Modern Electric, Hybrid Electric, and Fuel Cell Vehicles

Fundamentals, Theory, and Design

SECOND EDITION

Mehrdad Ehsani

Yimin Gao

Ali Emadi

CRC Press
Taylor & Francis Group

Modern Electric, Hybrid Electric, *and* Fuel Cell Vehicles

Fundamentals, Theory, and Design

SECOND EDITION

POWER ELECTRONICS AND APPLICATIONS SERIES

Muhammad H. Rashid, Series Editor
University of West Florida

PUBLISHED TITLES

Advanced DC/DC Converters
Fang Lin Luo and Hong Ye

Alternative Energy Systems: Design and Analysis with Induction Generators, Second Edition
M. Godoy Simões and Felix A. Farret

Complex Behavior of Switching Power Converters
Chi Kong Tse

DSP-Based Electromechanical Motion Control
Hamid A.Toliyat and Steven Campbell

Electric Energy: An Introduction, Second Edition
Mohamed A. El-Sharkawi

Electrical Machine Analysis Using Finite Elements
Nicola Bianchi

Fuel Cells: Modeling, Control, and Applications
Bei Gou, Woon Ki Na, and Bill Diong

Integrated Power Electronic Converters and Digital Control
Ali Emadi, Alireza Khaligh, Zhong Nie, and Young Joo Lee

Modern Electric, Hybrid Electric, and Fuel Cell Vehicles: Fundamentals, Theory, and Design, Second Edition
Mehrdad Ehsani, Yimin Gao, and Ali Emadi

Uninterruptible Power Supplies and Active Filters
Ali Emadi, Abdolhosein Nasiri, and Stoyan B. Bekiarov

Modern Electric, Hybrid Electric,

and

Fuel Cell Vehicles

Fundamentals, Theory, and Design

S E C O N D   E D I T I O N

Mehrdad Ehsani
Texas A&M University
College Station, Texas, U.S.A.

Yimin Gao
Texas A&M University
College Station, Texas, U.S.A.

Ali Emadi
Illinois Institute of Technology
Chicago, Illinois, U.S.A.

Contents

Preface

The development of internal combustion engine automobiles is one of the greatest achievements of modern technology. However, the highly developed automotive industry and the increasingly large number of automobiles in use around the world are causing serious problems for the environment and hydrocarbon resources. The deteriorating air quality, global warming issues, and depleting petroleum resources are becoming serious threats to modern life. Progressively more rigorous emissions and fuel efficiency standards are stimulating the aggressive development of safer, cleaner, and more efficient vehicles. It is now well recognized that electric, hybrid electric, and fuel-cell-powered drive train technologies are the most promising vehicle solutions for the foreseeable future.

To meet this challenge, an increasing number of engineering schools, in the United States and around the world, have initiated academic programs in advanced energy and vehicle technologies at the undergraduate and graduate levels. We started our first graduate course, in 1998, on "Advanced Vehicle Technologies—Design Methodology of Electric and Hybrid Electric Vehicles" for students in mechanical and electrical engineering at Texas A&M University. While preparing the lectures for this course, we found that although there is a wealth of information in the form of technical papers and reports, there was no rigorous and comprehensive textbook for students and professors who may wish to offer such a course. Furthermore, practicing engineers also needed a systematic reference book to fully understand the essentials of this new technology. The first edition of this book was our attempt to fill this need. The second edition introduces newer topics and deeper treatments than the first edition.

The book deals with the fundamentals, theoretical bases, and design methodologies of conventional internal combustion engine (ICE) vehicles, electric vehicles (EVs), hybrid electric vehicles (HEVs), and fuel cell vehicles (FCVs). It comprehensively covers vehicle performance characteristics, configurations, control strategies, design methodologies, modeling, and simulations for modern vehicles with mathematical rigor. It includes drive train architecture analysis, ICE-based drive trains, EV and HEV configurations, electric propulsion systems, series/parallel/mild hybrid electric drive train design methodologies, energy storage systems, regenerative braking, fuel cells and their applications in vehicles, and fuel cell hybrid electric drive train design. The book's perspective is from the overall drive train system and not just individual components. The design methodology is

described in mathematical terms, step by step. Furthermore, in explaining the design methodology of each drive train, design examples are presented with simulation results.

More specifically, the second edition contains many corrections and updates of the material in the first edition. Three new chapters and one appendix have been added. They are Chapter 9: Design and Control Methodology of Series–Parallel (Torque and Speed Coupling) Hybrid Drive Train; Chapter 10: Design and Control Principles of Plug-In Hybrid Electric Vehicles; Chapter 16: Design of Series Hybrid Drive Train for Off-Road Vehicles, and Appendix: Technical Overview of Toyota Prius. Chapter 13: Fundamentals of Regenerative Braking has been completely rewritten, based on our new research. In addition, plenty of new materials have been added to the old chapters. All these new contributions to the second edition make it more complete and useful to the reader.

This book consists of 16 chapters and one appendix. In Chapter 1, the social and environmental importances of modern transportation is discussed. This mainly includes the air pollution, global warming, and petroleum resource depletion issues associated with the development of modern transportation. In this chapter, the impact of future vehicle technologies on oil supplies is analyzed. The results are helpful for the development strategies of the next generation of vehicles. In addition, the development history of EVs, HEVs, and FCVs is briefly reviewed.

In Chapter 2, basic understandings of vehicle performance, power plant characteristics, transmission characteristics, and the equations used to describe vehicle performance are introduced. The main purpose of this chapter is to provide the basic knowledge that is necessary for vehicle drive train design. As an improvement to the first edition, material on the brake system and its design and performance has been strengthened in order to provide a more solid base for the hybrid brake system designs in EVs, HEVs, and FCVs.

In Chapter 3, major operating characteristics of different heat engines are introduced. As the primary power plant, the engine is the most important subsystem in conventional and hybrid drive train systems. Full understanding of the characteristics of engine is necessary for the design and control of conventional as well as HEVs.

In Chapter 4, EVs are introduced. This chapter mainly includes the design of the electric propulsion system and its energy storage device, the design of the traction motor and its transmission, methodology of prediction of vehicle performance, and system simulation results.

In Chapter 5, the basic concept of hybrid traction is established first. Then, various configurations of HEVs are discussed. These include series hybrid, parallel hybrid, torque-coupling and speed-coupling hybrids, and other configurations. The main operating characteristics of these configurations are also presented.

In Chapter 6, several electric power plants are introduced. These include DC, AC, permanent magnet brushless DC, and switched reluctance motor

drives. Their basic structure, operating principles, control and operational characteristics are described from a traction system point of view.

In Chapter 7, the design methodology of series hybrid electric drive trains is presented. This chapter focuses on the system-oriented design of the engine and the energy storage, the traction motor, the transmission, the control strategy, and the power converters. A design example is also provided. As an improvement to the first edition, various power converter configurations have been added.

In Chapter 8, a design methodology of parallel hybrid electric drive trains is provided. This chapter includes driving patterns and driving mode analysis; control strategy; design of the major components, for example, the engine, the energy storage, and the transmission; and vehicle performance simulation. In addition to the material covered in the first edition, a constrained engine on and off control strategy, fuzzy logic control strategy, and the concept of control optimization based on dynamic programming have been added.

In Chapter 9, the operating characteristics, design methodology, and control strategies of a series–parallel hybrid drive train are presented. This is a new chapter in the second edition.

In Chapter 10, the design and control principles of the plug-in hybrid vehicle are introduced. This chapter mainly addresses the charge sustaining hybrid drive train with regard to the drive train control strategy, energy storage design, and electric motor design. This is also a new chapter.

In Chapter 11, a design methodology of mild hybrid drive trains is introduced with two major configurations of parallel torque coupling and series–parallel, torque–speed coupling. This chapter focuses on operational analysis, control system development, and system simulation.

In Chapter 12, different energy storage technologies are introduced, including batteries, ultracapacitors, and flywheels. The discussion focuses on power and energy capacities. The concept of hybrid energy storage is also introduced in this chapter.

In Chapter 13, the design and control principles of hybrid brake systems are introduced. Brake safety and recoverable energy are the main concerns. The available braking energy characteristics, with regard to vehicle speed, and the braking power in typical driving cycles are investigated. The brake force distribution on the front and rear wheels is discussed for guaranteeing the vehicle braking performance for safety. Furthermore, this chapter discusses the important issue of distributing the total braking force between the mechanical and the electrical regenerative brakes. Two advanced hybrid brake systems, including their control strategies, are introduced. This chapter has been rewritten based on our recent research.

In Chapter 14, different fuel cell systems are described, with a focus on their operating principles and characteristics, various technologies, and their fuels. Specifically, vehicle applications of fuel cells are explained.

In Chapter 15, a systematic design of fuel cell hybrid drive trains is introduced. First, the concept of fuel cell hybrid vehicles is established. Then, their

operating principles and drive train control systems are analyzed. Lastly, a design methodology is provided, focusing on the system designs of the fuel cell, the electric propulsion system, and the energy storage system. A design example and its corresponding performance simulation results are provided.

In Chapter 16, a design methodology of an off-road tracked series hybrid vehicle is developed. The discussion focuses on the motion resistance calculation on soft grounds, traction motor system design, the engine/generator system design, and the peaking power source system design. This is a new chapter for the second edition.

A case study appendix has been added to the second edition. This is an overview of the Toyota Prius hybrid system. The purpose is to give the reader a practical example of the architecture, operational modes, control system, among other things, of a commercial hybrid electric drive train.

This book is suitable for a graduate or senior-level undergraduate course in advanced vehicles. Depending on the backgrounds of the students in different disciplines such as mechanical or electrical engineering, course instructors have the flexibility of choosing the specialized material to suit their lectures. This text has been used at Texas A&M University in a graduate-level course for many years. The manuscript of this text has been revised many times and over many years, based on the comments and feedback from the students in our course. We are grateful to our students for their help.

This book is also an in-depth resource and a comprehensive reference in modern automotive systems for engineers, students, researchers, and other professionals who are working in automotive-related industries, as well as those in government and academia.

In addition to the work by others, many of the technologies and advances presented in this book are the collection of many years of research and development by the authors and other members of the Advanced Vehicle Systems Research Program at Texas A&M University. We are grateful to all the dedicated staff of the Advanced Vehicle Systems Research group and the Power Electronics and Motor Drives group at Texas A&M, who made great contributions to this book.

We would also like to express our sincere thanks to Mr. Glenn C. Krell, whose proofreading and corrections have improved this text. In addition, we would like to acknowledge the efforts and assistance of the staff of CRC Press, LLC, especially Ms. Nora Konopka. Last but not least, we thank our families for their patience and support during the long effort in the writing of this book.

<div style="text-align:right">

Mehrdad Ehsani
Yimin Gao
Ali Emadi

</div>

Authors

Mehrdad Ehsani received his BS and MS from the University of Texas at Austin in 1973 and 1974, respectively, and his PhD from the University of Wisconsin–Madison in 1981, all in electrical engineering.

From 1974 to 1977 he was with the Fusion Research Center, University of Texas, as a research engineer. From 1977 to 1981 he was with the Argonne National Laboratory, Argonne, Illinois, as a resident research associate, while simultaneously doing the doctoral work at the University of Wisconsin–Madison in energy systems and control systems. Since 1981 Dr. Ehsani has been at Texas A&M University, College Station, where he is now a professor of electrical engineering and director of the Advanced Vehicle Systems Research Program and the Power Electronics and Motor Drives Laboratory. He is the recipient of the Prize Paper Awards in Static Power Converters and motor drives at the IEEE-Industry Applications Society 1985, 1987, and 1992 annual meetings, as well as numerous other honors and recognitions. In 1984, Dr. Ehsani was named the Outstanding Young Engineer of the Year by the Brazos chapter of the Texas Society of Professional Engineers. In 1992, he was named the Halliburton Professor in the College of Engineering at Texas A&M. In 1994, he was also named the Dresser Industries Professor in the same college. In 2001, he was selected as the Ruth & William Neely/Dow Chemical Faculty Fellow of the College of Engineering for 2001–2002, for "contributions to the Engineering Program at Texas A&M, including classroom instruction, scholarly activities, and professional service." In 2003, he received the BP Amoco Faculty Award for Teaching Excellence in the College of Engineering. He was awarded the IEEE Vehicular Society 2001 Avant Garde Award for "contributions to the theory and design of hybrid electric vehicles." In 2003, Dr. Ehsani was awarded the IEEE Undergraduate Teaching Award "for outstanding contributions to advanced curriculum development and teaching of power electronics and drives." In 2004, he was elected to the Robert M. Kennedy endowed Chair in Electrical Engineering at Texas A&M University. In 2005, he was elected as the Fellow of Society of Automotive Engineers. Dr. Ehsani is the author of over 300 publications in pulsed-power supplies, high-voltage engineering, power

electronics, motor drives, and advanced vehicle systems, and is the coauthor of 12 books on power electronics, motor drives, and advanced vehicle systems, including *Vehicular Electric Power Systems*, Marcel Dekker, Inc. 2003 and *Modern Electric Hybrid Vehicles and Fuel Cell Vehicles—Fundamentals, Theory, and Design*, CRC Press, 2004. He has over 23 granted or pending U.S. and EC patents. His current research work is in power electronics, motor drives, hybrid vehicles and their control systems.

Dr. Ehsani has been a member of the IEEE Power Electronics Society (PELS) AdCom, past chairman of the PELS Educational Affairs Committee, past chairman of the IEEE-IAS Industrial Power Converter Committee, and past chairman of the IEEE Myron Zucker Student–Faculty Grant program. He was the general chair of the IEEE Power Electronics Specialist Conference for 1990. He is the founder of the IEEE Power and Propulsion Conference, the founding chairman of the IEEE VTS Vehicle Power and Propulsion Committee, and chairman of the Convergence Fellowship Committees. In 2002, he was elected to the board of governors of VTS. He also serves on the editorial board of several technical journals and is the associate editor of *IEEE Transactions on Industrial Electronics* and *IEEE Transactions on Vehicular Technology*. He is a fellow of IEEE, an IEEE Industrial Electronics Society and Vehicular Technology Society Distinguished Speaker, and an IEEE Industry Applications Society and Power Engineering Society Distinguished Lecturer. He is also a registered professional engineer in the state of Texas.

Yimin Gao received his BS, MS, and PhD in mechanical engineering (major in development, design, and manufacturing of automotive systems) in 1982, 1986, and 1991, respectively, all from Jilin University of Technology, Changchun, Jilin, China. From 1982 to 1983, he worked as a vehicle design engineer for the DongFeng Motor Company, Shiyan, Hubei, China. He finished a layout design of a 5-ton truck (EQ144) and participated in prototyping and testing. From 1983 to 1986, he was a graduate student in the Automotive Engineering College of Jilin University of Technology, Changchun, Jilin, China. His working field was the improvement of vehicle fuel economy by optimal matching of engine and transmission.

From 1987 to 1992, he was a PhD student in the Automotive Engineering College of Jilin University of Technology, Changchun, Jilin, China. During this period, he worked on research and development of legged vehicles, which can potentially operate in harsh environments, where mobility is difficult for wheeled vehicles. From 1991 to 1995, Dr. Gao was an associate professor and automotive design engineer in the Automotive Engineering College of Jilin

University of Technology. During this period, he taught undergraduate students in a course entitled *Automotive Theory and Design* for several semesters and graduate students in a course entitled *Automotive Experiment Technique* for two semesters. Meanwhile, he also conducted vehicle performance, chassis, and components analyses, and conducted automotive design including chassis design, power train design, suspension design, steering system design, and brake design.

Dr. Gao joined the Advanced Vehicle Systems Research Program at Texas A&M University in 1995 as a research associate. Since then, he has been working in this program on research and development of electric and hybrid electric vehicles. His research areas are mainly on the fundamentals, architecture, control, modeling, and design of electric and hybrid electric drive trains and major components. He is a member of the Society of Automotive Engineers.

Ali Emadi received his BS and MS in Electrical Engineering with highest distinction from Sharif University of Technology, Tehran, Iran. He also received his PhD in Electrical Engineering from Texas A&M University, College Station, Texas. He is currently the Harris Perlstein Endowed chair professor of Electrical Engineering and the director of the Electric Power and Power Electronics Center and Grainger Laboratories at Illinois Institute of Technology (IIT) in Chicago, where he has established research and teaching facilities as well as courses in power electronics, motor drives, and vehicular power systems. In addition, Dr. Emadi is the founder, president, and chief technology officer of Hybrid Electric Vehicle Technologies, Inc. (HEVT)—a university spin-off company of IIT.

Dr. Emadi is the recipient of numerous awards and recognitions. He has been named a Chicago Matters Global Visionary in 2009. He was named the Eta Kappa Nu Outstanding Young Electrical Engineer of the Year 2003 (single international award) by virtue of his outstanding contributions to hybrid electric vehicle conversion by the Electrical Engineering Honor Society. He also received the 2005 Richard M. Bass Outstanding Young Power Electronics Engineer Award from the IEEE Power Electronics Society. In 2005, he was selected as the Best Professor of the Year by the students at IIT. Dr. Emadi is the recipient of the 2002 University Excellence in Teaching Award from IIT as well as the 2004 Sigma Xi/IIT Award for Excellence in University Research. He directed a team of students to design and build a novel motor drive, which won the First Place Overall Award of the 2003 IEEE/DOE/DOD International Future Energy Challenge for Motor Competition.

Dr. Emadi is the principal author and coauthor of over 250 journals and conference papers as well as several books including *Vehicular Electric Power Systems: Land, Sea, Air, and Space Vehicles*, Marcel Dekker, 2003; *Energy Efficient Electric Motors*, Marcel Dekker, 2004; *Uninterruptible Power Supplies and Active Filters*, CRC Press, 2004; *Modern Electric, Hybrid Electric, and Fuel Cell Vehicles: Fundamentals, Theory, and Design*, CRC Press, 2004; and *Integrated Power Electronic Converters and Digital Control*, CRC Press, 2009. Dr. Emadi is also the editor of the *Handbook of Automotive Power Electronics and Motor Drives*, Marcel Dekker, 2005.

Dr. Emadi was the founding general chair of the 1st IEEE Vehicle Power and Propulsion Conference (VPPC'05), which was colocated under his chairmanship with the SAE International Future Transportation Technology Conference. He is currently the chair of the IEEE Vehicle Power and Propulsion Steering Committee, chair of the Technical Committee on Transportation Power Electronics of the IEEE Power Electronics Society, and Chair of the Power Electronics Technical Committee of the IEEE Industrial Electronics Society. He has also served as the Chair of the 2007 IEEE International Future Energy Challenge.

Dr. Emadi is the editor (North America) of the *International Journal of Electric and Hybrid Vehicles*. He has been the guest editor-in-chief of the Special Issue on Automotive Power Electronics and Motor Drives, *IEEE Transactions on Power Electronics*. He has also been the guest editor of the Special Section on Hybrid Electric and Fuel Cell Vehicles, *IEEE Transactions on Vehicular Technology* and guest editor of the Special Section on Automotive Electronics and Electrical Drives, *IEEE Transactions on Industrial Electronics*. He has served as an associate editor of the *IEEE Transactions on Vehicular Technology*, *IEEE Transactions on Power Electronics*, and *IEEE Transactions on Industrial Electronics*.

1

Environmental Impact and History of Modern Transportation

The development of internal combustion (IC) engine vehicles, and especially automobiles, is one of the greatest achievements of modern technology. Automobiles have made great contributions to the growth of modern society by satisfying many of the needs for mobility in everyday life. The rapid development of the automotive industry, unlike that of any other industry, has prompted the progress of human beings from a primitive security to a highly developed industrial one. The automobile industry and the other industries that serve it constitute the backbone of the world's economy and employ the greatest share of the working population.

However, the large number of automobiles in use around the world has caused and continues to cause serious problems for environment and human life. Air pollution, global warming, and the rapid depletion of the Earth's petroleum resources are now problems of paramount concern.

In recent decades, the research and development activities related to transportation have emphasized the development of high-efficiency, clean, and safe transportation. Electric vehicles (EVs), hybrid electric vehicles (HEVs), and fuel cell vehicles have been typically proposed to replace conventional vehicles in the near future.

This chapter reviews the problems of air pollution, gas emissions causing global warming, and petroleum resource depletion. It also gives a brief review of the history of EVs, HEVs, and fuel cell technology.

1.1 Air Pollution

At present, all vehicles rely on the combustion of hydrocarbon (HC) fuels to derive the energy necessary for their propulsion. Combustion is a reaction between the fuel and the air that releases heat and combustion products. The heat is converted to mechanical power by an engine and the combustion

products are released to the atmosphere. An HC is a chemical compound with molecules made up of carbon and hydrogen atoms. Ideally, the combustion of an HC yields only carbon dioxide and water, which do not harm the environment. Indeed, green plants "digest" carbon dioxide by photosynthesis. Carbon dioxide is a necessary ingredient in vegetal life. Animals do not suffer from breathing carbon dioxide unless its concentration in air is such that oxygen is almost absent.

Actually, the combustion of HC fuel in combustion engines is never ideal. Besides carbon dioxide and water, the combustion products contain a certain amount of nitrogen oxides (NO_x), carbon monoxides (CO), and unburned HCs, all of which are toxic to human health.

1.1.1   Nitrogen Oxides

Nitrogen oxides (NO_x) result from the reaction between nitrogen in the air and oxygen. Theoretically, nitrogen is an inert gas. However, the high temperatures and pressures in engines create favorable conditions for the formation of nitrogen oxides. Temperature is by far the most important parameter in nitrogen oxide formation. The most commonly found nitrogen oxide is nitric oxide (NO), although small amounts of nitric dioxide (NO_2) and traces of nitrous oxide (N_2O) are present. Once released into the atmosphere, NO reacts with the oxygen to form NO_2. This is later decomposed by the Sun's ultraviolet radiation back to NO and highly reactive oxygen atoms that attack the membranes of living cells. Nitrogen dioxide is partly responsible for smog; its brownish color makes smog visible. It also reacts with atmospheric water to form nitric acid (HNO_3), which dilutes in rain. This phenomenon is referred to as "acid rain" and is responsible for the destruction of forests in industrialized countries.[1] Acid rain also contributes to the degradation of historical monuments made of marble.[1]

1.1.2   Carbon Monoxide

Carbon monoxide results from the incomplete combustion of HCs due to a lack of oxygen.[1] It is a poison to human beings and animals who inhale/breathe it. Once carbon monoxide reaches the blood cells, it fixes to the hemoglobin in place of oxygen, thus diminishing the quantity of oxygen that reaches the organs and reducing the physical and mental abilities of affected living beings.[1] Dizziness is the first symptom of carbon monoxide poisoning, which can rapidly lead to death. Carbon monoxide binds more strongly to hemoglobin than oxygen. The bonds are so strong that normal body functions cannot break them. People intoxicated by carbon monoxide must be treated in pressurized chambers, where the pressure makes it easier to break the carbon monoxide–hemoglobin bonds.

1.1.3 Unburned HCs

Unburned HCs are a result of the incomplete combustion of HCs.[1,2] Depending on their nature, unburned HCs may be harmful to living beings.[2] Some of these unburned HCs may be direct poisons or carcinogenic chemicals such as particulates, benzene, or others. Unburned HCs are also responsible for smog: the Sun's ultraviolet radiations interact with the unburned HCs and NO in the atmosphere to form ozone and other products. Ozone is a molecule formed of three oxygen atoms. It is colorless but very dangerous, and is poisonous because as it attacks the membranes of living cells, causing them to age prematurely or die. Toddlers, older people, and asthmatics suffer greatly from exposure to high ozone concentrations. Annually, deaths from high ozone peaks in polluted cities have been reported.[3]

1.1.4 Other Pollutants

Impurities in fuels result in the emission of pollutants. The major impurity is sulfur: mostly found in diesel and jet fuel, but also in gasoline and natural gas.[1] The combustion of sulfur (or sulfur compounds such as hydrogen sulfide) with oxygen releases sulfur oxides (SO_x). Sulfur dioxide (SO_2) is the major product of this combustion. On contact with air, it forms sulfur trioxide, which later reacts with water to form sulfuric acid, a major component of acid rain. It should be noted that sulfur oxide emissions originate from transportation sources but also largely from the combustion of coal in power plants and steel factories. In addition, there is debate over the exact contribution of natural sources such as volcanoes.

   Petroleum companies add chemical compounds to their fuels in order to improve the performance or lifetime of engines.[1] Tetraethyl lead, often referred to simply as "lead," was used to improve the knock resistance of gasoline and therefore allow better engine performance. However, the combustion of this chemical releases lead metal, which is responsible for a neurological disease called "saturnism." Its use is now forbidden in most developed countries and it has been replaced by other chemicals.[1]

1.2 Global Warming

Global warming is a result of the "greenhouse effect" induced by the presence of carbon dioxide and other gases, such as methane, in the atmosphere. These gases trap the Sun's infrared radiation reflected by the ground, thus retaining the energy in the atmosphere and increasing the temperature. An increased Earth temperature results in major ecological damages to its ecosystems and in many natural disasters that affect human populations.[2]
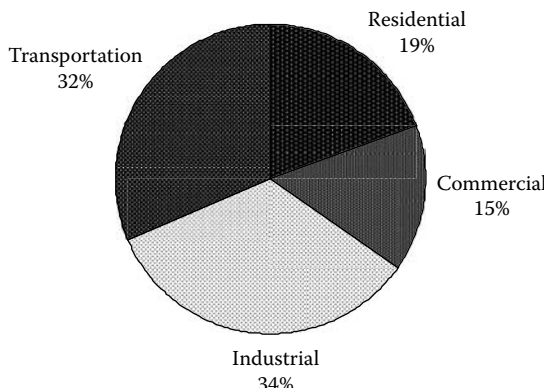
Considering the ecological damages induced by global warming, the disappearance of some endangered species is a concern because this destabilizes the natural resources that feed some populations. There are also concerns about the migration of some species from warm seas to previously colder northern seas, where they can potentially destroy indigenous species and the economies that live off those species. This may be happening in the Mediterranean Sea, where barracudas from the Red Sea have been observed.

Natural disasters command our attention more than ecological disasters because of the amplitude of the damages they cause. Global warming is believed to have induced meteorological phenomena such as "El Niño," which disturbs the South Pacific region and regularly causes tornadoes, inundations, and dryness. The melting of the polar icecaps, another major result of global warming, raises the sea level and can cause the permanent inundation of coastal regions and sometimes of entire countries.
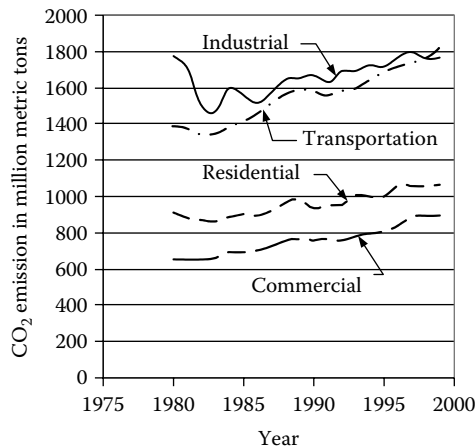
Carbon dioxide is the result of the combustion of HCs and coal. Transportation accounts for a large share (32% from 1980 to 1999) of carbon dioxide emissions. The distribution of carbon dioxide emissions is shown in Figure 1.1.[4]

Figure 1.2 shows the trend in carbon dioxide emissions. The transportation sector is clearly now the major contributor to carbon dioxide emissions. It should be noted that developing countries are rapidly increasing their transportation sector, and these countries represent a very large share of the world population. Further discussion is provided in the next subsection.
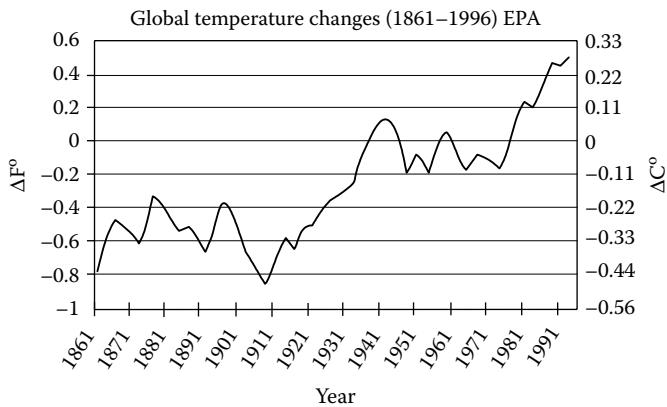
The large amounts of carbon dioxide released into the atmosphere by human activities are believed to be largely responsible for the increase in the global Earth temperature observed during the last decades (Figure 1.3). It is important to note that carbon dioxide is indeed digested by plants and sequestrated by oceans in the form of carbonates. However, these natural

FIGURE 1.1   Carbon dioxide emission distribution from 1980 to 1999.

FIGURE 1.2 Evolution of CO_2 emission.

FIGURE 1.3 Global Earth atmospheric temperature. (*Source:* IPCC (1995) updated.)

assimilation processes are limited and cannot assimilate all of the emitted carbon dioxide, resulting in an accumulation of carbon dioxide in the atmosphere.

1.3 Petroleum Resources

The vast majority of fuels for transportation are liquid fuels originating from petroleum. Petroleum is a fossil fuel, resulting from the decomposition of living matters that were imprisoned millions of years ago (Ordovician,

600–400 million years ago) in geologically stable layers. The process is roughly the following: living matters (mostly plants) die and are slowly covered by sediments. Over time, these accumulating sediments form thick layers and transform to rock. The living matters are trapped in a closed space, where they encounter high pressures and temperatures and slowly transform into either HCs or coal, depending on their nature. This process takes millions of years to accomplish. This is what makes the Earth's resources in fossil fuels finite.

Proved reserves are "those quantities that geological and engineering information indicates with reasonable certainty can be recovered in the future from known reservoirs under existing economic and operating conditions."[5] Therefore, they do not constitute an indicator of the Earth's total reserves. The proved reserves, as they are given in the British Petroleum 2001 estimate,[5] are given in billion tons in Table 1.1. The R/P ratio is the number of years that the proved reserves would last if the production were to continue at its current level. This ratio is also given in Table 1.1 for each region.[5]

The oil extracted nowadays is the easily extractable oil that lies close to the surface, in regions where the climate does not pose major problems. It is believed that far more oil lies underneath the Earth's crust in regions such as Siberia, or the American and Canadian Arctic. In these regions, the climate and ecological concerns are major obstacles to extracting or prospecting for oil. The estimation of the total Earth's reserves is a difficult task for political and technical reasons. A 2000 estimation of the undiscovered oil resources by the US Geological Survey is given in Table 1.2.[6]

Although the R/P ratio does not include future discoveries, it is significant. Indeed, it is based on proved reserves, which are easily accessible to this day. The amount of future oil discoveries is hypothetical, and the newly discovered oil will not be easily accessible. The R/P ratio is also based on the hypothesis that the production will remain constant. It is obvious, however, that consumption (and therefore production) is increasing yearly to keep up with the growth of developed and developing economies. Consumption is likely to increase in gigantic proportions with the rapid development of some

TABLE 1.1

Proved Petroleum Reserves in 2000

Region	Proved Reserves in 2000 in Billion Tons	R/P Ratio
North America	8.5	13.8
South and Central America	13.6	39
Europe	2.5	7.7
Africa	10	26.8
Middle East	92.5	83.6
Former USSR	9.0	22.7
Asia Pacific	6.0	15.9
Total world	142.1	39.9
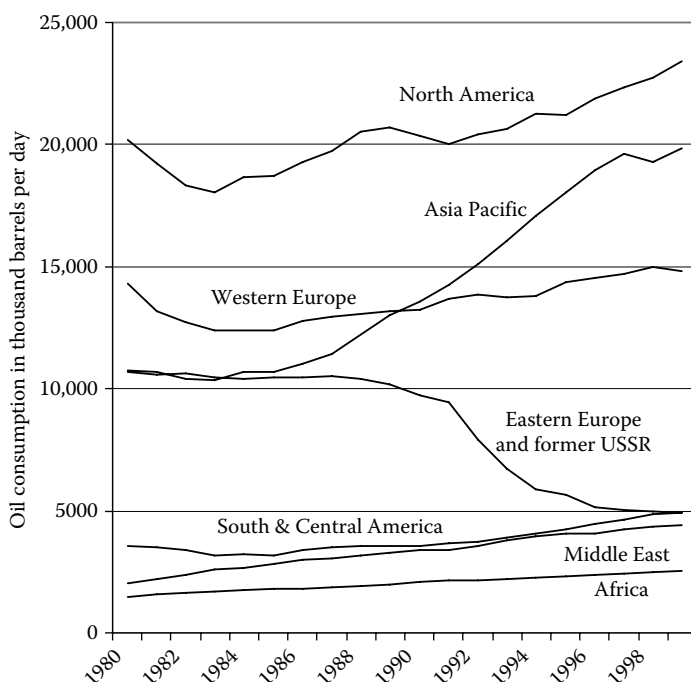
TABLE 1.2
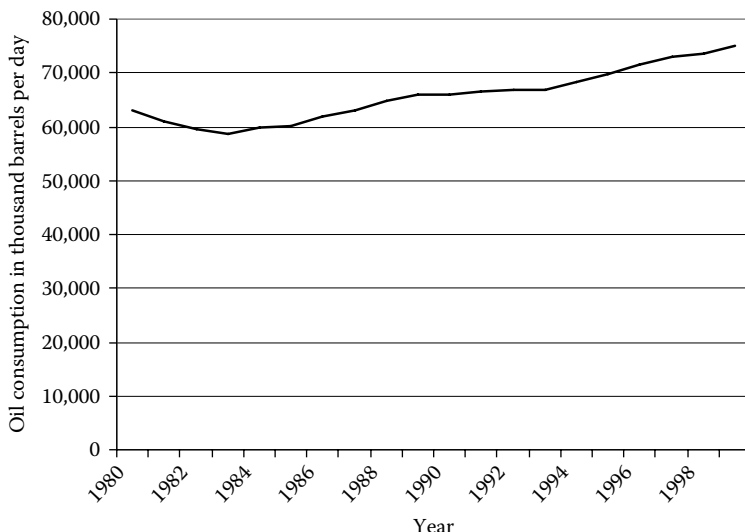
U.S. Geological Survey Estimate of Undiscovered Oil in 2000

Region	Undiscovered Oil in 2000 in Billion Tons
North America	19.8
South and Central America	14.9
Europe	3.0
Sub-Saharan Africa and Antarctic	9.7
Middle East and North Africa	31.2
Former USSR	15.7
Asia Pacific	4.0
World (potential growth)	98.3 (91.5)

largely populated countries, particularly in the Asia-Pacific region. Figure 1.4 shows the trend in oil consumption over the last 20 years.[7] Oil consumption is given in thousand barrels per day (one barrel is about 8 metric tons).

Despite the drop in oil consumption for Eastern Europe and the former USSR, the world trend is clearly increasing, as shown in Figure 1.5. The fastest-growing region is Asia Pacific, where most of the world's population lives. An

FIGURE 1.4   Oil consumption per region.

FIGURE 1.5   World oil consumption.

explosion in oil consumption is to be expected, with a proportional increase in pollutant emissions and CO_2 emissions.

1.4 Induced Costs

The problems associated with the frenetic combustion of fossil fuels are many: pollution, global warming, and foreseeable exhaustion of resources, among others. Although difficult to estimate, the costs associated with these problems are huge and indirect,[8] and may be financial, human, or both.

Costs induced by pollution include, but are not limited to, health expenses, the cost of replanting forests devastated by acid rain, and the cost of cleaning and fixing monuments corroded by acid rain. Health expenses probably represent the largest share of these costs, especially in developed countries with socialized medicine or health-insured populations.

Costs associated with global warming are difficult to assess. They may include the cost of the damages caused by hurricanes, lost crops due to dryness, damaged properties due to floods, and international aid to relieve the affected populations. The amount is potentially huge.

Most of the petroleum-producing countries are not the largest petroleum-consuming countries. Most of the production is located in the Middle East, while most of the consumption is located in Europe, North America, and Asia Pacific. As a result, consumers have to import their oil and depend on the producing countries. This issue is particularly sensitive in the Middle

East, where political turmoil affected the oil delivery to Western countries in 1973 and 1977. The Gulf War, the Iran–Iraq war, and the constant surveillance of the area by the United States and allied forces come at a cost that is both human and financial. The dependency of Western economies on a fluctuating oil supply is potentially expensive. Indeed, a shortage in oil supply causes a serious slowdown of the economy, resulting in damaged perishable goods, lost business opportunities, and the eventual impossibility to run businesses.

In searching for a solution to the problems associated with oil consumption, one has to take into account those induced costs. This is difficult because the cost is not necessarily asserted where it is generated. Many of the induced costs cannot be counted in asserting the benefits of an eventual solution. The solution to these problems will have to be economically sustainable and commercially viable without government subsidies in order to sustain itself in the long run. Nevertheless, it remains clear that any solution to these problems—even if it is only a partial solution—will indeed result in cost savings, which will benefit the payers.

1.5 Importance of Different Transportation Development Strategies to Future Oil Supply

The number of years that oil resources of the Earth can support our oil supply completely depends on the new discovery of oil reserves and cumulative oil production (as well as cumulative oil consumption). Historical data show that the new discovery of oil reserves grows slowly. On the other hand, the consumption shows a high growth rate, as shown in Figure 1.6. If oil discovery and consumption follow the current trends, the world oil resource will be used up by about 2038.[9,10]

It is becoming more and more difficult to discover new reserves of petroleum in the Earth. The cost of exploring new oil fields is becoming higher and higher. It is believed that the scenario of oil supply will not change much if the consumption rate cannot be significantly reduced.

As shown in Figure 1.7, the transportation sector is the primary user of petroleum, consuming 49% of the oil used in the world in 1997. The patterns of consumption of industrialized and developing countries are quite different, however. In the heat and power segments of the markets in industrialized countries, nonpetroleum energy sources were able to compete with and substitute for oil throughout the 1980s; by 1990, the oil consumption in other sectors was less than that in the transportation sector.

Most of the gains in worldwide oil use occur in the transportation sector. Of the total increase (11.4 million barrels per day) projected for industrialized countries from 1997 to 2020, 10.7 million barrels per day are attributed to the
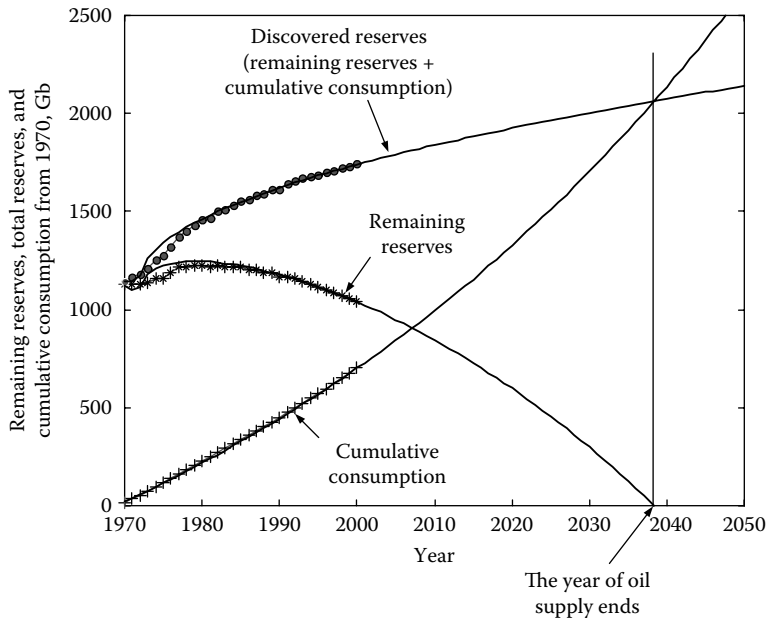
FIGURE 1.6   World oil discovery, remaining reserves, and cumulative consumption.
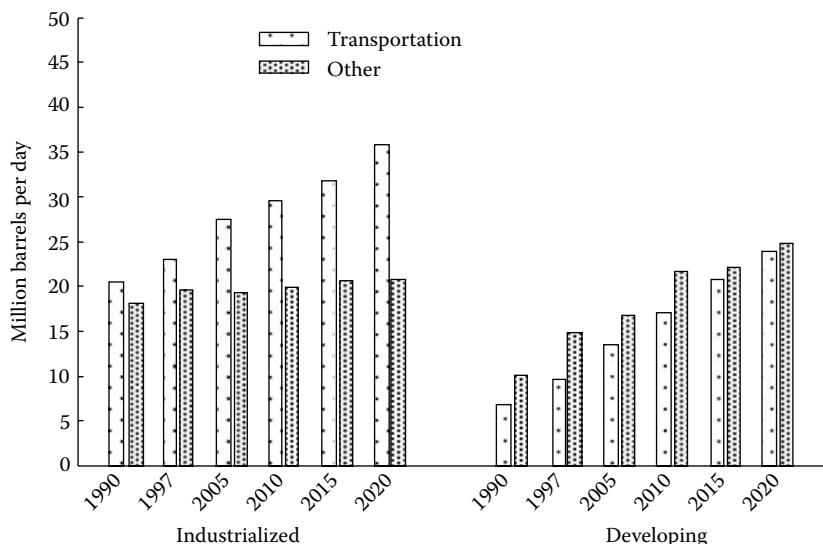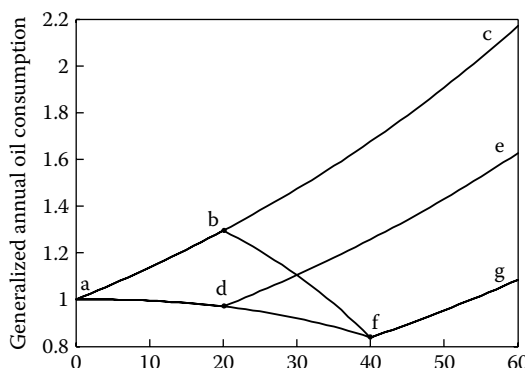
FIGURE 1.7   World oil consumption in transportation and others.

transportation sector, where few alternatives are economical until late in the forecast.
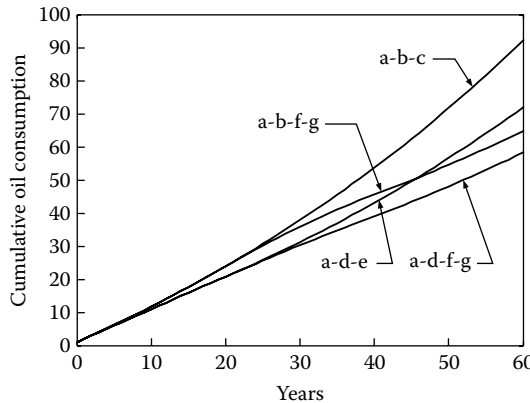
In developing countries, the transportation sector also shows the fastest projected growth in petroleum consumption, promising to rise nearly to the level of nontransportation energy use by 2020. In the developing world however, unlike in industrialized countries, oil use for purposes other than transportation is projected to contribute 42% of the total increase in petroleum consumption. The growth in nontransportation petroleum consumption in developing countries is caused in part by the substitution of petroleum products for noncommercial fuels (such as wood burning for home heating and cooking).

Improving the fuel economy of vehicles has a crucial impact on oil supply. So far, the most promising technologies are HEVs and fuel cell vehicles. Hybrid vehicles, using current IC engines as their primary power source and batteries/electric motor as the peaking power source, have a much higher operation efficiency than those powered by IC engine alone. The hardware and software of this technology are almost ready for industrial manufacturing. On the other hand, fuel cell vehicles, which are potentially more efficient and cleaner than HEVs, are still in the laboratory stage and it will take a long time to overcome technical hurdles for commercialization.

Figure 1.8 shows the generalized annual fuel consumptions of different development strategies of next-generation vehicles. Curve a–b–c represents the annual fuel consumption trend of current vehicles, which is assumed to have a 1.3% annual growth rate. This annual growth rate is assumed to be the annual growth rate of the total vehicle number. Curve a–d–e represents a development strategy in which conventional vehicles gradually become hybrid vehicles during the first 20 years, and after 20 years all the vehicles will be hybrid vehicles. In this strategy, it is assumed that the hybrid vehicle is 25% more efficient than a current conventional vehicle (25% less fuel consumption). Curve a–b–f–g represents a strategy in which, in the first 20 years,

FIGURE 1.8 Comparison of the annual fuel consumption between different development strategies of the next-generation vehicles.

FIGURE 1.9   Comparison of the cumulative fuel consumption between different development strategies of the next-generation vehicles.

fuel cell vehicles are in a developing stage while current conventional vehicles are still on the market. In the second 20 years, the fuel cell vehicles will gradually go to market, starting from point b and becoming totally fuel cell powered at point f. In this strategy, it is assumed that 50% less fuel will be consumed by fuel cell vehicles than by current conventional vehicles. Curve a–d–f–g represents the strategy that the vehicles become hybrid in the first 20 years and fuel cell powered in the second 20 years.

Cumulative oil consumption is more meaningful because it involves annual consumption and the time effect, and is directly associated with the reduction of oil reserves as shown in Figure 1.6. Figure 1.9 shows the scenario of generalized cumulative oil consumptions of the development strategies mentioned above. Although fuel cell vehicles are more efficient than hybrid vehicles, the cumulative fuel consumption by strategy a–b–f–g (a fuel cell vehicle in the second 20 years) is higher than the strategy a–d–e (a hybrid vehicle in the first 20 years) within 45 years, due to the time effect. From Figure 1.8, it is clear that strategy a–d–f–g (a hybrid vehicle in the first 20 years and a fuel cell vehicle in the second 20 years) is the best. Figures 1.6 and 1.9 reveal another important fact: that fuel cell vehicles should not rely on oil products because of the difficulty of future oil supply 45 years later. Thus, the best development strategy of next-generation transportation would be to commercialize HEVs immediately, and at the same time do the best to commercialize nonpetroleum fuel cell vehicles as soon as possible.

1.6   History of EVs

The first EV was built by Frenchman Gustave Trouvé in 1881. It was a tricycle powered by a 0.1 hp DC motor fed by lead-acid batteries. The whole vehicle

and its driver weighed approximately 160 kg. A vehicle similar to this was built in 1883 by two British professors.[11] These early realizations did not attract much attention from the public because the technology was not mature enough to compete with horse carriages. Speeds of 15 km/h and a range of 16 km were nothing exciting for potential customers. The 1864 Paris to Rouen race changed it all: the 1135 km were run in 48 h and 53 min at an average speed of 23.3 km/h. This speed was by far superior to that possible with horse-drawn carriages. The general public became interested in horseless carriages or automobiles as these vehicles were now called.

The following 20 years were an era during which EVs competed with their gasoline counterparts. This was particularly true in America, where there were not many paved roads outside a few cities. The limited range of EVs was not a problem. However, in Europe, the rapidly increasing number of paved roads called for extended ranges, thus favoring gasoline vehicles.[11]

The first commercial EV was the Morris and Salom's Electroboat. This vehicle was operated as a taxi in New York City by a company created by its inventors. The Electroboat proved to be more profitable than horse cabs despite a higher purchase price (around $3000 vs. $1200). It could be used for three shifts of 4 h with 90-min recharging periods in between. It was powered by two 1.5 hp motors that allowed a maximum speed of 32 km/h and a 40 km range.[11]

The most significant technical advance of that era was the invention of regenerative braking by Frenchman M. A. Darracq on his 1897 coupe. This method allows recuperating the vehicle's kinetic energy while braking and recharging the batteries, which greatly enhances the driving range. It is one of the most significant contributions to electric and HEV technology as it contributes to energy efficiency more than anything else in urban driving.

In addition, among the most significant EVs of that era was the first vehicle ever to reach 100 km. It was "La Jamais Contente" built by Frenchman Camille Jenatzy. Note that Studebaker and Oldsmobile got started in business by building EVs.

As gasoline automobiles became more powerful, more flexible, and above all easier to handle, EVs started to disappear. Their high cost did not help, but it is their limited driving range and performance that really impaired them versus their gasoline counterparts. The last commercially significant EVs were released around 1905. During nearly 60 years, the only EVs sold were common golf carts and delivery vehicles.

In 1945, three researchers at Bell Laboratories invented a device that was meant to revolutionize the world of electronics and electricity: the transistor. It quickly replaced vacuum tubes for signal electronics and soon the thyristor was invented, which allowed switching high currents at high voltages. This made it possible to regulate the power fed to an electric motor without the very inefficient rheostats and allowed the running of AC motors at variable frequency. In 1966, General Motors (GM) built the Electrovan, which was propelled by induction motors that were fed by inverters built with thyristors.

The most significant EV of that era was the Lunar Roving Vehicle, which the Apollo astronauts used on the Moon. The vehicle itself weighed 209 kg

and could carry a payload of 490 kg. The range was around 65 km. The design of this extraterrestrial vehicle, however, has very little significance down on Earth. The absence of air and the lower gravity on the Moon, and the low speed made it easier for engineers to reach an extended range with a limited technology.

During the 1960s and 1970s, concerns about the environment triggered some research on EVs. However, despite advances in battery technology and power electronics, their range and performance were still obstacles.

The modern EV era culminated during the 1980s and early 1990s with the release of a few realistic vehicles by firms such as GM with the EV1 and Peugeot Société Anonyme (PSA) with the 106 Electric. Although these vehicles represented a real achievement, especially when compared with early realizations, it became clear during the early 1990s that electric automobiles could never compete with gasoline automobiles for range and performance. The reason is that in batteries the energy is stored in the metal of the electrodes, which weigh far more than gasoline for the same energy content. The automotive industry abandoned the EV to conduct research on hybrid electric vehicles. After a few years of development, these are far closer to the assembly line for mass production than EVs have ever been.

In the context of the development of EVs, it is the battery technology that is the weakest, blocking the way of EVs to the market. Great effort and investment have been put into battery research, with the intention of improving performance to meet the EV requirement. Unfortunately, progress has been very limited. Performance is far behind the requirement, especially energy storage capacity per unit weight and volume. This poor energy storage capability of batteries limits EVs to only some specific applications, such as at airports, railroad stations, mail delivery routes, golf courses, and so on. In fact, basic study[12] shows that the EV will never be able to challenge the liquid-fueled vehicle even with the optimistic value of battery energy capacity. Thus, in recent years, advanced vehicle technology research has turned to HEVs as well as fuel cell vehicles.

1.7 History of HEVs

Surprisingly, the concept of a HEV is almost as old as the automobile itself. The primary purpose, however, was not so much to lower the fuel consumption but rather to assist the IC engine to provide an acceptable level of performance. Indeed, in the early days, IC engine engineering was less advanced than electric motor engineering.

The first hybrid vehicles reported were shown at the Paris Salon of 1899.[13] These were built by the Pieper establishments of Liège, Belgium and by the Vendovelli and Priestly Electric Carriage Company, France. The Pieper vehicle was a parallel hybrid with a small air-cooled gasoline engine assisted

by an electric motor and lead-acid batteries. It is reported that the batteries were charged by the engine when the vehicle coasted or was at a standstill. When the driving power required was greater than the engine rating, the electric motor provided additional power. In addition to being one of the two first hybrid vehicles, and the first parallel hybrid vehicle, the Pieper was undoubtedly the first electric starter.

The other hybrid vehicle introduced at the Paris Salon of 1899 was the first series HEV and was derived from a pure EV commercially built by the French firm Vendovelli and Priestly.[13] This vehicle was a tricycle, with the two rear wheels powered by independent motors. An additional 3/4 hp gasoline engine coupled to a 1.1 kW generator was mounted on a trailer and could be towed behind the vehicle to extend the range by recharging the batteries. In the French case, the hybrid design was used to extend its range by recharging the batteries. Also, the hybrid design was used to extend the range of an EV and not to supply additional power to a weak IC engine

Frenchman Camille Jenatzy presented a parallel hybrid vehicle at the Paris Salon of 1903. This vehicle combined a 6 hp gasoline engine with a 14 hp electric machine that could either charge the batteries from the engine or assist them later. Another Frenchman, H. Krieger, built the second reported series hybrid vehicle in 1902. His design used two independent DC motors driving the front wheels. They drew their energy from 44 lead-acid cells that were recharged by a 4.5 hp alcohol spark-ignited engine coupled to a shunt DC generator.

Other hybrid vehicles, both of the parallel and series type, were built during a period ranging from 1899 until 1914. Although electric braking has been used in these early designs, there is no mention of regenerative braking. It is likely that most, possibly even all, designs used dynamic braking by short circuiting or by placing a resistance in the armature of the traction motors. The Lohner-Porsche vehicle of 1903 is a typical example of this approach.[13] The frequent use of magnetic clutches and magnetic couplings should be noted.

Early hybrid vehicles were built in order to assist the weak IC engines of that time or to improve the range of EVs. They made use of the basic electric technologies that were then available. In spite of the great creativity that featured in their design, these early hybrid vehicles could no longer compete with the greatly improved gasoline engines that came into use after World War I. The gasoline engine made tremendous improvements in terms of power density, the engines became smaller and more efficient, and there was no longer a need to assist them with electric motors. The supplementary cost of having an electric motor and the hazards associated with the lead-acid batteries were key factors in the disappearance of hybrid vehicles from the market after World War I.

However, the greatest problem that these early designs had to cope with was the difficulty of controlling the electric machine. Power electronics did not become available until the mid-1960s and early electric motors were controlled by mechanical switches and resistors. They had a limited operating

range incompatible with efficient operation. Only with great difficulty could they be made compatible with the operation of a hybrid vehicle.

Dr. Victor Wouk is recognized as the modern investigator of the HEV movement.[13] In 1975, along with his colleagues, he built a parallel hybrid version of a Buick Skylark.[13] The engine was a Mazda rotary engine, coupled to a manual transmission. It was assisted by a 15 hp separately excited DC machine, located in front of the transmission. Eight 12 V automotive batteries were used for energy storage. A top speed of 80 mph (129 km/h) was achieved with acceleration from 0 to 60 mph in 16 s.

The series hybrid design was revived by Dr. Ernest H. Wakefield in 1967, when working for Linear Alpha Inc. A small engine coupled to an AC generator, with an output of 3 kW, was used to keep a battery pack charged. However, the experiments were quickly stopped because of technical problems. Other approaches studied during the 1970s and early 1980s used range extenders, similar in concept to the French Vendovelli and Priestly 1899 design. These range extenders were intended to improve the range of EVs that never reached the market. Other prototypes of hybrid vehicles were built by the Electric Auto Corporation in 1982 and by the Briggs & Stratton Corporation in 1980. These were both parallel hybrid vehicles.

Despite the two oil crises of 1973 and 1977, and despite growing environmental concerns, no HEV made it to the market. The researchers' focus was drawn by the EV, of which many prototypes were built during the 1980s. The lack of interest in HEVs during this period may be attributed to the lack of practical power electronics, modern electric motor, and battery technologies. The 1980s witnessed a reduction in conventional IC engine-powered vehicle sizes, the introduction of catalytic converters, and the generalization of fuel injection.

The HEV concept drew great interest during the 1990s when it became clear that EVs would never achieve the objective of saving energy. The Ford Motor Corporation initiated the Ford Hybrid Electric Vehicle Challenge, which drew efforts from universities to develop hybrid versions of production automobiles.

Automobile manufacturers around the world built prototypes that achieved tremendous improvements in fuel economy over their IC engine-powered counterparts. In the United States, Dodge built the Intrepid ESX 1, 2, and 3. The ESX-1 was a series hybrid vehicle, powered by a small turbocharged three-cylinder diesel engine and a battery pack. Two 100 hp electric motors were located in the rear wheels. The U.S. government launched the Partnership for a New Generation of Vehicles (PNGV), which included the goal of a mid-size sedan that could achieve 80 mpg. The Ford Prodigy and GM Precept resulted from this effort. The Prodigy and Precept vehicles were parallel HEVs powered by small turbocharged diesel engines coupled to dry clutch manual transmissions. Both of them achieved the objective but production did not follow.

Efforts in Europe are represented by the French Renault Next, a small parallel hybrid vehicle using a 750 cc spark-ignited engine and two electric motors.

This prototype achieved 29.4 km/L (70 mpg) with maximum speed and acceleration performance comparable to conventional vehicles. Volkswagen also built a prototype, the Chico. The base was a small EV, with a nickel-metal hydride battery pack and a three-phase induction motor. A small two-cylinder gasoline engine was used to recharge the batteries and provide additional power for high-speed cruising.

The most significant effort in the development and commercialization of HEVs was made by Japanese manufacturers. In 1997, Toyota released the Prius sedan in Japan. Honda also released its Insight and Civic Hybrid. These vehicles are now available throughout the world. They achieve excellent figures of fuel consumption. Toyota's Prius and Honda's Insight vehicles have historical value in that they are the first hybrid vehicles commercialized in the modern era to respond to the problem of personal vehicle fuel consumption.

1.8   History of Fuel Cell Vehicles

As early as 1839, Sir William Grove (often referred to as the "Father of the Fuel Cell") discovered that it may be possible to generate electricity by reversing the electrolysis of water. It was not until 1889 that two researchers, Charles Langer and Ludwig Mond, coined the term "fuel cell" as they were trying to engineer the first practical fuel cell using air and coal gas. Although further attempts were made in the early 1900s to develop fuel cells that could convert coal or carbon into electricity, the advent of IC engine temporarily quashed any hopes of further development of the fledgling technology.

Francis Bacon developed what was perhaps the first successful fuel cell device in 1932, with a hydrogen–oxygen cell using alkaline electrolytes and nickel electrodes—inexpensive alternatives to the catalysts used by Mond and Langer. Due to a substantial number of technical hurdles, it was not until 1959 that Bacon and company first demonstrated a practical 5-kW fuel cell system. Harry Karl Ihrig presented his now-famous 20-hp fuel-cell-powered tractor that same year.

National Aeronautics and Space Administration (NASA) also began building compact electric generators for use on space missions in the late 1950s. NASA soon came to fund hundreds of research contracts involving fuel cell technology. Fuel cells now have a proven role in the space program, after supplying electricity for several space missions.

In more recent decades, a number of manufacturers—including major automakers—and various federal agencies have supported ongoing research into the development of fuel cell technology for use in fuel cell vehicles and other applications.[14] Hydrogen production, storage, and distribution are the biggest challenges. Truly, fuel-cell-powered vehicles still have a long way to go to enter the market.

References

1. C. R. Ferguson and A. T. Kirkpatrick, *Internal Combustion Engines—Applied Thermo-Sciences*, Second Edition, John Wiley & Sons, New York, 2001.
2. U.S. Environmental Protection Agency (EPA), "Automobile emissions: An overview," *EPA 400-F-92-007*, Fact Sheet OMS-5, August 1994.
3. U.S. Environmental Protection Agency (EPA), "Automobiles and ozone," *EPA 400-F-92-006*, Fact Sheet OMS-4, January 1993.
4. Energy Information Administration, U.S. Department of Energy, "Carbon dioxide emissions from energy consumption by sector, 1980–1999," 2001, available at http://www.eia.doe.gov/emeu/aer/txt/tab1202.htm.
5. "BP statistical review of world energy—oil," 2001, available at http://www.bp.com/downloads/837/global_oil_section.pdf.
6. USGS World Energy Assessment Team, "World undiscovered assessment results summary," *U.S. Geological Survey Digital Data Series 60,* available at http://greenwood.cr.usgs.gov/energy/WorldEnergy/DDS-60/sum1.html#TOP.
7. International Energy Database, Energy Information Administration, U.S. Department of Energy, "World petroleum consumption, 1980–1999," 2000.
8. D. Doniger, D. Friedman, R. Hwang, D. Lashof, and J. Mark, "Dangerous addiction: Ending America's oil dependence," *National Resources Defense Council and Union of Concerned Scientists*, 2002.
9. M. Ehsani, D. Hoelscher, N. Shidore, and P. Asadi, "Impact of hybrid electric vehicles on the world's petroleum consumption and supply," *Society of Automotive Engineers (SAE) Future Transportation Technology Conference*, Paper No. 2003-01-2310, 2003.
10. J. E. Hake, "International energy outlook—2000 with projection to 2020," available at http://tonto.eia.doe.gov/FTPROOT/presentations/ieo2000/sld008.htm.
11. E. H. Wakefield, *History of the Electric Automobile: Battery-only Powered Cars*, Society of Automotive Engineers (SAE), ISBN: 1-56091-299-5, Warrendale, PA, 1994.
12. Y. Gao and M. Ehsani, "An investigation of battery technologies for the Army's hybrid vehicle application," in *Proceedings of the IEEE 56th Vehicular Technology Conference,* Vancouver, British Columbia, Canada, September 2002.
13. E. H. Wakefield, *History of the Electric Automobile: Hybrid Electric Vehicles*, Society of Automotive Engineers (SAE), ISBN: 0-7680-0125-0, Warrendale, PA, 1998.
14. California Fuel Cell Partnership, available at http://www.fuelcellpartnership.org/.

2

Fundamentals of Vehicle Propulsion and Brake

Vehicle operation fundamentals mathematically describe vehicle behavior, based on the general principles of mechanics. A vehicle, consisting of thousands of components, is a complex system. To describe its behavior fully, sophisticated mechanical and mathematical knowledge is needed. A great amount of literature in this field already exists. Since this book proposes to discuss electric, hybrid electric, and fuel cell power trains, the discussion of vehicle fundamentals will be restricted to one-dimensional movement. This chapter will, therefore, focus on vehicle performance, such as speed, gradeability, acceleration, fuel consumption, and braking performance.
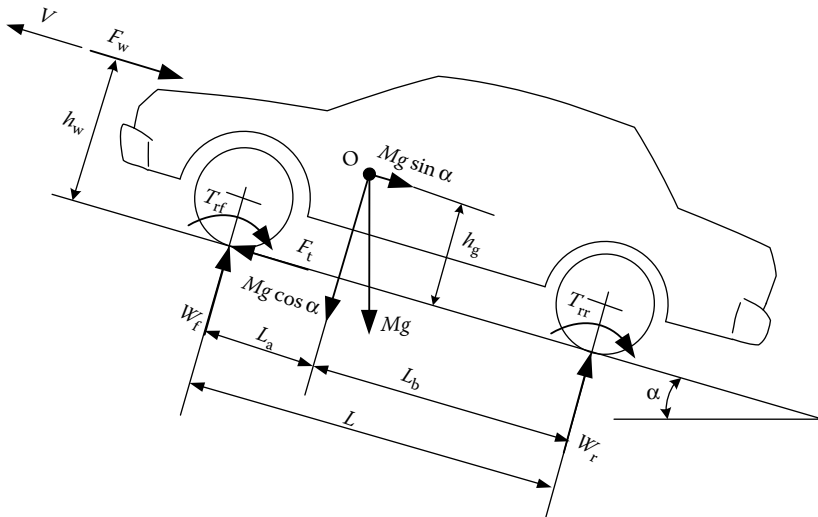
2.1 General Description of Vehicle Movement

The movement behavior of a vehicle along its moving direction is completely determined by all the forces acting on it in this direction. Figure 2.1 shows the forces acting on a vehicle moving up a grade. The tractive effort, F_t, in the contact area between the tires of the driven wheels and the road surface propels the vehicle forward. It is produced by the power plant torque and transferred through transmission and final drive to the drive wheels. While the vehicle is moving, there is resistance that tries to stop its movement. The resistance usually includes tire rolling resistance, aerodynamic drag, and uphill resistance. According to Newton's second law, vehicle acceleration can be written as

$$\frac{dV}{dt} = \frac{\sum F_t - \sum F_r}{\delta M},$$
(2.1)

where V is the speed of the vehicle, $\sum F_t$ is the total tractive effort of the vehicle, $\sum F_r$ is the total resistance, M is the total mass of the vehicle, and δ is the mass factor that equivalently converts the rotational inertias of rotating components into translational mass.
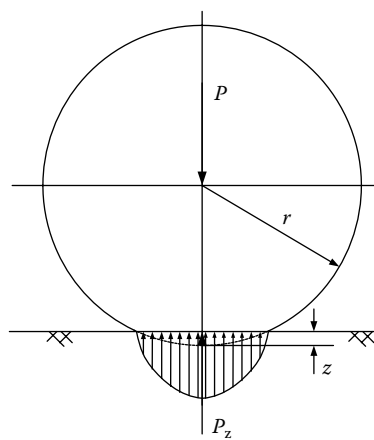
FIGURE 2.1   Forces acting on a vehicle moving uphill.

2.2   Vehicle Resistance

As shown in Figure 2.1, vehicle resistances opposing its movement include rolling resistance of the tires, appearing in Figure 2.1 as rolling resistance torques T_{rf} and T_{rr}, aerodynamic drag, F_w, and hill climbing resistance (the term $Mg \sin \alpha$ in Figure 2.1). All of the resistances will be discussed in detail in the following sections.

2.2.1   Rolling Resistance

The rolling resistance of tires on hard surfaces is primarily caused by hysteresis in the tire materials. Figure 2.2 shows a tire at standstill, on which a force, P, is acting at its center. The pressure in the contact area between the tire and ground is distributed symmetrically to the central line and the resultant reaction force, P_z, is aligned to P. The deformation, z, versus the load, P, in the loading and unloading process is shown in Figure 2.3. Due to hysteresis in the deformation of rubber material, the load at loading is larger than that at unloading at the same deformation, z, as shown in Figure 2.3. When the tire is rolling, as shown in Figure 2.4a, the leading half of the contact area is loading and the trailing half is unloading. Consequently, the hysteresis causes an asymmetric distribution of the ground reaction forces. The pressure in the leading half of the contact area is larger than that in the trailing half, as shown in Figure 2.4a. This phenomenon results in the ground reaction force shifting forward somewhat. This forwardly shifted ground reaction force, with the normal load acting on the wheel center, creates a moment, which opposes

FIGURE 2.2 Pressure distribution in contact area.
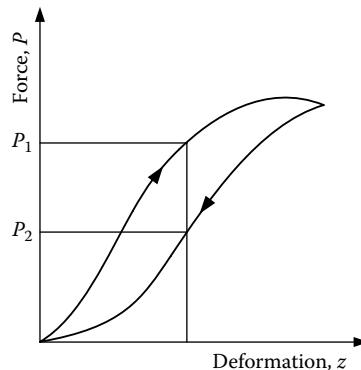
rolling of the wheel. On soft surfaces, the rolling resistance is primarily caused by deformation of the ground surface as shown in Figure 2.4b. The ground reaction force almost completely shifts to the leading half.

The moment produced by the forward shift of the resultant ground reaction force is called rolling resistant moment, as shown in Figure 2.4a, and can be expressed as
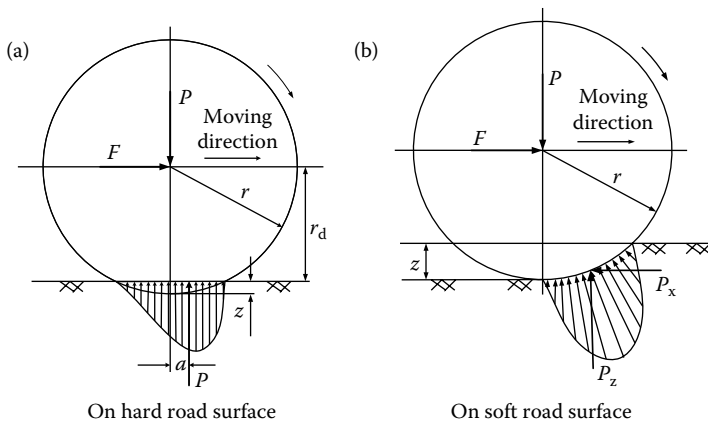
$$T_r = Pa. \tag{2.2}$$

To keep the wheel rolling, a force, F, acting on the center of the wheel is required to balance this rolling resistant moment. This force is expressed as

$$F = \frac{T_r}{r_d} = \frac{Pa}{r_d} = Pf_r, \tag{2.3}$$

FIGURE 2.3 Force acting on a tire versus tire deformation in loading and unloading.

FIGURE 2.4   Tire deflection and rolling resistance on a (a) hard and (b) soft road surface.

where r_d is the effective radius of the tire and $f_r = a/r_d$ is called the rolling resistance coefficient. In this way, the rolling resistant moment can be equivalently replaced by a horizontal force acting on the wheel center in the opposite movement direction of the wheel. This equivalent force is called rolling resistance with a magnitude of

$$F_r = Pf_r, \tag{2.4}$$

where P is the normal load acting on the center of the rolling wheel. When a vehicle is operated on a slope road, the normal load, P, should be replaced by the component that is perpendicular to the road surface. That is,

$$F_r = Pf_r \cos \alpha, \tag{2.5}$$

where α is the road angle (refer to Figure 2.1).

The rolling resistance coefficient, f_r, is a function of tire material, tire structure, tire temperature, tire inflation pressure, tread geometry, road roughness, road material, and presence or absence of liquids on the road. Typical values of rolling resistance coefficients on various roads are given in Table 2.1.[1] For fuel saving in recent years, low-resistance tires for passenger cars have been developed. Their rolling resistance coefficient is less than 0.01.

The values given in Table 2.1 do not take into account their variations with speed. Based on experimental results, many empirical formulas have been proposed for calculating the rolling resistance on a hard surface. For example, the rolling resistance coefficient of passenger cars on a concrete road may be calculated from the following equation:

$$f_r = f_0 + f_s \left(\frac{V}{100} \right)^{2.5}, \tag{2.6}$$

TABLE 2.1

Rolling Resistance Coefficients

Conditions	Rolling Resistance Coefficient
Car tires on a concrete or asphalt road	0.013
Car tires on a rolled gravel road	0.02
Tar macadam road	0.025
Unpaved road	0.05
Field	0.1–0.35
Truck tire on a concrete or asphalt road	0.006–0.01
Wheel on iron rail	0.001–0.002

where V is vehicle speed in km/h, and f_0 and f_s depend on the inflation pressure of the tire.[2]

In vehicle performance calculation, it is sufficient to consider the rolling resistance coefficient as a linear function of speed. For the most common range of inflation pressure, the following equation can be used for a passenger car on a concrete road[2]:

$$f_r = 0.01\left(1 + \frac{V}{160}\right). \tag{2.7}$$
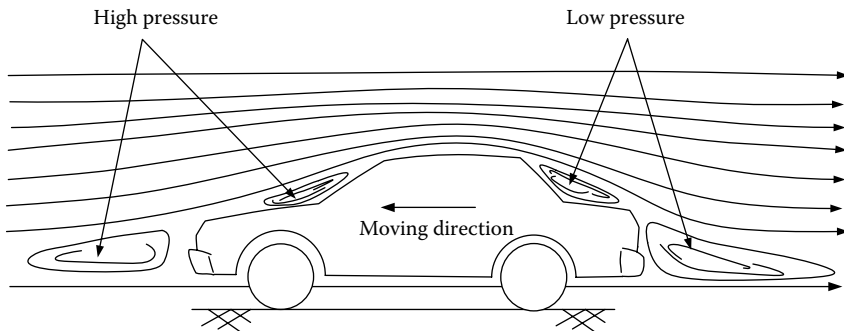
This equation predicts the values of f_r with acceptable accuracy for speeds up to 128 km/h.

2.2.2 Aerodynamic Drag

A vehicle traveling at a particular speed in air encounters a force resisting its motion. This force is referred to as aerodynamic drag. It mainly results from two components: shape drag and skin friction.

Shape drag: The forward motion of the vehicle pushes the air in front of it. However, the air cannot instantaneously move out of the way and its pressure is thus increased, resulting in high air pressure. In addition, the air behind the vehicle cannot instantaneously fill the space left by the forward motion of the vehicle. This creates a zone of low air pressure. The motion of the vehicle, therefore, creates two zones of pressure that oppose the motion by pushing (high pressure in front) and pulling it backwards (low pressure at the back) as shown in Figure 2.5. The resulting force on the vehicle is the shape drag. The name "shape drag" comes from the fact that this drag is completely determined by the shape of the vehicle body.

Skin friction: Air close to the skin of the vehicle moves almost at the speed of the vehicle while air away from the vehicle remains still. In between, air molecules move at a wide range of speeds. The difference in speed between two air molecules produces a friction that results in the second component of aerodynamic drag.

FIGURE 2.5 Shape drag.

Aerodynamic drag is a function of vehicle speed V, vehicle frontal area, A_f, shape of the vehicle body, and air density, ρ:

$$F_w = \frac{1}{2}\rho A_f C_D (V - V_w)^2, \tag{2.8}$$

where C_D is the aerodynamic drag coefficient that characterizes the shape of the vehicle body and V_w is component of the wind speed on the vehicle moving direction, which has a positive sign when this component is in the same direction of the moving vehicle and a negative sign when it is opposite to the vehicle speed. The aerodynamic drag coefficients for typical vehicle body shapes are shown in Figure 2.6.

2.2.3 Grading Resistance
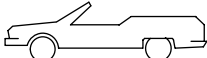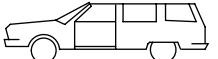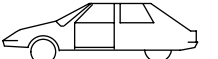
When a vehicle goes up or down a slope, its weight produces a component that is always directed in the downward direction, as shown in Figure 2.7. This component either opposes the forward motion (grade climbing) or helps the forward motion (grade descending). In vehicle performance analysis, only uphill operation is considered. This grading force is usually called grading resistance.

Grading resistance, referring to Figure 2.7, can be expressed as

$$F_g = Mg \sin \alpha. \tag{2.9}$$

To simplify the calculation, the road angle, α, is usually replaced by the grade value, when the road angle is small. As shown in Figure 2.7, grade is defined as
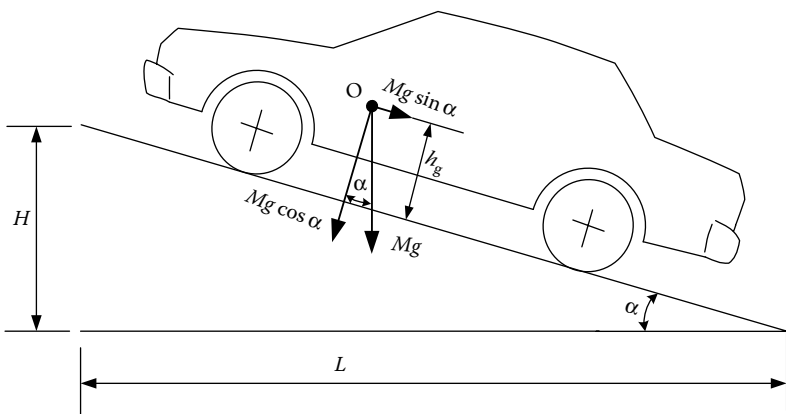
$$i = \frac{H}{L} = \tan \alpha \approx \sin \alpha. \tag{2.10}$$

Vehicle type	Coefficient of aerodynamic resistance
Open convertible	0.5…0.7
Van body	0.5…0.7
Ponton body	0.4…0.55
Wedged-shaped body; headlamps and bumpers are integrated into the body, covered underbody, optimized cooling air flow	0.3…0.4
Headlamp and all wheels in body, covered underbody	0.2…0.25
K-shaped (small breakaway section)	0.23
Optimum streamlined design	0.15…0.20
Trucks, road trains	0.8…1.5
Buses	0.6…0.7
Streamlined buses	0.3…0.4
Motorcycles	0.6…0.7

FIGURE 2.6 Indicative drag coefficients for different body shapes.

In some literature, the tire rolling resistance and grading resistance together are called road resistance, which is expressed as

$$F_{rd} = F_f + F_g = Mg(f_r \cos\alpha + \sin\alpha). \tag{2.11}$$

FIGURE 2.7 Vehicle climbing a grade.

When the road angle is small, the road resistance can be simplified as

$$F_{rd} = F_f + F_g = Mg(f_r + i). \tag{2.12}$$

2.3 Dynamic Equation

In the longitudinal direction, the major external forces acting on a two-axle vehicle, as shown in Figure 2.1, include the rolling resistance of the front and rear tires F_{rf} and F_{rr}, which are represented by rolling resistance moment, T_{rf} and T_{rr}, aerodynamic drag, F_w, climbing resistance, F_g ($Mg \sin \alpha$), and tractive effort of the front and rear tires, F_{tf} and F_{tr}. F_{tf} is zero for a rear-wheel-driven vehicle, whereas F_{tr} is zero for a front-wheel-driven vehicle.

The dynamic equation of vehicle motion along the longitudinal direction is expressed by

$$M\frac{dV}{dt} = (F_{tf} + F_{tr}) - (F_{rf} + F_{rr} + F_w + F_g), \tag{2.13}$$

where dV/dt is the linear acceleration of the vehicle along the longitudinal direction and M is the vehicle mass. The first term on the right-hand side of Equation 2.13 is the total tractive effort and the second term is the resistance.

To predict the maximum tractive effort that the tire–ground contact can support, the normal loads on the front and rear axles have to be determined. By summing the moments of all the forces about point R (center of the tire–ground area), the normal load on the front axle W_f can be determined as

$$W_f = \frac{MgL_b \cos \alpha - (T_{rf} + T_{rr} + F_w h_w + Mgh_g \sin \alpha + Mh_g \, dV/dt)}{L}. \tag{2.14}$$

Similarly, the normal load acting on the rear axle can be expressed as

$$W_r = \frac{MgL_a \cos \alpha + (T_{rf} + T_{rr} + F_w h_w + Mgh_g \sin \alpha + Mh_g \, dV/dt)}{L}. \tag{2.15}$$

For passenger cars, the height of the center of application of aerodynamic resistance, h_w, is assumed to be near the height of the gravity center of the vehicle, h_g. Equations 2.14 and 2.15 can be simplified as

$$W_f = \frac{L_b}{L}Mg \cos \alpha - \frac{h_g}{L}\left(F_w + F_g + Mgf_r\frac{r_d}{h_g}\cos \alpha + M\frac{dV}{dt}\right) \tag{2.16}$$

and

$$W_r = \frac{L_a}{L}Mg \cos \alpha + \frac{h_g}{L}\left(F_w + F_g + Mgf_r\frac{r_d}{h_g}\cos \alpha + M\frac{dV}{dt}\right), \tag{2.17}$$

where r_d is the effective radius of the wheel. Referring to Equations 2.5 and 2.13, Equations 2.16 and 2.17 can be rewritten as

$$W_f = \frac{L_b}{L} Mg \cos \alpha - \frac{h_g}{L} \left(F_t - F_r \left(1 - \frac{r_d}{h_g} \right) \right) \tag{2.18}$$

and

$$W_r = \frac{L_a}{L} Mg \cos \alpha + \frac{h_g}{L} \left(F_t - F_r \left(1 - \frac{r_d}{h_g} \right) \right), \tag{2.19}$$

where $F_t = F_{tf} + F_{tr}$ is the total tractive effort of the vehicle and F_r is the total rolling resistance of the vehicle. The first term on the right-hand side of Equations 2.18 and 2.19 is the static load on the front and rear axles when the vehicle is at rest on level ground. The second term is the dynamic component of the normal load.

The maximum tractive effort that the tire–ground contact can support (any small amount over this maximum tractive effort will cause the tire to spin on the ground) is usually described by the product of the normal load and the coefficient of road adhesion, μ, or referred to as frictional coefficient in some of the literature (more details are given in Section 2.4). For a front-wheel-driven vehicle,

$$F_{t \, max} = \mu W_f = \mu \left[\frac{L_b}{L} Mg \cos \alpha - \frac{h_g}{L} \left(F_{t \, max} - F_r \left(1 - \frac{r_d}{h_g} \right) \right) \right] \tag{2.20}$$

and

$$F_{t \, max} = \frac{\mu Mg \cos \alpha [L_b + f_r(h_g - r_d)]/L}{1 + \mu h_g/L}, \tag{2.21}$$

where f_r is the coefficient of the rolling resistance. Similarly, for a rear-wheel-driven vehicle,

$$F_{t \, max} = \mu W_r = \mu \left[\frac{L_a}{L} Mg \cos \alpha + \frac{h_g}{L} \left(F_{t \, max} - F_r \left(1 - \frac{r_d}{h_g} \right) \right) \right] \tag{2.22}$$

and

$$F_{t \, max} = \frac{\mu Mg \cos \alpha [L_a - f_r(h_g - r_d)]/L}{1 - \mu h_g/L}. \tag{2.23}$$

In vehicle operation, the maximum tractive effort on the driven wheels, transferred from power plant through transmission, should not exceed the maximum values that are limited by the tire–ground cohesion in Equations 2.21 and 2.23. Otherwise, the driven wheels will spin on the ground, leading to vehicle instability.

2.4   Tire–Ground Adhesion and Maximum Tractive Effort

When the tractive effort of a vehicle exceeds the limitation of the maximum tractive effort due to the adhesive capability between the tire and ground, the driven wheels will spin on the ground. Actually, the adhesive capability between the tire and the ground sometimes is the main limitation of vehicle performance. This is especially true when the vehicle drives on wet, icy, snow-covered, or soft soil roads. In this case, a tractive torque on the driven wheel would cause the wheel to slip significantly on the ground. The maximum tractive effort on the driven wheel depends on the longitudinal force that the adhesive capability between the tire and ground can supply, rather than the maximum torque that an engine can supply.

Experimental results show that, on various types of ground, the maximum tractive effort of the drive wheel closely relates to the slipping of the running wheel. This is also true on a good paved, dry road where the slipping is very small due to the elasticity of the tire. The slip, s, of a tire is defined in traction as

$$s = \left(1 - \frac{V}{r\omega}\right) \times 100\%, \tag{2.24}$$

where V is the translatory speed of the tire center, ω is the angular speed of the tire, and r is the rolling radius of the free rolling tire. In traction, the speed, V, is less than $r\omega$; therefore the slip of a tire has a positive value between 0 and 1.0. During braking, however, the slip of a tire can be defined as
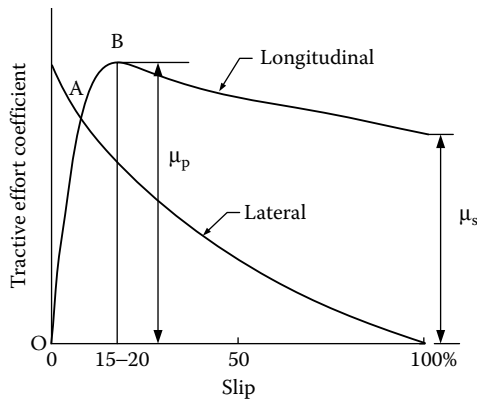
$$s = \left(1 - \frac{r\omega}{V}\right) \times 100\%, \tag{2.25}$$

which has a positive value between 0 and 1.0, similar to traction. The maximum traction effort of a tire corresponding to a certain tire slip is usually expressed as

$$F_x = P\mu(s), \tag{2.26}$$
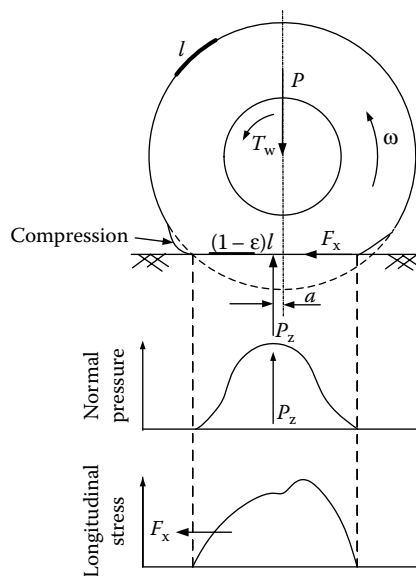
where P is the vertical load of the tire and μ is the tractive effort coefficient, which is a function of tire slip. The tractive effort coefficient and the tire slip have the relationship as shown in Figure 2.8.

In the small-slip range (section OA in Figure 2.8), the tractive effort is almost linearly proportional to the slip value. This small slip is caused by the elasticity of the tire rather than the relative slipping between the tire and ground at the contact patch, as shown in Figure 2.9. When a tractive torque is applied to the tire, a tractive force is developed at the tire–ground contact patch. At the same time, the tire tread in front and within the contact patch is subjected to compression. A corresponding shear deformation of the side wall of the tire is also developed. As tread elements are compressed before entering the contact region, the distance that the tire travels will be less than

FIGURE 2.8 Variation of tractive effort coefficient with longitudinal slip of a tire.

the distance in a free rolling tire. Because of the nearly linear elastic property of the tire, the tractive effort–slip curve is almost linear. Further increase of wheel torque and tractive force results in part of the tire tread sliding on the ground. Under these circumstances, the relationship between tractive force and slip is nonlinear. This corresponds to section AB of the curve, as shown in Figure 2.8. The peak tractive effort is reached at a slip of 15–20%. Further increase of the slip beyond that results in an unstable condition. The tractive effort coefficient falls rapidly from the peak value to the purely sliding value as shown in Figure 2.8. For normal driving, the slip of the tire must be limited

FIGURE 2.9 Behavior of a tire under the action of driving torque.

TABLE 2.2
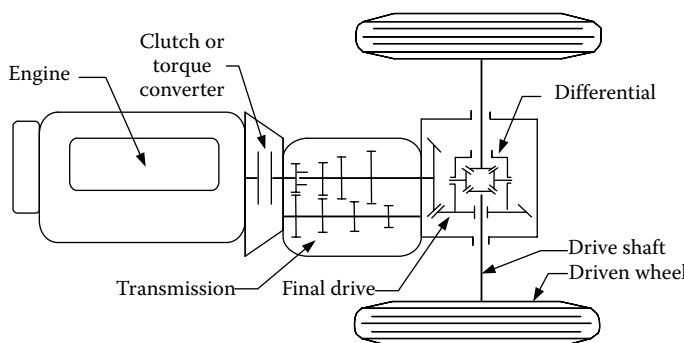
Average Values of Tractive Effort Coefficient on Various Roads

Surface	Peaking Values, μ_p	Slipping Values, μ_s
Asphalt and concrete (dry)	0.8–0.9	0.75
Concrete (wet)	0.8	0.7
Asphalt (wet)	0.5–0.7	0.45–0.6
Gravel	0.6	0.55
Earth road (dry)	0.68	0.65
Earth road (wet)	0.55	0.4–0.5
Snow (hard packed)	0.2	0.15
Ice	0.1	0.07

in the range less than 15–20%. Table 2.2 shows the average values of tractive effort coefficients on various roads.[2]

2.5 Power Train Tractive Effort and Vehicle Speed

An automotive power train, as shown in Figure 2.10, consists of a power plant (engine or electric motor), a clutch in manual transmission or a torque converter in automatic transmission, a gearbox (transmission), final drive, differential, drive shaft, and driven wheels. The torque and rotating speed from the output shaft of the power plant are transmitted to the driven wheels through the clutch or torque converter, gearbox, final drive, differential, and drive shaft. The clutch is used in manual transmission to couple or decouple the gearbox to the power plant. The torque converter in automatic transmission is a hydrodynamic device, functioning as the clutch in manual transmission with a continuously variable gear ratio (for more details, see

FIGURE 2.10 Conceptual illustration of an automobile power train.

Section 2.6). The gearbox supplies a few gear ratios from its input shaft to its output shaft for the power plant torque–speed profile to match the requirements of the load. The final drive is usually a pair of gears that supply a further speed reduction and distribute the torque to each wheel through the differential.

The torque on the driven wheels, transmitted from the power plant, is expressed as

$$T_w = i_g i_0 \eta_t T_p, \tag{2.27}$$

where i_g is the gear ratio of the transmission defined as $i_g = N_{in}/N_{out}$ (N_{in}— input rotating speed, N_{out}—output rotating speed), i_0 is the gear ratio of the final drive, η_t is the efficiency of the driveline from the power plant to the driven wheels, and T_p is the torque output from the power plant.

The tractive effort on the driven wheels, as shown in Figure 2.11, can be expressed as

$$F_t = \frac{T_w}{r_d}. \tag{2.28}$$

Substituting Equation 2.27 into Equation 2.28 yields the following result:

$$F_t = \frac{T_p i_g i_0 \eta_t}{r_d}. \tag{2.29}$$
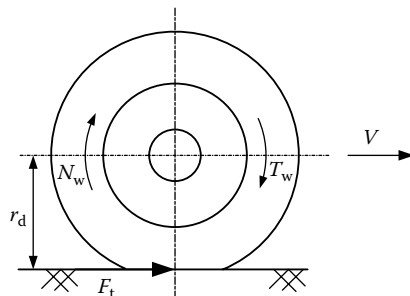
The friction in the gear teeth and bearings creates losses in the mechanical gear transmission. The following are representative values of the mechanical efficiency of various components:

Clutch: 99%.
Each pair of gears: 95–97%.
Bearing and joint: 98–99%.

The total mechanical efficiency of the transmission between the engine output shaft and driven wheels is the product of the efficiencies of all the

FIGURE 2.11 Tractive effort and torque on a driven wheel.

components in the driveline. As a first approximation, the following average values of the overall mechanical efficiency of a manual gear-shift transmission may be used:

Direct gear: 90%.
Other gear: 85%.
Transmission with very high reduction ratio: 75–80%.

The rotating speed (rpm) of the driven wheel can be expressed as

$$N_w = \frac{N_p}{i_g i_0},\tag{2.30}$$

where N_p is the transmission rotating speed (rpm), which is equal to the engine speed in the vehicle with a manual transmission and the turbine speed of a torque converter in the vehicle with an automatic transmission (for more details, see Section 2.6). The translational speed of the wheel center (vehicle speed) can be expressed as

$$V = \frac{\pi N_w r_d}{30}\ \text{(m/s)}.\tag{2.31}$$

Substituting Equation 2.30 into Equation 2.31 one obtains
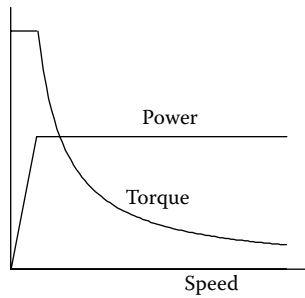
$$V = \frac{\pi N_p r_d}{30 i_g i_0}\ \text{(m/s)}.\tag{2.32}$$

2.6 Vehicle Power Plant and Transmission Characteristics

There are two limiting factors to the maximum tractive effort of the vehicle. One is the maximum tractive effort that the tire–ground contact can support (Equation 2.21 or 2.23) and the other is the tractive effort that the maximum torque of the power plant can produce with given driveline gear ratios (Equation 2.29). The smaller of these two factors will determine the performance potential of the vehicle. For on-road vehicles, the performance is usually limited by the second factor.

2.6.1 Power Plant Characteristics
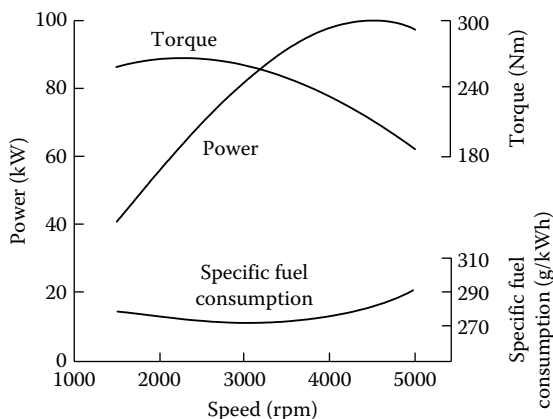
For vehicular applications, the ideal performance characteristic of a power plant is a constant power output over the full speed range. Consequently, the torque varies with speed hyperbolically as shown in Figure 2.12. With this ideal profile, the maximum power of the power plant will be available at
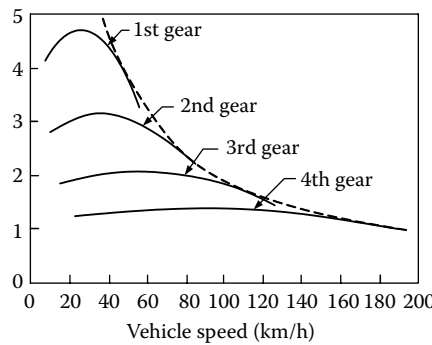
FIGURE 2.12 Ideal performance characteristics for a vehicle traction power plant.

any vehicle speed, therefore yielding optimal vehicle performance. However, in practice, the torque is constrained to be constant in low speed, so as not to be over the maxima limited by the adhesion between the tire–ground contact area. This constant power characteristic will provide the vehicle with high tractive effort at low speeds where demands for acceleration, drawbar pull, or grade climbing capability are high.

IC engines are the most commonly used power plants for land vehicles to date. Representative characteristics of a gasoline engine in wide open throttle are shown in Figure 2.13, which has torque–speed characteristics far from the ideal performance characteristic required by traction. It starts operating smoothly at the idle speed. Good combustion quality and maximum torque are reached at an intermediate engine speed. As the speed further increases, the torque decreases due to less air induced into the cylinders, caused by the growing losses in the air-induction manifold and grossing power losses caused by mechanical frication and hydraulic viscosity. Power output, however, increases to its maximum at a certain higher speed. Beyond this speed,

FIGURE 2.13 Typical performance characteristics of gasoline engines.
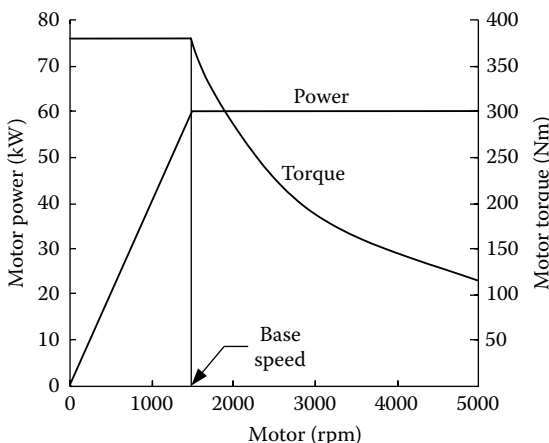
FIGURE 2.14 Tractive effort of an IC engine and a multigear transmission vehicle versus vehicle speed.
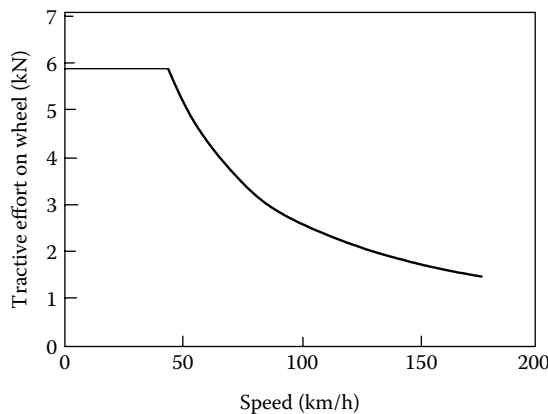
the engine power starts declining. In vehicular applications, the maximum permissible speed of the engine is usually set just a little above the speed of the maximum power output. The IC engine has a relatively flat torque–speed profile (as compared with an ideal power plant), as shown in Figure 2.13. Consequently, a multigear transmission is usually employed to modify it, as shown in Figure 2.14.

The electric motor is another candidate as a vehicle power plant, and becoming more and more important with the rapid development of electric, hybrid electric, and fuel cell vehicles. Electric motors with good speed adjustment control usually have a speed–torque characteristic that is much closer to the ideal, as shown in Figure 2.15.

Generally, the electric motor starts from zero speed. As it increases to its base speed, the voltage increases to its rated value while the flux remains

FIGURE 2.15 Typical performance characteristics of electric motors for traction.

FIGURE 2.16 Tractive effort of a single-gear EV versus vehicle speed.
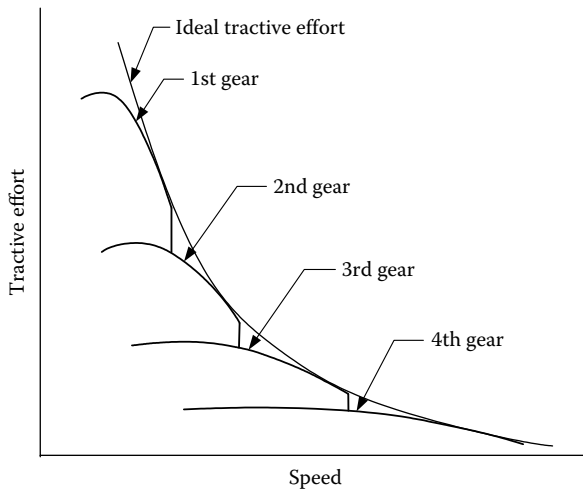
constant. In this speed range of zero to base speed, the electric motor produces a constant torque. Beyond the base speed, the voltage remains constant and the flux is weakened. This results in a constant output power while the torque declines hyperbolically with speed. Since the speed–torque profile of an electric motor is close to the ideal, a single-gear or double-gear transmission may be employed to meet the vehicle performance requirement, as shown in Figure 2.16.

2.6.2 Transmission Characteristics

The transmission requirements of a vehicle depend on the characteristics of the power plant and the performance requirements of the vehicle. As mentioned previously, a well-controlled electric machine, such as the power plant of an EV, would not need a multigear transmission. However, an IC engine has to use multigear or continuously varying transmission to multiply its torque at low speed. The term transmission here includes all those systems employed for transmitting the engine power to the drive wheels. For automobile applications, there are usually two basic types of transmission: manual gear transmission and hydrodynamic transmission.

2.6.3 Manual Gear Transmission

Manual gear transmission consists of a clutch, a gearbox, a final drive, and a drive shaft as shown in Figure 2.10. The final drive has a constant gear ratio. The common practice of requiring direct drive (nonreducing) in the gearbox to be in the highest gear determines this ratio. The gearbox provides a number of gear ratios ranging from three to five for passenger cars and more for heavy commercial vehicles that are powered with gasoline or diesel engines.

FIGURE 2.17 Tractive effort characteristics of a gasoline-engine-powered vehicle.

The maximum speed of the vehicle determines the gear ratio of the highest gear (i.e., the smallest ratio). On the other hand, the gear ratio of the lowest gear (i.e., the maximum ratio) is determined by the requirement of the maximum tractive effort or the gradeability. Ratios between them should be spaced in such a way that they will provide the tractive effort–speed characteristics as close to the ideal as possible, as shown in Figure 2.17. In the first iteration of transmission design, gear ratios between the highest and the lowest gear may be selected in such a way that the engine can operate in the same speed range for all the gears. This approach would benefit the fuel economy and performance of the vehicle. For instance, in normal driving, the proper gear can be selected, according to vehicle speed, to operate the engine in its optimum speed range for fuel-saving purposes. In fast acceleration, the engine can be operated in its speed range with high power output. This approach is depicted in Figure 2.18.
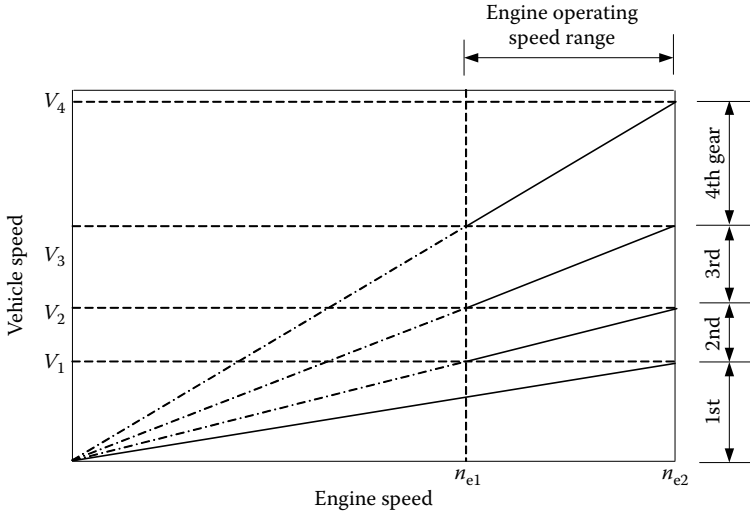
For a four-speed gearbox, the following relationship can be established (see Figure 2.18):

$$\frac{i_{g1}}{i_{g2}} = \frac{i_{g2}}{i_{g3}} = \frac{i_{g3}}{i_{g4}} = K_g \qquad (2.33)$$

and

$$K_g = \sqrt[3]{\frac{i_{g1}}{i_{g4}}}, \qquad (2.34)$$

where i_{g1}, i_{g2}, i_{g3}, and i_{g4} are the gear ratios for the first, second, third, and fourth gear, respectively. In the more general case, if the ratio of the highest gear, i_{gn} (smallest gear ratio), and the ratio of the lowest gear, i_{g1} (largest gear

FIGURE 2.18 Demonstration of vehicle and speed ranges for each gear.

ratio), have been determined and the number of the gear n_g is known, the factor K_g can be determined as

$$K_g = \sqrt[n_g-1]{\frac{i_{g1}}{i_{gn}}}, \tag{2.35}$$
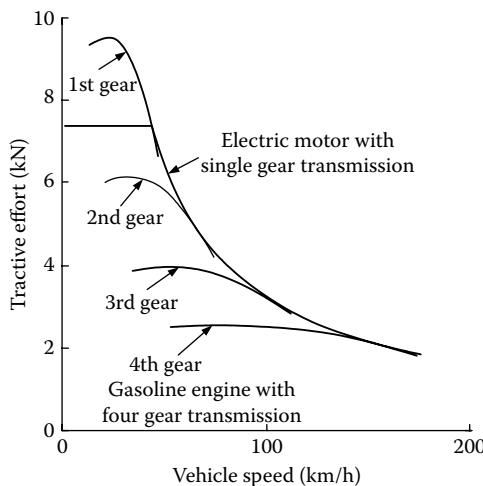
and each gear ratio can be obtained by

$$i_{gn-1} = K_g i_{gn},$$
$$i_{gn-2} = K_g^2 i_{gn},$$
$$\vdots \tag{2.36}$$
$$i_{g2} = K_g^{n_g-1} i_{gn}.$$

For passenger cars that usually use high gear in normal driving, the step between the ratios of the upper two gears is often slightly closer than that calculated from Equation 2.36. That is,

$$\frac{i_{g1}}{i_{g2}} > \frac{i_{g2}}{i_{g3}} > \frac{i_{g3}}{i_{g4}}. \tag{2.37}$$

This, in turn, affects the selection of the ratios of the lower gears. For commercial vehicles, however, the gear ratios in the gearbox are often arranged based on Equation 2.37.

FIGURE 2.19 Tractive efforts of a gasoline engine vehicle with a four-gear transmission and EV with a single-gear transmission.
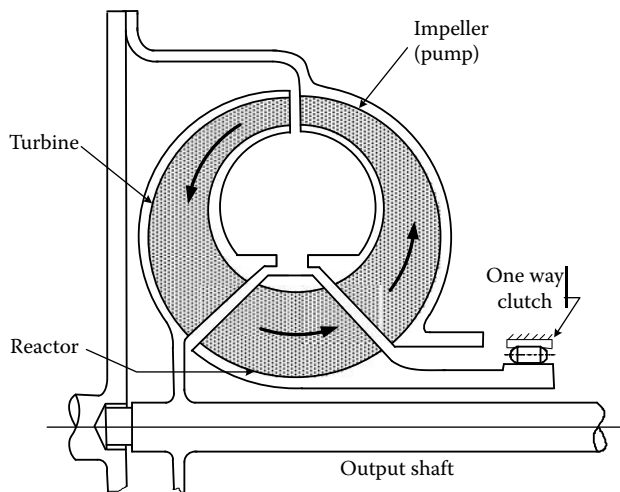
Figure 2.19 shows the tractive effort of a gasoline engine vehicle with a four-gear transmission and that of an EV with a single-gear transmission. It is clear that electric machines with favorable torque–speed characteristics can satisfy the tractive effort with a simple single-gear transmission.

2.6.3.1 Hydrodynamic Transmission

Hydrodynamic transmissions use fluid to transmit power in the form of torque and speed. Hydrodynamic transmissions are widely used in passenger cars. They consist of a torque converter and an automatic gearbox. The torque converter consists of at least three rotary elements known as the impeller (pump), the turbine, and the reactor, as shown in Figure 2.20. The impeller is connected to the engine shaft and the turbine is connected to the output shaft of the converter, which in turn is coupled with the input shaft of the multispeed gearbox. The reactor is coupled to external housing to provide a reaction on the fluid circulating in the converter. The function of the reactor is to enable the turbine to develop output torque higher than the input torque of the converter, thus obtaining torque multiplication. The reactor is usually mounted on a free wheel (one-way clutch) so that when the starting period has been completed and the turbine speed is approaching that of the pump, the reactor is in free rotation. At this point, the converter operates as a fluid coupler with a 1-to-1 ratio of output torque to input torque.

The major advantages of hydrodynamic transmission may be summarized as follows:

- When properly matched, the engine will not stall.
- It provides flexible coupling between the engine and the driven wheels.

FIGURE 2.20 Schematic view of a torque converter.

- Together with a suitably selected multispeed gearbox, it provides torque–speed characteristics that approach the ideal.

The major disadvantages of hydrodynamic transmission are its low efficiency in a stop–go driving pattern and complex structure.

The performance characteristics of a torque converter are described in terms of the following four parameters:

$$\text{Speed ratio } C_{sr} = \frac{\text{output\_speed}}{\text{input\_speed}}, \tag{2.38}$$

which is the reciprocal of the gear ratio mentioned before.

$$\text{Torque ratio } C_{tr} = \frac{\text{output\_torque}}{\text{input\_torque}}. \tag{2.39}$$

$$\text{Efficiency } \eta_c = \frac{\text{output\_speed} \times \text{output\_torque}}{\text{input\_speed} \times \text{input\_torque}} = C_{sr} C_{tr}. \tag{2.40}$$

$$\text{Capacity factor (size factor) } K_{tc} = \frac{\text{speed}}{\sqrt{\text{torque}}}. \tag{2.41}$$

The capacity factor, K_c, is an indicator of the ability of the converter to absorb or transmit torque, which is closely related to the size and geometric shape of the blades.

Typical performance characteristics of the torque converter are shown in Figure 2.21, in which torque ratio, efficiency, and input capacity factor (the ratio of input speed to the square root of input torque) are plotted against speed ratio. Torque ratio has the maximum value at stall condition where the
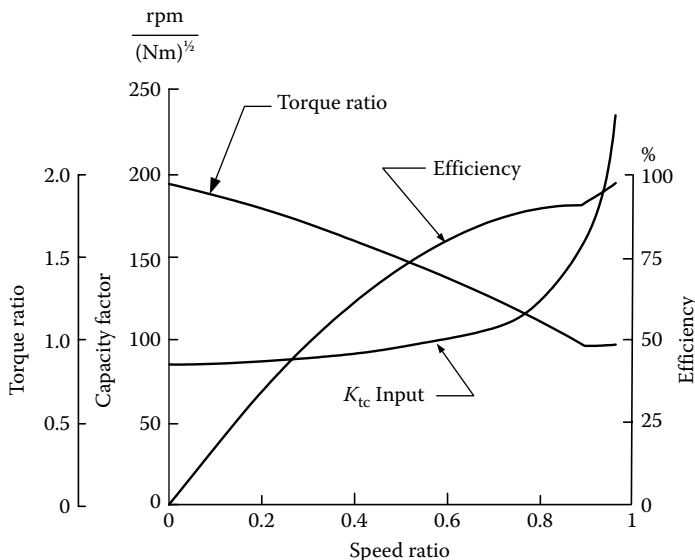
FIGURE 2.21 Performance characteristics of a torque converter.

output speed is zero. The torque ratio decreases as the speed ratio increases (gear ratio decreases) and the converter eventually acts as a hydraulic coupling with a torque ratio of 1.0. At this point, a small difference between the input and output speed exists because of the slip between the impeller (pump) and the turbine. The efficiency of the torque converter is zero at stall condition (zero speed ratio) and increases with an increase in the speed ratio. It reaches the maximum when the converter acts as a fluid coupling (torque ratio equal to 1.0).
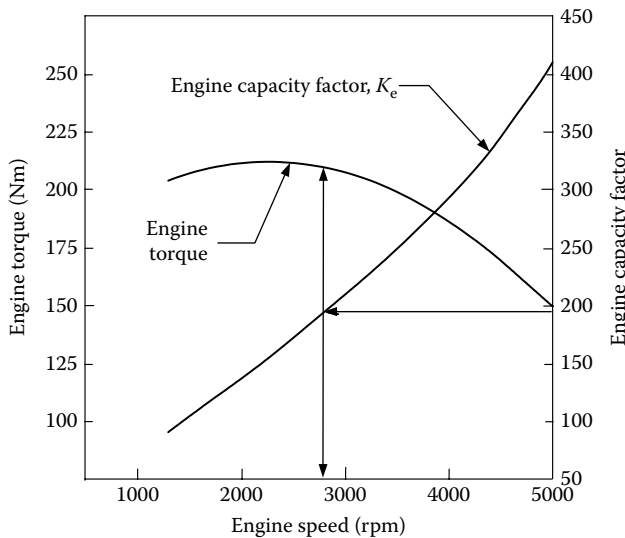
To determine the actual operating condition of the torque converter, the engine operating point has to be specified since the engine directly drives the torque converter. To characterize the engine operating condition for the purpose of determining the combined performance of the engine and the converter, an engine capacity factor, K_e, is introduced and defined as

$$K_e = \frac{n_e}{\sqrt{T_e}}, \tag{2.42}$$

where n_e and T_e are engine speed and torque, respectively. The variation of the capacity factor with speed for a typical engine is shown in Figure 2.22. To achieve proper matching, the engine and the torque converter should have a similar range in the capacity factor.

As mentioned above, the engine shaft is usually directly connected to the input shaft of the torque converter. That is,

$$K_e = K_{tc}. \tag{2.43}$$

FIGURE 2.22 Capacity factor of a typical engine.

The matching procedure begins by specifying engine speed and engine torque. Knowing the engine operating point, one can determine the engine capacity factor, K_e, using Equation 2.42 (see Figure 2.22). Since $K_e = K_{tc}$, the input capacity factor of the torque converter corresponding to the specific engine operating point is then known. As shown in Figure 2.21, for a particular value of the input capacity factor of the torque converter, K_{tc}, the converter speed ratio, C_{sr}, and the torque ratio, C_{tr}, can be determined from the torque converter performance characteristics as shown in Figure 2.21. The output torque and the output speed of the converter are then given by

$$T_{tc} = T_e C_{tr} \tag{2.44}$$

and

$$n_{tc} = n_e C_{sr}, \tag{2.45}$$

where T_{tc} and n_{tc} are the output torque and the output speed of the converter, respectively.

Since the torque converter has a limited torque ratio range (usually less than 2), a multispeed gearbox is usually connected to it. The gearbox comprises several planetary gear sets and is automatically shifted. With the gear ratios of the gearbox, the tractive effort and speed of the vehicle can be calculated (see Equations 2.27 and 2.32) by

$$F_t = \frac{T_e C_{tr} i_g i_0 \eta_t}{r} \tag{2.46}$$

and

$$V = \frac{\pi n_e C_{sr} r}{30 i_g i_0} \text{ (m/s)} = 0.377 \frac{n_e C_{sr} r}{i_t} \text{ (km/h).} \qquad (2.47)$$

Figure 2.23 shows the variation of the tractive effort with speed for a passenger car equipped with a torque converter and a three-speed gearbox.

2.6.3.2 Continuously Variable Transmission
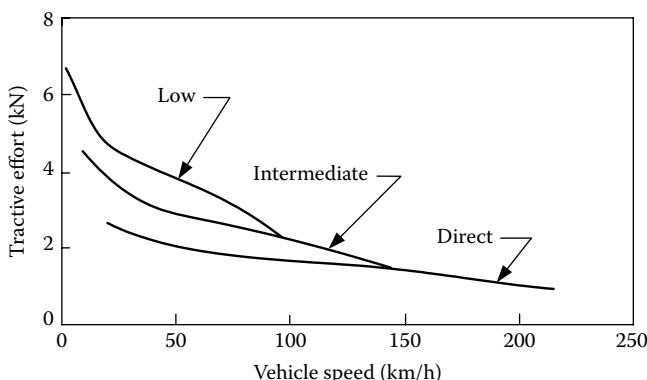
A continuously variable transmission (CVT) has a gear ratio that can be varied continuously within a certain range, thus providing an infinite number of gears. The continuous variation allows for matching virtually any engine speed and torque to any wheel speed and torque. It is therefore possible to achieve an ideal torque–speed profile (constant power profile).

The commonly used CVT in automobiles uses a pulley and belt assembly. One pulley is connected to the engine shaft, while the other is connected to the output shaft. The belt links the two pulleys. The distance between the two half pulleys can be varied, thus varying the effective diameter on which the belt grips. The transmission ratio is a function of the two effective diameters:

$$i_g = \frac{D_2}{D_1}, \qquad (2.48)$$

where D_1 and D_2 are the effective diameters of the output pulley and the input pulley, respectively.

Until recently, this implementation was affected by the limited belt–pulley adhesive contact. The design has been improved by the use of metallic belts that provide better solidity and improved contact. Furthermore, an interesting concept has been developed and is being used by Nissan. This concept

FIGURE 2.23 Tractive effort–speed characteristics of a passenger car with automatic transmission.

uses three friction gears: one is connected to the engine shaft, another to the output shaft, and the third grips on the particular profile of the other two gears. It can be rotated to grip on different effective diameters, thus achieving variable gear ratio.
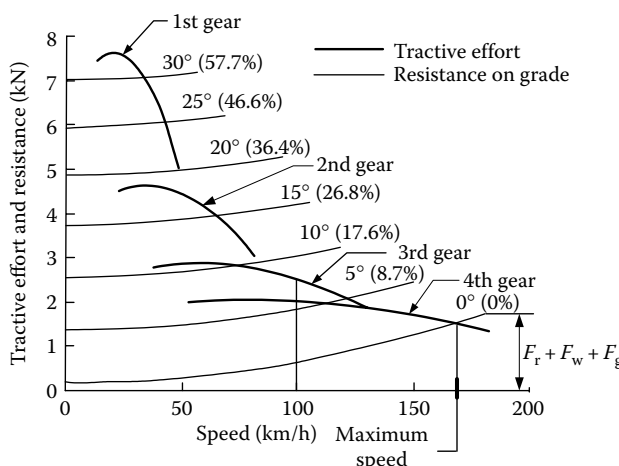
2.7 Vehicle Performance
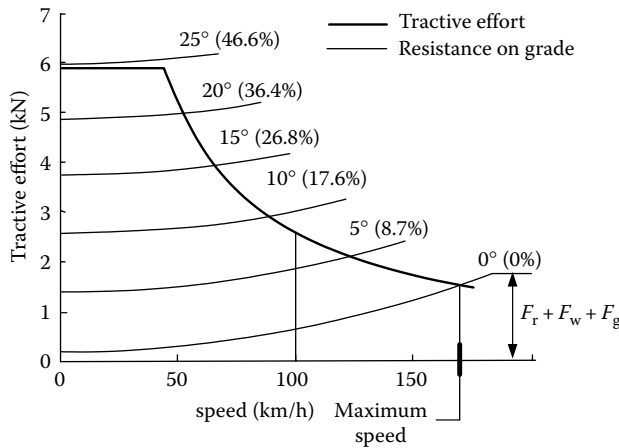
The performance of a vehicle is usually described by its maximum cruising speed, gradeability, and acceleration. The prediction of vehicle performance is based on the relationship between tractive effort and vehicle speed discussed in Sections 2.5 and 2.6. For on-road vehicles, it is assumed that the maximum tractive effort is limited by the maximum torque of the power plant, rather than the road adhesion capability. Depicted tractive effort (Equation 2.29 or 2.46) and resistance ($F_r + F_w + F_g$) on a diagram are used for vehicle performance analysis, as shown in Figures 2.24 and 2.25, for a gasoline-engine-powered, four-gear manual transmission vehicle and an electric-motor-powered, single-gear transmission vehicle, respectively.

2.7.1 Maximum Speed of a Vehicle

The maximum speed of a vehicle is defined as the constant cruising speed that the vehicle can develop with full power plant load (full throttle of engine or full power of motor) on a flat road. The maximum speed of the vehicle is

FIGURE 2.24 Tractive effort of a gasoline-engine-powered vehicle with manual multispeed transmission and its resistance.

FIGURE 2.25 Tractive effort of an electric-motor-powered vehicle with single-speed transmission and its resistance.

determined by the equilibrium between the tractive effort of the vehicle and the resistance or the maximum speed of the power plant and gear ratios of the transmission. The tractive effort and resistance equilibrium can be expressed as

$$\frac{T_p i_g i_0 \eta_t}{r_d} = M g f_r \cos\alpha + \frac{1}{2}\rho_a C_D A_f V^2. \tag{2.49}$$

This equation indicates that the vehicle reaches its maximum speed when the tractive effort, represented by the left-hand-side term in Equation 2.49, equals the resistance, represented by the right-hand-side terms. The intersection of the tractive effort curve and the resistance curve is the maximum speed of the vehicle, as shown in Figures 2.24 and 2.25.

It should be noted that for some vehicles, no intersection exists between the tractive effort curve and the resistance curve, because of a large power plant or a large gear ratio. In this case, the maximum speed of the vehicle is determined by the maximum speed of the power plant. Using Equation 2.32 or 2.47, the maximum speed of the vehicle can be obtained by

$$V_{max} = \frac{\pi n_{p\,max} r_d}{30 i_0 i_{g\,min}} \ (\text{m/s}), \tag{2.50}$$

where $n_{p\,max}$ and $i_{g\,min}$ are the maximum speed of the engine (or electric motor) and the minimum gear ratio of the transmission, respectively.

2.7.2   Gradeability

Gradeability is usually defined as the grade (or grade angle) that the vehicle can overcome at a certain constant speed, for instance the grade at a speed of

100 km/h (60 mph). For heavy commercial vehicles or off-road vehicles, the gradeability is usually defined as the maximum grade or grade angle that the vehicle can overcome in the whole speed range.

When the vehicle drives on a road with relative small grade and constant speed, the tractive effort and resistance equilibrium can be written as

$$\frac{T_p i_0 i_g \eta_t}{r_d} = Mg f_r + \frac{1}{2} \rho_a C_D A_f V^2 + Mgi. \tag{2.51}$$

Thus,

$$i = \frac{T_p i_0 i_g \eta_t / r_d - Mg f_r - 1/2 \, \rho_a C_D A_f V^2}{Mg} = d - f_r, \tag{2.52}$$

where

$$d = \frac{F_t - F_w}{Mg} = \frac{T_p i_0 i_g \eta_t / r_d - 1/2 \, \rho_a C_D A_f V^2}{Mg} \tag{2.53}$$

is called the performance factor. When the vehicle drives on a road with a large grade, the gradeability of the vehicle can be calculated as

$$\sin \alpha = \frac{d - f_r \sqrt{1 - d^2 + f_r^2}}{1 + f_r^2}. \tag{2.54}$$

The gradeability of the vehicle can also be obtained from the diagram in Figure 2.24 or 2.25, in which the tractive effort and resistance are plotted.
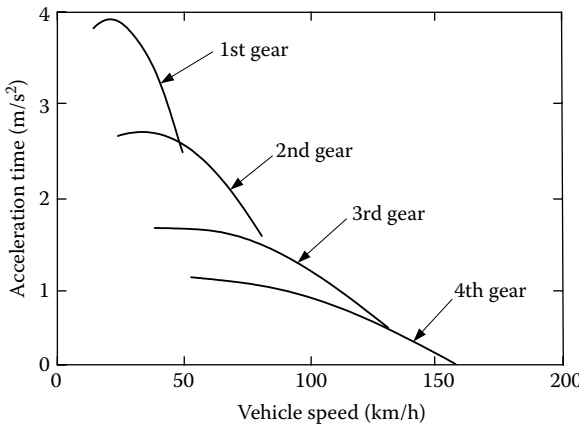
2.7.3 Acceleration Performance

The acceleration performance of a vehicle is usually described by its acceleration time and distance covered from zero speed to a certain high speed (0 to 96 km/h or 60 mph, for example) on level ground. Using Newton's second law (Equation 2.13), the acceleration of the vehicle can be written as

$$a = \frac{dV}{dt} = \frac{F_t - F_f - F_w}{M\delta}$$

$$= \frac{T_p i_0 i_g \eta_t / r_d - Mg f_r - 1/2 \, \rho_a C_D A_f V^2}{M\delta} = \frac{g}{\delta}(d - f_r), \tag{2.55}$$

where δ is called rotational inertia factor, considering the equivalent mass increase due to the angular moments of the rotating components. The mass factor can be written as

$$\delta = 1 + \frac{I_w}{Mr_d^2} + \frac{i_0^2 i_g^2 I_p}{Mr^2}, \tag{2.56}$$

FIGURE 2.26 Acceleration rate of a gasoline-engine-powered vehicle with four-gear transmission.

where I_w is the total angular inertial moment of the wheels and I_p is the total angular inertial moment of the rotating components associated with the power plant. Calculation of the mass factor, δ, requires knowing the values of the mass moments of inertia of all the rotating parts. In the case where these values are not known, the rotational inertia factor, δ, for a passenger car would be estimated using the following empirical relation:

$$\delta = 1 + \delta_1 + \delta_2 i_g^2 i_0^2, \tag{2.57}$$

where δ_1 represents the second term on the right-hand side of Equation 2.56, with a reasonable estimate value of 0.04, and δ_2 represents the effect of the power-plant-associated rotating parts, with a reasonable estimate value of 0.0025.

Figures 2.26 and 2.27 show the acceleration rate along with vehicle speed for a gasoline-engine-powered vehicle with a four-gear transmission and an electric-motor-powered vehicle with a single-gear transmission.
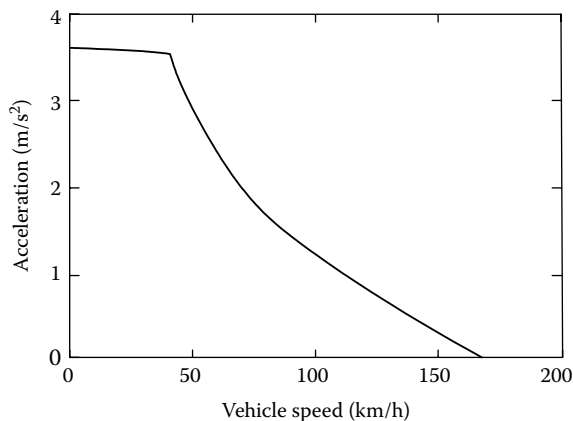
From Equation 2.55, the acceleration time, t_a, and distance, S_a, from low-speed V_1 to high-speed V_2 can be written, respectively, as

$$t_a = \int_{V_1}^{V_2} \frac{M\delta}{T_p i_g i_0 \eta_t / r_d - Mg f_r - 1/2 \rho_a C_D A_f V^2} \, dV \tag{2.58}$$
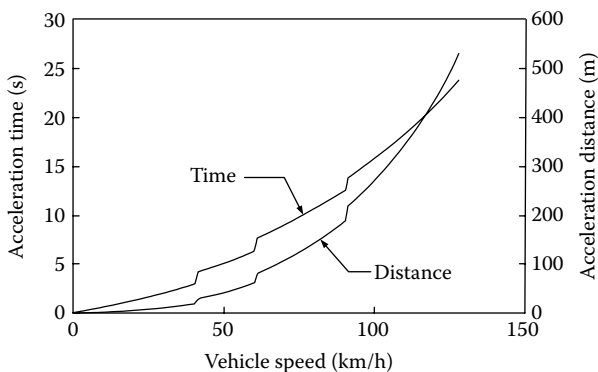
and

$$S_a = \int_{V_1}^{V_2} \frac{M\delta V}{T_p i_g i_0 \eta_t / r_0 - Mg f_r - 1/2 \, \rho_a C_D A_f V^2} \, dV. \tag{2.59}$$
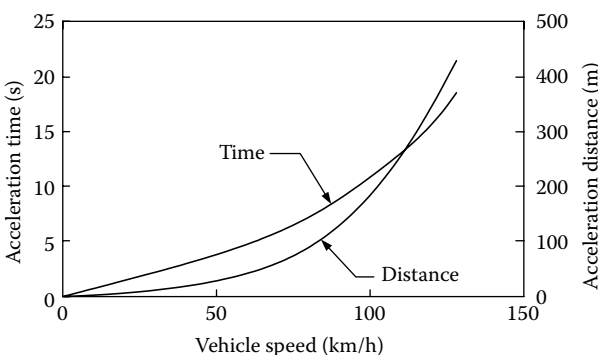
In Equations 2.58 and 2.59, the torque of the power plant T_p is a function of speed (see Figures 2.13 and 2.14), which in turn is a function of vehicle speed

FIGURE 2.27 Acceleration rate of an electric-machine-powered vehicle with a single-gear transmission.

FIGURE 2.28 Acceleration time and distance along with vehicle speed for a gasoline-engine-powered passenger car with four-gear transmission.

FIGURE 2.29 Acceleration time and distance along with vehicle speed for an electric-machine-powered passenger car with single-gear transmission.
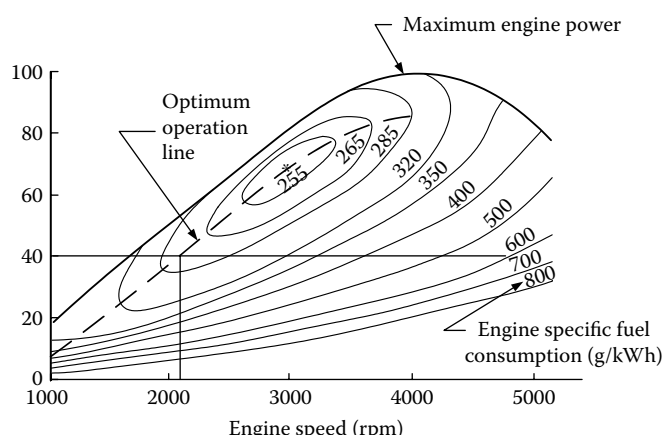
(see Equations 2.23 and 2.37) and gear ratio of the transmission. This makes it difficult to solve Equations 2.58 and 2.59 analytically. Numeral methods are usually used. Figures 2.28 and 2.29 show the acceleration time and distance along with vehicle speed for a gasoline-engine-powered vehicle and an electric-machine-powered EV, respectively.

2.8   Operating Fuel Economy

The fuel economy of a vehicle is evaluated by the amount of fuel consumption per 100 km traveling distance (liters/100 km) or mileage per gallon fuel consumption (miles/gallon), which is currently used in the United States. The operating fuel economy of a vehicle depends on a number of factors, including fuel consumption characteristics of the engine, gear number and ratios, vehicle resistance, vehicle speed, and traffic conditions.

2.8.1   Fuel Economy Characteristics of IC Engines

The fuel economy characteristic of an IC engine is evaluated by the amount of fuel per kWh energy output, which is referred to as the specific fuel consumption (g/kWh). The typical fuel economy characteristic of a gasoline engine is shown in Figure 2.30. The fuel consumption is quite different from one operating point to another. The optimum operating points are close to the points of full load (wide open throttle). The speed of the engine also has a significant influence on the fuel economy. With a given power output, the fuel consumption is usually lower at low speed than at high speed. For instance, when

FIGURE 2.30   Fuel economy characteristics of a typical gasoline engine.

the engine shown in Figure 2.30 has a power output of 40 kW, its minimum specific fuel consumption would be 270 g/kWh, at a speed of 2080 rpm.

For a given power output at a given vehicle speed, the engine operating point is determined by the gear ratio of the transmission (refer to Equations 2.32 and 2.47). Ideally, a continuous variable transmission can choose the gear ratio, in a given driving condition, to operate the engine at its optimum operating point. This advantage has stimulated the development of a variety of continuous variable transmissions, including frictional drive, hydrodynamic drive, hydrostatic drive, and hydro-mechanical variable drive.

2.8.2 Computation of Vehicle Fuel Economy

Vehicle fuel economy can be calculated by finding the load power and speed, and thus the specific fuel consumption of the engine. The engine power output is always equal to the resistance power plus the dynamic power for acceleration of the vehicle, that is,

$$P_e = \frac{V}{\eta_t}\left(F_f + F_w + F_g + M_v\delta\frac{dV}{dt}\right). \tag{2.60}$$

Equation (2.60) can be written as

$$P_e = \frac{V}{1000\eta_t}\left(Mgf_r\cos\alpha + \frac{1}{2}\rho_aC_DA_fV^2 + Mg\sin\alpha + M\delta\frac{dV}{dt}\right)(\text{kW}). \tag{2.61}$$

The engine speed, related to vehicle speed and gear ratio, can be expressed as
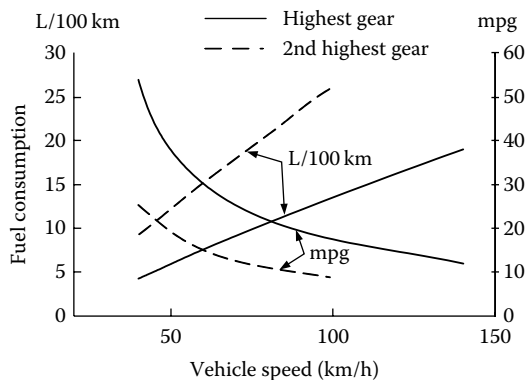
$$N_e = \frac{30Vi_gi_0}{\pi r_d}. \tag{2.62}$$

After determination of the engine power and speed by Equations 2.60 and 2.61, the value of the specific fuel consumption, g_e, can be found in the graph of the engine fuel economy characteristics as shown in Figure 2.30. The time rate of fuel consumption can be calculated by

$$Q_{fr} = \frac{P_eg_e}{1000\gamma_f}(\text{l/h}), \tag{2.63}$$

where g_e is the specific fuel consumption of the engine in g/kWh and γ_f is the mass density of the fuel in kg/L. The total fuel consumption within the total distance, S, at a constant cruising speed, V, is obtained by
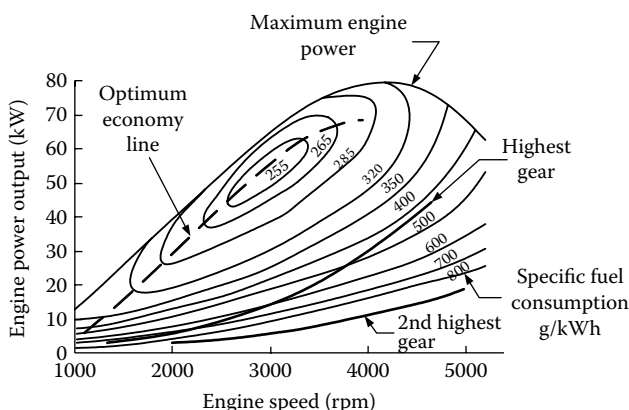
$$Q_s = \frac{P_eg_e}{1000\gamma_f}\frac{S}{V}. \tag{2.64}$$
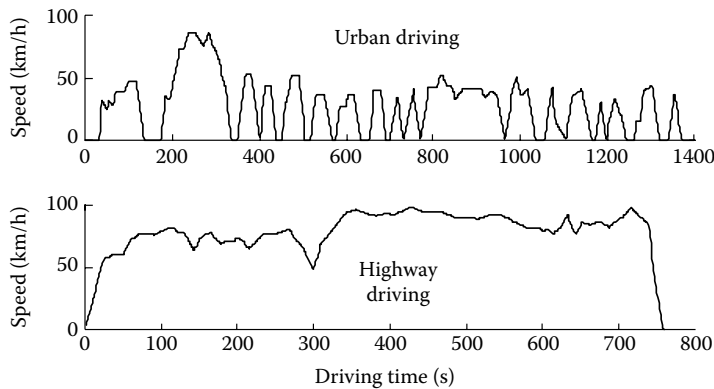
FIGURE 2.31   Fuel economy characteristics of a typical vehicle at constant speed.

Figure 2.31 shows an example of the fuel economy characteristics of a gasoline vehicle at a constant cruising speed on level ground. This figure indicates that with high speed, the fuel consumption increases because the aerodynamic resistance power increases with the speed cubed. This figure also indicates that with a high-speed gear (small gear ratio), the fuel economy of the vehicle can be enhanced due to the reduced engine speed at a given vehicle speed and decreased gear ratio.

Figure 2.32 shows the operating points of the engine at a constant vehicle speed, with the highest gear and the second highest gear. It indicates that the engine has a much lower operating efficiency in low gear than in high gear. This is the reason why the fuel economy of a vehicle can be improved with more gear transmission and continuous variable transmission.

FIGURE 2.32   Operating point of the engine at a constant speed with highest gear and second highest gear.

FIGURE 2.33 EPA FTP75 urban and highway drive cycles.

It should be noted that because of the complexity of vehicle operation in the real world, fuel consumption at a constant speed (as shown in Figure 2.12) cannot accurately represent fuel consumption for a vehicle under real driving conditions. Thus, various drive cycles have been developed to simulate real driving conditions, such as EPA FTP75 urban and highway, LA92, ECE-15, Japan1015, and so on. The drive cycles are usually represented by the speed of the vehicle along with the driving time. Figure 2.33 shows the urban and highway drive cycles of EPA FTP75 used in the United States.

To calculate fuel consumption in a drive cycle, the total fuel consumption can be obtained by the summation of fuel consumption in each time interval, Δt_i,
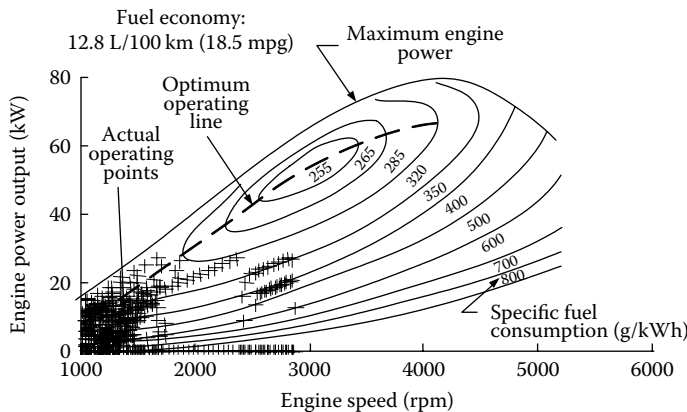
$$Q_{tc} = \sum_i \frac{P_{ei} g_{ei}}{1000 \gamma_f} \Delta t_i \tag{2.65}$$

where P_{ei} is the average power of the engine in the ith time interval in kW, g_{ei} is the average specific fuel consumption of the engine in the ith time interval in g/kWh, and Δt_i is the ith time interval in h. This calculation can be performed with a numerical method using a computer program. Figures 2.34 and 2.35 show examples of the fuel economy and engine operating points in EPA FTP75 urban and highway drive cycle, respectively.

2.8.3 Basic Techniques to Improve Vehicle Fuel Economy
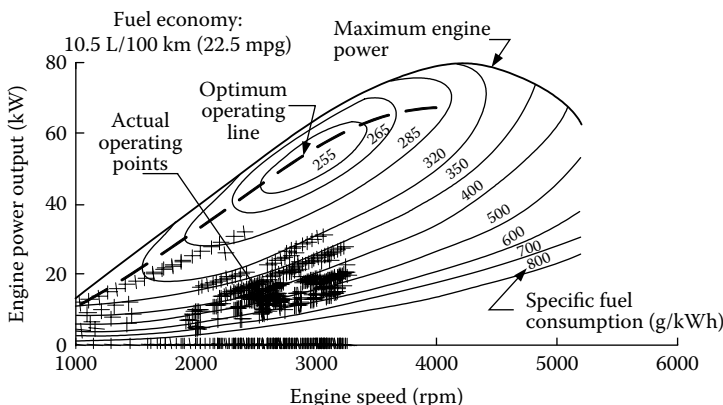
The effort to improve the fuel economy of vehicles has always been an ongoing process in the automobile industry. Fundamentally, the techniques used mainly include the following aspects:

1. *Reducing vehicle resistance*: Using light materials and advanced manufacturing technologies can reduce the weight of vehicles, in turn

FIGURE 2.34 Fuel economy and engine operating points in EPA FTP75 urban drive cycle overlapped on engine fuel consumption characteristics map.

reducing the rolling resistance and inertial resistance in acceleration, and therefore reducing the demanded power on the engine. The use of advanced technologies in tire production is another important method in reducing the rolling resistance of vehicles. For instance, steel wire plied radial tires have a much lower rolling resistance coefficient than conventional bias ply tires. Reducing aerodynamic resistance is also quite important at high speeds. This can be achieved by using a flow-shaped body style, a smooth body surface, and other techniques. Furthermore, improving transmission efficiency can reduce energy losses in the transmission. Proper transmission construction, good lubrication, proper adjustment and tightening of moving parts in the transmission, and so on will achieve this purpose.

FIGURE 2.35 Fuel economy and engine operating points in EPA FTP75 highway drive cycle overlapped on engine fuel consumption characteristics map.
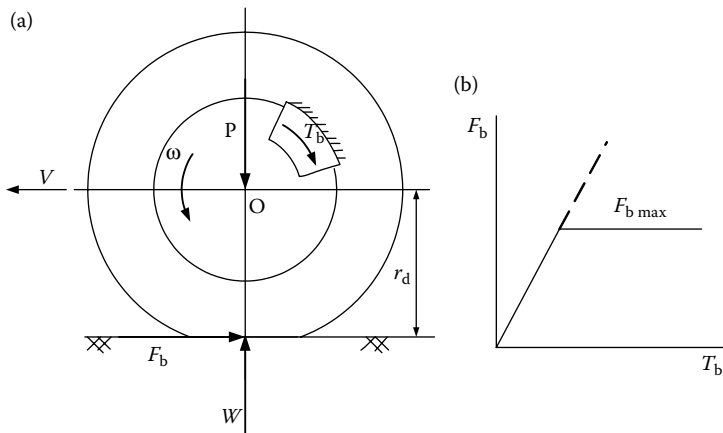
2. *Improving engine operation efficiency*: Improving engine operation efficiency has great potential to contribute to the improvement of vehicle fuel economy. There are many effective advanced techniques, such as accurate air/fuel ratio control with computer-controlled fuel injection, high thermal isolated materials for reducing thermal loss, varying ignition-timing techniques, active controlled valve and port, and so on.

3. *Properly matched transmission*: Parameters of the transmission, especially gear number and gear ratios, have much influence on operating fuel economy as described previously. In the design of the transmission, the parameters should be constructed so that the engine will operate close to its fuel optimum region.

4. *Advanced drive trains*: Advanced drive trains developed in recent years, such as new power plants, various hybrid drive trains, etc., can greatly improve the fuel economy of vehicles. Fuel cells have higher efficiency and lower emissions than conventional IC engines. Hybridization of a conventional combustion engine with an advanced electric motor drive may greatly enhance the overall efficiency of vehicles.

2.9 Brake Performance

The braking performance of a vehicle is undoubtedly one of the most important concerns that affect vehicle safety. In urban area driving, a significant amount of energy is consumed in braking. In recent years, more and more electric drives have been involved in vehicle traction, such as EVs, HEVs, and fuel-cell-powered vehicles; the electrification of the vehicle drive train makes it feasible to recover some of the energy lost in braking. Nevertheless, braking performance is still the first concern in the design of the vehicle brake system. Actually, when electric braking is introduced for braking energy recovery, mechanical braking by using frication is still required to ensure that the vehicle is stopped quickly. Consequently, a hybrid braking system is established. The design and control objectives of such a hybrid braking system are (1) sufficient braking force to quickly reduce the vehicle speed; (2) proper braking force distribution on the front and rear wheels to ensure vehicle stability during braking; and (3) recovery of as much braking energy as possible. This chapter discusses only the design principle of the vehicle brake system from the braking performance point of view. Regenerative braking will be discussed in Chapter 13.

2.9.1 Braking Force

The function of the vehicle brake system is to quickly reduce the vehicle speed while keeping the vehicle traveling direction stable and controllable

FIGURE 2.36   (a) Braking torque and braking force; (b) relationship between braking torque and braking force.

under various road conditions. These requirements are satisfied by applying sufficient braking force on the wheels and properly allocate the total braking force on the front and rear wheels.

Figure 2.36a shows a wheel during braking. The brake pad is pressed against the brake plate hydraulically or pneumatically, thus developing a frictional torque on the brake plate. This braking torque results in a braking force in the tire–ground contact area. It is just this braking force that tries to stop the vehicle. The braking force can be expressed as
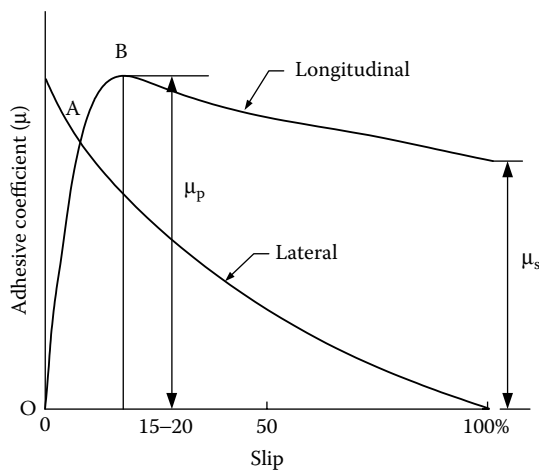
$$F_b = \frac{T_b}{r_d}. \tag{2.66}$$

The braking force increases with an increase in the braking torque. However, when the braking force reaches the maximum braking force that the tire–ground adhesion can support, it will not increase further, although the braking torque may still increase as shown in Figure 2.36b. This maximum braking force limited by the adhesive capability can be expressed as

$$F_{b\,max} = \mu W, \tag{2.67}$$

where μ is the adhesive coefficient of the tire–ground contact. Similar to the traction case, the adhesive coefficient varies with the slipping of the tire as shown in Figure 2.37. However, the slip is defined in braking as

$$s = \left(1 - \frac{r\omega}{V}\right) \times 100\%, \tag{2.68}$$

FIGURE 2.37 Variation of tractive effort coefficient with longitudinal slip of a tire.

where V is the vehicle translatory speed, ω is the wheel rotation speed, and r is the wheel radius. In this definition, when $\omega = 0$, that is, the wheel is completely locked, $s = 100\%$. Figure 2.37 shows the typical relationship between adhesive coefficient and wheel slip. There exists a maximum value in the slip range of 15–20%, and somewhat declining at 100% slip. Table 2.3 shows the average values of tractive effort coefficients on various roads.[2]
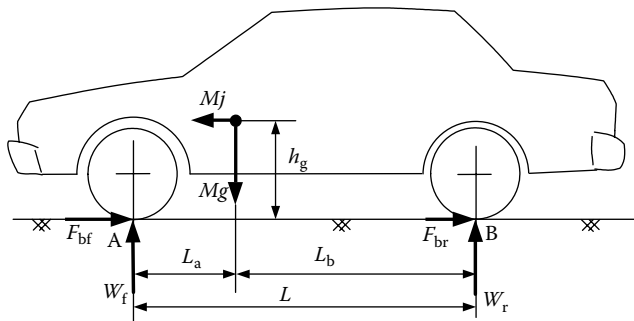
2.9.2 Braking Distribution on Front and Rear Axles

Figure 2.38 shows the forces acting on a vehicle during braking on a flat road. Rolling resistance and aerodynamic drag are ignored in this figure, because they are quite small compared to the braking forces. j is the deceleration of

TABLE 2.3

Average Values of Tractive Effort Coefficient on Various Roads

Surface	Peaking Values, μ_p	Slipping Values, μ_s
Asphalt and concrete (dry)	0.8–0.9	0.75
Concrete (wet)	0.8	0.7
Asphalt (wet)	0.5–0.7	0.45–0.6
Gravel	0.6	0.55
Earth road (dry)	0.68	0.65
Earth road (wet)	0.55	0.4–0.5
Snow (hard packed)	0.2	0.15
Ice	0.1	0.07

FIGURE 2.38   Force acting on a vehicle during braking on a flat road.

the vehicle during braking, which can be easily expressed as

$$j = \frac{F_{bf} + F_{br}}{M},$$ (2.69)

where F_{bf} and F_{br} are the braking forces acting on the front and rear wheels, respectively.

The maximum braking force is limited by the tire–ground adhesion and is proportional to the normal load acting on the tire. The actual braking force developed by the brake torque should also be proportional to the normal load so that both the front and the rear wheels obtain their maximum braking force at the same time. During braking, there is load transfer from the rear axle to the front axle. By considering the equilibrium of moments about the front and rear tire–ground contact points A and B, as shown in Figure 2.38, the normal loads on the front and rear axles W_f and W_r, with a vehicle deceleration rate, j, can be expressed as

$$W_f = \frac{Mg}{L}\left(L_b + h_g \frac{j}{g}\right)$$ (2.70)
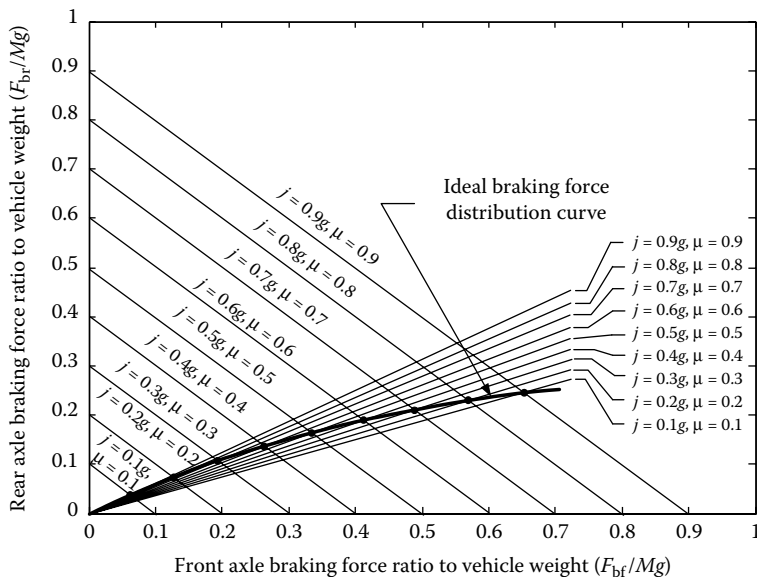
and

$$W_r = \frac{Mg}{L}\left(L_a - h_g \frac{j}{g}\right).$$ (2.71)

The braking forces applied on the front axle and the rear axle should be proportional to their normal load, respectively; thus, one obtains

$$\frac{F_{bf}}{F_{br}} = \frac{W_f}{W_r} = \frac{L_b + h_g j/g}{L_a - h_g j/g}.$$ (2.72)

Combining Equations 2.69 and 2.72, the ideal braking force distribution on the front and rear axles can be obtained as shown in Figure 2.39. When the braking is strong, both the front and rear wheels obtain their maximum ground

FIGURE 2.39 Ideal braking force distribution curve on the front and rear axles.

braking force, which is limited by the capability of the tire–ground adhesion [wheel lock for non-antilock brake system (ABS), or ABS starting to function to limit the braking force rising to avoid the wheels being locked]. In this case, the vehicle achieves its maximum deceleration rate as

$$|j_{\max}|_\mu = \frac{F_{bf\text{-}\max} + F_{br\text{-}\max}}{M} = \frac{(W_f + W_r)\mu}{M} = g\mu. \qquad (2.73)$$

The ideal braking force distribution curve (simply, I curve), as shown in Figure 2.39, is a nonlinear hyperbolic curve. If it is desired for the front and rear wheels to lock or the ABS to function at the same time on any road, the braking force on the front and rear axles must exactly follow this curve.

Completely following the I curve for the braking force distribution makes the system very complex in structure and control. However, with rapid advancement of electronics and microcontrol technologies, electric braking systems (EBSs) are being developed, which can greatly improve the braking performance compared with the traditional design used in most vehicles at the present. This technology will be briefly described in the regenerative braking chapter (Chapter 13).

Traditionally, the actual braking forces applied to the front and rear axles by the brake system are usually designed to have a fixed linear proportion. This proportion is represented by the ratio of the front axle braking force to

the total braking force of the vehicle, that is,

$$\beta = \frac{F_{bf}}{F_b},$$

(2.74)

where F_b is the total braking force of the vehicle ($F_b = F_{bf} + F_{br}$). β depends only upon the braking system design, such as the diameters of wheel cylinders in the front and rear wheels, and has nothing to do with the vehicle parameters. With a value of β, the actual braking forces on the front and rear axles, produced by the brake system, can be expressed as

$$F_{bf} = \beta F_b$$

(2.75)
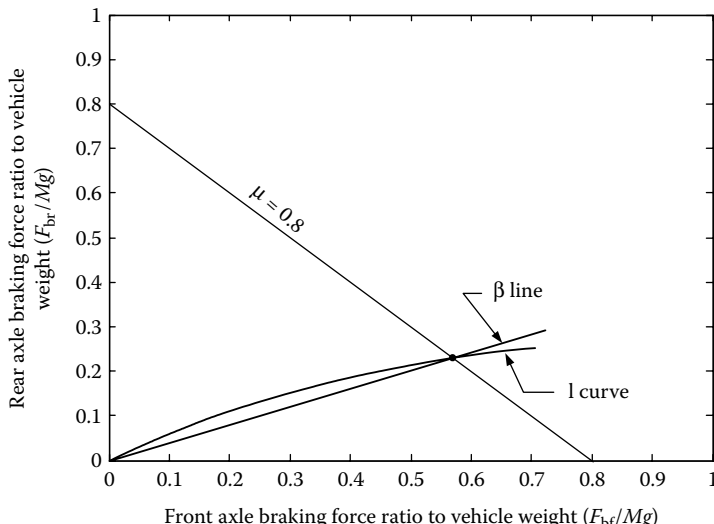
and

$$F_{br} = (1 - \beta)F_b.$$

(2.76)

Thus, one obtains

$$\frac{F_{bf}}{F_{br}} = \frac{\beta}{1 - \beta}.$$

(2.77)

Figure 2.40 shows the ideal and actual braking force distribution curves (labeled I and β curve). It is obvious that only one intersection point exists, at which the front and rear axles lock at the same time. This point represents

FIGURE 2.40   Ideal and actual braking force distribution curves.

one specific road adhesive coefficient, μ_0. Referring to Equation 2.72 in which j/g is replaced by μ_0 and Equation 2.77, one obtains

$$\frac{\beta}{1-\beta} = \frac{L_b + \mu_0 h_g}{L_a - \mu_0 h_g}. \tag{2.78}$$

From Equation (2.78) one can obtain μ_0 and β by
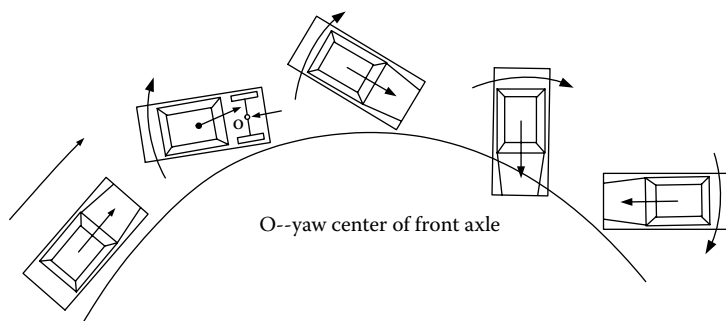
$$\mu_0 = \frac{L\beta - L_b}{h_g} \tag{2.79}$$

and
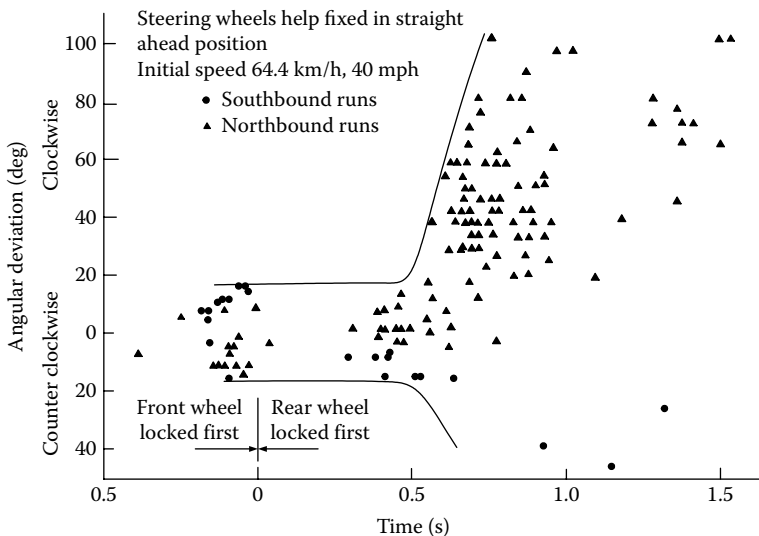
$$\beta = \frac{\mu_0 h_g + L_b}{L}. \tag{2.80}$$

During braking on the roads with the adhesive coefficient less than μ_0 (the region in which the β curve is below the I curve), the front wheels lock first, whereas when the road adhesive coefficient is larger than μ_0 (the region in which the β curve is above the I curve), the rear wheels lock first.

When the rear wheels lock first, the vehicle will lose directional stability, as shown in Figure 2.41, which shows the top view of a two-axle vehicle acted upon by the braking force and the inertia force. When the rear wheels lock, the capability of the rear tires to resist lateral forces is reduced to zero (refer to Figure 2.37). If some slight lateral movement of the rear wheels is initiated by side wind, road camber, or centrifugal force, a yawing moment due to the inertia force about the yaw center of the front axle will be developed. As the yaw motion progresses, the moment arm of the inertia force increases, resulting in an increase in yaw acceleration. As the rear end of the vehicle swings around 90°, the moment arm gradually decreases and eventually the vehicle rotates 180° with the rear end leading the front end.

O--yaw center of front axle

FIGURE 2.41 Loss of directional stability due to the lockup of rear wheels.

FIGURE 2.42 Angular deviation of a car when all four wheels do not lock at the same instant.

The lockup of front wheels will cause a loss of directional control, and the driver will no longer be able to exercise effective steering. It should be pointed out, however, that front wheel lockup does not cause directional instability. This is because whenever the lateral movement of the front wheels occurs, a self-correcting moment due to the inertial force of the vehicle about the yaw center of the rear axle will be developed. Consequently, it tends to bring the vehicle back to a straight line path. Figure 2.42 shows the measured angular deviation of a vehicle when the front and rear wheels do not lock at the same instant.[2]

Loss of steering control may be detected more readily by the driver and control may be regained by release or partial release of the brakes. Contrary to the case of front wheel lockup, when rear wheels lock and the angular deviation of the vehicle exceeds a certain level, control cannot be regained even by complete release of the brakes and by the most skilful driving. This suggests that rear wheel lockup is a more critical situation, particularly on a road with a low adhesive coefficient. Because the value of the braking force is low on slippery surfaces, the kinetic energy of the vehicle will dissipate at a low rate and the vehicle will experience a serious loss of directional stability over a considerable distance. Therefore, designers of vehicle brake systems must ensure that the rear wheels do not lock first.

The ABS, developed in recent years, can effectively prevent the wheels from lockup. This system employs speed sensors to detect the wheel rotating speed. When a wheel lockup is detected, the braking pressure control system reduces the pressure and brings the wheel back to its rotation.[3]

2.9.3 Braking Regulation and Braking Performance Analysis

2.9.3.1 Braking Regulation

As described above, if the real braking force distribution line β is below the ideal braking force distribution curve I as shown in Figure 2.40, the front wheels will be locked earlier than the rear wheels. This situation leads to stable behavior of the vehicle. This usually is the design, especially for passenger cars, which run at high speed. However, when the β line is much below the I curve, most of the braking force will be applied to the front wheel and a very small force to the rear wheels. This design will cause the problem of reduced utilization of road adhesive capability. That is, when the front wheels are locked and the rear wheels are not locked, the maximum braking force on the rear wheels will never be used. In order to avoid this situation, some brake design regulations have been developed. A typical one is ECE brake regulation.

The ECE brake design regulation for passenger cars is expressed by

$$\frac{F_{bf}}{W_f} \geq \frac{F_{br}}{W_r}. \tag{2.81}$$

Equation 2.81 shows that the rear wheels are never locked before the front wheels. In other words, the real braking force distribution curve β is always below the I curve. ECE also dictates the minimum braking force on rear wheels, as expressed by

$$\frac{j}{g} \geq 0.1 + 0.85(\mu - 0.2), \tag{2.82}$$
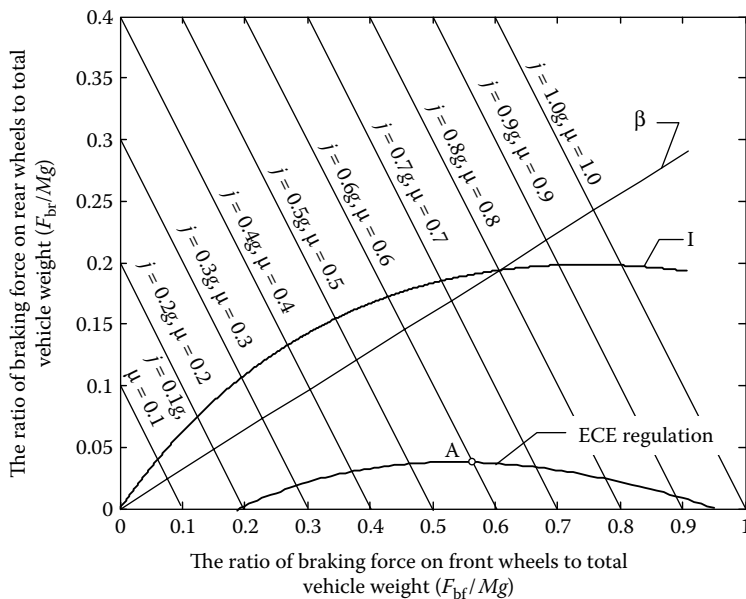
where j is the deceleration rate of the vehicle when the front wheels are locked on the road with adhesive coefficient, μ. The physical meaning of this equation is that when the front wheels are locked, the rear braking force must be large enough to make the vehicle yield a deceleration rate not smaller than the value dictated by Equation 2.82.

Braking forces of the front and rear wheels on the boundary of ECE regulation described by Equation 2.82 can be calculated as follows.

ECE regulation stipulates that the condition for Equation 2.81 is the front wheels being locked. Thus the braking force on the front wheels on the road with the adhesive coefficient, μ, is

$$F_{bf} = W_f \mu, \tag{2.83}$$

where W_f is the vertical loading on the front wheels, which is expressed at the vehicle deceleration rate by Equation 2.70, and the total braking force of the vehicle at the deceleration rate, j, is expressed by Equations 2.69 and 2.82 related to μ. Using all the equations mentioned above, the front and rear braking force can be calculated as shown in Figure 2.43. It must be noted that

FIGURE 2.43   Minimum braking force on rear wheels stipulated by ECE regulation.

in Figure 2.43, the front and rear wheel braking forces on the ECE regulation curve at a deceleration rate j (point A with $j = 0.6g$, for example) does not mean that the road adhesive coefficient is $\mu = 0.6$, but larger than it, due to the unlocked rear wheels.

Obviously, the real braking force distribution achieved by brake system design must fall into the area between the I curve and the ECE regulation curve.

2.9.3.2 Braking Performance Analysis

As mentioned above, the vehicle with the traditional brake system design of a straight line real braking force distribution locks up its front and rear wheels simultaneously only on one kind of road with adhesive coefficient μ_0. On other roads, the front or the rear wheels will lock up before the other one. For fully understanding the braking force scenarios on the front and rear wheels after the front or rear wheels lock, further analysis is introduced. This is helpful for the design of advanced braking systems for electric, hybrid electric, and fuel cell vehicles, which not only need to meet the braking performance requirements, but also are capable of recapturing braking energy as much as possible.

1. *The case of locked front wheels and unlocked rear wheels*: When the front wheels are locked, the braking force on them is expressed as

Equation 2.83. With the vehicle deceleration rate, j, the vertical load on the front wheels is expressed as Equation 2.70. Thus, the braking force on the front wheels can be expressed as

$$F_{bf} = \frac{Mg\mu}{L}\left(L_b + \frac{j}{g}h_g\right). \tag{2.84}$$

Since

$$F_{bf} + F_{br} = Mj, \tag{2.85}$$

thus

$$F_{bf} = \frac{Mg\mu}{L}\left(L_b + \frac{F_{bf} + F_{br}}{Mg}h_g\right). \tag{2.86}$$

Finally, we obtain

$$F_{br} = \frac{L - \mu h_g}{\mu h_g}F_{bf} - \frac{MgL_b}{h_g}. \tag{2.87}$$

With different road adhesive coefficient, μ, Equation 2.87 generates a group of lines (referred to as f lines) to represent the relationship of the braking forces on the front and rear wheels when the front wheels are locked and the rear wheels are not locked, as shown in Figure 2.44.
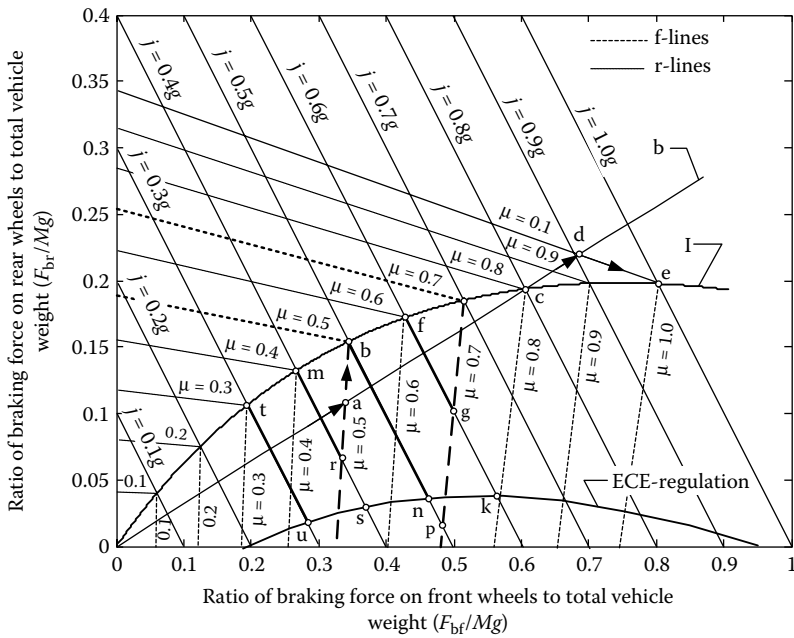
2. *The case of locked rear wheels and unlocked front wheels*: Similarly, when the rear wheels are locked and the front wheels are not, the braking force on the rear wheels against the braking force on the front wheels on roads with different adhesive coefficients can be expressed as

$$F_{br} = \frac{-\mu h_g}{L + \mu h_g}F_{bf} + \frac{\mu MgL_a}{L + \mu h_g}. \tag{2.88}$$

The lines generated by Equation 2.88 on roads with different adhesive coefficients are referred to as r lines as shown in Figure 2.44.

3. *Braking process analysis*: Using the diagram in which the I curve, the β line, the ECE regulation curve, the f lines, and the r lines are plotted, as shown in Figure 2.44, the detailed braking process can be analyzed as follows:

(a) *On a road with $\mu < \mu_0$ ($\mu = 0.5$ and $\mu_0 = 0.8$ in Figure 2.44 as the analyzing case)* On a road with $\mu < \mu_0$, the braking forces on the front and rear wheels are increased, as the brake pedal is depressed, along the real braking distribution line β, until point a: the intersection point of the β line and the f line with $\mu = 0.5$, where the front wheels are locked, but the rear wheels are not. Further depressing the brake pedal will cause faster increase in

FIGURE 2.44   Braking process analysis on roads with different adhesive coefficients.

the braking force on the rear wheels and slow increase in the braking force on the front wheels, along the f line of $\mu = 0.5$, until we reach point b, where the rear wheels are also locked and the vehicle achieves its maximum deceleration of $j = \mu g = 0.5g$. This case will not cause vehicle instability.

(b) *On a road with $\mu > \mu_0$ ($\mu = 1.0$ and $\mu_0 = 0.8$ in Figure 2.44 as the analyzing case)*   Similarly, when the brake pedal is depressed, the braking forces on the front and rear wheels rise along the β line until point d: the intersection point of the β line and the r line with $\mu = 1.0$, where the rear wheels are locked but the front wheels are not. Further depressing the brake pedal will cause the braking forces to develop along the r line with $\mu = 1.0$, finally reaching point e, where the front wheels are locked and the vehicle achieves its maximum deceleration rate of $j = \mu g = 1.0g$. In this process, the braking force on the rear wheels has slightly decreased due to the load shifting from the rear to the front wheels. This case will cause vehicle instability.

(c) *On a road with $\mu = \mu_0$ ($\mu = 0.8$ and $\mu_0 = 0.8$ in Figure 2.44 as the analyzing case)*   Obviously, the front and rear wheels will be locked simultaneously at point c, where the vehicle achieves its

maximum deceleration rate of $j = \mu g = 0.8g$. This is the ideal case.

4. *Maximum available braking force on front wheels*:   In electric, hybrid electric, and fuel cell passenger cars, electric motors are mostly employed to drive the front wheels. This means that regenerative braking is only available for the front wheels. In the braking system design and control (mechanical and electrical), more braking energy should be allocated to the front wheels so as to increase the braking energy that is available for recovering, under the conditions of meeting brake regulation.

As shown in Figure 2.44, when the commanded braking deceleration rate, j, is smaller than μg, the braking forces on the front and rear wheels can be varied in a range rather than a specified point. For example, when $\mu = 0.7$ and $j = 0.6g$, this range is between point f and point g specified by the heavy solid line in Figure 2.44. Obviously, the maximum braking force on the front wheels is dictated by point g. However, if less deceleration rate is commanded on the same road, the variation range of the braking force will be larger. For instance, when $j = 0.5g$ and $\mu = 0.7$, the range is from point b to point p. However, it violates the ECE regulation, and therefore the maximum braking force on the front wheels is dictated by point n. Similarly, when $\mu = 0.5$ and $j = 0.4g$, the maximum braking on the front wheels is specified by point r, rather than s, and when $j = 0.3$ by point u. It is obvious that, with a small difference between deceleration rate (g) and road adhesive coefficient, the maximum braking force is usually dictated by the f lines, and naturally meeting the ECE regulation. However, when the deceleration rate (g) is much smaller than the road adhesive coefficient (e.g., slight braking on a good road), the ECE regulation will dictate the maximum braking force on the front wheels.

The analysis above provides the basis for design and control of the hybrid brake system (mechanical plus electrical) of electric, hybrid electric, and fuel cell vehicles. More details will be discussed in the regenerative braking chapter.

References

1. J. Y. Wong, *Theory of Ground Vehicles*, John Wiley & Sons, New York, 1978.
2. Bosch, *Automotive Handbook*, Robert Bosch GmbH, Karlsruhe, Germany, 2000.
3. S. Mizutani, *Car Electronics*, Sankaido Co., Minato-Ku, Tokyo, Japan, 1992.

3

Internal Combustion Engines

The IC engine is the most popular power plant for motor vehicles. In the foreseeable future, it will still be the dominant vehicular power plant. In HEVs, the IC engine will also be the first selection as a primary power source. However, the operation of an HEV differs from that of a conventional motor vehicle. The engine in an HEV runs for a longer time at high power and does not require its power to be changed frequently. A specifically designed and controlled engine for hybrid vehicle applications has not been fully developed. In this chapter, the commonly used four-stroke (4S) IC engine and other types of engines, which can be possibly used in hybrid vehicles, such as two-stroke (2S) engines, rotary engines, Stirling engines, and gas turbine engines, are reviewed. For more details, readers may consult the relevant literature.
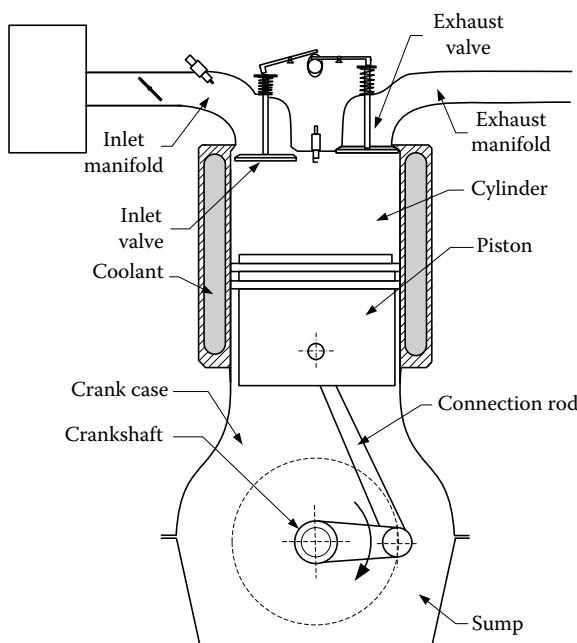
3.1 4S, Spark-Ignited IC Engines

3.1.1 Operating Principles

A 4S, spark-ignited (SI), IC engine is illustrated in Figure 3.1. It consists of subsystems including powering (crankshaft, connection rod, pistons and cylinders), intake and exhaust (air filter, throttle, inlet and exhaust manifolds, inlet and exhaust valves, and valve control cams), fuel supply [fuel tank (not shown), fuel pump (not shown), and fuel injectors], ignition [battery (not shown), ignition coils (not shown), distributor (not shown), and spark plugs], cooling [coolant, water pump (not shown), radiator (not shown)], and lubricating (not shown).
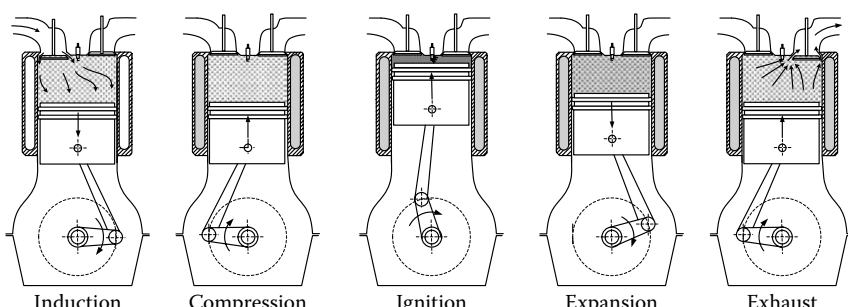
The combustion of the air/fuel mixture formed within the inlet manifold and trapped in the cylinder produces heat, so that the temperature and pressure in the cylinder increase quickly. Thus, the piston is forced to move down. The connection rod transfers the linear movement of the piston into rotary motion of the crankshaft.

A 4S, SI engine has four instinctive processes corresponding to the four strokes of each piston[1,2] (Figure 3.2).

FIGURE 3.1   4S, SI gasoline engine.

1. *Induction stroke (cylinder-filling process)*: The inlet valve is open, the exhaust valve is closed, and the piston travels down the cylinder, drawing in a charge of the air/fuel mixture formed within the inlet manifold.

2. *Compression stroke*: Both inlet and exhaust valves are closed, and the piston goes up the cylinder, compressing the fuel/air mixture in the cylinder. As the piston approaches the top dead center (TDC), the spark plug produces a spark to ignite the air/fuel mixture.

FIGURE 3.2   Four strokes of a spark-ignition engine.

3. *Expansion stroke (power producing or working process)*: There is combustion propagation through the charge, raising the temperature and pressure in the cylinder, moving the piston down. At the end of the expansion stroke, the exhaust valve opens and irreversible expansion of the exhaust gases blows out the exhaust valve, which is termed "blow-down."

4. *Exhaust stroke*: The exhaust valve remains open, and as the piston travels up the cylinder, the remaining gases in the cylinder are expelled. At the end of the exhaust stroke, the exhaust valve closes. However, some exhaust gas residuals will be left. This exhaust dilutes the next charge. Following this stroke, the induction stroke of the next cycle starts.

Since the cycle is completed only once every two revolutions of the crankshaft, the gear driven camshaft (for opening and closing the valves) has to be driven by the mechanism operating at half crankshaft speed (engine speed). Some of the power from the expansion stroke is stored in the flywheel to provide the energy for another three strokes.

3.1.2 Operation Parameters

3.1.2.1 Rating Values of Engines

The most common parameters for engine performance are as follows:

Maximum rated power: The highest power that an engine is allowed to develop for a short period of operation.
Normal rated power: The highest power that an engine is allowed to develop in continuous operation.
Rated speed: The rotational speed of the crankshaft, at which the rated power is developed.
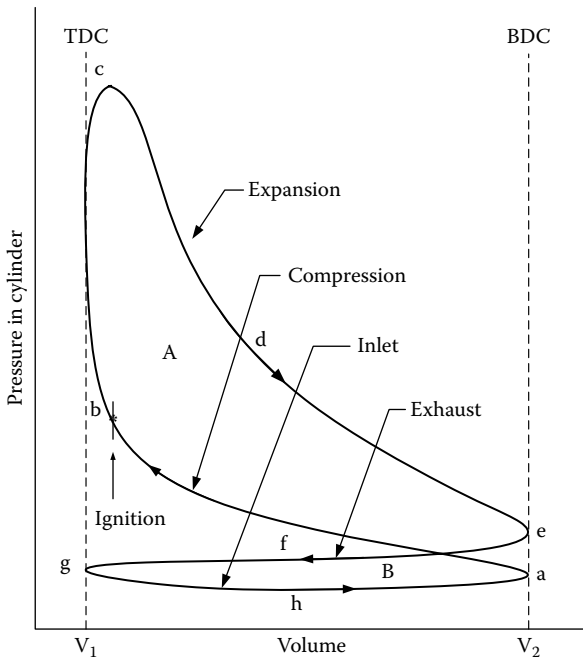
For vehicle application, engine performance is more precisely defined by the following:

1. The maximum power (or maximum torque) available at each speed within the useful engine operating range.
2. The range of speed and the power over which engine operation is satisfactory.

3.1.2.2 Indicated Work per Cycles and Mean Effective Pressure

The torque performance of the 4S SI engine is determined by the pressure within the cylinder, as shown in Figure 3.3. In the induction stroke (g–h–a), the pressure in the cylinder is usually lower than the atmospheric pressure

FIGURE 3.3   Diagram of pressure versus volume.

because of the resistance of the airflow into the cylinder. In the compression stroke (a–b–c), the pressure increases with the upward movement of the piston. When the piston approaches the TDC, the spark plug produces a spark to ignite the air/fuel mixture trapped in the cylinder, and the pressure increases quickly. In the expansion stroke (c–d–e), the high-pressure gases in the cylinder push the piston downward, producing torque on the crankshaft. In the exhaust stroke (e–f–g), the gases in the cylinder are propelled out of the cylinder with a higher pressure than in the induction stroke.

The torque performance is usually evaluated by the gross work done in one cycle, usually called gross indicated work, $W_{c,in}$. The gross indicated work can be calculated by

$$W_{c,in} = \int_{area\ A} p\,dV - \int_{area\ B} p\,dV, \qquad (3.1)$$

where p is the pressure in the cylinder and V is the volume. The work done in area B is negative, because the pressure in the induction stroke is lower than that in the exhaust stroke. In order to achieve much work in one cycle, area A should be made as large as possible by increasing the pressure in the expansion stroke, and area B should be made as small as possible by increasing the pressure in the induction stroke and decreasing it in the exhaust stroke.

When the pressure in the induction stroke is greater than that in the exhaust stroke, the work in this area will become positive. This is the case of the supercharged engine.

The torque of an engine depends on engine size [engine displacement, which is defined as the volume that the piston sweeps from TDC to bottom dead center (BDC)]. A more useful relative performance measure is the mean effective pressure (mep), which is defined as the work per cycle per displacement:

$$\text{mep} = \frac{\text{work per cycle}}{\text{displacement of cylinder}}. \tag{3.2}$$

The mean effective pressure can be expressed in terms of torque as

$$\text{mep (kPa)} = \frac{2\pi n_R T \text{ (Nm)}}{V_d \text{ (dm}^3)}, \tag{3.3}$$

where n_R is the number of revolutions of the crankshaft for each power stroke per cylinder ($n_R = 2$ for 4S engines and $n_R = 1$ for 2S engines), T is the torque in N m, and V_d is the displacement of the engine. The torque of an engine depends only on the mean effective pressure in the cylinder and the engine displacement V_d. For a given engine size, increasing the mean effective pressure is the only method of increasing the engine torque. It should be noted that when dealing with mean effective pressure, one must clearly state whether it is *indicated* mep (imep), which is measured within the cylinder, or brake mep (bmep), which is measured on the crankshaft. The difference between them is that the imep includes the engine mechanical loss (it is gross) and bmep does not include the engine mechanical loss (it is net). Mechanical loss is discussed in the following section.

3.1.2.3 Mechanical Efficiency

Not all the power produced in the cylinder (indicated power) is available on the crankshaft. Part of it is used to drive engine accessories and overcome the frictions inside the engine. All of these power requirements are grouped together and called friction power P_f; thus

$$P_{ig} = P_b + P_f, \tag{3.4}$$

where P_b is brake power (useful power on the crankshaft). It is quite difficult to determine the friction accurately. In practice, one common approach for automotive engines is to drive or motor the engine on a dynamometer (operate the engine without firing it) and measure the power supplied by the dynamometer.

The ratio of brake power (useful power on the crankshaft) to indicated power is called mechanical efficiency, η_m:

$$\eta_m = \frac{P_b}{P_{ig}} = 1 - \frac{P_f}{P_{ig}}. \tag{3.5}$$

The mechanical efficiency of an engine depends on the throttle position as well as on the design and engine speed. Typical values for modern automotive engines with wide-open throttles are 90% at speeds below about 1800–2400 rpm, decreasing to 75% at maximum rated speed. As the engine is throttled, the mechanical efficiency decreases eventually to zero at idle operation.

By removing the engine mechanical loss from the indicated work or imep, one can obtain the network or bmep that is measured on the crankshaft. The maximum bmep of good engine designs is well established, and is essentially constant over a large range of engine sizes. Typical values for bmep are as follows. For naturally aspirated spark-ignition engines, maximum values are in the range 850–1059 kPa (125–150 psi) at the engine speed where maximum torque is produced. At the maximum rated power, bmep values are 10–15% lower. For turbocharged automotive spark-ignition engines, the maximum bmep is in the range 1250–1700 kPa (180–250 psi). At the maximum rated power, bmep is in the range of 900–1400 kPa (130–200 psi).

3.1.2.4   Specific Fuel Consumption and Efficiency

In engine tests, fuel consumption is measured as a flow rate—mass flow per unit time, $\dot{m}_f$. A more useful parameter is the *specific fuel consumption* (sfc)—the fuel flow rate per useful power output. It measures how efficiently an engine is using the fuel supplied to produce work:

$$\text{sfc} = \frac{\dot{m}_f}{P}, \tag{3.6}$$

where $\dot{m}_f$ is fuel flow rate and P is engine power. If the engine power P is measured as the net power from the crankshaft, the specific fuel consumption is called *brake specific fuel consumption* (bsfc). The sfc or bsfc is usually measured in SI units by the gram numbers of fuel consumed per kW power output per hour (g/kWh). Low values of sfc (bsfc) are obviously desirable. For SI engines, typical best values of bsfc are about 250–270 g/kWh.

Normally, a dimensionless parameter that relates the desirable engine output (work per cycle or power) to the necessary input (fuel flow) would have more fundamental value. The ratio of the work produced per cycle to the amount of fuel energy supplied per cycle that can be released in the combustion process is commonly used for this purpose. It is a measure of the

engine efficiency (fuel conversion efficiency) given as

$$\eta_f = \frac{W_c}{m_f Q_{HV}} = \frac{P}{\dot{m}_f Q_{HV}},$$ (3.7)

where W_c is the work done in one cycle, m_f is the fuel mass consumed per cycle, and Q_{HV} is the heating value of the fuel, which is defined as the heat released from unit fuel with complete combustion at standard conditions and the combustion products cooling down to their original temperature. Typical heating values for commercial HC fuels used in engines are in the range of 42–44 MJ/kg (11.7–12.2 kWh/kg). The dimensionless efficiency can be expressed by sfc as

$$\eta_f = \frac{1}{\text{sfc } Q_{HV}}.$$ (3.8)

3.1.2.5 Specific Emissions

The level of emission of oxides of nitrogen [nitric oxide (NO) and nitrogen dioxide (NO₂) usually grouped together as NO_x], carbon monoxide (CO), unburned HCs, and particulates are important engine operating characteristics. The concentrations of gaseous emissions in engine exhaust are usually measured in parts per million or percent by volume (mole fraction). Specific emissions are the flow rate of pollutant per power output:

$$sNO_x = \frac{\dot{m}_{NO_x}}{P},$$ (3.9)

$$sCO = \frac{\dot{m}_{CO}}{P},$$ (3.10)

$$sHC = \frac{\dot{m}_{HC}}{P},$$ (3.11)

$$s\text{part} = \frac{\dot{m}_{\text{part}}}{P}.$$ (3.12)

Alternatively, emission rates can be normalized by the fuel flow rate; an emissions index (EI) is commonly used as

$$EI_{NO_x} = \frac{\dot{m}_{NO_x}(\text{g/s})}{\dot{m}_f(\text{kg/s})},$$ (3.13)

with similar expressions for CO, HC, and particulates.

3.1.2.6 Fuel/Air and Air/Fuel Ratios

In engine testing, both the air mass flow rate, $\dot{m}_a$, and fuel mass flow rate, $\dot{m}_f$, are normally measured. The ratio of these flow rates is useful in defining

engine operating conditions:

$$\text{fuel/air ratio } (F/A) = \frac{\dot{m}_f}{\dot{m}_a} \quad \text{and} \quad \text{air/fuel ratio } (A/F) = \frac{\dot{m}_a}{\dot{m}_f}. \qquad (3.14)$$

The stoichiometric fuel/air ratio is defined as the mass ratio of fuel to air such that, with this mass ratio, the combustion can be chemically completed. For gasoline, the stoichiometric fuel/air ratio is 0.0685 (air/fuel ratio: 14.6). More conveniently, fuel/air equivalent ratio, ϕ, and air/fuel equivalent ratio, λ, are commonly used. The fuel/air equivalent ratio is defined as

$$\phi = \frac{(F/A)_{\text{actual}}}{(F/A)_s} \qquad (3.15)$$

and

$$\lambda = \frac{(A/F)_{\text{actual}}}{(A/F)_s}. \qquad (3.16)$$

For fuel-rich mixtures: $\phi > 1, \lambda < 1$.
For stoichiometric mixtures: $\phi = \lambda = 1$.
For fuel-lean mixtures: $\phi < 1, \lambda > 1$.
The normal operating range for a conventional SI engine using gasoline is $0.82 \leq \phi \leq 1.23$ or $0.056 \leq F/A \leq 0.083$.

3.1.2.7   Volumetric Efficiency

The intake system—air filter, intake manifold, throttle plate, intake port, and intake valve—restricts the amount of air that an engine of a given displacement can induct. The parameter used to measure the effectiveness of an engine's induction process is volumetric efficiency, η_v. Volumetric efficiency is defined as the volume flow rate of air into the intake system divided by the rate at which volume is displaced by the piston:

$$\eta_v = \frac{2\dot{m}_a}{\rho_{a,i} V_d N}, \qquad (3.17)$$

where $\rho_{a,i}$ is the inlet air density and N is the rpm of the engine. An alternative equivalent definition for volumetric efficiency is

$$\eta_v = \frac{m_a}{\rho_{a,i} V_d}, \qquad (3.18)$$

where m_a is the mass of air induced into the cylinder per cycle.

The inlet density may be taken either as the atmospheric air density (in which case η_v measures the pumping performance of the entire inlet system) or as the density in the inlet manifold (in which case η_v measures the pumping

performance of the inlet port and valve only). Typical maximum values of η_v for naturally aspirated engines are in the range of 80–90%. The volumetric efficiency for diesel is somewhat higher than for SI engines.

3.1.3 Relationships between Operation and Performance Parameters

The importance of the above-discussed parameters to engine performance becomes evident when power, torque, and mean effective pressure are expressed in terms of these parameters. For power P,

$$P = \frac{\eta_f m_a N Q_{HV}(F/A)}{n_R}.$$ (3.19)

For 4S engines, volumetric efficacy can be introduced, and Equation 3.19 can be expressed as

$$P = \frac{\eta_f \eta_v N V_d Q_{HV} \rho_{a,i}(F/A)}{n_R}.$$ (3.20)

For torque T,

$$T = \frac{\eta_f \eta_v V_d Q_{HV} \rho_{a,i}(F/A)}{4\pi}.$$ (3.21)

For mean effective pressure,

$$\text{mep} = \eta_f \eta_v Q_{HV} \rho_{a,i}(F/A).$$ (3.22)

The power per unit piston area, often called specific power, is a measure of the engine designer's success in using the available piston area regardless of cylinder size. From Equation 3.20, the specific power is

$$\frac{P}{A_p} = \frac{\eta_f \eta_v N L Q_{HV} \rho_{a,i}(F/A)}{2}.$$ (3.23)

Mean piston speed can be introduced using Equation 3.23:

$$\frac{P}{A_p} = \frac{\eta_f \eta_v \bar{S}_p Q_{HV} \rho_{a,i}(F/A)}{4},$$ (3.24)

where $\bar{S}_p$ is the mean piston speed.

These relationships illustrate the direct importance of the following parameters to engine performance:

1. High fuel conversion efficiency.
2. High volumetric efficiency.

3. Increasing the output of a given displacement engine by increasing the inlet air density.

4. Maximum fuel/air ratio that can be usefully burned in the engine.

5. High mean piston speed.

3.1.4 Engine Operation Characteristics

3.1.4.1 Engine Performance Parameters

The practical engine performance parameters of interest are power, torque, specific fuel consumption, and specific emissions. The power of the 4S engine can be expressed as

$$P = \frac{mep A_p \bar{S}_p}{4},\tag{3.25}$$

where mep is mean effective pressure, A_p is area of the piston head, and $\bar{S}_p$ is mean piston speed. The torque, T, is given by

$$T = \frac{mep V_d}{4\pi}.\tag{3.26}$$

Thus for well-designed engines, the maximum values of mean effective pressure and piston speed are either flow limited (in naturally aspirated engines) or stress limited (in turbocharged engines). Power is proportional to piston area and torque to displaced volume. For 4S engines, the mean effective pressure can be expressed as

$$mep = \eta_f \eta_v Q_{LHV} \rho_{a,i} \left(\frac{F}{A} \right).\tag{3.27}$$

The importance of high fuel conversion efficiency, volumetric efficiency (breathing capacity), and inlet air density is clear. Specific fuel consumption is related to the fuel conversion efficiency by

$$sfc = \frac{1}{\eta_f Q_{LHV}}.\tag{3.28}$$

These parameters have both brake and indicated values. The difference between these two quantities is the engine's friction (and pumping) requirements and their ratio is the mechanical efficiency (see Equation 3.5).
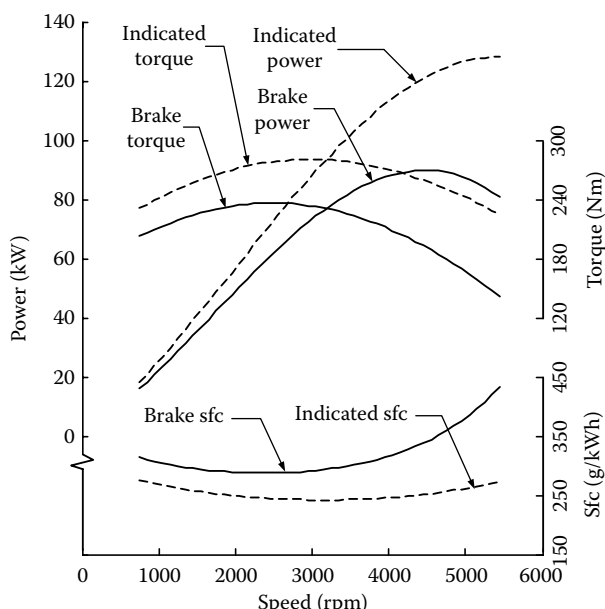
The relative importance of these parameters varies over an engine's operation speed and load range. The maximum rated or normal rated brake power and quantities such as bmep define an engine's full potential. The maximum brake torque (MBT) (and bmep derived from it) over the full speed range

indicates the engine's ability to obtain a high airflow through itself over the full speed range and to use that air effectively. Over the whole operating range—and most especially in those parts of that range where the engine will operate for a long period of time—engine fuel consumption, efficiency, and engine emissions are important.
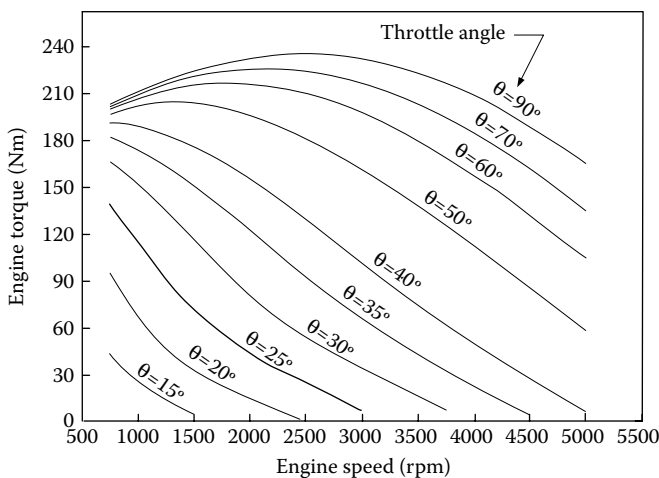
3.1.4.2 Indicated and Brake Power and Torque

The wide-open throttle operating characteristics of an SI engine are shown in Figure 3.4. Indicated power is the average rate of work transfer from gases in the cylinders to the piston during the compression and expansion strokes. Brake power is obtained by subtracting friction power from indicated power. The brake power shows a maximum value at about a speed slightly less than the maximum speed of the engine. Indicated torque shows a maximum value in the mid-speed range, which approximately corresponds to the speed at which volumetric efficiency has the maximum value. Brake torque decreases more than indicated torque at high speed because of more friction loss.

At partial load and fixed throttle position, these parameters behave similarly; however, at high speeds, torque decreases more rapidly than at full

FIGURE 3.4 Indicated and brake powers, torques, and specific fuel consumptions varying with engine speed.

FIGURE 3.5   Torque characteristics with engine throttle opening and engine speed.
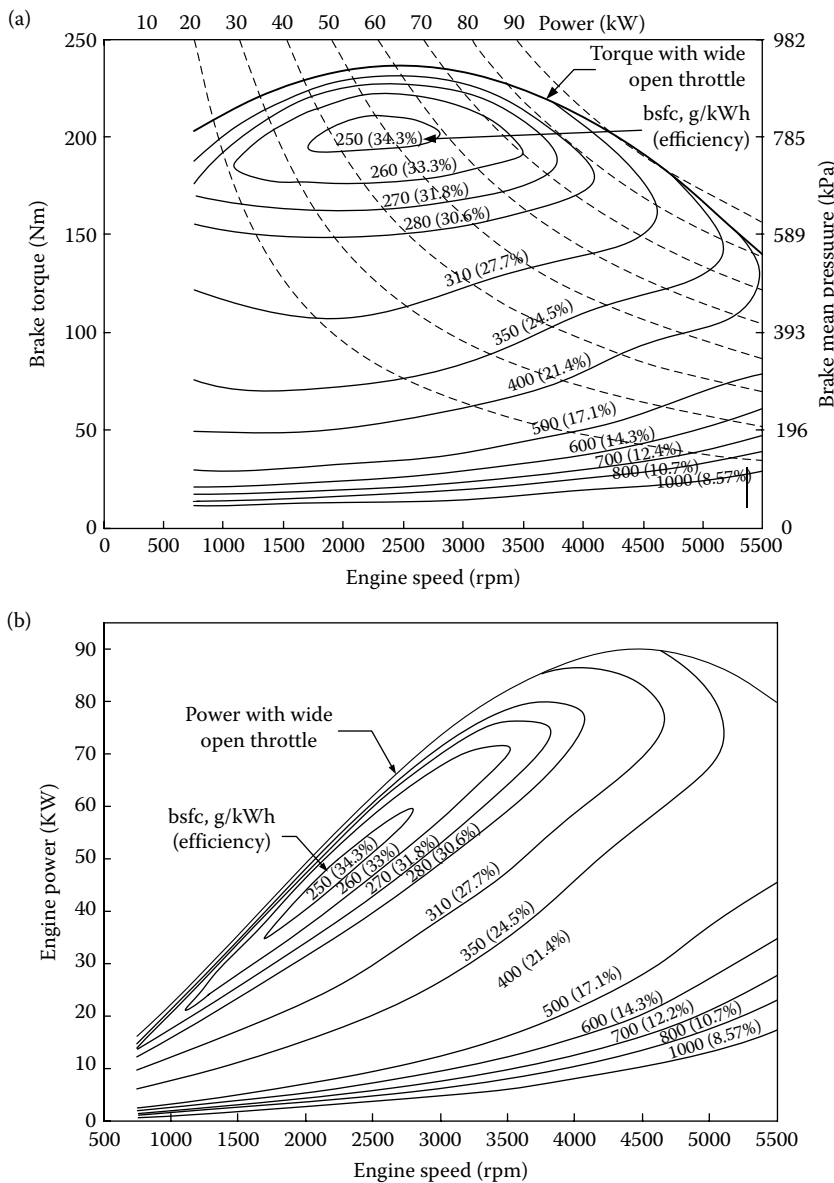
load as shown in Figure 3.5. The partially opened throttle causes more resistance to flowing air at higher speed and volumetric efficiency decreases. The pumping components of total friction also increase as the engine is throttled.

3.1.4.3   Fuel Consumption Characteristics

The fuel consumption characteristics (brake specific fuel consumption) of an engine vary widely with engine speed and load, as shown in Figure 3.6. Generally, an engine has its optimal operating region, in which the fuel consumption is minimized. This region usually locates in the middle of the speed range, corresponding to the maximum torque, where the losses in the induction and exhaust strokes are minimized. On the other hand, this region is close to full load operation (wide-open throttle), where the percentage of losses to the total indicated power is small. In vehicle design, the operating points of the engine should be close to this region in order to achieve high operating fuel economy.

3.1.5   Design and Operating Variables Affecting SI Engine Performance, Efficiency, and Emission Characteristics

The major design and operating variables that affect SI engine performance, efficiency, and emission characteristics are compression ratio, spark timing, valve timing, air/fuel ratio, and fraction of exhaust gases that are recycled for NO_x emission control.

FIGURE 3.6 Fuel consumption characteristics of a typical SI engine: (a) along with engine speed and torque and (b) along with engine speed and power.

3.1.5.1 Compression Ratio

The compression ratio of an engine is defined as the ratio of the total volume of a cylinder (V_2, as shown in Figure 3.3) to the volume when the piston moves to the TDC (V_1, as shown in Figure 3.3). Generally, a higher compression
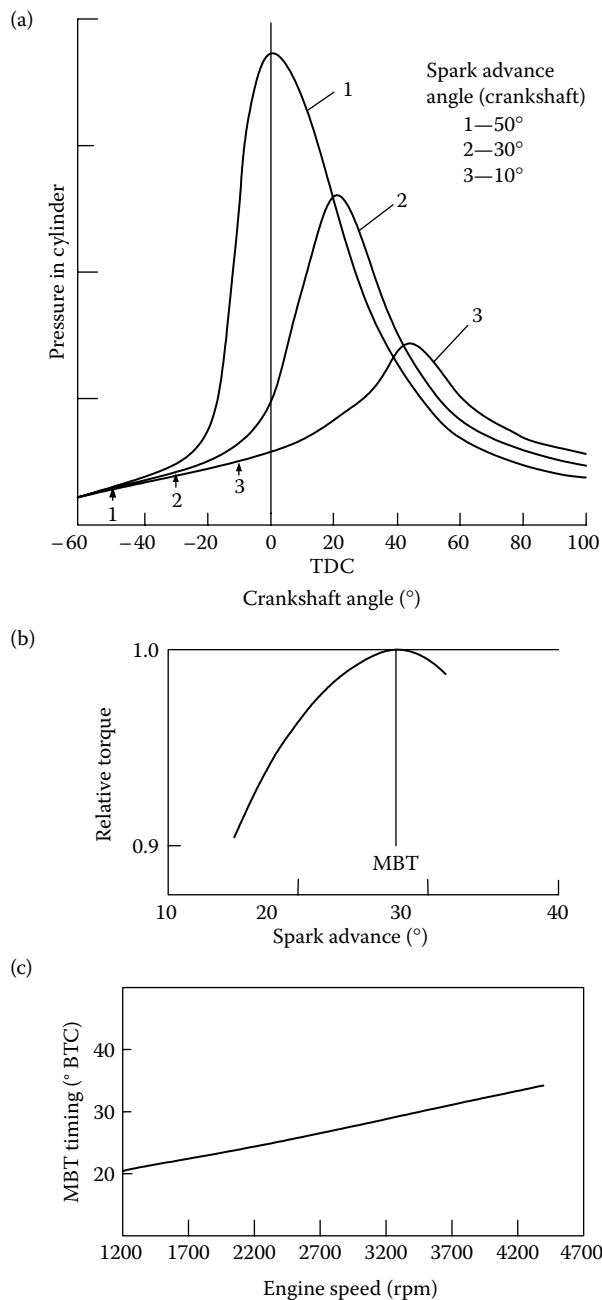
ratio yields high fuel conversion efficiency. The highest compression ratio of an SI engine is restricted by the octane number of the fuel. A high octane number allows higher compression ratio. For automotive gasoline SI engines, the compression ratio is in the range of 8–10.[1] Some additives are usually added to gasoline to enhance its octane number. Typical additives are lead and tetraethyl lead, which are very effective in enhancing the octane number of gasoline and have been widely used. However, lead and tetraethyl lead are very poisonous and have been prohibited in most places in the world. Other gasoline additives include methyl *tert*-butyl ether (MTBE), *tert*-amyl methyl ether and ethyl *tert*-butyl ether. Alcohols, such as methanol and ethanol, are also used as gasoline additives to enhance the octane number of gasoline.

3.1.5.2   Spark Timing

For SI engines under normal operating conditions, towards the end of the compression stroke, the spark plug produces a spark to ignite the mixture in the cylinder and combustion is initiated. Because propagation of the flame in the cylinder needs time, ignition must start before the end of the compression stroke. The degree of the crankshaft angle, from ignition starting to the end of the compression stroke, is called *spark advance* in degrees of crankshaft. Spark timing has a considerable effect on engine performance, efficiency, and exhaust emission.

Figure 3.7a shows the gas pressure in the cylinder with the crankshaft angle at different spark timings. Starting the ignition too soon (50° before TDC in Figure 3.7a) results in a high gas pressure acting on the piston in the compression stroke. Consequently, the negative work in the compression stroke increases and the positive work in the expansion stroke decreases, resulting in low average torque. Sometimes, too-early ignition causes abnormal combustion in the cylinder, which usually causes piston "knocking." "Knocking" is the most serious abnormal combustion phenomenon, which usually causes damage to mechanical parts such as crankshaft, bearings, and connection rods. Too-late ignition (10° before TDC in Figure 3.7a) results in low gas pressure in the cylinder, and thus low effective work. There exists an optimal spark timing at which the average engine torque reaches its maximum value. This optimal spark timing is called MBT timing as shown in Figure 3.7b. Spark timing, which is advanced or retarded from MBT timing, gives lower average torque. MBT timing is associated with the rate of flame development and propagation, the length of the flame travel path across the combustion chamber, and the details of the flame termination process after it reaches the wall. These depend on engine design, operating conditions, properties of fuel, air, burned gas mixture, etc. With a given design, engine speed has a great influence on MBT timing, and therefore the sparking timing should be adjusted with engine speed.

The time from ignition starting to reaching the maximum gas pressure in the cylinder changes slightly. Thus, with increasing engine speed, the sparking
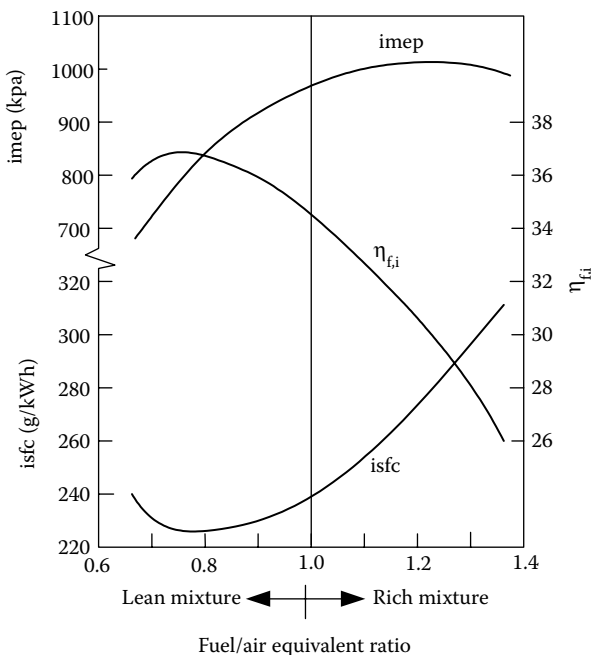
FIGURE 3.7 Effect of spark advance on engine performance: (a) cylinder pressure, (b) torque, and (c) MBT timing with engine speed.

advance should be increased as shown in Figure 3.7c. Correct spark timing is important, because NO and HC emissions vary significantly with spark timing.
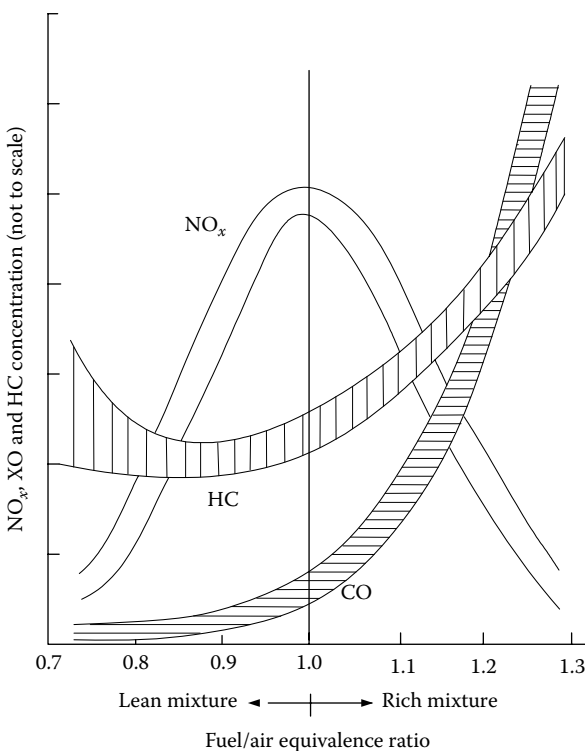
3.1.5.3   Fuel/Air Equivalent Ratio

Proper fuel/air (or air/fuel) ratio in the fuel/air mixture is a crucial factor that affects the performance, efficiency, and emission characteristics of an engine, as shown in Figure 3.8. The mean effective pressure peaks at slightly rich stoichiometry (between $\phi = 1$ and $\phi = 1.2$). However, the fuel conversion efficiency decreases as the mixture is enriched above the stoichiometry ($\phi > 1$) because part of the fuel is left after the combustion. When ϕ decreases, the fuel conversion efficiency increases because there exists sufficient oxygen in the cylinder to oxidize the fuel and the energy of the fuel is almost completely released as thermal energy. In SI engines, too lean mixtures will cause misfire. $\phi = 0.8$ would be the bottom limit. With lean mixtures, the combustion produces lower temperature in the cylinder and thus results in low mean effective pressure.

The fuel/air ratio has a dominant effect on emissions of SI engines as shown in Figure 3.9. Leaner mixtures produce lower emissions (NO_x, CO, and HC) until combustion becomes poor (and eventually misfire occurs).
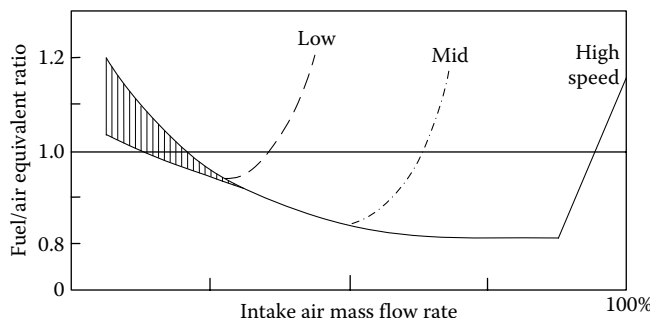
FIGURE 3.8   Fuel/air ratio effect on imep, fuel conversion efficiency, and isfc.

FIGURE 3.9   Fuel/air ratio effect on emissions.

When the fuel/air ratio is lower than a certain point (0.85 in Figure 3.9), HC emissions rise sharply and engine operation becomes erratic. The NO_x emissions have a different curve shape from those of CO and HC. they have a peak value close to the stoichiometric mixture, because NO_x tends to form at high temperature and pressure, which is the case of stoichiometric combustion.

Figure 3.9 indicates the complexities of emission control. In a cold engine with slow fuel vaporization, fuel flow is increased to provide an easily combustible fuel-rich mixture in the cylinder, until the engine warms up and this enrichment is removed. At part-load conditions, a lean mixture in the cylinder, which would produce lower HC and CO emissions and moderate NO_x emissions, could be used. The use of recycled exhaust to dilute the engine intake mixture lowers NO_x level (decreasing the temperature in the cylinder), and also deteriorates combustion quality. In practice, the fuel/air ratio varies with engine speed and intake mass flow rate as shown in Figure 3.10. At low mass flow rate (small throttle opening), the mixture is close to stoichiometric or richer, especially in an engine with carburetor fuel metering (the upper curve in Figure 3.10), due to less fuel atomization in the

FIGURE 3.10 Fuel/air ratio varies with engine speed and intake mass flow.

mixture and for smooth engine operation. With a fuel injection system, fuel atomization is better than with a carburetor. With a high intake mass flow rate, the mixture becomes richer for high torque output. In the middle, the mixture is lean for better efficiency and emissions.

3.1.6   Emission Control

Today emissions are treated at three points: fuel, engine, and exhaust (after-treatment). Gasoline is modified by means of additives and refining processes to adapt its composition in order to reduce the formation of pollutant species and facilitate after-treatment. For example, a reformulated gasoline may contain MTBE, which increases the fuel octane ratio in replacement of lead. MTBE is less harmful to the atmosphere than lead compounds used previously; however, it is no longer used because of its danger to water sources in case of spill. Gasoline is also treated for its sulfur content. Some after-treatment techniques can only tolerate very small amounts of sulfur compounds in gases.

A good example of engine design techniques that limit the formation of species is exterior air intake. Previously, the engine would breathe air from underneath the hood. This air is much hotter than ambient air, thus resulting in higher temperatures during compression and combustion and therefore resulting in high nitric oxide formation. Today, the engine breathes air from the outside, which is much cooler and therefore results in lower nitric oxide formation. Other design or operation parameters that affect the formation of polluting species include the following: high-pressure fuel injection and turbulent intake flows that improve the homogeneity of the mixture; combustion chamber design; aluminum engine blocks that allow running the engine cooler; sodium-filled exhaust valves that can therefore be cooled more easily; exhaust gas oxygen sensing that tells the engine controller what the fuel/air ratio really is, etc.

The most powerful means of controlling the emission of polluting species is exhaust after-treatment. The most widespread technique, which is now mandatory in most Western countries, is through the catalytic converter. It

is composed of a mesh of catalytic material such as platinum and rhodium. These catalysts react with the polluting species and transform them to harmless species. Nitric oxides are reduced to oxygen and air, carbon monoxide is oxidized to carbon dioxide, and unburned HCs are combusted to carbon dioxide and water. A catalytic converter that can take care of all three species at the same time is referred to as a three-way catalytic converter.

Catalytic converters need a slight excess of oxygen in order to oxidize CO and HC species. Therefore, the fuel/air ratio must be precisely controlled in order to maintain a constant oxygen concentration in the exhaust. This is done by means of exhaust oxygen sensing and fuel injections. Catalytic converters are the primary reason for the replacement of carburetors by fuel injection. The catalysts operate efficiently only at high temperature. They do not work for about 1 min when the engine is cold-started. It is during this lapse of time that the engine emits most of its pollutants. It should be noted that some emission control techniques do impair fuel consumption. This is especially true for the catalytic converter that acts as a restriction in the exhaust flow.

3.1.7 Basic Techniques for Improving Engine Performance, Efficiency, and Emissions

3.1.7.1 Forced Induction

The amount of torque produced in an IC engine depends on the amount of air induced into its cylinders. An easy way of increasing the amount of air induced is to increase the pressure in the intake manifold. This can be done by three means: variable intake manifold, supercharging, or turbocharging.

The intake manifold is like a wind instrument: it has resonant frequencies. A variable intake manifold tunes itself according to engine speed in order to exploit those resonant frequencies. If the tuning is proper, the amount of air induced into the cylinders can be optimized because the pressure in the intake manifold is increased. This technique improves the "breathing" of the engine but does not result in a very large increase of torque output.

A supercharger is an air compressor turned by the engine crankshaft. The air thus compressed is fed to the intake manifold. The advantage of a supercharger is that it can significantly increase the pressure in the intake manifold, even at low speed. The most significant disadvantage is that the supercharging power is taken from the engine crankshaft. This reduces the engine output and harms fuel consumption.

A turbocharger consists of a turbine driven by exhaust gases and of a compressor turned by the turbine. A turbocharger has the great advantage of taking its energy from the exhaust gases, which are normally wasted. Therefore, the efficiency of the engine does not suffer from the addition of the turbocharger. Turbocharging can tremendously increase the power output of the engine, especially if coupled to a charge cooling system. It also significantly improves the efficiency because the higher intake pressure reduces

the negative work associated with the induction stroke. The disadvantages of turbocharging include slow response, little or no effectiveness at low engine speed, and high rotational speed for the turbocharger, which increases the cost of forced induction.

Supercharging and turbocharging both suffer from two disadvantages: knock and emissions. Compressing the intake air also increases its temperature. An increased temperature means a greater risk of auto-ignition and knocks for the mixture, and increased nitric oxide emissions. The solution to this problem consists in cooling down the intake air after compression by means of an intercooler or heat exchanger. The compressed air is passed through a radiator, while the ambient air or water is passed on the exterior of the radiator, removing the heat from the charge. The temperature of induced air can be reduced sufficiently to avoid auto-ignition and knock. Nitric oxide emissions are also reduced. It should be noted that an engine designed for forced induction has a lower compression ratio than an engine that is designed for normal induction. Cooling the induced air is also beneficial for torque production, because cooler air is denser air. Therefore, more air can be induced into the cylinder if it is cooler.

3.1.7.2   Gasoline Direct Injection and Lean-Burn Engines

HC and CO emissions can be reduced if the engine burns a lean mixture. If a SI engine could run on extremely lean mixtures, then the emissions would be very significantly reduced. However, ultralean mixtures pose problems because the flame has trouble propagating.

Gasoline direct injection is one means of achieving a very efficient mixing. Because the injector is located in the cylinder, it must inject the fuel at high pressure, which reduces the size of the fuel droplets. The fuel can be injected close to the spark plug, thus enriching locally the mixture and allowing better ignition of the intake air. Additional advantages of gasoline direct injection include the cooling of intake air, which reduces knock and allows operating at a higher compression ratio. This further improves the engine efficiency. Besides the cost increase, gasoline direct injection results in higher NO_x emissions.

3.1.7.3   Multi- and Variable-Valve Timing

While many engines use only two valves, high-performance engines use three, four, or five valves in order to increase the intake flow area. Multiple valves provide a significant increase of torque at high engine speed, but sacrifice the low-speed torque because the larger intake flow area results in slower flows at low speed. Multiple valves imply multiple camshafts, which increase the cost and complexity of the engine.

It has been previously shown that valve timing needs to be optimized for each engine but also for specific operating conditions in order to avoid reverse

flows. While conventional engines use a fixed, compromised valve timing, some advanced engines use a variable valve timing. This allows a better control of the amount of mixture and therefore helps in reducing fuel consumption and emissions. The major drawbacks are the cost and complexity of variable valve systems.

3.1.7.4   Throttle-Less Torque Control

Because most of the losses at partial torque output result from the throttle, eliminating the throttle eliminates these losses and improves the partial torque fuel consumption. Torque control is achieved by means of variable valve timing or by varying the fuel/air ratio in lean-burn engines.

3.1.7.5   Variable Compression Ratio

A variable compression ratio allows operating a forced induction engine at optimal compression ratio at any intake pressure. If the charging mechanism does not provide maximum intake pressure, then the compression ratio of the engine can be increased without risking auto-ignition or knock. The increased compression ratio results in improved fuel economy at partial torque output.

3.1.7.6   Exhaust Gas Recirculation

Exhaust gas recirculation (EGR) consists in readmitting some of the exhaust gases into the combustion chamber in order to reduce the effective displacement of the engine. This technique is used in conventional vehicles to decrease the fuel consumption at partial torque output, while preserving the acceleration capabilities of the engine. The greatest benefit of EGR is in emission reduction because it reduces the amount of fuel burned in the chamber and therefore the temperature of the exhaust gases. The nitric oxide emissions are greatly reduced.

3.1.7.7   Intelligent Ignition

Intelligent ignition systems can set the spark advances at their optimum valve at any operating speed and load for optimum performance, efficiency, and exhaust emissions. High-power ignition systems can prevent losing fire in any cylinder, especially for engines with a lean mixture combination.

3.1.7.8   New Engine Materials

New materials developed for engine components will contribute to better fuel economy in two ways. Firstly, ceramic materials can be expected to offer better thermal insulation than metallic ones, with corresponding lower heat transfer (and therefore lower heat loss) and hence higher thermal efficiency.

Secondly, lightweight materials such as fiber-reinforced plastics with high tensile strength can save a lot of weight.

3.2   4S, Compression-Ignition IC Engines

Compression-ignition (CI) engines normally use diesel as their fuel. The 4S, CIIC engine has operation principles similar to the 4S, SI engine. It also has four distinctive strokes—induction, compression, expansion, and exhaust. However, in CI engines, air alone is induced into the cylinder. The fuel is injected directly into the cylinder just before the piston moves up to the TDC. High temperature in the compressed air ignites the fuel. Airflow at a given engine speed is essentially unchanged and load control is achieved by varying the amount of fuel injected at each cycle. Compared with SI engines, a CI engine works differently as follows:

1. The compression ratio is higher.
2. During the initial part of compression, only air is present.
3. The fuel/air mixture is always stoichiometrically weak.

These operation characteristics result in a better fuel efficiency than a SI engine. Furthermore, the CI engine is, in general, designed to operate at lower speeds, and consequently the friction losses are smaller.

Since the fuel/air ratio in a CI engine is always lean, CO emission is much lower than in SI engines, and can be negligible. Unburned HCs in a properly regulated diesel engine come from two sources. Firstly, around the perimeters of the reaction zone there is a mixture that is too lean to burn, and the longer the delay period, the greater the amount of HC emissions from this source. However, there is a delay period below which no further reductions in HC emissions are obtained. Under these conditions, the HC emissions mostly originate from a second source: the fuel retained in the nozzle sac (the space between the nozzle seat and the spray holes) and the spray holes. Fuel from these sources can enter the combustion chamber late in the cycle, thereby producing HC emissions.

The formation of NO_x is strongly dependent on temperature, the local concentration of oxygen, and the duration of combustion. Thus, in diesel engines, NO_x is formed during the diffusion combustion phase, on the weak side of the reaction zone. Reducing the diffusion-controlled combustion duration by increasing the rate of injection leads to a reduction in NO_x emissions. Retarding the injection timing also reduces the NO_x emissions, since the later injection leads to lower temperature. However, injection retarding will reduce the fuel efficiency of the engine.
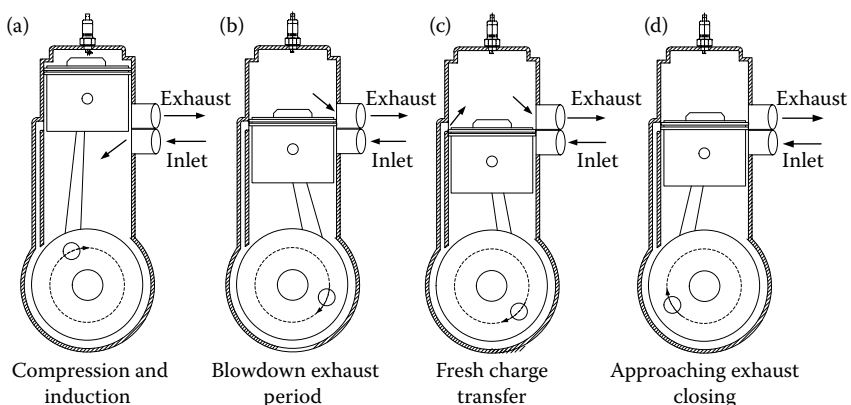
The black smoke from diesel engine originates from the fuel-rich side of the reaction zone in the diffusion-controlled combustion phase. After the rapid combustion at the end of the delay period, the subsequent combustion of the fuel is controlled by the rates of diffusion of air into the fuel vapor and vice versa, and the diffusion of the combustion products away from the reaction zone. Carbon particles are formed by the thermal decomposition (cracking) of the large HC molecules, and soot particles form by agglomeration. The soot particles can be oxidized when they enter the lean side of the reaction zone and further oxidation occurs during the expansion stroke, after the end of the diffusion combustion phase.

Smoke generation is increased by high temperature in the fuel-rich zone during diffusion combustion. The smoke emission can be reduced by shortening the diffusion combustion phase, because this gives less time for soot formation and more time for soot oxidation. The diffusion phase can be shortened by increased swirl, more rapid rejection, and a finer fuel spray. Advancing the injection timing can also reduce the smoke.

3.3   2S Engines

The 2S cycle combines the necessary processes of induction, exhaust, compression, and expansion in a single crankshaft rotation, unlike a 4S cycle that requires two rotations.[3] A basic 2S cycle is shown in Figure 3.11. 2S engines eliminate the separate induction and exhaust strokes. The basic operation principle is illustrated in Figure 3.11 and explained below.

1. In Figure 3.11a, the piston is approaching the top center. Above the piston, the trapped air and fuel charge is ignited by the spark plug,

FIGURE 3.11   Basic 2S cycle.

producing a rapid rise in temperature and pressure that will drive the piston down on the power stroke. Below the piston, the opened inlet port induces air from the atmosphere into the crankcase due to the increasing volume of the crankcase lowering the pressure below the atmospheric value. To induce fuel into the engine, various options exist: placing a carburetor in the inlet tract, injecting fuel into the inlet tract, injecting fuel into the crankcase transfer ducts, or injecting fuel directly into the cylinder before or after the closure of the exhaust port. If one operates the engine as a diesel power unit, the latter is the only option.
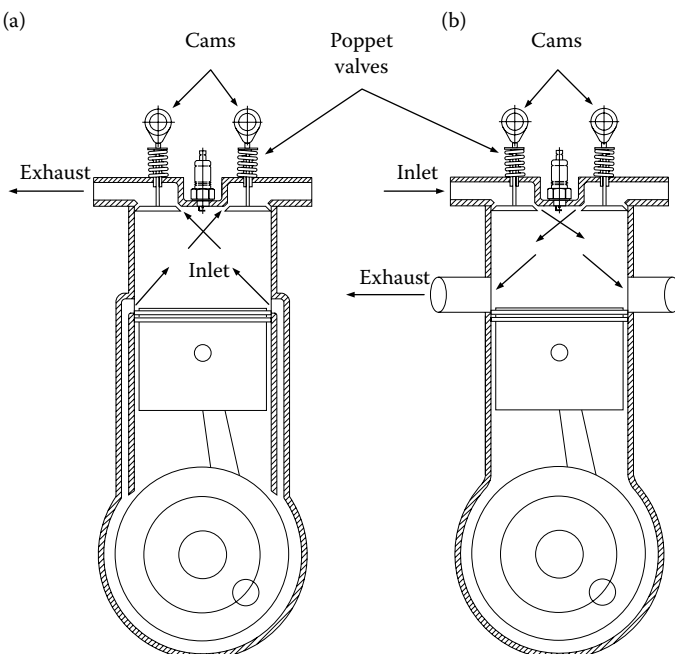
2. In Figure 3.11b, the exhaust port above the piston has been opened. It is often called the "release" point in the cycle and this allows the transmission of a pulse of hot, high-pressure exhaust gas from the combustion process into the exhaust duct. As the area of the port increases with crankshaft angle and the cylinder pressure falls with time, it is clear that the exhaust duct pressure profile with time is one that increases to a maximum value and then decays. Such a flow process is described as unsteady gas flow and such a pulse can be reflected from all pipe area changes, or at the pipe end termination to the atmosphere. These reflections have a dramatic influence on engine performance. Below the piston, the compression of the fresh charge is taking place. The pressure and temperature achieved will be a function of the proportion reduction of the crankcase volume, that is, the crankcase compression ratio.

3. In Figure 3.11c, above the piston, the initial exhaust process referred to as "blow-down" is nearing completion. The piston uncovers the transfer ports and connects the cylinder directly to the crankcase through the transfer ducts. If the crankcase pressure exceeds the cylinder pressure, then the fresh charge enters the cylinder in what is known as the "scavenge process." Clearly, if the transfer ports are badly directed then the fresh charge can exit directly out of the exhaust port and be totally lost from the cylinder. Such a process, referred to as "short-circuiting," would result in the cylinder being filled only with exhaust gas at the onset of the next combustion process, and no pressure rise or power output would ensue. Worse, all of the fuel in a carbureted configuration would be lost to the exhaust—a consequentially monstrous emission of unburned HC. This is the main reason why a conventional 2S engine has a lower efficiency and bad emissions.

4. In Figure 3.11d, in the cylinder, the piston is approaching what is known as the "trapping" point. The scavenge process has been completed and the cylinder is now filled with a mix of air, fuel if a carbureted design, and exhaust gas. As the piston rises, the cylinder pressure also rises, but the exhaust port is still open and, barring the intervention of some unsteady gas-dynamic effect generated in the exhaust pipe, the piston will spill fresh charge into the exhaust duct

to the detriment of resulting power output, fuel consumption, and pollutant emissions.
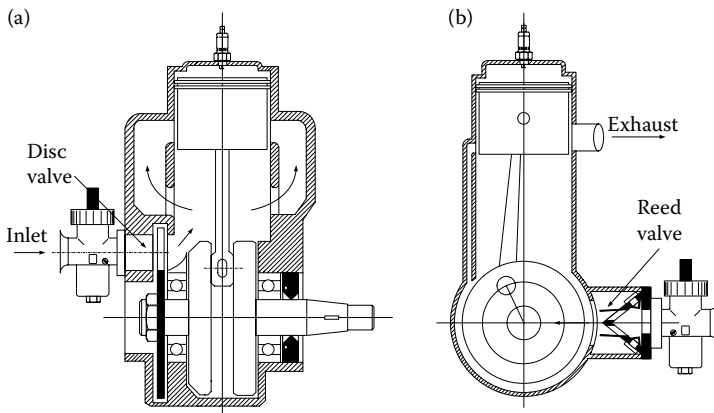
The simplest method of allowing fresh charge access into, and exhaust gas discharge from, the 2S engine is by the movement of the piston exposing port in the cylinder wall as shown in Figure 3.11. This means that all port timing events are symmetrical with respect to TDC and BDC. It is possible to produce asymmetrical inlet and exhaust timing events by the use of disc valves, reed valves, and poppet valves.

The use of poppet valves for both inlet and exhaust timing control is sketched in Figure 3.12 as an example of uniflow scavenging. This design is commonly used in 4S engines. Generally, the poppet valves' design is considered to be difficult to design so as to adequately flow sufficient charge into a 2S engine, compared with using the port in a cylinder wall with the same access area.[4]

The disc valves and reed valves are another two valves for 2S engines, as shown in Figure 3.13. The disc valve can provide asymmetric porting timing by designing the disc. However, the porting timing can be varied with the engine speed. Consequently, the porting timing is optimized only at a specified speed, and at other speeds the engine performance will be as good as at
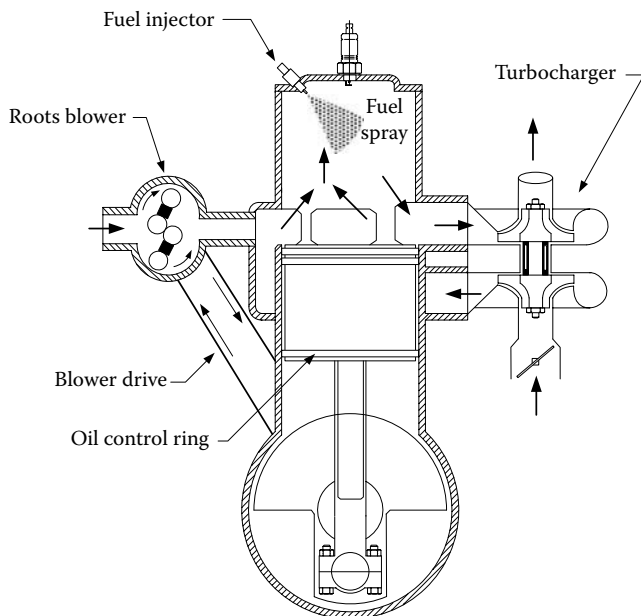
FIGURE 3.12 Uniflow scavenged with crankcase compression: (a) top exhaust and (b) top inlet design.

FIGURE 3.13   (a) Disc valve and (b) reed valve with crankcase compression.

this speed. Reed valves have always been popular as they provide an effective automatic valve whose timings vary with both engine load and engine speed. The high-performance outboard racing engine demonstrated that high specific power output was possible with reed valves.[4] Racing motorcycle organizations developed this further. Today, most reed valves are designed as V-blocks (refer to Figure 3.13b).

The essential element of the original 2S engines was the use of a crankcase as the air pumping device. The conventional lubrication method has been to mix the lubricant with the gasoline and supply it through the carburetor in ratios of gasoline to lubricant from 25:1 to 100:1, depending on the application. Combined with some fuel charge being short-circuited to the exhaust duct along with the air, the resulting exhaust is rich in unburned HCs and lubricant, some partially burned and some totally unburned. It is consequently visible as smoke. This is ecologically unacceptable. By definition, an external air pump can be utilized to replace the crankcase air pumping. This can be either a positive displacement blower of a Roots type or a centrifugal blower driven from the crankshaft. Clearly, it would be more efficient thermodynamically to use a turbocharger, where the exhaust energy to the exhaust turbine is available to drive the air compressor. This arrangement is shown in Figure 3.14, where the engine has both a blower and a turbocharger. The blower is used as a starting aid and as an air supplementary device at low loads and speeds, with the turbocharger being used as the main air supply unit at higher torque and power levels at any speed. To prevent any short-circuiting fuel to the exhaust, a fuel injector is used to supply fuel directly to the cylinder, after the exhaust port is closed and not in the position as shown in Figure 3.14, at BDC. Such an engine type has already demonstrated excellent fuel economy behavior, good exhaust emission characteristics of unburned HCs and carbon monoxide, and
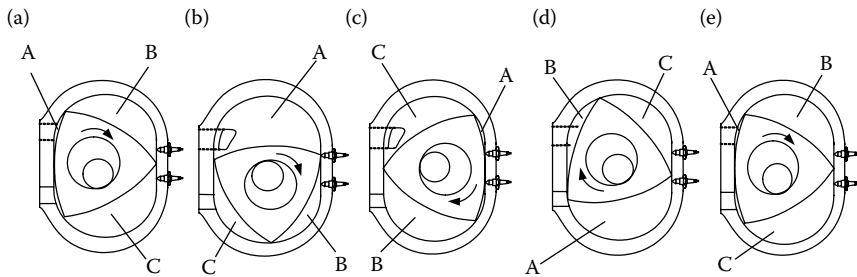
FIGURE 3.14   A supercharged and turbocharged fuel-injection 2S engine.

superior emission characteristics of oxides of nitrogen, in comparison with an equivalent 4S engine.

3.4   Wankel Rotary Engines

The rotary-piston engine (or Wankel engine, named by its inventor) generates power by the compression, ignition, and expansion of a gasoline/air mixture in a 4S cycle in the same way as conventional IC engines. The completely different mechanical design allows all moving parts to have a continuous rotary motion instead of a reciprocating movement. The rotor (or piston) is roughly triangular shaped and rotates on an eccentric shaft on the output shaft within a housing of epitrochoid shape. The term is given to the path described by a point within a circle rolling around another circle. The two-lobe epitrochoid of the Wankel is generated when the interior circle is twice the radius of the rolling circle.

   The four strokes of the cycle occur in the spaces formed between the three sides of the rotor and the two-lobed trochoidal chamber or housing; the spaces are expanded and contracted as the rotor turns. Figure 3.15 illustrates the operating cycle. The three separate working chambers are labeled A, B, and C. As the intake port is uncovered, volume A expands and draws a fresh fuel/air charge into the engine (Figure 3.15a). Next the trailing apex seal

FIGURE 3.15   The Wankle rotary engine cycle: (a) three separate working chambers and air/fuel intake into chamber A, (b) starting compression in chamber A, (c) ignition and starting expansion in chamber A, (d) starting exhaust in chamber A, and (e) starting intake in chamber A.

isolates volume A from the intake port and the charge is compressed as volume A steadily decreases with rotation of the rotor, reaching the minimum shown at the point of ignition (Figure 3.15b and c). While this sequence of events is occurring, the other two faces of the rotor are defining volumes B and C, which experience exactly the same sequence, each offset by one-third of a rotation.

Unlike the piston in a conventional engine, which requires a connecting rod to transmit power to the crankshaft, the rotor (or "rotary piston") runs directly on an eccentric shaft, from which torque output is derived. The Wankel also differs from the conventional automobile engine in having no valves. The fuel/air inlet port and the exhaust port are opened and closed at the appropriate time in the combustion cycle by the passage of the rotor itself.

The advantages of the Wankel engine are as follows:

Because the engine delivers one power stroke for each full crankshaft rotation, the Wankel uses its displacement volume twice as often as the SI engine does. One immediate advantage is that for equivalent power output, a Wankel engine is only about half the size and weight of a conventional engine.

Another advantage of the rotary engine is the reduced number of parts—typically 40% of the number of parts moving in a V-8 engine, although the advantage over a four-cylinder engine would be less. This has certain implications for easier and faster manufacturing of the engine.

Since the Wankel engine possesses only rotary motion, all the unbalanced forces are simple harmonic and can be fully canceled with rotating counterweights to produce very little vibration as compared with one-quarter of a revolution in the 4S engine. This dispersed application of torque adds to the basic smoothness of the Wankel with consequent lower noise (aided by the absence of a valve train). A single-rotor Wankel is as smooth as a three-cylinder piston engine. Most rotary engines being developed for automotive use have two rotors.

The engine is capable of burning fuel of a lower octane rating than a conventional piston engine with a slightly better performance gained from unleaded petrol. It can run at the stoichiometric fuel/air ratio allowing NO_x control (raw NO_x emissions are generally lower than a conventional petrol engine

due to the slower combustion) with a combination of EGR and a reduction catalyst, and HC and CO control with an oxidation catalyst.

The Wankel engine breathes well because of a greater length (crank degrees) of induction period and because of a relatively unrestricted flow path for the incoming mixture and exhaust gases. Volumetric efficiency in excess of 100% has been claimed for some designs. In the one- and two-rotor versions, the induction system is simple, which reduces problems associated with bad distribution of the fuel/air mixture. Also, the speed range of the engine is broad (i.e., higher than a conventional reciprocating engine) due to better breathing characteristics, potentially lower mechanical friction, no limitations imposed by valve train dynamics, and the absence of reciprocating parts.

Perhaps the most far-reaching economic significance of the Wankel lies outside the engine itself in the potential it offers for the redesign of the passenger car. The comparatively small size and light weight of the engine would permit vehicle aerodynamic improvements by way of lower hood lines and weight reduction because of the lower engine mass and the requirement for a smaller engine compartment.
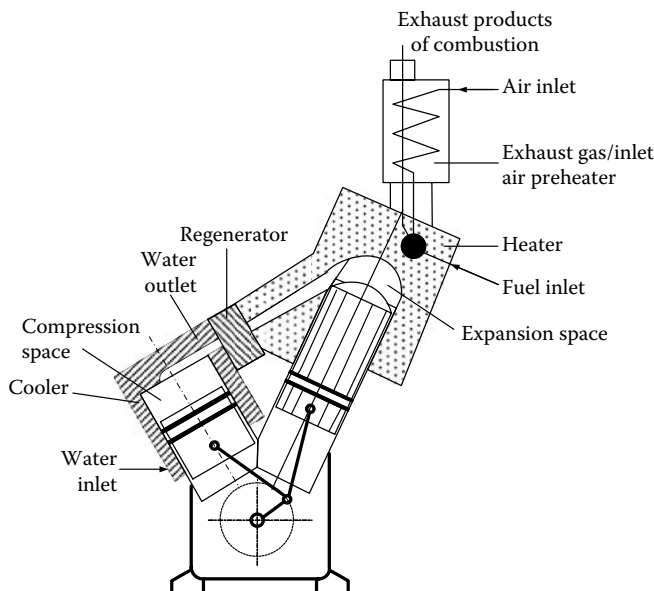
The Wankel engine's main disadvantages are reported to be its expensive construction materials, its requirement for high-precision manufacturing techniques, poor fuel economy, and high emissions of unburned HCs. The high HC emissions are because of poor sealing between the rotor and housing. The apex seal especially suffered from reliability and durability problems and has been unable to match conventional piston rings. But newly developed sealing materials are expected to provide a much higher level of service. The apex seal in current rotary engines is composed of a single piece of carbon impregnated with an aluminum alloy.

The high HC emissions have also contributed to the generally poor fuel economy. The other main factor is that combustion in the Wankel engine tends to be slower and hence less efficient than in the conventional piston engine. In most new designs, the combustion is accelerated by using two spark plugs in each combustion chamber. Continuing efforts to improve engine efficiency via direct injection and stratified charge have been reported. Stratification of the charge can readily be accomplished by injecting the fuel and creating a rich mixture in the vicinity of the TDC position of the rotor, which will substantially reduce the peak temperature and therefore decrease the NO_x produced. A lean mixture in the leading section of the chamber will enhance the oxidation of CO and HCs.

3.5 Stirling Engines

The Stirling engine is a reciprocating, continuous external combustion (EC) engine that has a piston and cylinder similar to a conventional IC engine as shown in Figure 3.16.[5] However, inside the engine, the working fluid (usually
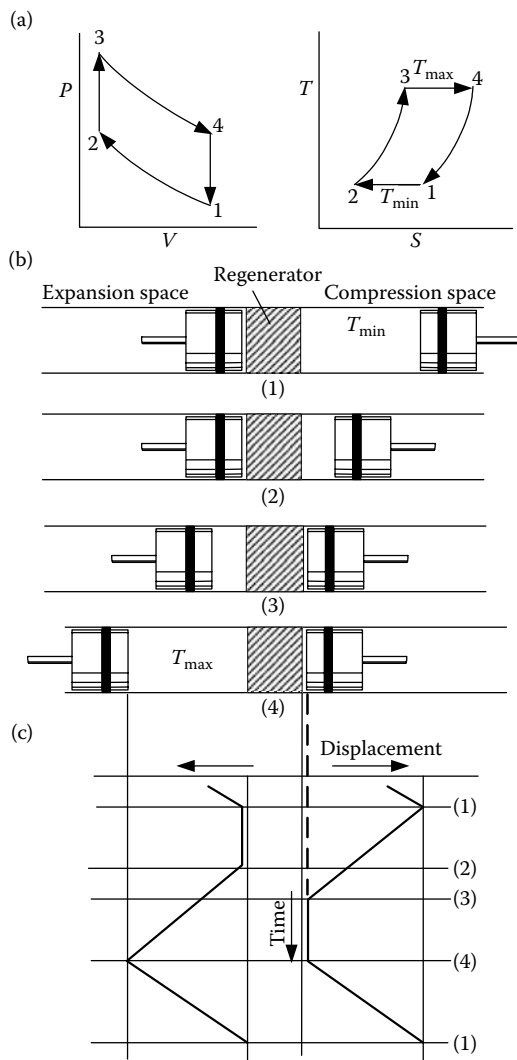
FIGURE 3.16   Diagram of a practical opposed-piston Stirling engine.

hydrogen or helium) is sealed. Alternately heating and cooling the working fluid causes pressure fluctuation that acts on the piston to produce power. A Stirling engine has a high-temperature heat source and a low-temperature heat sink. The heat source sounds the compression space and the heat sink sounds the expansion space. Both the source and the heat sink are separated by a regenerator (thermodynamics sponge), as shown in Figure 3.17.

   The Stirling engine works based on the Stirling thermodynamic cycle. The ideal Stirling cycle is illustrated in Figure 3.17,[5,6] which consists of a cylinder containing two opposed pistons, with a regenerator between the pistons. The regenerator, a thermodynamic sponge, is usually a matrix of finely divided metal in the form of wires or strips. One of the two volumes between the regenerator and the pistons is the expansion space, in which high temperature, T_{max}, is maintained by a heat source surrounding it. The other volume is the compression space, in which low temperature, T_{min}, is maintained by the heat sink surrounding it. Therefore, there is a temperature gradient ($T_{max} - T_{min}$) across the transverse faces of the regenerator. It is usually assumed that there is no thermal conduction in the longitudinal direction.

   To start the cycle, we assume that the compression-space piston is at the outer dead point and the expansion-space piston is at the inner dead point, close to the face of the regenerator. All the working fluid is then in the cold compression space. The volume is maximum, so that the pressure and temperature are at their minimum values, represented as 1 on the *P–V* and *T–S* diagrams as shown in Figure 3.17a. During compression (process 1–2), the

FIGURE 3.17 Ideal Stirling cycle: (a) *P–V* and *T–S* diagram, (b) piston arrangement at the terminal points of the cycle, and (c) time–displacement diagram.

compression piston moves towards the inner dead point and the expansion-space piston remains stationary. The working fluid is compressed in the compression space, and the pressure increases. The temperature is maintained constant because heat Q_c is abstracted from the compression-space cylinder to the surroundings (heat sink).

In the transfer process 2–3, both pistons move simultaneously, the compression piston towards (and the expansion piston away from) the regenerator, so that the volume between them remains constant. Therefore, the working

fluid is transferred, through the porous metallic matrix of the regenerator, from the compression space to the expansion space. In its passage through the regenerator, the working fluid is heated from T_{min} to T_{max}, by heat transfer from the matrix, and emerges from the regenerator into the expansion space at temperature T_{max}. The gradual increase in temperature in passage through the matrix, at constant volume, causes an increase in pressure.

In the expansion process 3–4, the expansion piston continues to move away from the regenerator towards the outer dead center point; the compression piston remains stationary at the inner dead center point, adjacent to the regenerator. As the expansion progresses, the pressure decreases as the volume increases; the temperature remains constant because heat Q_E is added to the system from an external heat source.
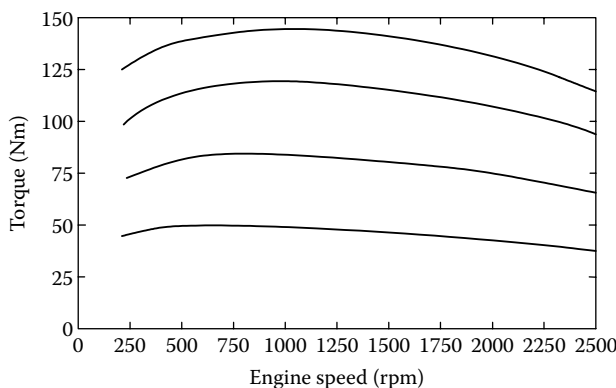
The final process in the cycle is the transfer process 4–1, during which both pistons move simultaneously to transfer the working fluid (at constant volume) back, through the regenerative matrix, so that the working fluid decreases in temperature and emerges at T_{min} into the compression space. Heat transferred in the process is contained in the matrix, for transfer to the gas in process 2–3 of the subsequent cycle.

The cycle is composed of heat transfer; therefore, there are four heat-transfer processes:

1. Process 1–2: isothermal compression: heat transfer from the working fluid at T_{min} to the external heat sink.
2. Process 2–3: constant volume: heat transfer to the working fluid from the regenerative matrix.
3. Process 3–4: isothermal expansion: heat transfer to the working fluid at T_{max} from an external heat source.
4. Process 4–1: constant volume: heat transfer from the working fluid to the regenerative matrix.

If the heat transferred in process 2–3 has the same magnitude as in process 4–1, then the only heat transfer between the engine and its surroundings are (a) heat supply at T_{max} and (b) heat rejection at T_{min}. This heat supply and heat rejection at constant temperature satisfy the requirement of the second law of thermodynamics for maximum thermal efficiency, so that the efficiency of the Stirling engine is the same as the Carnot cycle, that is, $\eta = (T_{max} - T_{min})/T_{max}$. The principal advantage of the Stirling cycle over the Carnot cycle lies in the replacement of two isentropic processes by two constant-volume processes, which greatly increase the area of the P–V diagram. Therefore, to obtain a reasonable amount of work from the Stirling cycle, it is not necessary to resort to the impractically high pressures and swept volumes, as in the Carnot cycle.
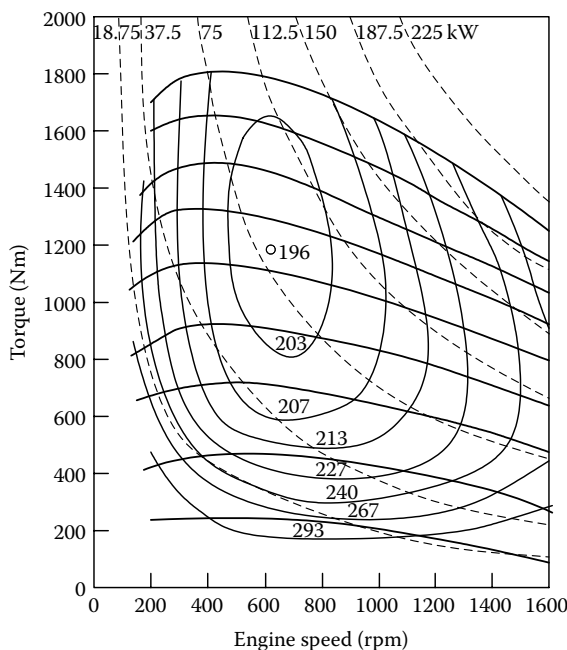
The torque–speed characteristic of a Stirling engine is relatively flat as shown in Figure 3.18. This is particularly favorable for automotive

FIGURE 3.18 Torque/speed characteristics of typical Stirling engines.

applications where high torque at low speed is advantageous to achieve good acceleration.

The performance and fuel consumption characteristic map for a Stirling engine is shown in Figure 3.19.[5] Compared with IC engines, the outstanding feature of the Stirling engine is that the fuel consumption at part load is

FIGURE 3.19 Performance and fuel consumption map for a four-cylinder Stirling engine for traction applications.

higher compared to its optimum fuel consumption operating point, much less than that of IC engines. This outstanding characteristic will lead to good fuel economy for a vehicle that operates in partial load most of the time.

The exhaust emissions are low and easy to control because combustion is isolated from the cycle changes in pressure and temperature experienced by the working fluid. An excess of air of between 20% and 80%, continuous combustion, and no "quench" of flame by a "cold" metal surface also help to ensure almost complete combustion. Because continuous combustion replaces the intermittent explosive nature of combustion in other piston engines, the Stirling engine usually has low noise.

Other important advantages of the Stirling engine for its application of vehicles are the multifuel and self-starting characteristics. Because the combustion is isolated from its working fluid, and only heat is transferred to the working fluid from a heat source, a variety of fuels can be used.

However, Stirling engines also have some disadvantages. The main disadvantages have traditionally been high manufacture cost, a heavy and bulky end result, and difficulty in controlling the power output accurately. Also it has so far proven impossible to hold the leakage rate of hydrogen or helium from the system down to a level that would be acceptable. The durability of piston seals has been as much of a problem as the effectiveness of the seals to prevent leakage.

In practical everyday automotive operations, there are some additional shortcomings. First, EC prolongs the start-up time. Power cannot be drawn from a cold engine until the heater head reaches a reasonable operating temperature. Second, fuel energy is spent in raising the heater head to operating temperature, and when the engine is shut down, that stored energy is dissipated without performing useful work.
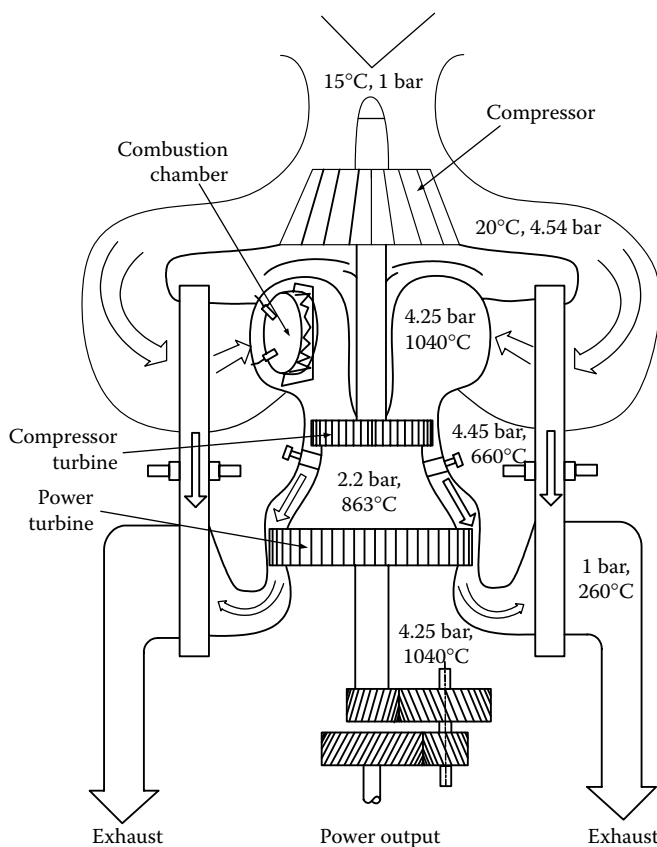
3.6   Gas Turbine Engines

The gas turbine engine is a rotary, continuous IC engine where the fuel is supplied to a burner and burned with an excess of compressed air (lean burn). The hot combustion gases then expand and pass through a turbine, which generates power and is transferred to the output shaft by gearing, as shown in Figure 3.20.[7]

The gas turbine engine operates in accordance with the principles described below:
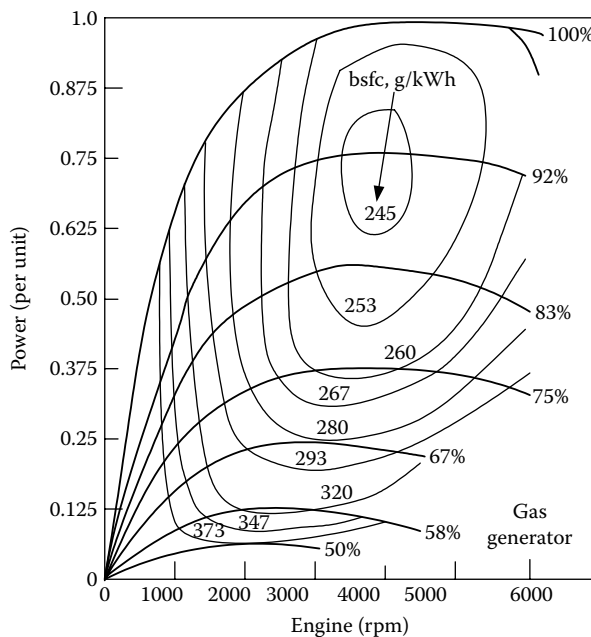
1. *Compression*: Air enters the gas turbine and is compressed.
2. *Heat exchange*: Heat is drawn from the exhaust gases and communicated to the compressed air. There is recuperation of the exhaust gases' energy that is otherwise lost.
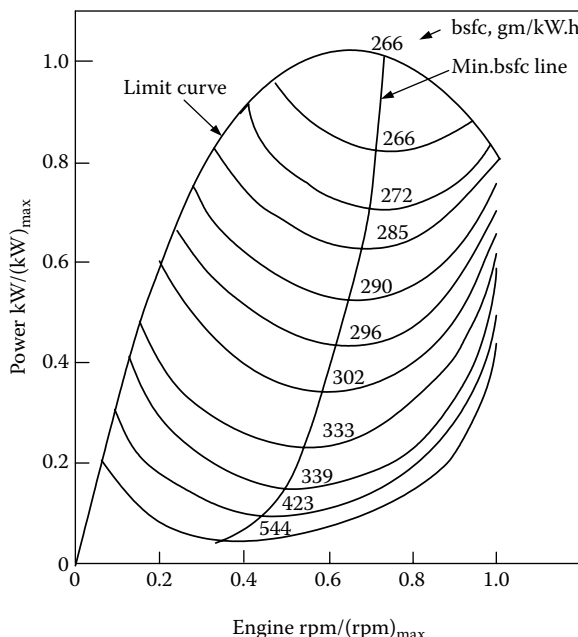
FIGURE 3.20 Gas turbine engine with heat exchanger.

3. *Combustion*: Fuel is mixed with the hot air and ignited. The pressure increases.
4. *Expansion*: The hot exhaust gases drive the turbine, thus releasing their energy. The turbine turns the compressor and the output shaft.

Figures 3.21 and 3.22 show the bsfc map for a complete range of output power and speed. The shape of the bsfc map of a turbine engine is quite different from that of SI and CI engines. The speed of a turbine engine can start from zero, and extend to its maximum. The drop in the fuel economy at partial load from full load is much smaller than that of the SI and CI engines. The bsfc values are more sensitive to speed than to power. Therefore, a turbine engine favors running at constant speed, and load variations have less influence on the fuel economy.

FIGURE 3.21 Fuel consumption characteristics of a Kronograd KTT gas turbine.

FIGURE 3.22 Fuel consumption characteristics of a Chrysler upgraded turbine.

The advantages of gas turbines include the following:

1. A very compact engine because of its high rotational speed.
2. Vibration-free operation due to the rotating movement.
3. Ability to operate on a wide variety of fuels.
4. Reduced HC and CO emissions compared to IC engines because the combustion is continuous and therefore easier to control.

However, gas turbines suffer from some major disadvantages for automotive applications:

1. High noise levels due to the quenching of gases by the turbine and compressor.
2. High fuel consumption because the gas turbine does not scale down efficiently: the efficiency of a dynamic compressor and turbine is low for small sizes (below a few hundred kilowatts).
3. High rotating speeds are required for small (below a few hundred kilowatts) turbines to operate at their maximum efficiency. This requires sophisticated materials to withstand the mechanical constraints.
4. The high temperatures continuously encountered by the turbine require expensive materials that also have to withstand high rotational speeds.
5. The efficiency is extremely speed dependent, thus requiring a speed decoupling.
6. No torque output at low speed.
7. High cost of the heat exchanger.

3.7 Quasi-Isothermal Brayton Cycle Engines

The quasi-isothermal Brayton cycle engine (QIBCE) is an invention of Prof. Mark Holtzapple at Texas A&M University. It is a variation of the gas turbine, with two major differences intended to improve on the most crippling disadvantages of the gas turbine.

The most significant improvement is the compressor and turbine principle. Instead of being of the dynamic type, and therefore bound to operate at very high speed, these elements are of the positive displacement type that operate effectively and efficiently at low speeds. The principle is that of a gear pump, of the kind used in automobiles for oil.

The second improvement is the quasi-isothermal compression, which requires less energy than the adiabatic compression in conventional Brayton cycles. This is achieved by spraying water in the compressor. The liquid water

"captures" the heat resulting from the compression, while remaining as liquid or slightly vaporizing. This keeps the overall flow temperature from rising, therefore reducing the energy necessary for the compression.

The claimed advantages of the QIBCE engine are as follows:

1. Potential for very high efficiency
2. Compactness
3. Continuous combustion that results in low HC and CO emissions
4. Reduced noise emissions compared to a gas turbine because of the absence of quenching of gases
5. Simplicity due to a reduced number of parts

The disadvantages are as follows:

1. Specialized and potentially expensive materials for the turbine because it is permanently exposed to high temperatures. However, these materials should be less stressed than in a gas turbine because of the lower operating speeds
2. High cost of the heat exchanger

To this day, this engine is only a concept and a prototype must be implemented to verify the claimed advantages.

References

1. J. B. Heywood, *Internal Combustion Engine Fundamentals*, McGraw-Hill Inc., New York, 1988.
2. R. Stone, *Introduction to Combustion Engines*, Second Edition, Society of Automotive Engineers (SAE), Warrendale, PA, 1992.
3. P. Duret, *A New Generation of Two-Stroke Engines for The Future?*, Edison's Technip, Paris, 1993.
4. G. P. Blair, *Design and Simulation of Two Stroke Engines*, Society of Automotive Engineers (SAE), Warrendale, PA, 1996.
5. G. Walker, G. Reader, O. R. Fauvel, and E. R. Bingham, *The Stirling Alternative— Power System, Refrigerants and Heat Pumps*, Gordon and Breach Science Publishers, London, 1994.
6. M. J. Collie, *Stirling Engine Design and Feasibility for Automotive Use*, Noyes Data Corporation, New Jersey, 1979.
7. J. P. O'Brien, *Gas Turbines for Automotive Use*, Noyes Data Corporation, New Jersey, 1980.

4

Electric Vehicles

EVs use an electric motor for traction, and chemical batteries, fuel cells, ultracapacitors, and/or flywheels for their corresponding energy sources. The EV has many advantages over the conventional internal combustion engine vehicle (ICEV), such as absence of emissions, high efficiency, independence from petroleum, and quiet and smooth operation. The operational and fundamental principles in EVs and ICEVs are similar, as described in Chapter 2. There are, however, some differences between ICEVs and EVs, such as the use of a gasoline tank versus batteries, ICE versus electric motor, and different transmission requirements. This chapter will focus on the methodology of power train design and will investigate the key components, including traction motor, energy storage, and so on.
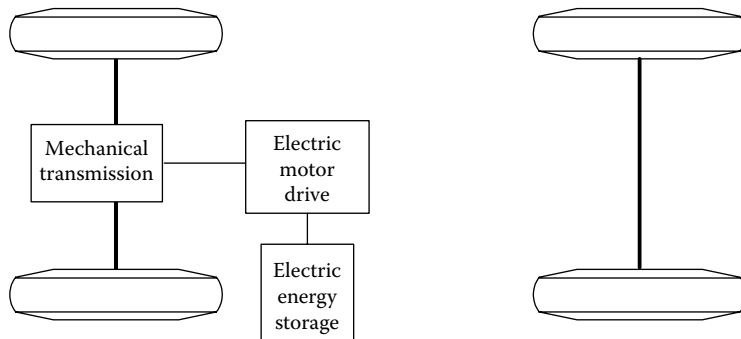
4.1   Configurations of EVs

Previously, the EV was mainly converted from the existing ICEV by replacing the IC engine and fuel tank with an electric motor drive and battery pack while retaining all the other components, as shown in Figure 4.1. Drawbacks such as its heavy weight, lower flexibility, and performance degradation have caused the use of this type of EV to fade out. In its place, the modern EV is purposely built, based on original body and frame designs. This satisfies the structure requirements unique to EVs and makes use of the greater flexibility of electric propulsion.[1]
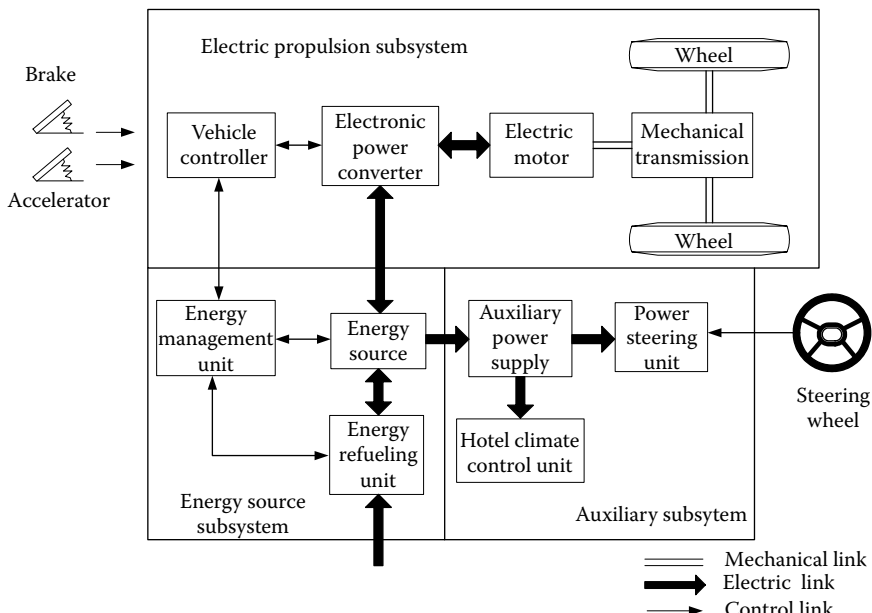
A modern electric drive train is conceptually illustrated in Figure 4.2.[1] The drive train consists of three major subsystems: electric motor propulsion, energy source, and auxiliary. The electric propulsion subsystem is comprised of the vehicle controller, the power electronic converter, the electric motor, mechanical transmission, and driving wheels. The energy source subsystem involves the energy source, the energy management unit, and the energy refueling unit. The auxiliary subsystem consists of the power steering unit, the hotel climate control unit, and the auxiliary supply unit.

Based on the control inputs from the accelerator and brake pedals, the vehicle controller provides proper control signals to the electronic power

FIGURE 4.1   Primary EV power train.

converter, which functions to regulate the power flow between the electric motor and energy source. The backward power flow is due to the regenerative braking of the EV and this regenerated energy can be restored into the energy source, provided the energy source is receptive. Most EV batteries as well as ultracapacitors and flywheels readily possess the ability to accept regenerative energy. The energy management unit cooperates with the vehicle controller to control the regenerative braking and its energy recovery. It also works with the energy refueling unit to control the refueling unit and to monitor the usability of the energy source. The auxiliary power supply
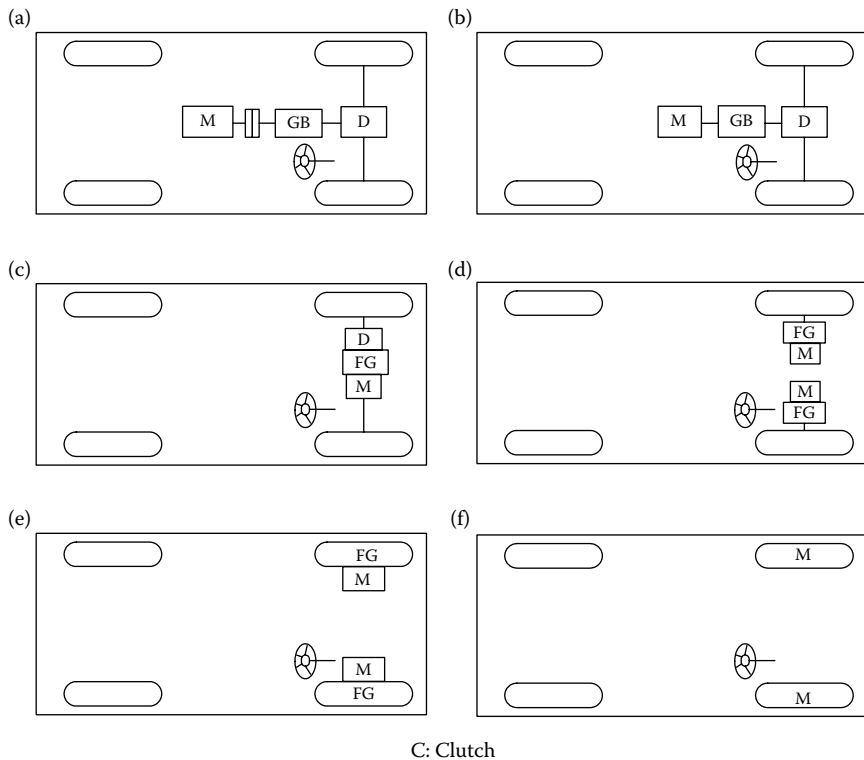
FIGURE 4.2   Conceptual illustration of a general EV configuration.[1]

provides the necessary power with different voltage levels for all the EV auxiliaries, especially the hotel climate control and power steering units.

There are a variety of possible EV configurations due to the variations in electric propulsion characteristics and energy sources, as shown in Figure 4.3.[1]

a. Figure 4.3a shows the configuration of the first alternative, in which an electric propulsion replaces the IC engine of a conventional vehicle drive train. It consists of an electric motor, a clutch, a gearbox, and a differential. The clutch and gearbox may be replaced by an automatic transmission. The clutch is used to connect or disconnect the power of the electric motor from the driven wheels. The gearbox provides a set of gear ratios to modify the speed–power (torque) profile to match the load requirement (refer to Chapter 2). The differential is a mechanical device (usually a set of planetary gears), which enables the wheels of

C: Clutch
D: Differential
FG: Fixed gearing
GB: Gearbox
M: Electric motor

FIGURE 4.3 Possible EV configuration: (a) conventional driveline with multigear transmission and clutch, (b) single-gear transmission without need of a clutch, (c) integrated fixed gearing and differential, (d) two separate motors and fixed gearing with their driveshaft, (e) direct drive with two separate motors and fixed gearing, and (f) two separate in-wheel motor drives.[1]

both sides to be driven at different speeds when the vehicle runs along a curved path.

b. With an electric motor that has a constant power in a long speed range (refer to Chapter 2), a fixed gearing can replace the multispeed gearbox and reduce the need for a clutch. This configuration not only reduces the size and weight of the mechanical transmission, it also simplifies the drive train control because gear shifting is not needed.

c. Similar to the drive train in (b), the electric motor, the fixed gearing, and the differential can be further integrated into a single assembly while both axles point at both driving wheels. The whole drive train is further simplified and compacted.

d. In Figure 4.3d, the mechanical differential is replaced by using two traction motors. Each of them drives one side wheel and operates at a different speed when the vehicle is running along a curved path.

e. In order to further simplify the drive train, the traction motor can be placed inside a wheel. This arrangement is the so-called in-wheel drive. A thin planetary gear set may be employed to reduce the motor speed and enhance the motor torque. The thin planetary gear set offers the advantage of a high-speed reduction ratio as well as an inline arrangement of the input and output shaft.

f. By fully abandoning any mechanical gearing between the electric motor and the driving wheel, the out-rotor of a low-speed electric motor in the in-wheel drive can be directly connected to the driving wheel. The speed control of the electric motor is equivalent to the control of the wheel speed and hence the vehicle speed. However, this arrangement requires the electric motor to have a higher torque to start and accelerate the vehicle.
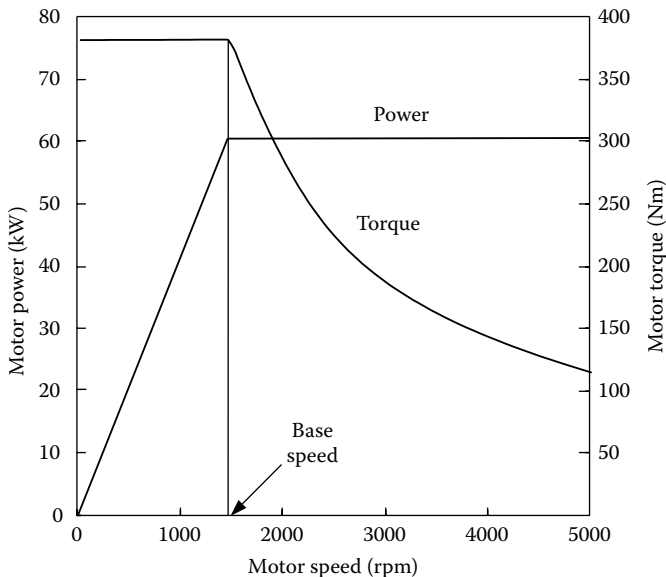
4.2   Performance of EVs

A vehicle's driving performance is usually evaluated by its acceleration time, maximum speed, and gradeability. In EV drive train design, proper motor power rating and transmission parameters are the primary considerations to meet the performance specification. The design of all these parameters depends mostly on the speed–power (torque) characteristics of the traction motor, as mention in Chapter 2, and will be discussed in this chapter.

4.2.1   Traction Motor Characteristics

Variable-speed electric motor drives usually have the characteristics shown in Figure 4.4. At the low-speed region (less than the base speed as marked in Figure 4.4), the motor has a constant torque. In the high-speed region (higher

FIGURE 4.4 Typical variable-speed electric motor characteristics.
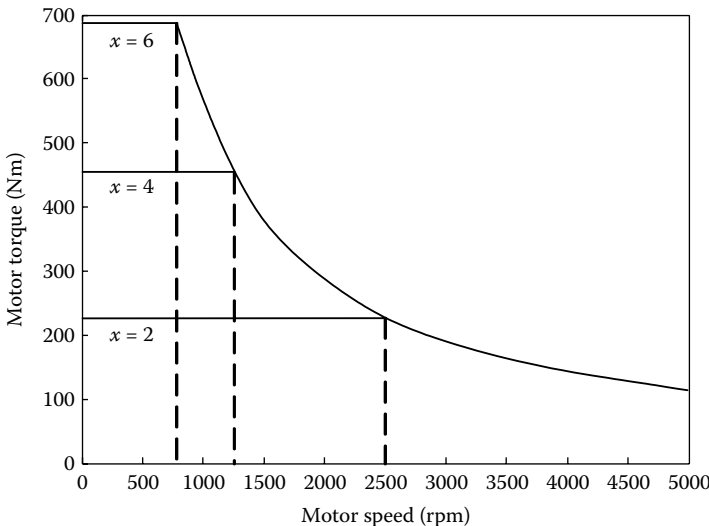
than the base speed), the motor has a constant power. This characteristic is usually represented by a speed ratio x, defined as the ratio of its maximum speed to its base speed. In low-speed operation, voltage supply to the motor increases with the increase of speed through the electronic converter while the flux is kept constant. At the point of base speed, the voltage of the motor reaches the source voltage. After the base speed, the motor voltage is kept constant and the flux is weakened, dropping hyperbolically with increasing speed. Hence, its torque also drops hyperbolically with increasing speed.[2-4]

Figure 4.5 shows the torque–speed profiles of a 60 kW motor with different speed ratios x ($x = 2$, 4, and 6). It is clear that with a long constant power region, the maximum torque of the motor can be significantly increased, and hence vehicle acceleration and gradeability performance can be improved and the transmission can be simplified. However, each type of motor inherently has its limited maximum speed ratio. For example, a permanent magnet motor has a small x (<2) because of the difficulty of field weakening due to the presence of the permanent magnet. Switched reluctance motors may achieve $x > 6$ and induction motors about $x = 4$.[2,5]

4.2.2 Tractive Effort and Transmission Requirement

The tractive effort developed by a traction motor on driven wheels and the vehicle speed are expressed as

$$F_t = \frac{T_m i_g i_0 \eta_t}{r_d} \tag{4.1}$$
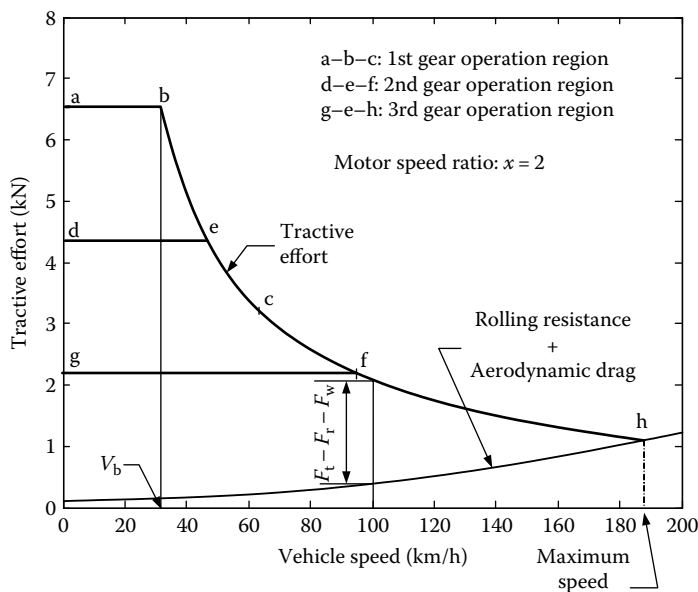
FIGURE 4.5 Speed–torque profile of a 60-kW electric motor with $x = 2, 4,$ and 6.

and
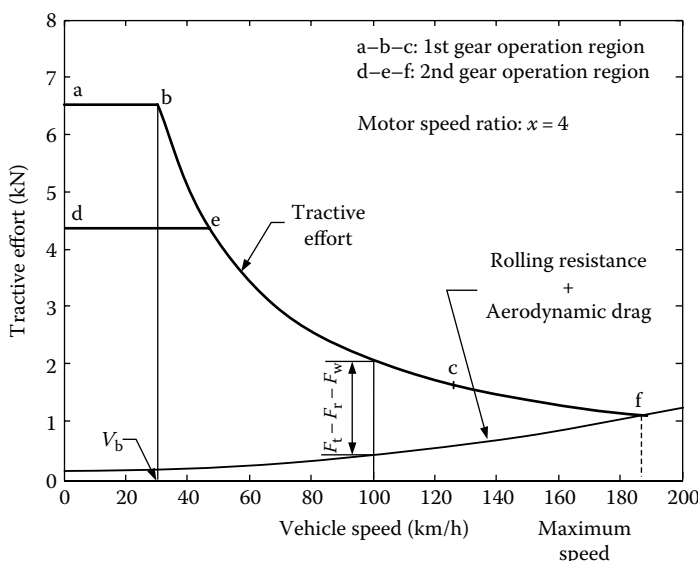
$$V = \frac{\pi N_m r_d}{30 i_g i_0} \ (\text{m/s}),\tag{4.2}$$

where T_m and N_m are the motor torque output in N m and speed in rpm, respectively, i_g is the gear ratio of transmission, i_0 is the gear ratio of final drive, η_t is the efficiency of the whole driveline from the motor to the driven wheels, and r_d is the radius of the driven wheels.
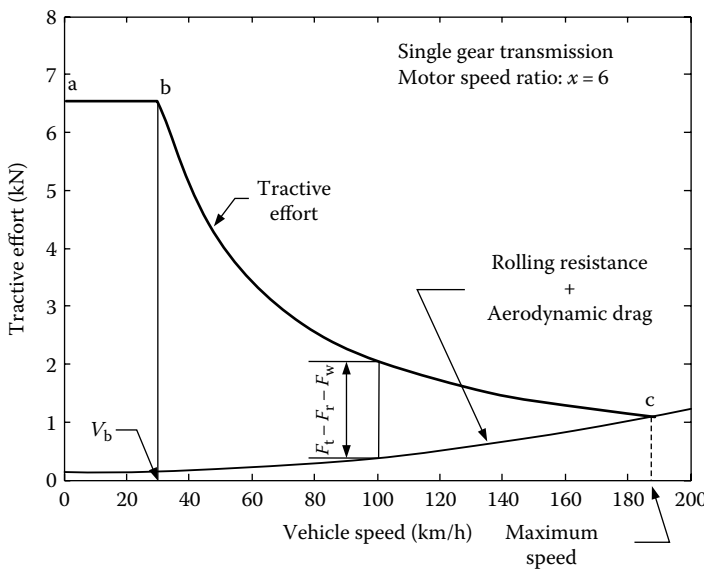
The use of a multigear or single-gear transmission depends mostly on the motor speed–torque characteristic. That is, at a given rated motor power, if the motor has a long constant power region, a single-gear transmission would be sufficient for a high tractive effort at low speeds. Otherwise, a multigear (more than two gears) transmission has to be used. Figure 4.6 shows the tractive effort of an EV, along with the vehicle speed with a traction motor of $x = 2$ and a three-gear transmission. The first gear covers the speed region of a–b–c, the second gear covers d–e–f, and the third gear covers g–f–h. Figure 4.7 shows the tractive effort with a traction motor of $x = 4$ and a two-gear transmission. The first gear covers the speed region of a–b–c and the second gear d–e–f. Figure 4.8 shows the tractive effort with a traction motor of $x = 6$ and a single-gear transmission. These three designs have the same tractive effort versus vehicle speed profiles. Therefore, the vehicles will have the same acceleration and gradeability performance.

FIGURE 4.6 Tractive effort versus vehicle speed with a traction motor of $x = 2$ and three-gear transmission.

FIGURE 4.7 Tractive effort versus vehicle speed with a traction motor of $x = 4$ and two-gear transmission.

FIGURE 4.8 Tractive effort versus vehicle speed with a traction motor of $x = 6$ and single-gear transmission.

4.2.3 Vehicle Performance

Basic vehicle performance includes maximum cruising speed, gradeability, and acceleration. The maximum speed of a vehicle can be easily found by the intersection point of the tractive effort curve with the resistance curve (rolling resistance plus aerodynamic drag), in the tractive effort versus vehicle speed diagram shown in Figures 4.6 through 4.8. It should be noted that such an intersection point does not exist in some designs, which usually use a larger traction motor or a large gear ratio. In this case, the maximum vehicle speed is determined by the maximum speed of the traction motor as

$$V_{max} = \frac{\pi N_{m\ max} r_d}{30 i_{g\ min} i_0} \ (m/s),\tag{4.3}$$

where $N_{m\ max}$ is the allowed maximum rpm of the traction motor and $i_{g\ min}$ is the minimum gear ratio of the transmission (highest gear).

Gradeability is determined by the net tractive effort of the vehicle, F_{t-net} ($F_{t-net} = F_t - F_r - F_w$), as shown in Figures 4.6 through 4.8. The gradeability at mid- and high speeds is smaller than that at low speeds. The maximum grade that the vehicle can overcome at the given speed can be calculated by

$$i = \frac{F_{t-net}}{Mg} = \frac{F_t - (F_r + F_w)}{Mg},\tag{4.4}$$

where F_t is the tractive effort on the driven wheels, F_r is the tire rolling resistance, and F_w is the aerodynamic drag. However, at low speeds, the gradeability is much larger. Calculations based on Equation 4.4 will cause significant error; instead, Equation 4.5 should be used:

$$\sin \alpha = \frac{d - f_r\sqrt{1 - d^2 + f_r^2}}{1 + f_r^2}. \tag{4.5}$$

$d = F_t - F_w/Mg$ is called the vehicle performance factor (refer to Chapter 2) and f_r is the tire rolling resistance coefficient.

Acceleration performance of a vehicle is evaluated by the time used to accelerate the vehicle from a low speed V_1 (usually zero) to a higher speed (100 km/h for passenger cars). For passenger cars, acceleration performance is more important than maximum cruising speed and gradeability, since it is the acceleration requirement rather than the maximum cruising speed or the gradeability that dictate the power rating of the motor drive. Referring to Equation 2.58 and Figures 2.28 and 2.29, the acceleration time for an EV can be expressed as

$$t_a = \int_0^{V_b} \frac{M\delta}{P_t/V_b - Mg \quad f_r - 1/2\rho_a C_D A_f V^2} \, dV$$
$$+ \int_{V_b}^{V_f} \frac{M\delta}{P_t/V - Mg \quad f_r - 1/2\rho_a C_D A_f V^2} \, dV, \tag{4.6}$$

where V_b and V_f are the vehicle base speed (as shown in Figures 4.6 through 4.8) and the final acceleration speed, respectively, and P_t is the tractive power on the driven wheels transmitted from the traction motor corresponding to the vehicle base speed. The first term on the right-hand side of Equation 4.6 is in correspondence with the speed region less than the vehicle base speed; the second term is in correspondence with the speed region beyond the vehicle base speed.

It is difficult to obtain the analytical solution from Equation 4.6. For initial evaluation of acceleration time versus tractive power, one can ignore rolling resistance and aerodynamic drag and obtain

$$t_a = \frac{\delta M}{2P_t}\left(V_f^2 + V_b^2\right), \tag{4.7}$$

where the vehicle rotational inertial factor, δ, is a constant. The tractive power, P_t, can then be expressed as

$$P_t = \frac{\delta M}{2t_a}\left(V_f^2 + V_b^2\right). \tag{4.8}$$

It should be noted that the power rating obtained from Equation 4.8 is only the power consumed for vehicle acceleration. To accurately determine the tractive power rating, the power consumed in overcoming the rolling resistance and dynamic drag should be considered. The average drag power during acceleration can be expressed as

$$\bar{P}_{drag} = \frac{1}{t_a} \int_0^{t_a} \left(Mg f_r V + \frac{1}{2} \rho_a C_D A_f V^3 \right) dt. \tag{4.9}$$

Referring to Figures 2.28 and 2.29, the vehicle speed V may be expressed, using time t, as

$$V = V_f \sqrt{\frac{t}{t_a}}. \tag{4.10}$$

Substituting Equation 4.10 into Equation 4.9 and integrating, one obtains

$$\bar{P}_{drag} = \frac{2}{3} Mg f_r V_f + \frac{1}{5} \rho_a C_D A_f V_f^3. \tag{4.11}$$

The total tractive power for accelerating the vehicle from zero to speed V_f in t_a seconds can be finally obtained as

$$P_t = \frac{\delta M}{2t_a} \left(V_f^2 + V_b^2 \right) + \frac{2}{3} Mg f_r V_f + \frac{1}{5} \rho_a C_D A_f V_f^3. \tag{4.12}$$

Equation 4.12 indicates that for a given acceleration performance, low vehicle base speed will result in a small motor power rating. However, the power rating decline rate to the vehicle base speed reduction is not identical. Differentiating Equation 4.12 with respect to vehicle speed V_b, one can obtain

$$\frac{dP_t}{dV_b} = \frac{\delta M_v}{t_a} V_b. \tag{4.13}$$

Figure 4.9 shows an example of the tractive power rating and the power rating decline rate to the vehicle speed reduction (dP_t/dV_b) versus the speed factor x. In this example, the acceleration time is 10 s, the vehicle mass is 1200 kg, the rolling resistance coefficient is 0.01, the aerodynamic drag coefficient is 0.3, and the front area is 2 m^2. This figure clearly indicates that a low x (high V_b) reduction in V_b will result in significant decline in the power rating requirement. But with a high x (low V_b), $x > 5$ for example, it is not so effective. Figure 4.10 gives an example of the acceleration time and distance versus vehicle speed, using Equation 4.6 and numerical methods.
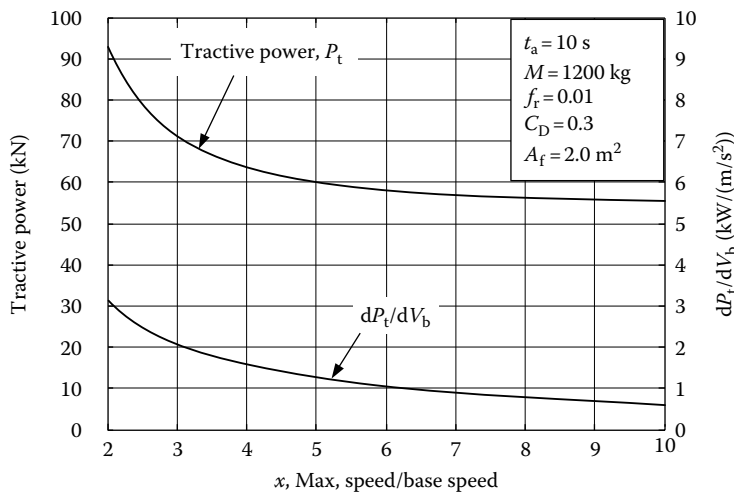
FIGURE 4.9 Power rating versus speed factor.
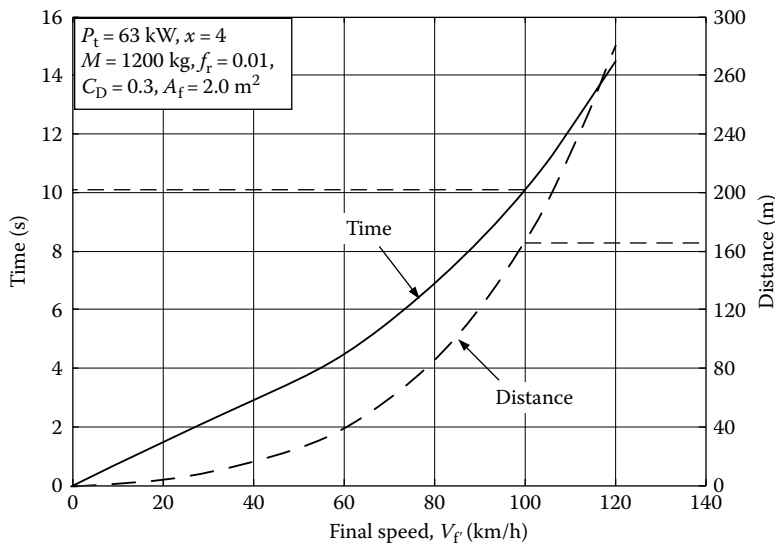
FIGURE 4.10 Acceleration time and distance versus final speed.

4.3 Tractive Effort in Normal Driving

The vehicle performance described in the previous section dictates vehicle capabilities with respect to speed, gradeability, and acceleration, thus

dictating the power capacity of the power train. However, in normal driving conditions these maximum capabilities are rarely used. During most of the operation time, the power train operates with partial load. Actual tractive effort (power) and vehicle speed vary widely with operating conditions such as acceleration, deceleration, uphill and downhill motion, and so on. These variations are associated with traffic environment as well as type of vehicle. City and highway traffic conditions vary greatly, as do the different functionality of vehicles, such as passenger cars and vehicles with regular operation routes and schedules.
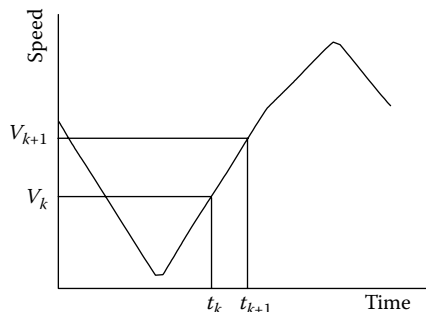
It is difficult to describe the tractive effort and vehicle speed variations in all actual traffic environments accurately and quantitatively. However, some representative driving cycles (driving schedules) have been developed to emulate typical traffic environments. These driving cycles are represented by vehicle speeds versus operating time while driving on a flat road. Some typical drive cycles are illustrated in Figure 4.12, which include (a) FTP75 urban cycle, (b) FTP75 highway cycle, (c) US06 cycle, which is a high-speed and high-acceleration drive cycle, (d) J227a schedule B, (e) J227a schedule C, and (f) J227a schedule D. The J227a series are recommended by the Society of Automotive Engineers in the United States[6] and is applied in the evaluation of EVs and batteries.

In a specific drive cycle, the tractive effort of a vehicle can be expressed as
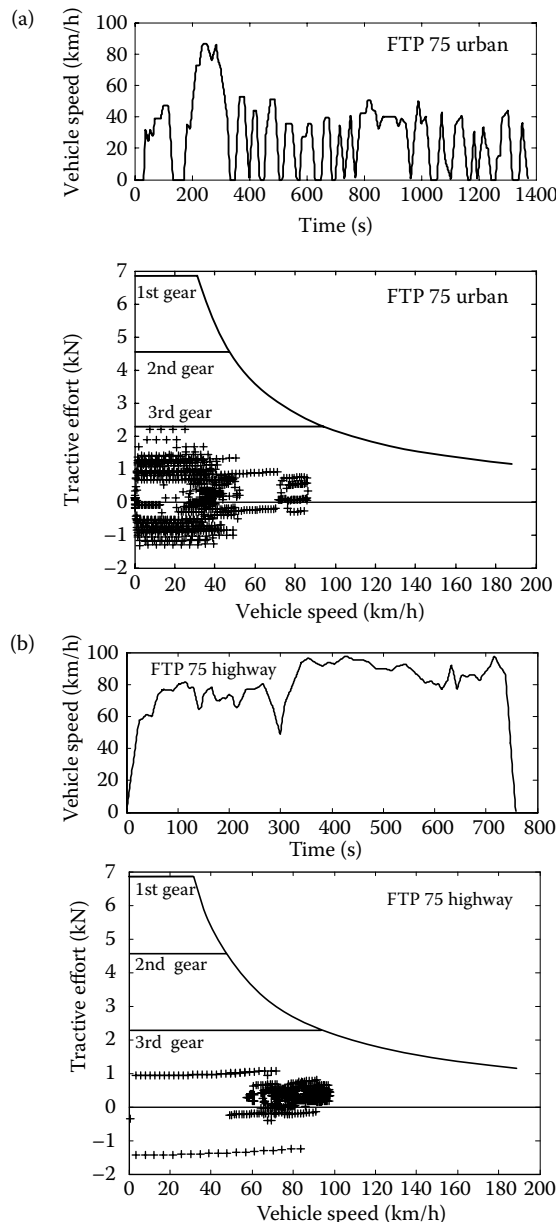
$$F_t = Mg f_r \cos \alpha + \frac{1}{2} \rho_a C_D A_f V^2 + M\delta \frac{dV}{dt}. \tag{4.14}$$

In a short time period, the speed is assumed to be linear with time, and acceleration is constant as shown in Figure 4.11. The acceleration, dV/dt in a driving cycle, can be obtained by
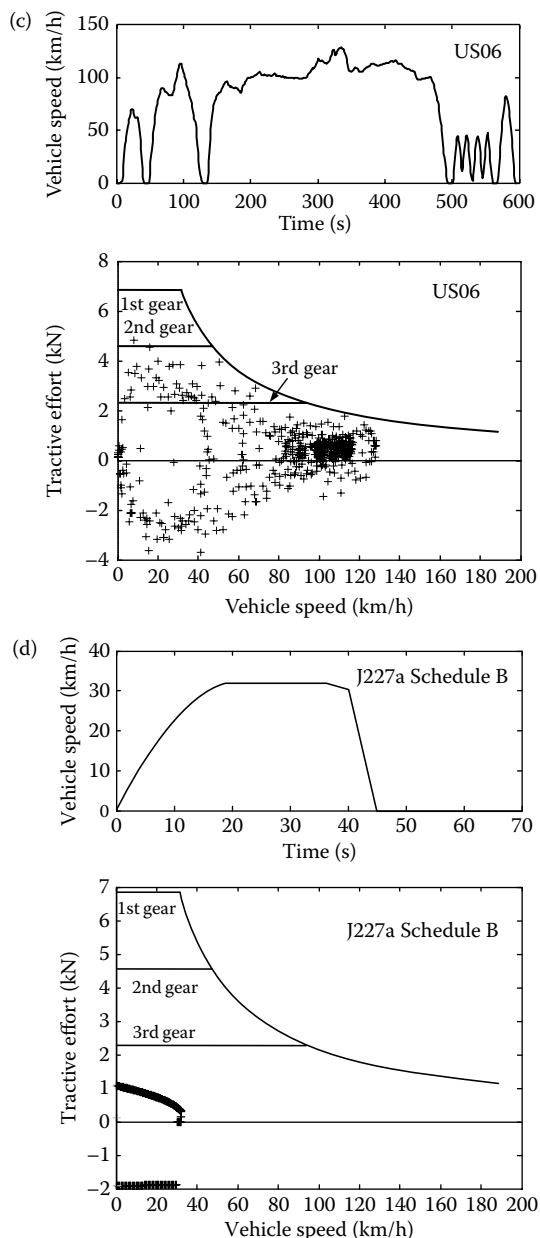
$$\frac{dV}{dt} = \frac{V_{k+1} - V_k}{t_{k+1} - t_k} \quad (k = 1, 2, \ldots, n, n - \text{total number of points}). \tag{4.15}$$

FIGURE 4.11   Acceleration being assumed constant with a short time period.

FIGURE 4.12 Speed profile and tractive effort in different representative drive cycles; operating points are marked by '+': (a) FTP75 urban, (b) FTP75 highway, (c) US06, (d) J227a schedule B, (e) J227a schedule C, and (f) J227a schedule D.

(c)

(d)

FIGURE 4.12   Continued.

(e)

(f)
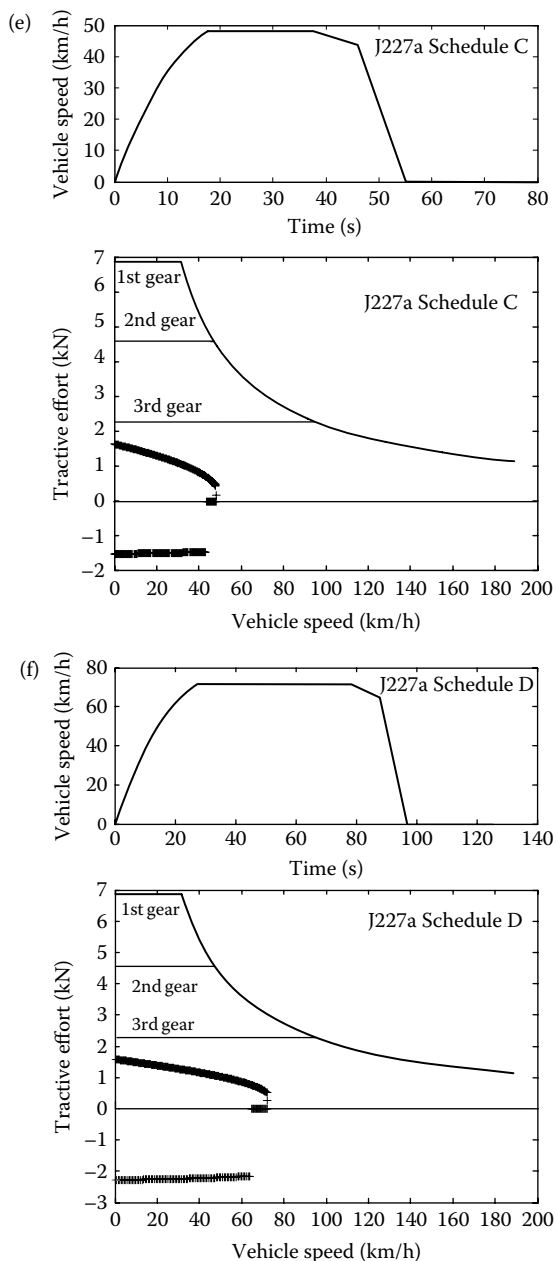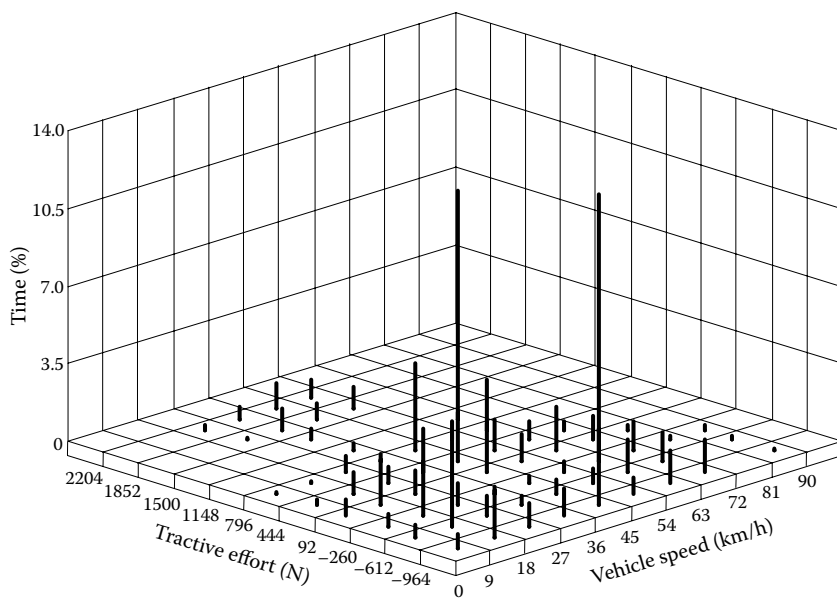
FIGURE 4.12 Continued.

FIGURE 4.13   Time distribution on vehicle speed and tractive effort in an FTP75 urban cycle.

By using Equation 4.14, the tractive efforts in any instant in a driving cycle can be calculated, as shown in Figure 4.12. The operating points of tractive effort versus vehicle speed scatter over the plane, and clearly show the operating area in which the power train operates most of the time. Furthermore, the time distribution of vehicle speed and tractive effort can be generated as shown in Figure 4.13. This time distribution information is very helpful for power train design, in which the most efficient region of the power train is designed to overlap the greatest operation time area.

4.4   Energy Consumption

In transportation, the unit of energy is usually kilowatt-hour (kWh) rather than joule or kilojoule (J or kJ). The energy consumption per unit distance in kWh/km is generally used to evaluate the vehicle energy consumption. However, for ICEVs the commonly used unit is a physical unit of fuel volume per unit distance, such as liters per 100 km (L/100 km). In the United States, the distance per unit volume of fuel is usually used; this is expressed as miles per gallon (mpg). On the other hand, for battery-powered EVs, the original energy consumption unit in kWh, measured at the battery terminals, is more suitable. The battery energy capacity is usually measured in kWh and the driving range per battery charge can be easily calculated. Similar to ICEVs,

L/100 km (for liquid fuels) or kg/100 km (for gas fuels such as hydrogen) or mpg or miles per kilogram is a more suitable unit of measurement for vehicles that use gaseous fuels.
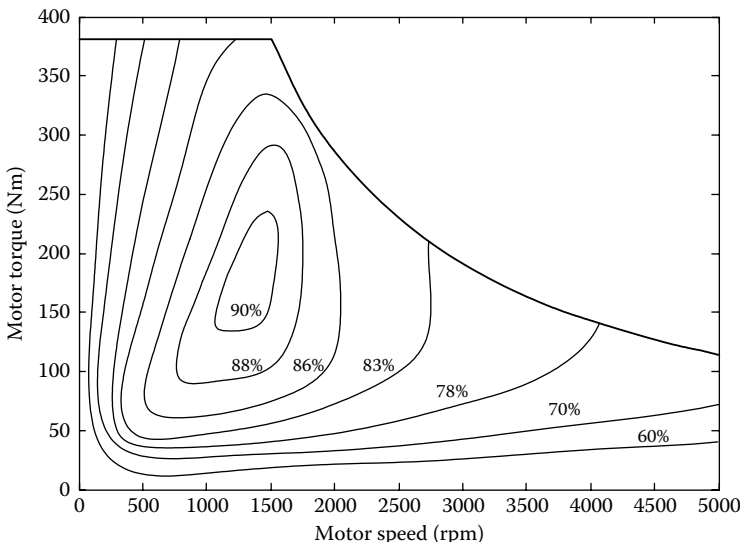
Energy consumption is an integration of the power output at the battery terminals. For propelling, the battery power output is equal to the resistance power and power losses in the transmission and motor drive, including power losses in the electronics. The power losses in transmission and motor drive are represented by their efficiencies η_t and η_m, respectively. Thus, the battery power output can be expressed as

$$P_{\text{b-out}} = \frac{V}{\eta_t \eta_m} \left(Mg(f_r + i) + \frac{1}{2} \rho_a C_D A_f V^2 + M\delta \frac{dV}{dt} \right). \qquad (4.16)$$

Here, the nontraction load (auxiliary load) is not included. In some cases, the auxiliary loads may be too significant to be ignored and should be added to the traction load. When regenerative braking is effective on an EV, a part of the braking energy—wasted in conventional vehicles—can be recovered by operating the motor drive as a generator and restoring it into the batteries. The regenerative braking power at the battery terminals can also be expressed as

$$P_{\text{b-in}} = \frac{\alpha V}{\eta_t \eta_m} \left(Mg(f_r + i) + \frac{1}{2} \rho_a C_D A_f V^2 + M\delta \frac{dV}{dt} \right), \qquad (4.17)$$

where road grade i or acceleration dV/dt or both are negative, and α ($0 < \alpha < 1$) is the percentage of the total braking energy that can be regenerated

FIGURE 4.14 Typical electric motor efficiency characteristics.

by the electric motor, called the regenerative braking factor. The regenerative braking factor α is a function of the applied braking strength and the design and control of the braking system, which will be discussed in detail in the later chapters. The net energy consumption from the batteries is

$$E_{\text{out}} = \underbrace{\int P_{\text{b-out}}\, dt}_{\text{traction}} + \underbrace{\int P_{\text{b-in}}\, dt}_{\text{braking}}. \tag{4.18}$$

It should be noted that the braking power in Equation 4.17 has a negative sign. When the net battery energy consumption reaches the total energy in the batteries, measured at their terminal, the batteries are empty and need to be charged. The traveling distance between two charges (usually called effective travel range) is determined by the total energy carried by the batteries, the resistance power, and the effectiveness of the regenerative braking (α).

The efficiency of a traction motor varies with its operating points on the speed–torque (speed–power) plane as shown in Figure 4.14, where the most efficient operating area exists. In power train design, this area should overlap or at least be as close as possible to the area of the greatest operation as mentioned in the previous section.

References

1. C. C. Chan and K. T. Chau, *Modern Electric Vehicle Technology*, Oxford University Press, New York, 2001.
2. Y. Gao, H. Maghbelli, M. Ehsani, G. Frazier, J. Kajs, and S. Bayne, "Investigation of proper motor drive characteristics for military vehicle propulsion," *Society of Automotive Engineers (SAE) Journal*, Paper No. 2003-01-2296, Warrendale, PA, 2003.
3. Z. Rahman, M. Ehsani, and K. Butler, "An investigation of electric motor drive characteristics for EV and HEV propulsion systems," *Society of Automotive Engineers (SAE) Journal*, Paper No. 2000-01-3062, Warrendale, PA, 2003.
4. Z. Rahman, M. Ehsani, and K. Butler, "Effect of extended-speed, constant-power operation of electric drives on the design and performance of EV-HEV propulsion system," *Society of Automotive Engineers (SAE) Journal*, Paper No. 2000-01-1557, Warrendale, PA, 2003.
5. K. M. Rahman and M. Ehsani, "Performance analysis of electric motor drives for electric and hybrid electric vehicle application," *IEEE Power Electronic in Transportation*, 49–56, ISBN 0-7803-3292-X, 1996.
6. D. A. J. Rand, R. Woods, and R. M. Dell, *Batteries for Electric Vehicles*, Research Studies Press, Ltd, Hertfordshire, UK, 1998.

5

Hybrid Electric Vehicles

Conventional vehicles with IC engines provide good performance and long operating range by utilizing the high-energy-density advantages of petroleum fuels. However, conventional IC engine vehicles have the disadvantages of poor fuel economy and environmental pollution. The main reasons for their poor fuel economy are (1) mismatch of engine fuel efficiency characteristics with the real operation requirement (refer to Figures 2.34 and 2.35); (2) dissipation of vehicle kinetic energy during braking, especially while operating in urban areas; and (3) low efficiency of hydraulic transmission in current automobiles in stop-and-go driving patterns (refer to Figure 2.21). Battery-powered EVs, on the other hand, possess some advantages over conventional IC engine vehicles, such as high-energy efficiency and zero environmental pollution. However, the performance, especially the operation range per battery charge, is far less competitive than IC engine vehicles, due to the much lower energy density of the batteries than that of gasoline. HEVs, which use two power sources(a primary power source and a secondary power source), have the advantages of both IC engine vehicles and EVs and overcome their disadvantages.[1,2] In this chapter, the basic concept and operation principles of HEV power trains are discussed.
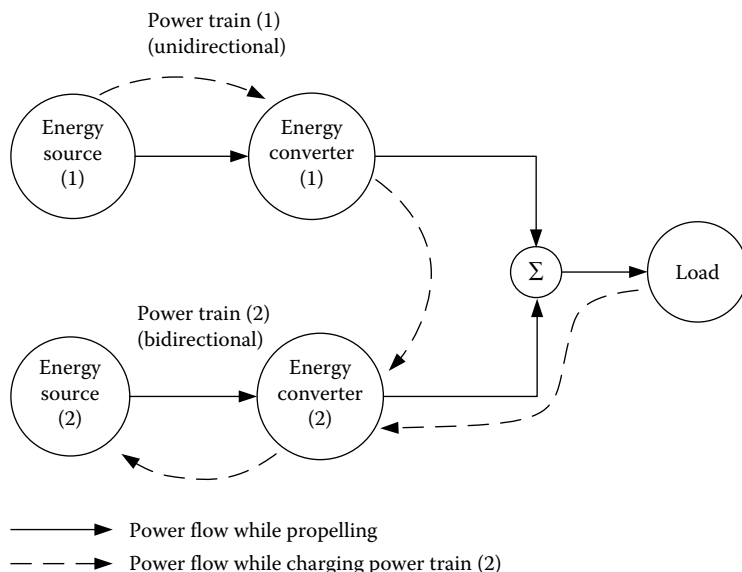
5.1 Concept of Hybrid Electric Drive Trains

Basically, any vehicle power train is required to (1) develop sufficient power to meet the demands of vehicle performance, (2) carry sufficient energy on-board to support the vehicle driving a sufficient range, (3) demonstrate high efficiency, and (4) emit few environmental pollutants. Broadly, a vehicle may have more than one power train. Here, the power train is defined as the combination of the energy source and the energy converter or power source, such as the gasoline (or diesel)–heat engine system, the hydrogen–fuel cell–electric motor system, the chemical battery–electric motor system, and so on. A vehicle that has two or more power trains is called a hybrid vehicle. A hybrid vehicle with an electrical power train is called an HEV. The drive train of a vehicle is defined as the aggregation of all the power trains.

A hybrid vehicle drive train usually consists of no more than two power trains. More than two power trains will make the drive train very complicated. For the purpose of recapturing braking energy that is dissipated in the form of heat in conventional IC engine vehicles, a hybrid drive train usually has a power train that allows energy to flow bidirectionally. The other one is either bidirectional or unidirectional. Figure 5.1 shows the concept of a hybrid drive train and the possible different power flow routes.

A hybrid drive train can supply its power to the load by a selective power train. There are many available patterns of operating two power trains to meet the load requirement:

1. Power train 1 alone delivers its power to the load.

2. Power train 2 alone delivers its power to the load.

3. Both power train 1 and power train 2 deliver their power to the load simultaneously.

4. Power train 2 obtains power from the load (regenerative braking).

5. Power train 2 obtains power from power train 1.

6. Power train 2 obtains power from power train 1 and the load simultaneously.

7. Power train 1 delivers power to the load and to power train 2 simultaneously.

FIGURE 5.1 Conceptual illustration of a hybrid electric drive train.

8. Power train 1 delivers its power to power train 2, and power train 2 delivers its power to the load.

9. Power train 1 delivers its power to the load, and the load delivers the power to power train 2.

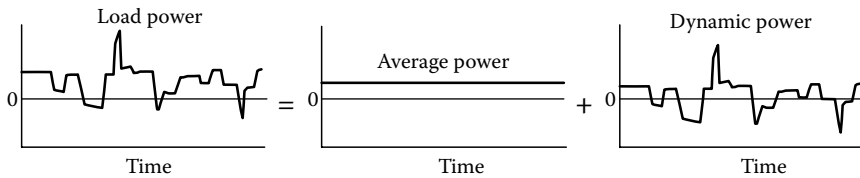In the case of hybridization with a gasoline (diesel)–IC engine (power train 1) and a battery–electric machine (power train 2), pattern (1) is the engine-alone propelling mode. This may be used when the batteries are almost completely depleted and the engine has no remaining power to charge the batteries, or when the batteries have been fully charged and the engine is able to supply sufficient power to meet the power demands of the vehicle. Pattern (2) is the pure electric propelling mode, in which the engine is shut off. This pattern may be used for situations where the engine cannot operate effectively, such as very low speed, or in areas where emissions are strictly prohibited. Pattern (3) is the hybrid traction mode and may be used when large power is needed, such as during sharp accelerating or steep hill climbing. Pattern (4) is the regenerative braking mode, by which the kinetic or potential energy of the vehicle is recovered through the electric motor functioning as a generator. The recovered energy is then stored in the batteries and reused later on. Pattern (5) is the mode in which the engine charges the batteries while the vehicle is at a standstill, coasting, or descending a slight grade, in which no power goes into or comes from the load. Pattern (6) is the mode in which both regenerating braking and the IC engine charge the batteries simultaneously. Pattern (7) is the mode in which the engine propels the vehicle and charges the batteries simultaneously. Pattern (8) is the mode in which the engine charges the batteries, and the batteries supply power to the load. Pattern (9) is the mode in which the power flows into the batteries from the heat engine through the vehicle mass. The typical configuration of this mode is that the two power trains are separately mounted on the front and rear axles of the vehicle, which will be discussed in the following sections.

The abundant operation modes in a hybrid vehicle create much more flexibility over a single power train vehicle. With proper configuration and control, applying a specific mode for a special operating condition can potentially optimize the overall performance, efficiency, and emissions. However, in a practical design, deciding which mode should be implemented depends on many factors, such as the physical configuration of the drive train, power train efficiency characteristics, load characteristics, and so on.

Operating each power train in its optimal efficiency region is essential for the overall efficiency of the vehicle. An IC engine generally has the best efficiency operating region with a wide throttle opening. Operating away from this region will cause low operating efficiency (refer to Figures 2.30, 2.32, 2.34, 2.35, and 3.6). On the other hand, efficiency suffering in an electric motor is not as detrimental when compared to an IC engine that operates away from its optimal region (refer to Figure 4.14).
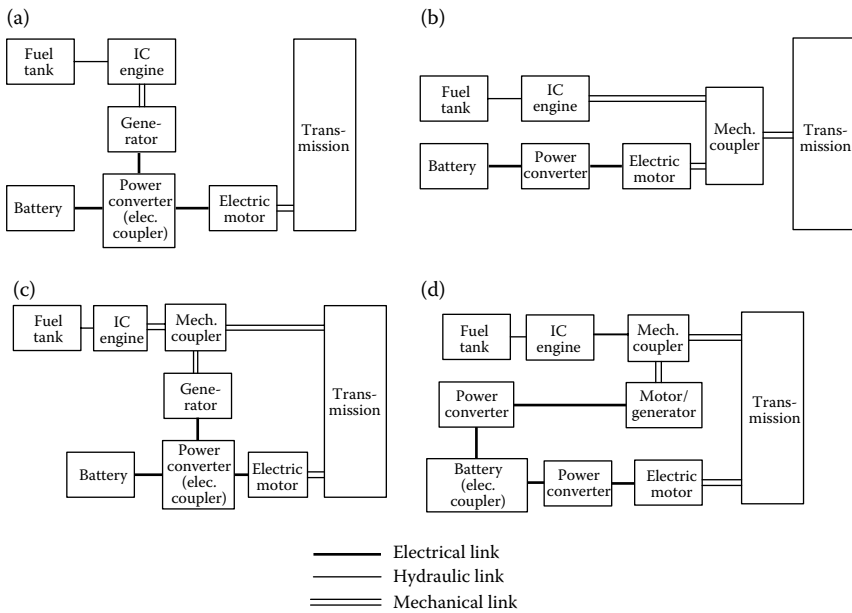
FIGURE 5.2   A load power is decomposed into steady and dynamic components.

The load power of a vehicle varies randomly in real operation due to frequent acceleration, deceleration, and climbing up and down grades, as shown in Figure 5.2. Actually, the load power is composed of two components: one is steady (average) power, which has a constant value, and the other is dynamic power, which has a zero average. In designing the control strategy of a hybrid vehicle, one power train that favors steady-state operation, such as an IC engine and fuel cell, may be used to supply the average power. On the other hand, another power train, such as an electric motor, may be used to supply the dynamic power. The total energy output from the dynamic power train will be zero in a whole driving cycle. This implies that the energy source of the dynamic power train does not lose energy capacity at the end of the driving cycle. It functions only as a power damper.

In a hybrid vehicle, steady power may be provided by an IC engine, a Stirling engine, a fuel cell, and so on. The IC engine or the fuel cell can be much smaller than that in a single power train design because the dynamic power is taken by the dynamic power source, and then can operate steadily in its most efficient region. The dynamic power may be provided by an electric motor powered by batteries, ultracapacitors, flywheels (mechanical batteries), and their combinations.[1,3]

5.2   Architectures of Hybrid Electric Drive Trains

The architecture of a hybrid vehicle is loosely defined as the connection between the components that define the energy flow routes and control ports. Traditionally, HEVs were classified into two basic types: series and parallel. It is interesting to note that, in 2000, some newly introduced HEVs could not be classified into these kinds.[4] Hence, HEVs are presently classified into four kinds—series hybrid, parallel hybrid, series–parallel hybrid, and complex hybrid—that are functionally shown in Figure 5.3.[5] Scientifically, the classifications above are not very clear and may cause confusion. Actually, in an HEV, there are two kinds of energy flowing in the drive train: one is mechanical energy and the other is electrical energy. Adding two powers together or splitting one power into two at the power merging point always occurs with the same power type, that is, electrical or mechanical,

FIGURE 5.3 Classifications of hybrid EVs. (a) Series (electrically coupling), (b) parallel (mechanical coupling), (c) series–parallel (mechanical and electrical coupling), and (d) complex (mechanical and electrical coupling).

not electrical and mechanical. So perhaps a more accurate definition for HEV architecture may be to take the power coupling or decoupling features such as an electrical coupling drive train, a mechanical coupling drive train, and a mechanical–electrical coupling drive train.

Figure 5.3a functionally shows the architecture that is traditionally called a series hybrid drive train. The key feature of this configuration is that two electrical powers are added together in the power converter, which functions as an electric power coupler to control the power flows from the batteries and generator to the electric motor, or in the reverse direction, from the electric motor to the batteries. The fuel tank, the IC engine, and the generator constitute the primary energy supply and the batteries function as the energy bumper.

Figure 5.3b is the configuration that is traditionally called a parallel hybrid drive train. The key of this configuration is that two mechanical powers are added together in a mechanical coupler. The IC engine is the primary power plant, and the batteries and electric motor drive constitute the energy bumper. The power flows can be controlled only by the power plants—the engine and electric motor.

Figure 5.3c shows the configuration that is traditionally called a series–parallel hybrid drive train. The distinguished feature of this configuration is the employment of two power couplers—mechanical and electrical. Actually, this configuration is the combination of series and parallel structures,
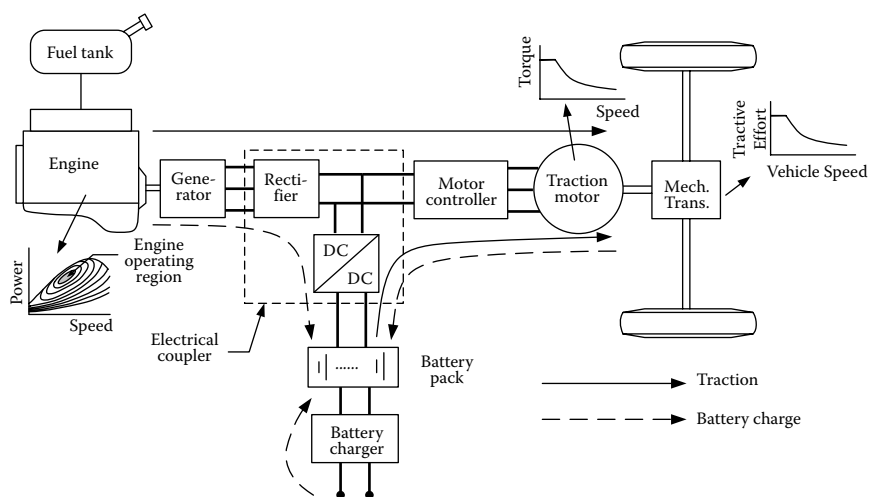
possessing the major features of both and more plentiful operation modes than those of the series or parallel structure alone. On the other hand, it is relatively more complicated and may be of higher cost.

Figure 5.3d shows a configuration of the so-called complex hybrid, which has a similar structure to the series–parallel one. The only difference is that the electric coupling function is moved from the power converter to the batteries and one more power converter is added between the motor/generator and the batteries.

We will concentrate more on the first three configurations—series, parallel, and series–parallel.

5.2.1   Series Hybrid Electric Drive Trains (Electrical Coupling)

A series hybrid drive train is a drive train in which two electrical power sources feed a single electrical power plant (electric motor) that propels the vehicle. The configuration that is most often used is the one shown in Figure 5.4. The unidirectional energy source is a fuel tank and the unidirectional energy converter (power plant) is an IC engine coupled to an electric generator. The output of the electric generator is connected to a power DC bus through a controllable electronic converter (rectifier). The bidirectional energy source is a battery pack connected to the power DC bus by means of a controllable, bidirectional power electronic converter (DC/DC converter). The power bus is also connected to the controller of the electric motor. The traction motor can be controlled as either a motor or a generator, and in forward or reverse motion. This drive train may need a battery charger to charge the batteries by wall plug-in from a power grid. The series hybrid drive train

FIGURE 5.4   Configuration of a series hybrid electric drive train.

originally came from an EV on which an additional engine–generator is added to extend the operating range that is limited by the poor energy density of the batteries.

The drive train needs a vehicle controller to control the operation and power flows based on the driver's operating command through accelerator and brake pedals and other feedback information from the components (not shown in Figure 5.4, but for details see Figure 7.1). The vehicle controller will control the IC engine through its throttle, electric coupler (controllable rectifier and DC/DC converter), and traction motor to produce the demanded propelling torque or regenerative braking torque with one of the following operation modes:

1. *Pure electric traction mode*: The engine is turned off and the vehicle is propelled only from the batteries.
2. *Pure engine traction mode*: The vehicle traction power comes only from the engine–generator, while the batteries neither supply nor accept any power from the drive train. The electric machines serve as an electric transmission from the engine to the driven wheels.
3. *Hybrid traction mode*: The traction powers are drawn from both the engine–generator and the batteries, merging together in the electrical coupler.
4. *Engine traction with battery charging mode*: The engine–generator supplies power to charge the batteries and to propel the vehicle simultaneously. The engine–generator power is split in the electric coupler.
5. *Regenerative braking mode*: The engine–generator is turned off and the traction motor is operated as a generator powered by the vehicle kinetic or potential energy. The power generated is charged to the batteries and reused in later propelling.
6. *Battery charging mode*: The traction motor receives no power and the engine–generator is operated only to charge the batteries.
7. *Hybrid battery charging mode*: Both the engine–generator and the traction motor operate as generators in braking to charge the batteries.

Series hybrid drive trains offer several advantages:

1. There is no mechanical connection between the engine and the driven wheels. Consequently, the engine can be potentially operated at any point on its speed–torque (power) map. This distinguished advantage, with a sophisticated power flow control, provides the engine with opportunities to be operated always within its maximum efficiency region, as shown in Figure 5.4. The efficiency and emissions of the engine in this narrow region may be further improved by some special design and control technologies, which is much easier than in the

whole operating domain. Furthermore, the mechanical decoupling of the engine from the driven wheels allows the use of high-speed engines, where it is difficult to directly propel the wheels through a mechanical link, such as gas turbines or power plants that have slow dynamic responses (e.g., Stirling engine, etc.).

2. Because electric motors have a torque–speed profile that is very close to the ideal for traction, as shown in Figures 2.12, 2.14, and 4.4, the drive train may not need multigear transmission, as discussed in Chapter 3. Therefore, the structure of the drive train can be greatly simplified and is of less cost. Furthermore, two motors may be used, each powering a single wheel, and the mechanical differential can be removed. Such an arrangement also has the following advantages of decoupling the speeds of two wheels, a similar function of a mechanical differential, and an additional function of antislip similar to the conventional traction control. Furthermore, four in-the-wheel motors may be used, each one driving a wheel. In such a configuration, the speed and torque of each wheel can be independently controlled. Consequently, the drivability of the vehicle can be significantly enhanced. This is very important for off-road vehicles which usually operate on difficult terrain, such as ice, snow, and soft ground.

3. The control strategy of the drive train may be simple, compared to other configurations, because of its fully mechanical decoupling between the engine and wheels.
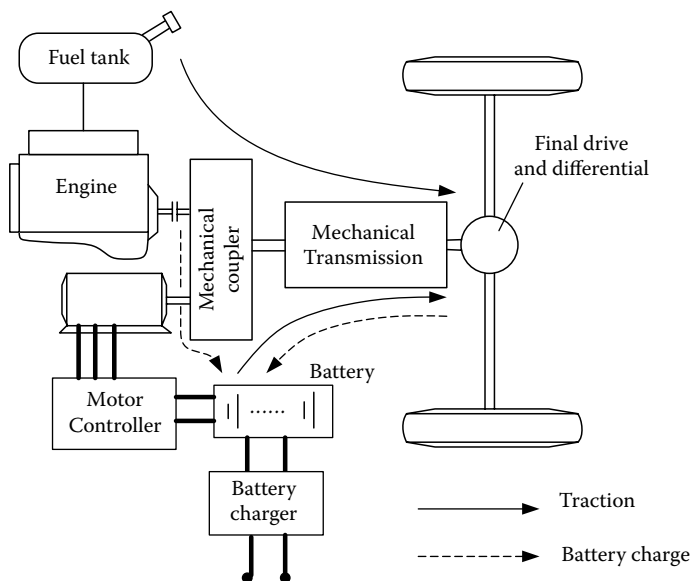
However, series hybrid electric drive trains have some disadvantages, such as the following:

1. The energy from the engine changes its form twice to reach its destination—driven wheels (mechanical to electrical in the generator and electrical to mechanical in the traction motor). The inefficiencies of the generator and traction motor may cause significant losses.

2. The generator adds additional weight and cost.

3. Because the traction motor is the only power plant propelling the vehicle, it must be sized to produce enough power for optimal vehicle performance in terms of acceleration and gradeability.

The design and control principle of a series HEV will be discussed in Chapter 7.

5.2.2 Parallel Hybrid Electric Drive Trains (Mechanical Coupling)

A parallel hybrid drive train is a drive train in which the engine supplies its mechanical power directly to the driven wheels in a manner similar to a conventional IC engine vehicle. The engine is assisted by an electric motor that is mechanically coupled to the driveline. The powers of the engine and electric

FIGURE 5.5 Configuration of a parallel hybrid electric drive train.

motor are coupled together by mechanical coupling, as shown in Figure 5.5. The distinguished feature of this architecture is that two mechanical powers from the engine and electric motor are added together by a mechanical coupler.

All the possible operating modes mentioned in the series hybrid drive train are still effective. The major advantages of the parallel hybrid drive train over the series one are the following: (1) both the engine and the electric motor directly supply torques to the driven wheels and no energy form conversion occurs, thus the energy loss may be less; and (2) it is compact because there is no need for an additional generator and the traction motor is smaller than in series. Its major disadvantage is the mechanical coupling between the engine and the driven wheels, since then the engine operating points cannot be fixed in a narrow speed and torque region. Another disadvantage may be the complex structure and control.

Generally, mechanical coupling consists of torque coupling and speed coupling. In torque coupling, the mechanical coupler adds the torques of the engine and motor together and delivers the total torque to the driven wheels. The engine and motor torque can be independently controlled. But the speeds of the engine, motor, and vehicle are linked together with a fixed relationship and cannot be independently controlled because of the power conservation constraint. Similarly in speed coupling, the speeds of the engine and motor can be added together and all the torques are linked together and cannot be independently controlled. The details of these two kinds of mechanical coupler are described hereafter.

5.2.2.1   Parallel Hybrid Drive Train with Torque Coupling

5.2.2.1.1   Torque-Coupling Devices

Figure 5.6 conceptually shows a mechanical torque coupling, which is a three-port, two-degree-of-freedom mechanical device. Port 1 is a unidirectional input and ports 2 and 3 are bidirectional input or output, but both are not input at the same time. Here input means the energy flow into the device and output means the energy flow out of the device. In a hybrid vehicle application, port 1 is connected to an IC engine directly or through a mechanical transmission. Port 2 is connected to the shaft of an electric motor directly or through a mechanical transmission. Port 3 is connected to the driven wheels through a mechanical linkage.

If the losses are ignored and in steady state, the power input to the torque coupler is always equal to the power output from it. Suppose here port 2 (electric motor) is in propelling, that is, input. The power output to the vehicle wheels is:
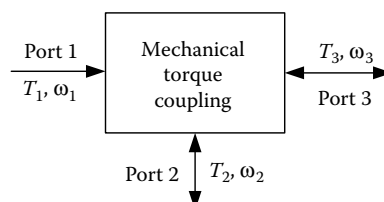
$$T_3\omega_3 = T_1\omega_1 + T_2\omega_2. \tag{5.1}$$

The torque coupler can be expressed as

$$T_3 = k_1 T_1 + k_2 T_2, \tag{5.2}$$
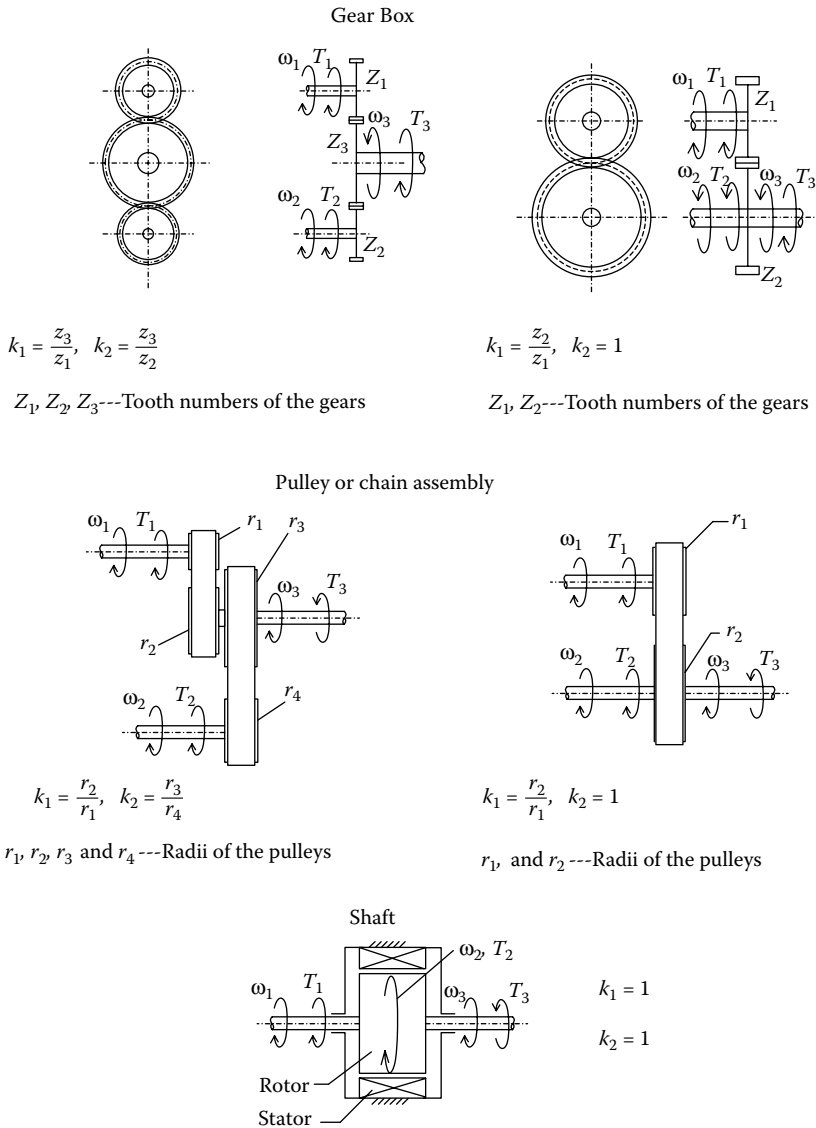
where k_1 and k_2 are the structural parameters of the torque coupler, which are described by the gear ratios and usually are constant when the device design is fixed. For the torque coupler, T_3 is load torque and T_1 and T_2 are propelling torques that are independent of each other and can be independently controlled. However, due to the constraint of Equation 5.1, the angular velocities ω_1, ω_2, and ω_3 are linked together and cannot be independently controlled, as expressed by

$$\omega_3 = \frac{\omega_1}{k_1} = \frac{\omega_2}{k_2}. \tag{5.3}$$

Figure 5.7 shows some common mechanical torque-coupling devices.

FIGURE 5.6   Torque-coupling device.

Gear Box

$k_1 = \dfrac{z_3}{z_1}, \quad k_2 = \dfrac{z_3}{z_2}$

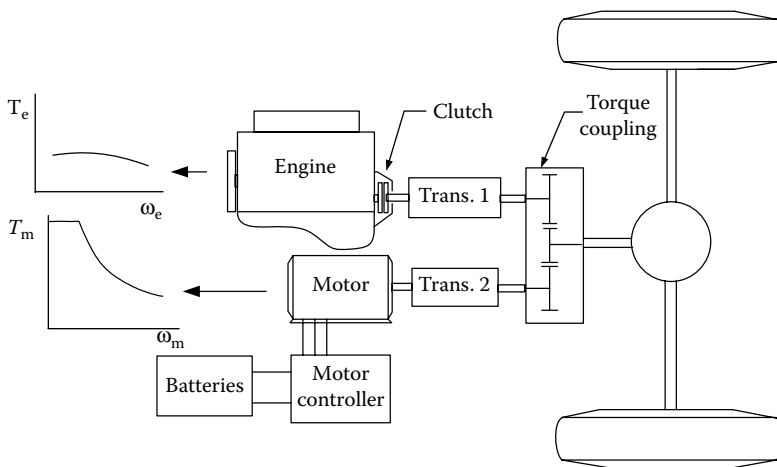Z_1, Z_2, Z_3---Tooth numbers of the gears

$k_1 = \dfrac{z_2}{z_1}, \quad k_2 = 1$

Z_1, Z_2---Tooth numbers of the gears

Pulley or chain assembly

$k_1 = \dfrac{r_2}{r_1}, \quad k_2 = \dfrac{r_3}{r_4}$

r_1, r_2, r_3 and r_4 ---Radii of the pulleys

$k_1 = \dfrac{r_2}{r_1}, \quad k_2 = 1$

$r_1,$ and r_2 ---Radii of the pulleys

Shaft

$k_1 = 1$

$k_2 = 1$

FIGURE 5.7 Commonly used mechanical torque-coupling devices.

5.2.2.1.2 *Drive Train Configurations with Torque Coupling*

Torque couplers can be used to constitute hybrid drive trains with many different configurations. Based on the torque coupler used, a two- or one-shaft configuration may be constituted. In each, transmission may be placed in different positions with different gears, resulting in various tractive characteristics.
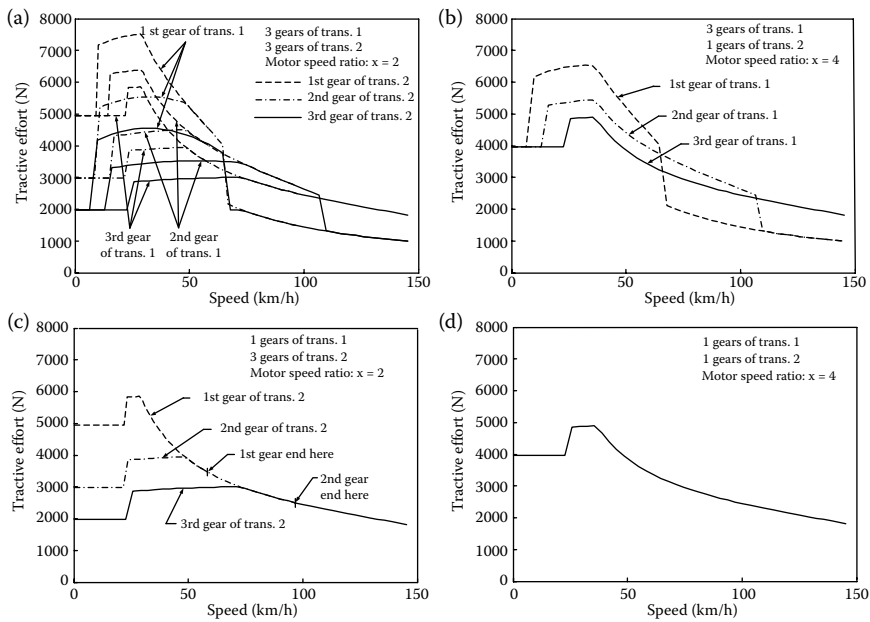
FIGURE 5.8   Two-shaft configuration.

A good design will depend mostly on the tractive requirements, engine size, motor size, and motor speed–torque characteristics.

Figure 5.8 shows a two-shaft configuration, in which two transmissions are used. One is placed between the engine and the torque coupler and the other between the motor and the torque coupler. Both transmissions may be single- or multigear. Figure 5.9 shows the general tractive effort–speed profiles of a vehicle with different transmission gears. It is evident that two multigear transmissions produce many tractive effort profiles. The performance and overall efficiency of the drive train may be superior to other designs, because two multigear transmissions provide more opportunities for both the engine and the electric traction system (electric machine and batteries) to operate in their optimum region. This design also provides great flexibility in the design of the engine and electric motor characteristics. However, two multigear transmissions will significantly complicate the drive train and increase the burden of the control system for selecting the proper gear in each transmission.[6,7]

In Figure 5.8, a multigear transmission, 1, and a single-gear transmission, 2, may be used. Referring to the relative positions of transmissions and the electric motor, this configuration is referred to as a pretransmission configuration (the electric motor is in front of the transmission). The tractive effort–speed profiles are shown in Figure 5.9b. In the design of a hybrid drive train, the maximum tractive effort with this transmission arrangement may be sufficient for hill climbing performance; greater tractive effort would not be needed because of the limitation of tire–ground contact adhesion. Utilizing a single-gear transmission, 2, takes advantage of the high torque of an electric machine at low speed. The multigear transmission, 1, is used to overcome the disadvantages of the IC engine speed–torque characteristics (flat torque output in its entire speed range). The multigear transmission, 1, also tends to improve the operating efficiency of the engine and reduces the speed range of the
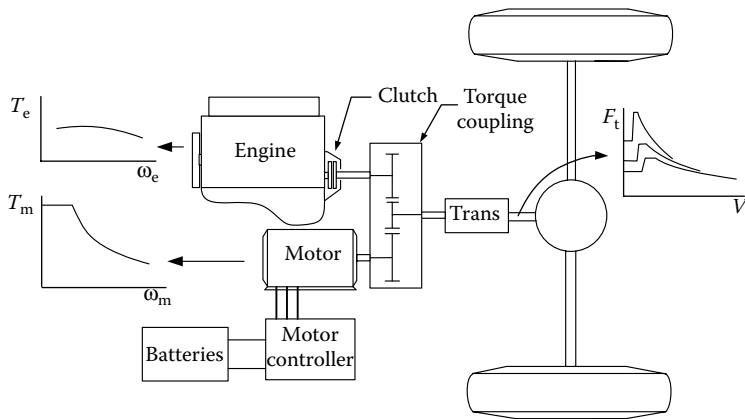
FIGURE 5.9 Tractive effort along with vehicle speed with different transmission schemes: (a) two multigear transmissions, (b) multigear engine transmission and single-gear motor transmission, (c) single-gear engine transmission and multigear motor transmission, and (d) both single-gear transmissions.

vehicle, in which the electric machine must propel the vehicle alone, thus preventing the batteries from quickly discharging.

In contrast to the above design, Figure 5.9c shows the tractive effort–speed profile of a drive train that has a single-gear transmission, 1, for the engine and a multigear transmission, 2, for the electric motor. This configuration is considered to be an unfavorable design, because it does not use the advantages of the two power plants.

Figure 5.9d shows the tractive effort–speed profile of a drive train that has two single-gear transmissions. This arrangement results in a simple configuration and control. The limitation to the application of this drive train is the maximum tractive effort of the drive train. When the power ratings of the engine, electric motor, batteries, and transmission parameters are properly designed, this drive train would serve the vehicle with satisfactory performance and efficiency.
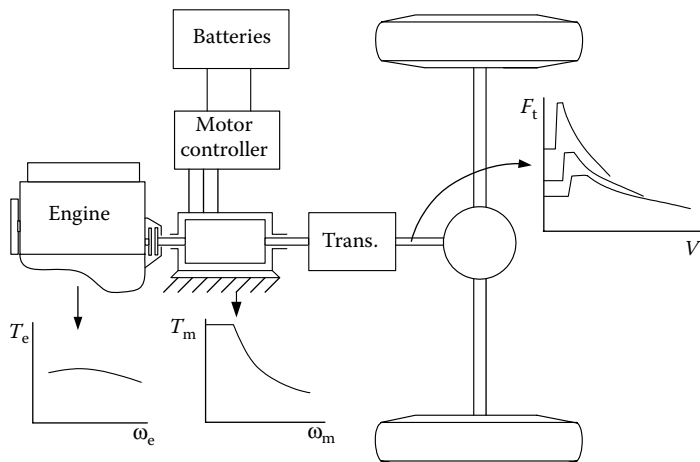
Another configuration of a two-shaft parallel hybrid drive train is shown in Figure 5.10, in which the transmission is located between the torque coupler and the drive shaft and may be categorized as a pretransmission. The transmission amplifies the torques of both the engine and the electric motor with the same scale. The design of the gear ratios k_1 and k_2 in the torque coupler (Equation 5.3) allows the electric motor and the engine to reach their
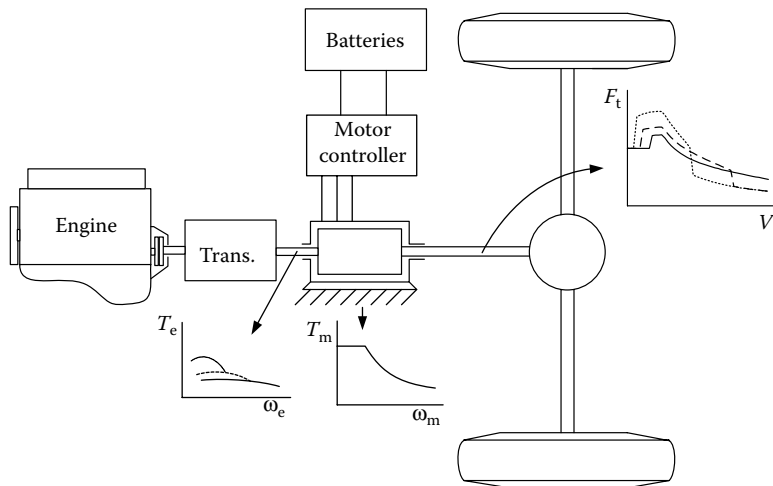
FIGURE 5.10 Two-shaft configuration.

maximum speeds at the same time. This configuration would be suitable when a relatively small engine and electric motor are used, where a multigear transmission is needed to enhance the tractive effort at low speeds.

The simplest and most compact architecture of the torque-coupling parallel hybrid is the single-shaft configuration, where the rotor of the electric motor functions as the torque coupler ($k_1 = 1$ and $k_2 = 1$ in Equations 5.2 and 5.3). The electric motor may be located either between the engine and transmission as shown in Figure 5.11, referred to as pretransmission, or between the transmission and final drive as shown in Figure 5.12, referred to as post-transmission.

FIGURE 5.11 Pretransmission single-shaft torque combination parallel hybrid electric drive train.
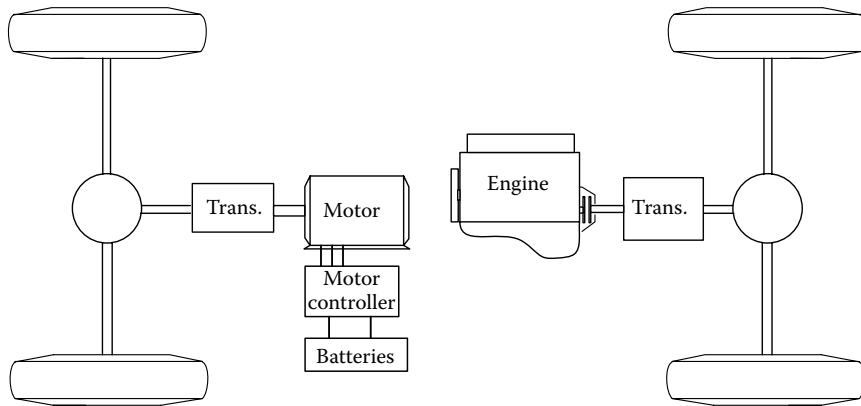
FIGURE 5.12 Post-transmission single-shaft torque combination parallel hybrid electric drive train.

In the pretransmission configuration as shown in Figure 5.11, torques of both the engine and motor are modified by the transmission. However, the engine and motor are required to have the same speed range. This configuration is usually used in the case of a small motor, referred to as a mild hybrid drive train, in which the electric motor functions as an engine starter, an electrical generator, an engine power assistant, and for regenerative braking.

In the post-transmission configuration as shown in Figure 5.12, the transmission only modifies the engine torque while the motor directly delivers its torque to the final drive without modification. This configuration may be used in a drive train where a large electric motor with a long constant power region is employed. The transmission is only used to change the engine operating points for improving the vehicle performance and engine operating efficiency. It should be noted that the batteries cannot be charged from the engine by running the electric motor as a generator when the vehicle is at a standstill, since the motor is rigidly connected to the driven wheels.

Another torque-coupling parallel hybrid drive train is the separated axle architecture, in which one axle is powered by the engine and the other by the electric motor, as shown in Figure 5.13. The tractive efforts produced by the two power trains are added together through the vehicle chassis and road. The operating principle is similar to the two-shaft configuration shown in Figure 5.8. Both transmissions for the engine and electric motor may be single-gear or multigear. This configuration has similar tractive effort characteristics, as shown in Figure 5.9.

The separated axle architecture offers some of the advantages of a conventional vehicle. It keeps the original engine and transmission unaltered and adds an electrical traction system on the other axle. It is also a four-wheel

FIGURE 5.13 Separated axle torque combination parallel hybrid electric drive train.
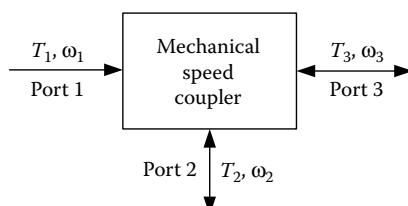
drive, which improves the traction on slippery roads and reduces the tractive effort on a single tire.

However, electric machines and the eventual differential gear system occupy a lot of space and may reduce the available passenger space and luggage space. This problem may be solved if the transmission behind the electric motor is single-gear and the single electric motor is replaced by two small-sized electric motors that can be placed within the two driven wheels. It should be noted that the batteries cannot be charged from the engine when the vehicle is at a standstill.

5.2.2.2 *Parallel Hybrid Drive Train with Speed Coupling*

5.2.2.2.1 *Speed-Coupling Devices*

The powers produced by the two power plants may be coupled together by adding their speeds, as shown in Figure 5.14. Similar to the mechanical torque coupler, the speed coupler is also a three-port, two-degree-of-freedom mechanical device. Port 1 may be connected to an IC engine with unidirectional energy flow. Ports 2 and 3 may be connected to an electric motor and to the load (final drive), both with bidirectional energy flow.

FIGURE 5.14 Speed coupling.

The mechanical speed coupler has the property

$$\omega_3 = k_1\omega_1 + k_2\omega_2, \tag{5.4}$$

where k_1 and k_2 are constants associated with the structural and geometric design. Among the three speeds, ω_1, ω_2, and ω_3, two of them are independent of each other and can be controlled independently. Due to the constraint of power conservation, the torques are linked together by
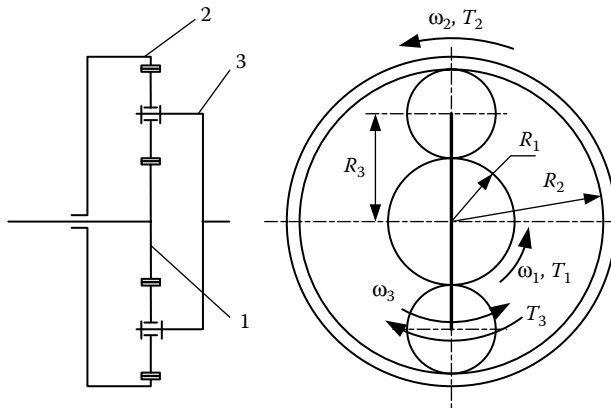
$$T_3 = \frac{T_1}{k_1} = \frac{T_2}{k_2}, \tag{5.5}$$

In which the minimum torque determines the other two.

A typical speed-coupling device is the planetary gear unit as shown in Figure 5.15. The planetary gear unit is a three-port unit consisting of sun gear, ring gear, and yoke labeled 1, 2, and 3, respectively. The speed relationship in the sun gear, ring gear, and yoke can be obtained as follows.

First, let the yoke be attached to a stationary frame, that is, $\omega_3 = 0$; the gear ratio from the sun gear to ring gear is

$$i_{1-2}^{3} = \frac{\omega_2^3}{\omega_1^3} = -\frac{R_2}{R_1} = -\frac{Z_2}{Z_1}, \tag{5.6}$$

where ω_1^3 and ω_2^3 are the angular velocities of the sun gear and ring gear with respect to the yoke (when the yoke is at a standstill), R_1 and R_2 are the radii of the sun gear and ring gear, respectively, and Z_1 and Z_2 are the tooth numbers of the sun gear and ring gear, respectively, which are proportional to the radii of the sun gear and ring gear. Here, rotating in the counterclockwise direction is defined as positive angular velocity, whereas rotating in the clockwise

FIGURE 5.15 Planetary gear unit used as a speed-coupling device.

direction is defined as negative angular velocity, as shown in Figure 5.15. Equation 5.6 indicates that ω_1^3 and ω_2^3 have different rotating directions and thus the gear ratio i_{1-2}^3 is negative. When the yoke is free from the stationary frame, the absolute angular velocities of the sun gear, ring gear, and yoke can be expressed by

$$\frac{\omega_1 - \omega_3}{\omega_2 - \omega_3} = i_{1-2}^3. \tag{5.7}$$

Then we obtain

$$\omega_1 - i_{1-2}^3 \omega_2 - (1 - i_{1-2}^3)\omega_3 = 0. \tag{5.8}$$

Conventionally, we are not accustomed to negative gear ratio. If we define the gear ratio as a positive number, as

$$i_g = -i_{1-2}^3 = \frac{R_2}{R_1} = \frac{Z_2}{Z_1}, \tag{5.9}$$

Equation 5.8 can be rewritten as

$$\omega_1 + i_g \omega_2 - (1 + i_g)\omega_3 = 0 \tag{5.10}$$

or

$$\omega_3 = \frac{1}{1 + i_g}\omega_1 + \frac{i_g}{1 + i_g}\omega_2. \tag{5.11}$$

Comparing Equation 5.11 with Equation 5.4, $k_1 = 1/(1 + i_g)$ and $k_2 = i_g/(1 + i_g)$ are obtained.

Similar to the definition of speed, when the torque acting on each element of the planetary gear unit is defined to be positive in the counterclockwise direction and negative in the clockwise direction, the total power into the unit should be zero (output power is negative) when the loss inside the unit is ignored, that is,

$$T_1 \omega_1 + T_2 \omega_2 + T_3 \omega_3 = 0. \tag{5.12}$$

Combining Equations 5.11 and 5.12 yields

$$T_3 = -(1 + i_g)T_1 = -\frac{1 + i_g}{i_g}T_2. \tag{5.13}$$

Equation 5.13 indicates that the torques acting on the sun gear, T_1, and ring gear, T_2, always have the same sign (both positive or negative), and the torque acting on the yoke, T_3, always has the direction opposite to T_1 and T_2, as shown in Figure 5.15.

When one element of the sun gear, ring gear, or yoke is locked to the stationary frame, that is, one degree of freedom is constrained, the unit will become

Element fixed	Speed	Torque
Sun gear	$\omega_3 = \dfrac{i_g}{1 + i_g}\, \omega_2$	$T_3 = -\dfrac{1 + i_g}{i_g}\, T_2$
Ring gear	$\omega_3 = \dfrac{1}{1 + i_g}\, \omega_1$	$T_3 = -(1 + i_g)\, T_1$
Yoke	$\omega_1 = -i_g\, \omega_2$	$T_1 = \dfrac{1}{i_g}\, T_2$

FIGURE 5.16 Speed and torque relationships while one element is fixed.

a single-gear transmission (one input and one output). The speed and torque relationships, while different elements are fixed, are shown in Figure 5.16.

Another interesting device used as a speed coupler is an electric motor with a floating stator (called transmotor in this book), in which the stator, generally fixed to a stationary frame in a traditional motor, is released to form a double-rotor machine—outer and inner rotor. The outer rotor, inner rotor, and air gap are the three ports. Electric power is converted into mechanical power through the air gap, as shown in Figure 5.17. The motor speed, in conventional terms, is the relative speed of the inner rotor with respect to the outer rotor. Because of the action and reaction effect, the torques acting on both rotors are always the same and result in constants $k_1 = 1$ and $k_2 = 1$. The speed relationship can be expressed as

$$\omega_{or} = \omega_{ir} + \omega_{oi}, \tag{5.14}$$

where ω_{io} is the inner rotor speed relative to the outer rotor stator. The torque relationship can be expressed as

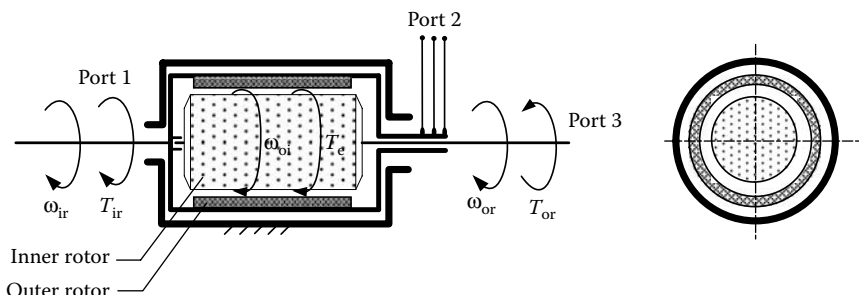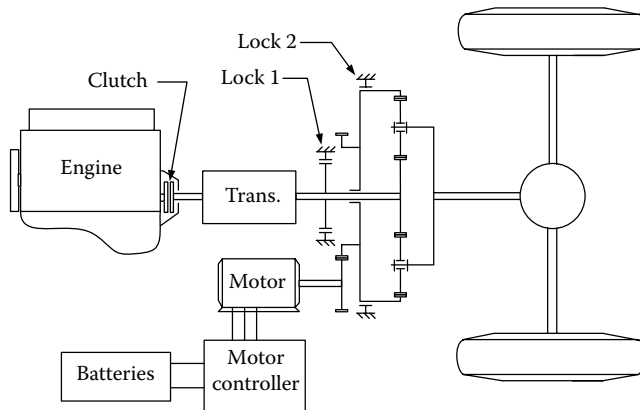$$T_{ir} = T_{os} = T_e. \tag{5.15}$$

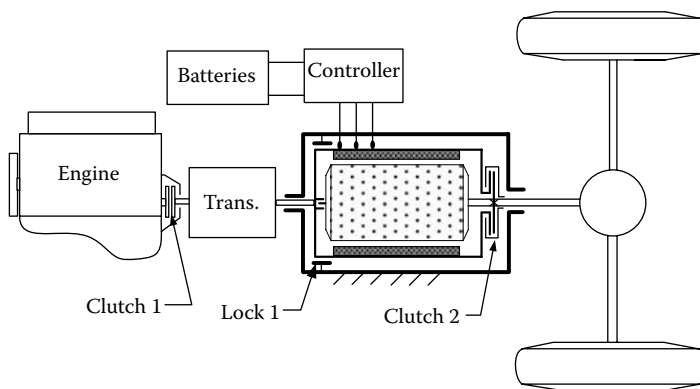**FIGURE 5.17** Transmotor used as a speed coupler.

FIGURE 5.18   Hybrid electric drive train with speed coupling of a planetary gear unit.

5.2.2.2.2   *Drive Train Configurations with Speed Coupling*

Similar to the torque-coupling device, the speed-coupling units can be used to constitute various hybrid drive trains. Figures 5.18 and 5.19 show two examples of hybrid drive trains with speed coupling using a planetary gear unit and an electric transmotor. In Figure 5.18, the engine supplies its power to the sun gear through a clutch and transmission. The transmission is used to modify the speed–torque profile of the engine so as to match the traction requirements. The transmission may be multigear or single-gear based on the engine speed–torque profile. The electric motor supplies its power to the ring gear through a pair of gears. Lock 1 and lock 2 are used to lock the sun gear and ring gear to the stationary frame of the vehicle in order to implement different operation modes. The following operation modes can be carried out:

1. *Hybrid traction*: When lock 1 and lock 2 are released (the sun gear and ring gear can rotate), both the engine and electric machine supply positive speed and torque (positive power) to the driven wheels. The output speed and torque from the yoke of the planetary unit is described by Equations 5.11 and 5.13. That is, the rotational speed of the yoke is the summation of the sun gear speed (engine speed, or proportional to engine speed) and the ring gear speed (electric motor speed, or proportional to motor speed). However, the output torque from the yoke is proportional to the engine torque and motor torque. Torque control will be studied in Chapter 8.

2. *Engine-alone traction*: When lock 2 locks the ring gear to the vehicle frame and lock 1 is released, the engine alone supplies power to the driven wheels. From Equations 5.11 and 5.13, the speed of the yoke is proportional to the speed of the sun gear as $\omega_3 = \omega_1/(1 + i_g)$, and the
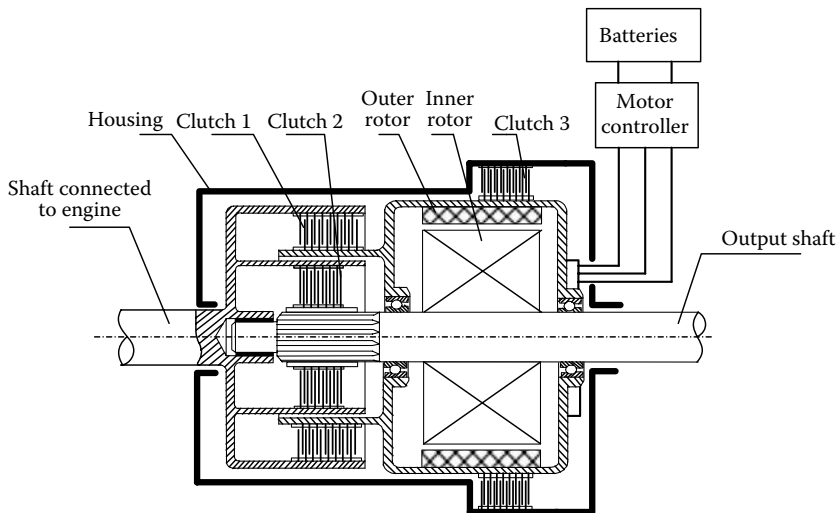
FIGURE 5.19 Hybrid electric drive train with speed coupling of an electric transmotor.

torque output from the yoke is proportional to the torque applied on the sun gear from the engine as $T_3 = (1 + i_g)T_1$.

3. *Motor-alone traction*: When lock 1 locks the sun gear to the vehicle frame (engine is shut off and engine clutch is disengaged) and lock 2 is released, only the electric motor supplies its power to the driven wheels. From Equations 5.11 and 5.13, the speed of the yoke is proportional to the speed of the ring gear as $\omega_3 = (\omega_2 i_g)/(1 + i_g)$, and the torque output from the yoke is proportional to the torque applied on the ring gear by the electric motor as $T_3 = (1 + i_g)/(i_g T_1)$.

4. *Regenerative braking*: The states of lock 1 and lock 2 are the same as in motor-alone traction, the engine is also shut off, the engine clutch is disengaged, and the electric machine is controlled in regenerating mode (negative torque). The kinetic or potential energy of the vehicle can be absorbed by the electric system.

5. *Battery charging from the engine*: The engine clutch and lock 1 and lock 2 are in the same state as in the hybrid traction mode. However, the electric motor is controlled to rotate in the opposite direction, that is, negative speed. Thus, the electric machine operates with positive torque and negative speed (negative power) and absorbs energy from the engine and delivers it to the batteries. In this case, the engine power is split into two parts by decomposing its speed.

The drive train, consisting of the transmotor as shown in Figure 5.19, has a similar structure as that in Figure 5.18. Lock 1 and clutch 2 are used to lock the outer rotor to the vehicle frame and the outer rotor to the inner rotor, respectively. This drive train can fulfill all the operation modes mentioned above. The operating modes analysis is left to the readers.

Figure 5.20 shows an implementation of speed coupling with a transmotor. Clutch 1 is the substitution for clutch 1 as shown in Figure 5.19, clutch 2 has

FIGURE 5.20   Implementation of speed coupling with a transmotor.

the same function as clutch 2 in Figure 5.19, and clutch 3 has the same function as lock 1 in Figure 5.19.
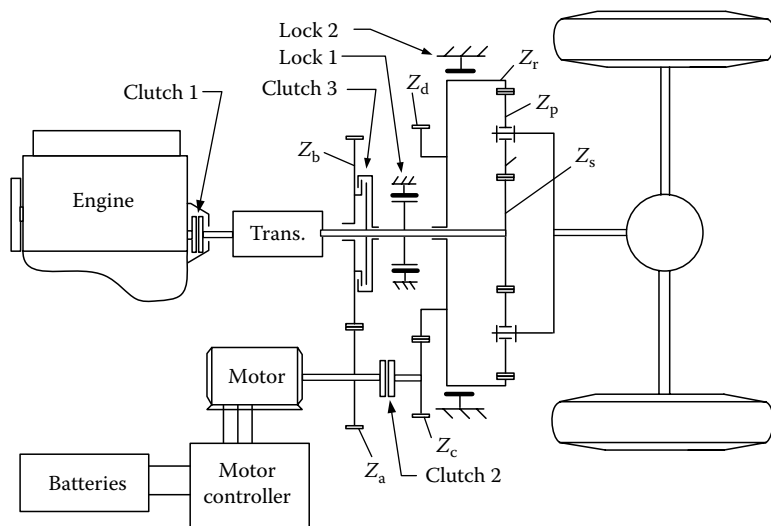
The main advantage of the hybrid drive train with speed coupling is that the speed of two power plants is decoupled from vehicle speed. Therefore, the speed of both power plants can be chosen freely. This advantage is important to power plants, such as the Stirling engine and the gas turbine engine, in which, the operating efficiencies are sensitive to speed and less sensitive to torque.

5.2.2.3   *Hybrid Drive Trains with Both Torque and Speed Coupling*

5.2.2.3.1   *With Optional Coupling Mode*

By combining torque and speed coupling, one may establish a hybrid drive train in which torque- and speed-coupling states can be alternatively chosen. Figure 5.21 shows such a drive train.[8] When the torque-coupling operation mode is chosen, lock 2 locks the ring gear of the planetary unit to the vehicle frame while clutches 1 and 3 are engaged and clutch 2 is disengaged. The power of the engine and the electric motor are added together by adding their torques together through gear Z_a, Z_b and clutch 3 to the sun gear shaft. In this case, the planetary gear unit functions only as a speed reducer. The gear ratio from the sun gear to yoke, defined as ω_1/ω_3, equals $(1 + i_g)$. This is a typical parallel hybrid drive train with torque coupling.

When the speed-coupling mode is chosen as the current operating mode, clutches 1 and 2 are engaged, whereas clutch 3 is disengaged, and locks 1 and 2 release the sun gear and ring gear. The speed of the yoke, connected to the
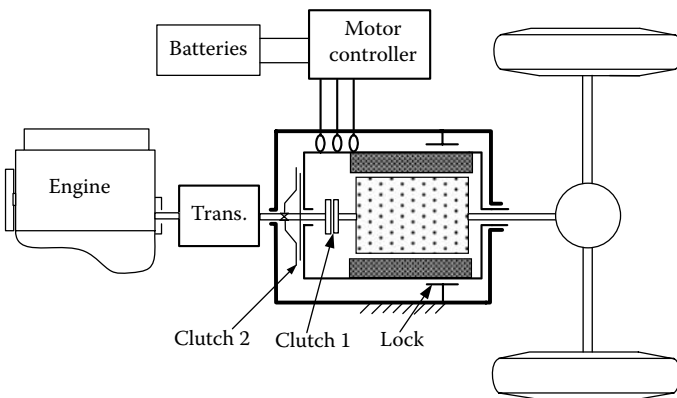
FIGURE 5.21 Alternative torque and speed hybrid electric drive train with a planetary gear unit.

drive wheels, is a combination of engine speed and motor speed (refer to Equation 5.11). But the engine torque, the electric motor torque, and torque on the driven wheels are kept in a fixed relationship as described by Equation 5.13.

With the option to choose the power-coupling mode (torque or speed coupling), the power plant has more opportunities to choose its operation manner and operation region so as to optimize their performance. For instance, at low vehicle speeds, the torque combination operation mode may be suitable for high acceleration or hill climbing. On the other hand, at high vehicle speeds, the speed combination mode would be used to keep the engine speed in its optimal region.

The planetary gear unit and the traction motor in Figure 5.21 can be replaced by a transmotor to constitute a similar drive train as shown in Figure 5.22. When clutch 1 is engaged to couple the output shaft of the transmission to the inner rotor shaft of the transmotor, clutch 2 is disengaged to release the engine shaft from the inner rotor of the transmotor and the lock is activated to fix the outer rotor of the transmotor to the vehicle frame. The drive train then works in the torque-coupling mode. On the other hand, when clutch 1 is disengaged and clutch 2 is engaged and the lock is released, the drive train works in the speed-coupling mode.

The distinguishable characteristic of the above hybrid drive trains is that the drive train can optionally choose the best coupling mode in different driving situations so as to achieve the best vehicle performance and efficiency. However, they cannot run on both coupling modes at the same time, since only two power plants are available.

FIGURE 5.22 Alternative torque- and speed-coupling hybrid electric drive train with a transmotor.

5.2.2.3.2   *With Both Coupling Modes*

By adding another power plant, a hybrid drive train with both speed- and torque-coupling modes at the same time can be realized. A good example is the one developed and implemented in the Toyota Prius by Toyota Motor Company.[9] This drive train is schematically illustrated in Figure 5.23. The drive train uses a planetary gear unit as the speed-coupling device and a set of fixed axle gears as the torque-coupling device. An IC engine is connected to the yoke of the planetary gear unit, and a small motor/generator (few kilowatts) is connected to the sun gear of a planetary gear unit to constitute the speed-coupling configuration. The ring gear is connected to the driven wheels through the axle-fixed gear unit (torque coupler). Meanwhile, a traction motor is also connected to the fixed axle gear unit to constitute the torque-coupling configuration.

From Equation 5.11, the rotational speed of the ring gear or gear Z_a, which is proportional to vehicle speed, is related to the rotational speed of the engine (yoke) and of the motor/generator (sun gear) and is expressed as

$$\omega_r = \frac{1 + i_g}{i_g}\omega_{ice} - i_g\omega_{m/g}, \tag{5.16}$$

where i_g is the gear ratio defined by Equation 5.9 and ω_{ice} and $\omega_{m/g}$ are the rotational speeds of the engine and motor/generator, respectively. The load torque, acting on the ring gear of the planetary gear unit by gear Z_4, is related to the engine torque and the motor/generator torque by
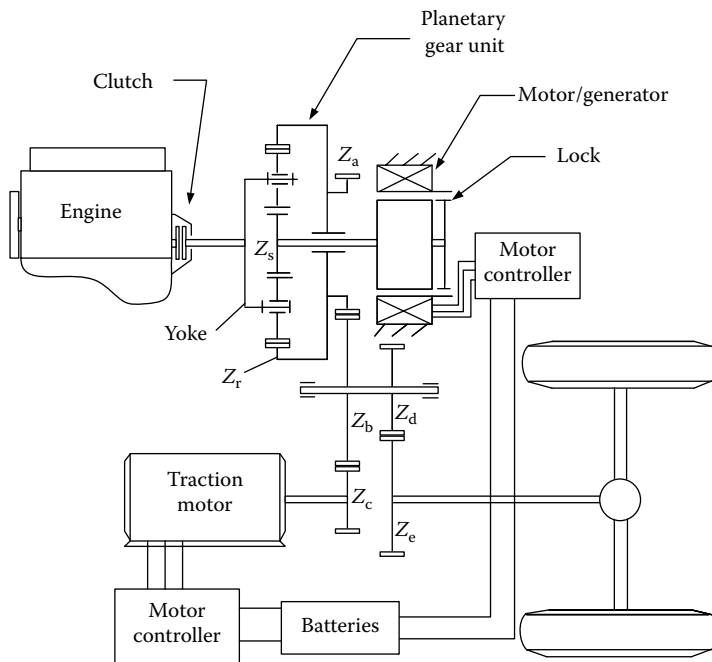
$$-T_r = \frac{i_g}{1 + i_g}T_{ice} = -i_g T_{m/g}. \tag{5.17}$$

Equation 5.17 indicates that the torque, acting on the sun gear, supplied by the motor/generator has opposite direction to engine torque and same direction
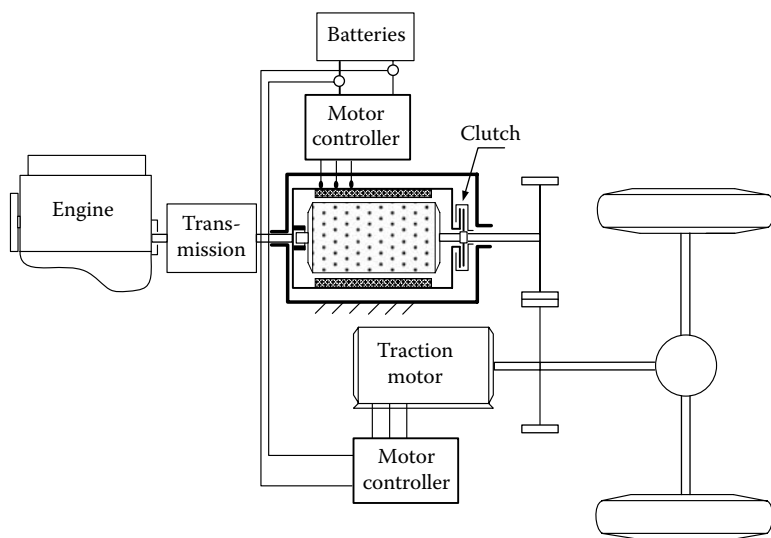
as load torque on the ring gear. With low vehicle speed (small ω_r) and a not very low engine speed (larger than its idle speed), the motor/generator has to rotate in the positive direction (same direction as engine speed). In this condition, the motor/generator operates with a negative power, that is, generating. The power of the engine is split into two parts: one part goes to the motor/generator and the other to vehicle load through the ring gear. This is how the drive train gets its name of power-split hybrid drive train. However, at high vehicle speed, while trying to maintain the engine speed below a given speed, for high engine operating efficiency, the motor/generator may be operated in negative speed, that is, rotating in the opposite direction to engine speed. In this case, the motor/generator delivers positive power to the planetary gear unit, that is, motoring. It becomes clear through the above analysis that the major function of a motor/generator is to control engine speed, that is, decouple engine speed from wheel speed.

The traction motor adds additional torque to the torque output from the ring gear of the planetary gear unit with a torque-coupling mode through gears Z_c, Z_b, Z_d, and Z_e, by which the engine torque is decoupled from the vehicle load.

The small motor and the planetary gear unit in Figure 5.23 can be replaced by an individual transmotor, as shown in Figure 5.24.[10] This drive train has very similar characteristics as the drive train shown in Figure 5.23.
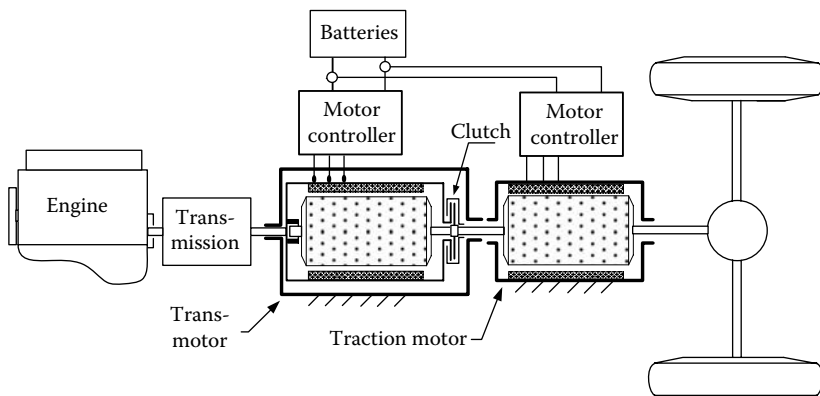

FIGURE 5.23 Integrated speed- and torque-coupling hybrid electric drive train.
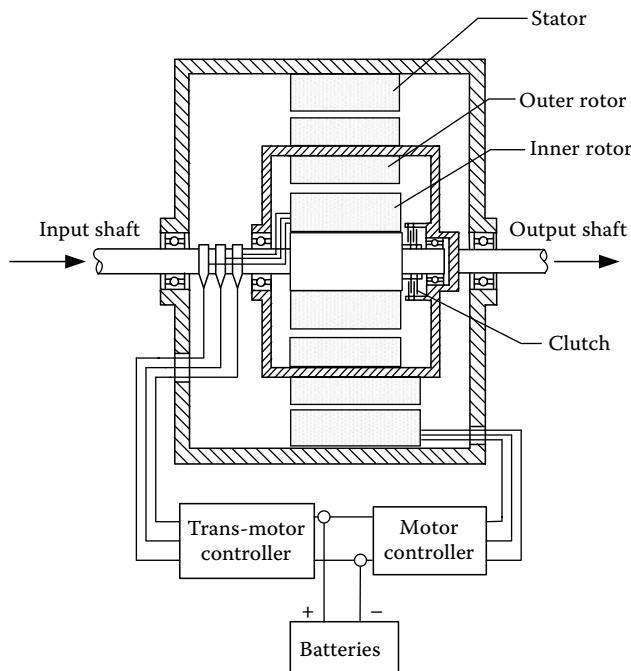
FIGURE 5.24   Hybrid electric drive train with speed and torque coupling of a transmotor and double shaft.

Another variation of the drive train in Figure 5.24 is the single-shaft design as shown in Figure 5.25. A more compact design of the drive train in Figure 5.25 is to integrate the transmotor and the traction motor together as shown in Figure 5.26. The design and control may be more complicated than the separated structure due to correlated magnetic field in the double air gaps.

FIGURE 5.25   Hybrid electric drive train with speed and torque coupling of a transmotor and single shaft.

FIGURE 5.26 Integrated transmotor and traction motor.

In the literature, the integrated or separated transmotor and traction motor in Figures 5.25 and 5.26 is called electrical variable transmission (EVS).[11,12] This name is derived from the fact that engine speed is electrically decoupled from vehicle speed by the speed-coupling device: the transmotor. The operating characteristics and drive train control will be discussed later.

References

1. M. Ehsani, Y. Gao, and J. M. Miller, "Hybrid electric vehicles: Architecture and motor drives," *Proceedings of the IEEE, Special issue on Electric, Hybrid Electric and Fuel Cells Vehicle*, Vol. 95, No. 4, April 2007.
2. M. Ehsani, K. L. Butler, Y. Gao, and K. M. Rahman, "Next generation passenger cars with better range, performance, and emissions: The ELPH car concept," *Horizon in Engineering Symposium*, Texas A&M University Engineering Program Office, College Station, Texas, September 1998.
3. M. Ehsani, *The Electrically Peaking Hybrid System and Method*, US Patent No. 5,586,613, December 1996.

4. K. Yamaguchi, S. Moroto, K. Kobayashi, M. Kawamoto, and Y. Miyaishi, "Development of a new hybrid system-dual system," *Society of Automotive Engineers (SAE) Journal*, Paper No. 960231, Warrendale, PA, 1997.

5. C. C. Chan and K. T. Chau, *Modern Electric Vehicle Technology*, Oxford University Press, New York, 2001.

6. Y. Gao, K. M. Rahman, and M. Ehsani, "The energy flow management and battery energy capacity determination for the drive train of electrically peaking hybrid," *Society of Automotive Engineers (SAE) Journal*, Paper No. 972647, Warrendale, PA, 1997.

7. Y. Gao, K. M. Rahman, and M. Ehsani, "Parametric design of the drive train of an electrically peaking hybrid (ELPH) vehicle," *Society of Automotive Engineers (SAE) Journal*, Paper No. 970294, Warrendale, PA, 1997.

8. Y. Gao and M. Ehsani, *New Type of Transmission for Hybrid Vehicle with Speed and Torque Summation*, US Patent pending.

9. Available at http://www.toyota.com, Toyota Motor Company, visited in September 2003.

10. Y. Gao and M. Ehsani, *Series–Parallel Hybrid Drive Train with an Electric Motor of Floating Stator and Rotor*, US Patent pending.

11. M. J. Hoeijimakes and J. A. Ferreira, "The electrical variable transmission," *IEEE on Industry Application*, 42 (4), 1092–1100, July–August 2006.

12. S. Cui, Y. Cheng, and C. C. Chan, "A basic study of electrical variable transmission and its application in hybrid electric vehicle," *IEEE on Vehicle Power and Propulsion Conference, (VPPC)*, 2006.
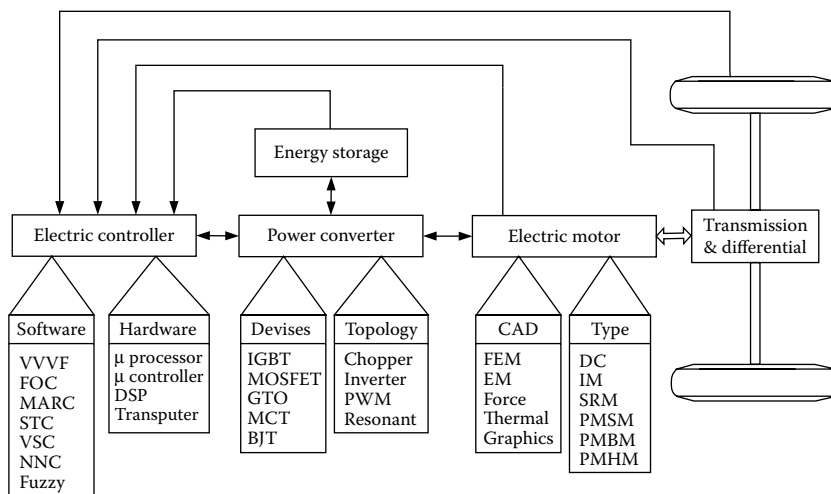
6

Electric Propulsion Systems

Electric propulsion systems are at the heart of EVs and HEVs. They consist of electric motors, power converters, and electronic controllers. The electric motor converts the electric energy into mechanical energy to propel the vehicle or vice versa, to enable regenerative braking and/or to generate electricity for the purpose of charging the on-board energy storage. The power converter is used to supply the electric motor with proper voltage and current. The electronic controller commands the power converter by providing control signals to it, and then controls the operation of the electric motor to produce proper torque and speed, according to the command from the driver. The electronic controller can be further divided into three functional units—sensor, interface circuitry, and processor. The sensor is used to translate the measurable quantities, such as current, voltage, temperature, speed, torque, and flux, into electric signals through the interface circuitry. These signals are conditioned to the appropriate level before being fed into the processor. The processor output signals are usually amplified via the interface circuitry to drive power semiconductor devices of the power converter. The functional block diagram of an electric propulsion system is illustrated in Figure 6.1.

The choice of electric propulsion systems for EVs and HEVs mainly depends on a number of factors, including the driver's expectation, vehicle constraints, and energy source. The driver's expectation is defined by a driving profile, which includes the acceleration, maximum speed, climbing capability, braking, and range. The vehicle constraints, including volume and weight, depend on the vehicle type, vehicle weight, and payload. The energy source relates to batteries, fuel cells, ultracapacitors, flywheels, and various hybrid sources. Thus, the process of identifying the preferred feature and package options for electric propulsion has to be carried out at the system level. The interaction of subsystems and the likely impacts of system trade-offs must be examined.

Differing from the industrial applications of motors, the motors used in EVs and HEVs usually require frequent starts and stops; high rates of acceleration/deceleration; high torque and low-speed hill climbing; low torque and high-speed cruising, and a very wide speed range of operation. The motor drives for EVs and HEVs can be classified into two main groups, namely the commutator motors and commutatorless motors, as illustrated in Figure 6.2. Commutator motors mainly are the traditional DC motors, which include
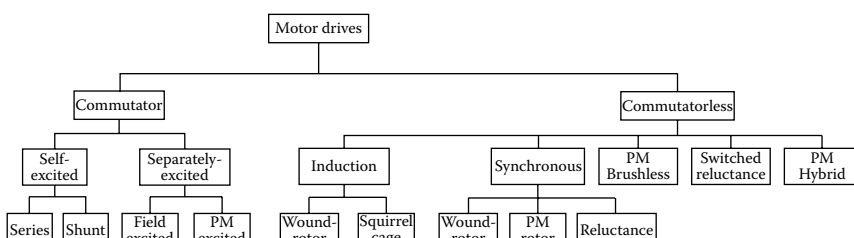
FIGURE 6.1   Functional block diagram of a typical electric propulsion system.[1]

series excited, shunt excited, compound excited, separately excited, and permanent magnets (PMs) excited motors. DC motors need commutators and brushes to feed current into the armature, thus making them less reliable and unsuitable for maintenance-free operation and high speed. In addition, winding-excited DC motors have low specific power density. Nevertheless, because of their mature technology and simple control, DC motor drives have been prominent in electric propulsion systems.

Technological developments have recently pushed commutatorless electric motors into a new era. Advantages include higher efficiency, higher power density, and lower operating cost. They are also more reliable and maintenance-free compared to commutator DC motors; thus, commutatorless electric motors have now become more attractive.

Induction motors are widely accepted as a commutatorless motor type for EV and HEV propulsion. This is because of their low cost, high reliability, and maintenance-free operation. However, conventional control of induction motors such as variable-voltage variable-frequency cannot provide

FIGURE 6.2   Classification of electric motor drives for EV and HEV applications.

the desired performance. With the advent of the power electronics and microcomputer era, the principle of field-oriented control (FOC) or vector control of induction motors has been accepted to overcome their control complexity due to their nonlinearity.[2] However, these EV and HEV motors using FOC still suffer from low efficiency at light loads and limited constant-power operating range.

By replacing the field winding of conventional synchronous motors with PMs, PM synchronous motors can eliminate conventional brushes, slip rings, and field copper losses.[3] Actually, these PM synchronous motors are also called PM brushless AC motors, or sinusoidal-fed PM brushless motors, because of their sinusoidal AC current and brushless configuration. Since these motors are essentially synchronous motors, they can run from a sinusoidal or pulsed waveform modulation supply (PWM supply) without electronic commutation. When PMs are mounted on the rotor surface, they behave as nonsalient synchronous motors because the permeability of PMs is similar to that of air. By burying those PMs inside the magnetic circuit of the rotor, the saliency causes an additional reluctance torque, which leads to facilitating a wider speed range at constant power operation. On the other hand, by abandoning the field winding or PMs while purposely making use of the rotor saliency, synchronous reluctance motors are generated. These motors are generally simple and inexpensive, but with relatively low output power. Similar to induction motors, these PM synchronous motors usually use FOC for high-performance applications.[3] Because of their inherently high power density and high efficiency, they have been accepted as having great potential to compete with induction motors for EV and HEV applications.

By virtually inverting the stator and rotor of PM DC motors (commutator), PM brushless DC (BLDC) motors are generated. It should be noted that the term "DC" may be misleading, since it does not refer to a DC current motor. Actually, these motors are fed by rectangular AC current and hence are also rectangular-fed PM brushless motors.[4] The most obvious advantage of these motors is the removal of brushes. Another advantage is the ability to produce a large torque because of the rectangular interaction between current and flux. Moreover, the brushless configuration allows more cross-sectional area for the armature windings. Since the conduction of heat through the frame is improved, an increase in electric loading causes higher power density. Different from PM synchronous motors, these PM BLDC motors generally operate with shaft position sensors. Recently, sensorless control technologies have been developed in the Power Electronics and Motor Drive Laboratory at Texas A&M University.

Switched reluctance motors (SRMs) have been recognized to have considerable potential for EV and HEV applications. Basically, they are direct derivatives of single-stack variable-reluctance stepping motors. SRMs have the definite advantages of simple construction, low manufacturing cost, and outstanding torque–speed characteristics for EV and HEV applications. Although they possess simplicity in construction, this does not imply any

simplicity of their design and control. Because of the heavy saturation of pole tips and the fringe effect of pole and slots, their design and control are difficult and subtle. Traditionally, SRMs operate with shaft sensors to detect the relative position of the rotor to the stator. These sensors are usually vulnerable to mechanical shock and sensitive to temperature and dust. Therefore, the presence of the position sensor reduces the reliability of SRMs and constrains some applications. Recently, sensorless technologies have been developed in the Power Electronics and Motor Drive Laboratory—again, at Texas A&M University. These technologies can ensure smooth operation from zero speed to maximum speed.[5] This will be discussed in detail in the following sections.

6.1 DC Motor Drives

DC motor drives have been widely used in applications requiring adjustable speed; good speed regulation; and frequent starting, braking, and reversing. Various DC motor drives have been widely applied to different electric traction applications because of their technological maturity and control simplicity.

6.1.1 Principle of Operation and Performance
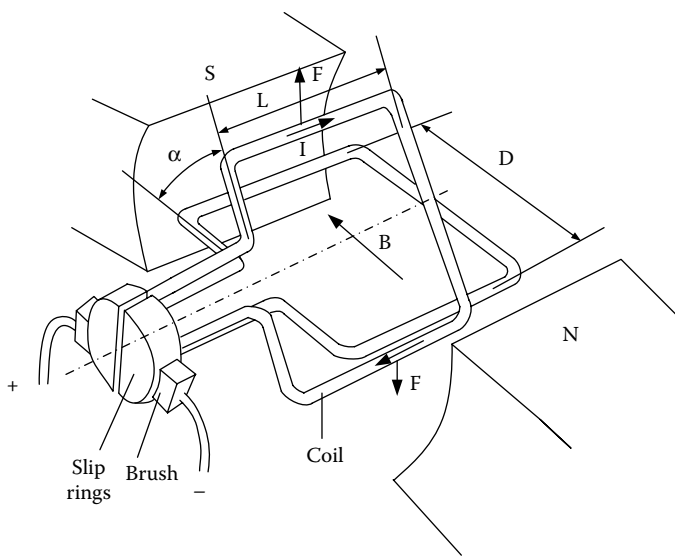
The operation principle of a DC motor is straightforward. When a wire carrying electric current is placed into a magnetic field, a magnetic force acting on the wire is produced. The force is perpendicular to the wire and the magnetic field as shown in Figure 6.3. The magnetic force is proportional to the wire length, magnitude of the electric current, and the density of the magnetic field; that is,

$$F = BIL. \tag{6.1}$$

When the wire is shaped into a coil, as shown in Figure 6.3, the magnetic forces acting on both sides produce a torque, which is expressed as

$$T = BIL \cos \alpha, \tag{6.2}$$

where α is the angle between the coil plane and the magnetic field as shown in Figure 6.3. The magnetic field may be produced by a set of windings or PMs. The former is called wound-field DC motor and the latter is called the PM DC motor. The coil carrying electric current is called the armature. In practice, the armature consists of a number of coils. In order to obtain continuous and
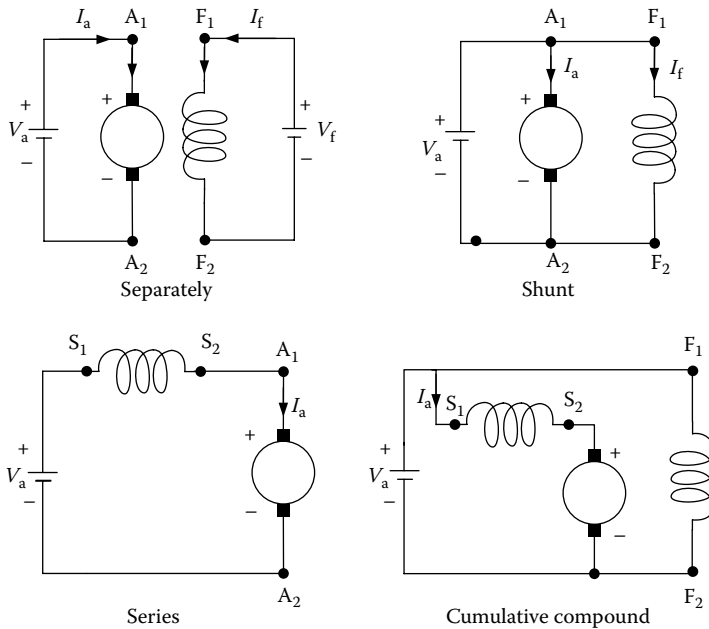
FIGURE 6.3 Operation principle of a DC motor.

maximum torque, slip rings and brushes are used to conduct each coil at the position of $\alpha = 0$.

Practically, the performance of DC motors can be described by the armature voltage, back electromotive force (EMF), and field flux.

Typically, there are four types of wound-field DC motors, depending on the mutual interconnection between the field and armature windings. They are separately excited, shunt excited, series excited, and compound excited as shown in Figure 6.4. In the case of a separately excited motor, the field and armature voltage can be controlled independently of one another. In a shunt motor, the field and armature are connected in parallel to a common source. Therefore, an independent control of field or armature currents can only be achieved by inserting a resistance in the appropriate circuit. This is an inefficient method of control. The efficient method is to use power electronics-based DC–DC converters in the appropriate circuit to replace the resistance. The DC–DC converters can be actively controlled to produce proper armature and field voltage. In the case of a series motor, the field current is the same as the armature current; therefore, field flux is a function of armature current. In a cumulative compound motor, the magnetomotive force (mmf) of a series field is a function of the armature current and is in the same direction as the mmf of the shunt field.[6]

The steady-state equivalent circuit of the armature of a DC motor is shown in Figure 6.5. The resistor R_a is the resistance of the armature circuit. For separately excited and shunt DC motors, it is equal to the resistance of the armature windings; for the series and compound motors, it is the sum of armature and series field winding resistances. The basic equations of
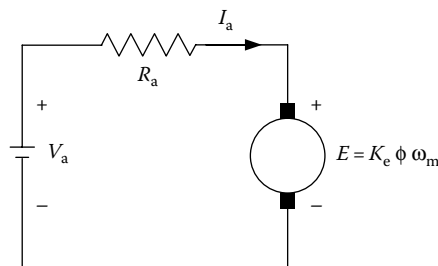
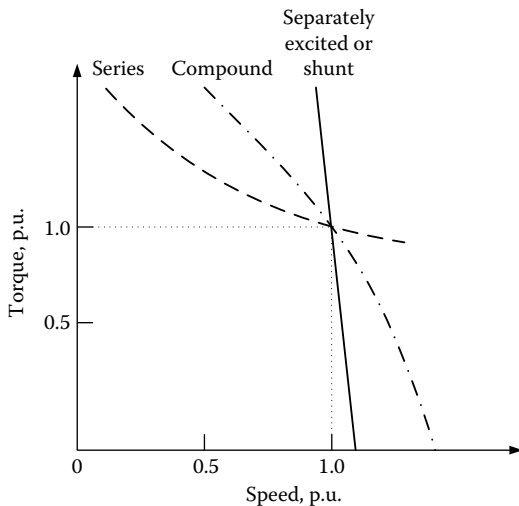**FIGURE 6.4**   Wound-field DC motors.

a DC motor are

$$V_a = E + R_a I_a, \quad E = K_e \phi \omega_m \qquad (6.3)$$

$$T = K_e \phi I_a, \qquad (6.4)$$

where ϕ is the flux per pole in webers, I_a is the armature current in A, V_a is the armature voltage in volts, R_a is the resistance of the armature circuit in ohms, ω_m is the speed of the armature in rad/s, T is the torque developed by the motor in N m, and K_e is a constant.

FIGURE 6.5   Steady-state equivalent circuit of the armature circuit of a DC motor.

FIGURE 6.6 Speed characteristics of DC motors.

From Equations 6.3 and 6.4, one can obtain

$$T = \frac{K_e\phi}{R_a}V - \frac{(K_e\phi)^2}{R_a}\omega_m. \tag{6.5}$$

Equations 6.3 through 6.5 are applicable to all the DC motors, namely separately (or shunt) excited, series, and compound motors. In the case of separately excited motors, if the field voltage is maintained as constant, one can assume the flux to be practically constant as the torque changes. In this case, the speed–torque characteristic of a separately excited motor is a straight line, as shown in Figure 6.6. The nonload speed ω_m is determined by the armature voltage and the field excitation. Speed decreases as torque increases, and speed regulation depends on the armature circuit resistance. Separately excited motors are used in applications requiring good speed regulation and proper adjustable speed.

In the case of series motors, the flux is a function of armature current. In an unsaturated region of the magnetization characteristic, ϕ can be assumed to be proportional to I_a. Thus

$$\phi = K_f I_a. \tag{6.6}$$

By Equations 6.4 through 6.6, the torque for series excited DC motors can obtained as

$$T = \frac{K_e K_f V_a^2}{(R_a + K_e K_f \omega_m)^2}, \tag{6.7}$$

where the armature circuit resistance R_a is now the sum of armature and field winding resistance.

A speed–torque characteristic of a series DC motor is shown in Figure 6.6. In the case of a series, any increase in torque is accompanied by an increase in the armature current and, therefore, an increase in magnetic flux. Because flux increases with the torque, the speed drops to maintain a balance between the induced voltage and the supply voltage. The characteristic, therefore, shows a dramatic drop. A motor of standard design works at the knee point of the magnetization curve at the rated torque. At heavy torque (large current) overload, the magnetic circuit saturates and the speed–torque curve approaches a straight line.

Series DC motors are suitable for applications requiring high starting torque and heavy torque overload, such as traction. This was just the case for electric traction before the power electronics and micro-control era. However, series DC motors for traction application bear some disadvantages. They are not allowed to operate without the load torque with full supply voltage. Otherwise, their speed will quickly increase up to a very high value (refer to Equation 6.7) Another disadvantage is the difficulty of regenerative braking.
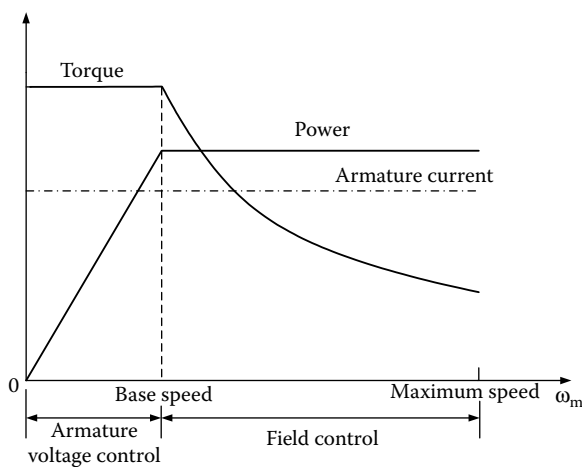
Performance equations for cumulative compound DC motors can be derived from Equations 6.3 and 6.4. The speed–torque characteristics are between series and separately excited (shunt) motors, as shown in Figure 6.6.

6.1.2   Combined Armature Voltage and Field Control

The independence of armature voltage and field provides more flexible control of the speed and torque than other types of DC motors. In EV and HEV applications, the most desirable speed–torque characteristic is to have a constant torque below a certain speed (base speed), and a constant power in the speed range of above the base speed, as shown in Figure 6.7. In the speed range of lower than the base speed, the armature current and field are set at their rated values, producing the rated torque. From Equations 6.3 through 6.4, it is clear that the armature voltage must be increased proportionally with the increase of the speed. At the base speed, the armature voltage reaches its rated value (equal to the source voltage) and cannot be increased further. In order to further increase the speed, the field must be weakened with the increase of the speed, then maintaining the back EMF E and armature current constant. The torque produced drops parabolically with the increase of the speed and the output power remains constant, as shown in Figure 6.7.

6.1.3   Chopper Control of DC Motors

Choppers are used for the control of DC motors because of a number of advantages such as high efficiency, flexibility in control, light weight, small size, quick response, and regeneration down to very low speeds. At present,
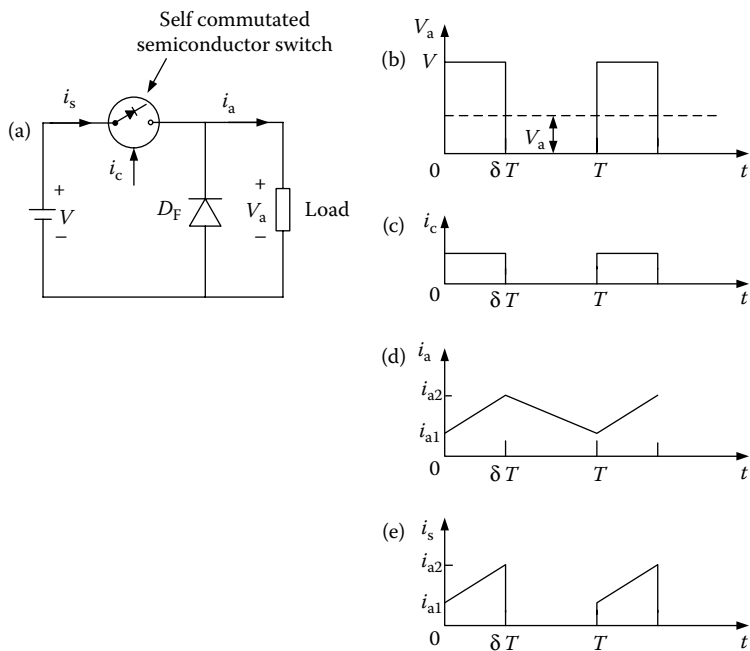
FIGURE 6.7 Torque and power limitations in combined armature voltage and field control.

the separately excited DC motors are usually used in traction, due to the control flexibility of armature voltage and field.

For a DC motor control in open-loop and closed-loop configurations, the chopper offers a number of advantages due to the high operation frequency. High operation frequency results in high-frequency output voltage ripple and therefore less ripples in the motor armature current and a smaller region of discontinuous conduction in the speed–torque plane. A reduction in the armature current ripple reduces the armature losses. A reduction or elimination of the discontinuous conduction region improves speed regulation and transient response of the drive.

The power electronic circuit and the steady-state waveform of a DC chopper drive are shown in Figure 6.8. A DC voltage source, V, supplies an inductive load through a self-commutated semiconductor switch S. The symbol of a self-commutated semiconductor switch has been used because a chopper can be built using any devices among thyristors with a forced commutation circuit: GTO, power transistor, MOSFET, and IGBT. The diode shows the direction in which the device can carry current. A diode D_F is connected in parallel with the load. The semiconductor switch S is operated periodically over a period T and remains closed for a time $t_{on} = \delta T$ with $0 < \delta < 1$. The variable $\delta = t_{on}/T$ is called the duty ratio or duty cycle of a chopper. Figure 6.8 also shows the waveform of control signal i_c. Control signal i_c will be the base current for a transistor chopper, and a gate current for the GTO of a GTO chopper or the main thyristor of a thyristor chopper. If a power MOSFET is used, it will be a gate to the source voltage. When the control signal is present, the semiconductor switch S will conduct, if forward biased. It is assumed that the circuit operation has been arranged such that the removal of i_c will turn off the switch.

FIGURE 6.8 Principle of operation of a step down (or class A) chopper: (a) basic chopper circuit; (b)–(e) waveforms.

During the on interval of the switch ($0 \leq t \leq \delta T$), the load is subjected to a voltage V and the load current increases from i_{a1} to i_{a2}. The switch is opened at $t = \delta T$. During the off period of the switch ($\delta T \leq t \leq 1$), the load inductance maintains the flow of current through diode D_F. The load terminal voltage stays zero (if the voltage drop on the diode is ignored in comparison to V) and the current decreases from i_{a2} to i_{a1}. The internal $0 \leq t \leq \delta T$ is called the duty interval and the interval $\delta T \leq t \leq T$ is known as the freewheeling interval. Diode D_F provides a path for the load current to flow when switch S is off, and thus improves the load current waveform. Furthermore, by maintaining the continuity of the load current at turn-off, it prevents transient voltage from appearing across switch S, due to the sudden change of the load current. The source current waveform is also shown in Figure 6.8e. The source current flows only during the duty interval and is equal to the load current.

The direct component or average value of the load voltage V_a is given by

$$V_a = \frac{1}{T} \int_0^T v_a \, dt = \frac{1}{T} \int_0^{\delta T} V \, dt = \delta V. \tag{6.8}$$

By controlling δ between 0 and 1, the load voltage can be varied from 0 to V; thus a chopper allows a variable DC voltage to be obtained from a fixed voltage DC source.

The switch S can be controlled in various ways for varying the duty ratio δ. The control technologies can be divided into two categories:

1. Time Ratio Control (TRC).
2. Current Limit Control (CLC).

In TRC, also known as pulse width control, the ratio of on time to chopper period is controlled. The TRC can be further divided as follows:

1. *Constant frequency TRC*: The chopper period T is kept fixed and the on period of the switch is varied to control the duty ratio δ.
2. *Varied frequency TRC*: Here δ is varied either by keeping t_{on} constant and varying T or by varying both t_{on} and T.

In variable frequency control with constant on time, low-output voltage is obtained at very low chopper frequencies. The operation of a chopper at low frequencies adversely affects the motor performance. Furthermore, the operation of a chopper with variable frequencies makes the design of an input filter very difficult. Thus, variable frequency control is rarely used.
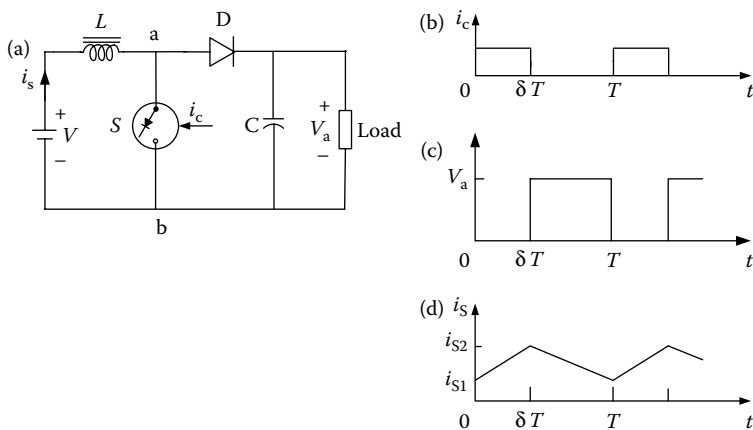
In CLC, also known as point-by-point control, δ is controlled indirectly by controlling the load current between certain specified maximum and minimum values. When the load current reaches a specified maximum value, the switch disconnects the load from the source and reconnects it when the current reaches a specified minimum value. For a DC motor load, this type of control is, in effect, a variable frequency variable on time control.

The following important points can be noted from the waveform of Figure 6.8.

1. The source current is not continuous but flows in pulses. The pulsed current makes the peak input power demand high and may cause fluctuation in the source voltage. The source current waveform can be resolved into DC and AC harmonics. The fundamental AC harmonic frequency is the same as the chopper frequency. The AC harmonics are undesirable because they interfere with other loads connected to the DC source and cause radio frequency interference through conduction and electromagnetic radiation. Therefore, an L-C filter is usually incorporated between the chopper and the DC source. At higher chopper frequencies, harmonics can be reduced to a tolerable level by a cheaper filter. From this point, a chopper should be operated at the highest possible frequency.
2. The load terminal voltage is not a perfect direct voltage. In addition to a direct component, it has the harmonics of the chopping frequency and its multiples. The load current also has an AC ripple.

The chopper of Figure 6.8 is called a class A chopper. It is one of the number of chopper circuits that are used for the control of DC motors. This chopper is capable of providing only a positive voltage and a positive current. It is called a single-quadrant chopper, only providing separately excited DC motor control in the first quadrant, that is, positive speed and positive torque. Since it can vary the output voltage from V to 0, it is also a step-down chopper or a DC-to-DC buck converter. The basic principle involved can also be used to realize a step-up chopper or DC-to-DC boost converter.

The circuit diagram and steady-state waveforms of a step-up chopper are shown in Figure 6.9. This chopper is known as a class B chopper. The presence of control signal i_c indicates the duration for which the switch can conduct if forward-biased. During a chopping period T, it remains closed for an interval $0 \leq t \leq \delta T$ and remains open for an interval $\delta T \leq t \leq T$. During the on period, i_S increases from i_{S1} to i_{S2}, thus increasing the magnitude of energy stored in inductance L. When the switch is opened, current flows through the parallel combination of the load and capacitor C. Since the current is forced against the higher voltage, the rate of change of the current is negative. It decreases from i_{S2} to i_{S1} in the switch's off period. The energy stored in the inductance L and the energy supplied by the low-voltage source are given to the load. The capacitor C serves two purposes. At the instant of opening of switch S, the source current, i_S, and load current, i_a, are not the same. In the absence of C, the turn-off of S will force the two currents to have the same values. This will cause high induced voltage in the inductance L and the load inductance. Another reason for using capacitor C is to reduce the load voltage ripple. The purpose of the diode D is to prevent any flow of current from the load into switch S or source V.

FIGURE 6.9 Principle of operation of a step-up (or class B) chopper: (a) basic chopper circuit; (b)–(d) waveforms.

For understanding of the step-up operation, capacitor C is assumed large enough to maintain a constant voltage V_a across the load. The average voltage across the terminals a and b is given as

$$V_{ab} = \frac{1}{T} \int_0^T v_{ab}\, dt = V_a(1 - \delta). \tag{6.9}$$

The average voltage across the inductance L is

$$V_L = \frac{1}{T} \int_0^T \left(L\frac{di}{dt} \right) dt = \frac{1}{T} \int_{i_{S1}}^{i_{S2}} L\, di = 0. \tag{6.10}$$

The source voltage

$$V = V_L + V_{ab}. \tag{6.11}$$

Substituting from Equations 6.9 and 6.10 into Equation 6.11 gives
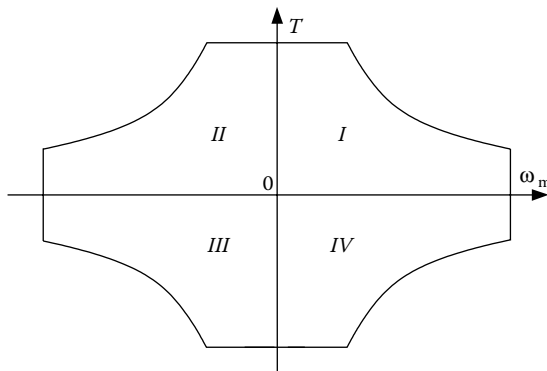
$$V = V_a(1 - \delta) \quad \text{or} \quad V_a = \frac{V}{1 - \delta}. \tag{6.12}$$

According to Equations 6.12, theoretically the output voltage V_a can be changed from V to ∞ by controlling δ from 0 to 1. In practice, V_a can be controlled from V to a higher voltage, which depends on the capacitor C, and the parameters of the load and chopper.

The main advantage of a step-up chopper is the low ripple in the source current. While most applications require a step-down chopper, the step-up chopper finds application in low-power battery-driven vehicles. The principle of the step-up chopper is also used in the regenerative braking of DC motor drives.

6.1.4 Multi-Quadrant Control of Chopper-Fed DC Motor Drives

The application of DC motors on EVs and HEVs requires the motors to operate in multiquadrants, including forward motoring, forward braking, backward motoring, and backward braking, as shown in Figure 6.10. For vehicles with reverse mechanical gears, two-quadrant operation (forward motoring and forward braking, or quadrant I and quadrant IV) is required. However, for the vehicles without reverse mechanical gears, four-quadrant operation is needed. Multiquadrant operation of a separately excited DC motor is implemented by controlling the voltage poles and magnitude through power electronics-based choppers.

FIGURE 6.10 Speed–torque profiles of a multiquadrant operation.
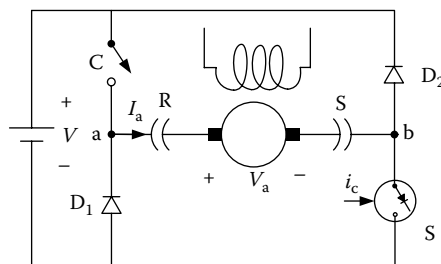
6.1.4.1 Two-Quadrant Control of Forward Motoring and Regenerative Braking

A two-quadrant operation consisting of forward motoring and forward regenerative braking requires a chopper capable of giving a positive voltage and current in either direction. This two-quadrant operation can be realized in the following two schemes.[6]

6.1.4.1.1 Single Chopper with a Reverse Switch

The chopper circuit used for forward motoring and forward regenerative braking is shown in Figure 6.11 where S is a self-commutated semiconductor switch, operated periodically such that it remains closed for a duration of δT and remains open for the duration of $(1 - \delta)T$. C is the manual switch. When C is closed and S is in operation, the circuit is similar to that of Figure 6.6, permitting the forward motoring operation. Under this condition, terminal a is positive and terminal b is negative.

The regenerative braking in the forward direction is obtained when C is opened and the armature connection is reversed with the help of the reversing switch RS, making terminal b positive and terminal a negative. During the on

FIGURE 6.11 Forward motoring and regenerative braking control with a single chopper.

period of the switch S, the motor current flows through a path consisting of the motor armature, switch S, and diode D_1, and increases the energy stored in the armature circuit inductance. When S is opened, the current flows through the armature diode D_2, source V, diode D_1 and back to the armature, thus feeding energy into the source.

During motoring, the change over to regeneration is done in the following steps. Switch S is deactivated and switch C is opened. This forces the armature current to flow through diode D_2, source V and diode D_1. The energy stored in the armature circuit is fed back to the source and the armature current falls to zero. After an adequate delay to ensure that the current has indeed become zero, the armature connection is reversed and switch S is reactivated with a suitable value of δ to start regeneration.
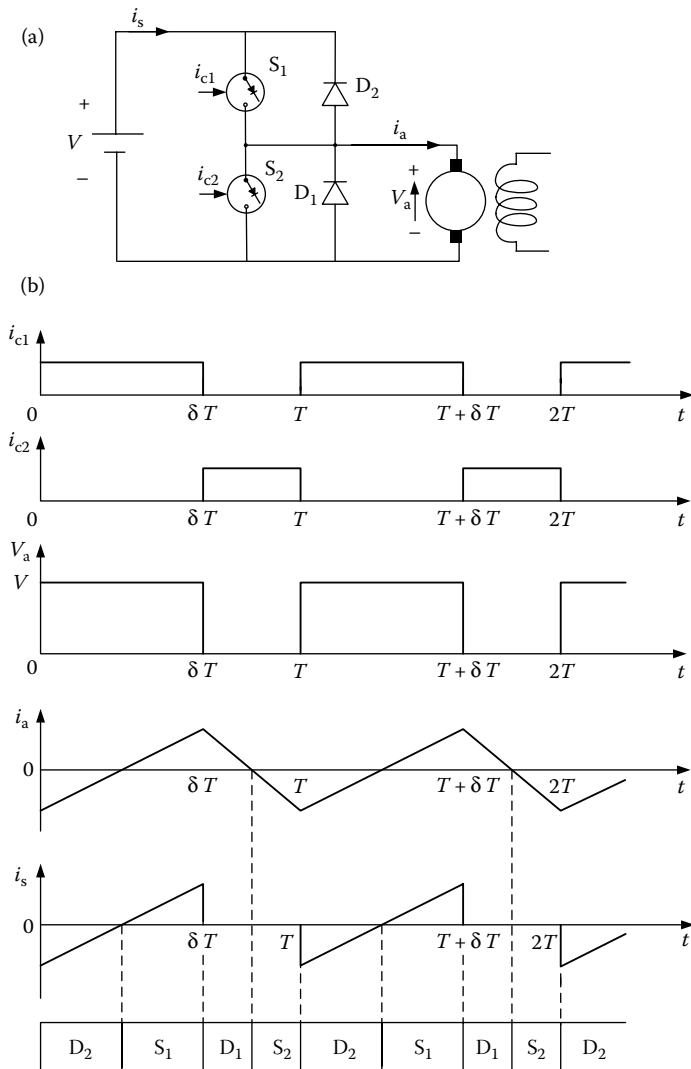
6.1.4.1.2 Class C Two-Quadrant Chopper

In some applications, a smooth transition from motoring to braking and vice versa is required. For such applications, the class C chopper is used as shown in Figure 6.12. The self-commutated semiconductor switch S_1 and diode D_1 constitute one chopper and the self-commutator switch S_2, and diode D_2 form another chopper. Both the choppers are controlled simultaneously, both for motoring and regenerative braking. The switches S_1 and S_2 are closed alternately. In the chopping period T, S_1 is kept on for a duration δT and S_2 is kept on from δT to T. To avoid a direct short-circuit across the source, care is taken to ensure that S_1 and S_2 do not conduct at the same time. This is generally achieved by providing some delay between the turn-off of one switch and the turn-on of another switch.

The waveforms of the control signals, v_a, i_a, and i_s and the devices under conducting during different intervals of a chopping period are shown in Figure 6.11b. In drawing these waveforms, the delay between the turn-off of one switch and turn-on of another switch has been ignored because it is usually very small. The control signals for the switches S_1 and S_2 are denoted by i_{c1} and i_{c2}, respectively. It is assumed that a switch conducts only when the control signal is present and the switch is forward biased.

The following points are helpful in understanding the operation of this two-quadrant circuit.

1. In this circuit, discontinuous conduction does not occur, irrespective of its frequency of operation. The discontinuous conduction occurs when the armature current falls to zero and remains zero for a finite interval of time. The current may become zero either during the freewheeling interval or in the energy transfer interval. In this circuit, freewheeling will occur when S_1 is off and the current is flowing through D_1. This will happen in interval $\delta T \leq t \leq T$, which is also the interval for which S_2 receives the control signal. If i_a falls to zero in the freewheeling interval, the back EMF will immediately drive a current through S_2 in the reverse direction, thus preventing the armature current from

FIGURE 6.12 Forward motoring and regenerative braking control using class C two-quadrant chopper: (a) chopper circuit; (b) waveforms.

remaining zero for a finite interval of time. Similarly, the energy transfer will be present when S_2 is off and D_2 is conducting—that is, during the interval $0 \leq t \leq \delta T$. If the current falls to zero during this interval, S_1 will conduct immediately because i_c is present and $V > E$. The armature current will flow, preventing discontinuous conduction.

2. Since discontinuous conditions are absent, the motor current will be flowing all the time. Thus, during the interval $0 \leq t \leq \delta T$, the motor

armature will be connected either through S_1 or D_2. Consequently, the motor terminal voltage will be V and the rated of change of i_a will be positive because $V > E$. Similarly, during the interval $\delta T \leq t \leq T$, the motor armature will be shorted either through D_1 or S_2. Consequently, the motor voltage will be zero and the rate of change of i_a will be negative.
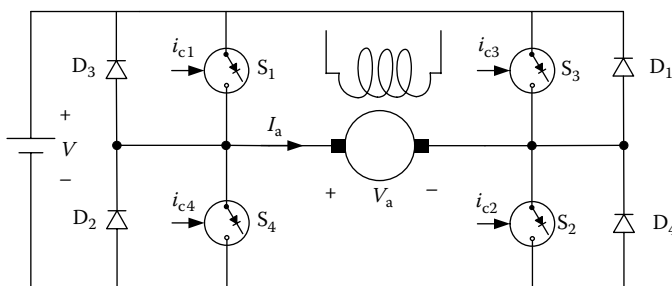
3. During the interval $0 \leq t \leq \delta T$, the positive armature current is carried by S_1 and the negative armature current is carried by D_2. The source current flows only during this interval and it is equal to i_a. During the interval $\delta T \leq t \leq T$, the positive current is carried by D_1 and the negative current is carried by S_2.

4. From the motor terminal voltage waveform of Figure 6.12b, $V_a = \delta V$. Hence,

$$I_a = \frac{\delta V - E}{R_a}. \tag{6.13}$$

Equation 6.13 suggests that the motoring operation takes place when $\delta > (E/V)$, and that regenerative braking occurs when $\delta < (E/V)$. The no-load operation is obtained when $\delta = (E/V)$.

6.1.4.2 Four-Quadrant Operation

The four-quadrant operation can be obtained by combining two class C choppers (Figure 6.12a) as shown in Figure 6.13, which is referred to as a class E chopper. In this chopper, if S_2 is kept closed continuously, and S_1 and S_4 are controlled, a two-quadrant chopper is obtained, which provides positive terminal voltage (positive speed) and the armature current in either direction (positive or negative torque), giving a motor control in quadrants I and IV. Now if S_3 is kept closed continuously and S_1 and S_4 are controlled, one gets a two-quadrant chopper that can supply a variable negative terminal voltage (negative speed), and the armature current can be in either direction (positive or negative torque), giving a motor control in quadrants II and III.

FIGURE 6.13 Class E four-quadrant chopper.

This control method has the following features: the utilization factor of the switches is low due to the asymmetry in the circuit operation. Switches S_3 and S_2 should remain on for a long period. This may create commutation problems when the switches are using thyristors. The minimum output voltage depends directly on the minimum time for which the switch can be closed, since there is always a restriction on the minimum time for which the switch can be closed, particularly in thyristor choppers.[7] The minimum available output voltage, and therefore the minimum available motor speed, is restricted.

To ensure that switches S_1 and S_4, or S_2 and S_3 are not on at the same time, some fixed time interval must elapse between the turn-off for one switch and the turn-on of another switch. This restricts the maximum permissible frequency of operation. It also requires two switching operations during a cycle of the output voltage.

Dubey[6] provided other control methods to solve the problems mentioned above.
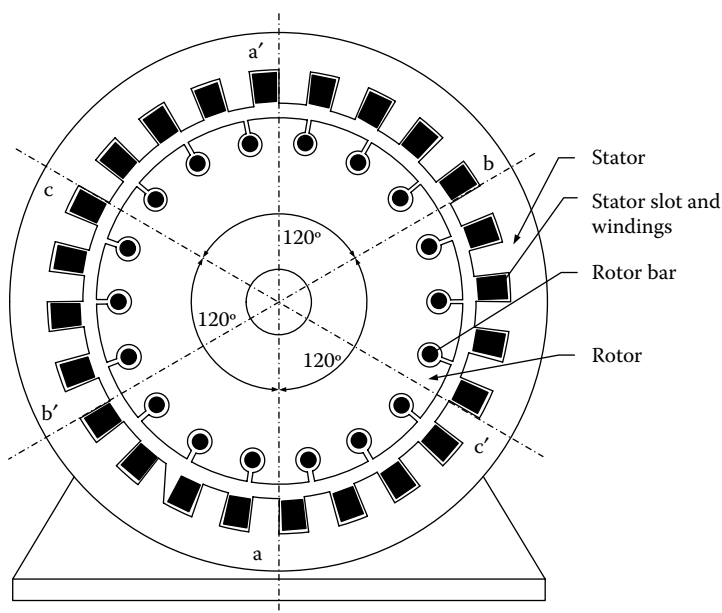
6.2   Induction Motor Drives

Commutatorless motor drives offer a number of advantages over conventional DC commutator motor drives for the electric propulsions of EVs and HEVs. At present, induction motor drives are the mature technology among commutatorless motor drives. Compared with DC motor drives, the AC induction motor drive has additional advantages such as lightweight nature, small volume, low cost, and high efficiency. These advantages are particularly important for EV and HEV applications.

There are two types of induction motors, namely, wound-rotor and squirrel-cage motors. Because of the high cost, need for maintenance, and lack of sturdiness, wound-rotor induction motors are less attractive than their squirrel-cage counterparts, especially for electric propulsion in EVs and HEVs. Hence, squirrel-cage induction motors are loosely named as induction motors.

A cross section of a two-pole induction motor is shown in Figure 6.14. Slots in the inner periphery of the stator are inserted with three phase windings, a–a', b–b', and c–c'. The turns of each winding are distributed such that the current in the winding produces an approximate sinusoidally distributed flux density around the periphery of the air gap. The three windings are spatially arranged by 120° as shown in Figure 6.14.
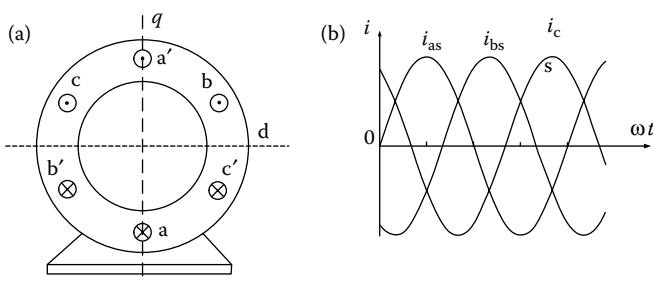
The most common types of induction motor rotors are the squirrel-cage motors in which aluminum bars are cast into slots in the outer periphery of the rotor. The aluminum bars are short-circuited together at both ends of the rotor by cast aluminum end rings, which also can be shaped as fans.

FIGURE 6.14 Cross section of an induction motor.

6.2.1   Basic Operation Principles of Induction Motors

Figure 6.15 shows, schematically, a cross section of the stator of a three-phase, two-pole induction motor. Each phase is fed with a sinusoidal AC current, which has a frequency of ω and a 120° phase difference between each other. Current i_{as}, i_{bs}, and i_{cs} in the three stator coils a–a′, b–b′, and c–c′ produce alternative magnetic motive forces (mmfs), F_{as}, F_{bs}, and F_{cs}, which are space vectors. The resultant stator mmf vector F_s^s constitutes a vector sum of the phase mmf vectors.

FIGURE 6.15 Induction motor stator and stator winding current: (a) spatially symmetric three-phase stator windings; (b) phase currents.

The mmfs produced by the phase currents can be written as

$$F_{as} = F_{as} \sin \omega t, \tag{6.14}$$

$$F_{bs} = F_{bs} \sin (\omega t - 120°), \tag{6.15}$$

$$F_{bs} = F_{cs} \sin (\omega t - 240°). \tag{6.16}$$

The resultant stator mmf vector, F_s^s, is expressed as

$$F_s^s = F_{as}^s e^{j0°} + F_{bs}^s e^{j120°} + F_{cs}^s e^{j240°}. \tag{6.17}$$

Assuming that the magnitudes of the three-phase mmfs are identical, equal to F_s, Equation 6.17 can be further expressed as

$$F_s^s = \frac{3}{2} F_s e^{(\omega t - 90°)}. \tag{6.18}$$
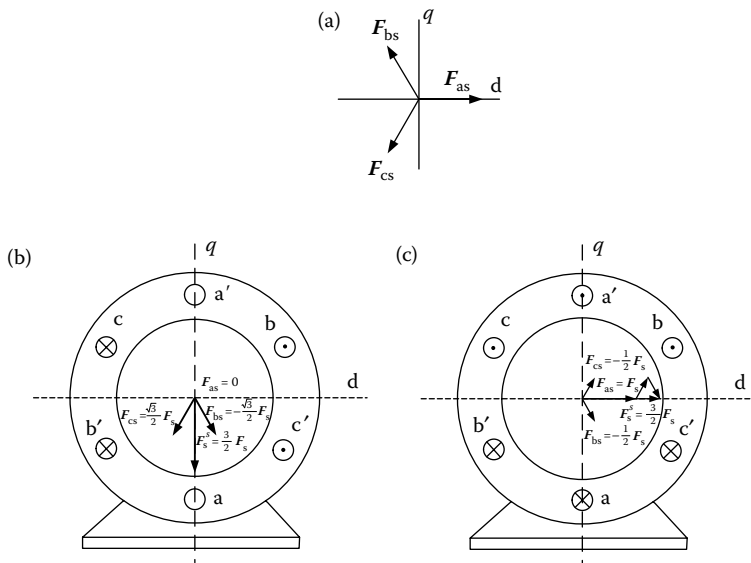
Equation 6.18 indicates that the resultant stator mmf vector is rotating with the frequency of the angle velocity of ω, and its magnitude is $3/2F_s$. Figure 6.16 graphically shows the stator mmf vectors at $\omega t = 0$ and $\omega t = 90°$; here, ωt is the angle in Equations 6.12 through 6.18, rather than the resultant stator mmf vector relative to the d-axis. Actually, if the ωt Equations 6.14 through 6.16 is taken as the reference, the resultant stator mmf vector is a 90° delay to the phase a–a' mmf.

The reaction between the rotating stator mmf and the rotor conductors induces a voltage in the rotor and hence electric current in the rotor. In turn, the rotating mmf produces a torque on the rotor, which is carrying the induced current. It is clear that the induced current in the rotor is essential for producing torque, and in turn the induced current depends on the relative movements between the stator mmf and the rotor. That is why there must exist a difference between the angular velocity of the rotating stator mmf and the angular velocity of the rotor.

The frequency ω, or angular velocity of the rotating stator mmf in equation, depends only on the frequency of the alternative current of the stator; thus it is referred to as electrical angular velocity. For the machine with two poles, the electrical angular velocity is identical to the mechanical angular velocity of the rotating stator mmf. However, for the machine with more than two poles, the mechanical angular velocity differs from the electrical one, which can be expressed as

$$\omega_{ms} = \frac{2}{p} \omega = \frac{4\pi f}{p} \text{ rad/s}, \tag{6.19}$$

where f is the frequency of the alternative current or angular velocity of the rotating stator mmf in cycle/s. When the angular velocity of the rotor is equal to the mechanical angular velocity of rotating stator mmf, there will

FIGURE 6.16 Stator mmf vectors: (a) positive direction of each phase mmf; (b) stator mmf vectors at $\omega t = 0$; (c) stator mmf vectors at $\omega t = 90°$.

be no induced current in the rotor, and then no torque is produced. Thus, the mechanical angular velocity of the rotating stator mmf is also called synchronous speed.

If the rotor speed is ω_m in rad/s, then the relative speed between the stator rotating field and the rotor is given by

$$\omega_{sl} = \omega_{ms} - \omega_m = s\omega_{ms} \tag{6.20}$$

where ω_{sl} is called slip speed. The parameter s, known as slip, is given by

$$s = \frac{\omega_{ms} - \omega_m}{\omega_{ms}} = \frac{\omega_{sl}}{\omega_{ms}}. \tag{6.21}$$

Because of the relative speed between the stator field and the rotor, balanced three-phase voltages are induced in the rotor mentioned before. The frequency of these voltages is proportional to the slip speed. Hence

$$\omega_r = \frac{\omega_{sl}}{\omega_{ms}}\omega = s\omega, \tag{6.22}$$

where ω_r is the frequency of the rotor voltage induced.

For $\omega_m < \omega_{ms}$, the relative speed is positive; consequently, the rotor-induced voltages have the same phase sequence as the stator voltages. The three-phase current flowing through the rotor produces a magnetic field,

which moves with respect to the rotor at the slip speed in the same direction as the rotor speed. Consequently, the rotor field moves in the space at the same speed as the stator, and a steady torque is produced. For $\omega_m = \omega_{ms}$, the relative speed between the rotor and stator field becomes zero. Consequently, no voltages are induced and no torque is produced by the motor. For $\omega_m > \omega_{ms}$, the relative speed between the stator field and the rotor speed reverses. Consequently, the rotor-induced voltages and currents also reverse and have a phase sequence opposite to that of the stator. Moreover, the developed torque has a negative sign, suggesting generator operation. (The generator is used to produce regenerative braking.)

6.2.2 Steady-State Performance

A per-phase equivalent circuit of an induction motor is shown in Figure 6.17a. The fields produced by the stator and rotor are linked together by an ideal transformer. a_{T1} is the transformer factor, which is equal to n_s/n_r, where n_s and n_r are the numbers of turns of stator and rotor windings, respectively. For a squirrel-cage rotor, $n_r = 1$. The equivalent circuit can be simplified by referring the rotor quantities to the stator frequency and number of turns. The resultant equivalent circuit is shown in Figure 6.17b, where R'_r and X'_r are the rotor resistance and reactance referred to the stator, and is given by the following equations:

$$R'_r = a_{T1}^2 R_r \quad \text{and} \quad X'_r = a_{T1}^2 X_r. \tag{6.23}$$

The stator reactance, mutual reactance, and rotor reactance referred to the stator can be expressed by the stator frequency and their inductances, L_s, L_m, and L_r, as shown in Figure 6.17. The impedances of stator, field, and rotor can be expressed as

$$Z_s = R_s + jL_s\omega \tag{6.24}$$

$$Z_m = jL_m\omega \tag{6.25}$$
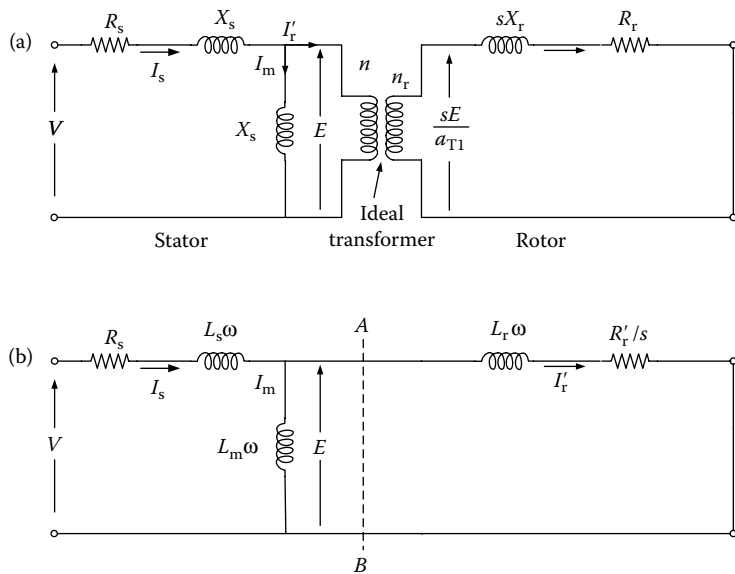
$$Z_r = \frac{R'_r}{s} + jL_r\omega \tag{6.26}$$

The driving-point impedance of the circuit is

$$Z = Z_s + \frac{Z_m Z_r}{Z_m + Z_r}. \tag{6.27}$$

Hence, the current I_s and I'_r can be calculated as

$$I_s = \frac{V}{Z}. \tag{6.28}$$

FIGURE 6.17 Per phase equivalent circuit of an induction motor: (a) with a transformer between rotor and stator and (b) refer rotor quantities to stator.

and

$$I'_r = \frac{Z_m}{Z_m + Z_r} I_s. \tag{6.29}$$

The total electrical power supplied to the motor for three phases is

$$P_{elec} = 3I'^2_r \frac{R'_r}{s}. \tag{6.30}$$

The mechanical power of the rotor can be obtained by subtracting the total power loss in the stator as

$$P_{mech} = P_{elec} - 3I'^2_r R'_r. \tag{6.31}$$
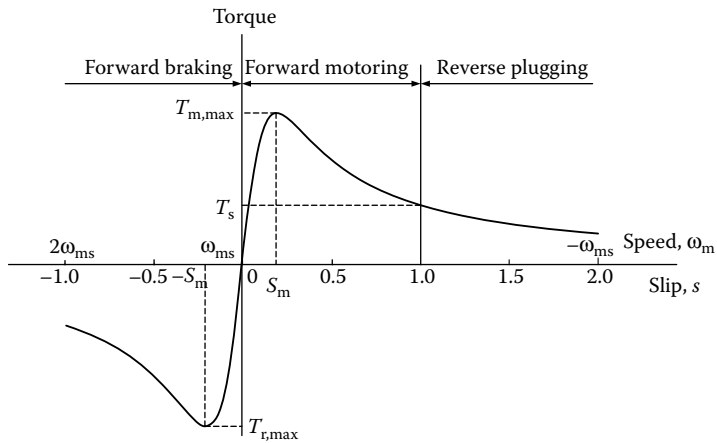
The angular velocity of the rotor, ω_m, is

$$\omega_m = \frac{2}{P} \omega (1 - s). \tag{6.32}$$

The torque developed by the motor can be determined by

$$T = \frac{P_{mech}}{\omega_m}. \tag{6.33}$$

Figure 6.18 shows the torque–slip characteristics of an induction motor, which has fixed voltage and frequency. In the region of $0 < s < s_m$, where s_m is

FIGURE 6.18 Torque–slip characteristics of an induction motor with fixed stator frequency and voltage.

the rated slip of the motor, the torque increases approximately linearly with the increase of slip until reaching its maximum at $s = s_m$, then it decreases with the further increase of the slip. At $s = 1$, the rotor speed is zero and the corresponding torque is the starting torque, which is less than its torque at $s = s_m$. The region of $0 < s < 1$ is the forward motoring region. In the region of $s > 1$, the rotor torque is positive and decreases further with the increase of slip, and the rotor speed is negative, according to Equation 6.21. Thus in this region, the operation of the motor is reverse braking. In the region of $s < 0$, that is, when the rotor speed is greater than the synchronous speed, the motor produces a negative torque.

It is clear that the speed–torque characteristic of a fixed voltage and fixed frequency induction motor is not appropriate to vehicle traction applications. This is due to the low starting torque, limited speed range, and unstable operation in the range of $s > s_m$, in which any additional disturbing torque in the load will lead the machine to stop as the torque decreases with the speed decreasing characteristically. The high slip also results in high current, which may cause damage in the stator windings. Actually, the operation of the fixed voltage and frequency induction motor are usually operated in the narrow slip range of $0 < s < s_m$. Thus, for traction application, an induction motor must be controlled to provide proper speed–torque characteristic as mentioned in Chapters 2 and 4.

6.2.3 Constant Volt/Hertz Control

For traction application, the torque–speed characteristic of an induction motor can be varied by simultaneously controlling the voltage and frequency, which

is known as the constant volt/hertz control. By emulating a DC motor at low speed, the flux may be kept constant. According to Figure 6.17b, the field current I_m should be kept constant and equal to its rated value. That is,

$$I_{mr} = \frac{E}{X_m} = \frac{E_{rated}}{\omega_r L_m},$$ (6.34)

where I_{mr} is the rated field current, E_{rated} and ω_r are the rated mmf and frequency of the stator, respectively. To maintain the flux at constant, the E/ω should be kept constant and equal to E_{rated}/ω_r. Ignoring the voltage drop in the stator impedance Z_s results in a constant V/ω until the frequency and voltage reach their rated values. This approach is known as constant volt/hertz control.[6]

From Figure 6.17b, the rotor current can be calculated as

$$I_r' = \frac{(\omega/\omega_r)E_{rated}}{jL_r\omega + R_r'/s}.$$ (6.35)

The torque produced can be obtained as

$$T = \frac{3}{\omega}I_r'^2 R_r'/s = \frac{3}{\omega}\left[\frac{(\omega/\omega)^2 E_{rated}^2 R_r'/s}{\left(R_r'/s\right)^2 + (L_r\omega)^2}\right].$$ (6.36)

The slip s_m corresponding to the maximum torque is
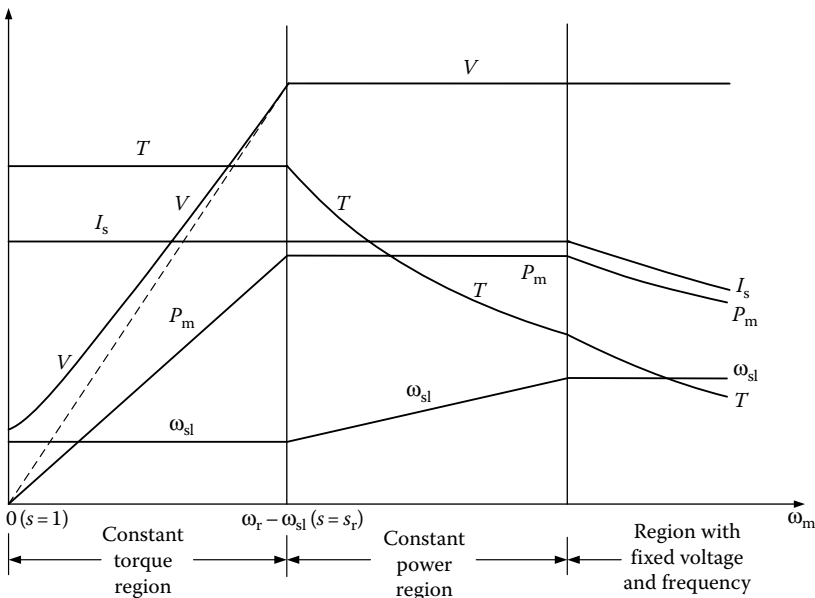
$$s_m = \pm\frac{R_r'}{L_r\omega}.$$ (6.37)

And then, the maximum torque is

$$T_{max} = \frac{3}{2}\frac{E_{rated}^2}{L_r\omega_r^2}.$$ (6.38)

Equation 6.38 indicates that with the constant E/ω, the maximum torque is constant with varying frequency. Equation 6.37 indicates that $s_m\omega$ is constant, resulting in constant slip speed, ω_{sl}. In practice, due to the presence of stator impedance and the voltage drop, the voltage should be somewhat higher than that determined by constant E/ω, as shown in Figure 6.19.

When motor speed is beyond its rated speed, the voltage reaches its rated value and cannot be increased with the frequency. In this case, the voltage is fixed to its rated value and the frequency increases continuously with the motor speed. The motor goes into the field weakening operation. The slip s is fixed to its rated value corresponding to the rated frequency, and the slip speed ω_{sl} increases linearly with the motor speed. This control approach results in constant power operation as shown in Figure 6.19.
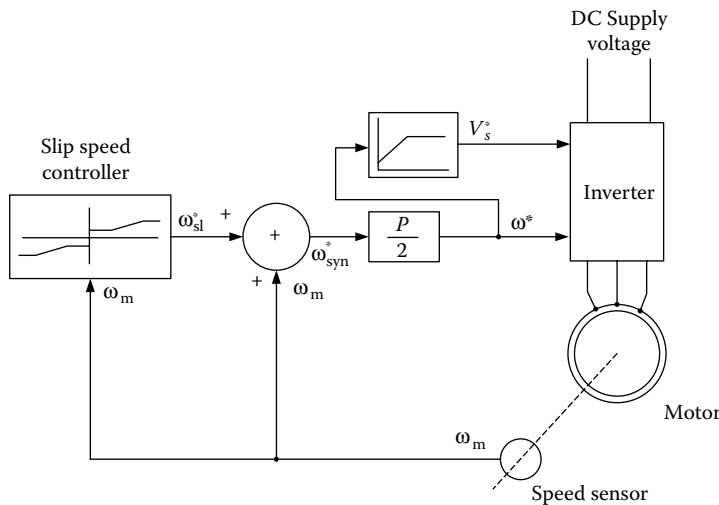
FIGURE 6.19   Operating variables varying with motor speed.

In traction applications, speed control in a wide range is usually required and the torque demand in the high-speed range is low. Control beyond constant power range is required. To prevent the torque from exceeding the breakdown torque, the machine is operated at a constant slip speed and the machine current and power are allowed to decrease as shown in Figure 6.19. Figure 6.20 shows a general block diagram where constant V/f control is implemented.

6.2.4   Power Electronic Control

As EV and HEV propulsion, an induction motor drive is usually fed with a DC source (battery, fuel cell, etc.), which has approximately constant terminal voltage. Thus a variable frequency and variable voltage DC/AC inverter is needed to feed the induction motor. The general DC/AC inverter is constituted by power electronic switches and power diodes. The commonly used topology of a DC/AC inverter is shown in Figure 6.21a, which has three legs (S_1 and S_4, S_3 and S_6, and S_5 and S_2), feeding the phase a, phase b, and phase c of the induction motor. When switches S_1, S_3, and S_5 are closed, S_4, S_6, and S_2 are opened, and phases a, b, and c are supplied with a positive voltage ($V_d/2$). Similarly, when S_1, S_3, and S_5 are opened and S_4, S_6, and S_2 are closed, the phases a, b, and c is supplied with a negative voltage. All the diodes provide a path for the reverse current of each phase.
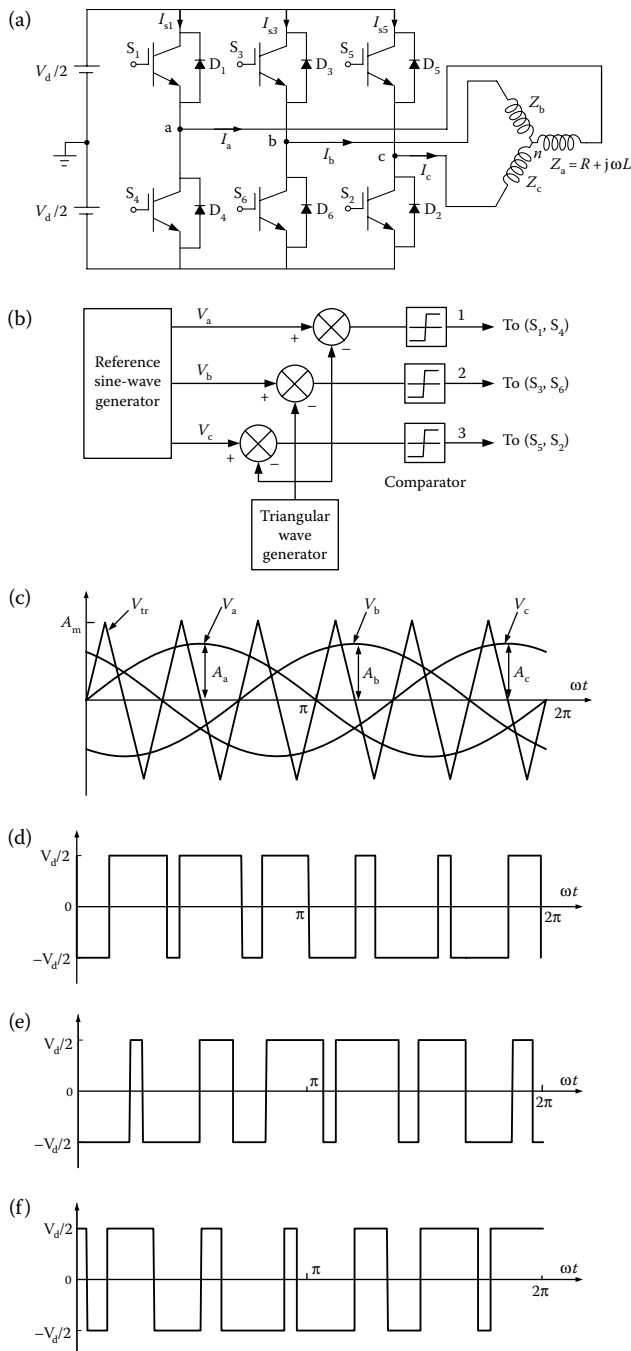
FIGURE 6.20 General configuration of constant V/f control.

For constant volt/hertz control of an induction motor, sinusoidal pulse width modulation (PWM) is used exclusively. Three-phase reference voltage V_a, V_b and V_c of variable amplitude A_a, A_b, and A_c are compared with a common isosceles triangular carrier wave V_{tr} of a fixed amplitude A_m as shown in Figure 6.21c. The outputs of comparators 1, 2, and 3 form the control signals for the three legs of the inverter. When the sinusoidal reference voltage V_a, V_b, and V_c, at a time t is greater than the triangular waved voltage, turn-on signals are sent to the switches S_1, S_3, and S_5 and turn-off signals to S_4, S_6, and S_6. Thus the three phases of the induction motor have positive voltage. On the other hand, when the reference sinusoidal voltage is smaller than the triangular wave voltage, turn-on signals are sent to the switches S_1, S_3, and S_5 and turn-off signals to S_4, S_6, and S_2. The three phases of the induction motor then have a negative voltage. The voltages of the three phases are shown in Figure 6.21d through 6.21f.

The frequency of the fundamental component of the motor terminal voltage is the same as that of the reference sinusoidal voltage. Hence, the frequency of the motor voltage can be changed by changing the frequency of the reference voltage. The ratio of the amplitude of the reference wave to that of the triangular carrier wave, m, is called the modulation index; therefore,

$$m = \frac{A}{A_m}, \tag{6.39}$$

where A is the multitude of the reference sinusoidal voltage, V_a, V_b, or V_c, and A_m is the multitude of angular carrier voltage. The fundamental (rms)

FIGURE 6.21 DC/AC inverter with sinusoidal pulse-width modulation: (a) inverter topology; (b) control signals; (c) three phase reference voltage and triangular carrier waveforms; (d) voltage of phase a; (e) voltage of phase b; and (f) voltage of phase c.

component in the phase waveform V_{ao}, V_{bo}, or V_{co} is given by

$$V_f = \frac{mV_d}{2\sqrt{2}}. \tag{6.40}$$

Thus, the fundamental voltage increases linearly with m until $m = 1$ (i.e., when the amplitude of the reference wave becomes equal to that of the carrier wave). For $m > 1$, the number of pulses in V_{ao}, V_{bo}, or V_{co}, becomes less and the modulation ceases to be sinusoidal.[6]

6.2.5 Field Orientation Control

The constant volt/hertz control of the induction motor is more suitably applied to the motors that operate with relative slow speed regulation. However, this approach shows poor response to frequent and fast speed varying, and also results in poor operation efficiency due to the poor power factor. In the last two decades, FOC or vector control technology has been successfully developed. This technology mostly overcomes the disadvantages of the constant volt/hertz control in AC motor drives.

6.2.5.1 Field Orientation Principles

The aim of FOC is to maintain the stator field perpendicular to the rotor field so as to always produce the maximum torque as in DC motors. However, for induction motors, phase voltages are the only accesses for the purpose of control.

As mentioned in Section 6.2.1, when balanced three-phase sinusoidal currents flow through the three phases of the stator of an induction motor, the rotating field is developed; current is induced in the rotor. In turn, the current induced in the rotor is also three-phase and produces a field, which rotates with the same angular velocity of the stator rotating field. The rotating fields of both stator and rotor can be described by two retorting vectors, referring to a common, stationary reference frame, d–q, as shown in Figure 6.16. The mmf of the stator field is expressed by Equation 6.17. For convenience, it is repeated as follows:

$$F_s^s = F_{as}e^{j0°} + F_{bs}e^{j120°} + F_{cs}e^{j240°}. \tag{6.41}$$

Similarly, the stator voltage, stator current, and stator flux can be expressed as vectors in the same way. That is,

$$v_s^s = v_{as}^s e^{j0°} + v_{bs}^s e^{j120°} + v_{cs}^s e^{j240°}, \tag{6.42}$$

$$i_s^s = i_{as}^s e^{j0°} + i_{bs}^s e^{j120°} + i_{cs}^s e^{j240°}, \tag{6.43}$$

$$\lambda_s^s = \lambda_{as}^s e^{j0°} + \lambda_{bs}^s e^{j120°} + \lambda_{cs}^s e^{j240°}. \tag{6.44}$$

The subscript s refers to the stator and as, bs, and cs refer to phases a, b, and c of the stator. The superscript s refers to the variable that is referred to the stator fixed frame. Bold symbols stand for vector variables. The vectors of stator voltage, current, and flux can be also described by its components in d and q axes as follows:

$$\begin{bmatrix} v_{ds}^s \\ v_{qs}^s \end{bmatrix} = \begin{bmatrix} 1 & -\dfrac{1}{2} & -\dfrac{1}{2} \\ 0 & \dfrac{\sqrt{3}}{2} & -\dfrac{\sqrt{3}}{2} \end{bmatrix} \begin{bmatrix} v_{as} \\ v_{bs} \\ v_{cs} \end{bmatrix}, \tag{6.45}$$

$$\begin{bmatrix} i_{ds}^s \\ i_{qs}^s \end{bmatrix} = \begin{bmatrix} 1 & -\dfrac{1}{2} & -\dfrac{1}{2} \\ 0 & \dfrac{\sqrt{3}}{2} & -\dfrac{\sqrt{3}}{2} \end{bmatrix} \begin{bmatrix} i_{as} \\ i_{bs} \\ i_{cs} \end{bmatrix}, \tag{6.46}$$

$$\begin{bmatrix} \lambda_{ds}^s \\ \lambda_{qs}^s \end{bmatrix} = \begin{bmatrix} 1 & -\dfrac{1}{2} & -\dfrac{1}{2} \\ 0 & \dfrac{\sqrt{3}}{2} & -\dfrac{\sqrt{3}}{2} \end{bmatrix} \begin{bmatrix} \lambda_{as} \\ \lambda_{bs} \\ \lambda_{cs} \end{bmatrix}. \tag{6.47}$$

In a real induction motor, the rotor winding differs from the stator winding, that is, the effective number of turns per phase of the rotor winding, N_r, is not equal to that of the stator winding, N_s. Therefore the turns ratio, $v = N_s/N_r$, must be taken into account. The vectors of rotor current, voltage, and magnetic flux can be described by i_r^r, v_r^r, and λ_r^r in the rotor frame. However, it is necessary to transform the vectors from the rotor frame to the stator frame for the purpose of easy analysis. The transformations of these vectors (refer to Figure 6.22) are described by

$$i_r^s = \frac{e^{j\theta_0}}{v} i_r^r, \tag{6.48}$$
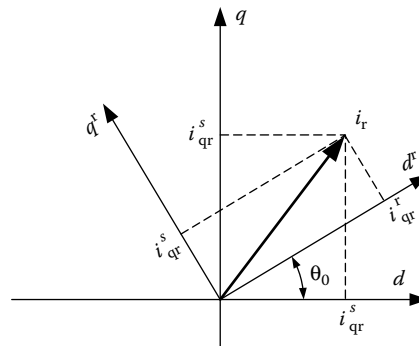
$$v_r^s = v e^{j\theta_0} v_r^r, \tag{6.49}$$

$$\lambda_r^s = v e^{j\theta_0} \lambda_r^r. \tag{6.50}$$

Using vector notation, either the stator or rotor windings can be represented by a simple resistive-plus-inductive circuit, using current, voltage, and magnetic flux space vector as illustrated in Figure 6.23.

Using the vector version of Kirchhoff's voltage law, the equation of the stator winding can be written as

$$v_s^s = R_s i_s^s + \frac{d\lambda_s^s}{dt} \tag{6.51}$$

FIGURE 6.22 Transformation of rotor current vector from rotor frame to stator frame.

and that of rotor winding as
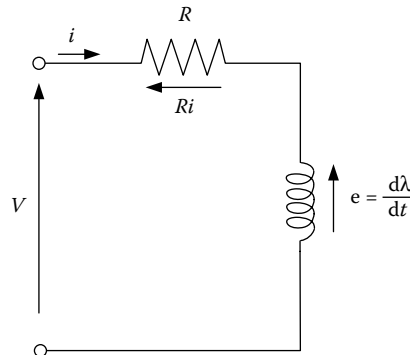
$$v_r^r = R_r^r i_r^r + \frac{d\lambda_r^r}{dt},$$ (6.52)

where R_s and R_r^r are the actual stator and rotor resistances per phase, respectively. As is known from the steady-state theory of induction machines, the relation between R_r^r and the rotor resistance referred to the stator is

$$R_r^r = \frac{1}{v^2} R_r.$$ (6.53)

Hence from Equations 6.48 and 6.53, the first term of Equation 6.52 is

$$R_r^r i_r^r = \frac{e^{-j\theta_0}}{v} R_r i_r^s.$$ (6.54)

FIGURE 6.23 Resistive-plus-inductive equivalent circuit of either the stator or rotor windings.

The second term, from Equation 6.50, gives

$$\frac{d\boldsymbol{\lambda}_r^r}{dt} = \frac{e^{j\theta_0}}{v}\left(\frac{d\boldsymbol{\lambda}_r^s}{dt} - j\omega_0\right). \tag{6.55}$$

Finally, substituting Equations 6.54 and (6.55) into Equation 6.52 gives

$$v_r^s = R_r i_r^s + \frac{d\boldsymbol{\lambda}_r^s}{dt} - j\omega_0\boldsymbol{\lambda}_r^s. \tag{6.56}$$

Introducing a differentiation operator $p \equiv d/dt$, the voltage equation of an induction motor can be written as

$$v_s^s = R_s i_s^s + p\boldsymbol{\lambda}_s^s, \tag{6.57}$$

$$v_r^s = R_r i_r^s + (p - j\omega_0)\boldsymbol{\lambda}_r^s. \tag{6.58}$$

The flux vector $\boldsymbol{\lambda}_s^s$ and $\boldsymbol{\lambda}_r^s$ can then be expressed in terms of current vector i_s^s and i_r^s, and the motor inductances as

$$\begin{bmatrix} \boldsymbol{\lambda}_s^s \\ \boldsymbol{\lambda}_r^s \end{bmatrix} = \begin{bmatrix} L_s & L_m \\ L_m & L_r \end{bmatrix} \begin{bmatrix} i_s^s \\ i_r^s \end{bmatrix}, \tag{6.59}$$

where L_m is the mutual inductance; L_s is the stator inductance calculated as the sum of the stator leakage inductance L_{ls} and the mutual inductance L_m; and L_r is the rotor inductance calculated as the sum of the rotor leakage inductance L_{lr} and the mutual inductance L_m.

Finally, the voltage equation can be written in matrix format as

$$\begin{bmatrix} v_{ds}^s \\ v_{qs}^s \\ v_{dr}^s \\ v_{qr}^s \end{bmatrix} = \begin{bmatrix} R_s & 0 & 0 & 0 \\ 0 & R_s & 0 & 0 \\ 0 & \omega_0 L_m & R_r & \omega_0 L_r \\ -\omega_0 L_m & 0 & -\omega_0 L_r & R_r \end{bmatrix} \begin{bmatrix} i_{ds}^s \\ i_{qs}^s \\ i_{dr}^s \\ i_{dr}^s \end{bmatrix}$$

$$+ \begin{bmatrix} L_s & 0 & L_m & 0 \\ 0 & L_s & 0 & L_m \\ L_m & 0 & L_r & 0 \\ 0 & L_m & 0 & L_r \end{bmatrix} \frac{d}{dt} \begin{bmatrix} i_{ds}^s \\ i_{qs}^s \\ i_{dr}^s \\ i_{dr}^s \end{bmatrix}. \tag{6.60}$$

Because the rotor circuit of the induction motor is shorted, v_{dr}^s and v_{qr}^s are zero. At a given rotor speed, ω_0, the stator and rotor currents can be obtained by solving Equation 6.60. The torque developed by the motor can be expressed as

$$T = \frac{P}{3}L_m\left(i_{qs}^s i_{dr}^s - i_{ds}^s i_{qr}^s\right) = \frac{P}{3}L_m\,\mathrm{Im}\left(i_s^s i_r^{s*}\right), \tag{6.61}$$

where Im stands for the imaginary part of the production of vector i_s^s and conjugate vector of i_r^{s*}.
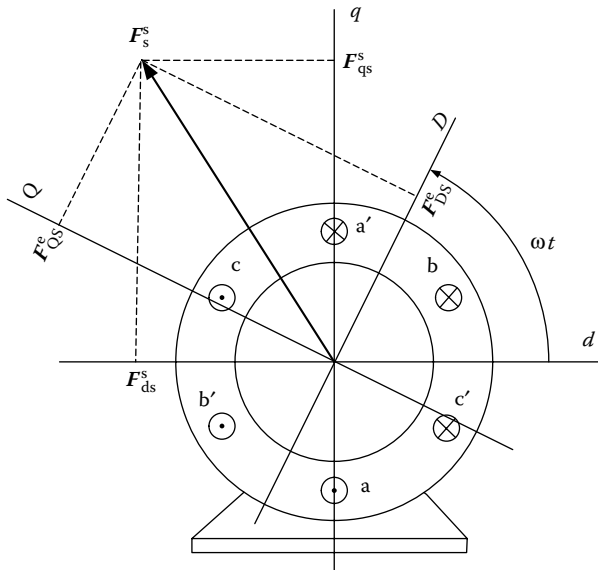
Transferring three-phase variables (voltage, current, and flux) into a stationary stator-based *dq* frame does not change the alternate characteristics of the variable with time. AC quantities are somewhat inconvenient for control purposes. For instance, control systems are usually represented by block diagrams in which the variables are time-varying DC signals. Therefore, another transformation is necessary, which allows the conversion of the AC *dq* components of the motor vectors into DC variables. To do this, a transformation is conducted from a stationary stator reference frame, *dq*, to the so-called excitation reference frame *DQ*, which rotates with the angular speed ω, in the same direction as does mmf, F_s^s. As a result, in the steady state, coordinates of motor vectors in the new reference frame do not vary in time. This is illustrated in Figure 6.24, which shows the stator mmf vector in both reference frames.

The voltage vector of the stator in excitation reference frame can be expressed as

$$v_S^e = v_s^s e^{-j\omega t} \tag{6.62}$$

Considering $e^{-j\omega t} = \cos(\omega t) - \sin(\omega t)$, the components of stator voltage on *DQ* frame is

$$\begin{bmatrix} v_{DS}^e \\ v_{QS}^e \end{bmatrix} = \begin{bmatrix} \cos(\omega t) & \sin(\omega t) \\ -\sin(\omega t) & \cos(\omega t) \end{bmatrix} \begin{bmatrix} v_{ds}^s \\ v_{qs}^s \end{bmatrix}. \tag{6.63}$$

FIGURE 6.24 Stator mmf vector in the stator and excitation reference frames.

Thus, the motor equation in excitation reference frame can be expressed as

$$v_S^e = R_s i_s^e + (p + j\omega)\,\lambda_s^e, \tag{6.64}$$

$$v_R^e = R_r i_R^e + (p + j\omega - j\omega_0)\,\lambda_R^e = R_r i_R^e + (p + j\omega_r)\,\lambda_R^e, \tag{6.65}$$

where $\omega_r = \omega - \omega_0$ as the slip speed, and

$$\begin{bmatrix} \lambda_S^e \\ \lambda_R^e \end{bmatrix} = \begin{bmatrix} L_s & L_m \\ L_m & L_r \end{bmatrix} \begin{bmatrix} i_S^e \\ i_R^e \end{bmatrix}. \tag{6.66}$$

Again, the rotor voltage vector is normally assumed to be zero because of the shorted rotor winding.

The torque equation in the excitation reference frame is similar to that in the stator frame as

$$T = \frac{P}{3} L_m \left(i_{QS}^e i_{DR}^e - i_{DS}^e i_{QR}^e \right) = \frac{P}{3} L_m \, \mathrm{Im} \left(i_S^e i_e^{e*} \right). \tag{6.67}$$

In general, accurate control of instantaneous torque produced by a motor is required in high-performance drive systems, such as EV and HEV propulsions. The torque developed in the motor is a result of the interaction between current in the armature winding and the magnetic field produced in the stator field of the motor. The field should be maintained at a certain optimal level, sufficiently high to yield a high torque per unit of ampere, but not too high to result in excessive saturation of the magnetic circuit of the motor. With a fixed field, the torque is proportional to the armature current.

Independent control of the field and armature currents is desirable. In a similar manner to that of a DC motor, the armature winding in induction motors is also on the rotor, while the field is generated by currents in the stator winding. However, the rotor current is not directly derived from an external source, but results from the EMF induced in the winding as a result of the relative motion of the rotor conductors with respect to the stator field. In the most commonly used squirrel-cage motors, only the stator current can be directly controlled, since the rotor winding is not accessible. Optimal torque production conditions are not inherent due to the absence of a fixed physical disposition between the stator and rotor fields, and the torque equation is nonlinear. FOC or vector control can realize the optimal control for transient operation of an induction drive. The FOC can decouple the field control from the torque control. A field-oriented induction motor emulates a separately excited DC motor in two aspects:

1. Both the magnetic field and the torque developed in the motor can be controlled independently.

2. Optimal conditions for torque production, resulting in the maximum torque per unit ampere, occur in the motor both in the steady state and in transient conditions of operations.

As mentioned in Section 6.1.1, the optimal torque production conditions are inherently satisfied in a DC motor (refer to Figure 6.3). The armature current i_a, supplied through brushes, is always orthogonal to the flux vector (field flux), λ_f, produced in the stator and linking the rotor winding. In effect, the developed torque, T, is proportional both to the armature current and the field flux, that is,

$$T = K_T i_a \lambda_f, \tag{6.68}$$

where K_T is a constant depending on the physical parameters of the motor. Thus, the torque of separately excited DC motors can be controlled by independently controlling the armature current and flux as mentioned in Section 6.1.2.

To emulate this independent armature and field control characteristic of a DC motor, the torque Equation 6.67 can be rearranged so that the torque is expressed in terms of the stator current and rotor flux. From Equation 6.66, the flowing equation can be obtained as

$$i_R^e = \frac{1}{L_r} \left(\lambda_R^e - L_m i_S^e \right). \tag{6.69}$$

Torque Equation 6.67 can be rewritten as

$$T = \frac{P}{3R_r} \frac{L_m}{\tau_r} \left(i_{QS}^e \lambda_{DR}^e - i_{DS}^e \lambda_{QR}^e \right), \tag{6.70}$$

where $\tau_r = L_r / R_r$ is the rotor time constant.

In Equation 6.70, if

$$\lambda_{QR}^e = 0, \tag{6.71}$$

then

$$T = \frac{P}{3R_r} \frac{L_m}{\tau_r} \lambda_{DR}^e i_{QS}^e. \tag{6.72}$$

Clearly, Equation 6.72 is analogous to Equation 6.68, describing a separately excited DC motor.

Substituting $v_R^e = 0$ (shorted rotor winding) into Equation 6.65 yields

$$R_r i_R^e + (p + j\omega_r) \lambda_R^e = 0, \tag{6.73}$$

and substituting Equation 6.69 into Equation 6.73 yields

$$p\lambda_R^e = \frac{1}{\tau_r} \left[L_m i_S^e - (1 + j\omega_r \tau_r) \lambda_R^e \right]. \tag{6.74}$$

Thus,

$$p\lambda_{DR}^e = \frac{L_m}{\tau_r} i_{DS}^e - \frac{1}{\tau_r} \lambda_{DR}^e. \tag{6.75}$$
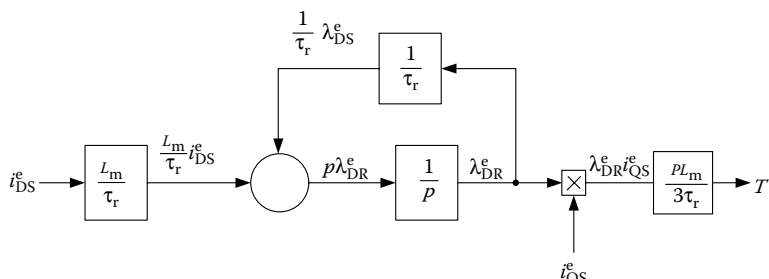
Equation 6.75 indicates that the flux λ_{DR}^e is produced by the current, i_{DS}^e. Thus, the torque produced can be represented by the block diagram as shown in Figure 6.25.

Furthermore, Equation 6.75 can be expressed into a transfer function as
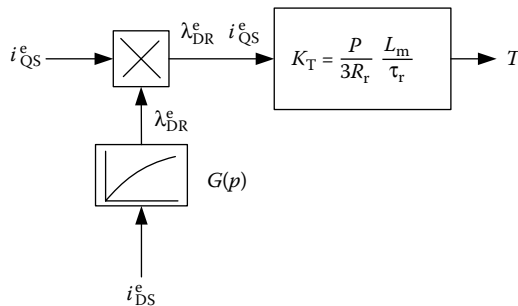
$$G(p) = \frac{\lambda_{DR}^e}{i_{DS}^e} = \frac{L_m}{\tau_r p + 1}. \tag{6.76}$$

Thus, the block diagram in Figure 6.25 can be further reduced as shown in Figure 6.26.

If conditions (6.71) and $\lambda_{DR}^e = $ constant t are satisfied, that is, $\lambda_{QR}^e = 0$ and $p\lambda_{DR}^e = 0$, then Equation 6.64 yields $i_{DR}^e = 0$, that is, $i_R^e = j i_{QR}^e$. At the same time, $\lambda_R^e = \lambda_{DR}^e$. Consequently, vectors i_R^e and λ_R^e are orthogonal, which represents the optimal conditions for the torque production, analogous to a DC motor. In an induction motor, the optimal torque-production conditions are always satisfied in the steady state. However, in transient operation, the motor needs delicate control to achieve this optimal torque production.

FIGURE 6.25   Block diagram of an induction motor with $\lambda_{QR}^e = 0$.

FIGURE 6.26 Block diagram of a field-orientated induction motor.
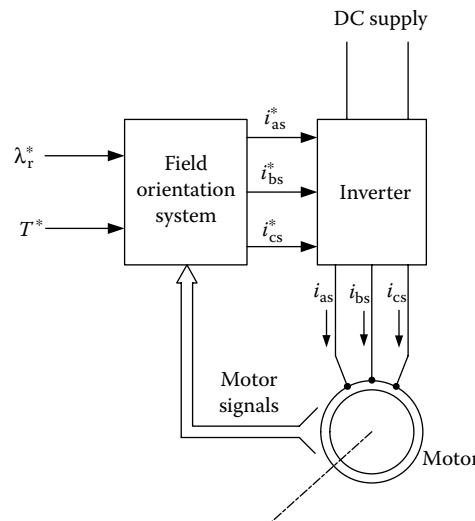
6.2.5.2 Control

As demonstrated in the above section, the field orientation principle defines the conditions of optimal torque production. Orthogonality of the rotor current and stator flux vectors must be maintained at all times. This is inherently satisfied in the steady state when the rotor settles down to such a speed that the developed torque matches the load torque. Under transient conditions, however, in order to meet the field orientation principle conditions, special techniques are required to provide an algorithmic equivalent of the actual physical disposition between the stator and rotor fields of the emulated DC motor.

The general block diagram of a vector control system for an induction motor drive is shown in Figure 6.27. A field orientation system produces reference signals, i_{as}^*, i_{bs}^*, and i_{cs}^*, of the stator currents, based on the input reference values, λ_r^* and T^*, of the rotor flux and motor torque, respectively, and the signals corresponding to selected variables of the motor. An inverter supplies the motor currents, i_{as}, i_{bs}, and i_{cs}, such that their waveforms follow the reference waveform, i_{as}^*, i_{bs}^* and i_{cs}^*.

As shown in Figure 6.26, in a field orientated induction motor, the i_{DS}^e and i_{QS}^e components of the stator current vector, i_S^e, in the excitation frame can be used for independent control of the motor field and torque, respectively. Hence, the field orientation system as shown in Figure 6.27 first converts λ_r^* and T^* into the corresponding reference signals, i_{DS}^{e*} and i_{QS}^{e*}, of the vector of the stator current and then transfers these into the reference signals, i_{as}^*, i_{bs}^*, and i_{cs}^*, of the stator phase current, which are to be produced by the inverter. The stator phase currents, i_{as}^*, i_{bs}^*, and i_{cs}^*, can be calculated using dq to abc transformation (see Equation 6.46) if the corresponding reference signals, i_{ds}^{s*} and i_{qs}^{s*}, in the stator reference frame are known. This is a simple scalar, or static, transformation, since the elements of the transformation matrix used to perform this operation are constant.
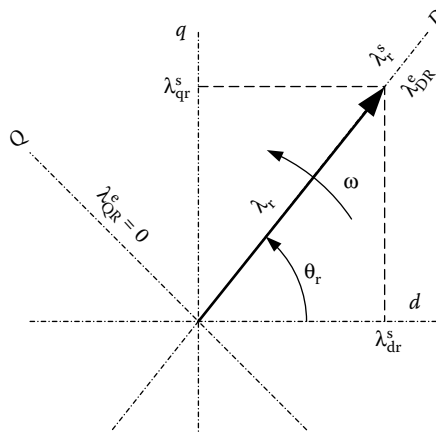
However, it can be seen from Equation 6.63 that a dynamic transformation, that is, one involving time, is required to determine i_{ds}^{s*} and i_{qs}^{s*} from i_{DS}^{e*} and i_{QS}^{e*}.

FIGURE 6.27   General block diagram of a vector control system for an induction motor.

In Figure 6.24, it does not indicate which vector the excitation reference frame DQ aligns with. Clearly, any one of the vectors can be used as a reference with which the excitation frame is to be aligned. Usually, it is the rotor flux vector, λ_r^s, along which the excitation frame is orientated. This method is usually referred to as the rotor flux orientation scheme,[8] as shown in Figure 6.28.

If the angular position of the rotor flux vector in the stator reference frame is denoted by θ_r, the DQ to dq transformation in the described scheme is

FIGURE 6.28   Orientation of the excitation reference frame along the rotor flux vector.

expressed as

$$\begin{bmatrix} i_{ds}^{s*} \\ i_{qs}^{s*} \end{bmatrix} = \begin{bmatrix} \cos(\theta_r) & -\sin(\theta_r) \\ \sin(\theta_r) & \cos(\theta_r) \end{bmatrix} \begin{bmatrix} i_{DS}^{e*} \\ i_{QS}^{e*} \end{bmatrix}. \tag{6.77}$$

It can be observed that this orientation of the orientation frame inherently satisfies the field orientation principle condition in Equation 6.71. The rotor flux is controlled by adjusting the i_{DS}^{e} component of the stator current vector—independently of the torque control, which is realized by means of the i_{QS}^{e} component. The only requirement for this scheme is an accurate identification of angle θ_r, that is, the position of λ_r^s. This can be done in either a direct or indirect way.
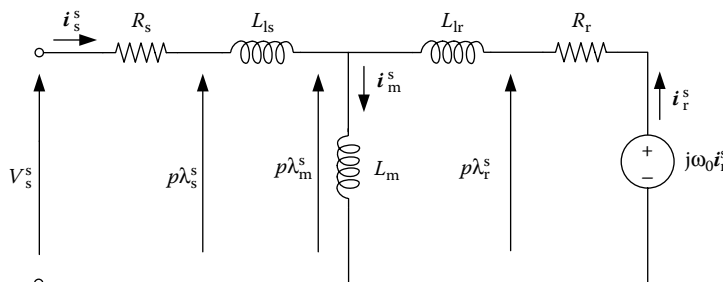
6.2.5.3 Direction Rotor Flux Orientation Scheme

In direct field orientation systems, the magnitude and angular position (phase) of the reference flux vector, λ_r^e, are either measured or estimated from the stator voltage and current using flux observers. For example, Hall sensors can be used to measure magnetic fields. Placing the sensors in the air gap of the motor, on the d and q axes, allows determination of the corresponding components of vector λ_m^s of the mutual flux (air gap flux). However, this air gap flux differs from the rotor flux, which is taken as the reference flux vector and needs derivation from the air gap flux λ_m^s. Referring to the dynamic T equivalent circuit shown in Figure 6.29, the flux appearing across the mutual inductance L_m is
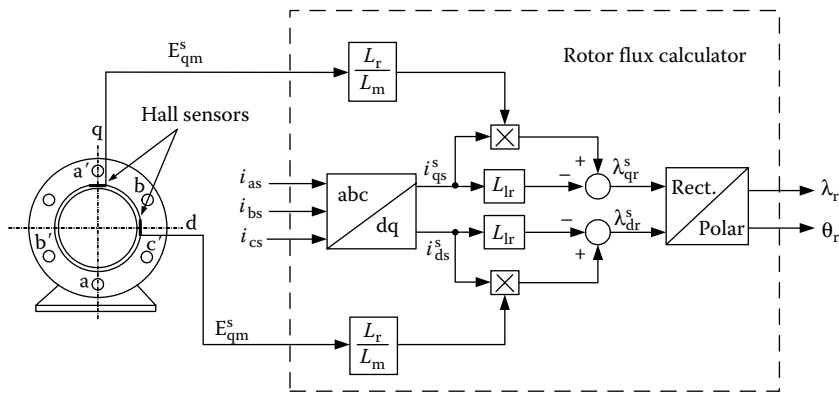
$$\lambda_m^s = L_m i_m^s = L_m \left(i_s^s + i_r^s \right) \tag{6.78}$$

or

$$i_r^s = \frac{1}{L_m} \lambda_m^s - i_s^s. \tag{6.79}$$

FIGURE 6.29 Dynamic T equivalent circuit of an induction motor.

FIGURE 6.30 Determination of the magnitude and position of the rotor flux vector using a Hall sensor and a rotor flux calculator.[3]

Since λ_r^s differs from the λ_m^s by only the leakage flux in the rotor, then

$$\lambda_r^s = \lambda_m^s + L_{lr}i_r^s = \lambda_m^s + L_{lr}\left(\frac{1}{L_m}\lambda_m^s - \lambda_s^s\right) = \frac{L_r}{L_m}\lambda_m^s - L_{lr}i_s^s. \qquad (6.80)$$
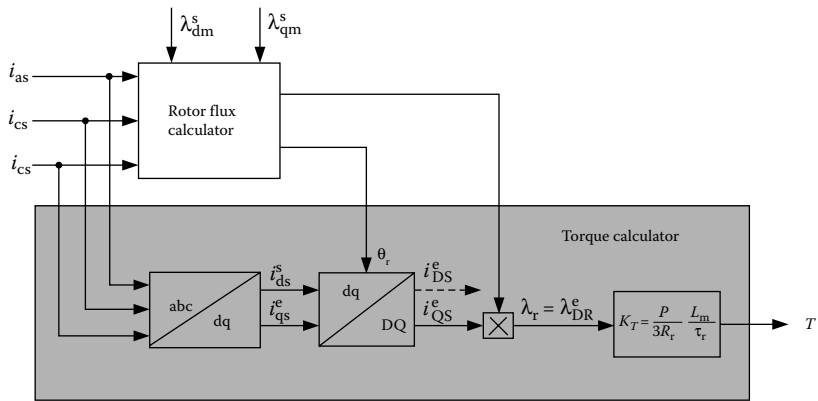
A microprocessor-based rotor flux calculator is shown in Figure 6.30. It performs the algebraic operations as the follows:

1. Signals i_{ds}^s and i_{qs}^s are calculated from the actual stator phase currents, i_{as}, i_{bs}, and i_{cs}, using the abc to dq transformation expressed in Equation 6.46.
2. Using Equation 6.80, signals λ_{dr}^s and λ_{qr}^s are calculated.
3. Magnitude λ_r and the phase θ_r of the rotor flux vector are determined using the rectangular to polar coordinate transformation.

It must be pointed out that the orthogonal spacing of the flux sensors in Figure 6.30 applies only to two-pole machines. In a P-pole machine, the sensors must be placed $180/P$ from each other.

Since $\lambda_{DR}^e = \lambda_r$ (see Figure 6.28), then the output variable, λ_r, of the rotor flux calculator can be used as a feedback signal in the field control loop. The same variables can also be used for calculation of the developed torque as shown in Figure 6.31. The torque calculator computes torque in the following steps:

1. The static abc to dq transformation is performed on the stator currents i_{as}, i_{bs}, and i_{cs} to obtain i_{ds}^s and i_{qs}^s.
2. Angle θ_r supplied by the rotor flux calculator is substituted into Equation 6.63 for ωt in order to transfer signals i_{ds}^s and i_{qs}^s into i_{DS}^e and i_{QS}^e components of the stator current vector in the excitation frame.
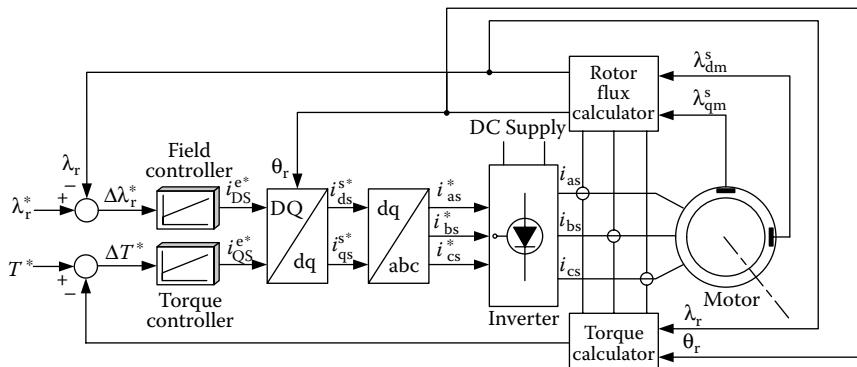
FIGURE 6.31 Torque calculator.

3. Magnitude, λ_r, of the rotor flux, also supplied by the rotor flux calculator and presumed equal to λ_{DS}^e, is multiplied by i_{QS}^e and by the torque constant K_T to calculate the developed torque.

Figure 6.31 shows the torque calculation process block diagram.

Figure 6.32 illustrates an independent flux and torque control block diagram, based on the vector control of an induction motor with direct rotor flux orientation. In the system, proportional-plus-integral (PI)-based field and torque controllers are used to generate the control signals i_{DS}^{e*} and i_{QS}^{e*} in excitation frame by comparing the target rotor flux, λ_r^*, and target torque T^*, with the actual rotor flux, λ_r, and torque, T. Then, i_{DS}^{e*} and i_{QS}^{e*} in excitation frame are transferred into i_{ds}^{s*} and i_{qs}^{s*} in stator reference frame using rotor flux angle (see Equation 6.63). Furthermore, i_{ds}^{s*} and i_{qs}^{s*} in stator reference

FIGURE 6.32 Vector control system for an induction motor with direct rotor flux orientation.

frame are transferred into phase current signals i_{as}^*, i_{bs}^*, and i_{cs}^* through static transformation (see Equation 6.46). The phase current signals, as the reference signals, are used to control the power electronics of the inverter to generate corresponding phase current i_{as}, i_{bs}, and i_{cs}.

In practice, the ratio of L_r to L_m, and the rotor leakage inductance, L_{ls}, which are used in the rotor flux calculator (see Figure 6.30), are not significantly affected by changes in the operation conditions of the motor, such as the winding temperature or saturation of the magnetic circuit. Therefore, the field orientation techniques described are considered to be the most robust and accurate. However, it requires the placement of vulnerable Hall sensors in the air gap of the motor, to the detriment of the cost and reliability of the drive system.

6.2.5.4   Indirect Rotor Flux Orientation Scheme

The presence of vulnerable Hall sensors in vector control with direct rotor flux orientation would weaken the reliability and enhance the cost of the motor drive. The indirect approach is to obtain the rotor flux position by the calculation of the slip speed, ω_r, required for correct field orientation, and the imposition of this speed on the motor.

If the synchronous speed necessary to maintain the orthogonal orientation of vectors λ_R^e and i_R^e in the given operating conditions of the motor is denoted by ω^*, the θ_r angle can be expressed as

$$\theta_r = \int_0^t \omega^* \, dt = \int_0^t \omega_r^* \, dt + \int_0^t \omega_0 \, dt = \int_0^t \omega_r^* \, dt + \theta_0, \quad (6.81)$$

where ω^*, ω_r, and ω_0 are the synchronous speed, slip speed, and rotor speed, respectively, and θ_0 is the angular displacement of the rotor, which is easy to measure using a shaft position sensor.

The required value of the slip speed ω_r^* can be computed from Equation 6.69. Since $\lambda_R^e = \lambda_{DR}^e$, Equation 6.69 becomes
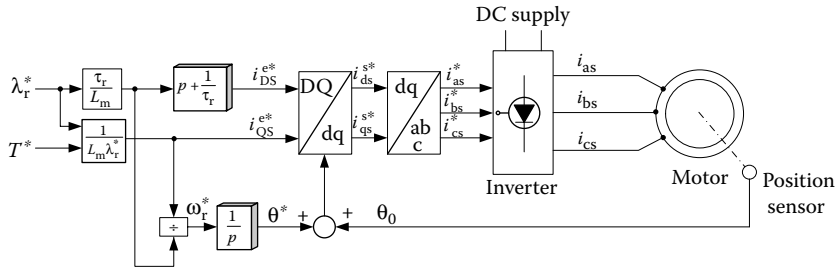
$$i_R^e = \frac{1}{L_r} \left(\lambda_{DR}^e - L_m i_S^e \right). \quad (6.82)$$

Substituting Equation 6.82 into Equation 6.73 gives the real and imaginary parts as

$$\lambda_{DR}^e \left(1 + \tau_r p \right) = L_m i_{DS}^e, \quad (6.83)$$

and

$$\omega_r \tau_r \lambda_{DR}^e = L_m i_{QS}^e. \quad (6.84)$$

FIGURE 6.33 Vector control system for an induction motor with indirect rotor flux orientation.

Replacing ω_r, λ_{DR}^e, and i_{QS}^e with ω_r^*, λ_r^*, and i_{QS}^{e*}, respectively, in Equation 6.84 yields

$$\omega_r^* = \frac{L_m}{\tau_r} \frac{i_{QS}^{e*}}{\lambda_r^*}. \tag{6.85}$$

Replacing λ_{Dr}^e and i_{DS}^e in Equation 6.83 with λ_r^* and i_{DR}^{e*} yields

$$i_{DS}^{e*} = \frac{1 + \tau_r p}{L_m} \lambda_R^*. \tag{6.86}$$
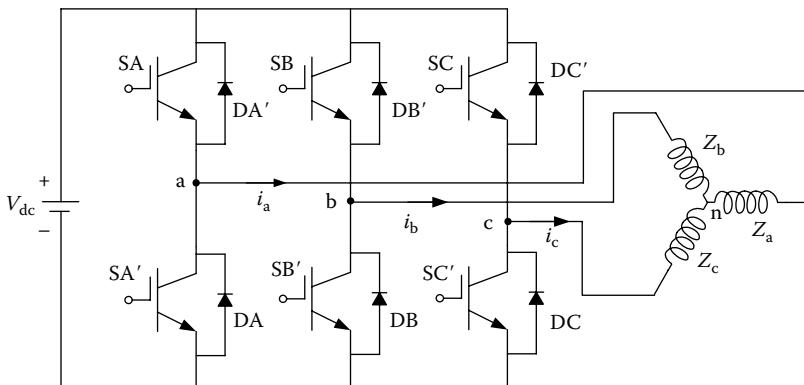
From the torque Equation 6.68, the signal i_{QS}^{e*} can be obtained as

$$i_{QS}^{e*} = \frac{T^*}{K_T \lambda_r^*}. \tag{6.87}$$

A vector control system for an induction motor based on the indirect rotor flux orientation scheme is shown in Figure 6.33. The rotor flux and developed torque are controlled in a feedforward manner. As a consequence of this, performance of the system strongly depends on an accurate knowledge of motor parameters, a requirement that is difficult to satisfy in practical applications. On the other hand, a major advantage of such a system is that a standard motor can be used, whose rotor position is easily measurable by an external sensor. Since the control scheme presented here constitutes an extension of the scalar torque control methods, the reference flux and torque values must satisfy the safe operation area condition described.[9]

6.2.6 Voltage Source Inverter for FOC

The power electronic inverter for FOC of induction motor drives has the same topology as shown in Figure 6.21a, which is repeatedly illustrated in Figure 6.34. The power switches in a given leg (a, b, or c) must never both be in ON-state, since this would cause a short-circuit. On the other hand, if both the switches on the same leg are in OFF-state, then the potential of

FIGURE 6.34 Circuit diagram of a three-phase voltage source inverter.

the corresponding output terminal is unknown to the control system of the inverter. The circuit can be completed through either the upper or lower diode and, consequently, the potential can be equal to that of either positive bus (+) or negative bus (−). Therefore the inverter is controlled in such a way that, in a given leg, either the upper switch (SA, SB, or SC) is ON and the lower switch (SA′, SB′, or SC′) is OFF or vice versa, the upper switch is OFF and the lower switch is ON.

Since only two combinations of states of the switches in each leg are allowed, a switching variable can be assigned to each phase of the inverter. In effect, only eight logic states are permitted for the whole power circuit. Defining the switching variables as

$$a = \begin{cases} 0 & \text{if SA is OFF and SA′ is ON,} \\ 1 & \text{if SA is ON and SB′ is OFF,} \end{cases} \tag{6.88}$$

$$b = \begin{cases} 0 & \text{if SB is OFF and SB′ is ON,} \\ 1 & \text{if SB is ON and SB′ is OFF,} \end{cases} \tag{6.89}$$

$$c = \begin{cases} 0 & \text{if SC is OFF and SC′ is ON,} \\ 1 & \text{if SC is ON and SC′ is OFF.} \end{cases} \tag{6.90}$$

The instantaneous values of the line-to-line output voltage of the inverter are given by

$$v_{ab} = V_{dc}(a - b), \tag{6.91}$$

$$v_{bc} = V_{dc}(b - c), \tag{6.92}$$

$$v_{ca} = V_{dc}(c - a), \tag{6.93}$$

where V_{dc} is the voltage of the DC supply of the inverter.

In a balanced three-phase system, the line-to-neutral voltage can be calculated from the line-to-line voltages as[9]

$$v_a = \frac{1}{3}(v_{ab} - v_{ca}),\tag{6.94}$$

$$v_b = \frac{1}{3}(v_{bc} - v_{ab}),\tag{6.95}$$

$$v_c = \frac{1}{3}(v_{ca} - v_{bc}).\tag{6.96}$$

Hence, after substituting Equations 6.88 through 6.90 into Equations 6.94 through 6.96, the line-to-neutral voltages are given by

$$v_a = \frac{V_{dc}}{3}(2a - b - c),\tag{6.97}$$

$$v_b = \frac{V_{dc}}{3}(2b - c - a),\tag{6.98}$$

$$v_c = \frac{V_{dc}}{3}(2c - a - b).\tag{6.99}$$
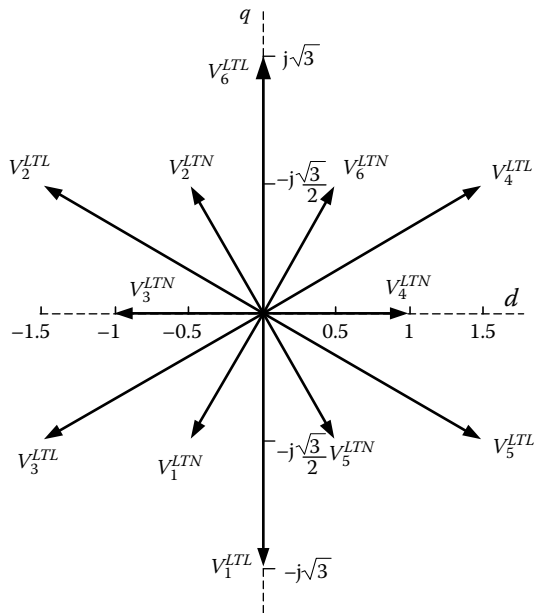
From Equations 6.91 through 6.93, line-to-line voltages can assume only three values: $-V_{dc}$, 0, and V_{dc}. However, Equations 6.97 through 6.99 give out five line-to-neutral voltage values: $(-2/3)V_{dc}$, $(-1/3)V_{dc}$, 0, $(1/3)V_{dc}$, and $(2/3)V_{dc}$. The eight logic states of the inverter can be numbered from 0 to 7 using the decimal equivalent of binary number abc_2. For example, if $a = 1$, $b = 0$, and $c = 1$, then $abc_2 = 101_2 = 5_{10}$, and the inverter is said to be in state 5. Taking V_{dc} as the base voltage, and at state 5, the per-unit output voltages are: $v_{ab} = 1$, $v_{bc} = -1$, $v_{ca} = 0$, $v_a = 1/3$, $v_b = -2/3$, and $v_c = 1/3$.

Performing the abc to dq transformation, the output voltage can be represented as space vectors, the stator reference frame, each vector corresponding to a given state of the inverter. The space vector diagrams of line-to-line voltages, identified by the superscript of LTL, and line-to-neutral voltages, identified by the superscript LTN, of voltage source inverter are shown in Figure 6.35. The vectors are presented in the per-unit format.

6.2.6.1 Voltage Control in Voltage Source Inverter
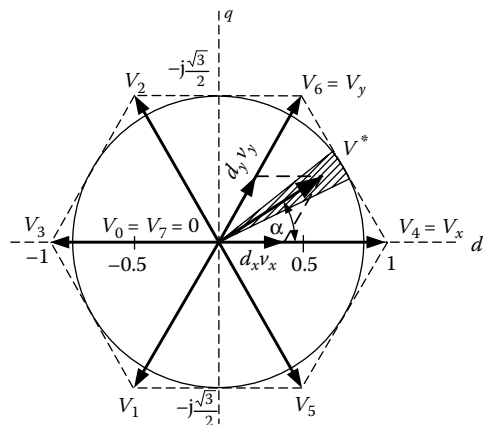
A large number of different (PWM) technologies have been developed and implemented in practical inverters. Currently, one of the most popular methods is based on the concept of space vectors of the inverter voltages, as shown in Figure 6.35. This method is more suitable for application with the field orientation control of induction motor drives.

For a wye-connected induction motor, the load currents are generated by the line-to-neutral voltages of the inverter. Thus, the motor operation is controlled by the line-to-neutral voltage inverter voltages.

FIGURE 6.35 Space vectors of output voltage of a voltage source inverter.

Space vectors of the line-to-neutral voltages are shown in Figure 6.36, together with an arbitrary vector v^*, to be generated by the inverter. In addition to showing six nonzero vectors (state 1 to state 6), another two zero vectors, corresponding to state 0 and state 7, are also shown. Clearly, only vectors v_0 to v_7, further referred to as base vectors, can be produced at a

FIGURE 6.36 Illustration of the space vector PWM strategy.

given instant of time. Therefore, vector v^* represents an average rather than an instantaneous value, the average being taken over a period of switching, or sampling, interval, which, in practice, constitutes a small fraction of the cycle of the output frequency. The switching interval, at the center of which the reference vector is located, is shown in Figure 6.36 as the shaded segment.

The nonzero base vectors divided the cycle into six, 60°-wide sectors. The desired voltage vector v^*, located in a given sector, can be synthesized as a linear combination of the two adjacent base vectors, v_x and v_y, which are framing the sector, and either one of the two zero vectors. That is,

$$v^* = d_x v_x + d_r v_y + d_z v_z, \tag{6.100}$$

where v_z is the zero vector, d_x, d_y, and d_z denote the duty ratios of the states of x, y, and z within the switching interval, respectively. For instance, the reference voltage vector $v*$, in Figure 6.36, is located within the first sector in which $v_x = v_4$ and $v_y = v_6$; hence, it can be produced by an appropriately timed sequence of states 4, 6, and 0 or 7 of the inverter.

The state duty ratio is defined as the ratio of the duration of the state to the duration of the switching interval. Therefore,

$$d_x + d_y + d_z = 1. \tag{6.101}$$

It can be seen that under this condition the locus of the maximum available vectors v^* constitutes the hexagonal envelope of the base vectors, as shown in Figure 6.36. To avoid low-order voltage harmonics, resulting from the non-circular shape of the envelope, the locus of the synthesized voltage vectors is, in practice, limited to the circle as shown in Figure 6.36. Consequently, the maximum available magnitude, V_{max}, of the resulting voltage is $(\sqrt{3}/2)V_{dc}$. With respect to vector v^*, in Figure 6.36, Equation 6.100 can be written as

$$v^* = MV_{max}e^{j\alpha} = d_x v_4 + d_y v_6 + d_z v_z, \tag{6.102}$$

where M is the modulation index, adjustable within the 0 to 1 range, and α denotes the angular position of the vector v^* inside the sector, that is, the angular distance between vectors v^* and v_x. As seen in Figure 6.36, $v_x = v_4 = 1 + j0$ p.u., $v_y = v_6 = 1/2 + j\sqrt{3}/2$ p.u., and v_z (either v_0 or v_7) is zero, and $V_{max} = (\sqrt{3}/2)V_{dc}$, Equation 6.100 can be rewritten as

$$\frac{\sqrt{3}}{2}M\cos(\alpha) = d_x + \frac{1}{2}d_y, \tag{6.103}$$

and

$$\frac{\sqrt{3}}{2}M\sin(\alpha) = \frac{\sqrt{3}}{2}d_y. \tag{6.104}$$

Thus, d_x and d_y can be expressed as

$$d_x = M \sin(60° - \alpha), \tag{6.105}$$

$$d_y = M \sin(\alpha), \tag{6.106}$$

and

$$d_z = 1 - d_x - d_y. \tag{6.107}$$

The same equations can be applied to the other sectors.

The simple algebraic formulas 6.105 through 6.107 allow duty ratios of the consecutive logic states of an inverter to be computed in real time. Due to the freedom of choice of the zero vectors, various state sequences can be enforced in a given sector. Particularly efficient operation of the inverter is obtained when the state sequence in consecutive switching intervals is

$$\left| x - y - z \right| z - y - x \left| \ldots , \tag{6.108} \right.$$

where $z = 0$ in sectors $v_6 - v_2, v_3 - v_1$ and $v_5 - v_4$, and $z = 7$ in the remaining sectors. Figure 6.37 shows an example of switching signals and output voltages for a voltage source inverter in the previously described PWM mode with $M = 0.7$ and 20° width of the switching interval.[9]
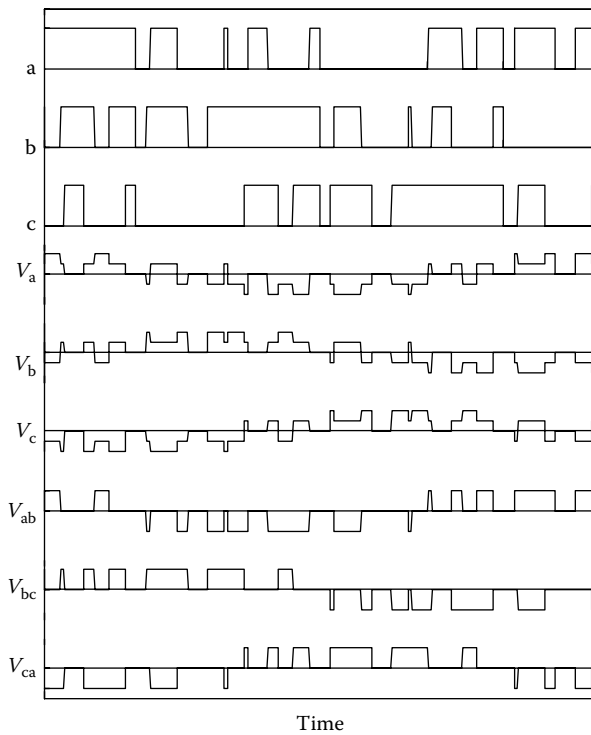
6.2.6.2 *Current Control in Voltage Source Inverter*

Since the output currents of an inverter depend on load, feedforward current control is not feasible and a feedback from current sensors is required. There exist a number of different control technologies. The simplest one is the controller, based on the so-called "hysteretic" or "bang-bang."
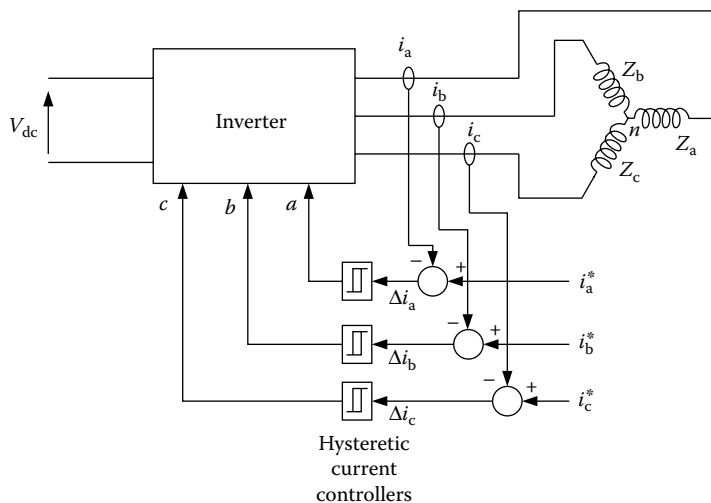
The block diagram of a current control voltage source inverter is shown in Figure 6.38. The output currents i_a, i_b, and i_c of the inverter are sensed and compared with the reference current signals i_a^*, i_b^*, and i_c^*. Current error signals Δi_a, Δi_b, and Δi_c are then applied to the hysteresis current controller, which generates switching signals, a, b, and c, for the inverter switches.

The input–output characteristic of the phase-a hysteretic current controller is shown in Figure 6.39. The width of the hysteretic loop, denoted by h, represented the tolerance bandwidth for the controlled current. If the current error, Δi_a, is greater than $h/2$, that is, i_a is unacceptably lower than the reference current, i_a^*, the corresponding line-to-neutral voltage, v_a, must be increased. From Equation 6.97, this voltage is most strongly affected by the switch variable a; hence, it is this variable that is regulated by the controller, and is set 1 to a in the described situation. Conversely, an error of less than $-h/s$ results in $a = 0$; in order to decrease the current i_a that stays within the tolerance band, the other two controllers are operated in a similar manner.
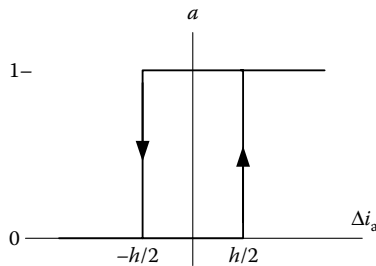
The width, h, of the tolerance band affects the switching frequency of the inverter. The narrower the band, the more frequently the switching takes place and the higher the quality of the current will be. This is illustrated in Figures
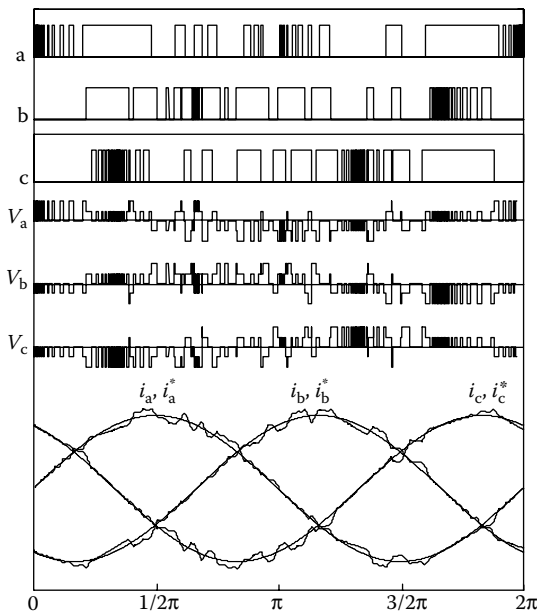
FIGURE 6.37 Example switching signals and output voltage for voltage source inverter in the PWM operation mode.

FIGURE 6.38 Block diagram of a current-controlled voltage source inverter.

FIGURE 6.39   Input–output characteristics of a hysteresis current controller.
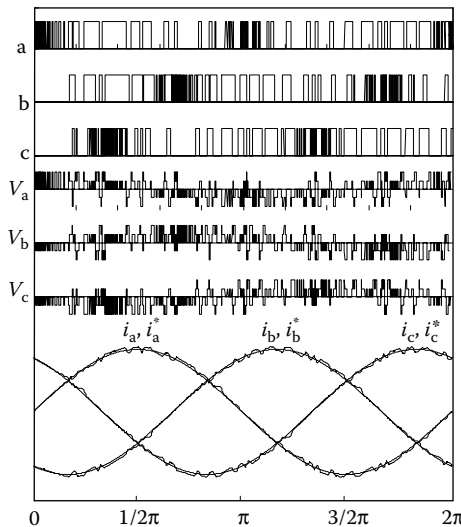
FIGURE 6.40   Current-controlled voltage source inverter (10% tolerance bandwidth).

6.40 and 6.41, in which the switching variables, line-to-neutral voltages, and currents for an inverter supplying a resistive-plus-inductive load are at values of $h = 10$ and 5% of the amplitude of the reference current, respectively. In practice, the tolerance bandwidth should be set to a value that represents an optimal trade-off between the quality of the currents and the efficiency of the inverter.

6.3   Permanent Magnetic BLDC Motor Drives

By using high-energy PMs as the field excitation mechanism, a PM motor drive can be potentially designed with high power density, high speed, and

FIGURE 6.41 Current-controlled voltage source inverter (5% tolerance bandwidth).

high operation efficiency. These prominent advantages are quite attractive for their application in EVs and HEVs. Of the family of PM motors, the BLDC motor drive is the most promising candidate for EV and HEV applications.[4]

The major advantages of BLDC motor includes the following:

- *High efficiency*: BLDC motors are the most efficient of all electric motors. This is due to the use of PMs for the excitation, which consume no power. The absence of mechanical commutator and brushes means low mechanical friction losses and therefore higher efficiency.

- *Compactness*: The recent introduction of high-energy density magnets (rare-earth magnets) has allowed achieving very high flux densities in the BLDC motor. This allows achieving accordingly high torques, which in turns allows making the motor small and light.

- *Ease of control*: The BLDC motor can be controlled as easily as a DC motor because the control variables are easily accessible and constant throughout the operation of the motor.

- *Ease of cooling*: There is no current circulation in the rotor. Therefore, the rotor of a BLDC motor does not heat up. The only heat production is on the stator, which is easier to cool than the rotor because it is static and on the periphery of the motor.

- *Low maintenance, great longevity, and reliability*: The absence of brushes and mechanical commutators suppresses the need for associated regular maintenance and suppresses the risk of failure associated with these elements. The longevity is therefore only a function of the winding insulation, bearings, and magnet life-length.

- *Low noise emissions*: There is no noise associated with the commutation because it is electronic and not mechanical. The driving converter switching frequency is high enough so that the harmonics are not audible.

However, BLDC motor drives also suffer from some disadvantages as follows:

- *Cost*: Rare-earth magnets are much more expensive than other magnets and result in an increased motor cost.
- *Limited constant power range*: A large constant power range is crucial to achieving high vehicle efficiencies. The PM BLDC motor is incapable of achieving a maximum speed greater than twice the base speed.
- *Safety*: Large rare-earth PMs are dangerous during the construction of the motor because flying metallic objects are attracted towards them. There is also a danger in the case of vehicle wreck if the wheel is spinning freely: the motor is still excited by its magnets and high voltage is present at the motor terminals that can possibly endanger the passengers or rescuers.
- *Magnet demagnetization*: Magnets can be demagnetized by large opposing magnetomotive forces and high temperatures. The critical demagnetization force is different for each magnet material. Great care must be brought to cooling the motor, especially if it is built compact.
- *High-speed capability*: The surface-mounted PM motors cannot reach high speeds because of the limited mechanical strength of the assembly between the rotor yoke and the PMs.
- *Inverter failures in BLDC motor drives*: Because of the PMs on the rotor, BLDC motors present major risks in the case of short-circuit failures of the inverter. Indeed, the rotating rotor is always energized and constantly induces an EMF in the short-circuited windings. A very large current circulates in those windings and an accordingly large torque tends to block the rotor. The dangers of blocking one or several wheels of a vehicle are non-negligible. If the rear wheels are blocked while the front wheels are spinning, the vehicle will spin uncontrollably. If the front wheels are blocked, the driver has no directional control over the vehicle. If only one wheel is blocked, it will induce a yaw torque that will tend to spin the vehicle, which will be difficult to control. In addition to the dangers to the vehicle, it should be noted that the large current resulting from an inverter short circuit poses a risk to demagnetize and destroy the PMs.

Open circuit faults in BLDC motor drives are no direct threat to the vehicle stability. The impossibility of controlling a motor due to an open circuit may,

however, pose problems in terms of controlling the vehicle. Because the magnets are always energized and cannot be controlled, it is difficult to control a BLDC motor in order to minimize the fault. This is a particularly important issue when the BLDC motor is operated in its constant power region. Indeed, in this region, a flux is generated by the stator to oppose the magnet flux and allow the motor to rotate at higher speeds. If the stator flux disappears, the magnet flux will induce a large EMF in the windings, which can be harmful to the electronics or passengers.
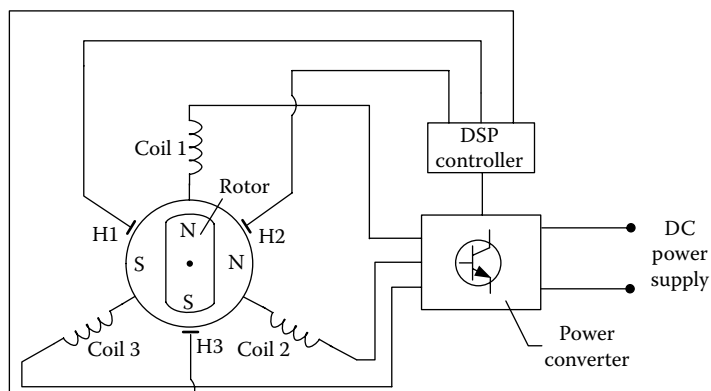
6.3.1 Basic Principles of BLDC Motor Drives

A BLDC motor drive consists mainly of the BLDC machine, the digital signal processor (DSP) based controller, and the power electronics-based power converter, as shown in Figure 6.42. Position sensors H1, H2, and H3 sense the position of the machine rotor. The rotor position information is fed to the DSP-based controller, which, in turn, supplies gating signals to the power converter by turning on and turning off the proper stator pole windings of the machine. In this way, the torque and speed of the machines are controlled.
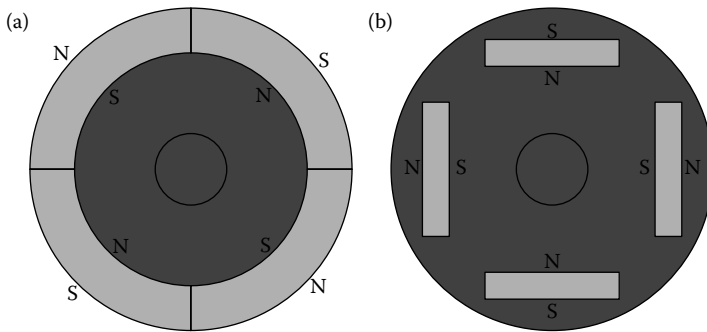
6.3.2 BLDC Machine Construction and Classification

BLDC machines can be categorized by the position of rotor PM, geometrically, according to the way in which the magnets are mounted on the rotor. The magnets can either be surface mounted or interior mounted.

Figure 6.43a shows the surface-mounted PM rotor. Each PM is mounted on the surface of the rotor. It is easy to build, and specially skewed poles are easily magnetized on this surface-mounted type to minimize cogging torque. But there is a possibility that it will fly apart during high-speed operation.

FIGURE 6.42 BLDC motor.

FIGURE 6.43 Cross sectional view of the PM rotor: (a) surface-mounted PM rotor; and (b) interior-mounted PM rotor.

Figure 6.43b shows the interior-mounted PM rotor. Each PM is mounted inside the rotor. It is not as common as the surface-mounted type but it is a good candidate for high-speed operation. Note that there is inductance variation for this type of rotor because the PM part is equivalent to air in the magnetic circuit calculation.
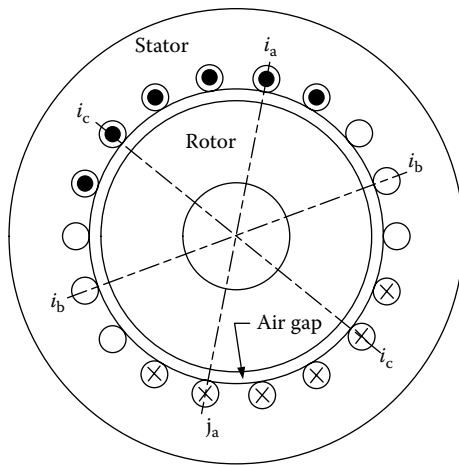
In the case of the stator windings, there are two major classes of BLDC motor drives, both of which can be characterized by the shapes of their respective back EMF waveforms, namely trapezoidal and sinusoidal.

The trapezoidal-shaped back EMF BLDC motor is designed to develop trapezoidal back EMF waveforms. It has the following ideal characteristics:

- Rectangular distribution of magnet flux in the air gap.
- Rectangular current waveform.
- Concentrated stator windings.

Excitation waveforms take the form of quasisquare current waveforms with two 60° electrical intervals of zero current excitation per cycle. The nature of the excitation waveforms for trapezoidal back EMF permits some important system simplifications compared to sinusoidal back EMF machines. In particular, the resolution requirements for the rotor position sensor are much lower since only six commutation instants are necessary per electrical cycle. Figure 6.44 shows the winding configuration of the trapezoidal-shaped back EMF BLDC machine.

Figure 6.45a shows equivalent circuit and (b) shows trapezoidal back EMF, current profiles, and Hall sensor signals of the three-phase BLDC motor drive. The voltages seen in this figure, e_a, e_b, and e_c, are the line-to-neutral back EMF voltages, the result of the PM flux crossing the air gap in a radial direction, and cutting the coils of the stator at a rate proportional to the rotor speed. The coils of the stator are positioned in the standard three-phase full-pitch, concentrated arrangement, and thus the phase trapezoidal back EMF waveforms are displaced by 120° electrical degrees. The current pulse

FIGURE 6.44   Winding configuration of the trapezoidal-shaped back EMF BLDC.

generation is a "120°-on and 60°-off" type, meaning each phase current is flowing for 2/3 of an electrical 360° period, 120° positively and 120° negatively. To drive the motor with maximum and constant torque per ampere, it is desired that the line current pulses be synchronized with the line-neutral back EMF voltages of the particular phase.

A sinusoidal-shaped back EMF BLDC motor is designed to develop sinusoidal back EMF waveforms. It has the following ideal characteristics:
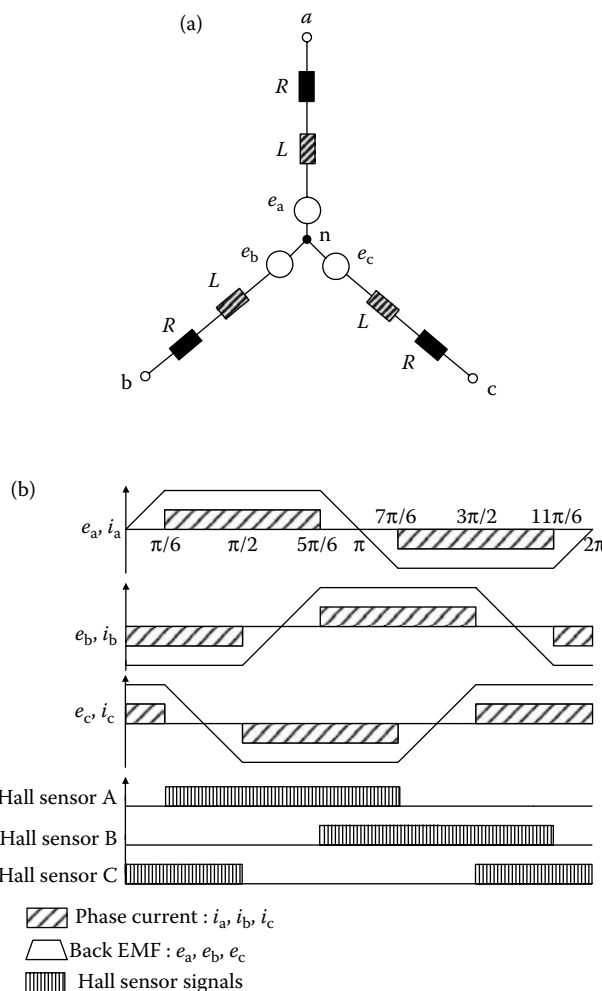
1. Sinusoidal distribution of magnet flux in the air gap.
2. Sinusoidal current waveforms.
3. Sinusoidal distribution of stator conductors.

The most fundamental aspect of the sinusoidal-shaped back EMF motor is that the back EMF generated in each phase winding by the rotation of the magnet should be a sinusoidal wave function of rotor angle. The drive operation of the sinusoidal-shaped back EMF BLDC machine is similar to the AC synchronous motor. It has a rotating stator MMF wave like a synchronous motor and therefore can be analyzed with a phasor diagram. Figure 6.46 shows the winding configuration of the sinusoidal-shaped back EMF BLDC machine.

6.3.3   Properties of PM Materials

There are three classes of PMs currently used for electric motors:

1. Alnicos (Al, Ni, Co, Fe).
2. Ceramics (ferrites), for example, barium ferrite ($BaO \times 6Fe_2O_3$) and strontium ferrite ($SrO \times 6Fe_2O_3$).
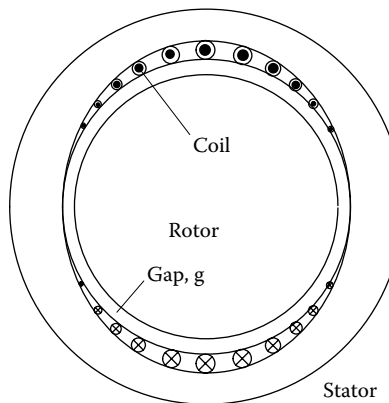
FIGURE 6.45 (a) Three-phase equivalent circuit and (b) back EMFs, currents, and Hall sensor signals of a BLDC motor.

3. Rare-earth materials, that is, samarium–cobalt (SmCo), and neodymium–iron–boron (NdFeB).
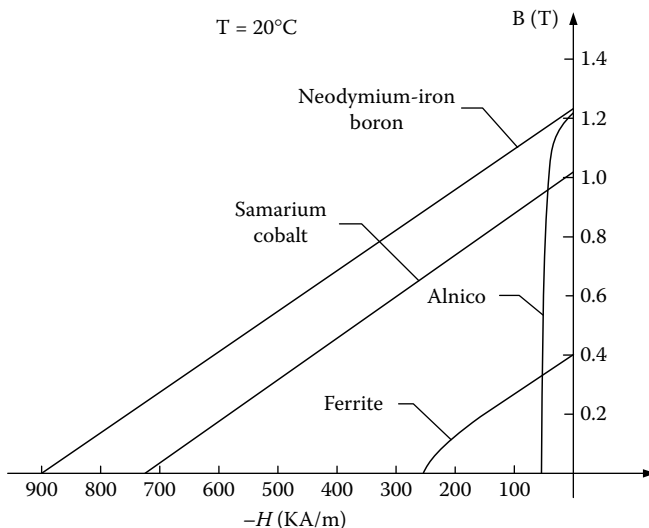
Demagnetization curves of the above PM materials are shown in Figure 6.47.[10]

6.3.3.1 Alnico

The main advantages of Alnico are its high magnetic remanent flux density and low-temperature coefficients. The temperature coefficient of its remanent

FIGURE 6.46 Winding configuration of sinusoidal-shaped back EMF BLDC.

FIGURE 6.47 Demagnetization curves for different PM materials.

magnetic flux density B_r, or remanence, is 0.02%/°C and the maximum service temperature is 520°C. These advantages allow quite a high air gap flux density and high operating temperature. Unfortunately, coercive force is very low and the demagnetization curve is extremely nonlinear. Therefore, it is very easy not only to magnetize but also to demagnetize Alnico. Alnico magnets have been used in motors having ratings in the range from a few watts to 150 kW. Alnicos dominated the PM industry from the mid-1940s to about 1970, when ferrites became the most widely used materials.[10]

6.3.3.2 Ferrites

Barium and strontium ferrites were invented in the 1950s. A ferrite has a higher coercive force than that of Alnico, but at the same time has a lower remanent magnetic flux density. Temperature coefficients are relatively high, that is, the coefficient of B_r is 0.20%/°C and the coefficient of coercive field strength, H_c, or coercivity is 0.27%/°C. The maximum service temperature is 400°C. The main advantages of ferrites are their low cost and very high electric resistance, which means no eddy-current losses in the PM volume.

6.3.3.3 Rare-Earth PMs

During the last three decades, greater progress regarding available energy density $(BH)_{max}$ has been achieved with the development of rare-earth PMs. The first generation of the rear-earth PMs based on the composition of samarium–cobalt ($SmCo_5$) was inverted in the 1960s and has been commercially produced since the early 1970s. Today, it is a well-established hard magnetic material. $SmCo_5$ has the advantages of high remanent flux density, high coercive force, high-energy product, linear demagnetization curve, and low-temperature coefficient. The temperature coefficient of B_r is 0.03–0.045%/°C and the temperature coefficient of H_c is $0.14 - 0.40$%/°C. The maximum service temperature is 250–300°C. It is well suited to build motors with low volume and consequently high specific power and low moment of inertia. The cost is the only drawback. Both Sm and Co are relatively expensive due to their supply restriction.

With the discovery in recent years of a second generation of rare-earth magnets on the basis of inexpensive neodymium (Nd) and iron, remarkable progress with regard to lowering raw material cost has been achieved. NdFeB magnets, which are now produced in increasing quantities, have better magnetic properties than those of SmCo, but only at room temperature. The demagnetization curves, especially the coercive force, are strongly temperature dependent. The temperature coefficient of B_r is $0.095 - 0.15$%/°C and the temperature coefficient of H_c is $0.40 - 0.7$%/°C. The maximum service temperature is 150°C and the Curie temperature is 310°C.

The latest grades of NdFeB have better thermal stability, enabling an increase in working temperature by 50°C, and offer greatly improved resistance to corrosion.[10]

6.3.4 Performance Analysis and Control of BLDC Machines

Speed–torque performance is most important for traction and other applications. As any other electric machine, the torque is produced by the interaction of magnetic field and current. The magnetic field is produced in BLDC by the PM, and the current depends on the source voltage, control, and the back EMF, which is determined by the magnetic field and speed of the machine.

To obtain the desired torque and speed at a given load, the current needs to be controlled.

6.3.4.1 Performance Analysis

The performance analysis of the BLDC machines is based on the following assumption for simplification:

1. The motor is not saturated.
2. Stator resistances of all the windings are equal and self- and mutual inductances are constant.
3. Power semiconductor devices in the inverter are ideal.
4. Iron losses are negligible.

A simplified equivalent circuit of one phase is shown in Figure 6.48, where V_t is the voltage of the power supply, R_s is the resistance of the winding, L_s is the leakage inductance ($L_s = L - M$, where L is the self-inductance of the winding and M is the mutual inductance), and E_s is the back EMF induced in the winding by the rotating rotor.

Based on the equivalent circuit of Figure 6.48, the performance of the BLDC motor can be described by
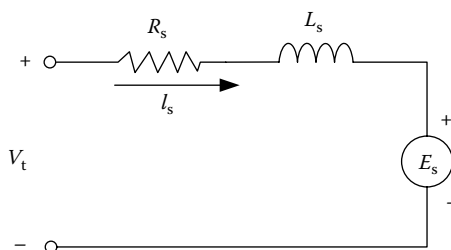
$$V_t = R_s I_s + L_s \frac{dI_s}{dt} + E_s, \tag{6.109}$$

$$E_s = k_E \omega_r, \tag{6.110}$$
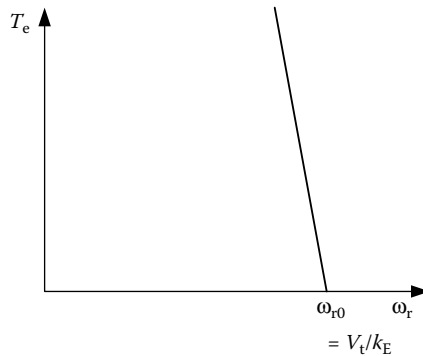
$$T_e = k_T I_s, \tag{6.111}$$

$$T_e = T_L + J \frac{d\omega_r}{dt} + B\omega_r, \tag{6.112}$$

where k_E is the back EMF constant, which is associated with the PMs and rotor structure, ω_r is the angular velocity of the rotor, k_T is the torque constant, T_L

FIGURE 6.48 Simplified equivalent circuit of the BLDC motor.

FIGURE 6.49 Speed–torque curve in the steady state with constant voltage.

is the load torque, and B is the viscous resistance coefficient. For steady-state operation, Equations 6.109 through 6.111 can be simply reduced to

$$T_e = \frac{(V_t - k_E \omega_r) k_T}{R_s}. \tag{6.113}$$

The speed–torque performance with constant voltage supply is shown in Figure 6.49. It can be seen from Equation 6.113 and Figure 6.49 that at low speed, especially while starting, very high torque is produced, which results in very high current due to the low back EMF. This very high current would damage the stator windings.

With variable voltage supply, the winding current can be restricted to its maximum by actively controlling the voltage; thus a maximum constant torque can be produced as shown in Figure 6.50.

For dynamic or transient operation, the performance of the BLDC machine is described by Equations 6.109 through 6.112. However, Laplace transform is helpful to simplify the analysis. Equations 6.109 through 6.112 can be expressed by their Laplace forms as

$$V_t(s) = E_s(s) + (R_s + sL_s) I_s(s), \tag{6.114}$$
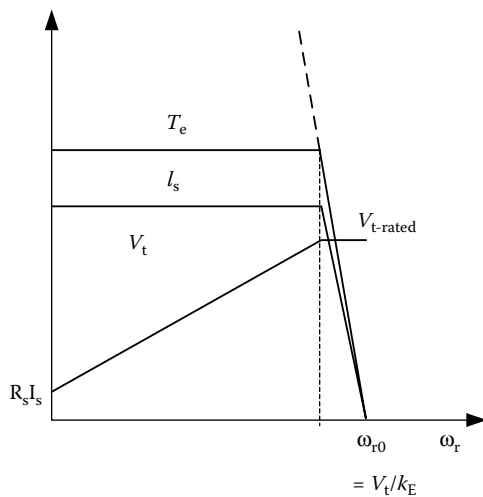
$$E_s(s) = k_E \omega_r(s), \tag{6.115}$$

$$T_e(s) = k_T I_s(s), \tag{6.116}$$

$$T_e(s) = T_L(s) + (B + sJ) \omega_r(s). \tag{6.117}$$

Thus, the transfer function of the BLDC motor drive system is

$$\omega_r(s) = \frac{k_T}{(R_s + sL_s)(sJ + B) + k_T k_E} V_t(s) - \frac{R_s + sL_s}{(R_s + sL_s)(sJ + B) + k_T k_E} T_L(s). \tag{6.118}$$

FIGURE 6.50 Speed–torque curve in the steady state with variable voltage supply.
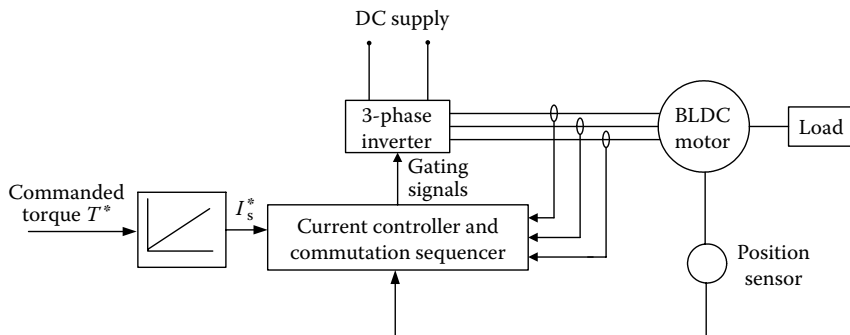
L_s and J in Equation 6.118 represent the electrical and mechanical delay in transient operation. L_s determines how quickly the armature current builds up in response to a step change in the terminal voltage, where the rotor speed is assumed to be constant. J determines how quickly the speed builds up in response to a step change in the terminal voltage.

6.3.4.2 Control of BLDC Motor Drives

In vehicle traction application, the torque produced is required to follow the torque desired by the driver and commanded through the accelerator and brake pedals. Thus, torque control is the basic requirement.
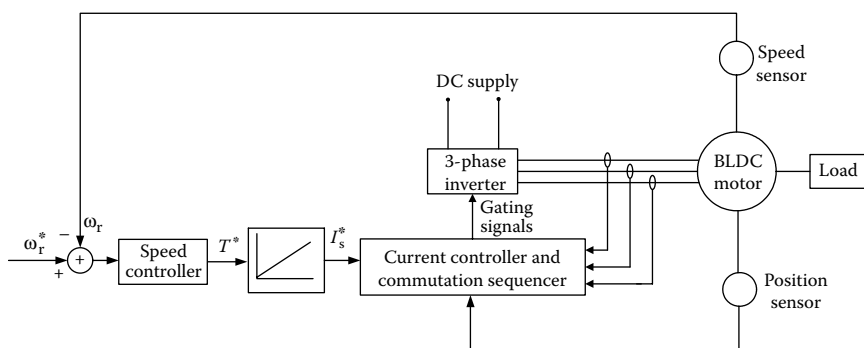
Figure 6.51 shows a block diagram of a torque control scheme for a BLDC motor drive. The desired current I^* is derived from the commanded torque T^* through a torque controller. The current controller and commutation sequencer receive the desired current I^*, position information from the position sensors, and perhaps the current feedback through current transducers, and then produce gating signals. These gating signals are sent to the three-phase inverter (power converter) to produce the desired phase current to the BLDC machine.

In traction application, speed control may be required, cruising control operation for example (see Figure 6.52). Many high-performance applications include current feedback for torque control. At the minimum, a DC bus current feedback is required to protect the drive and machine from over-currents. The controller blocks, "speed controller" may be any type of classical controller such as a proportional-integral (PI) controller or a more advanced controller such as an artificial intelligence control. The "current controller and

FIGURE 6.51   Block diagram of the torque control of the BLDC motor.

commutation sequencer" provides the properly sequenced gating signals to the "three-phase inverter" while comparing sensed currents to a reference to maintain a constant peak current control by hysteresis (current chopping) or with a voltage source (PWM)-type current control. Using position information, the commutation sequencer causes the inverter to "electronically commutate," acting as the mechanical commutator of a conventional DC machine. The commutation angle associated with a brushless motor is normally set so that the motor will commutate around the peak of the torque angle curve. Considering a three-phase motor, connected in Delta or wye, commutation occurs at electrical angles, which are plus or minus 30° (electrical) from the peaks of the torque–angle curves. When the motor position moves beyond the peaks by an amount equal to 30° (electrical), then the commutation sensors cause the stator phase excitation to switch to move the motor suddenly to −30° relative to the peak of the next torque–angle curve.[11]

FIGURE 6.52   Block diagram of the speed control of the BLDC motor.
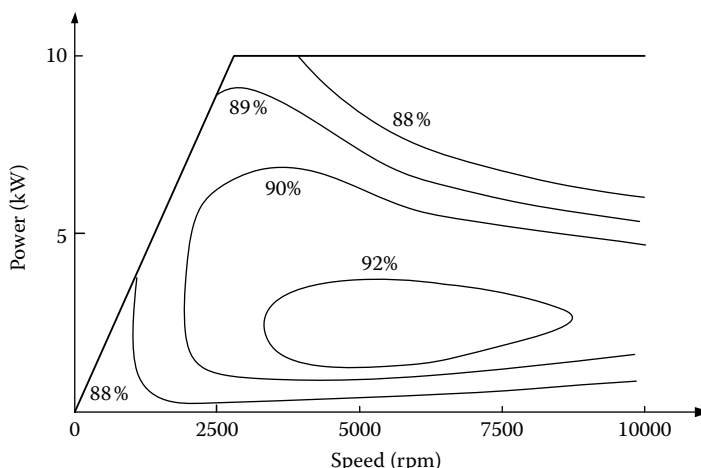
6.3.5 Extend Speed Technology

As discussed above, PM BLDC machines inherently have a short constant power range due to their rather limited field weakening capability. This is a result of the presence of the PM field, which can only be weakened through production of a stator field component, which opposes the rotor magnetic field. The speed ratio, x, is usually less than 2.[12]

Recently, the use of additional field windings to extend the speed range of PM BLDC motors has been developed.[1] The key is to control the field current in such a way that the air gap field provided by PMs can be weakened during high-speed, constant-power operation. Due to the presence of both PMs and the field windings, these motors are the so-called PM hybrid motors. The PM hybrid motor can achieve a speed ratio of around 4. The optimal efficiency profiles of a PM hybrid motor drive are shown in Figure 6.53.[1] However, the PM hybrid motors have the drawback of a relatively complex structure. The speed ratio is still not enough to meet the vehicle performance requirement, especially to an off-road vehicle. Thus a multigear transmission is required.

6.3.6 Sensorless Techniques

As mentioned above, the operation of the BLDC motor drives relies mostly on position sensors for obtaining the rotor position information so as to properly perform the turn-on or turn-off of each phase properly.[8] The position sensor is usually either a three-element Hall-effect sensor or an optical encoder. These position sensors are high-cost, fragile elements. Thus, its presence not only enhances the cost of the motor drive but also seriously lowers its reliability and limits its application in some environments, such as the military one.

FIGURE 6.53 Optimal efficiency profiles of a PM hybrid motor drive.[1]

Position sensorless technology can effectively continue the operation of the system in case the position sensors lose their function. This is crucial in some applications, such as military vehicles.

Several sensorless technologies have been developed. The majority of them are based on the voltage, current, and back EMF detection. These techniques can be primarily grouped into four categories:

1. Those using measured currents, voltages, fundamental machine equations, and algebraic manipulations.
2. Those using observers.
3. Those using back EMF methods.
4. Those with novel techniques not falling into the previous three categories.

6.3.6.1   Methods Using Measurables and Math

The method consists of two subtypes: (1) those that calculate the flux linkages using measured voltages and currents and (2) those that utilize a model's prediction of a measurable voltage or current, compare the model's value with the actual measured voltage or current and calculate the change in position, which is proportional to the difference between the measured and actual voltage or current.

The first subtype is seen in some studies.[13−20] The fundamental idea is to calculate the flux linkage from the measured voltage and current

$$\Psi = \int_0^t (V - Ri)\, d\tau. \qquad (6.119)$$

With the knowledge of initial position, machine parameters, and the flux linkages' relationship with rotor position, the rotor position can be estimated. By determining the rate of change of the flux linkage from the integration results, the speed can also be determined. An advantage of the flux-calculating method is that line–line voltages may be used in the calculations and thus no motor neutral is required.[8] This is beneficial, as the most common BLDC configuration is Y-connected with no neutral.

The second subtype is seen in some other studies.[21−24] This method consists of first developing an accurate d–q model of the machine. Utilizing the measured currents and a d–q transformation, the output voltages of the model are compared to the measured and transformed voltages. The difference is proportional to the difference in angular reference between the model's coordinate system and the actual coordinate system, which is the rotor position with reference to the actual coordinate system's reference. Conversely, they have also used the measured voltages and found the differences in the currents. In either case, the difference between the measured (and transformed) and the calculated is used as the multiplier in an update equation for the rotor position.

6.3.6.2 Methods Using Observers

These methods determine the rotor position and/or speed using observers. The first of these considered are those utilizing the well-known Kalman filter as a position estimator.[25–30] One of the first of these to appear in the literature was by M. Schroedl in 1988. In his many publications, Schroedl utilized various methods of measuring system voltages and currents, which could produce rough estimates of the angular rotor position. The Kalman filtering added the additional refinements to the first estimates of position and speed. Other observer-based systems include those utilizing nonlinear,[31–33] full-order,[13,34,35] and sliding-mode observers.[15,22,36]

6.3.6.3 Methods Using Back EMF Sensing

Using back EMF sensing is the main approach in sensorless control technology of the BLDC motor drive. This approach consists of several methods, such as (1) the terminal voltage sensing method, (2) the third-harmonic back EMF sensing method, (3) freewheeling diode conduction, and (4) back EMF integration.

Terminal voltage sensing: In normal operation of the BLDC motors, the flat part of a phase back EMF is aligned with the phase current. The switching instants of the converter can be obtained by knowing the zero crossing of the back EMF and a speed-dependent period of time delay.[37]

Since back EMF is zero at rest and proportional to speed, it is not possible to use the terminal voltage sensing method to obtain a switching pattern at low speeds. As the speed increases, the average terminal voltage increases and the frequency of excitation increases. The capacitive reactance in the filters varies with the frequency of excitation, introducing a speed-dependent delay in switching instants. This speed-dependent reactance disturbs current alignment with the back EMF and field orientation, which causes problems at higher speeds. In this method, a reduced speed operating range is normally used, typically around 1000–6000 rpm. This method is a good method for the steady state; however, phase differences in the circuits used due to speed variations do not allow optimal torque per ampere over a wide speed range.

Third harmonic back EMF sensing: Rather than using the fundamentals of the phase back EMF waveform as in the previous technique, the third harmonic of the back EMF can be used in the determination of the switching instants in the wye-connected 120° current conduction operating mode of the BLDC motor.[38] This method is not as sensitive to phase delay as the zero voltage crossing method, since the frequency to be filtered is three times as high. The reactance of the filter capacitor in this case dominates the phase angle output of the filter more so than at the lower frequency. This method provides a wider speed range than the zero-crossing method, does not introduce as much phase delay as the zero-crossing method, and requires less filtering.

Freewheeling diode conduction: This method uses indirect sensing of the zero crossing of the phase back EMF to obtain the switching instants of the BLDC motor.[39] In the 120° conducting *Y*-connected BLDC motor, one of the phases is always open-circuited. For a short period after opening the phase, there-phase current remains flowing, via a free-wheeling diode, due to the inductance of the windings. This open-phase current becomes zero in the middle of the commutation interval, which corresponds to the point where back EMF of the open phase crosses zero. The largest downfall of this method is the requirement of six additional isolated power supplies for the comparator circuitry for each free-wheeling diode.

Back EMF *integration*: In this method, position information is extracted by integrating the back EMF of the unexcited phase.[40−43] The integration is based on the absolute value of the open phase's back EMF. Integration of the voltage divider scaled-down back EMF starts when the open phase's back EMF crosses zero. A threshold is set to stop the integration that corresponds to a commutation instant. As the back EMF is assumed to vary linearly from positive to negative (trapezoidal back EMF assumed), and this linear slope is assumed to be speed insensitive, the threshold voltage is kept constant throughout the speed range. If desired, current advance can be implemented by the change of the threshold. Once the integrated value reaches the threshold voltage, a reset signal is asserted to zero the integrator output.

This approach is less sensitive to switching noise, automatically adjusts to speed changes, but the low-speed operation is poor. With this type of sensorless operation scheme, up to 3600 rpm has been reported.[43]

6.3.6.4   Unique Sensorless Techniques

The following sensorless methods are completely original and unique. These range from artificial intelligence methods to variations in the machine structure. The first of the novel methods to be considered are those utilizing artificial intelligence, that is, artificial neural networks (ANNs) and fuzzy logic. Peters and Harth[43] utilized a neural network using the back-propagation training algorithm (BPN) to act as a nonlinear function implementation between measured phase voltages and currents, which were inputs, and rotor position, which was the output. Using the equations in the above method, the flux linkage can be calculated using the measured voltages, currents, and system parameters.

Utilizing fuzzy logic, Hamdi and Ghribi[44] proposed two fuzzy logic subsystems in an application. Using the conventional equations of phase voltages and currents, the rotor position can be calculated.[8] With the knowledge of the relationships between these measurables and the rotor position, a fuzzy Mamdami-type system was developed to produce rotor position estimates. It was noted that this could have been accomplished just as easily with look-up tables; however, for the desired resolution the size of the look-up tables becomes unmanageably large. The second fuzzy system used took as

input the estimated rotor position and produced reference current values for two different drive strategies: unity power factor and maximum torque per ampere.

In Hesmondhalgh et al.,[45] an additional stator lamination with equally spaced slots around the periphery is added to the end of the machine. Each of the slots contains a small sensing coil. The local magnetic circuit variations for each of the sensing coils are affected by the PM rotor's position. A 20-kHz signal is injected through the coils. The signal distortions are analyzed at the terminals of the sensing coils, the second harmonic yielding position information. An artificial saliency was created in Hesmondhalgh et al.[45] by attaching small pieces of aluminum to the surface of the PMs. The flow of eddy currents in the aluminum acts to increase the reluctance of the various windings' magnetic circuits, thus causing changes in the winding's inductances with rotor position.
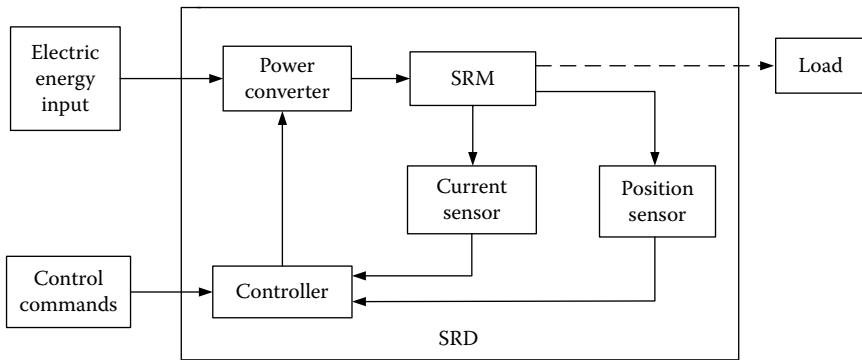
6.4   SRM Drives

The SRM drive is considered as an attractive candidate for variable speed motor drives due to its low cost, rugged structure, reliable converter topology, high efficiency over a wide speed range, and simplicity in control.[46,47] These drives are suitable for EVs, HEV traction applications, aircraft starter/generator systems, mining drives, washing machines, door actuators, and so on.[48–51]

The SRM has a simple, rugged, and low-cost structure. It has no PM or winding on the rotor. This structure not only reduces the cost of the SRM, but also offers high-speed operation capability for this motor. Unlike the induction and PM machines, the SRM is capable of high-speed operation without the concern of mechanical failures that result from the high-level centrifugal force. In addition, the inverter of the SRM drive has a reliable topology. The stator windings are connected in series with the upper and lower switches of the inverter. This topology can prevent the shoot-through fault that exists in the induction and permanent motor drive inverter. Moreover, high efficiency over a wide speed range and control simplicity are known merits of the SRM drive.[46,47]

A conventional SRM drive system consists of the SRM, power inverter, sensors such as voltage, current, and position sensors, and control circuitry such as the DSP controller and its peripherals as shown in Figure 6.54. Through proper control, high performance can be achieved in the SRM drive system.[46,47] The SRM drive inverter is connected to a DC power supply, which can be derived from the utility lines through a front-end diode rectifier or from batteries. The phase windings of the SRM are connected to the power inverter, as shown in Figure 6.55. The control circuit provides a gating signal to the switches of the inverter according to particular control strategies and the signals from various sensors.

FIGURE 6.54 SRM drive system.
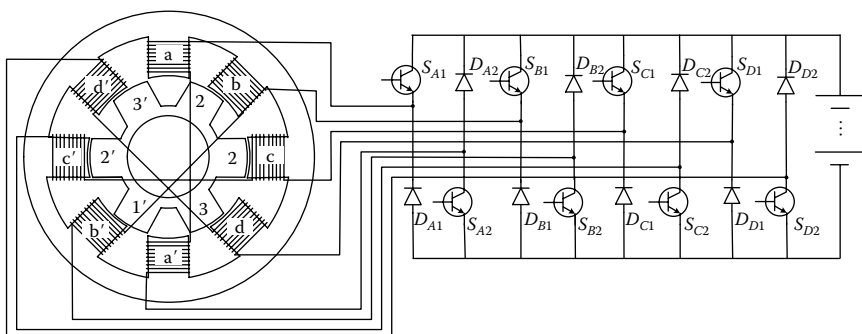
6.4.1 Basic Magnetic Structure

The SRM has salient poles on both the stator and rotor. It has concentrated windings on the stator and no winding or PM on the rotor. There are several configurations for SRM depending on the number and size of the rotor and stator poles. The configurations of the 8/6 and 6/4 SRMs, which are more common, are shown in Figure 6.56.
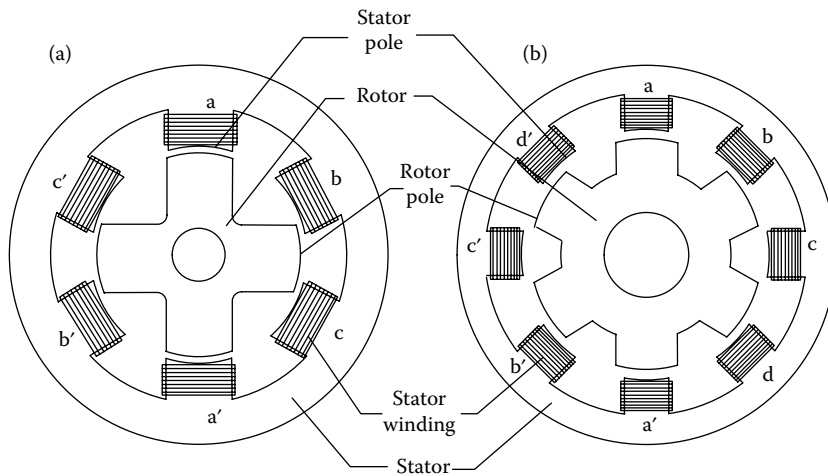
Due to its double saliency structure, the reluctance of the flux path for a phase winding varies with the rotor position. Also, since the SRM is commonly designed for high-degree saturation at high phase current, the reluctance of the flux path also varies as the phase current. As a result, the stator flux linkage, phase bulk inductance, and phase incremental inductance all vary with the rotor position and phase current.

The phase voltage equation of the SRM (Figure 6.55) is given by

$$V_j = Ri_j + \frac{\mathrm{d}}{\mathrm{d}t} \sum_{k=1}^{m} \lambda_{jk}, \tag{6.120}$$

FIGURE 6.55 SRM and its power supply.
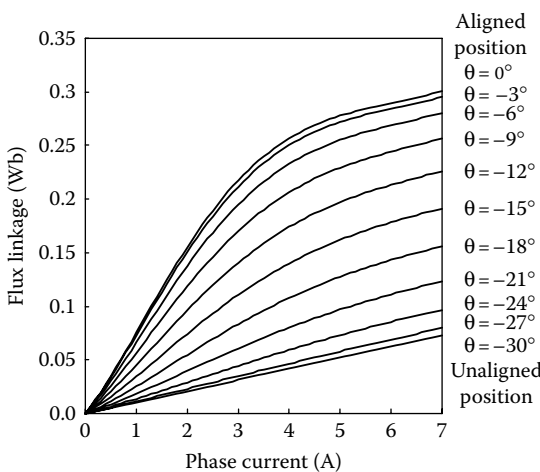
FIGURE 6.56 Cross section of common SRM configurations: (a) a 6/4 SRM and (b) an 8/6 SRM.

where m is the total number of phases, V_j is the applied voltage to phase j, i_j is the current in phase j, R is the winding resistance per phase, λ_{jk} is the flux linkage of phase j due to the current of phase k, and t is the time. The phase flux linkage λ_{jk} is given by

$$\lambda_{jk} = L_{jk}(i_{k,\theta}, \theta)i_k, \tag{6.121}$$

where L_{jk} is the mutual inductance between phase k and phase j. The mutual inductance between phases is usually small compared to the bulk inductance and is neglected in equations.
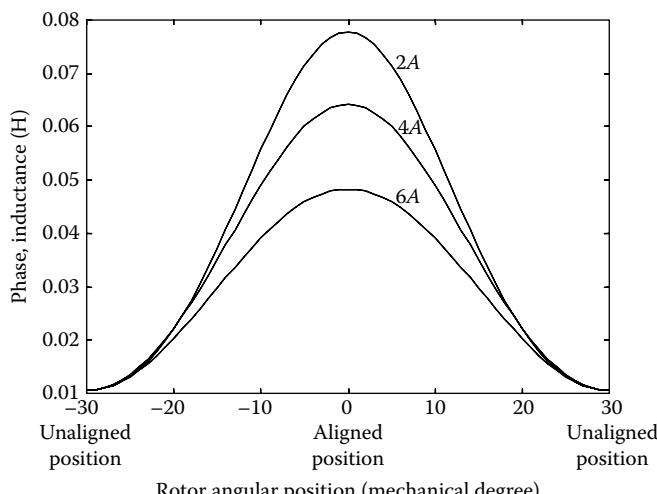
At a fixed phase current, as the rotor moves from the unaligned to the aligned position, the reluctance of the flux path reduces due to the reduction in the air gap. As a result, the phase inductance and flux linkage increases as the rotor moves. At a fixed rotor position, as the phase current increases, the flux path becomes more and more saturated. Hence, the reluctance of the flux path reduces as the phase current increases. As a result, the phase bulk inductance drops with an increase in the phase current. But the phase flux linkage still increases as the phase current increases due to the enhancement in the excitation. The variations of the phase bulk inductance and flux linkage with respect to the phase current and rotor position for an 8/6 SRM are shown in Figures 6.57 and 6.58, respectively. In those figures, $\theta = -30°$ and $\theta = 0°$ represent the unaligned and aligned rotor positions of the referred SRM, respectively.

FIGURE 6.57 Variation of phase flux linkage with rotor position and phase current.

Substituting Equation 6.121 into Equation 6.120, one can have

$$
\begin{aligned}
V_j &= Ri_j + \frac{\mathrm{d}}{\mathrm{d}t} \sum_{k=1}^{m} \boldsymbol{\lambda}_{jk} = Ri_j + \sum_{k=1}^{m} \left\{ \frac{\partial \boldsymbol{\lambda}_{jk}}{\partial i_k} \frac{\mathrm{d}i_k}{\mathrm{d}t} + \frac{\partial \boldsymbol{\lambda}_{jk}}{\partial \theta} \frac{\mathrm{d}\theta}{\mathrm{d}t} \right\} \\
&= Ri_j + \sum_{k=1}^{m} \left\{ \frac{\partial (L_{jk}i_k)}{\partial i_k} \frac{\mathrm{d}i_k}{\mathrm{d}t} + \frac{\partial (L_{jk}i_k)}{\partial \theta} \omega \right\} \\
&= Ri_j + \sum_{k=1}^{m} \left\{ \left(L_{jk} + i_k \frac{\partial L_{jk}}{\partial i_k} \right) \frac{\mathrm{d}i_k}{\mathrm{d}t} + i_k \frac{\partial L_{jk}}{\partial \theta} \omega \right\}.
\end{aligned}
\tag{6.122}
$$

FIGURE 6.58 Variation of phase bulk inductance with rotor position and phase current.

When only one phase is energized in the operation, Equation 6.122 can be written as
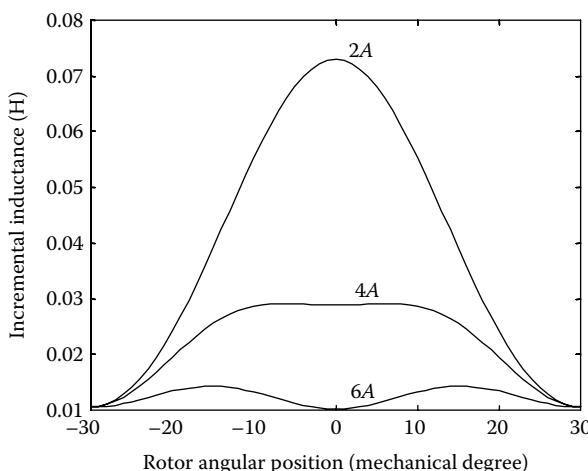
$$V_j = Ri_j + \left(L_{jj} + i_j \frac{\partial L_{jj}}{\partial i_j} \right) \frac{di_j}{dt} + i_j \frac{\partial L_{jj}}{\partial \theta} \omega. \tag{6.123}$$

The third term on the right-hand side of Equation 6.123 is the back EMF. The phase incremental inductance is defined as the derivative of the phase flux linkage against the phase current as

$$\ell_{jj} = \frac{\partial \lambda_{jj}}{i_j} = L_{jj} + i_j \frac{\partial L_{jj}}{\partial i_j}, \tag{6.124}$$

where $\ell_{jj}(i, \theta)$ and $L_{jj}(i, \theta)$ are phase incremental inductance and bulk inductance, respectively. Figure 6.57 shows a typical example of flux linkage varying with rotor position, θ, and phase current i of an SRM. Figure 6.58 shows typical variation of phase bulk inductance with rotor position and phase current.

When the magnetic flux is not saturated, the flux linkage varies linearly with the phase current. The incremental inductance can be viewed as equal to the phase bulk inductance. However, if the machine is saturated at a certain phase current and rotor position, the phase incremental inductance does not equal the phase bulk inductance any more. The variation of the phase incremental inductance with respect to the phase current and rotor position can be derived from the variation of the phase linkage with respect to the phase current and rotor position. The variation of the phase incremental inductance with respect to the phase current and rotor position for an 8/6 SRM is shown in Figure 6.59.

FIGURE 6.59 Variation of phase incremental inductance with rotor position and phase current for a typical 8/6 SRM.

6.4.2 Torque Production

Torque in SRM is produced by the tendency of the rotor to get into alignment with the excited stator poles. The analytical expression of the torque can be derived using the derivative of the coenergy against the rotor position at a given current.

For a phase coil with current i linking a flux λ, the stored field energy W_f and the coenergy W'_f are indicated as shaded regions as shown in Figure 6.60. Coenergy can be found from the definite integral:

$$W'_f = \int_0^i \lambda \, di. \tag{6.125}$$
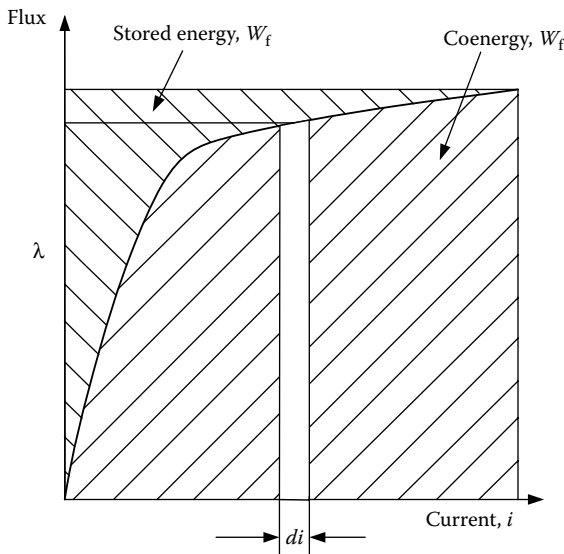
The torque produced by one phase coil at any rotor position is given by

$$T = \left[\frac{\partial W'_f}{\partial \theta} \right]_{i=\text{constant}}. \tag{6.126}$$

In the case of flux being linear with current, for example, unsaturated field, the magnetization curve in Figure 6.60 would be a straight line and the coenergy would be equal to the stored field energy. The instantaneous torque can be given as

$$T = \frac{1}{2} i^2 \frac{dL(\theta)}{d\theta}, \tag{6.127}$$

where L is the unsaturated phase bulk inductance.

FIGURE 6.60 Stored field energy and coenergy.

In the case of saturated phase, the torque cannot be calculated by a simple algebra equation; instead, an integral equation such as
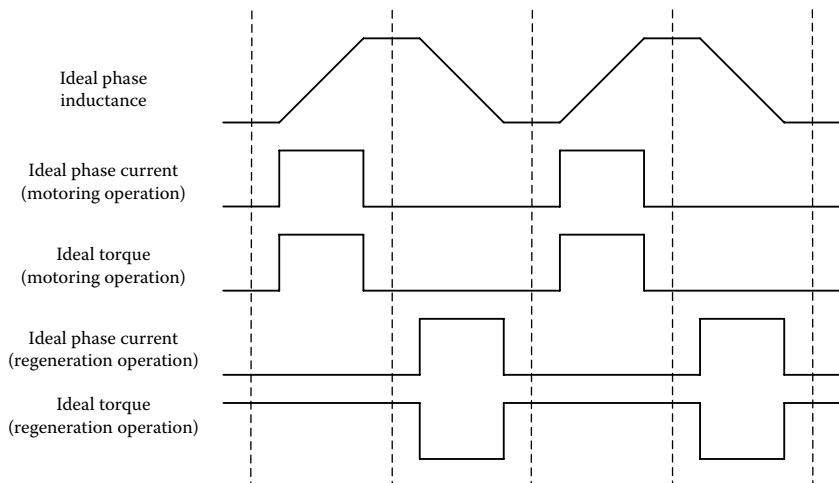
$$T = \int_0^i \frac{\partial L(\theta, i)}{\partial \theta} i \, di \qquad (6.128)$$

is used.

From Equations 6.127 and 6.128, it can be seen that in order to produce positive torque (motoring torque) in SRM, the phase has to be excited when the phase bulk inductance increases as the rotor rotates. It can also be observed from Equation 6.127 and 6.128 that the phase current can be unidirectional for motoring torque production. Hence, low-cost and reliable inverter topology introduced in the later section can be employed for the SRM drive. Figure 6.61 shows the ideal phase inductance, current, and torque of the SRM. Positive (motoring) torque is produced if the phase is excited when the phase inductance is increasing as the rotor rotates. Negative torque is generated if the phase is excited when the phase inductance is decreasing as the rotor moves.[52,53] This implies that the position information is necessary for control of the SRM drive.

The output torque of an SRM is the summation of torque of all the phases:

$$T_m = \sum_{i=1}^{N} T(i, \theta), \qquad (6.129)$$

FIGURE 6.61 Idealized inductance, current, and torque profiles of the SRM.

where T_m and N are the output torque and phase number of the motor. The relation between the motor torque and mechanical load is usually given by

$$T_m - T_l = J\frac{d\omega}{dt} + B\omega, \tag{6.130}$$

where J, B, and T_l are the moment of inertia, viscous friction, and load torque, respectively. The relation between position and speed is given by

$$\omega = \frac{d\theta}{dt}. \tag{6.131}$$

6.4.3 SRM Drive Converter
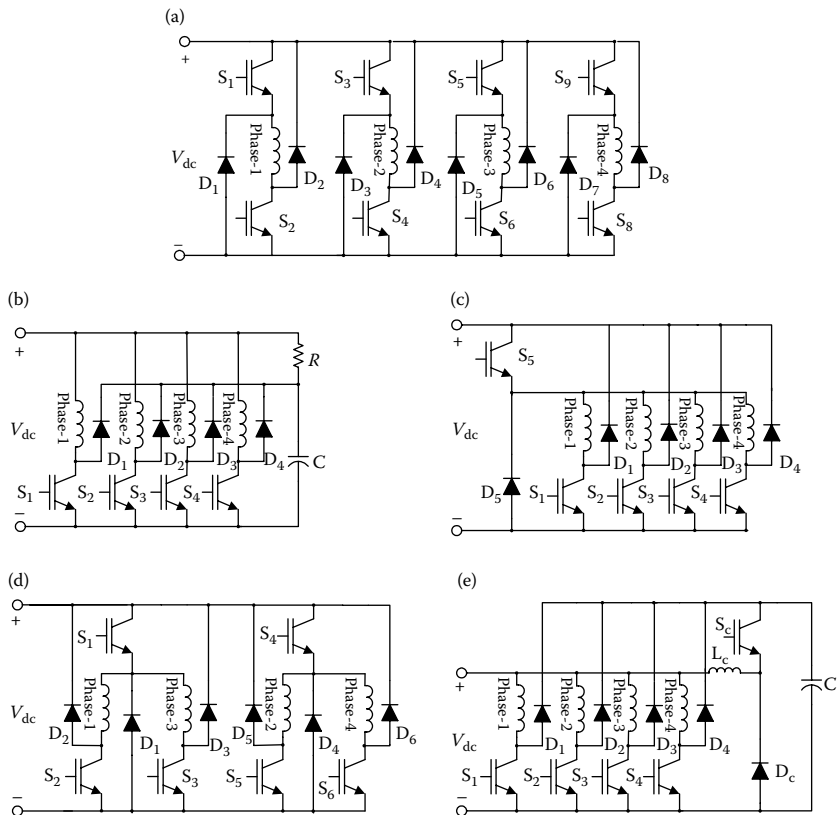
It can be seen from Figure 6.61 that the torque developed by the motor can be controlled by varying the amplitude and the timing of the current pulses in synchronism with the rotor position. In order to control the amplitude and pulse width of the phase current, a certain type of inverter should be used.

The input to the SRM drive is DC voltage, which is usually derived from the utility through a front-end diode rectifier or from batteries. Unlike other AC machines, the currents in SRMs can be unidirectional. Hence, conventional bridge inverters used in AC motor drives are not used in SRM drives. Several configurations have been proposed for an SRM inverter in the literature,[54,55] some of the most commonly used ones are shown in Figure 6.62.

The most commonly used inverter uses two switches and two freewheeling diodes per phase and is called the classic converter. The configuration of the classic converter is shown in Figure 6.62a. The main advantage of the classic converter is the flexibility in control. All the phases can be controlled independently, which is essential for very high-speed operation where there will be considerable overlap between the adjacent phase currents.[56]
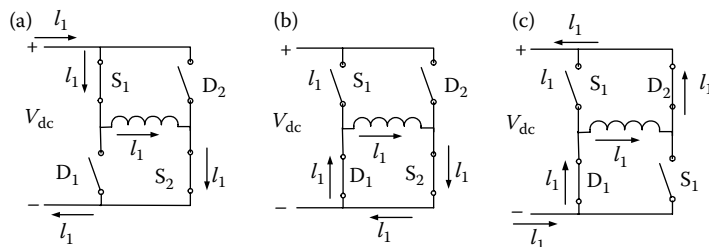
The operation of the classic converter is shown in Figure 6.63 by taking phase-1 as an example. When the two switches S_1 and S_2 are turned on as in Figure 6.62a, the DC bus voltage, V_{dc}, will be applied to the phase-1 winding. Phase-1 current will increase as it flows through the path consisting of the V_{dc} positive terminal, S_1, phase-1 winding, S_2, and the V_{dc} negative terminal. By turning off S_1 and holding on S_2 (i.e., Figure 6.63b), when the phase is energized, the current freewheels through the S_2 and D_1. In this mode, phase-1 is not getting or giving energy to the power supply. When S_1 and S_2 are turned off (Figure 6.63c), the phase-1 current will flow through D_2, the V_{dc} positive terminal, the V_{dc} negative terminal, D_1, and phase-1 winding. During this time, the motor phase is subjected to negative DC bus voltage through the freewheeling diodes. The energy trapped in the magnetic circuit is returned to the DC link. The phase current drops due to the negative applied phase voltage. By turning on and off S_1 and S_2, the phase-1 current can be regulated.

The half-bridge converter uses $2n$ switches and $2n$ diodes for an n-phase machine. There are several configurations that use less switches; for example,

FIGURE 6.62 Different inverter topologies for SRM drives: (a) classic half-bridge converter; (b) R-dump; (c) n + 1 switches (Miller converter); (d) 1.5*n* switch converter; and (e) C-dump.

the R-dump-type inverter (Figure 6.62b) uses one switch and one diode per phase. This drive is not efficient; during turn-off, the stored energy of the phase is charging capacitor C to the bus voltage and dissipating in resistor R. Also zero voltage mode does not exist in this configuration.

FIGURE 6.63 Modes of operation for the classic converter: (a) turn-on mode, (b) zero voltage mode, and (c) turn-off mode.

An alternative configuration is $(n + 1)$ switch inverter. In this inverter, all the phases are sharing a switch and diode so that overlapping operation between phases is not possible, which is inevitable in high-speed operation of this motor. This problem has been solved by sharing switches of each couple nonadjacent phases, as shown in Figure 6.62d. This configuration is limited to an even number of phases of SRM drives.
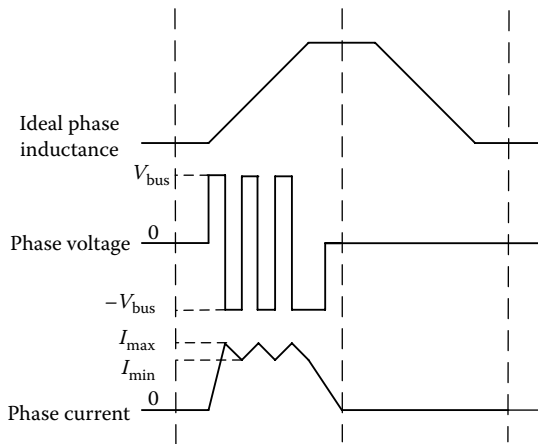
One of the popular inverter configurations is C-dump (Figure 6.62e), which has the advantage of less switches and allows independent phase current control. In this configuration, during the turn-off time, the stored magnetic energy is charging capacitor C, and if the voltage of the capacitor reaches a certain value, for example V_c, it is transferred to the supply through the switch S_c. The main disadvantage of this configuration is that the negative voltage across the phase coil is limited to the difference between the voltage across the capacitor V_c and the system power supply voltage.

6.4.4   Modes of Operation

For SRM, there is a speed at which the back EMF is equal to the DC bus voltage. This speed is defined as the base speed. Below the base speed, the back EMF is lower than the DC bus voltage. From Equation 6.125, it can be seen that when the converter switches are turned on or off to energize or de-energize the phase, the phase current will rise or drop accordingly. The phase current amplitude can be regulated from 0 to the rated value by turning on or off the switches. Maximum torque is available in this case when the phase is turned on at an unaligned position and turned off at the aligned position and the phase current is regulated at the rated value by hysteresis or PWM control. The typical waveforms of the phase current, voltage, and flux linkage of the SRM below the base speed are shown in Figure 6.64.

Above the base speed, the back EMF is higher than the DC bus voltage. At the rotor position—at which the phase has a positive inductance slope with respect to the rotor position—the phase current may drop even if the switches of the power inverter are turned on. The phase current is limited by the back EMF. In order to build high current and therefore produce high motoring torque in the SRM, the phase is usually excited ahead of the unaligned position, and the turn-on position is gradually advanced as the rotor speed increases. The back EMF increases with the rotor speed. This leads to a decrease in the phase current and hence the torque drops. If the turn-on position is advanced for building as high as possible a current in the SRM phase, the maximum SRM torque almost drops as a linear function of the reciprocal of the rotor speed. The maximum power of the SRM drive is almost constant. The typical waveforms at high-speed operation are shown in Figure 6.65.

The advancing of the phase turn-on position is limited to the position at which the phase inductance has a negative slope with respect to the rotor position. If the speed of the rotor further increases, no phase advancing is available
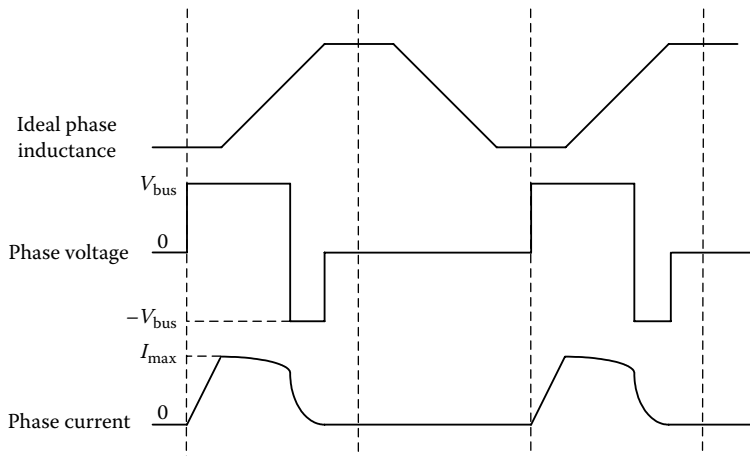
FIGURE 6.64 Low-speed (below the base speed) operation of SRM.
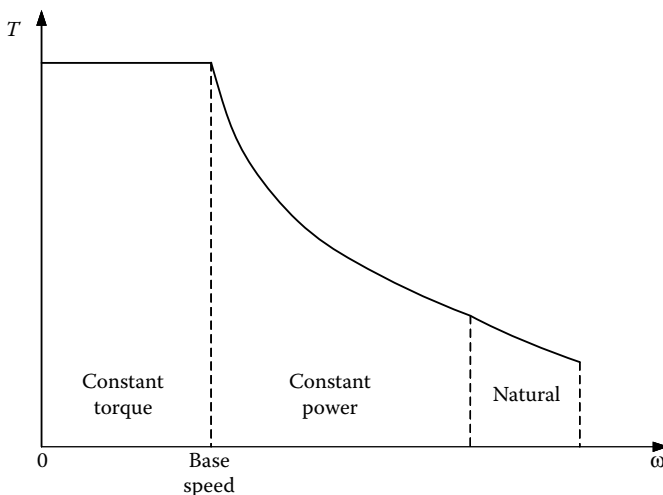
for building higher current in the phase and the torque of the SRM will drop significantly.[11] The mode is referred to as the natural mode operation. The torque–speed characteristic of the SRM is shown in Figure 6.66.

6.4.5 Generating Mode of Operation (Regenerative Braking)

Torque in the SRMs is created based on the principle of reaching the minimum reluctance for the excited phase. Therefore, if the rotor pole is approaching the excited phase, which means the bulk inductance is increasing, the torque produced is in the direction of the rotor and it is in motoring mode. But if the

FIGURE 6.65 High-speed (above the base speed) operation of SRM.
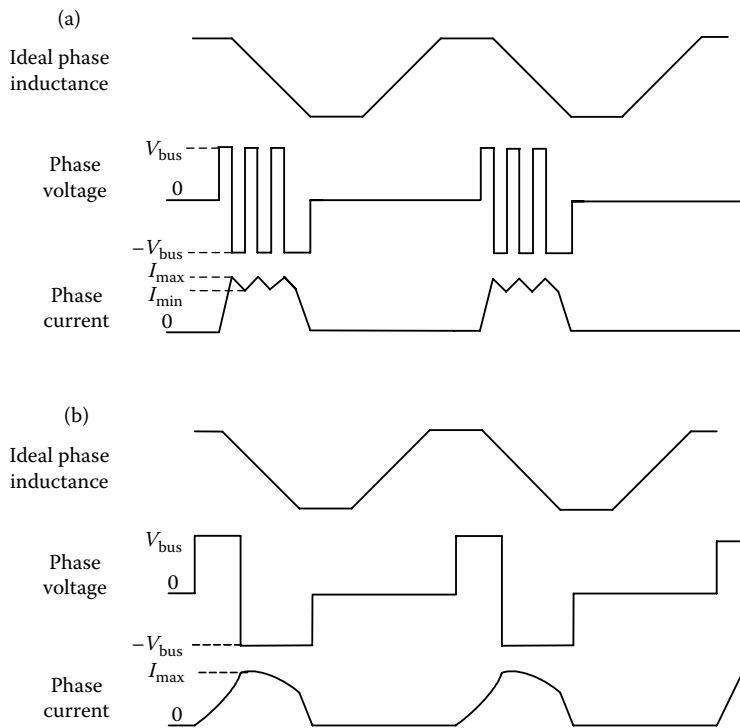
FIGURE 6.66 Torque–speed characteristic of SRM.

rotor pole is leaving the stator phase—which means the negative slope of the bulk inductance—the stator tries to keep it in alignment; the torque produced is then in the opposite direction of the movement of the rotor, and the SRM works in the generating mode.

Regenerative braking is an important issue in the propulsion drive of EVs and HEVs. There is a duality in operation of generating and motoring modes and the current waveforms in the generating modes are simply the mirror images of the waveforms in the motoring region around the alignment rotor position.[57] The switched reluctance generator (SRG) is a singly excited machine, so in order to get power from it, it should be excited near the rotor aligned position and then turned off before the unaligned region (Figure 6.67).

As in motoring operation, current can be controlled by changing the turn-on and turn-off angles and current level while at low speed. Alternatively, at speeds higher than the base speed, only the turn-on and turn-off angles can be used for control.
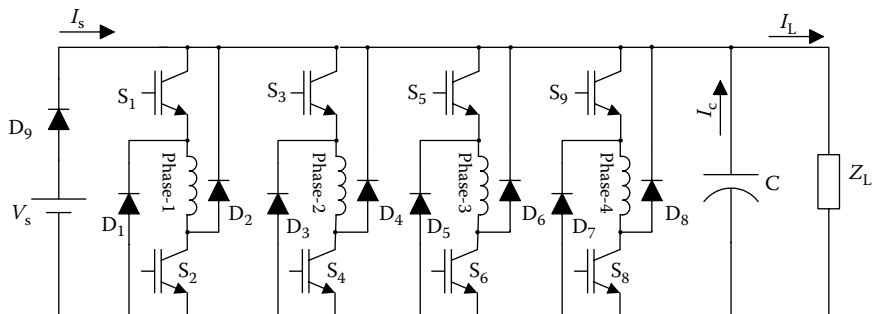
The driving circuit for SRG is similar to the SRMs; one of the common configurations is shown in Figure 6.68. When the switches are turned on, the phase gets energy from the supply and capacitor. During the turn-off period, the freewheeling current from the motor charges up the capacitor and delivers energy to the load. Since there is no PM in this motor, during the start-up and initial condition, it needs an external source such as a battery to deliver energy to the phase; after taking transient time, the capacitor is then charged up to the output voltage. Depending on the output voltage during phase-on time, both the capacitor and external source, or just the capacitor, provide the current to
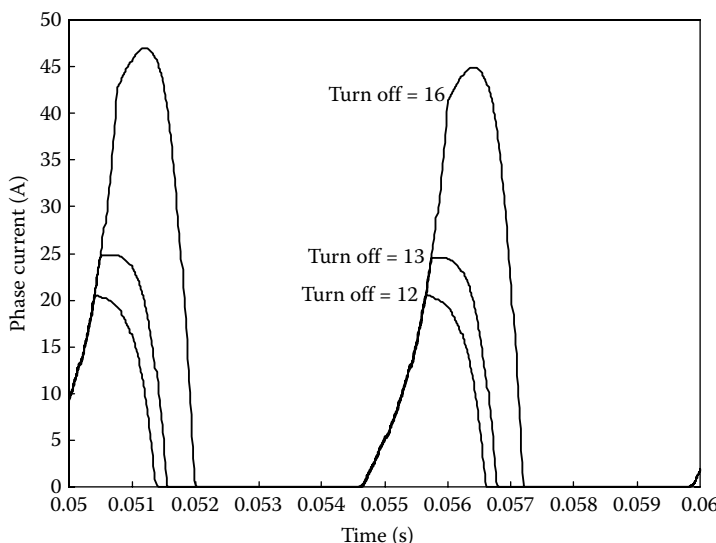
FIGURE 6.67 Low- and high-speed operation in generating mode: (a) low speed operation and (b) high speed operation.

the load and the phase coil. The external source can be designed to be charged, or can be disconnected from the system after the system reaches its operating point.

In the generating region, the back EMF is negative so it helps the phase to be charged very fast; then during turn-off the back EMF opposes the negative

FIGURE 6.68 A driving circuit example for the SRG.

FIGURE 6.69 Effect of the turn-off angle in maximum current level in generating mode in an 8/6 switched reluctance machine.

supply voltage, and it decreases slowly.

$$V_C - e = L\frac{di}{dt} + Ri, \quad e > 0 \text{ (during phase-on period).} \qquad (6.132)$$

$$-V_C - e = L\frac{di}{dt} + Ri, \quad e > 0 \text{ (during phase-off period).} \qquad (6.133)$$

In Equations 6.132 and 6.133, V_c is the bus voltage of the inverter or, equivalently, the voltage of the bus capacitor and e is the back EMF voltage.

In certain conditions such as high speed and high loads, the back EMF voltage is greater than the bus supply voltage, so the current increases even after turning off the phase. In addition to uncontrollable torque, this necessitates an oversized converter, thereby adding to the cost and overall size of the system. Due to variations in speed of the prime mover, the power electronic converter should be designed for the worst possible case. This will magnify the additional cost and size issues. By properly selecting the turn-off angle, this maximum generating current can be coaxed into the safe region.[58] Figure 6.69 shows the effect of turn-off angle in the maximum generating current.

6.4.6 Sensorless Control

Excitation of the SRM phases needs to be properly synchronized with the rotor position for effective control of speed, torque, and torque pulsation.

A shaft position sensor is usually used to provide the rotor position. However, these discrete position sensors not only add complexity and cost to the system but also tend to reduce the reliability of the drive system and restrict their application in some specific environments, such as military applications. Position sensorless technology can effectively continue the operation of the system, in case the position sensors lose their function. This is crucial in some applications, such as military vehicles.

Several sensorless control methods have been reported in the literature over the past two decades.[15−28] Most of these techniques are based on the fact that the magnetic status of the SRM is a function of the angular rotor position. As the rotor moves from the unaligned position toward the aligned position, the phase inductance increases from the minimum value to the maximum value. It is obvious that if the phase bulk inductance can be measured and the functional relation between the phase bulk inductance and the rotor position is known, the rotor position can be estimated according to the measured phase bulk inductance.[59]

Some sensorless techniques do not use the magnetic characteristic and voltage equation of the SRM directly to sense the rotor position. Instead, these sensorless control methods are based on the observer theory or synchronous operation method similar to that applied to conventional AC synchronous machines.
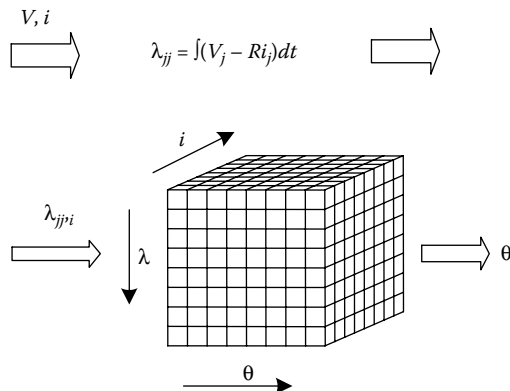
Generally, the existing sensorless control methods can be classified as follows:

1. The phase flux linkage-based method.
2. The phase inductance-based method.
3. Modulated signal injected methods.
4. The mutual-induced voltage-based method.
5. Observer-based methods.

6.4.6.1 *Phase Flux Linkage-Based Method*[60]

This method uses the phase voltage and current data of the active phases to estimate the rotor position. The basic principle of this method is to use the functional relation between the phase flux linkage, phase current, and rotor position for rotor position detection. From Figure 6.57, it can be observed that if the flux linkage and phase current are known, the rotor position can be estimated accordingly, as shown in Figure 6.70.

The problem with this sensorless control method is the inaccurate estimation of the phase flux linkage at low speed. At high speed (above the base speed), the phase voltage keeps its positive polarity until the phase is turned off. The V term dominates in $V–Ri$, and integration of $V–Ri$ in a relatively short period will not lead to a huge error in flux estimation. However, at low speed

FIGURE 6.70 Flux linkage-based rotor position estimation method.

(below the base speed) the phase voltage changes its polarity from one hysteresis cycle to the next hysteresis cycle. When V–Ri is integrated in a relatively long period, the phase voltage term cancels itself due to the excursions, while the Ri term keeps its polarity during the integration period—and becomes significant after a long time of integration. The error in R or i may lead to a huge error in the flux estimation in this case. Therefore, this sensorless control method is only suitable for high-speed operation of SRM.

6.4.6.2 Phase Inductance-Based Method

Similar to the phase flux linkage, the phase bulk and incremental inductances are both functions of the phase current and rotor position. Hence, they can also be used for rotor position estimation.

6.4.6.2.1   Sensorless Control Based on Phase Bulk Inductance[61]

Using the phase flux linkage obtained as shown in Figure 6.70, the phase inductance can be obtained as

$$L_{jj} = \frac{\lambda_{jj}}{i_j}. \tag{6.134}$$

The estimated phase bulk inductance and measured phase current can be input to a prestored look-up table storing the functional relation between the phase bulk inductance and phase current and rotor position, to find the corresponding rotor position. Instead of using a look-up table, one can also use an analytical model to represent the functional relation between phase bulk inductance, phase current, and rotor position.[61]

Like the flux linkage-based method, since integration of V–Ri is used for phase inductance estimation, this method is only suitable for high-speed operation. Some sensorless control method that can work both at standstill and low speed, such as the open-loop method, has to be used to start the SRM

and bring the rotor speed to a certain level. After the rotor speed has reached a threshold, the phase flux linkage and/or inductance are calculated using the integration method and the rotor position is estimated according to the calculated phase flux linkage and inductance.

6.4.6.2.2 *Sensorless Control Based on Phase Incremental Inductance*

The position estimation method using the phase incremental inductance utilizes the current and voltage data of the active phase for estimation of the incremental inductance of this phase, and consequently, of the rotor position.

Neglecting the mutual couplings and, at very low speeds [neglectable motional-EMF term $i_j(\partial L_{jj}/\partial\theta)\omega$], the incremental inductance can be obtained from Equations 6.123 and 6.124 as

$$\ell_{jj} = \frac{V_j - Ri_j}{di_j/dt}. \tag{6.135}$$

Thus, the phase incremental inductance can be measured from the phase voltage and current. If the relation between the phase incremental inductance and rotor position is known, the rotor position can be estimated according to the estimated phase incremental inductance.

At low phase current—and therefore at unsaturated phase—the phase incremental inductance can be viewed as equal to the phase bulk inductance, and monotonically increases as the rotor moves from the unaligned position to the aligned position. The incremental inductance has a one-to-one relation with the rotor position in this case. However, at high phase current, and therefore at saturated phase, when the rotor moves from the unaligned position to the aligned position, the phase incremental inductance may be the same value at two or more rotor positions.[62]

Even though the phase incremental inductance does not have a one-to-one relation with the rotor position at high phase current, it can still be used for rotor position estimation. Some SRMs are designed with a high degree saturation such that the phase incremental inductance at the aligned position has the minimum value at high current. In this case, the phase incremental inductance at the aligned position is unique; hence, it can be used to detect the aligned rotor position. This rotor position estimation technique will give one rotor position at one electrical cycle.

This method does not require any extra sensing circuitry. However, it is applicable only for very low speeds, less than 10% of the base speed, because the back EMF term is neglected for calculation of the phase incremental inductance.

6.4.6.3 **Modulated Signal Injection Methods**

These methods are to apply a voltage to the idle phase winding and measure the resultant phase current to detect the phase inductance. This derived phase

inductance will provide the rotor position information. Both an extra-low amplitude voltage source and the power converter can be used to apply a voltage to the phase winding. When an extra voltage source is used, a sinusoidal voltage is usually used for sensing the phase inductance. The phase angle and the amplitude of the resultant phase current contain the phase inductance; hence the rotor position information can be obtained. This is the idea behind the amplitude modulation (AM) and phase modulation (PM) methods. When the power converter is used for sensing purpose, a short period voltage pulse is usually applied to the idle phase and a triangular current is induced in the corresponding phase. The changing rate of the phase current contains the phase inductance, and hence the rotor position information. This is the basic idea of the diagnostic pulse-based method.

6.4.6.3.1   *Frequency Modulation Method*[49,63]

This method is used to first generate a train of square wave voltage whose frequency is in reverse proportion to the instantaneous inductance of the idle phase. The circuitry used for generating a square wave voltage train whose frequency is in reverse proportion to the inductance is referred to as an *L–F* converter.

To detect the frequency of this square wave voltage train, and hence the phase inductance, the timer of a microcontroller can be used to count the frequency of the square wave voltage train. Another approach is to use a frequency-to-voltage converter (*F–V* converter) to obtain a voltage proportional to the frequency of the square wave voltage train, and sample this voltage using an A/D converter. In order to connect the phase winding, which is in the power circuit, to the sensing circuitry, which is in the control circuit, two photovoltaic BOSFET switches are used for each phase.

Since the signal used for position estimation in this method is an inductance-encoded frequency signal, this method is referred to as the frequency modulation (FM) method. This method is easy to implement and is robust. However, at high-speed operation, the phase energizing current exists—even when the phase inductance is decreasing as the rotor moves. This restricts the signal injection to the SRM phases. Another problem with this method is that it requires additional circuitry for implementation. The cost associated with this additional circuitry may be a concern in some applications. Furthermore, it is very sensitive to mutual coupling since the current in the active phase induces voltage in the unenergized phases, which strongly distorts the probing pulses.

6.4.6.3.2   *AM and PM Methods*[64]

The PM and AM techniques are based on the phase and amplitude variations, respectively, of the phase current due to the time-varying inductance when a sinusoidal voltage is applied to the phase winding in series with a resistance *R*. The current flowing through the circuit in response to the applied voltage

is a function of the circuit impedance. Since the coil inductance varies periodically, the phase angle between the current and the applied voltage also varies in a periodic manner. With a large inductance, the lagging angle of the current wave behind the voltage wave is large and the peak current is small. The PM encoder technique measures the instantaneous phase angle on a continuous basis, while the AM encoder technique measures the amplitude. These instantaneous measurements contain the phase inductance information that can be obtained after passing the signals through a demodulator. The demodulator generates a signal that represents the phase inductance as a function of the rotor position. Using an inverse function or a conversion table, the rotor position can be estimated.

Since the PM and AM methods need the injection of a low-amplitude signal to one of the idle phases, the photovoltaic BOSFET switches are needed to connect the phase winding to the sensing circuitry.

Like the FM method, signal injection to one of the idle phases is restricted at high-speed operation where the torque producing current occupies most of the electrical cycle and makes the signal injection impossible. Another disadvantage of these methods is that they require additional hardware for indirect position sensing. As stated before, it is very sensitive to mutual coupling.

6.4.6.3.3 Diagnostic Pulse-Based Method[65]

Instead of using an additional voltage source to inject the sensing signal to the idle phase, the power converter of the SRM drive can be used to provide a short period voltage pulse to the idle phase, and low-amplitude current is produced. Therefore, the back EMF, saturation effect, and the voltage drop on the winding resistance can all be neglected. From Equations 6.123 and 6.124, the changing rate of the phase current is given as

$$\frac{\mathrm{d}i_j}{\mathrm{d}t} = \frac{V}{L_{jj}}. \tag{6.136}$$

Equation 6.136 indicates that the phase current changing rate contains the phase inductance, and hence the rotor position information.

Similar to the case of switches being turned on, when the switches connected to the phase are turned off, the phase current freewheels through the diodes. The phase voltage equals the negative DC bus voltage; the change rate of the current has the same expression as Equation 6.136, but with a negative sign.

Either the current growing rate or dropping rate can be used for sensing the phase inductance. When the current changing rate is found to exceed a threshold that is dictated by the phase inductance at the commutation position, the phase can be commutated. This method does not require additional hardware for indirect rotor position sensing. However, at high-speed operation, the phase excitation current occupies the majority of one electrical cycle and restricts the injection of the testing signal. And like FM, AM, and PM methods, it is very sensitive to mutual coupling.

6.4.6.4   *Mutual-Induced Voltage-Based Method*[66]

The idea of this method is based on measuring the mutually induced voltage in an idle phase, which is either adjacent or opposite to the energized phase of an SRM. The mutual voltage in the "off" phase, induced due to the current in the active phase, varies significantly with respect to the rotor position. This mutually induced voltage variation can be sensed by a simple electronic circuit. If the functional relation between the mutually induced voltage in the inactive phase due to the current in the active phase and the rotor position is known, the rotor position information can be extracted from the mutually measured induced voltage in the inactive phase. This method is only suitable for low-speed operation. Furthermore, it is very sensitive to noise since the ratio between induced voltage and system noise is small.

6.4.6.5   *Observer-Based Methods*[67]

In this method, state-space equations are used to describe the dynamic behavior of the SRM drive. An observer is then developed based on these nonlinear state-space differential equations for estimation of the rotor position. The input and output of this observer are phase voltage and phase current, respectively. The state variables of this observer are stator flux linkage, rotor position angle, and rotor speed. The phase current, flux linkage, rotor position, and rotor speed can be estimated using this observer. The phase current estimated by this observer is compared to the actual phase current of the SRM, and the resultant current errors are used to adjust the parameters of the observer. When the current estimated by the observer matches the actual current, the observer is considered as a correct representation of the dynamic behavior of the actual SRM drive and the rotor position estimated by the observer is used to represent the actual rotor position.

The main disadvantages of these methods are real-time implementation of complex algorithms, which require a high-speed DSP and a significant amount of stored data. This increases the cost and speed limitations by the DSP. However, high resolution in detecting rotor position and applicability to the whole speed range are some merits of these methods.

6.4.7   Self-Tuning Techniques of SRM Drives

As discussed in previous sections, the SRM drive has a simple and rugged construction—favorable characteristics for traction application. But its control is very complicated due to the nonlinearity of its magnetic circuit and the fact that control depends heavily on the mechanical and electrical parameters, such as air gap, resistance, and so on.[53] In mass production and real-world operation, it is important for these parameters to have the exact values and remain unchanged. For example, the air gap would be changed due to mechanical vibration wearing, and the resistance in windings and

inductance would vary with temperature. These parameter variations would cause significant degradation of the drive performance if the control system cannot "know" these variations and implement corresponding corrections in the control process. Self-tuning techniques are referred to as methods of updating the control strategy in a control system.

The major purpose of self-tuning control for the SRM drive is to update the control variables in the presence of motor parameters' variations, so as to optimize the torque per ampere.[68] There are two approaches to this problem: the arithmetic mean method and the neural network-based method.

6.4.7.1 Self-Tuning with Arithmetic Method

To optimize the SRM drive performance, it is necessary to maximize torque per ampere through real-time optimization. The SRM drive control variables are phase current, turn-on angle, and turn-off angle. In a low-speed region, hysteresis-type current control is used to keep the commanded current constant. The chopping current band has to be optimally chosen, as there is a trade-off between the width of the band and the chopping frequency. Assuming the selected band is optimal, maximum torque per ampere can be obtained by aptly tuning the turn-on angle (θ_{on}) and the turn-off angle (θ_{off}) of the phase current excitation. Computer simulations, based on a simple mathematical model, have been performed to prove the existence of a unique (θ_{on}, θ_{off}) optimal pair, which gives the maximum torque per ampere for a given current and speed.[31] It has been shown that the optimal values of θ_{on} and θ_{off} are bounded within the following limits:

$$\theta_{on}^{min} < \theta_{on} < 0°, \tag{6.137}$$

$$\theta_{off}^{max} < \theta_{off} < 180°, \tag{6.138}$$

where θ_{on}^{min} is the turn-on angle such that the current reaches the desired value at $0°$, and θ_{off}^{max} is the turn-off angle such that the current reduces to zero at $180°$.

The intuitive selections for control angles are such as to turn on each phase exactly at its unaligned position and turn off the phase just before its aligned position. The optimal θ_{on} is not very susceptible to the change in inductance due to the parameter variations because of the large air gap at the unaligned position.[46] Hence, optimal θ_{on} calculated off-line based on the linear model is sufficient to give the optimal torque per ampere. Therefore, the optimization problem reduces to calculation of θ_{off} on-line that gives maximum torque per ampere.

6.4.7.1.1 Optimization with Balanced Inductance Profiles

To minimize the phase current for a given torque and speed, a heuristic search algorithm for finding the optimum turn-off angle[69] can be used in which both

the reference current and the turn-off angle are varied, while the PI controller maintains the speed.

The optimization algorithm is explained as follows. Initially the default turn-off angle is used to reach the commanded speed. Then, the turn-off angle is reduced in steps. With the turn-off angle variation, the torque will either decrease or increase, and the PI controller adjusts the phase reference current accordingly to a new value so that the speed remains at its set value. If the current reduces with change in the turn-off angle, then the direction of search is correct and is continued till the current starts increasing with further change in the turn-off angle. The step size for the turn-off angle can be a function of the operating point itself.

Once the optimization is completed for a given operating point, the optimum values of control variables—that is, the reference current and the control angles—can be stored in look-up tables so that the controller can directly pick up these values if the same operating point is to be reached in future. This will save some amount of time and effort.
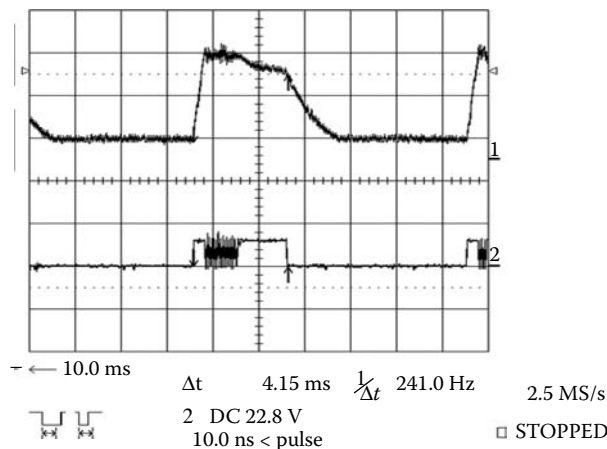
6.4.7.1.2   *Optimization in the Presence of Parameter Variations*

Initially, when optimization is performed, the reference currents for all the phases are kept the same, assuming that the phase inductances are balanced. If there are parameter variations, then different phases will have different optimal reference currents and turn-off angles. In order to take care of this problem, once the general optimization is complete, the control variables for the individual phases are tuned separately, that is, the reference current and turn-off angle for only one of the phases is varied at a time, while these parameters for the other phases are kept fixed. Finally, when all the phases are tuned, the optimum reference current and turn-off angle for different phases will be different if there is any parameter variation. The main advantage of using this method is that the optimization algorithm does not require any information about the degree of imbalance present in the inductance profile, which may change considerably over a period of time.

Figure 6.71 shows the current waveform of the SRM phase with default values of turn-on and turn-off angles and Figure 6.72 shows the current waveform after applying the self-tune algorithm, which is running almost at the same operating point. By comparing the two figures, it can be seen that there is a considerable reduction in the both the amplitude and the width of the phase current and hence its rms value. The operating speeds are also the same before and after optimization for both the cases.

6.4.7.2   Self-Tuning Using an ANN
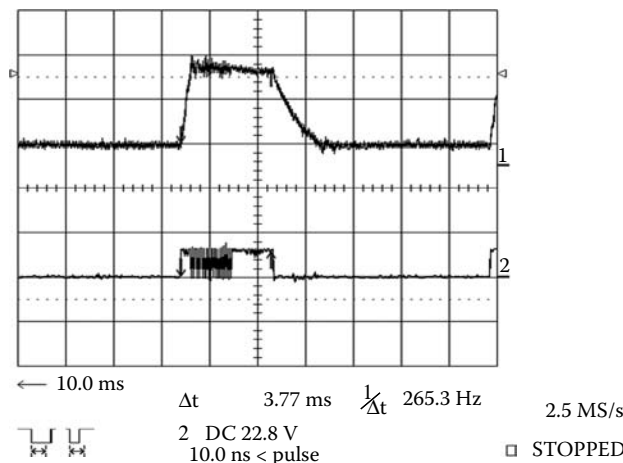
ANNs with highly nonlinear and adaptive structure have been used in many applications. ANNs have inherent interpolation property, so they are an ideal candidate for storing turn-on and turn-off angles instead of storing them in look-up tables. Figure 6.73 shows a three-layer feedforward neural network
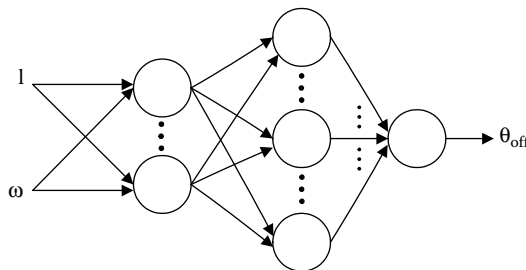
FIGURE 6.71 Phase current and gating pulse without optimization, terminal voltage: 50 V, load: 120 W, reference current: 5.5 A, speed: 1200 rpm, conduction angle: 30°.

with two inputs—current and speed—and one output—the optimum turn-off angle.[70]

The proposed self-tuning control technique incorporates a heuristic search method along with an adaptive-type ANN-based method. The weights of ANN are initially set to default values. The control technique incorporates a periodic heuristic search of optimal θ_{off} to verify the accuracy of the θ_{off} obtained from the ANN. If there is a variation in the inductance profile due to parameter drift, the optimal θ_{off} obtained from the ANN will no longer be

FIGURE 6.72 Phase current and gating pulse with optimization, terminal voltage: 50 V, load: 120 W, reference current: 4.7 A, speed: 1200 rpm, conduction angle: 27.25°.

FIGURE 6.73   A three-layer feedforward ANN for holding optimal turn-off angles.

valid. This prompts the controller to activate the heuristic search by modifying the θ_{off} in small steps until the current reaches the minimum value. This new optimal θ_{off} at that particular operating point is now used to adapt the weights of the ANN. Hence this novel ANN-based control technique coupled with the heuristic search learns and adapts to any parameter drift to give the optimal θ_{off}.
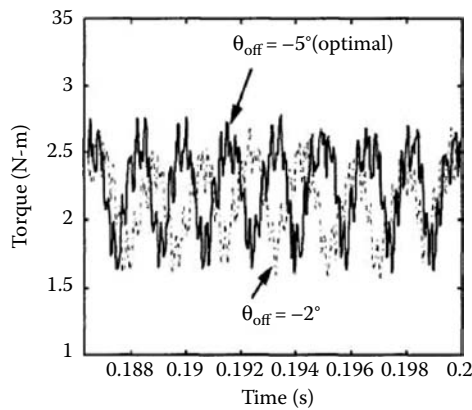
ANNs have been successfully used for many applications in control systems. But the ANN learning algorithm shows a great performance when used off-line. This means that they have to be fully trained before being applied. Neural networks with incremental learning capability and stable adaptation of network parameters are essential for on-line adaptive control. The adaptive learning is based on the assumption that the ANN to start with is well trained in such a way that it can perform input/output mapping for the initial training set with a high degree of accuracy. This can be achieved by training the ANN with sufficient amount of data to a very low error rate. In this application, this training can be done off-line as it may require more time.

Now when new training data are obtained, the already trained ANN is used to generate additional examples. These additional examples with the newly obtained training data are then used to retrain the current ANN. This ensures that the original ANN mapping is retained with only a change localized around the neighborhood of the new training data. This makes the network gradually adapt to the new data. The above method ensures the stability of the network weight variations by slow adaptation as the new optimal θ_{off} will be in the neighborhood of the old value.

Some simulation results[70] that show the ability of this algorithm are shown in Figure 6.74. These results belongs to an 8/6, 12 V, 0.6 kW SRM. This plot clearly shows the improvement in torque per ampere with optimization, which is about 13.6%.

6.4.8 Vibration and Acoustic Noise in SRM

Despite the excellent attributes, SRM drives exhibit high levels of torque ripple and audible noise. Indeed, in some noise-sensitive applications such as

FIGURE 6.74 Developed torque before and after optimization.
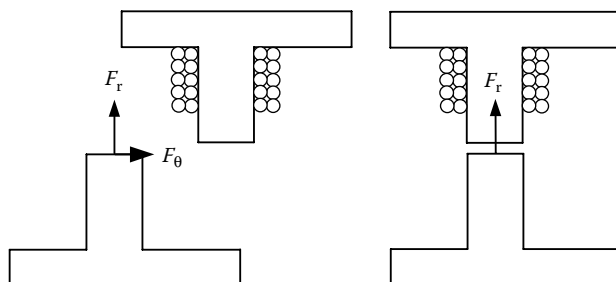
domestic products, the problem of acoustic noise and vibration appears to be particularly important. The acoustic noise in SRM is mainly due to the varying magnetic forces between the stator and rotor poles, as shown in Figures 6.75 and 6.76.[71,72] The tangential and radial components of the electromagnetic force density in the air gap are given by

$$F_\theta = v_0 \int B_\theta B_r d\theta, \qquad (6.139)$$
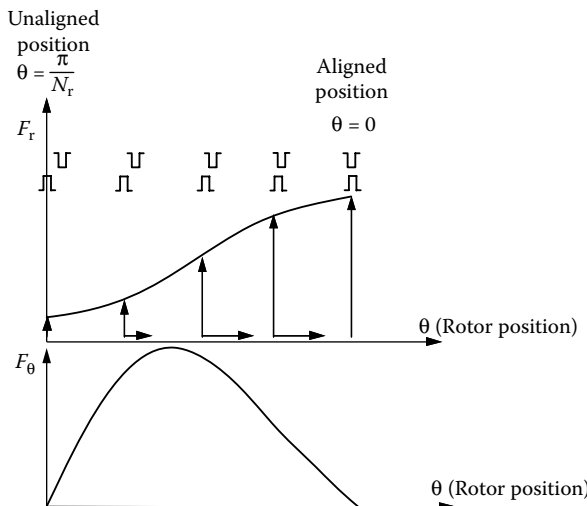
$$F_r = v_0 \int (B_r^2 - B_\theta^2) d\theta, \qquad (6.140)$$

where v_0, B_θ, B_r, and θ stand for reluctivity of the air, tangential, and radial components of the flux density, and rotor position, respectively.

The varying magnetic forces, especially the radial force, cause the deformation of the stator and, therefore, radial vibrations of the stator and acoustic noise.

FIGURE 6.75 Static profile of the radial component of the force.

FIGURE 6.76 Distribution of radial (F_r) and tangential (F_θ) forces.

The results of structural study of SRM show that back iron is the most significant parameter in the dynamic behavior of the stator deformations.[60,73] Increasing the back-iron length results in larger natural frequencies and smaller deformation, which consequently reduce the chance of a mechanical resonance even at high speeds.

Increasing the air gap length will reduce the radial forces.[74] However, it will vitiate the performance of the SRM. Radial vibration of the stator experiences a severe acceleration during the turn-off process. This is due to a large magnitude of the attraction forces and their fast rate of change. This is effectively the point of impact of a hammer on the stator structure. Smoothing of the radial force during the turn-off process has been found to be the most direct method for reducing the vibration.[75]

The current profiling algorithm has to make sure that no negative torque will be generated. In other words, the phase current has to be completely removed at or before the aligned position. Also, it must be noted that a high number of steps in controlling the tail current will increase the switching losses. Moreover, unconstrained reduction of vibration using this method will vitiate the performance of the machine. Therefore, study of other objectives such as efficiency and torque ripple under the proposed control method is an essential step.[71]

Fahimi et al.[76] showed that, for practical implementation two levels of current will provide a smooth variation in radial force. Therefore, turn-off instant, the position at which the second current limit is assigned and the position at which final hard chopping of the phase current occurs, is considered a controlled variable. These parameters are computed at various operating points using the analytical model of the SRM drive.[77]

6.4.9 SRM Design

SRM has a simple construction. However, this does not mean its design is simple. Actually, due to the double-salient structure, continuously varying inductance and high saturation of pole tips, and the fringing effect of pole and slots, the design of SRM suffers great difficulty in using the magnetic circuit approach. In most cases, the electromagnetic finite element analysis is used to determine the motor parameters and performances. Typical electromagnetic field distributions of an 8/6 SRM are shown in Figure 6.77. Nevertheless, there are some basic criteria to initialize the design process of SRM for EVs and HEVs.[78,79]

6.4.9.1 Number of Stator and Rotor Poles
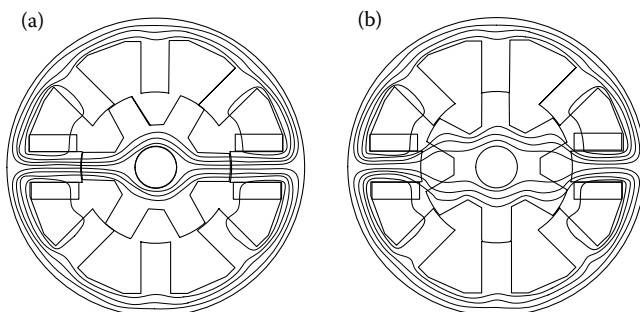
For continuous rotating, the stator and rotor poles should satisfy some special conditions, that is, stator poles and rotor poles must be equally distributed on the circumferences, and pole numbers of the stator and rotor must satisfy the relationship as

$$N_s = 2mq, \tag{6.141}$$

$$N_r = 2(mq \mp 1), \tag{6.142}$$

where N_s and N_r are the pole numbers of the stator and rotor, respectively, q is the phase number of the machine, and m is equal to 1 or 2. In order to reduce the switch frequency and the minimum inductance, the rotor pole number is less than the stator pole number, that is, a minus sign is used in Equation 6.142. The most common combination of q, m, N_s, and N_r is listed in Table 6.1.

Four-phase 8/6 and three-phase 6/4 configurations are the most commonly used SRM structures. A three-phase 6/4 configuration has the advantage of having more room for phase advancing in high-speed applications. In addition, compared to an 8/6 configuration, this structure will minimize the effects of mutual coupling between adjacent phases. However, it results in more

FIGURE 6.77 Typical electromagnetic field distribution of an 8/6 SRM: (a) aligned position and (b) unaligned position.

TABLE 6.1

Common Combination of q, N_s, and N_r

		N_r				
		$m = 1$			$m = 2$	
q	N_s	"−"	"+"	N_s	"−"	"+"
3	6	4	8	12	10	14
4	8	6	10	16	14	18
5	10	8	12	20	18	22

torque pulsation due to its torque–angle characteristics, which contains large dead zones. Furthermore, starting torque can be a problem associated with this configuration. On the other hand, an 8/6 structure can be used to reduce the torque ripple and improve the starting torque.[11] However, by selecting an 8/6 machine, the cost of the silicon will increase. By increasing the number of poles per phase (12/8 and 16/12 configuration), one can minimize demerits of a 6/4 machine while maintaining the same cost of silicon. In this design study an 8/6 configuration has been selected.

6.4.9.2 Stator Outer Diameter

Stator outer diameter is mainly designed based on the available space given in desired specifications. In fact, the main compromise has to be made between the length of the machine and its outer diameter. A pancake (the length of the machine is less than the stator outer radius) type of the design is subject to three-dimensional effects of coils' endings,[80] whereas a very long structure will face cooling and rotor bending issues, which are of particular importance for large machines.

6.4.9.3 Rotor Outer Diameter

The relationship between the developed torque by SRM and machine parameters can be represented by the following equation:

$$T \propto D_r^2 l (N_i)^2, \tag{6.143}$$

where D_r, N_i, and l are the outer diameter of the rotor, equivalent ampere-turn of one phase, and length of the machine. Once the outer diameter of the SRM is fixed, any increase in rotor outer diameter will result in a reduction of N_i, thereby reducing the torque developed by SRM. Because of this and considering the fact that SRM is highly saturated, rotor boring should be equal or slightly larger than the stator outer radius. It must be noted that the rotor geometry enhances the moment of inertia and vibrational modes of the machine.

6.4.9.4 Air Gap

Air gap has an important impact on the generated torque and dynamic behavior of the SRM. In fact, by reducing the air gap, inductance at the aligned position will increase, resulting in higher torque density. On the other hand, a very small air gap will cause severe saturation in stator and rotor pole areas.[74] In addition, mechanical manufacture of a very small air gap might not be feasible. The following empirical formula can be used as a reference for selecting the air gap in large machines[81]:

$$\delta(\text{mm}) = 1 + \frac{D_s}{1000}, \tag{6.144}$$

where δ and D_s are the air gap and the stator outer boring in (mm) and (m), respectively. By investigating the value of the flux density (B) in the stator and rotor poles, the level of saturation and consequently air gap can be finalized.

6.4.9.5 Stator Arc

Since the developed torque depends on the area available for the coils, it is important to design the stator arc in such a way that maximum space for inserting the coils is provided. A very narrow stator arc will result in the tangential vibration of the stator pole. Moreover, it reduces the effective region in the torque–angle characteristics, which increases the torque ripple and reduces the average torque. An optimal value for the stator arc can be chosen using the following inequality[77]:

$$0.3\,\frac{\pi D_R}{N_S} \le \lambda_S \le 0.35\frac{\pi D_R}{N_S}, \tag{6.145}$$

where D_R, N_S, and λ_S are, respectively, the rotor diameter, number of stator poles, and stator arc.

6.4.9.6 Stator Back Iron
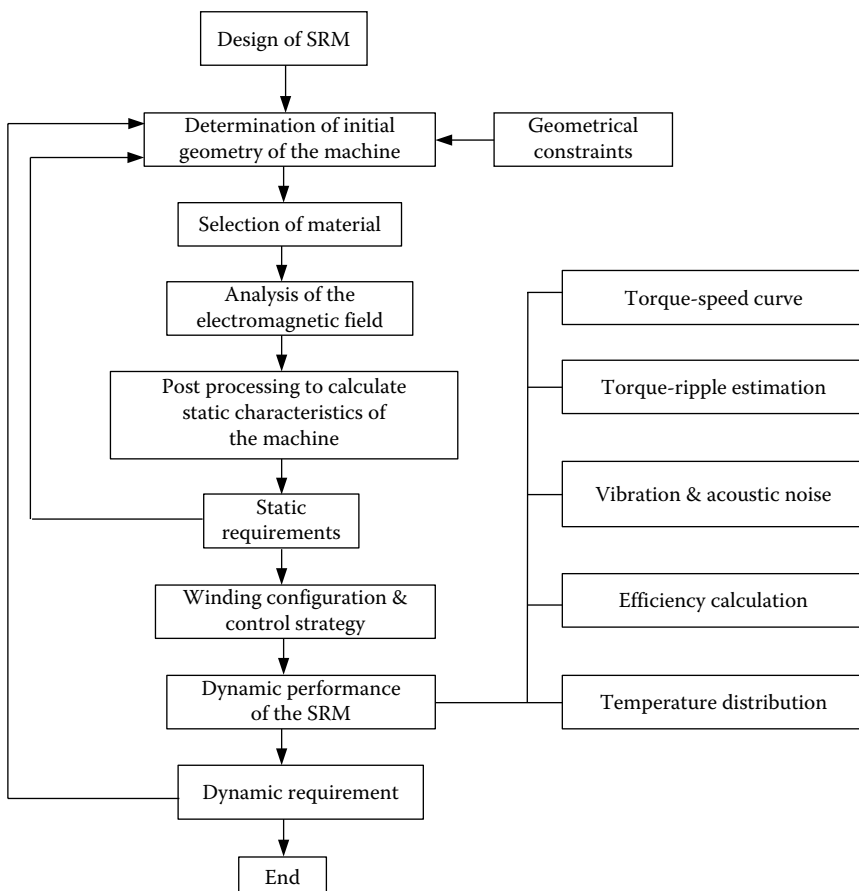
For designing the back iron, the following constraints have to be considered:

1. Radial vibration of the stator body has to be minimized.
2. There should be enough space for cooling of the stator.
3. Back iron should be capable of carrying half of the flux existing in the stator poles without getting saturated.
4. The area available for inserting the coils should not be reduced.

6.4.9.7   Performance Prediction

Clearly, most of the performance requirements are related to the dynamic performance of the drive and hence call for an overall modeling of the drive system including control and power electronics considerations. However, in order to predict the dynamic performance of the drive, static characteristics of the machine (phase inductance and torque–angle profiles) should be available.

The improved magnetic equivalent circuit (IMEC)[82] approach is a shortcut method that gives an approximation of the steady-state parameters of the SRM. Indeed, by replacing all of the magnetomotive sources (ampere-turn) with voltage sources and various parts of the magnetic structure with their equivalent reluctances, one can perform a magnetic analysis. Furthermore, by dividing the stator and rotor poles into several smaller portions, accuracy of

FIGURE 6.78   Basic design strategy.

this method can be arbitrarily improved. It must be noted that finite element analysis of SRM is a time-consuming procedure. Therefore, the IMEC method is more appropriate for developing first design examples.

Figure 6.78 depicts a general design strategy for the SRM drive.

References

1. C. C. Chan and K. T. Chau, *Modern Electric Vehicle Technology*, Oxford University Press, Oxford, 2001.
2. D. W. Novotny and T. A. Lipo, *Vector Control and Dynamics of AC Drives*, Oxford Science Publications, Oxford, ISBN: 0-19-856439-2, 1996.
3. D. C. Hanselman, *Brushless Permanent-Magnet Motor Design*, McGraw-Hill, New York, 1994.
4. F. Huang and D. Tien, "A neural network approach to position sensorless control of brushless DC motors," in *Proceedings of the IEEE 22nd International Conference on Industrial Electronics, Control, and Instrumentation*, Vol. 2, pp. 1167–1170, August 1996.
5. S. Vukosavic, L. Peric, E. Levi, and V. Vuckovic, "Sensorless operation of the SR motor with constant dwell," in *Proceedings of the 1990 IEEE Power Electronics Specialists Conference*, pp. 451–454, 1990.
6. G. K. Dubey, *Power Semiconductor Controlled Drives*, Prentice-Hall, Englewood Cliffs, NJ, 1989.
7. S. R. MacMinn and J. W. Sember, "Control of a switched-reluctance aircraft starter-generator over a very wide speed range," in *Proceedings of the Intersociety Energy Conversion Engineering Conference*, 1989, pp. 631–638.
8. M. Ehsani, *Method and Apparatus for Sensing the Rotor Position of a Switched Reluctance Motor,* U.S. Patent No. 5,410,235, April 1995.
9. A. M. Trzynadlowski, *The Field Orientation Principle in Control of Induction Motor*, Kluwer Academic Publishers, Dordrecht, 1994.
10. J. F. Gieras and M. Wing, *Permanent Magnet Motor Technology, Design and Applications*, Marcel Dekker, New York, 1997.
11. I. Husain, "Minimization of torque ripple in SRM drives," *IEEE Transactions on Industrial Electronics*, 49 (1), 28–39, February 2002.
12. K. M. Rahman and M. Ehsani, "Performance analysis of electric motor drives for electric and hybrid electric vehicle application," *IEEE Power Electronics in Transportation*, 1996, 49–56.
13. T. Senjyu and K. Uezato, "Adjustable speed control of brushless DC motors without position and speed sensors," in *Proceedings of the IEEE/IAS Conference on Industrial Automation and Control: Emerging Technologies*, pp. 160–164, 1995.
14. A. Consoli, S. Musumeci, A. Raciti, and A. Testa, "Sensorless vector and speed control of brushless motor drives," *IEEE Transactions on Industrial Electronics*, 41, 91–96, February 1994.
15. P. Acarnley, "Sensorless position detection in permanent magnet drives," *IEE Colloquium on Permanent Magnet Machines and Drives*, pp. 10/1–10/4, 1993.

16. T. Liu and C. Cheng, "Adaptive control for a sensorless permanent-magnet synchronous motor drive," *IEEE Transactions on Aerospace and Electronic Systems*, 30, 900–909, July 1994.

17. R. Wu and G. R. Slemon, "A permanent magnet motor drive without a shaft sensor," *IEEE Transactions on Industry Applications*, 27, 1005–1011, September/October 1991.

18. T. Liu and C. Cheng, "Controller design for a sensorless permanent magnet synchronous drive system," *IEE Proc.—B*, 140, 369–378, November 1993.

19. N. Ertugrul, P. P. Acarnley, and C. D. French, "Real-time estimation of rotor position in PM motors during transient operation," *IEE Fifth European Conference on Power Electronics and Applications*, pp. 311–316, 1993.

20. N. Ertugrul and P. Acarnley, "A new algorithm for sensorless operation of permanent magnet motors," *IEEE Transactions on Industry Applications*, 30, 126–133, January/February 1994.

21. T. Takeshita and N. Matsui, "Sensorless brushless DC motor drive with EMF constant identifier," *IEEE International Conference on Industrial Electronics, Control, and Instrumentation*, Vol. 1, pp. 14–19, 1994.

22. N. Matsui and M. Shigyo, "Brushless DC motor control without position and speed sensors," *IEEE Transactions on Industry Applications*, 28, 120–127, January/February 1992.

23. N. Matsui, "Sensorless operation of brushless DC motor drives," *Proceedings of the IEEE International Conference on Industrial Electronics, Control, and Instrumentation*, Vol. 2, pp. 739–744, November 1993.

24. N. Matsui, "Sensorless PM brushless DC motor drives," *IEEE Transactions on Industrial Electronics*, 43, 300–308, April 1996.

25. M. Schrodl, "Digital implementation of a sensorless control algorithm for permanent magnet synchronous motors," *Proceedings of the International Conference "SM 100,"* ETH Zurich, Switzerland, pp. 430–435, 1991.

26. M. Schrodl, "Operation of the permanent magnet synchronous machine without a mechanical sensor," *IEE Proceedings on the International Conference on Power Electronics and Variable Speed Drives*, pp. 51–56, July 1990.

27. M. Schrodl, "Sensorless control of permanent magnet synchronous motors," *Electric Machines and Power Systems*, 22, 173–185, 1994.

28. B. J. Brunsbach, G. Henneberger, and T. Klepsch, "Position controlled permanent magnet excited synchronous motor without mechanical sensors," *IEE Conference on Power Electronics and Applications*, Vol. 6, pp. 38–43, 1993.

29. R. Dhaouadi, N. Mohan, and L. Norum, "Design and implementation of an extended Kalman filter for the state estimation of a permanent magnet synchronous motor," *IEEE Transactions on Power Electronics*, 6, 491–497, July 1991.

30. A. Bado, S. Bolognani, and M. Zigliotto, "Effective estimation of speed and rotor position of a PM synchronous motor drive by a Kalman filtering technique," in *Proceedings of the 23rd IEEE Power Electronics Specialist Conference*, Vol. 2, pp. 951–957, 1992.

31. K. R. Shouse and D. G. Taylor, "Sensorless velocity control of permanent-magnet synchronous motors," in *Proceedings of the 33rd Conference on Decision and Control*, pp. 1844–1849, December 1994.

32. J. Hu, D. M. Dawson, and K. Anderson, "Position control of a brushless DC motor without velocity measurements," *IEE Proceedings on Electronic Power Applications*, 142, 113–119, March 1995.

33. J. Solsona, M. I. Valla, and C. Muravchik, "A nonlinear reduced order observer for permanent magnet synchronous motors," *IEEE Transactions on Industrial Electronics*, 43, 38–43, August 1996.

34. R. B. Sepe and J. H. Lang, "Real-time observer-based (adaptive) control of a permanent-magnet synchronous motor without mechanical sensors," *IEEE Transactions on Industry Applications*, 28, 1345–1352, November/December 1992.

35. L. Sicot, S. Siala, K. Debusschere, and C. Bergmann, "Brushless DC motor control without mechanical sensors," in *Proceedings of the IEEE Power Electronics Specialist Conference*, pp. 375–381, 1996.

36. T. Senjyu, M. Tomita, S. Doki, and S. Okuma, "Sensorless vector control of brushless DC motors using disturbance observer," in *Proceedings of the 26th IEEE Power Electronics Specialists Conference*, Vol. 2, pp. 772–777, 1995.

37. K. Iizuka, H. Uzuhashi, and M. Kano, "Microcomputer control for sensorless brushless motor," *IEEE Transactions on Industry Applications*, IA-27, 595–601, May–June 1985.

38. J. Moreira, "Indirect sensing for rotor flux position of permanent magnet AC motors operating in a wide speed range," *IEEE Transactions on Industry Applications Society*, 32, 401–407, November/December 1996.

39. S. Ogasawara and H. Akagi, "An approach to position sensorless drive for brushless DC motors," *IEEE Transactions on Industry Applications*, 27, 928–933, September/October 1991.

40. T. M. Jahns, R. C. Becerra, and M. Ehsani, "Integrated current regulation for a brushless ECM drive," *IEEE Transactions on Power Electronics*, 6, 118–126, January 1991.

41. R. C. Becerra, T. M. Jahns, and M. Ehsani, "Four-quadrant sensorless brushless ECM drive," in *Proceedings of the IEEE Applied Power Electronics Conference and Exposition*, pp. 202–209, March 1991.

42. D. Regnier, C. Oudet, and D. Prudham, "Starting brushless DC motors utilizing velocity sensors," in *Proceedings of the 14th Annual Symposium on Incremental Motion Control Systems and Devices*, Champaign, IL, Incremental Motion Control Systems Society, pp. 99–107, June 1985.

43. D. Peters and J. Harth, "I.C.s provide control for sensorless DC motors," *EDN*, pp. 85–94, April 1993.

44. M. Hamdi and M. Ghribi, "A sensorless control scheme based on fuzzy logic for AC servo drives using a permanent-magnet synchronous motor," *IEEE Canadian Conference on Electrical and Computing Engineering*, pp. 306–309, 1995.

45. D. E. Hesmondhalgh, D. Tipping, and M. Amrani, "Performance and design of an electromagnetic sensor for brushless DC motors," *IEE Proceedings*, 137, 174–183, May 1990.

46. T. J. E. Miller, *Switched Reluctance Motors and Their Control*, Oxford Science Publications, London, 1993.

47. P. J. Lawrenson, J. M. Stephenson, P. T. Blenkinsop, J. Corda, and N. N. Fulton, "Variable-speed switched reluctance motors," *Proceedings of IEE*, 127, Part B (4), 253–265, July 1980.

48. E. Richter, J. P. Lyons, C. A. Ferreira, A. V. Radun, and E. Ruckstatder, "Initial testing of a 250 kW starter/generator for aircraft applications," in *Proceedings of the SAE Aerospace Atlantic Conference Expo.*, Dayton, OH, April 18–22, 1994.

49. M. Ehsani, *Phase and Amplitude Modulation Techniques for Rotor Position Sensing in Switched Reluctance Motors,* U.S. Patent No. 5,291,115, March 1994.

50. D. A. Torrey, "Variable-reluctance generators in wind-energy systems," in *Proceedings of the IEEE PESC '93*, pp. 561–567, 1993.

51. J. M. Kokernak, D. A. Torrey, and M. Kaplan, "A switched reluctance starter/alternator for hybrid electric vehicles," in *Proceedings of the PCIM '99*, pp. 74–80, 1999.

52. J. T. Bass, M. Ehsani, and T. J. E. Miller, "Simplified electronics for torque control of sensorless switched reluctance motor," *IEEE Transactions on Industrial Electronics*, 34 (2), 1987.

53. M. Ehsani, *Self-Tuning Control of Switched Reluctance Motor Drives System*, U.S. Patent Pending, File Number 017575.0293.

54. M. Ehsani, *Switched Reluctance Motor Drive System*, U.S. Patent Pending, Filing Date: January 1997, Serial Number 60/061,087.

55. R. Krishnan, *Switched Reluctance Motors Drives: Modeling, Simulation Analysis, Design and Applications*, CRC Press, Boca Raton, FL, 2001.

56. N. Mohan, T. M. Undeland, and W. P. Robbins, *Power Electronics—Converters, Applications, and Design*, John Wiley & Sons, New York, ISBN: 0-471-58408-8, 1995.

57. A. Radun, "Generating with the switched-reluctance motor," in *Proceedings of the IEEE APEC '94*, pp. 41–47, 1994.

58. B. Fahimi, "A switched reluctance machine based starter/generator for more electric cars," in *Proceedings of the IEEE Electric Machines and Drives Conference*, pp. 73–78, 2000.

59. H. Gao, F. R. Salmasi, and M. Ehsani, "Sensorless control of SRM at standstill," in *Proceedings of the 2000 IEEE Applied Power Electronics Conference*, Vol. 2, pp. 850–856, 2000.

60. J. P. Lyons, S. R. MacMinn, and M. A. Preston, "Discrete position estimator for a switched reluctance machine using a flux-current map comparator," U.S. Patent 5140243, 1991.

61. G. Suresh, B. Fahimi, K. M. Rahman, and M. Ehsani, "Inductance based position encoding for sensorless SRM drives," in *Proceedings of the 1999 IEEE Power Electronics Specialists Conference,* Vol. 2, pp. 832–837, 1999.

62. H. Gao, *Sensorless Control of the Switched Reluctance Motor at Standstill and Near-Zero Speed*, Ph.D. Dissertation, Texas A&M University, December 2001.

63. M. Ehsani, *Position Sensor Elimination Technique for the Switched Reluctance Motor Drive*, U.S. Patent 5072166, 1990.

64. M. Ehsani, I. Husain, S. Mahajan, and K. R. Ramani, "New modulation encoding techniques for indirect rotor position sensing in switched reluctance motors," *IEEE Transactions on Industry Applications*, 30 (1), 85–91, 1994.

65. G. R. Dunlop and J. D. Marvelly, "Evaluation of a self commuted switched reluctance motor," in *Proceedings of the 1987 Electric Energy Conference*, pp. 317–320, 1987.

66. M. Ehsani and I. Husain, "Rotor position sensing in switched reluctance motor drives by measuring mutually induced voltages," in *Proceedings of the 1992 IEEE Industry Application Society Annual Meeting*, Vol. 1, pp. 422–429, 1992.

67. A. Lumsdaine and J. H. Lang, "State observer for variable reluctance motors," *IEEE Transactions on Industrial Electronics*, 37 (2), 133–142, 1990.

68. K. Russa, I. Husain, and M. E. Elbuluk, "A self-tuning controller for switched reluctance motors," *IEEE Transactions on Power Electronics,* 15 (3), pp. 545–552, May 2000.

69. P. Tandon, A. Rajarathnam, and M. Ehsani, "Self-tuning of switched reluctance motor drives with shaft position sensor," *IEEE Transactions on Industry Applications*, 33 (4), pp. 1002–1010, July/August 1997.
70. A. Rajarathnam, B. Fahimi, and M. Ehsani, "Neural network based self-tuning control of a switched reluctance motor drive to maximize torque per ampere," in *Proceedings of the IEEE Industry Applications Society Annual Meeting,* Vol. 1, pp. 548–555, 1997.
71. B. Fahimi, *Control of Vibration in Switched Reluctance Motor Drive,* Ph.D. Dissertation, Texas A&M University, May 1999.
72. D. E. Cameron, J. H. Lang, and S. D. Umans, "The origin and reduction of acoustic noise an doubly salient variable reluctance motor," *IEEE Transactions on Industry Applications*, IA-28 (6), 1250–1255, November/December 1992.
73. H. Gao, B. Fahimi, F. R. Salmasi, and M. Ehsani, "Sensorless control of the switched reluctance motor drive based on the stiff system control concept and signature detection," in *Proceedings of the 2001 IEEE Industry Applications Society Annual Meeting*, pp. 490–495, 2001.
74. B. Fahimi and M. Ehsani, "Spatial distribution of acoustic noise caused by radial vibration in switched reluctance motors: application to design and control," in *Proceedings of the 2000 IEEE Industry Application Society Annual Meeting*, Rome, Italy, October 2000.
75. B. Fahimi, G. Suresh, K. M. Rahman, and M. Ehsani, "Mitigation of acoustic noise and vibration in switched reluctance motor drive using neural network based current profiling," in *Proceedings of the 1998 IEEE Industry Application Society Annual Meeting,* Vol. 1, pp. 715–722, 1998.
76. B. Fahimi and M. Ehsani, *Method and Apparatus for Reducing Noise and Vibration in Switched Reluctance Motor Drives*, U.S. Patent pending.
77. G. S. Buja and M. I. Valla, "Control characteristics of the SRM drives—part I: Operation in the linear region," *IEEE Transactions on Industrial Electronics*, 38 (5), 313–321, October 1991.
78. B. Fahimi, G. Suresh, and M. Ehsani, "Design considerations of switched reluctance motors: vibration and control issues," in *Proceedings of the 1999 IEEE Industry Application Society Annual Meeting,* Phoenix, AZ, October 1999.
79. J. Faiz and J. W. Finch, "Aspects of design optimization for switched reluctance motors," *IEEE Transactions on Energy Conversion*, 8 (4), 704–712, December 1993.
80. A. M. Michaelides and C. Pollock, "Effect of end core flux on the performance of the switched reluctance motor," *IEE on Electronic Power Applications*, 141 (6), 308–316, November 1994.
81. G. Henneberger, *Elektrische Maschinen I, II, III*, RWTH Aachen, Manuscripts at Institut fuer Elektrische Maschinen, 1989.
82. B. Fahimi, G. Henneberger, and M. Moallem, "Prediction of transient behavior of SRM drive using improved equivalent magnetic circuit method," *PCIM Conference Records*, pp. 285–291, 1995.

7
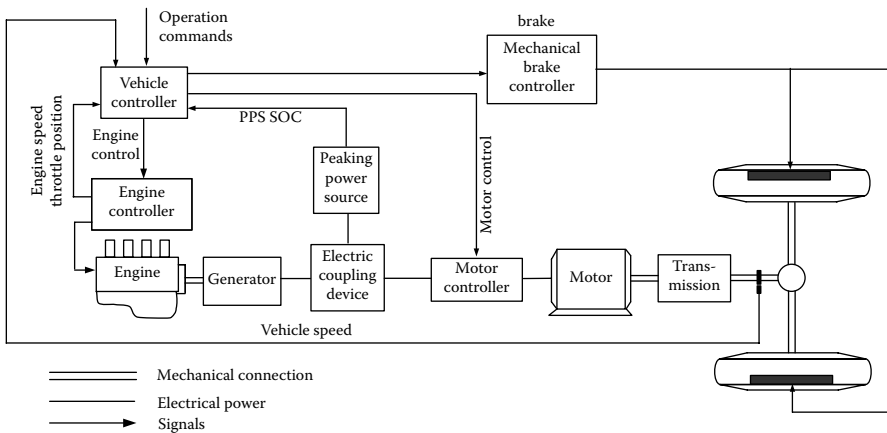
Design Principle of Series (Electrical Coupling) Hybrid Electric Drive Train

The concept of a series hybrid electric drive train was developed from the EV drive train.[1] As mentioned in Chapter 4, EVs, compared with conventional gasoline- or diesel-fueled vehicles, have the advantages of zero mobile pollutant emissions, multienergy sources, and high efficiency. However, EVs using present technologies have some disadvantages: a limited drive range due to the shortage of energy storage in the on-board batteries, limited payload and volume capacity due to heavy and bulky batteries, and long battery charging time. The initial objective of developing a series HEV was aimed at extending the drive range by adding an engine/alternator system to charge the batteries on-board.

A typical series hybrid electric drive train configuration is shown in Figure 7.1. The vehicle is propelled by a traction motor. The traction motor is powered by a battery pack and/or an engine/generator unit. The powers of both power sources are merged together in a power electronics-based and controllable electrical coupling device. Many operation modes are available to choose, according to the power demands of the driver and the operation status of the drive train system.

Vehicle performance (in terms of acceleration, gradeability, and maximum speed) is completely determined by the size and characteristics of the traction motor drive. Motor power capability and transmission design are the same as in the EV design discussed in Chapter 4. However, the drive train control is essentially different from the pure electric drive train due to the involvement of the additional engine/generator unit. This chapter will focus on the design principles of the engine/alternator system, the drive train control, and the energy and power capacity of the battery pack. In this chapter, the term "peak power source" will replace "battery pack" because, in HEVs, the major function of the batteries is to supply peaking power and they can be replaced with other kinds of sources such as ultracapacitors, flywheels, or combinations.

FIGURE 7.1   Configuration of a typical series hybrid electric drive train.
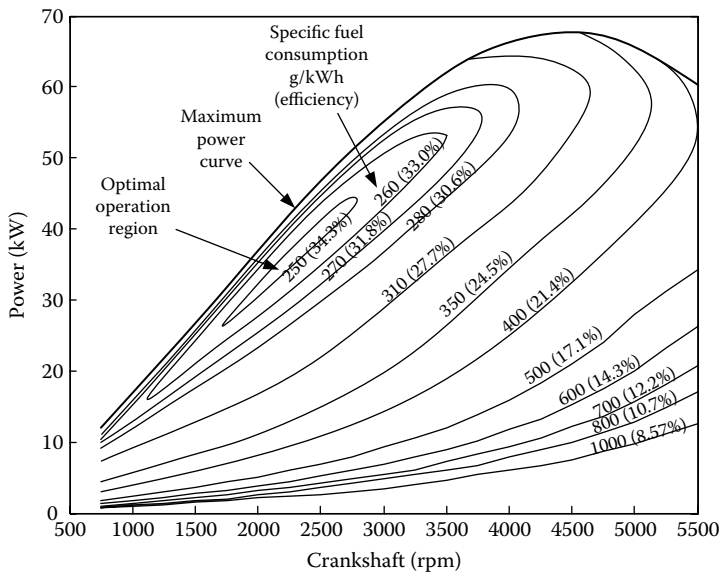
7.1 Operation Patterns

In series hybrid electric drive trains, the engine/generator system is
mechanically decoupled from the driven wheels as shown in Figure 7.1. The
speed and torque of the engine are independent of vehicle speed and traction
torque demand, and can be controlled to any operating point on its speed-
torque plane.[2,3] Generally, the engine should be controlled in such a way
that it always operates in its optimal operation region, where fuel consump-
tion and emissions of the engine are minimized (see Figure 7.2). Due to the
mechanical decoupling of the engine from the driven wheels, this optimal
engine operation is realizable. However, it heavily depends on the operating
modes and control strategy of the drive train.

The drive train has several operating modes, which can be used selectively
according to the driving conditions and wish of the driver. These operating
modes are as follows:

1. *Hybrid traction mode*: When a large amount of power is demanded,
   that is, the driver depresses the accelerator pedal deeply, both
   engine/generator and peaking power source (PPS) supply their pow-
   ers to the electric motor drive. In this case, the engine should be
   controlled to operate in its optimal region for efficiency and emis-
   sion reasons as shown in Figure 7.2. The PPS supplies the additional
   power to meet the traction power demand. This operation mode can
   be expressed as

$$P_{\text{demand}} = P_{\text{e/g}} + P_{\text{pps}}, \tag{7.1}$$

FIGURE 7.2 Example of engine characteristics and optimal operating region.

where P_{demand} is the power demanded by the driver, $P_{e/g}$ is the engine/generator power, and P_{pps} is the PPS power.

2. *Peak power source-alone traction mode*: In this operating mode, the peak power source alone supplies its power to meet the power demand, that is,

$$P_{demand} = P_{pps}. \qquad (7.2)$$

3. *Engine/generator-alone traction mode*: In this operating mode, the engine/generator alone supplies its power to meet the power demand, that is,

$$P_{demand} = P_{e/g}. \qquad (7.3)$$

4. *PPS charging from the engine/generator*: When the energy in the PPS decreases to a bottom line, the PPS must be charged. This can be done by regenerative braking or by the engine/generator. Usually, engine/generator charging is needed, since regenerative braking charging is insufficient. In this case, the engine/generator power is divided into two parts: one to propel the vehicle and the other to charge the PPS. That is,

$$P_{demand} = P_{e/g} + P_{pps}. \qquad (7.4)$$

It should be noticed that the operation mode is only effective when the power of the engine/generator is greater than the load power

demand. It should be noted that PPS power is given a negative sign when it is being charged.

5. *Regenerative braking mode*: When the vehicle is braking, the traction motor can be used as a generator, converting part of the kinetic energy of the vehicle mass into electric energy to charge the PPS.

As shown in Figure 7.1, the vehicle controller commands the operation of each component according to the traction power (torque) command from the driver, the feedback from each of the components, and also the drive train and the preset control strategy. The control objectives are to (1) meet the power demand of the driver, (2) operate each component with optimal efficiency, (3) recapture braking energy as much as possible, and (4) maintain the state of charge (SOC) of the PPS in a preset window.

7.2   Control Strategies
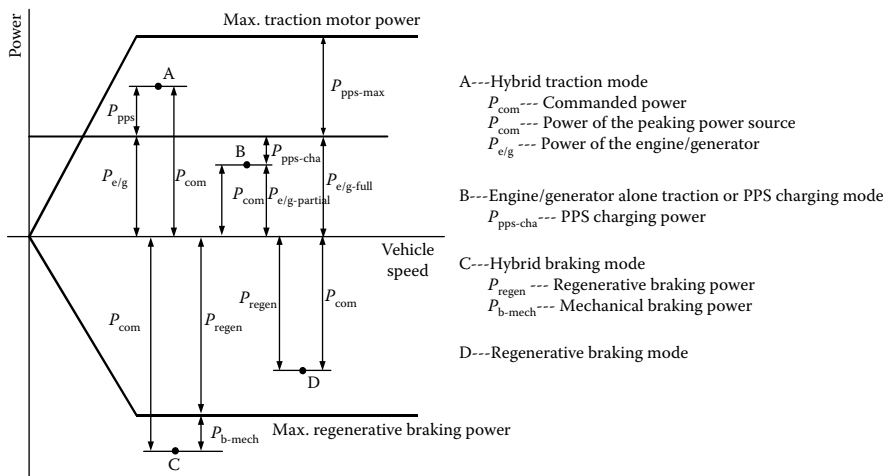
A control strategy is a control rule that is preset in the vehicle controller and commands the operation of each component. The vehicle controller receives operation commands from the driver and feedback from the drive train and all the components, and then makes decisions to use proper operation modes. Obviously, the performance of the drive train relies mainly on control quality, in which control strategy plays a crucial role.

In practice, there are a number of control strategies that can be employed in a drive train for vehicles with different mission requirements. In this chapter, two typical control strategies are introduced: (1) maximum state-of-charge of peaking power source (Max. SOC-of-PPS) and (2) engine turn-on and turn-off (engine on/off) or thermostat control strategies.[4]

7.2.1   Max. SOC-of-PPS Control Strategy

The target of this control strategy is to meet the power demand commanded by the driver and, at the same time, maintain the SOC of the PPS at its high level. The engine/generator is the primary power source, and the PPS is the secondary source. This control strategy is considered to be the proper design for vehicles in which performance (speed, acceleration, gradeability, etc.) is the first concern, such as vehicles with frequent stop–go driving patterns and military vehicles in which carrying out their mission is the most important objective. A high SOC level in the PPS will guarantee the high performance of vehicles at any time.

The Max. SOC-of-PPS control strategy is depicted in Figure 7.3, in which points A, B, C, and D represent the power demands that the driver commanded in either traction mode or braking mode. Point A represents the commanded traction power that is greater than the power that the
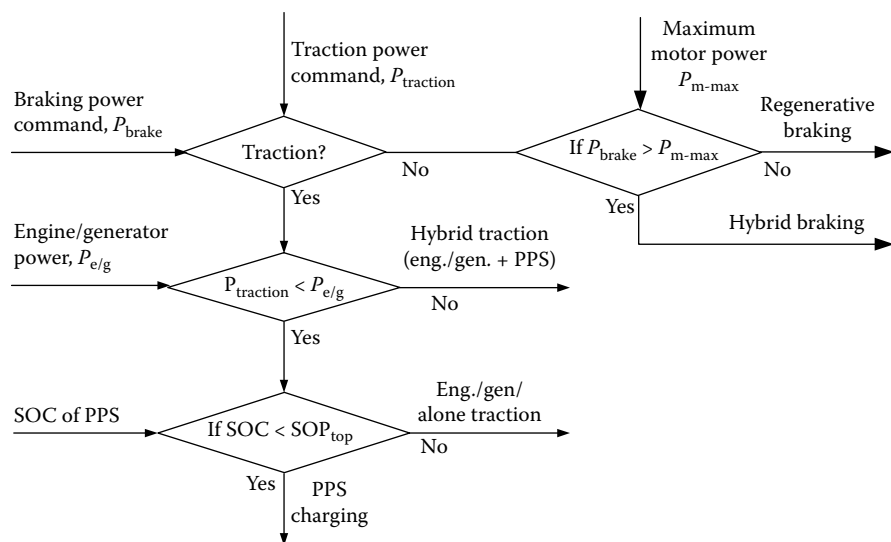
FIGURE 7.3 Illustration of the maximum PPS SOC control strategy.

engine/generator can produce. In this case, the PPS must produce its power to make up the power shortage of the engine/generator. Point B represents the commanded power that is less than the power that the engine/generator produces when operating in its optimal operation region (refer to Figure 7.2). In this case, two operating modes may be used, depending on the SOC level of the PPS. If the SOC of the PPS is below its top line, such as less than 70%, the engine/generator is operated with full load. (The operating point of the engine/generator with full load depends on the engine/generator design. For details, see the next section.) Part of its power goes to the traction motor to propel the vehicle and the other part goes to the PPS to increase the energy level. On the other hand, if the SOC of the PPS has reached its top line, the engine/generator traction mode alone is supplied, that is, the engine/generator is controlled to produce power equal to the demanded power, and the PPS is set at idle. Point C represents the commanded braking power that is greater than the braking power the motor can produce (maximum regenerative braking power). In this case, a hybrid braking mode is used, in which the electric motor produces its maximum braking power and the mechanical braking system produces the remaining braking power. Point D represents the commanded braking power that is less than the maximum braking power that the motor can produce. In this case, only regenerative braking is used. The control flowchart of the Max. SOC-of-PPS is illustrated in Figure 7.4.
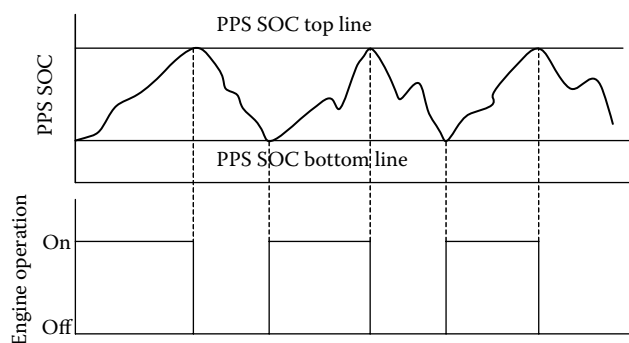
7.2.2 Engine On–Off or Thermostat Control Strategy

The Max. SOC-of-PPS control strategy emphasizes maintaining the SOC of the PPS at a high level. However, in some driving conditions, such as driving

FIGURE 7.4 Control flowchart of the Max. SOC-of-PPS control strategy.

for a long time (with a low load) on a highway at constant speed, the PPS can be easily charged to its full level, and the engine/generator is forced to operate with power output smaller than its optimum. Hence, the efficiency of the drive train is reduced. In this case, the engine on–off or thermostat control strategy would be appropriate. This control strategy is illustrated in Figure 7.5. The operation of the engine/generator is completely controlled by the SOC of the PPS. When the SOC of the PPS reaches its preset top line, the engine/generator is turned off and the vehicle is propelled only by the PPS. On the other hand, when the SOC of the PPS reaches its bottom line, the engine/generator is turned on. The PPS gets its charging from the engine/generator. In this way, the engine can be always operated within its optimal deficiency region.

FIGURE 7.5 Illustration of thermostat control.
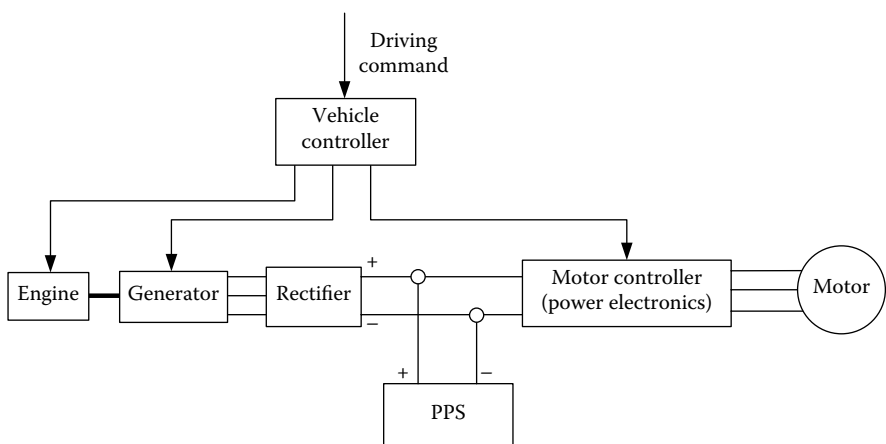
7.3 Design Principles of a Series (Electrical Coupling) Hybrid Drive Train

Successful design of the drive train system means ensuring the vehicle being capable of achieving the desired performance, such as acceleration, gradeability, high speed, and high operating efficiency. The traction motor drive, engine/generator unit, PPS, and electrical coupling device are the major design components of concern. Their design should primarily be considered at the system level so as to ensure that all the components work harmoniously.

7.3.1 Electrical Coupling Device

As mentioned above, the electrical coupling device is the sole linkage point for combining the three sources of powers together: engine/generator, PPS, and traction motor. Its major function is to regulate the power (electric current) flow between these power sources and sinks. The power (current) regulation is carried out based on the proper control of the terminal voltages. The simplest structure is to connect the three terminals together directly as shown in Figure 7.6.

This configuration is the simplest and has the lowest cost. Its major feature is that the bus voltage is equal to the rectified voltage of the generator and that of the PPS. The bus voltage is determined by the minimum of the two voltages above. The power flow is solely controlled by the voltage of the generator. To deliver its power to the traction motor and/or the PPS, the open circuit voltage (zero current) of the generator, rectified, must be higher than the PPS voltage. This can be done by controlling the engine throttle and/or the magnetic field
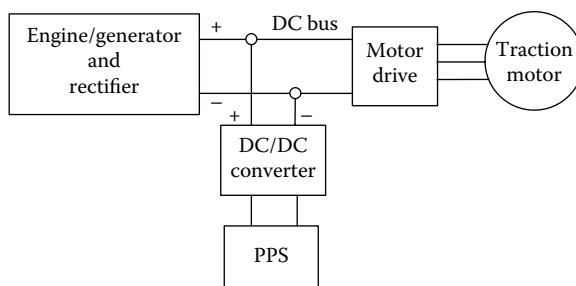
FIGURE 7.6 Directly connected power source and sink.
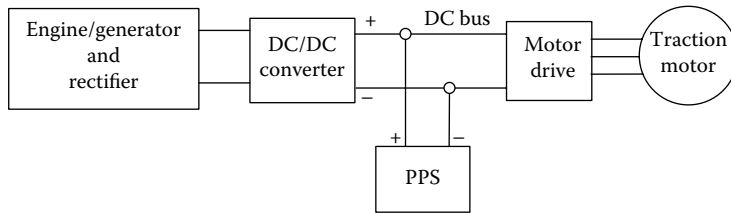
of the generator. When the engine/generator is controlled to generate the rectified terminal voltage equal to the open circuit voltage of the PPS, the PPS does not deliver power and the engine/generator alone powers the electric motor. When the rectified voltage of the engine/generator is lower than the PPS voltage, the PPS alone powers the electric motor. In regenerative braking, the generated bus voltage by the traction motor must be higher than the PPS voltage. However, the voltage generated by the traction motor is usually proportional to the rotational speed of the motor. Therefore, the regenerative braking capability in low speed will be rather limited for this design. It is also obvious that this simple design requires the engine/generator and the PPS to have the same rated voltage. This constraint may result in a heavy PPS due to the high voltage.

Adding a DC/DC converter, and thus releasing the voltage constraints, may significantly improve the performance of the drive train.[5,6] Two alternative configurations are shown in Figures 7.7 and 7.8. In the configuration of Figure 7.7, the DC/DC converter is placed between the PPS and the DC bus and the engine–generator–rectifier is connected directly to the DC bus. In this configuration, the PPS voltage is allowed to be different from the DC bus voltage, and the rectified voltage of the engine/generator is always equal to the DC bus voltage. In the configuration of Figure 7.8, the DC/DC converter is placed between the engine–generator–rectifier and the DC bus and the PPS is directly connected to the DC bus. Contrary to the configuration of Figure 7.7, the DC/DC converter conditions the rectified voltage of the engine/generator and the voltage of the PPS is always equal to the DC bus voltage.

Among these two configurations, the one in Figure 7.7 seems to be more appropriate. Its advantages over the other one are mainly the following: (1) changes in the voltage of PPS do not affect the DC bus voltage, (2) the energy in the PPS can be fully used, (3) the voltage of the DC bus can be maintained by controlling the engine throttle and/or the magnetic field of the generator, (4) a low PPS voltage can be used, which may lead to small and light PPS pack and less cost, and (5) the charging current of PPS can be regulated during regenerative braking and charging from the engine/generator.

FIGURE 7.7   Configuration with the DC/DC converter on the PPS side.

FIGURE 7.8 Configuration with the DC/DC converter on the engine/generator side.
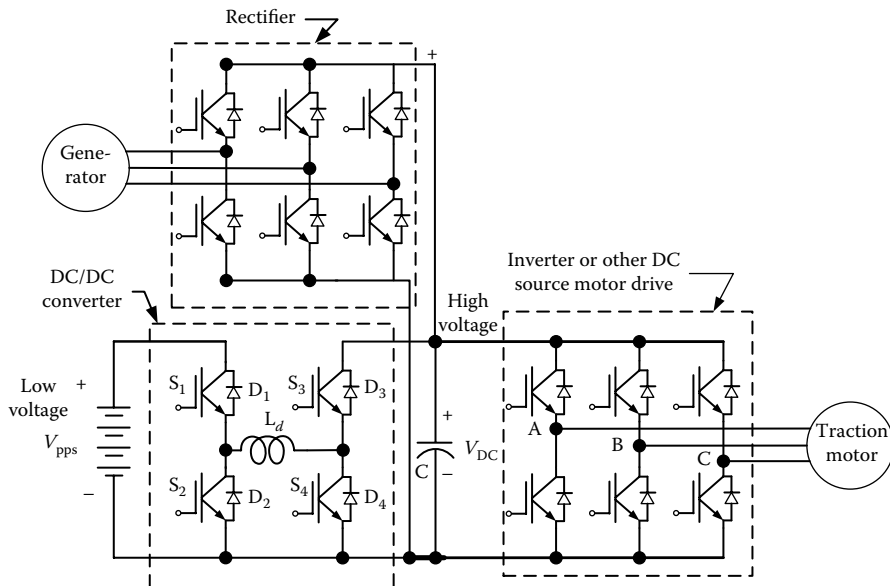
It is obvious that the DC/DC converter in this configuration has to be bidirectional. In the case of the rated voltage of the PPS being lower than the DC bus voltage, the DC/DC converter has to boost the PPS voltage to the level of the DC bus to deliver its power to the DC bus and buck the DC bus voltage to the level of the PPS charging voltage to charge the PPS. In regenerative braking, if the voltage generated by the traction motor at a given low speed is still higher than the voltage of the PPS, the buck DC/DC converter in the PPS charging direction is still usable. However, if the voltage generated by the traction motor at the given low speed is lower than the terminal voltage of the PPS, the DC/DC converter may need to boost the DC bus voltage to charge the battery. In this case, a buck/boost (step down/step up) converter is needed. The basic functions of the DC/DC required converter are summarized in Figure 7.9.

Figure 7.10 shows a bidirectional DC/DC converter connected between the low voltage of PPS and the high-voltage of the DC bus, boosting for PPS discharging (traction) and bucking for PPS charging from the engine/generator or from regenerative braking.[6] In the PPS discharging (traction) mode, switch S_1 is turned off, and switch S_2 is turned on and off periodically. In the on period of S_2, the inductor L_d is charged with energy from the PPS and the load is powered by the capacitor C, as shown in Figure 7.11a. In the off period of S_2, both the PPS and the inductor supply energy to the load and the charging of capacitor C, as shown in Figure 7.11b.
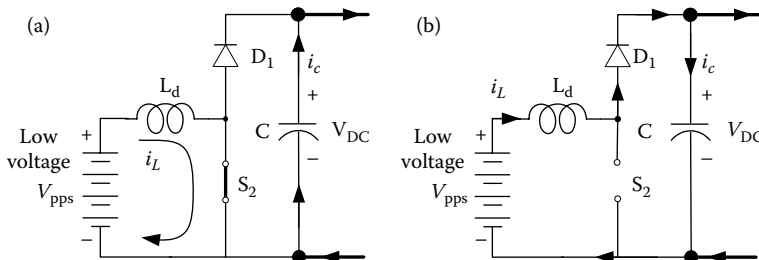
In the PPS charging mode from the engine/generator or traction motor in regenerative braking, the DC/DC converter bucks the high voltage of the DC bus to the low voltage of the PPS. Switch S_1 and diode D_2 serve as a

Energy flow	PPS discharging	PPS charging
PPS traction	Boost	—
PPS charging from e/g	—	Buck
Regenerative braking	—	Buck or buck/boost

FIGURE 7.9 Basic functions of the DC/DC converter.

FIGURE 7.10   Bidirectional DC/DC with low-voltage PPS and high-voltage DC bus.
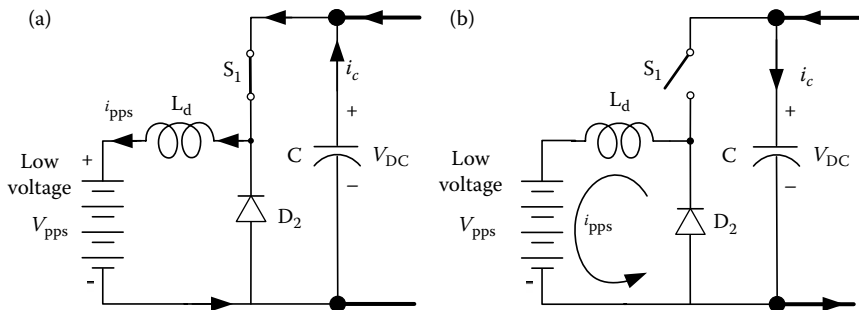
FIGURE 7.11   Current flow during the on and off periods of S_2 in the PPS discharging mode: (a) in S_2 on period and (b) in S_2 off period.
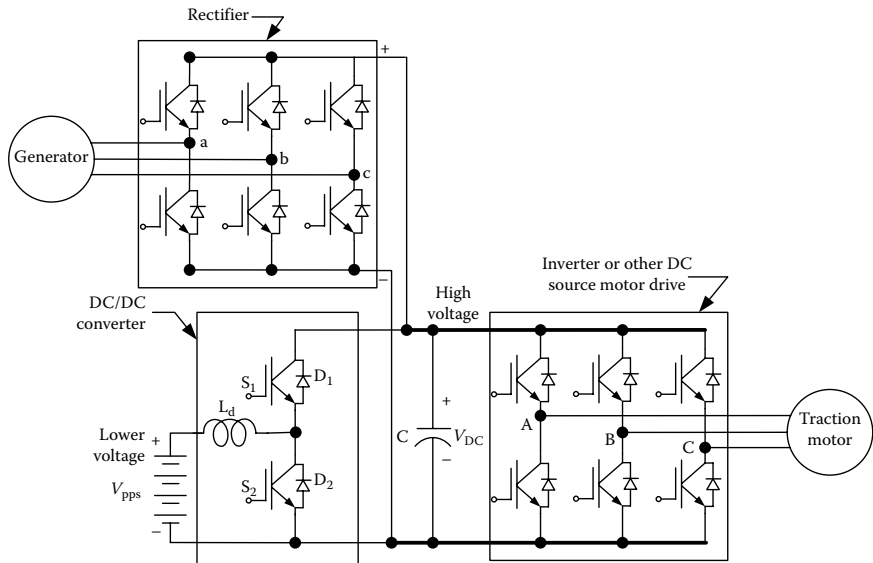
unidirectional buck converter. The current flows during the on and off periods of S_1 are shown in Figure 7.12.

As mentioned above, when the generated voltage by the traction motor at low speed, in regenerative braking, is lower than the voltage of the PPS, a bidirectional boost/buck DC/DC converter is required. Such a bidirectional buck/boost DC/DC converter is shown in Figure 7.13. Its basic operations in PPS discharging and charging modes are as follows.

In the PPS discharging mode, that is, boosting the PPS voltage to the DC bus level, switch S_1 is always on, S_2 and S_3 are always off, and S_4 are turned on and off periodically in the same manner as S_2 in Figure 7.11. In the PPS charging mode with the DC bus voltage higher than the PPS voltage in regenerative

FIGURE 7.12 Current flow during the on and off periods of S_1 in PPS charging mode: (a) in S_1 on period and (b) in S_2 off period.

FIGURE 7.13 A boost/buck DC/DC converter.

braking or engine/generator charging mode, that is, bucking the DC bus voltage to PPS level, switches S_1, S_2, and S_4 are turned off, and S_3 are turned on and off periodically in the same manner as shown in Figure 7.12. In the PPS charging mode with the DC bus voltage lower than the PPS voltage (regenerative braking at low speed), that is, boosting the DC bus voltage to the PPS level, switches S_1 and S_4 are kept off, S_3 on, and S_2 is turned on and off periodically. In the on period of S_2, the inductor L_d is charged by the DC bus through S_3 and S_2 In the off period of S_2, both the DC bus and the inductor charge the PPS through S_3 and D_1.
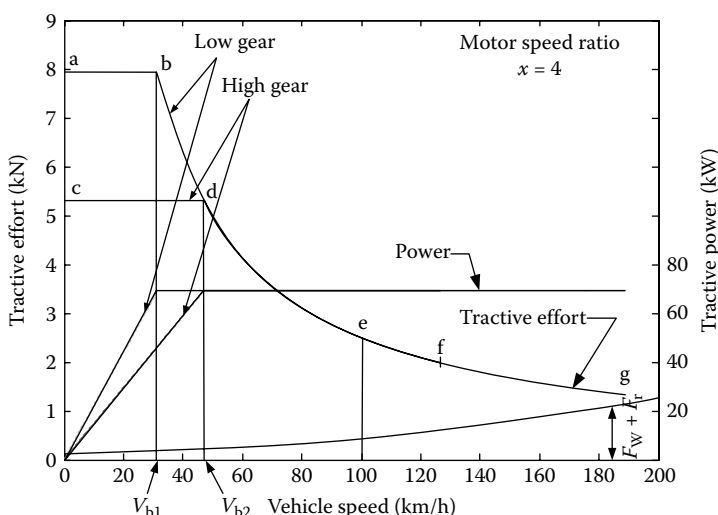
Actually in the DC/DC converter in Figure 7.13, there is a spare function, which is bucking the PPS voltage to bus voltage if the PPS voltage is higher than the DC bus voltage. This case would never occur in this application.

7.3.2 Power Rating Design of the Traction Motor

Similar to the pure EV discussed in Chapter 4, the power rating of the electric motor drive in series HEV is completely determined by vehicle acceleration performance requirement, motor characteristics, and transmission characteristics (refer Chapter 4). At the beginning of the design, the power rating of the motor drive can be estimated, according to the acceleration performance (time used to accelerate the vehicle from zero speed to a given speed), using the following equation:

$$P_t = \frac{\delta M}{2t_a}\left(V_f^2 + V_b^2\right) + \frac{2}{3}Mgf_rV_f + \frac{1}{5}\rho_a C_D A_f V_f^3, \tag{7.5}$$

where M is the total vehicle mass in kg, t_a is the expected acceleration time in s, V_b is the vehicle speed in m/s, corresponding to the motor-based speed (see Figure 7.14), V_f is the final speed of the vehicle during acceleration in m/s, g is the gravity acceleration in 9.80 m/s^2, f_r is the tire rolling resistance coefficient, ρ_a is the air density in 1.202 kg/m^3, A_f is the front area of the vehicle in m^2, and C_D is the aerodynamic drag coefficient.

FIGURE 7.14 Speed–torque (power) characteristics of an electric motor.

The first term in Equation 7.5 represents the power used to accelerate the vehicle mass, and the second and third terms represent the average power for overcoming the tire rolling resistance and aerodynamic drag.

Figure 7.14 shows the tractive effort and tractive power versus vehicle speed with a two-gear transmission. During acceleration, starting from low gear, the tractive effort follows the trace of a–b–d–e–f. At point f, the electric motor reaches its maximum speed and the transmission has to be shifted to high gear for further acceleration. In this case the base speed of the vehicle in Equation 7.5 is V_{b1}. However, when a single-gear transmission is used, that is, only high gear is available, the tractive effort follows the trace of c–d–e–f–g, and $V_b = V_{b2}$.

It is obvious that for a given final speed during acceleration, such as 100 km/h at point e, the vehicle with a two-gear transmission will have a short acceleration time, because the tractive effort at low speed in low gear, represented by a–b–d, is larger than that in higher gear, represented by a–d.

Figure 7.15 shows an example of the power rating of motor versus speed ratio, which is defined as the ratio of maximum speed to base speed as shown in Figure 7.14.

It should be noted that the rated motor power determined by Equation 7.5 is only an estimate for meeting acceleration performance. In some special applications, such as in off-road military vehicles, the cross-country operation may be the primary concern. In this case, the traction motor must be powerful enough to overcome the required maximum grade of an off-road trail. The
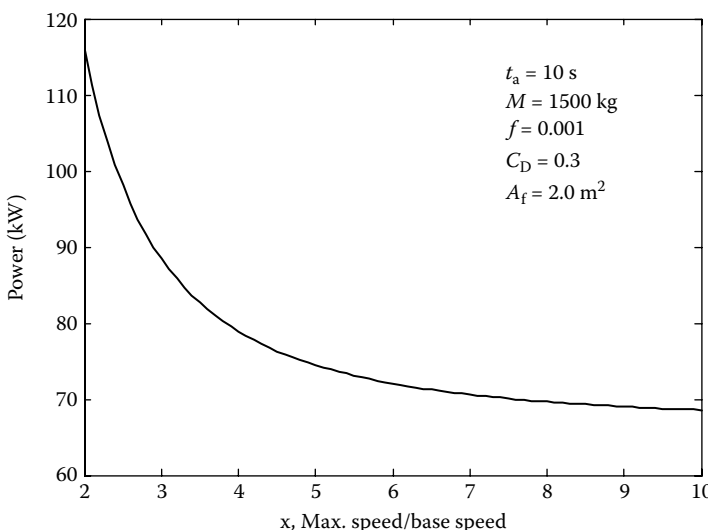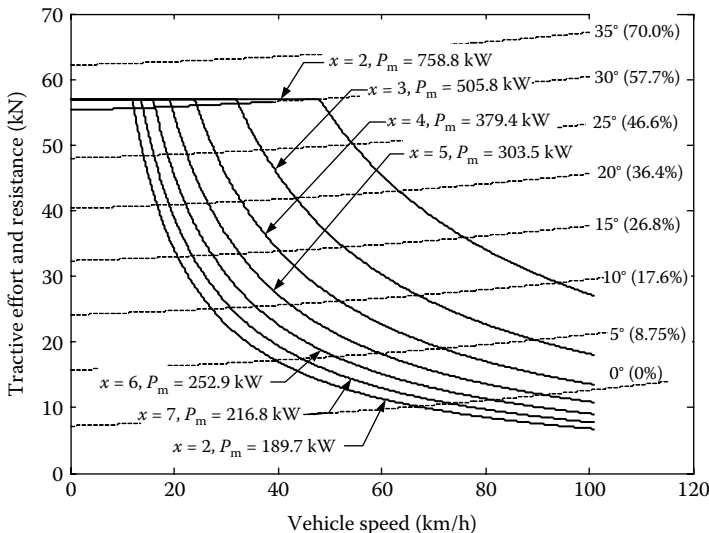
FIGURE 7.15 Power rating of traction power versus speed ratio of a drive train.

FIGURE 7.16 Tractive effort versus vehicle speed with different speed ratios and motor power.
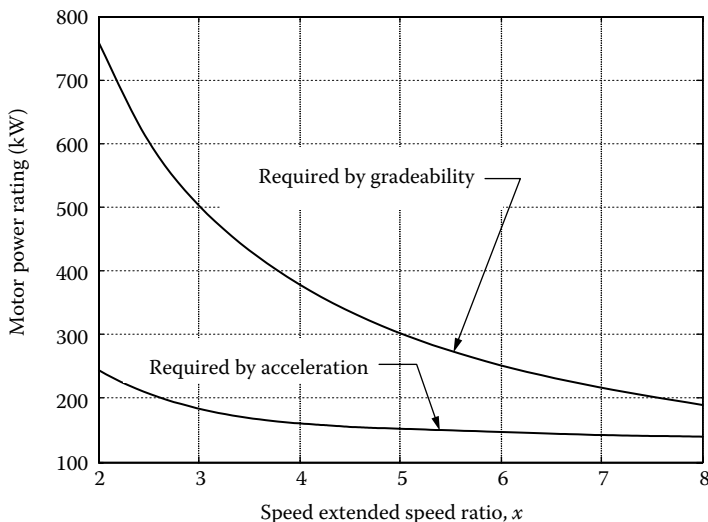
traction power in hill climbing can be expressed as

$$P_{grade} = \left(Mg f_r \cos\alpha + \frac{1}{2}\rho_a C_D A_f V^2 + Mg \sin\alpha \right) V (\text{W}), \qquad (7.6)$$

where α is the ground slope angle and V is the vehicle speed in m/s, specified by the gradeability requirement. When the off-road vehicle is climbing its required maximum slope, 60% or 31°, for example, at a speed of 10 km/h in real operation, the ground is usually unpaved and the rolling resistance is much larger than those of paved roads because of the road surface deformations. Therefore, in the calculation of motor power required for gradeability, additional resistance power should be added to reflect this situation.

Based on the specified gradeability requirement of 60% or 31° at 10 km/h, the tractive efforts versus vehicle speeds of a 10-ton military vehicle, with different extended speed ratios and motor power ratings, can be calculated by using Equation 7.6 as shown in Figure 7.16. It can be seen that larger extended speed ratios can effectively reduce the power rating requirement of the traction motor to meet the gradeability requirement. However, the speed on the maximum slope will be smaller. The large extended speed ratio can be implemented either by the motor itself or by a multigear transmission.

To ensure that the vehicle meets an acceleration requirement, for example, 8 s from zero to 48 km/h, the motor power rating requirement with different extended speed ratios on hard roads is also calculated by using Equation 7.5. Figure 7.17 shows the calculation results. It is obvious that motor power rating
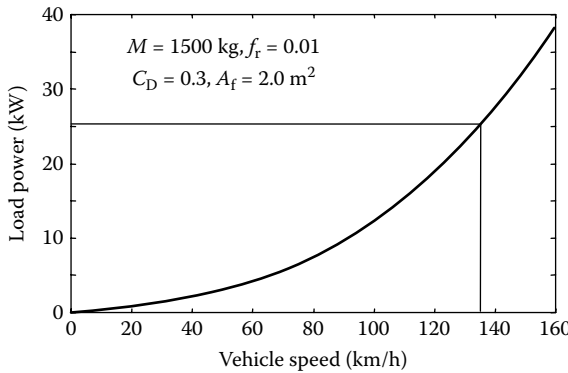
FIGURE 7.17 Motor power required by acceleration and gradeability along with extended speed ratios.

is determined by gradeability performance. This means that the power rating designed to meet the gradeability will naturally meet the acceleration requirement. In engineering design, trade-offs may need to be made between motor power rating and system complexity to design an appropriate motor extended speed ratio.

7.3.3 Power Rating Design of the Engine/Generator

As discussed in Chapter 5, the engine/generator in a series hybrid drive train is used to supply steady-state power in order to prevent the PPS from being discharged completely. In the design of the engine/generator, two driving conditions should be considered: driving for a long time at constant speed, such as highway driving and off-road driving on a soft road, and driving with a frequent stop–go pattern, such as driving in cities. With the first driving pattern, the vehicle should not rely on the PPS to support the operation at high speeds, for example, 130 km/h for on-road vehicles and 60 km/h for cross-country driving for off-road vehicles. The engine/generator should be able to produce sufficient power to support vehicle speed. For a frequent stop–go driving pattern, the engine/generator should produce sufficient power to maintain the energy store of the PPS at a certain level, so that enough power can be drawn to support vehicle acceleration and hill climbing. As mentioned above, the energy consumption of the PPS is closely related to the control strategy.

FIGURE 7.18 Load power of a 1500-kg passenger car at constant speed.

At a constant speed and on a flat road, the power output from the power source (engine/generator and/or the PPS) can be expressed as

$$P_{e/g} = \frac{V}{1000\eta_t\eta_m}\left(Mgf_r + \frac{1}{2}\rho_a C_D A_f V^2\right) \text{ (kW)}, \qquad (7.7)$$
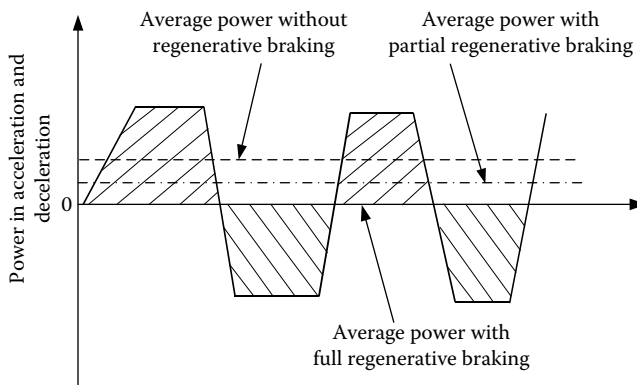
where η_t and η_m are the efficiencies of transmission and traction motor, respectively. Figure 7.18 shows an example of the load power (not including η_t and η_m, curve versus vehicle speed) for a 1500-kg passenger car. It indicates that the power demand at constant speed is much less than that for acceleration (refer to Figure 7.15). In this example, about 35 kW (including losses in the transmission and traction motor, $\eta_t = 0.9$, $\eta_m = 0.8$, for example) is needed at a constant speed of 130 km/h.

When the vehicle is driving in a stop-and-go pattern in urban areas, the power that the engine/generator produces should be equal to or slightly greater than the average load power in order to maintain balanced PPS energy storage. The average load power can be expressed as

$$P_{ave} = \frac{1}{T}\int_0^T \left(Mgf_r + \frac{1}{2}\rho_a C_D A_f V^2\right)V\,dt + \frac{1}{T}\int_0^T \delta M\frac{dV}{dt}\,dt, \qquad (7.8)$$
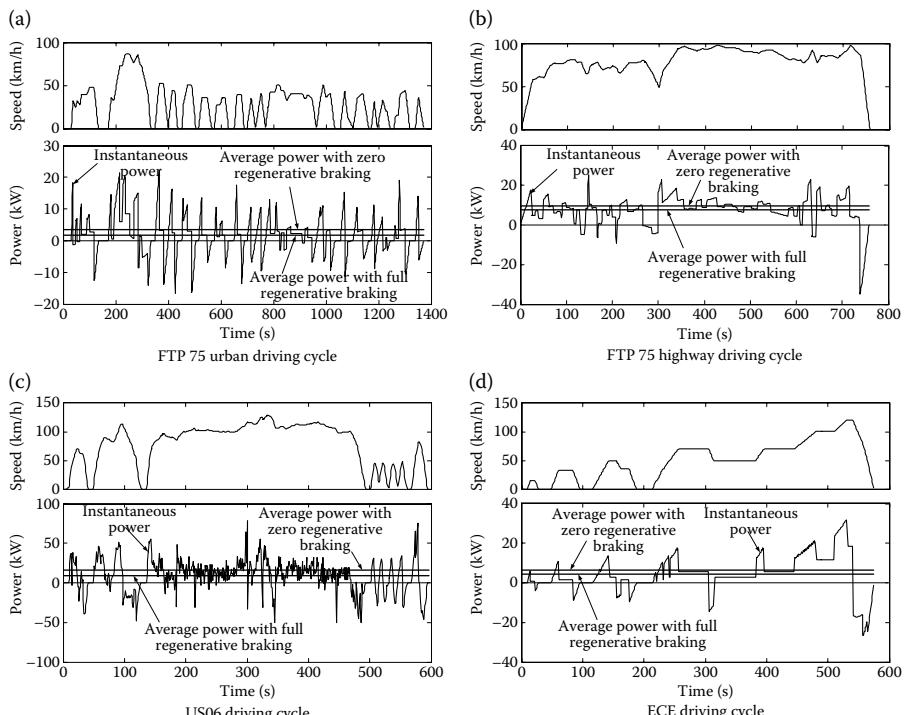
where δ is the vehicle rotational inertia factor (refer to Chapter 2) and dV/dt is the acceleration of the vehicle. The first term in Equation 7.8 is the average power that is consumed to overcome the tire rolling resistance and aerodynamic drag. The second term is the average power consumed in acceleration and deceleration. When the vehicle has the ability to recover all the kinetic energy of the vehicle, the average power consumed in acceleration and deceleration is zero. Otherwise, it will be greater than zero, as shown in Figure 7.19.

In the design of an engine/generator system, the power capability should be greater than, or at least not less than, the power that is needed to support
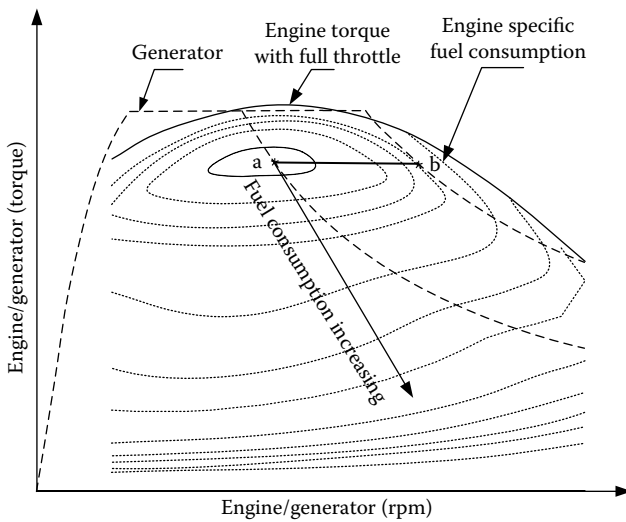
FIGURE 7.19 Average power consumed in acceleration and deceleration with full, partial, and zero regenerative braking.

the vehicle driving at a constant speed (highway driving) and at average power when driving in urban areas. In actual design, some typical urban drive cycles must be used to predict the average power of the vehicle, as shown in Figure 7.20.

FIGURE 7.20 Instantaneous power and average power with full and zero regenerative braking in typical drive cycles. (a) FTP75 urban, (b) FTP75 highway, (c) US06, and (d) ECE-15.

FIGURE 7.21   Operating point of the engine/generator.

In the engine/generator size design, the operating point at which the engine/generator produces the above power should be determined. In fact, there are two possible designs. One approach is to design the engine operating point at its most efficient point as shown by point a in Figure 7.21. At this operating point, the engine produces the needed power as discussed above. This design will lead to a somewhat larger engine, since its maximum power will not be used most of the time. This design has the advantage of more power being available for special situations. For instance, when the PPS is completely discharged or has failed, the engine/generator can be operated at a higher power (point b) to ensure that the vehicle performance has not suffered too much. The larger engine power can also be used to quickly charge the PPS. Shifting of the operating point from a to b, as shown in Figure 7.21, will cause the bus voltage to increase, due to the increase in the speed. With a properly designed traction motor control, higher voltage will not affect the operation of the traction motor. On the contrary, the higher DC bus voltage will enable the motor to produce higher power.

Another design approach is to design the operating point at point b, that is, close to the engine maximum power, to meet the acceleration and gradeability requirements as discussed above. This design will lead to a smaller engine. However, its operating efficiency is somewhat lower than the former design with no excess power to support the vehicle.

7.3.4   Design of PPS

The PPS must be capable of delivering sufficient power to the traction motor at any time. At the same time, the PPS must store sufficient energy to avoid failure of power delivery due to too-deep discharging.

7.3.4.1 Power Capacity of PPS

To fully utilize traction motor power capacity, the total power of the engine/generator and PPS should be greater than, or at least equal to, the rated maximum power of the electric motor. Thus, the power capacity of the PPS can be expressed as

$$P_{pps} \geq \frac{P_{m,max}}{\eta_m} - P_{e/g}, \tag{7.9}$$
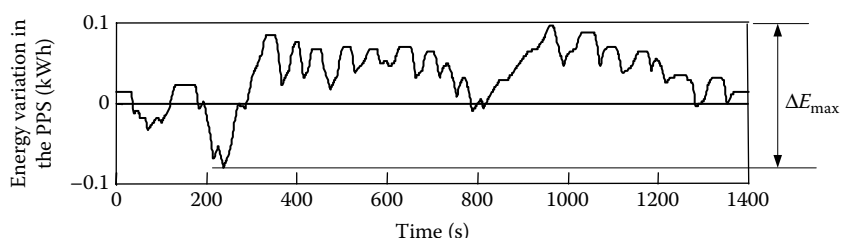
where $P_{m,max}$ is the maximum rated power of the motor, η_m is the efficiency of the motor, and $P_{e/g}$ is the power of the engine/generator system at its designed operating point.

7.3.4.2 Energy Capacity of PPS

In some driving conditions, a frequent accelerating/decelerating driving pattern would result in a low SOC in the PPS, thus losing its delivery power. To properly determine the energy capacity of the PPS, the energy variations in some typical drive cycles must be known. The energy variation in the PPS can be expressed as

$$\Delta E = \int_0^T P_{pps}\, dt, \tag{7.10}$$

where P_{pps} is the power of the PPS. Positive P_{pps} represents charging power and negative P_{pps} represents discharging power. It is obvious that the energy variation in the PPS is closely associated to the control strategy. Figure 7.22 shows an example in which the energy changes in the PPS vary with driving time in the FTP75 urban driving cycle with the maximum SOC control strategy. Figure 7.22 also shows the maximum amount of energy changes, ΔE_{max}, in the whole drive cycle, if the SOC of the PPS is allowed in the operating range between SOC_{top} and SOC_{bott}. The whole energy capacity of the PPS can be determined by Equation 7.11. The operating range of the SOC of the PPS depends on the operating characteristics of the PPS. For example, for efficiency reasons, chemical batteries would have an optimal operating range in

FIGURE 7.22 Energy variations in an FTP75 urban drive cycle with Max. SOC control strategy.

the middle (0.4–0.7), and for limited voltage variation reasons, ultracapacitors would only have a very limited energy change range (0.8–1.0).

$$E_{cap} = \frac{\Delta E_{max}}{SOC_{top} - SOC_{bott}}. \tag{7.11}$$

7.4 Design Example

Design specification
Parameters
Vehicle total mass: 1500 kg
Rolling resistance coefficient: 0.01
Aerodynamic drag coefficient: 0.3
Front area: 2.0 m^2
Transmission efficiency (single gear): 0.9
Performance specification
Acceleration time (from 0 to 100 km/h): 10 ± 1 s
Maximum gradeability: >30% at low speed and >5% at 100 km/h
Maximum speed: 160 km/h

7.4.1 Design of Traction Motor Size
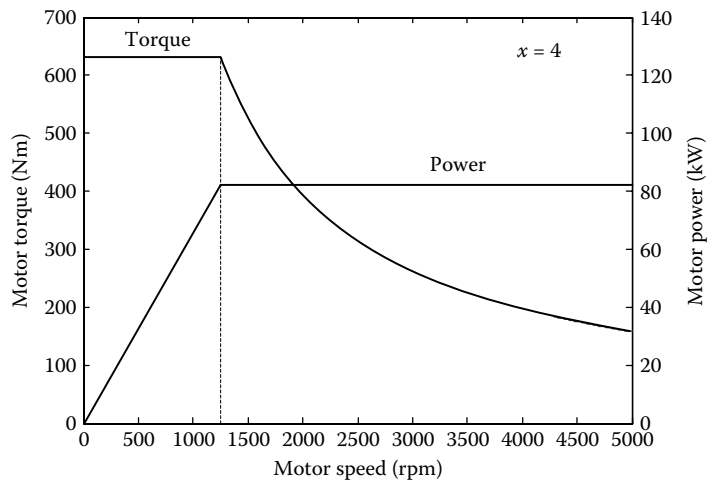
Using Equation 7.5 and assuming the motor drive has a speed ratio of $x = 4$, the motor drive power rating can be obtained as 82.5 kW for the specified acceleration time of 10 s from zero to 100 km/h. Figure 7.23 shows the speed–torque and speed–power profiles of the traction motor.

7.4.2 Design of the Gear Ratio

The gear ratio is designed so that the vehicle reaches its maximum speed at the motor maximum speed, that is,

$$i_g = \frac{\pi n_{m,max} r}{30 V_{max}}, \tag{7.12}$$
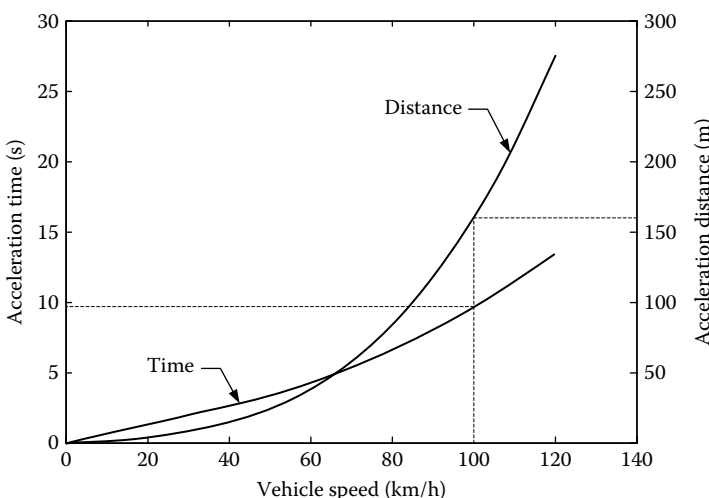
where $n_{m,max}$ is the maximum motor rpm, V_{max} is the maximum speed of the vehicle in m/s, and r is the radius of the tire. Suppose $n_{m,max} = 5000$ rpm and $V_{max} = 44.4$ m/s (160 km/h or 100 mph), and $r = 0.2794$ m (11 in.); $i_g = 3.29$ is obtained.

FIGURE 7.23 Characteristics of traction motor versus motor rpm.

7.4.3 Verification of Acceleration Performance
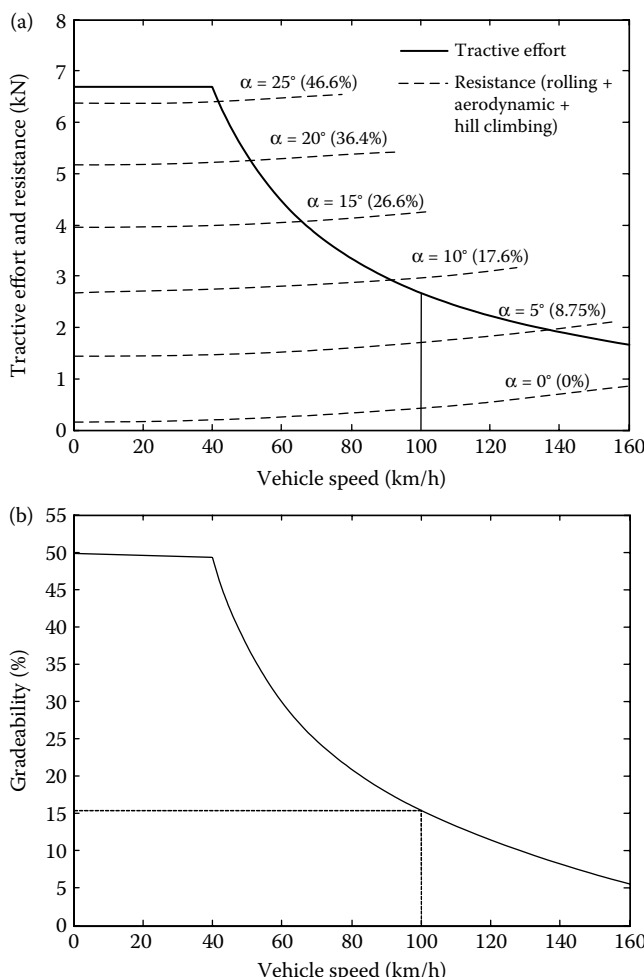
Based on the torque–speed profile of the traction motor, gear ratio, and vehicle parameters, and using the calculation method discussed in Chapters 2 and 4, vehicle acceleration performance (acceleration time and distance versus vehicle speed) can be obtained as shown in Figure 7.24. If the acceleration time obtained does not meet the design specification, the motor power rating should be redesigned.

FIGURE 7.24 Acceleration time and distance versus vehicle speed.

7.4.4 Verification of Gradeability

Using the motor torque–speed profile, gear ratio, and vehicle parameters, and the equations described in Chapters 2 and 4, the tractive effort and resistance versus vehicle speed can be calculated as shown in Figure 7.25a. Further, the gradeability of the vehicle can be calculated as shown in Figure 7.25b. Figure 7.25 indicates that the gradeability calculated is much greater than that specified in the design specification. This result implies that for a passenger car, the power needed for acceleration performance is usually larger than that needed for gradeability; the former determines the power rating of the traction motor.

FIGURE 7.25 Tractive effort, resistance, and gradeability of the vehicle versus speed: (a) tractive effort and resistance and (b) gradeability.
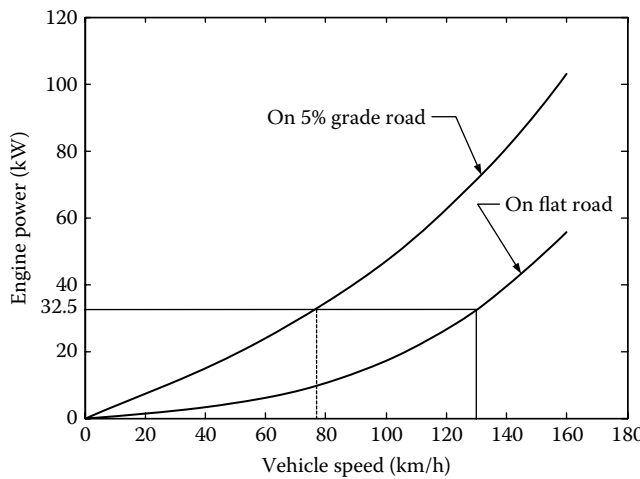
FIGURE 7.26   Engine power versus vehicle constant speed on a flat road and a 5% grade road.

7.4.5   Design of Engine/Generator Size

The power rating of the engine/generator is designed to be capable of supporting the vehicle at a regular highway speed (130 km/h or 81 mph) on a flat road. Figure 7.26 shows that the engine power needed at 130 km/h or 81 mph is 32.5 kW, in which energy losses in transmission (90% of efficiency), motor drive (85% of efficiency), and generator (90% of efficiency) are involved. Figure 7.26 also indicates that 32.5 kW of engine power can be capable of supporting the vehicle driving at 78 km/h (49 mph) on a 5% grade road.
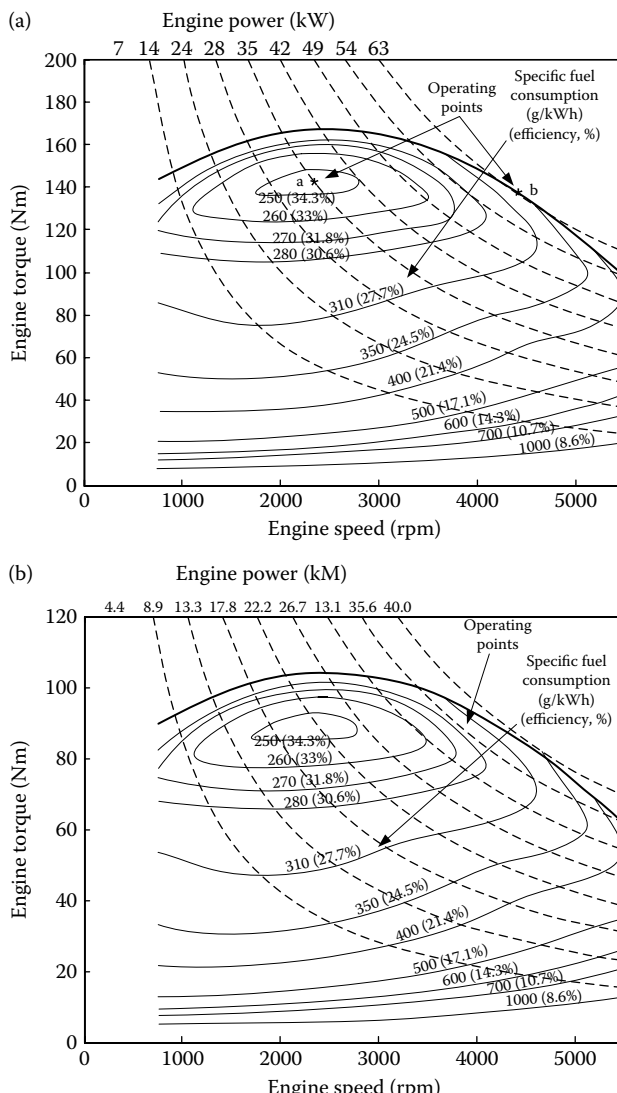
Another consideration in the design of the power rating of the engine/generator is the average power when driving with some typical stop-and-go driving patterns as illustrated in Figure 7.20. The typical data in these drive cycles are listed in Table 7.1.

TABLE 7.1

Typical Data of the Different Drive Cycles

	Max. Speed (km/h)	Average Speed (km/h)	Average Power with Full Regen. Braking (kW)	Average Power without Regen. Braking (kW)
FTP75 urban	86.4	27.9	3.76	4.97
FTP75 highway	97.7	79.6	12.6	14.1
US06	128	77.4	18.3	23.0
ECE-1	120	49.8	7.89	9.32

Compared with the power needed in Figure 7.25, the average power in these driving cycles is smaller. Hence, 32.5 kW of engine power can meet the power requirement in these drive cycles. Figure 7.27 shows the engine characteristics. The engine would need to supply additional power to support the continuous nontraction loads, such as lights, entertainment, ventilation, air conditioning, power steering, brake boosting, and so on. In summary, the engine needs to

FIGURE 7.27 Engine characteristics and operating points: (a) operating with best efficiency and (b) operating with close maximum power.

produce about 35 kW of power to support the vehicle at 130 km/h on a flat road, without the need for power assistance from the PPS. This power can sufficiently meet the average power requirement for the stop-and-go driving pattern in urban areas.

Figure 7.27a shows the engine fuel consumption map and the minimum fuel consumption operating point (point a) at which 35 kW of power is produced. It can be seen that the maximum engine power is about 63 kW at point b. Another design of the engine power is shown in Figure 7.27b, in which the engine operating point is designed close to its maximum power to produce the power demand of 35 kW. The engine size in this design is smaller than the former design, but the fuel consumption is higher than the former design at 35 kW power level. As discussed above, this power is for 130 km/h of constant speed on a flat road. At lower speeds or driving in urban areas in which the average load power is much less, the latter design may not show higher fuel consumption than the former.

7.4.6 Design of the Power Capacity of PPS

The sum of the output power of the engine/generator and PPS should be greater than, or at least equal to, the input power of the traction motor. That is,

$$P_{pps} = \frac{P_{motor}}{\eta_{motor}} - P_{e/g} = \frac{82.5}{0.85} - 32.5 = 64.5 \text{ kW}, \tag{7.13}$$
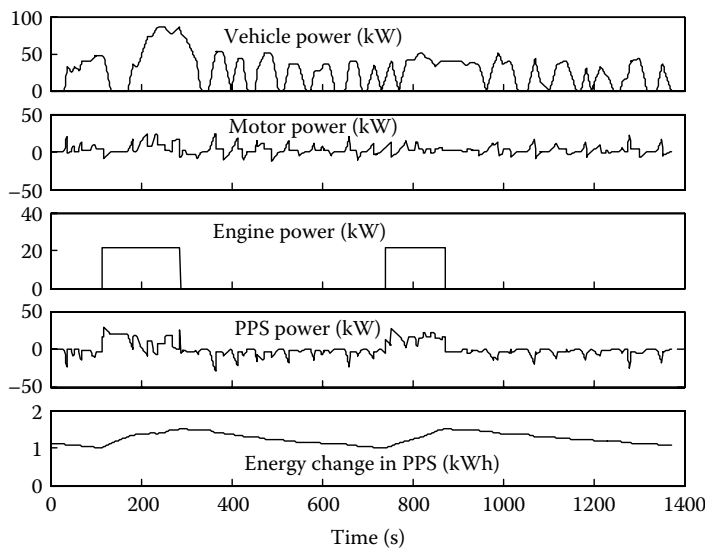
where 32.5 kW is the power of the engine/generator for traction.

7.4.7 Design of the Energy Capacity of PPS

The energy capacity of the PPS depends heavily on drive cycle and overall control strategy. In this design, because the power capacity of the engine/generator is much greater than the average load power (refer to Figure 7.20), the engine on–off (thermostat) control strategy is considered to be appropriate.
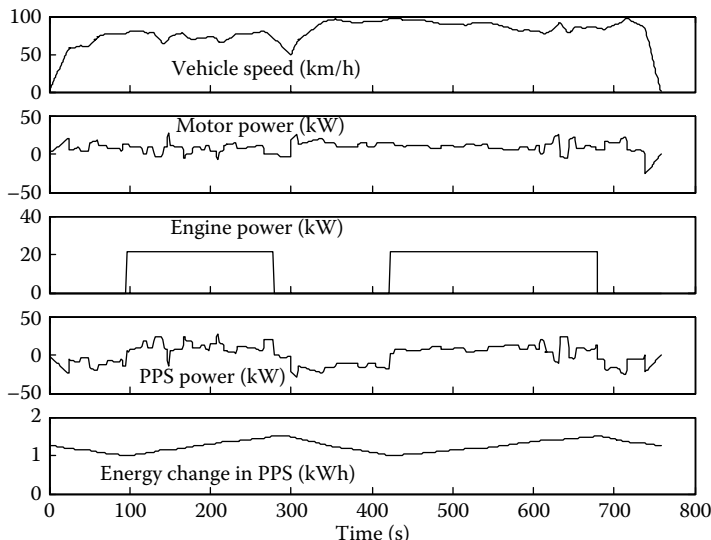
Figure 7.28 shows the simulation results of the above vehicle with engine on–off control strategy in the FTP75 urban drive cycle. In the simulation, regenerative braking is involved (see Chapter 13, Regenerative Braking). In the control, the allowed maximum energy variation in PPS is 0.5 kWh. Suppose that the PPS is allowed to operate in the SOC range of 0.2. Using batteries as the PPS, operating in the range of 0.4–0.6 of SOC will have optimal efficiency. Using ultracapacitors, 0.2 variation of SOC will limit the terminal voltage to 10%. The total storage energy in the PPS can be calculated as

$$E_{pps} = \frac{\Delta E_{max}}{\Delta SOC} = \frac{0.5}{0.2} = 2.5 \text{ kWh}. \tag{7.14}$$

FIGURE 7.28   Simulation results in an FTP75 urban drive cycle.

The weight and volume of the PPS are determined by its power capability or energy capability, depending on the power and energy density ratings of the PPS. For batteries, power density is usually the determining factor, whereas for ultracapacitors, energy density is usually the determining factor. A hybrid

FIGURE 7.29   Simulation results in an FTP75 highway drive cycle.

PPS, both battery and ultracapacitors, would be much smaller and lighter than using any one of the above. For details, refer to Chapter 12, Energy Storage.

7.4.8   Fuel Consumption

The fuel consumption in various drive cycles can be calculated by simulation. In the simulation in this example, the engine as shown in Figure 7.27b is used. When the engine is on, its power output is around 20 kW, corresponding to its best fuel efficiency operating point. In the FTP75 urban drive cycle (Figure 7.28), the vehicle has a fuel economy of 5.57 L/100 km or 42.4 miles per gallon (mpg), and in the FTP highway drive cycle (Figure 7.29), 5.43 L/100 km or 43.5 mpg. It is clear that a hybrid vehicle with a similar performance to a conventional vehicle is much more efficient, especially in the frequent stop-and-go environment. The main reasons are the high operating efficiency of the engine and the significant amount of braking energy recovered by regenerative braking. Regenerative braking techniques are described in Chapter 13.

References

1. C. C. Chan and K. T. Chau, *Modern Electric Vehicle Technology*, Oxford University Press, New York, 2001.
2. C. G. Hochgraf, M. J. Ryan, and H. L. Wiegman, "Engine control strategy for a series hybrid electric vehicle incorporating load-leveling and computer controlled energy management," *Society of Automotive Engineers (SAE) Journal*, Paper No. 960230, Warrendale, PA, 2002.
3. M. Ender and P. Dietrich, "Duty cycle operation as a possibility to enhance the fuel economy of an SI engine at part load," *Society of Automotive Engineers (SAE) Journal*, Paper No. 960227, Warrendale, PA, 2002.
4. M. Ehsani, Y. Gao, and K. Butler, "Application of electric peaking hybrid (ELPH) propulsion system to a full size passenger car with simulation design verification," *IEEE Transactions on Vehicular Technology*, 48 (6), November 1999.
5. C. C. Chan, "The state of the art of electric and hybrid, and fuel cell vehicles," *Proceedings of the IEEE, Special issue on Electric, Hybrid and Fuel Cell Vehicles*, Vol. 95, No. 4, April 2007.
6. Jih-sheng (Jason) Lai and D. J. Nelson, "Energy management power converters in hybrid hlectric and fuel cell vehicles," *Proceedings of the IEEE, Special issue on Electric, Hybrid and Fuel Cell Vehicles*, Vol. 95, No. 4, April 2007.

8

Parallel (Mechanically Coupled) Hybrid Electric Drive Train Design

Unlike the series hybrid drive train, the parallel or mechanically coupled hybrid drive train has features that allow both the engine and the traction motor to apply their mechanical power in parallel directly to the driven wheels. As mentioned in Chapter 5, the mechanical coupling has two forms: torque and speed couplings. When using conventional IC engines as the primary power source, torque coupling is more appropriate since the IC engine is essentially a torque source.
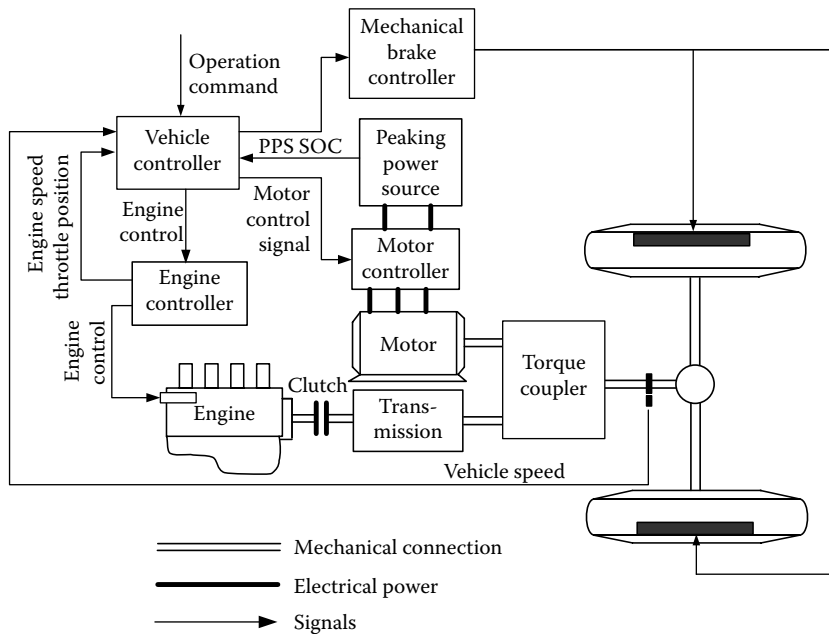
The major advantages of a torque-coupling parallel configuration over a series configuration are (1) nonnecessity of a generator, (2) a smaller traction motor, and (3) only part of the engine power going through multipower conversion. Hence, the overall efficiency can be higher than in the series hybrid.[1] However, control of the parallel hybrid drive train may be more complex than that of the series hybrid drive train, because of the simultaneous mechanical coupling between the engine and the driven wheels.

There are many possibilities of configurations in a parallel hybrid drive train, as mentioned in Chapter 5. The design methodology for one configuration may not be applicable to others. Each particular configuration may be only applicable to the specified operation environment and mission requirement. This chapter will focus on the design methodology of parallel drive trains with torque coupling, which operates with the electrically peaking principle. That is, the engine supplies its power to meet the base load (operating at a given constant speed on flat and mild grade roads, or the average of the load of a stop-and-go driving pattern) and the electric motor supplies the power to meet the peak load requirement. Other options, such as a mild hybrid drive train, are discussed in Chapter 11.

8.1 Drive Train Configuration and Design Objectives

The drive train structure of the parallel (torque coupling) hybrid vehicle is shown in Figure 8.1. The control system of the drive train consists of a vehicle controller, an engine controller to control the engine power, an electric motor

FIGURE 8.1   Configuration of the parallel torque-coupling hybrid drive train.
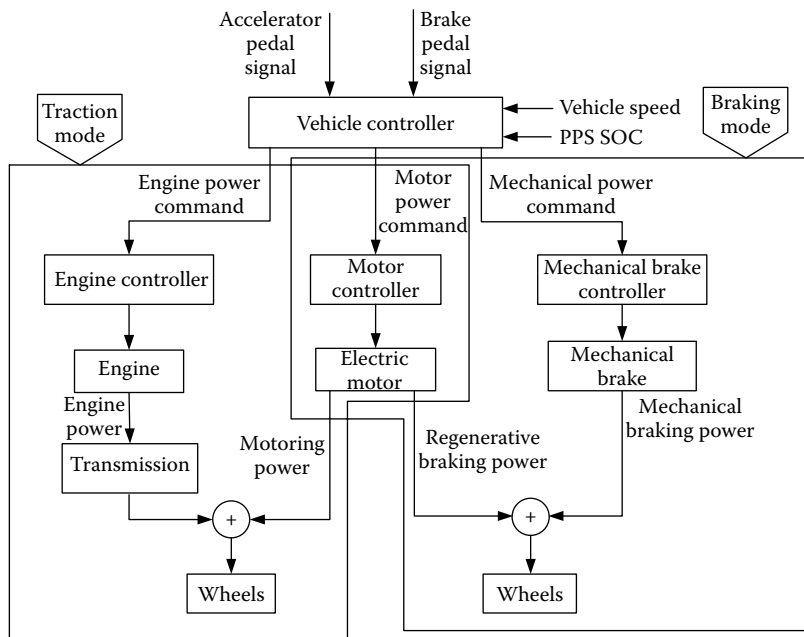
controller, and, perhaps, a mechanical brake controller and clutch controller. The vehicle controller is the highest level controller. It receives the operation command from the driver through the accelerator and brake pedals, and other operating variables of the vehicle and its components, which includes vehicle speed, engine speed and throttle position, SOC of the PPS, and so on. By processing all the signals received, based on the embedded drive train control algorithm, the vehicle controller generates control commands and sends the commands to the corresponding component controllers. The component controllers control the corresponding components to carry out the commands coming from the vehicle controller. Since the torque coupler is uncontrollable, the power flow in the drive train can only be controlled by controlling the power sources, that is, the engine, traction motor, clutch, and mechanical brake.

In the drive train design, the important factors are the power of the engine, motor and PPS and its energy capacity, transmission, and more importantly the control strategy of the drive train. The design objectives are as follows: (1) satisfying the performance requirements (gradeability, acceleration, and maximum cruising speed), (2) achieving high overall efficiency whenever possible, (3) maintaining the SOC of PPS at reasonable levels during driving on highways and in urban areas without the need of charging the PPS from outside the vehicle, and (4) recovering brake energy as much as possible.

8.2   Control Strategies

The available operation modes in a parallel torque-coupling hybrid drive train, as mentioned in Chapter 5, mainly include the following: (1) engine-alone traction, (2) electric-alone traction, (3) hybrid traction (engine plus motor), (4) regenerative braking, and (5) PPS charging from the engine. During operation, proper operation modes should be used so as to meet the traction torque requirement, achieve high overall efficiency, maintain a reasonable level of SOC of the PPS, and recover braking energy as much as possible.[2-6]

The overall control scheme is schematically shown in Figure 8.2. It consists of the vehicle controller, engine controller, electric motor controller, and mechanical brake controller. The vehicle controller is at the highest level. It collects data from the driver and all the components, such as the desired torque from the driver, vehicle speed, SOC of the PPS, engine speed and throttle position, electric motor speed, and so on. Based on these data, the component characteristics and the preset control strategy, the vehicle controller gives its control signals to each component controller. Each component controller then controls the operation of the corresponding component to meet the requirement of the drive train.

FIGURE 8.2   Overall control scheme of the parallel torque-coupling hybrid drive train.

The vehicle controller plays a central role in the operation of the drive train. The vehicle controller should fulfill various operation modes, according to the data collected from components and the driver's command, and should give the correct control command to each component controller. Hence, the control strategy in the vehicle controller is the key in the success of the drive train operation.

8.2.1   Max. SOC-of-PPS Control Strategy

When a vehicle is operating in a stop-and-go driving pattern, the PPS must deliver its power to the drive train frequently. Consequently, the PPS tends to be discharged quickly. In this case, maintaining a high SOC in the PPS is necessary to ensure that the PPS is capable of delivering sufficient power to the drive train to support the vehicle's frequent acceleration. The basic rules in this control strategy are using the engine as the primary power source as much as possible and charging the PPS whenever the engine has excess power over that required for propulsion, without the PPS SOC exceeding its full charge limit.[3]

The maximum control strategy can be explained by Figure 8.3. In this figure, the maximum power curves for hybrid traction (engine plus electric motor), engine-alone traction, and electric motor-alone traction and regenerative braking are plotted against vehicle speed. Power demands in different conditions are also plotted, represented by points A, B, C, and D.

1: Maximum power with hybrid mode
2: Maximum power with electric alone traction
3: Engine power on its optimum operating line
4: Engine power with partial load
5: Maximum generative power of electric motor

P_L : Load power, traction or braking
P_e : Engine power
P_m: Motor traction power
P_{mb}: Motor braking power
P_{mc}: PPS charging power
P_{mf}: Mechanical braking power
V_{eb} : Vehicle speed corresponding to the engine minimum rpm

FIGURE 8.3   Demonstration of various operating modes based on power demand.

The operation modes of the drive train are explained below.

Motor-alone propelling mode: When the vehicle speed is less than a preset value V_{eb}, which is considered to be the bottom line of the vehicle speed below which the engine cannot operate stably, or operates with high fuel consumption or high emissions, the electric motor alone propels the vehicle. Meanwhile the engine is shut down or idles with the clutch open. The engine power, electric traction power, and PPS discharge power can be written as

$$P_e = 0, \tag{8.1}$$

$$P_m = P_L, \tag{8.2}$$

$$P_{\text{pps-d}} = \frac{P_m}{\eta_m}. \tag{8.3}$$

where P_e is the engine power output, P_L is the propelling power commanded by the driver, from the accelerator pedal, P_m is the power output of the electric motor, $P_{\text{pps-d}}$ is the PPS discharge power, and η_m is the motor efficiency.

Hybrid propelling mode: When the commanded propelling power, P_L, by the driver, represented by point A in Figure 8.3, is greater than the power that the engine can produce, both the engine and electric motor must deliver their power to the driven wheels at the same time. In this case, engine operation is set on its optimum operation line (point a) by controlling the engine throttle to produce power P_e. The remaining power demand is supplied by the electric motor. The motor power output and PPS discharge power are

$$P_m = P_L - P_e, \tag{8.4}$$

$$P_{\text{pps-d}} = \frac{P_m}{\eta_m}. \tag{8.5}$$

PPS charge mode: When the commanded propelling power, P_L, represented by point B in Figure 8.3, is less than the power that the engine can produce while operating on its optimum operation line, and the SOC of the PPS is below its top line, the engine is operated on its optimum operating line (point b), producing its power P_e. In this case, the electric motor is controlled by its controller to function as a generator, powered by the remaining power of the engine. The input power to the electric motor and PPS charge power are

$$P_m = (P_e - P_L)\eta_{t,e,m}, \tag{8.6}$$

$$P_{\text{pps-c}} = P_m\eta_m, \tag{8.7}$$

where $\eta_{t,e,m}$ is the transmission efficiency from the engine to the electric motor.

Engine-alone propelling mode: When the commanded propelling power, represented by point B in Figure 8.3, is less than the power that the engine can

produce while operating on its optimum operation line, and the SOC of the PPS has reached its top line, the engine-alone propelling mode is used. In this case, the electric system is shut down, and the engine is operated to supply its power that meets the load power demand. The power output curve of the engine with a partial load is represented by the dashed line in Figure 8.3. The engine power, electric power, and battery power can be expressed by

$$P_e = P_L, \tag{8.8}$$

$$P_m = 0, \tag{8.9}$$

$$P_{pps} = 0. \tag{8.10}$$

Regenerative-alone brake mode: When the vehicle experiences braking and the demanded braking power is less than the maximum regenerative braking power that the electric system can supply (as shown in Figure 8.3 by point C), the electric motor is controlled to function as a generator to produce its braking power that equals the commanded braking power. In this case, the engine is shut down or set idling. The electric power output from the motor and PPS charging power are

$$P_{mb} = P_L \eta_m, \tag{8.11}$$

$$P_{pps-c} = P_{mb}. \tag{8.12}$$

Hybrid braking mode: When the demanded braking power is greater than the maximum regenerative braking power that the electric system can supply (as shown in Figure 8.3 by point D), the mechanical brake must be applied. In this case, the electric motor should be controlled to produce its maximum regenerative braking power, and the mechanical brake system handles the remaining portion. The motor output power, PPS charging power, and mechanical braking power are
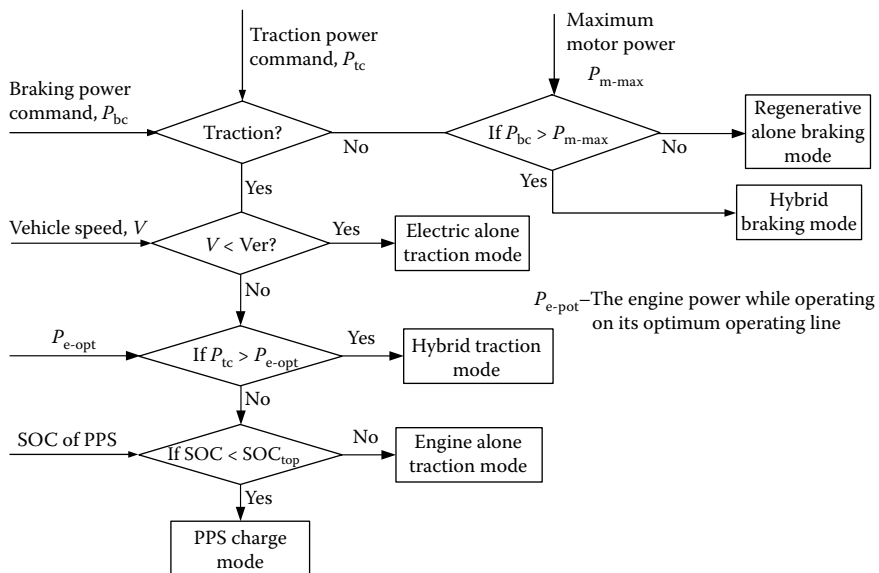
$$P_{mb} = P_{mb,max} \eta_m, \tag{8.13}$$

$$P_{pps-c} = P_{mb}, \tag{8.14}$$

$$P_{mf} = P_L - P_{mb}. \tag{8.15}$$

It should be noted that for good braking performance, the braking forces on the front and rear wheels should be proportional to their normal load on the wheels. Thus, braking power control will not be exactly that mentioned above (for more details, see Chapter 13, Regenerative Braking). The control flowchart of the Max. SOC-of-PPS is illustrated in Figure 8.4.

The major objective of this control strategy is using the engine as the vehicle primary mover as much as possible, with no pure electric traction, when the vehicle speed is higher than a present value. This control strategy minimizes

FIGURE 8.4 Flowchart of Max. SOC-of-PPS control strategy.
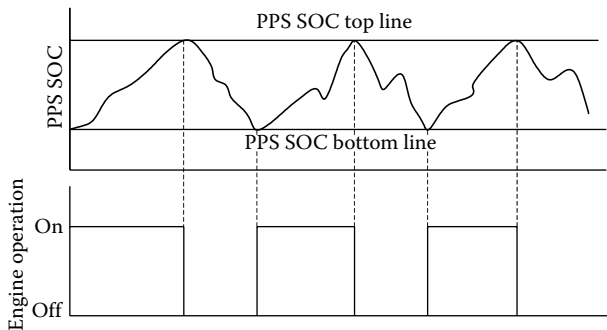
the part of engine energy that cycles through the electric motor and the PPS. This may reduce the engine energy transmission losses. However, when the PPS is fully charged and the vehicle load is small, the engine will be throttled down to meet the small load power. In this case, the engine will suffer a low operating efficiency.

8.2.2 Engine On–Off (Thermostat) Control Strategy

When the vehicle operates in a state in which the load power is less than the power that the engine produces with optimal operating efficiency, and the PPS is fully charged, the Max. PPS SOC control strategy will force the engine to operate away from its optimal operating region. Consequently, the overall efficiency of the vehicle would suffer. In this situation, the engine on–off (thermostat) control strategy may be used. In the engine on–off control strategy, the operation of the engine is controlled by the SOC of the PPS, as shown in Figure 8.5.

During the engine on period, the control is Max. PPS SOC strategy, in which the engine is always operated on its optimal curve. When the SOC of the PPS reaches its top line, the engine is turned off and the vehicle is propelled only by the electric motor. When the SOC of the PPS reaches its bottom line, the engine is turned on and the control again goes into Max. SOC-of-PPS.

It can be seen that this control strategy uses the electric motor as its primary power sources. The engine either operates in its optimal region or stops. Thus, the average operating efficiency of the engine is optimized. However, contrary

FIGURE 8.5   Illustration of engine on–off control strategy.

to the Max. SOC-of-PPS control strategy, the engine energy that goes through the electric motor and the PPS is also maximized, which may cause more energy losses in energy conversion.
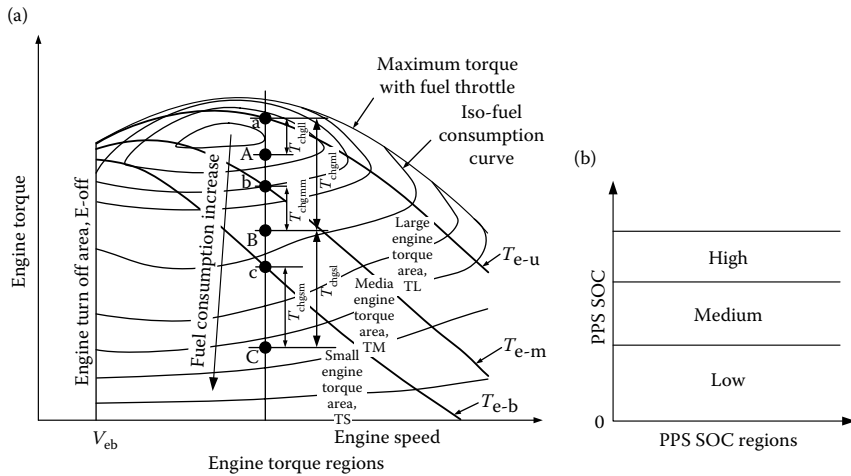
It should be noted that with this control strategy, the electric motor has to have sufficient power to meet the vehicle peaking power during the engine off periods.

8.2.3   Constrained Engine On–Off Control Strategy

The constrained engine on–off control strategy is the trade-off between the Max. SOC-of-PPS and engine on–off control strategies. The principle of this control strategy is to add the engine on and off operation in the Max. SOC-of-PPS control strategy. The control will be exactly the Max. SOC-of-PPS, when the vehicle speed is less than V_{eb}, and the commanded traction powers are at points A, C, and D as shown in Figure 8.3. However, when the commanded traction power is at point B shown in Figure 8.3, that is, less than the engine power with optimal efficiency, the engine can be operated with optimal throttle, partial throttle, or turned off, depending on the SOC of the PPS. This control strategy is explained by using the diagram of Figure 8.6.

The engine torque or power is divided into three special regions—the large torque area, TL, the medium torque area, TM, and the small torque area, TS—as shown in Figure 8.6a. These three torque areas are separated by the torque curves $T_{e\text{-}l}$, $T_{e\text{-}m}$, and $T_{e\text{-}s}$. These three curves may be generated by three special throttle openings. In Figure 8.6a, the isofuel consumption curves are also plotted. Similarly, the SOC of the PPS is also divided into three regions—high, medium, and low—as shown in Figure 8.6b. The engine control is based on the real-time commanded traction torque T_L and the SOC of the PPS. The suggested control strategy is illustrated in Figure 8.7.

When the commanded traction torque is in the TL area, as shown by point A in Figure 8.6a, and if the SOC of the PPS is in the medium or high region, the engine is controlled to produce its torque equal to the commanded traction

FIGURE 8.6 Illustration of the constrained engine on and off control strategy: (a) engine operation regions and (b) PPS SOC regions.

torque and no additional torque is produced to charge the PPS. However, if the SOC of the PPS is in the low region, the engine needs to produce more torque to charge the PPS. In this case, the engine is controlled to operate on its optimal efficiency line, represented by point a. The charging torque is T_{chgll} as shown in Figure 8.6a.

PPS SOC / Commanded torque, T_L	Low	Medium	High
In small area (point C)	$T_e = T_b$ $T_{chgsl} = T_b - T_c$	$T_e = T_c$ $T_{chgsm} = T_c - T_c$	$T_e = 0$ $T_{chgsh} = 0$
In medium area (point B)	$T_e = T_a$ $T_{chgml} = T_a - T_B$	$T_e = T_b$ $T_{chgmm} = T_b - T_B$	$T_e = T_B$ $T_{chgmh} = 0$
In large area (point A)	$T_e = T_a$ $T_{chgll} = T_a - T_A$	$T_e = T_A$ $T_{chglh} = 0$	$T_e = T_A$ $T_{chglh} = 0$

T_A, T_B, T_C --- Commanded traction torques in large, medium, and low torque areas, corresponding to point A, B, and C in Figure 8.6(a)

T_a, T_b, T_c --- Torques that engine is controlled to produce, corresponding to point a, b, and c

T_{chgxx} --- PPS charging torque, footnote xx = lh--- large torque, low SOC, and so on

T_e --- Engine torque

FIGURE 8.7 Engine torque control strategy with different commanded traction torque and PPS SOC.

When the commanded traction torque is in the TM area, as shown by point B in Figure 8.6a, and if the SOC of the PPS is in the high region, the engine is controlled to produce its torque equal to the commanded traction torque with no additional engine torque to charge the PPS. Otherwise if the SOC of the PPS is in the medium region, the engine torque is controlled on the top boundary line of this area, as shown by point b in Figure 8.6a. The PPS charging torque is T_{chgmm}. However, if the SOC of the PPS is in the low region, and in order to quickly bring the SOC of the PPS to the medium level, the engine is controlled to operate on the optimal efficiency line as shown by point a in Figure 8.6a. The PPS charging torque is T_{chgml}.

When the commanded traction torque is in the TS area as shown by point C in Figure 8.6a, and if the SOC of the PPS is in the high region, the engine is shut down and the electric motor alone propels the vehicle. If the SOC of the PPS is in the medium region, the engine is controlled to operate on the upper boundary line of this area, as shown by point c in Figure 8.6a. The PPS charging torque is T_{chgsm}. However, if the SOC of the PPS is in the low region, the engine is controlled to operate at point a, as shown in Figure 8.6a, to quickly bring the SOC of the PPS to the medium region. The PPS charging torque is T_{chgsl}.

Figure 8.7 summarizes engine control in all the commanded engine traction torque areas and SOC regions of the PPS.

8.2.4 Fuzzy Logic Control Technique

The above engine and electric motor control strategy can be further developed by using fuzzy logic control methods, based on the commanded traction torque and SOC of the PPS. In fuzzy logic language, input variables of the commanded traction torque and SOC of the PPS are described by linguistic values as high (H), medium (M), and low (L). The output variables of the commanded engine torque are described as high (H), medium (M), low (L), and a crisp value zero (Z). Similarly, the electric motor torques are described as negative high (NH), negative medium (NM), negative low (NL), zero (Z, a crisp value), positive low (PL), positive medium (PM), and positive high (PH). Positive torque is for traction and negative is for generating. The control rules are very similar to those described in Figure 8.7. The block diagram of the fuzzy logic control is shown in Figure 8.8.

In Figure 8.8, only the engine torque is determined by the fuzzy logic control rules, based on the SOC of the PPS and the commanded traction torque. The motor torque will be obtained from the commanded traction torque and the engine torque is obtained from fuzzy logic, that is,

$$T_m = T_{ct} - T_e.$$

Since this control strategy is for the operation mode in which the commanded traction torque, T_{ct}, is smaller than the maximum torque that the

Rule base					
T_{ct} T_e	SOC	L	M	H	
L		H	M	Z	
M		H	H	M	
H		H	H	H	

T_{ct} : Commanded traction torque
T_e : Engine torque
T_m : Motor torque
$\mu_{T_{ct}}$: Membership of T_{ct}
μ_{SOC}: Membership of PPS SOC
μ_{T_e} : Membership of T_e

PPS SOC → T_{ct} → Fuzzification → μ_{SOC}, $\mu_{T_{ct}}$ → Inference (Control rules) → μ_{T_e} → Defuzzification → T_e → $T_m = T_{ct} - T_e$ → T_m
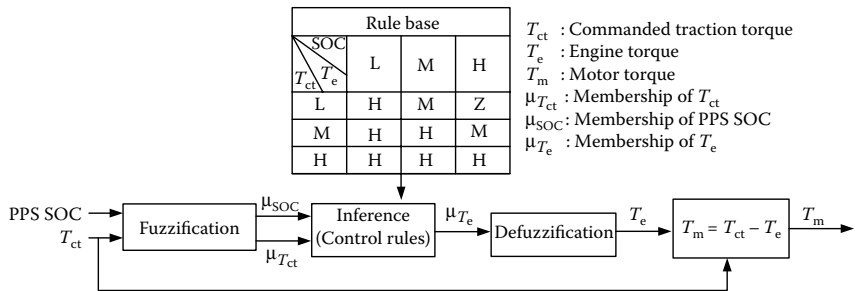
FIGURE 8.8   Block diagram of fuzzy logic control.

engine can produce with its optimal efficiency curve, as shown by point B in Figure 8.3, the commanded traction torque, T_{ct}, and the engine torque, T_e, have the same boundary, that is, from zero to maximum. Thus T_{ct} and T_e have the same membership function. A possible one is shown in Figure 8.9a, and a possible membership function of the SOC of PPS is shown in Figure 8.9b. The standard procedure to solve fuzzy logic control problems will not be discussed here. Readers should refer the associated references.[7–11]

It has to be noted that the threshold or fuzzy logic control strategies discussed above are based on the experience and knowledge about the drive train operation. Real-time operation is the most reliable way of obtaining this
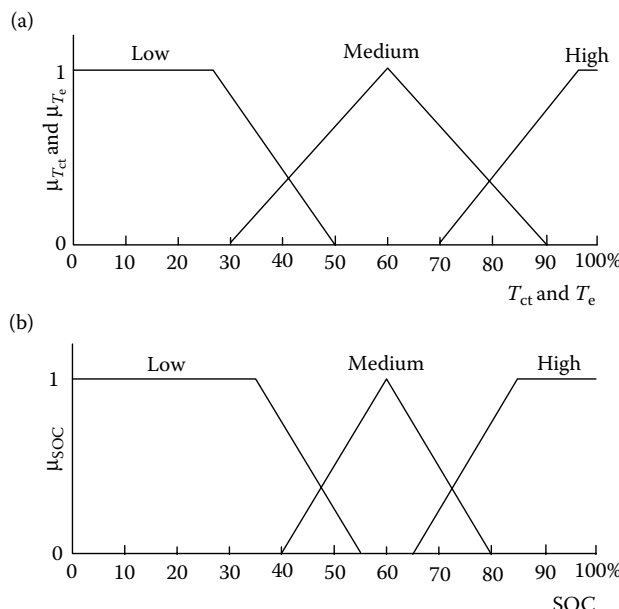
FIGURE 8.9   Membership functions of (a) T_{ct}, T_e and (b) SOC.

experience and knowledge. However, it requires a long time and involves high cost. Another effective way is by using simulation technologies to tune the control parameters iteratively until achieving optimal parameters for the specified operation environment. This work may be time consuming. It is easier to use off-line optimization technologies than iteratively running rules/fuzzy logic-based simulation to obtain the optimal control parameters. Dynamic programming is one of these techniques.[12,13]

8.2.5   Dynamic Programming Technique

The basic idea of the control algorithm using the dynamic programming technique considers the dynamic nature of the HEV system when performing the optimization. Furthermore, the optimization is with respect to the time horizon, rather than for an instant in time,[12,13,14] that is, for the whole driving cycle.

Contrary to the rule-based fuzzy logic control algorithm, the dynamic optimization approach usually relies on a drive train model to compute the best control strategy. The model can be either analytical or numerical. For a given driving cycle, the optimal operating strategy to achieve the best fuel economy can be obtained by solving a dynamic optimization problem. The problem formulation is described in the following.[12,13]

In the discrete-time format, a model of the HEV can be expressed as

$$x(k+1) = f(x(k), u(k)), \qquad (8.16)$$

where $u(k)$ is the vector of control variables such as engine throttle opening, desired motor torque, gear shift command of the transmission, and so on and $x(k)$ is the vector of state variables of the system, which is the response to control variables $u(k)$. The goals of the optimization are to find the optimal control input $u(k)$, to minimize the total fuel consumption, or the combination of total consumption and total emission over a given driving cycle.[14] The total fuel consumption or the combined fuel consumption and emission is defined as a cost function to be minimized. In the following expression, only the total fuel consumption is included in the cost function:

$$J = \text{Fuel} = \sum_{k=0}^{N-1} L(x(k), u(k)), \qquad (8.17)$$

where N is the time length of the driving cycle and L is the instantaneous fuel consumption rate, which is a function of the system state x and input u.

In the minimizing procedure of Equation 8.17, some constraints have to be imposed to ensure that all the operating parameters are within their valid

ranges. These constraints include

$$\omega_{e\text{-min}} \leq \omega_e \leq \omega_{e\text{-max}}, \tag{8.18}$$

$$0 \leq T_e \leq T_{e\text{-max}}, \tag{8.19}$$

$$0 \leq \omega_m \leq \omega_{m\text{-max}}, \tag{8.20}$$

$$T_{m\text{-min}} \leq T_m \leq T_{m\text{-max}}, \tag{8.21}$$

$$\text{SOC}_{\min} \leq \text{SOC} \leq \text{SOC}_{\max}, \tag{8.22}$$

where ω_e is the engine angular velocity; $\omega_{e\text{-min}}$ and $\omega_{e\text{-max}}$ are the specified minimum and maximum engine angular velocities, respectively; T_e is the engine torque, which must be greater than or equal to zero and smaller than or equal to its maximum torque at the corresponding angular velocity; ω_m is the motor angular velocity, which is defined in the range of zero to its maximum; T_m is the motor torque; $T_{m\text{-min}}$ is the minimum motor torque, which may be the maximum generating torque (negative); $T_{m\text{-max}}$ is the maximum motor torque in traction; and SOC is the SOC of the PPS, which is constrained to the range of its bottom $\text{SOC}_{\min}$ and top $\text{SOC}_{\max}$ levels. In order to sustain the charge of the PPS (PPS SOC at the end of the driving cycle is not lower than that at the beginning of the driving cycle), a final state constraint for the SOC of the PPS should be imposed. Thus a soft terminal constraint on PPS SOC (quadratic penalty function) is added to the cost function as follows[12,13]:

$$J = \text{Fuel} = \sum_{k=0}^{N-1} L(x(k), u(k)) + G(x(N)), \tag{8.23}$$

where $G(x(N)) = \alpha(\text{SOC}(N) - \text{SOC}_f)^2$ represents the penalty associated with the error in the SOC at the end of the driving cycle; SOC_f is the desired SOC at the end of the driving cycle, which may be set equal to the SOC at the beginning of the driving cycle, and α is a weight factor.

Dynamic programming is well known for requiring computations that grow exponentially with the number of states.[12,15] Therefore, a simplified vehicle and components model is necessary. The engine, electric motor, PPS, transmission, and so on may need to be reduced to static models with look-up tables for I/O mapping and efficiencies.

Standard procedures to solve the above optimization problem based on Bellman's principle of optimality are given by Lin et al.[12] and Betsekas.[15] The dynamic programming algorithm is presented as follows:

Step $N - 1$:

$$J_{N-1}^*(x(N - 1)) = \min_{u(N-1)} [L(x(N - 1), u(N - 1)) + G(x(N))]. \tag{8.24}$$

Step k, for $0 \leq k < N - 1$:
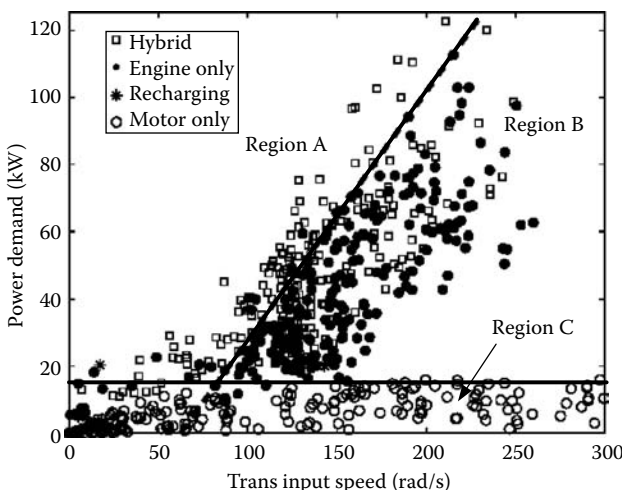
$$J_k^*(x(k)) = \min_{u(k)} \left[L(x(k), u(k)) + J_{k+1}^*(x(k+1)) \right]. \qquad (8.25)$$

The recursive equation is solved backward from step $N - 1$ to zero. Each minimization in a given driving cycle is performed subject to the constraints imposed by Equations 8.18 through 8.22.

The standard method to solve a dynamic programming problem numerically is to use quantization and interpolation.[12,13,16] The states and control values are first quantized into finite grids. At each step of the dynamic programming algorithm, the function $J_k(x(k))$ is evaluated only at the grid points. If the next states, $x(k + 1)$, do not fall exactly on to a quantized value, function interpolation is used to determine the value of $J_{k+1}^*(x(k + 1))$ in Equation 8.25 as well as $G(x(N))$ in Equation 8.24.

The dynamic programming procedure produces an optimal, time-varying, state-feedback control policy that is stored in a table for each of the quantized states and time stages, that is, $u^*(x(k), k)$. This function is then used as a state-feedback controller in the simulations. It should be noted that dynamic programming creates a family of optimal paths for all possible initial conditions. In this application, once the initial SOC is given, the optimal policy will find an optimal way of bringing the final SOC back to the terminal value (SOC$_f$) while achieving the minimal fuel consumption.

Although the dynamic programming approach provides an optimal solution for minimizing the fuel consumption, the resulting control policy is not implementable in real driving conditions because the optimal policy requires

FIGURE 8.10 Operating points of dynamic programming optimization over UDDSHDC cycle.[12]

a knowledge of the future speed and load profiles of the vehicle. Nevertheless, analytic optimal policies determined through dynamic programming can provide insight into how fuel economy improvement is achieved. Figure 8.10 shows an example of the operating points of different operating modes that can be used to refine the rules/fuzzy logic-based control strategy as discussed above.

8.3 Parametric Design of a Drive Train

Parameters of the parallel (torque coupling) hybrid drive train such as engine power, electric motor power, gear ratios of transmission, and power and energy capacity of the PPS are key parameters and exert considerable influence on vehicle performance and operation efficiency. However, as initial steps in the drive train design, these parameters should be estimated based on vehicle performance requirements. Such parameters should also be refined by more accurate simulations.

In the following sections, the parameters of a passenger car are used in calculations. These parameters are vehicle mass, $M = 1500$ kg; rolling resistance coefficient, $f_r = 0.01$; air density, $\rho_a = 1.205$ kg/m^3; front area, $A_f = 2.0$ m^2; aerodynamic drag coefficient, $C_D = 0.3$; radius of driven wheels, $r = 0.2794$ m; transmission efficiency from engine to drive wheels, $\eta_{t,e} = 0.9$; and transmission efficiency from motor to drive wheels, $\eta_{t,m} = 0.95$.
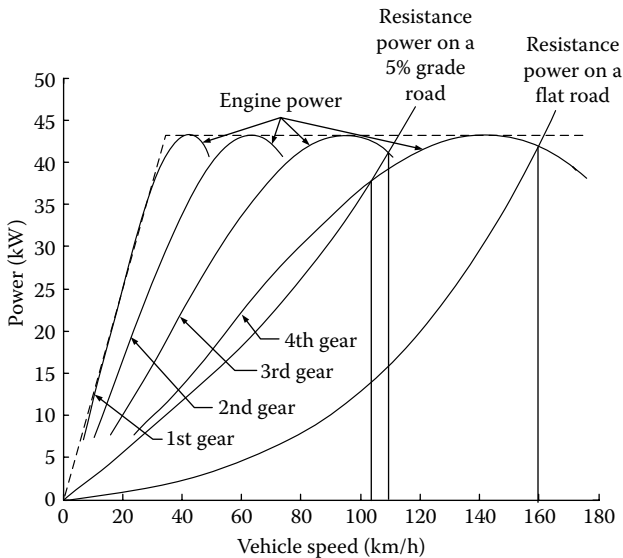
8.3.1 Engine Power Design

The engine should be able to supply sufficient power to support vehicle operation at normal constant speeds on both a flat and a mild grade road without the help of the PPS. The engine should also be able to produce an average power that is larger than the average load power when the vehicle operates with a stop-and-go operating pattern.

As a requirement of normal highway driving at a constant speed on a flat or a mild grade road, the power needed is expressed as

$$P_e = \frac{V}{1000\eta_{t,e}} \left(Mgf_r + \frac{1}{2}\rho_a C_D A_f V^2 + Mgi \right) \text{ (kW).} \qquad (8.26)$$

Figure 8.11 shows the load powers of a 1500-kg example passenger car, along with vehicle speed, on a flat road and a road with 5% grade. It is seen that on a flat road, a speed of 160 km/h (100 mph) needs a power of 43 kW. For a comprehensive analysis, the power curves of a 43-kW engine with a multigear transmission are also plotted in Figure 8.11. From Figure 8.11, it can also be seen that on a 5% grade road, the vehicle can reach maximum speeds of about 103 km/h and 110 km/h with fourth gear and third gear, respectively.

FIGURE 8.11   Engine power required at constant speed on a flat road and a 5% grade road.

Figure 8.12 is the same diagram as shown in Figure 8.11, with the addition of the engine fuel consumption map at each gear. This figure can be used to analyze the influence of transmission gears on vehicle performance, such as acceleration, gradeability, and fuel consumption of the vehicle (for more details, refer to the section of transmission design).
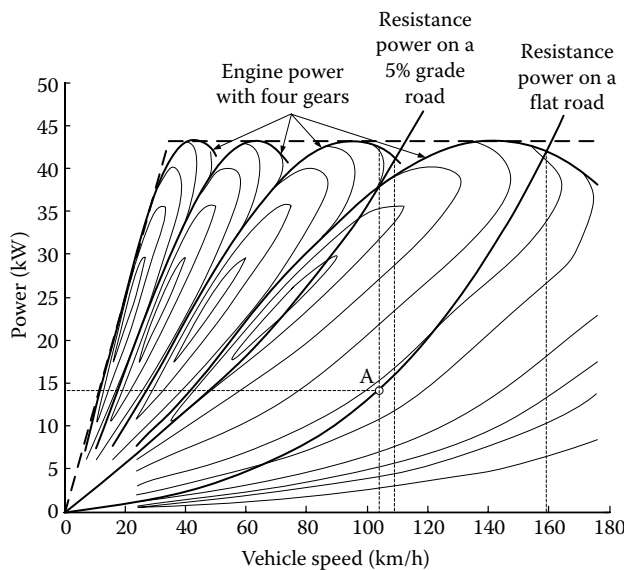
The above-designed engine power should be evaluated so that it meets the average power requirement while driving in a stop-and-go pattern. In a drive cycle, the average load power of a vehicle can be calculated by

$$P_{\text{ave}} = \frac{1}{T} \int_0^T \left(M g f_{\text{r}} V + \frac{1}{2} \rho_a C_D A_f V^3 + \delta M V \frac{dV}{dt} \right) dt. \qquad (8.27)$$

The average power varies with the degree of regenerative braking. The two extreme cases are the full and zero regenerative braking cases. Full regenerative braking recovers all the energy consumed in braking and the average power is calculated by Equation 8.27, where negative dV/dt (deceleration) will tend to reduce the average power, P_{ave}. However, when the vehicle has no regenerative braking, the average power is larger than that with full regenerative braking, which can be calculated from Equation 8.27 in such a way that when the instantaneous power is less than zero, it is given a zero.

Figure 8.13 shows vehicle speed, instantaneous load power, and average powers with full regenerative braking and zero regenerative braking in some typical drive cycles for a 1500-kg passenger car.

In the engine power design, the average power that the engine produces must be greater than the average load power as shown in Figure 8.13. In a
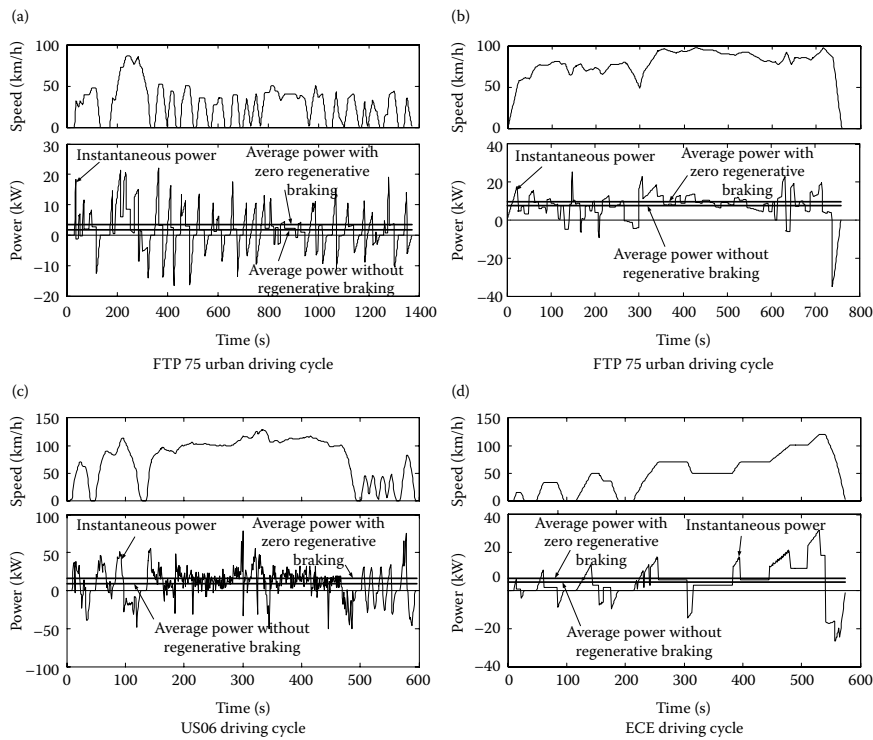
FIGURE 8.12 Engine power required at constant speed on a flat road and a 5% grade road with the engine fuel consumption map at each gear.

parallel drive train, the engine is mechanically coupled to the driven wheels. Hence, engine rotating speed varies with vehicle speed. On the other hand, engine power with full throttle varies with engine rotating speed. In other words, engine power with full throttle is associated with vehicle speed. Thus, the determination of engine power to meet the average power in a drive cycle is not as straightforward as in a series hybrid, in which the engine operating point can be fixed. The average power that the engine produces with full throttle can be calculated by

$$P_{\text{max-ave}} = \frac{1}{T} \int_0^T P_e(V) \, dt, \tag{8.28}$$

where T is the total time in the drive cycles and $P_e(V)$ is the engine power with full throttle, which is a function of vehicle speed when the gear ratio of the transmission is given, as shown in Figures 8.11 and 8.12.

The possible operating points of the engine with full throttle and the maximum possible average powers in some typical drive cycles are shown in Figure 8.14, in which the maximum engine power is 43 kW and transmission is single gear (fourth gear only in Figures 8.11 and 8.12). If a multigear transmission is used, the maximum average power of the engine is greater than that used in a single-gear transmission (refer to Figures 8.11 and 8.12). Comparing the maximum possible average powers to the load average powers in the typical driving cycles as shown in Figure 8.13, it is concluded that the
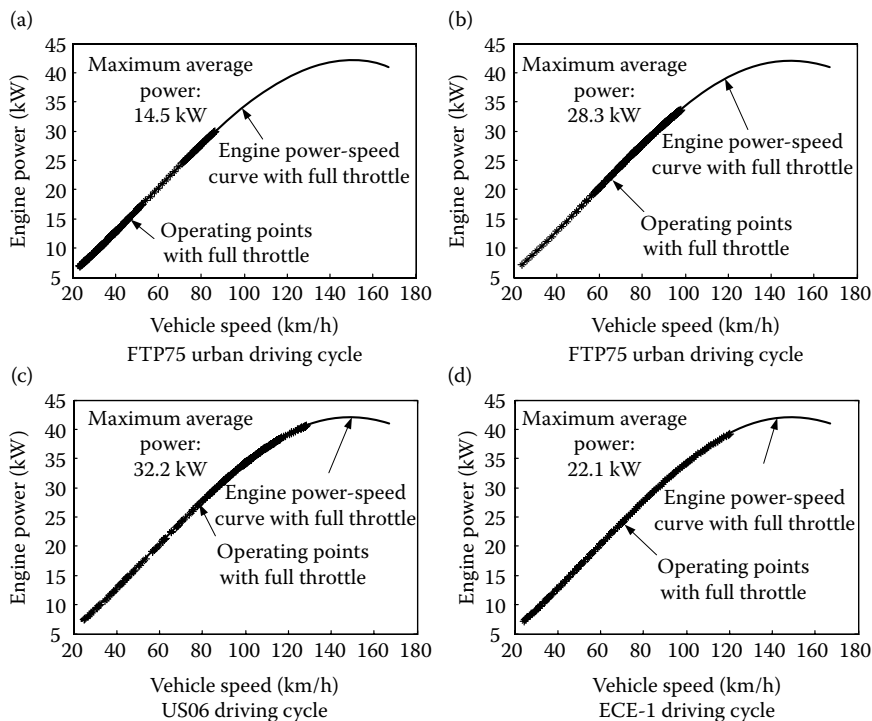
FIGURE 8.13 Instantaneous power and average power with full and zero regenerative braking in typical drive cycles: (a) FTP75 urban, (b) FTP75 highway, (c) US06, and (d) ECE-15.

engine power designed is sufficient to support a vehicle operating in these typical drive cycles.

8.3.2 Transmission Design

Multigear transmission can effectively increase the tractive effort of driven wheels, from the engine torque, especially at a low to medium speed range (refer to Figures 8.11 and 8.12). The direct benefit of the increased tractive effort is the reduction of acceleration time and enhanced gradeability with a given motor power rating. In other words, the motor power rating can be reduced to meet the given acceleration performance and gradeability. Another benefit is the large remaining engine torque for charging the PPS, in addition to propelling the vehicle. Thus the SOC of the PPS can be brought back to a high level quickly. However, a multigear transmission will add complexity to the drive train, especially for the control system in which a shifting control module must be added.

In real engineering, careful analysis is needed to make the decision of using a single-gear or multigear transmission. In the example mentioned above, the maximum average engine power in the typical driving cycle with

FIGURE 8.14 Maximum possible operating points of the engine and maximum average power in typical drive cycles: (a) FTP75 urban, (b) FTP75 highway, (c) US06, and (d) ECE-15.

a single-gear transmission, as shown in Figure 8.14, is significantly larger than the average load power even without regenerative braking as shown in Figure 8.13. Thus, the engine is considered powerful enough with a single-gear transmission if it meets the sustainability of the SOC of PPS. Of course, if a small engine is mandatorily used, a multigear transmission would be necessary.

The operating efficiency of the engine would not be expected to be significantly improved by using a multigear transmission. By referring to Figure 8.12, it can be seen that at most engine speeds, the engine will have higher operating efficiency at the highest gear (fourth gear in Figure 8.12) than with lower gears. However, with the highest gear, the low-speed range, in which the engine cannot stably operate and pure electric traction is used, is larger than that with other gears.

8.3.3 Electric Motor Drive Power Design

In HEV, the major function of the electric motor is to supply peak power to the drive train. In motor power capacity design, acceleration performance and peak load power in typical drive cycles are the major concerns.[17]

It is difficult to directly design the motor power from the acceleration performance specified. This is because we have two power sources and their maximum power relationship with the vehicle speed. An effective approach is to initially make an estimate of the motor power capacity based on the specified acceleration performance, and then complete the final design through iterative simulations.

As an initial estimate, one can assume that the steady-state load (rolling resistance and aerodynamic drag) is handled by the engine and the dynamic load (inertial load in acceleration) is handled by the motor. With this assumption, acceleration is directly related to the torque output of an electric motor by
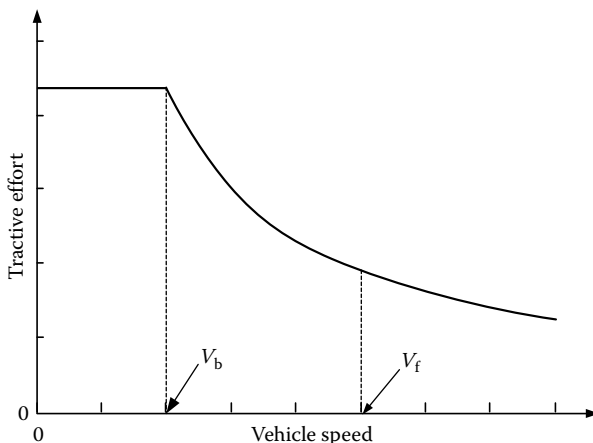
$$\frac{T_m i_{tm} \eta_{tm}}{r} = \delta_m M \frac{dV}{dt}, \tag{8.29}$$

where T_m is the motor torque, i_{tm} is the gear ratio from the motor to the driven wheels, where a single transmission is supposed, η_{tm} is the transmission efficiency from the motor to the driven wheels, and δ_m is the rotating inertia factor associated with the motor (refer to Chapter 2).

Using the output characteristics of the electric motor shown in Figure 8.15, and a specified acceleration time, t_a, from zero speed to a final high speed, V_f, and referring to Chapter 4, the motor power rating is expressed as

$$P_m = \frac{\delta_m M}{2\eta_{tm} t_a}(V_f^2 + V_b^2). \tag{8.30}$$

For a 1500-kg passenger car with a maximum speed of 160 km/h, a base speed of 50 km/h, a final acceleration speed of 100 km/h, acceleration time $t_a = 10$ s, and $\delta_m = 1.04$, the power rating of the electric motor is about 74 kW.

FIGURE 8.15 Tractive effort versus vehicle speed of an electric-motor-driven vehicle.
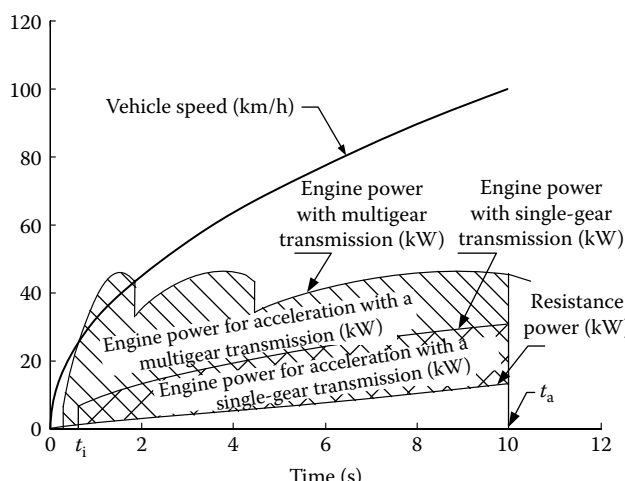
It should be noted that the motor power obtained above is somewhat overestimated. Actually, the engine has some remaining power to help the motor to accelerate the vehicle as shown in Figures 8.11 and 8.12. This is also seen in Figure 8.16, in which vehicle speed, engine power with full throttle, and resistance power (rolling resistance, aerodynamic drag, and power losses in transmission) with a multigear and single-gear transmission are plotted along acceleration time. The average remaining power of the engine, used to accelerate the vehicle, can be expressed as

$$P_{e,a} = \frac{1}{t_a - t_i} \int_{t_i}^{t_a} (P_e - P_r) \, dt, \tag{8.31}$$

where P_e and P_r are engine power and resistance power, respectively. It should be noted that the engine power transmitted to the driven wheels is associated with the gear number and gear ratios of the transmission. It is obvious from Figures 8.11 and 8.12 that a multigear transmission will effectively increase the remaining power at the driven wheels, therefore reducing the motor power required for acceleration.

Figure 8.16 shows the engine remaining power over that required for overcoming the rolling resistance and aerodynamic drag with a multigear and single-gear transmission during acceleration. This figure indicates that around 17- and 22-kW engines with a single-gear and multigear transmission, respectively, are available for assisting the motor in acceleration. Finally, the motor power rating is $74 - 17 = 57$ kW for a single-gear transmission and $74 - 22 = 52$ kW for a multigear transmission.

When the power ratings of the engine and electric motor as well as the transmission are initially designed, a more accurate calculation needs to be

FIGURE 8.16 Vehicle speed, engine power, and resistance power versus acceleration time.

performed to evaluate vehicle performance, mainly maximum speed, grade-ability, and acceleration. Maximum speed and gradeability can be obtained from the diagram of tractive effort and resistance versus vehicle speed. This diagram can be created by using the methods discussed in Chapter 2.
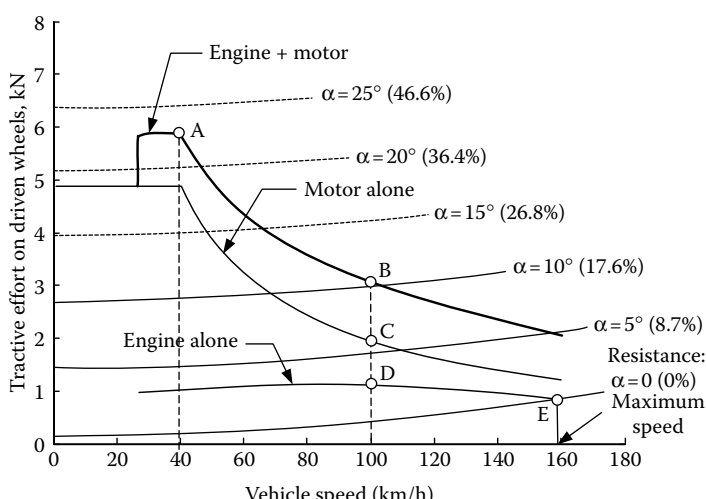
The diagram (as shown in Figure 8.17) shows the design results of the example passenger car with a single-gear transmission. It indicates that the maximum gradeability of the vehicle is about 42% or 22.8° at a vehicle speed of about 40 km/h (point A). At a vehicle speed of 100 km/h, the gradeabil-ity of the vehicle with full hybrid, motor-alone and engine-alone traction are 18.14% or 10.28° (point B), 10.36% or 5.91° (point C), and 4.6% or 2.65° (point D), respectively. The maximum speed of the vehicle is round 160 km/h with engine-alone traction, which is dictated by the engine power point (E). How-ever, if the engine and motor top speed can extend beyond this vehicle speed, the vehicle maximum speed with hybrid mode and motor-alone mode can be extended further.

Figure 8.18 shows the acceleration performance for the example passenger car with a single-gear transmission. It indicates that 10.7 s are used and 167 m are covered for accelerating the vehicle from zero speed to 100 km/h.
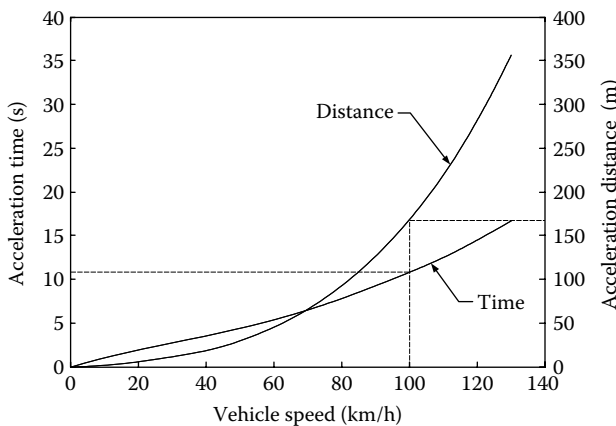
The calculation results for vehicle performance shown in Figures 8.17 and 8.18 indicate that the design of the engine and motor power capacities are appropriate.

8.3.4 PPS Design

The PPS design mainly includes the design for power capacity and energy capacity. The power capacity design is somewhat straightforward. The

FIGURE 8.17 Tractive effort and resistance on a slope versus vehicle speed.

FIGURE 8.18 Acceleration time and distance versus vehicle speed.

terminal power of the PPS must be greater than the input electric power of the electric motor, that is,

$$P_s \geq \frac{P_m}{\eta_m},$$ (8.32)

where P_m and η_m are motor power rating and efficiency, respectively.

The energy capacity design of the PPS is closely associated with the electrical energy consumption in various driving patterns—mainly the full load acceleration and typical urban driving cycles.

During the acceleration period, the energies drawn from the PPS and the engine can be calculated along with the calculation of acceleration time and distance by
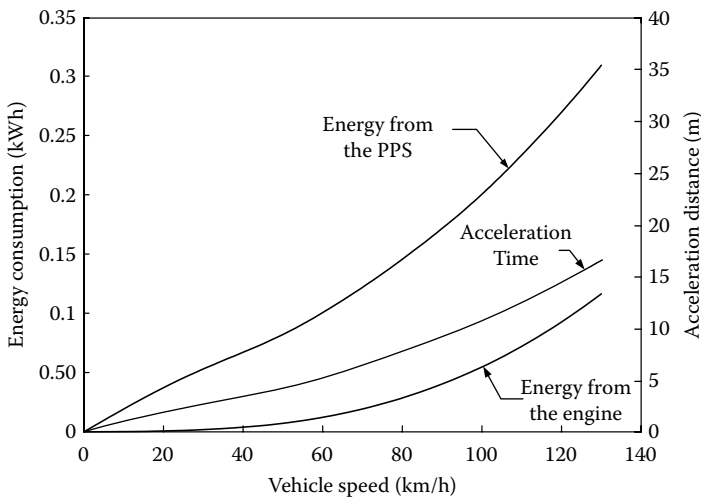
$$E_{pps} = \int_0^{t_a} \frac{P_m}{\eta_m}\, dt$$ (8.33)

and

$$E_{engine} = \int_0^{t_a} P_e\, dt,$$ (8.34)

where E_{pps} and E_{engine} are the energies drawn from the PPS and the engine, respectively, and P_m and P_e are the powers drawn from the motor and the engine, respectively. Figure 8.19 shows the energies drawn from the PPS and the engine in the period of full acceleration along the vehicle speed for the example passenger car. At an end speed of 120 km/h, about 0.3 kW h energy is drawn from the PPS.

The energy capacity of the PPS must also meet the requirement while driving in a stop-and-go pattern in typical drive cycles. In other words, the energy

FIGURE 8.19   Energies drawn from the PPS and engine during full acceleration period.
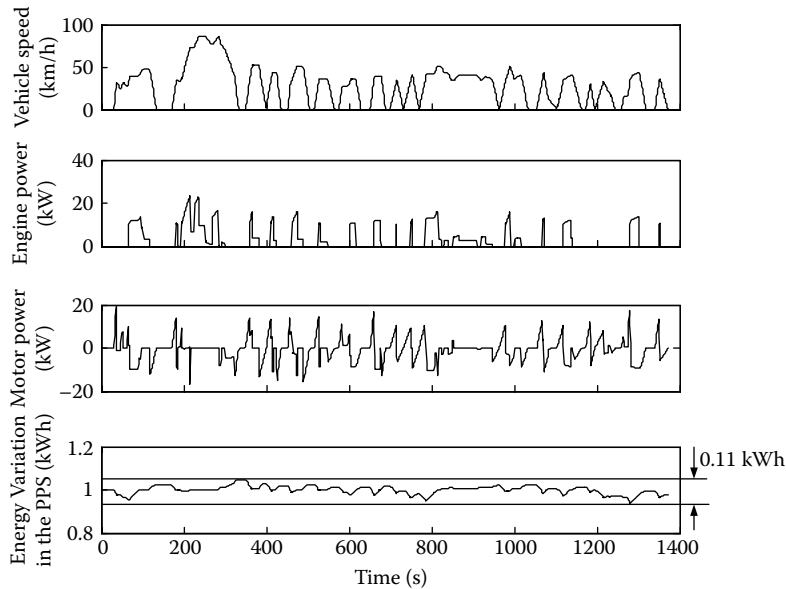
in the PPS will not be fully discharged. The energy changes in the PPS can be obtained by

$$E_{var} = \int_0^t \left(P_{pps\text{-}ch} - P_{pps\text{-}disch} \right) \, dt, \qquad (8.35)$$

where $P_{pps\text{-}ch}$ and $P_{pps\text{-}disch}$ are the instantaneous charging and discharging power of the PPS. With a given control strategy, the charging and discharging power of the PPS can be obtained by a drive train simulation in a typical driving cycle (refer to Section 8.4).

Figure 8.20 shows the simulation results of the example passenger car in an FTP75 urban drive cycle with maximum SOC control strategy. It can be seen that the maximum energy change in the PPS is about 0.11 kWh, which is less than that in full load acceleration (0.3 kWh). Thus, the energy consumption in full load acceleration determines the energy capacity of the energy storage. This conclusion is only valid for the Max. SOC control strategy and FTP75 urban driving cycle. When other control strategies and driving cycles are used, the conclusion may be different.

In fact, not all the energy stored in the PPS can be fully used to generate sufficient power for the drive train. In the case of using batteries as the PPS, low SOC will severely limit their power output, and will, at the same time, lead to low efficiency, due to an increase in internal resistance. In the case of using ultracapacitors as the PPS, low SOC will result in low terminal voltage that will affect the performance of the traction motor. Similarly when a flywheel is used, low SOC means the low flywheel speed at which the terminal voltage of the electric machine, functioning as the energy exchange port, is low. Thus only part of the energy stored in the PPS can be available for use, which can

FIGURE 8.20 Vehicle speed, engine power, motor power, and energy variation in PPS storage in an FTP75 urban drive cycle with the Max. SOC control strategy.

be represented by the SOC or state-of-energy. The energy capacity of the PPS can be obtained from
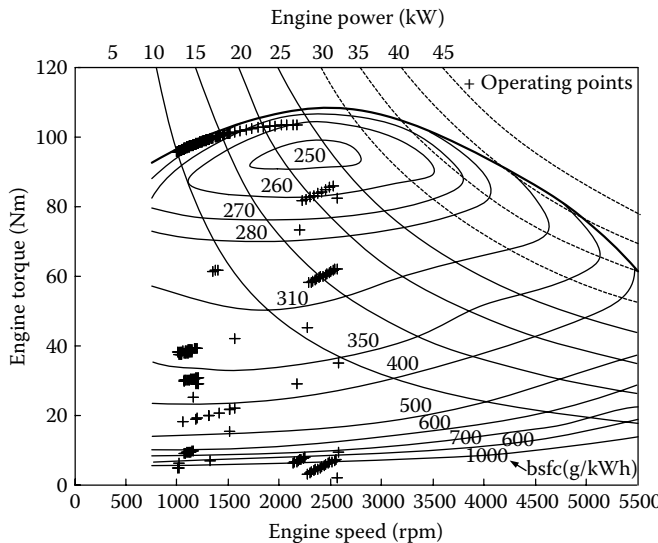
$$E_{\text{c-pps}} = \frac{E_{\text{dis-max}}}{SOC_t - SOC_b},$$ (8.36)

where $E_{\text{dis-max}}$ is the allowed maximum energy discharging from the PPS, and SOC_t and SOC_b are the top line and bottom line of the SOC of the PPS. In the example, $E_{\text{dis-max}} = 0.3$ kWh and assume that 30% of the total energy of the PPS is allowed to be used; then the minimum energy capacity of the PPS is 1 kWh.

8.4 Simulations
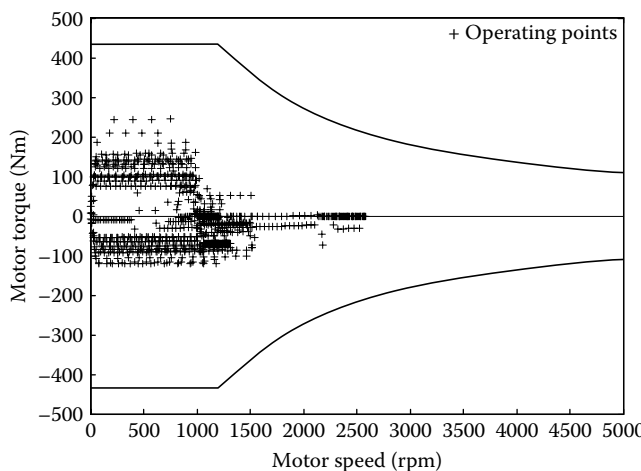
When all the major components have been designed, the drive train should be simulated by using a simulation program. The simulation in typical drive cycles can produce a great deal of useful information about the drive train, such as engine power, motor power, energy changes in the PPS, engine operating points, motor operating points, fuel consumption, and so on.

Figure 8.20 shows the vehicle speed, engine power, motor power, and energy changes in the PPS along with the driving time for the example passenger car in the FTP75 urban drive cycle. Figures 8.21 and 8.22 show the

FIGURE 8.21   Engine operating points overlap its fuel consumption map in an FTP75 urban drive cycle with maximum SOC control strategy.

engine and motor operating points, respectively. The simulation results of the fuel economy of the example passenger car are 4.66 L per 100 km or 50.7 miles per gallon (mpg) when the engine is turned off during the period of standstill and braking, and 5.32 L per 100 km or 44.4 mpg when the engine is set at idle during the period of standstill and braking.

FIGURE 8.22   Motor operating points in an FTP75 urban drive cycle with maximum SOC control strategy.

References

1. M. Ehsani, K. L. Butler, Y. Gao, K. M. Rahman, and D. Burke, "Toward a sustainable transportation without sacrifice of range, performance, or air quality: The ELPH car concept," *International Federation of Automotive Engineering Society Automotive Congress,* Paris, France, September/October 1998.

2. M. Ehsani, Y. Gao, and K. Butler, "Application of electric peaking hybrid (ELPH) propulsion system to a full size passenger car with simulation design verification," *IEEE Transactions on Vehicular Technology*, 48 (6), November 1999.

3. Y. Gao, K. M. Rahman, and M. Ehsani, "The energy flow management and battery energy capacity determination for the drive train of electrically peaking hybrid," *Society of Automotive Engineers (SAE) Journal*, Paper No. 972647, Warrendale, PA, 1997.

4. Y. Gao, K. M. Rahman, and M. Ehsani, "Parametric design of the drive train of an electrically peaking hybrid (ELPH) vehicle," *Society of Automotive Engineers (SAE) Journal*, Paper No. 970294, Warrendale, PA, 1997.

5. C. Liang, W. Weihua and W. Qingnian, "Energy Management Strategy and Parametric Design for Hybrid Electric Military Vehicle," SAE paper 2003-01-0086.

6. P. Pisu, and G. Rizzoni, "A comparative study of supervisory control strategies for hybrid electric vehicles," *IEEE Transaction on Control Systems Technology*, 15 (3), May 2007.

7. H.-D. Lee and S.-K. Sul, "Fuzzy-logic-based torque control strategy for parallel-type hybrid electric vehicle," *IEEE Transaction on Industrial Electronics*, 45 (4), August 1998.

8. G. Shi, Y. Jing, A. Xu, and J. Ma, "Study and simulation of based-fuzzy-logic parallel hybrid electric vehicles control strategy," *Proceedings of the Sixth International on Intelligent Systems Design and Application* (ISDA'06), 2006.

9. R. Langari and J.-S. Won, "Intelligent energy management agent for a parallel hybrid vehicle—part I: System architecture and design of the driving situation identification process," *IEEE Transactions on Vehicular Technology*, 54 (3), May 2005.

10. R. Langari and J.-S. Won, "Intelligent energy management agent for a parallel hybrid vehicle—part II: Torque distribution, charge sustenance strategies, and performance results," *IEEE Transactions on Vehicular Technology*, 54 (3), May 2005.

11. T. Heske and J. N. Heske, *Fuzzy Logic for Real World Design*, Annabooks, ISBN: 0-929392-24-8, 1996.

12. C.-C. Lin, H. Peng, J. W. Grizzle, and J.-M. Kang, "Power management strategy for a parallel hybrid electric truck," *IEEE Transactions on Control System Technology*, 11 (6), November 2003.

13. C.-C. Lin, J.-M. Kang, J. W. Grizzle, and H. Peng, "Energy management strategy for a parallel hybrid electric truck," *Proceedings of the American Control Conference*, Arlington, VA, June 25–27, 2001.

14. C.-C. Lin, H. Peng, S. Jeon, and J. M. Lee, "Control of a hybrid electric truck based on driving pattern recognition," *Proceedings of the 2002 Advanced Vehicle Control Conference*, Hiroshima, Japan, September 2002.

15. D. P. Betsekas, *Dynamic Programming and Optimal Control*, Athena Scientific, 1995.

16. C.-C. Lin, Z. Filipi, L. Louca, H. Peng, D. Assanis, and J. Stein, "Modeling and control of a medium-duty hybrid electric truck," *International Journal of Heavy Vehicle Systems*. 11 (3/4), 2004.
17. Y. Gao, H. Moghbelli, and M. Ehsani, "Investigation of proper motor drive characteristics for military vehicle propulsion," *Society of Automotive Engineers (SAE) Journal*, Paper No. 2003-01-2296, Warrendale, PA, 2003.

9

Design and Control Methodology of Series–Parallel (Torque and Speed Coupling) Hybrid Drive Train

As discussed in Chapter 5, the series–parallel or, more accurately, the torque/speed-coupling hybrid drive train has some advantages over the series (electrical coupling) and parallel (single torque or speed coupling) drive trains. The torque and speed couplings in this drive train free the engine from the driven wheels in the torque and speed constraints. Consequently, the instantaneous engine torque and speed can be independent of the load torque and speed of the vehicle. Therefore, the engine can be operated in its high-efficiency region in a similar way as that of the series (electrical coupling) drive train. On the other hand, part of the engine power is directly delivered to the driven wheels without experiencing multiform conversion.[1–3] This feature is more similar to the parallel (torque or speed coupling) drive train.

As discussed in Chapter 5, the series–parallel hybrid drive train can be composed of speed-coupling devices such as planetary gears and transmotors as shown in Figures 5.22 through 5.24. All these configurations have similar features, design, and control principles. This chapter focuses on the design and control principles of the configuration, which uses the planetary gear unit as its speed-coupling device as shown in Figure 5.22. For a more detailed example of a commercial series–parallel vehicle, see the Appendix in this book.

9.1 Drive Train Configuration

9.1.1 Speed-Coupling Analysis

A series–parallel hybrid drive train can be formed by using both torque and speed coupling. The well-known torque-coupling devices are mostly gear set, sprocket-chain set, or pulley-belt set.[4,5] However, speed-coupling devices are less familiar to the reader and more complex. The operating characteristics of

planetary gear functioning as a speed-coupling device are discussed in detail as follows.

A mechanical planetary unit has the structure as shown in Figure 9.1. It consists of a sun gear labeled s in Figure 9.1, a ring gear labeled r, several planetary gears labeled p (usually three or four for force balance), and a yoke labeled y, which is hinged to the centers of the planetary gears. As discussed in Chapter 5, the speeds in rpm of the sun gear, n_s, ring gear, n_r, and yoke, n_y, have the relationship

$$n_y = \frac{1}{1+i_g}n_s + \frac{i_g}{1+i_g}n_r, \tag{9.1}$$
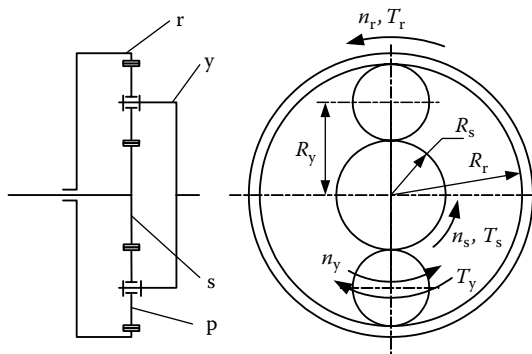
where i_g is the gear ratio defined as R_r/R_s as shown in Figure 9.1. The speeds n_s, n_r, and n_y are defined as positive in the direction shown in Figure 9.1. Defining $k_{ys} = (1+i_g)$ and $k_{yr} = (1+i_g)/i_g$, Equation 9.1 can be further expressed as

$$n_y = \frac{1}{k_{ys}}n_s + \frac{1}{k_{yr}}n_r. \tag{9.2}$$

Neglecting the energy losses in steady-state operation, the torques acting on the sun gear, ring gear, and yoke have the relationship

$$T_y = -k_{ys}T_s = -k_{yr}T_r. \tag{9.3}$$

Equation 9.3 indicates that the torques acting on the sun gear, T_s, and ring gear, T_r, always have the same sign; in other words, they have to be always in the same direction. However, the torque acting on the yoke, T_y, is always in the opposite direction of T_s and T_r. Equation 9.3 also indicates that with $i_g > 1$, which is the general case since $R_r > R_s$, T_s is the smallest, T_y is the largest, and T_r is in between. This means that the torque acting on the yoke is balanced by torques acting on the sun gear and ring gear.

FIGURE 9.1 Planetary gear unit used as a speed coupling.

Element fixed	Speed	Torque
Sun gear	$n_y = \dfrac{1}{k_{yr}} n_r$	$T_y = -k_{yr} T_r$
Ring gear	$n_y = \dfrac{1}{k_{ys}} n_s$	$T_y = -k_{ys} T_s$
Yoke	$n_s = -\dfrac{k_{ys}}{k_{yr}} n_r$	$T_s = \dfrac{k_{yr}}{k_{ys}} T_r$

FIGURE 9.2 Speed and torque relationships while one element is fixed.

When one element among the sum gear, ring gear, and yoke is locked to the vehicle frame, that is, one degree of freedom of the unit is constrained, the unit becomes a single-gear transmission (one input and one output); the speed and torque relationship, with one element fixed, is shown in Figure 9.2.

In composing a hybrid drive train with the planetary gear unit as a speed coupling, there are many options as shown in Figure 9.3. To reduce the torque capacity requirement, therefore reducing the motor/generator physical size and weight, connecting the motor/generator to the sun gear of the planetary gear unit may be the appropriate choice. The engine may be either connected to the yoke or to the ring gear as shown in Figure 9.3a and b. In the former design (Figure 9.3a), the torques of the engine and motor/generator have the relationship

$$T_e = -k_{ys} T_{m/g}, \tag{9.4}$$
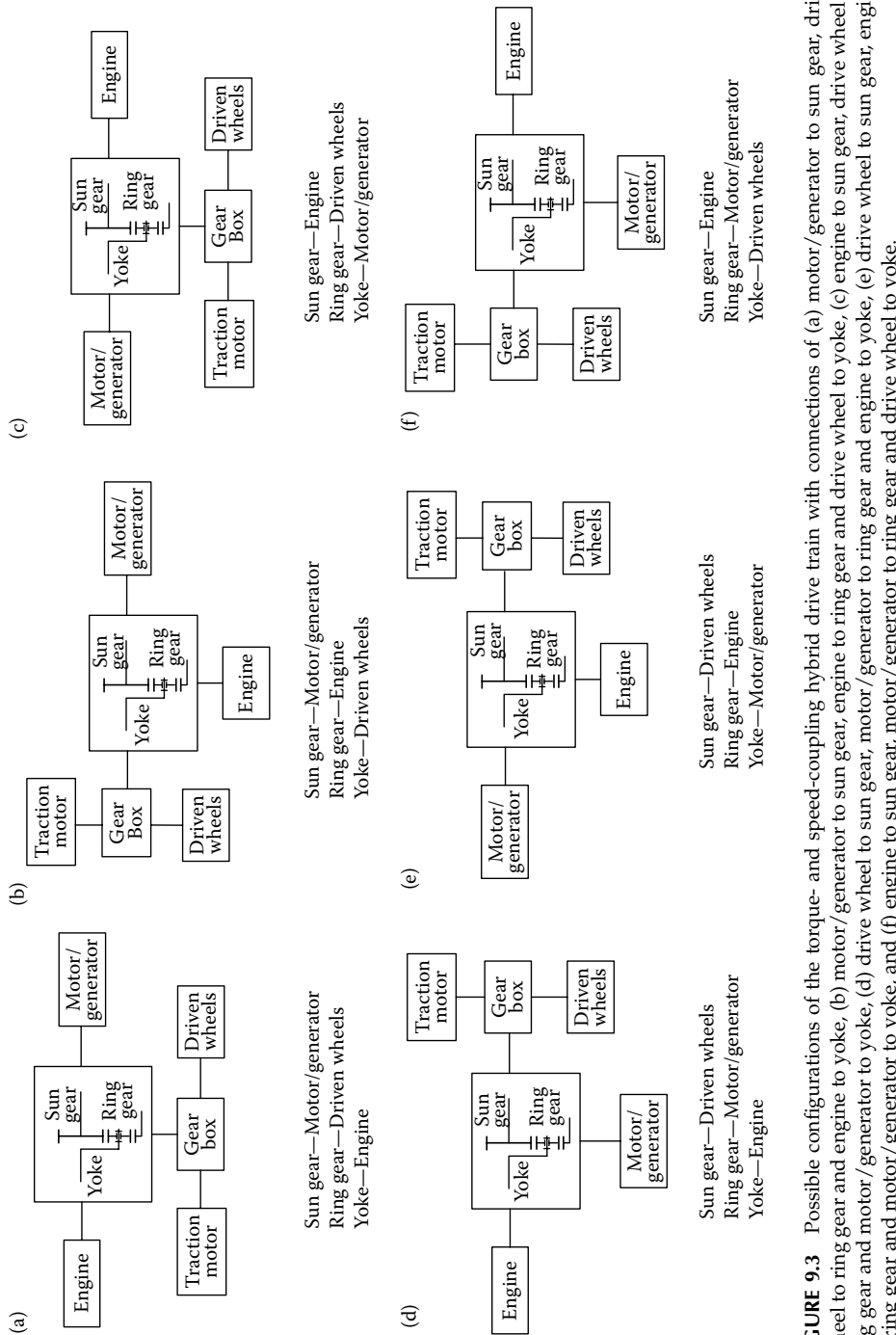
where T_e and $T_{m/g}$ are the torques acting on the yoke and sun gear, produced by the engine and the motor/generator. T_e and $T_{m/g}$ have opposite directions. The engine operates in the first quadrant, and the motor operates in the third and fourth quadrants as shown in Figure 9.4. Since the motor/generator has to produce its torque to balance the engine maximum torque at any speed, the motor/generator must have a constant maximum torque in its whole speed range as shown in Figure 9.4.

In the latter design (Figure 9.3b), the engine torque and motor/generator torque have the relationship
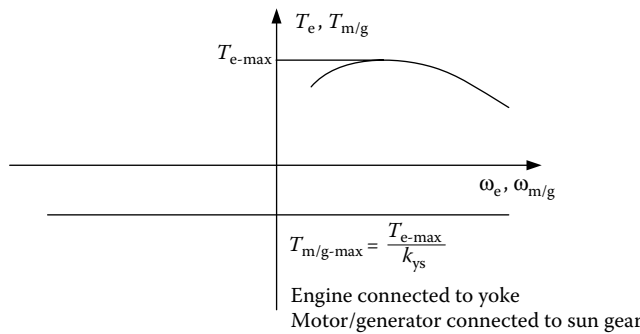
$$T_e = \frac{k_{yr}}{k_{ys}} T_{m/g}. \tag{9.5}$$

The engine and motor/generator operating areas are shown in Figure 9.5.

Comparing Figure 9.4 with Figure 9.5, with the same maximum engine torque, the former design (Figures 9.3a and 9.4) results in a smaller motor/generator (smaller motor/generator torque). However, the torque from the ring gear, delivered to the driven wheel through the gear box, is smaller than the engine torque (similar to the overdrive gear in the conventional transmission). Nevertheless, the gear ratio of the gear box can be

FIGURE 9.3 Possible configurations of the torque- and speed-coupling hybrid drive train with connections of (a) motor/generator to sun gear, drive wheel to ring gear and engine to yoke, (b) motor/generator to sun gear, engine to ring gear and drive wheel to yoke, (c) engine to sun gear, drive wheel to ring gear and motor/generator to yoke, (d) drive wheel to sun gear, motor/generator to ring gear and engine to yoke, (e) drive wheel to sun gear, engine to ring gear and motor/generator to yoke, and (f) engine to sun gear, motor/generator to ring gear and drive wheel to yoke.

(a) Sun gear—Motor/generator
Ring gear—Driven wheels
Yoke—Engine

(b) Sun gear—Motor/generator
Ring gear—Engine
Yoke—Driven wheels

(c) Sun gear—Engine
Ring gear—Driven wheels
Yoke—Motor/generator

(d) Sun gear—Driven wheels
Ring gear—Motor/generator
Yoke—Engine

(e) Sun gear—Driven wheels
Ring gear—Engine
Yoke—Motor/generator

(f) Sun gear—Engine
Ring gear—Motor/generator
Yoke—Driven wheels
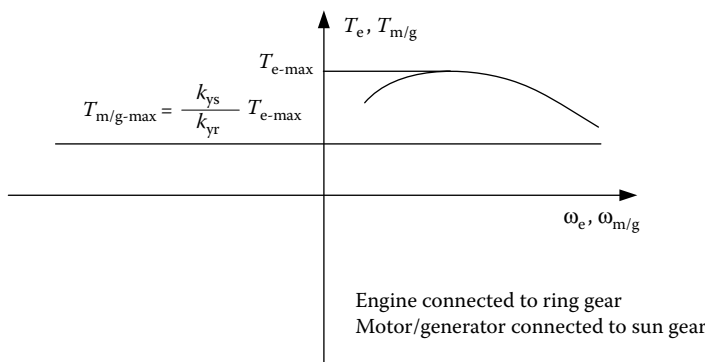
FIGURE 9.4 Operating areas of the engine and motor/generator.
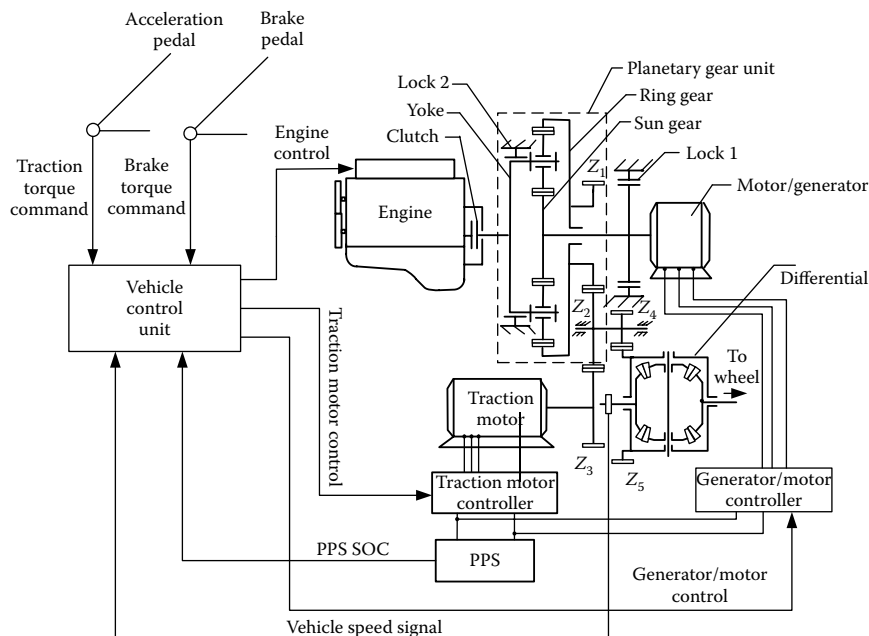
designed to meet the tractive torque requirement. Further discussion in the following section will be based on this design (Figures 9.3a and 9.4).

9.1.2 Drive Train Configuration

Figure 9.6 shows the detailed configuration of a series–parallel (torque/speed coupling) drive train.[6] The planetary gear unit constitutes the speed coupling that connects an engine and a motor/generator together. The engine and motor/generator are connected to the yoke and sun gear, respectively. The ring gear of the planetary gear is connected to the drive wheels through gears of Z_1, Z_2, Z_4, Z_5, and a differential. A traction motor is connected to the driven wheels through gears of Z_3, Z_2, Z_4, Z_5, and the differential, which couples the output torques of the ring gear and the traction motor together. In this configuration, one clutch and two locks are used. The clutch serves for connecting or disconnecting the engine to or from the yoke of the planetary gear unit. Lock 1 is used to lock or release the sun gear and the shaft of the
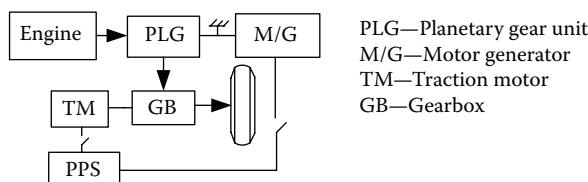
FIGURE 9.5 Operating areas of the engine and motor/generator.

FIGURE 9.6   Drive train configuration.

generator/motor to or from the stationary frame of the vehicle. Lock 2 is used to lock or release the yoke to or from the stationary frame of the vehicle. By controlling the clutch, locks, engine, motor/generator, and the traction motor, many operation modes are available to be used as follows.

1. *Speed-coupling mode*: In this mode, the traction motor is de-energized. There are three submodes:
   1.1. *Engine-alone traction*: The clutch is engaged to connect the engine to the yoke, lock 1 locks the sun gear to the vehicle stationary frame, and the motor/generator is de-energized. Lock 2 releases the yoke from the vehicle stationary frame. The energy flow route is shown in Figure 9.7.

PLG—Planetary gear unit
M/G—Motor generator
TM—Traction motor
GB—Gearbox

FIGURE 9.7   The traction energy flow route is from the engine alone.

In this case, the engine alone delivers its torque to the driven wheels. The speed relationship between the engine and the driven wheels is

$$n_{dw} = \frac{k_{yr}n_e}{i_{rw}}, \tag{9.6}$$

where n_{dw} and n_e are the speeds of the driven wheel and the engine, and i_{rw} is the gear ratio from the ring gear to the drive train wheels, which is expressed as

$$i_{rw} = \frac{Z_5 Z_2}{Z_1 Z_4}, \tag{9.7}$$

where Z_1, Z_2, Z_4, and Z_5 are the tooth numbers of the gears Z_1, Z_2, Z_4, and Z_5.

The torque relationship between the drive wheels and the engine is
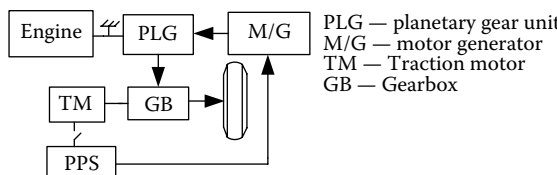
$$T_{dw} = \frac{i_{rw}\eta_{yr}\eta_{rw}T_e}{k_{yr}}, \tag{9.8}$$

where T_{dw} is the torque developed on the driven wheels by the engine torque T_e, η_{yr} is the efficiency from the yoke to the ring gear, and η_{rw} is the efficiency from the ring gear to the driven wheels.

1.2. *Motor/generator-alone traction*: In this mode, the engine is shut down; the clutch is engaged or disengaged and lock 1 releases the sun gear and the shaft of the motor/generator from the stationary frame; lock 2 locks the yoke to the stationary frame. In this case, the vehicle is propelled by the motor/generator alone. The energy flow route is shown in Figure 9.8.

The speed and torque relationship between the generator/motor and the driven wheels is

$$n_{dw} = -\frac{k_{yr}}{k_{ys}i_{rw}}n_{m/g} \tag{9.9}$$

FIGURE 9.8 Energy flow route in the mode of motor/generator traction.

and

$$T_{dw} = \frac{k_{ys} i_{rw} \eta_{sr} \eta_{rw}}{k_{yr}} T_{m/g}, \qquad (9.10)$$

where T_{dw} is the tractive torque on the driven wheels developed by the motor/generator torque $T_{m/g}$, and η_{sr} is the efficiency from the sun gear to the ring gear.

It should be noted that the motor/generator has to be operated in the third quadrant, that is, negative angular velocity and negative torque as defined in Figure 9.1.

1.3. *Engine and motor/generator with speed-coupling traction*: In this mode, the clutch is engaged. Locks 1 and 2 are released from the stationary frame. From Equation 9.2, the angular velocities of the driven wheels, engine, and motor/generator have the relationship

$$n_{dw} = \frac{k_{yr}}{i_{rw}} \left(n_e - \frac{1}{k_{ys}} n_{m/g} \right), \qquad (9.11)$$
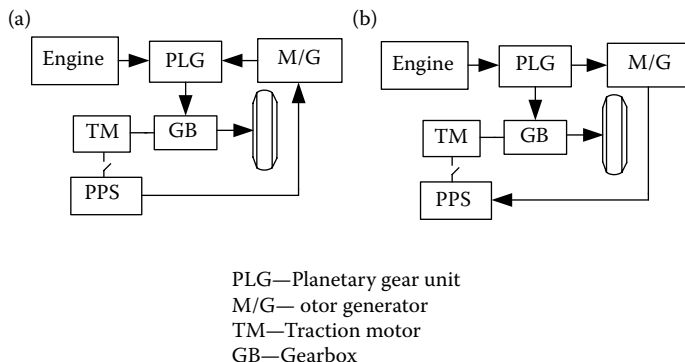
and the torques have the relationship

$$T_{dw} = \frac{i_{rw} \eta_{yr} \eta_{rw}}{k_{yr}} T_e = \frac{k_{ys} \eta_{sr}^b \eta_{rw}}{k_{yr}} T_{m/g}, \qquad (9.12)$$
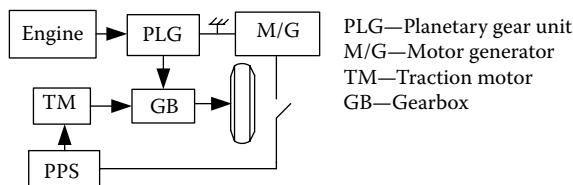
where b is an index, when the power flows from the motor/generator to the sun gear, that is, $n_{m/g} < 0$, $b = 1$, otherwise $b = -1$. Equation 9.11 implies that, at a given vehicle speed, the engine speed can be adjusted by the motor/generator speed. Equation 9.12 indicates that the engine torque, motor/generator torque, and load torque on the driven wheels always hold a fixed relationship. This implies that a change in one torque will cause a change in the other two torques, causing the operating points of the engine and motor/generator to change. For a detailed discussion, refer to the next section for drive train control.

The energy flow routes are shown in Figure 9.9.

2. *Torque-coupling mode*: When the traction motor is energized, its torque can be added to the torque output of the ring gear to constitute the torque-coupling mode. Corresponding to the three modes (1.1), (1.2), and (1.3), when the traction motor is controlled to operate in motoring and generating, six basic operation modes are constituted.

   2.1. *Engine alone in mode (1.1) plus traction motor motoring*: This mode is the same as the general parallel hybrid traction mode. The energy flow route is shown in Figure 9.10.

   2.2. *Engine alone in mode (1.1) plus traction motor generating*: This mode is the same as the PPS charging from the engine mode in the

(a)

(b)

PLG—Planetary gear unit
M/G— otor generator
TM—Traction motor
GB—Gearbox
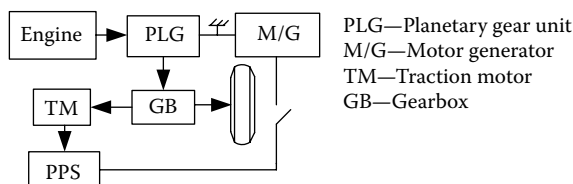
FIGURE 9.9 Energy flow route in speed-coupling mode: (a) M/G motoring and (b) M/G generating.

PLG—Planetary gear unit
M/G—Motor generator
TM—Traction motor
GB—Gearbox
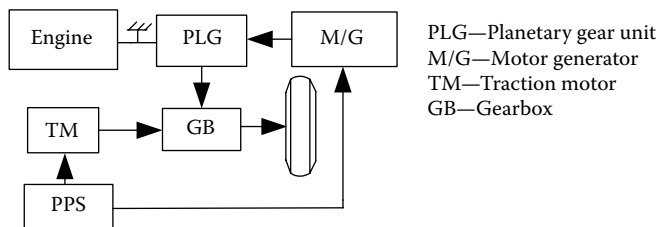
FIGURE 9.10 Energy flow route in parallel traction mode.

general hybrid drive train. The energy flow route is shown in Figure 9.11.
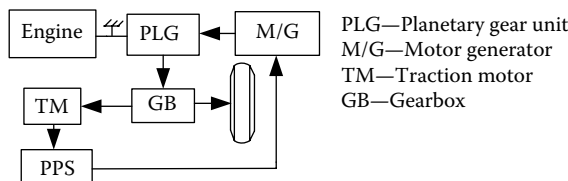
2.3. *Motor/generator-alone mode (1.2) plus traction motor motoring*: This mode is similar to mode (2.1), but the engine is replaced by the motor/generator. The energy flow route is shown in Figure 9.12.

2.4. *Motor/generator alone in mode (1.2) plus traction motor generating*: This mode is similar to mode (2.2) but the engine is replaced by the motor/generator. This mode may never be used because part of the motor/generator energy circles from the PPS and finally to the PPS through the motor/generator and traction motor as shown in Figure 9.13.

PLG—Planetary gear unit
M/G—Motor generator
TM—Traction motor
GB—Gearbox

FIGURE 9.11 Energy flow route in parallel PPS charging.
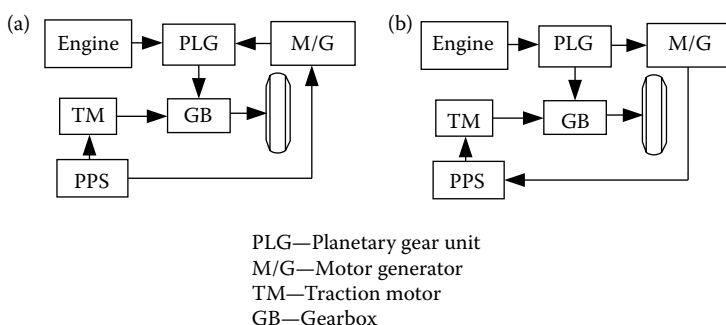
FIGURE 9.12   Energy flow route in the mode of two motor traction in parallel.
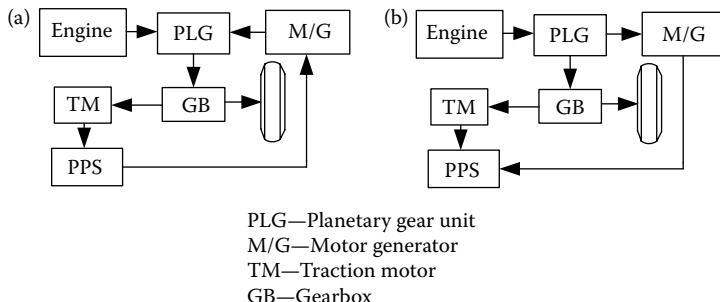
FIGURE 9.13   Energy flow route in the mode of motor/generator traction and PPS charging.

2.5. *Speed-coupling traction in mode (1.3) plus traction motor motoring*:
This mode uses the full functions of speed and torque coupling.
There are two operating states of the motor/generator: motoring
and generating as shown in Figure 9.14. The operating states of
the motor/generator in motoring (Figure 9.14a) may be used at
high vehicle speeds. In this case, the engine speed may be lim-
ited to somewhat lower than its medium speed to avoid too high
an engine speed where its operating efficiency may be low. The
motor generator contributes its speed to the drive train for sup-
porting the high vehicle speed as shown in Figure 9.14a. Similarly,
the operating states in Figure 9.14b may be used in the case of
low vehicle speed. In this case, the engine can be operated at

FIGURE 9.14   Energy flow route: (a) traction motor motoring and (b) traction motor generating.

PLG—Planetary gear unit
M/G—Motor generator
TM—Traction motor
GB—Gearbox
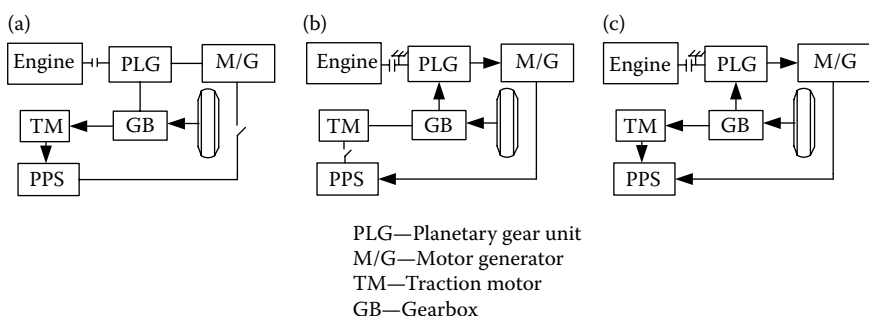
FIGURE 9.15 Energy flow route: (a) M/G motoring and (b) M/G generating.

speeds somewhat lower than its medium speed to avoid too low a speed operation, where its operating efficiency may be low. The motor/generator absorbs part of the engine speed.

2.6. *Speed-coupling traction in mode (1.3) plus traction motor generating*: Similar to mode (2.5), the engine and motor/generator operate in speed-coupling mode. But the traction motor operates in generating mode as shown in Figure 9.15.

3. *Regenerative braking*: When the vehicle is experiencing braking, the traction motor, motor/generator, or both can produce braking torque and recapture part of the braking energy to charge the PPS. In this case, the engine is shut down with the clutch opened. The possible energy flow is shown in Figure 9.16.

As discussed above, there are several operating modes available for use. In control scheme design, perhaps not all the operating modes are really used, depending on the drive train design, driving conditions, operating characteristics of the major components, and so on.

PLG—Planetary gear unit
M/G—Motor generator
TM—Traction motor
GB—Gearbox

FIGURE 9.16 Energy flow in regenerative braking: (a) traction motor alone, (b) M/G alone, and (c) both traction motor and M/G.

9.2   Drive Train Control Methodology
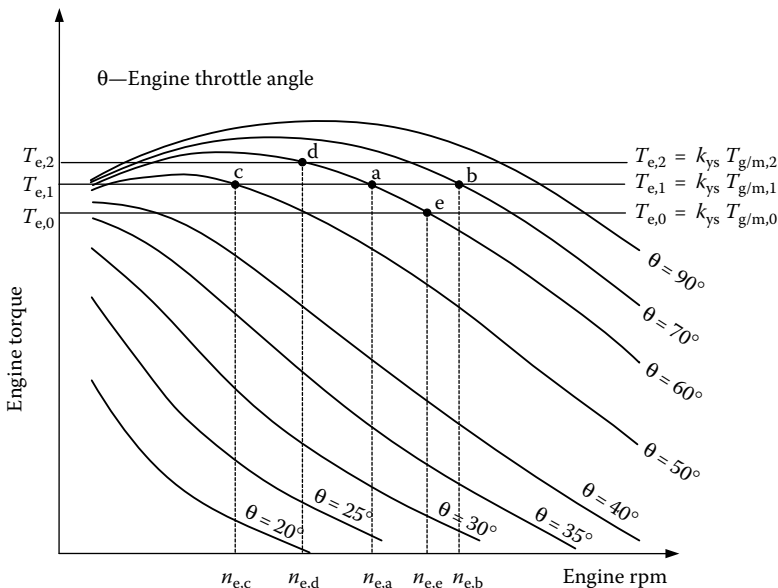
9.2.1   Control System

The control system of the drive train is shown in Figure 9.6. The vehicle controller unit (VCU) receives the traction or braking torque commands from the driver through the accelerator or brake pedals, and other necessary operating information, such as SOC of the PPS and vehicle speed. Based on the real-time information received and the control logic preset in the VCU, the VCU generates control signals to control the engine, motor/generator, traction motor, as well as clutch and locks, through engine throttle actuator, motor/generator controller, traction motor controller, clutch, and lock actuators.

9.2.2   Engine Speed Control Approach

Equation 9.11 indicates that the engine speed, n_e, can be adjusted by controlling the motor/generator speed, $n_{m/g}$, at a given wheel speed, n_{dw}. However, this control activity has to be carried out by controlling the engine throttle and the motor/generator torque as shown in Figure 9.17. The control procedure is as follows:

Suppose the engine is operating at point a with a speed of $n_{e,a}$, producing torque $T_{e,1}$, with a throttle angle of 60° as shown in Figure 9.17; the motor/generator has to produce its torque $T_{m/g,1} = T_{e,1}/k_{ys}$ (where the losses

FIGURE 9.17   Engine speed controlled by the engine throttle and motor/generator torque.

are ignored) to balance the engine torque. With a fixed motor/generator torque, and thus a fixed engine torque, increasing the engine throttle opening will cause the engine speed to increase, to point b with $\theta = 70°$ for example. Similarly, reducing the engine throttle opening will cause the engine speed to decrease, to point c at $\theta = 50°$ for example. The engine speed can also be changed by changing the motor/generator torque as shown in Figure 9.17. With a fixed engine throttle, reducing the motor/generator torque (and thus the engine torque) will cause the engine speed to increase from point a to point e, or increasing the motor/generator torque will cause the engine speed to decrease from point a to point d. Thus, the engine speed can be potentially controlled within its optimal speed range by instantaneously controlling the engine throttle and/or the motor/generator torque.

9.2.3   Traction Torque Control Approach
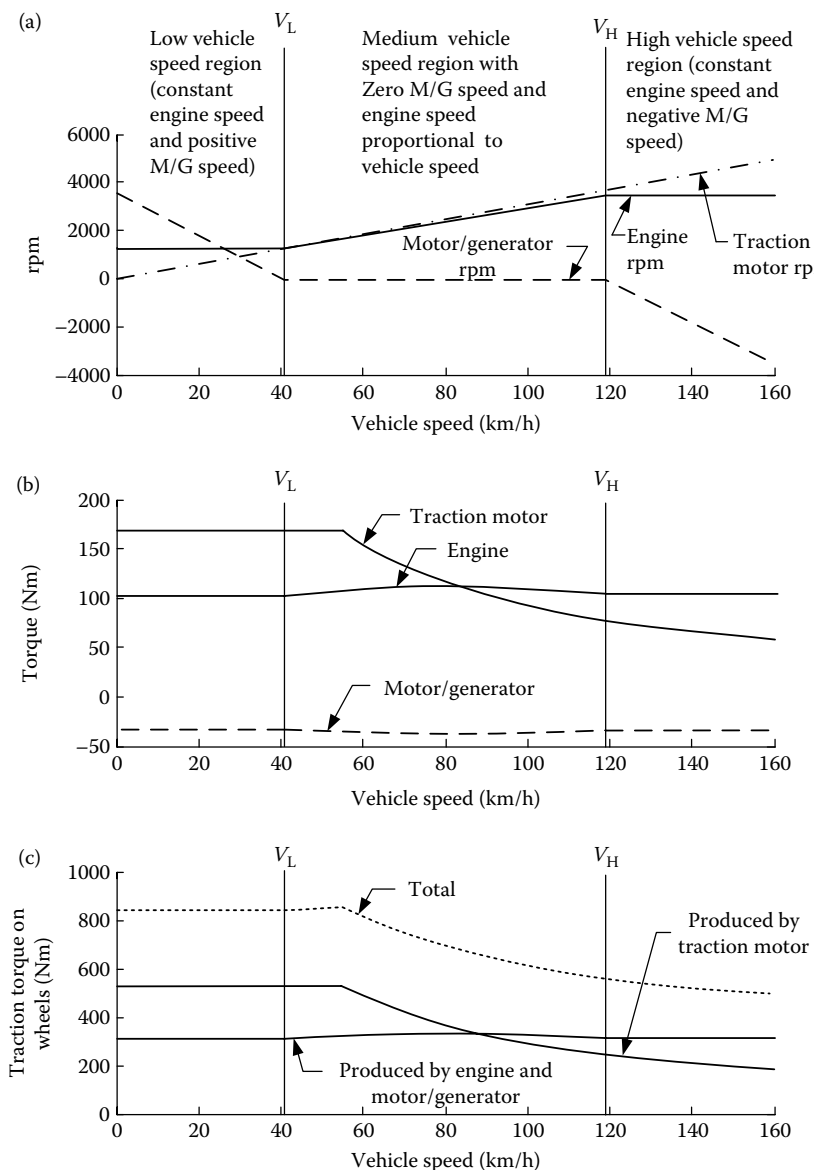
The traction torque on the driven wheels is the sum of the torques transmitted from the ring gear of the planetary gear units and the traction motor. The traction torque on the driven wheels can be expressed as

$$T_{tdw} = i_{rw}\eta_{rw}T_{ring} + i_{mw}\eta_{mw}T_{tm}, \tag{9.13}$$

where T_{tdw} is the total tractive effort on the driven wheels, T_{ring} is the torque output from the ring gear of the planetary gear unit, which is generated by the engine and the motor/generator, i_{rw} and η_{rw} are the gear ratio and transmission efficiency from the ring gear to the driven wheels, respectively, T_{tm} is the traction motor torque, and η_{mw} and i_{mw} are the transmission efficiency and gear ratio from the traction motor to the driven wheels, where $i_{mw} = (Z_2Z_5)/(Z_3Z_4)$ (Z_2, Z_3, Z_4, and Z_5 are the tooth numbers of the corresponding gears as shown in Figure 9.6).

The total traction torque request on the driven wheels, which is commanded by the driver through the accelerator pedal, can be met by the torque outputs from the ring gear, T_{ring}, and the traction motor, T_{tm}. As mentioned above, T_{ring} can be obtained by controlling the engine throttle and the motor/generator torque to operate the engine with high efficiency. The contributions of T_{ring} and T_{tm} to the total depend on the control strategy of the drive train, which will be discussed in the next section.

Figure 9.18 illustrates the simulation results of an example drive train with full engine throttle opening and full traction motor load (maximum torque vs. motor speed). In the simulation, the engine rpm is controlled such that, at low vehicle speeds, the engine operates with a constant speed (1200 rpm in this example) and the motor/generator operates with positive speeds. At medium vehicle speeds, the motor/generator is locked to the vehicle frame and the engine speed linearly increases with vehicle speed (pure parallel or pure torque-coupling operation). At high vehicle speeds, the engine again operates with a constant speed (3500 rpm in this example) and the motor/generator

FIGURE 9.18 Torques and speeds of the engine, traction motor, motor/generator, and driven wheels with full engine throttle opening and full loading of the traction motor along vehicle speed: (a) speeds, (b) torques of the power plants, and (c) torques on the driven wheels.

operates with negative speed (rotating in the opposite direction of the engine). With the pervious engine speed control, the engine operating speeds are constrained in the medium range in which the engine efficiency may be higher. It is noted that the motor/generator is de-energized in the medium vehicle

speed range for using the high engine torque and closing the energy flow through the motor/generator, which may cause more energy loss.

Similar to the series (electrical coupling) and parallel (mechanical coupling) drive trains, the maximum torque on the driven wheels, corresponding to full accelerator pedal position, full engine throttle opening, and full traction motor load, dictates vehicle performance, such as acceleration and gradeability. On the other hand, with a partially depressed accelerator pedal (partial load request), the engine or traction motor or both have to reduce their torques to meet the traction torque demand. Thus, a control strategy is needed to properly allocate the total load power to the power sources.

9.2.4 Drive Train Control Strategies

The distinct property of the above hybrid drive train is that the engine speed and torque can be decoupled completely or partially from the driven wheels through speed coupling and torque coupling. It also has much more flexibility than series or parallel hybrid drive trains in the choice of the active operation mode. Thus, this drive train has more potential for the improvement of drive train efficiency and emissions. But it heavily relies on system control. There are much more varieties of control strategies, due to more available operation modes. Nevertheless, the control objectives are the same as in the series and parallel drive trains, that is, high overall fuel utilization efficiency and low emission under conditions of (1) always meeting the driver's torque command (traction and braking) and (2) always maintaining the SOC of the PPS at a reasonable level, for example, around 70% and never lower than 30%.

9.2.4.1 Engine Speed Control Strategy

The vehicle speed range is divided into three regions, low, medium, and high as shown in Figures 9.18 and 9.19. When the vehicle speed is lower than a given speed V_L, the speed-coupling mode is used to avoid too low engine speed. The vehicle speed V_L is determined by the lowest engine speed allowed with zero motor/generator speed (lock 1 locks the sun gear to the stationary frame) and can be expressed as
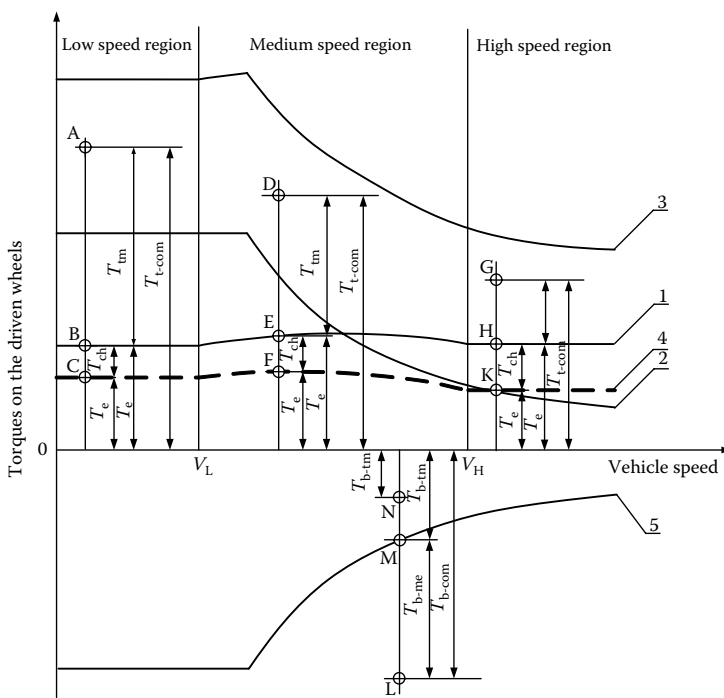
$$V_L = \frac{\pi k_{yr} r_w n_{e\text{-min}}}{30 i_{rw}} \, (\text{m/s}), \tag{9.14}$$

where $n_{e\text{-min}}$ is the minimum engine rpm allowed and r_w is the wheel radius of the vehicle in m.

In this low vehicle speed region, the motor/generator has to be operated with a positive speed, which, from Equation 9.2, can be expressed as

$$n_{m/g} = k_{ys} \left(n_{e\text{-min}} - \frac{30 i_{rw} V}{\pi k_{yr} r_w} \right), \tag{9.15}$$

where V is the vehicle speed in m/s ($V \leq V_L$).

FIGURE 9.19 Schematic illustration of the MAX. SOC control strategy.

1—The traction torque developed by the maximum torque with optimal throttle

2—Traction torque developed by the maximum traction motor torque

3—The maximum traction torque developed by both the engine and traction motor

4—The traction torque developed by the engine with partial throttle

5—The maximum braking torque developed by the traction motor

$T_{t\text{-com}}$—Commanded traction torque by the driver

$T_{t\text{-e}}$—Traction torque developed by the engine torque

$T_{t\text{-tm}}$—Traction torque developed by the traction motor

T_{ch}—Equivalent traction torque for PPS charging

$T_{b\text{-com}}$—Commanded braking torque

$T_{b\text{-tm}}$—Braking torque produced by the traction motor

$T_{b\text{-me}}$—Braking torque produced by mechanical brake

As indicated by Equation 9.3, the torque produced by the motor/generator, applied to the sun gear of the planetary unit, has the direction opposite to its speed. Therefore, in this case, the motor/generator absorbs part of the engine power to charge the PPS. The power on the motor/generator shaft,

with ignored losses, can be expressed as

$$P_{m/g} = \frac{2\pi}{60} T_{m/g} n_{m/g} = \frac{2\pi}{60} T_e n_{e\text{-min}} - \frac{i_{rw}}{k_{yr} r_w} T_e V. \tag{9.16}$$

The first term on the right-hand side is the power that the engine produces, and the second term is the power that is delivered to the driven wheels.

When the vehicle speed is higher than V_L, but lower than a given speed V_H, the motor/generator is de-energized and the sun gear (the shaft of the motor/generator) is locked to the stationary frame of the vehicle. The drive train operates in the torque-coupling mode. The engine speed is proportional to the vehicle speed. Speed V_H is determined by the maximum engine speed allowed $n_{e\text{-max}}$, beyond which the engine operating efficiency may be reduced. When the vehicle speed is higher than V_H, the engine speed is kept constant at $n_{e\text{-max}}$, and the motor/generator starts working again with a negative speed to compensate for the engine speed. V_H can be expressed as

$$V_H = \frac{\pi k_{yr} r_w n_{e\text{-max}}}{30 i_{rw}} \text{(m/s)}, \tag{9.17}$$

where $n_{e\text{-max}}$ is the maximum engine rpm allowed.

In this medium-speed region, all the engine power is delivered to the driven wheels.

When the vehicle speed is higher than V_H, for limiting the engine speed below the maximum engine speed allowed $n_{e\text{-max}}$, the motor/generator has to be operated in the direction opposite to the engine speed, which can be expressed as

$$n_{m/g} = k_{ys} \left(n_{e\text{-max}} - \frac{30 k_{ys} i_{rw} V}{\pi k_{yr} r_w} \right), \tag{9.18}$$

where $V \geq V_H$.

The motor/generator is in motoring. The motoring power can be expressed as

$$P_{m/g} = \frac{2\pi}{60} T_{m/g} n_{m/g} = \frac{i_{rw}}{k_{yr} r_w} T_e V - \frac{2\pi}{60} T_e n_{e\text{-max}}. \tag{9.19}$$

The first term on the right-hand side is the total power delivered to the driven wheels and the second term is the power that the engine produces. The motor/generator accepts power from the PPS.

9.2.4.2 Traction Torque Control Strategy

Similar to the torque (power) control in the parallel hybrid drive train, Figure 9.19 conceptually shows the allocation of the total traction torque

commanded by the driver to the engine (motor/generator) and the traction motor, or the total braking torque commanded to the traction motor and the mechanical braking system.

9.2.4.2.1 In Low Vehicle Speed Region

As mentioned above, when the vehicle speed is lower than V_L, the engine is operated at a specified speed, $n_{e\text{-min}}$. The engine torque labeled 1 in Figure 9.19 is produced with an engine throttle at which the engine has maximum fuel utilization efficiency at this speed. This engine throttle is possibly near its full opening point.

Point A represents a traction torque commanded by the driver, which is larger than the torque that the engine can produce with the optimal engine throttle as shown in Figure 9.16. In this case, the engine alone cannot handle this commanded torque, and needs the help of the traction motor. In this case, the engine should be controlled with its optimal throttle as shown by point B in Figure 9.19. However, the torque that the traction motor can produce depends on the energy level of the PPS. When the SOC of the PPS is lower than a specified value SOC_L (30% for example), the PPS should not be further discharged. In this case, the maximum power of the traction motor is the power generated by the motor/generator described by Equation 9.16. Neglecting the losses, the traction motor torque can be expressed as

$$T_{mt} = \frac{60}{2\pi} \frac{P_{m/g}}{n_{tm}} = \left(\frac{n_{e\text{-min}}}{n_{tm}} - \frac{i_{rw}}{k_{yr} i_{mw}} \right) T_e = \left(\frac{2\pi r_w}{60 i_{mw}} \frac{n_{e\text{-min}}}{V} - \frac{i_{rw}}{i_{mw} k_{yr}} \right) T_e,$$

$$(9.20)$$

where i_{mw} is the gear ratio from the traction motor to the driven wheels described by $i_{mw} = (Z_2 Z_5)/(Z_3 Z_4)$ as shown in Figure 9.6.

In this case, the planetary gear unit, the motor/generator, and the traction motor together function as an EVT, because no energy goes into or comes out of the PPS.

When the SOC is higher than the bottom line, SOC_L, that is, the PPS has sufficient energy to support the traction motor, the traction motor should be controlled to produce its torque, T_{tm}, to meet the commanded traction torque as shown in Figure 9.19. In this case, the PPS supplies its power to the traction motor.

When the commanded torque, $T_{t\text{-com}}$, is smaller than the engine torque produced with optimal throttle as shown by point B in Figure 9.19, there are several options in choosing the engine and traction motor operations: (1) With the SOC of the PPS lower than SOC_L, the engine may be operated with the speed of $n_{e\text{-min}}$ and optimal throttle (point B in Figure 9.19). The PPS is charged by the motor/generator with the power of $P_{m/g}$ (refer to Equation 9.16) and the traction motor torque, T_{ch}, as shown in Figure 9.19. (2) With the SOC of the PPS in between the SOC_L and SOC_H ($SOC_L < SOC < SOC_H$), the engine and

the motor/generator may be controlled so that the engine operates with the speed of $n_{e\text{-min}}$ and produces the torque that meets the commanded traction torque. The traction motor is idling (de-energized). The PPS is charged only by the motor/generator. (3) With the SOC of the PPS higher than SOC_H, the engine is shut down and the traction motor alone produces its torque to meet the traction torque demand.

9.2.4.2.2 In Medium Vehicle Speed Region

When the vehicle speed is in a range higher than V_L but lower than V_H as shown in Figures 9.18 and 9.19, only the torque-coupling (traditionally parallel) mode is employed, that is, lock 1 locks the sun gear of the planetary gear unit (the shaft of the motor/generator) to the stationary vehicle frame. In this mode, engine speed is proportional to vehicle speed. The engine and traction motor control strategy, based on the commanded traction torque and SOC of the PPS, is exactly the same as that discussed in Chapter 8.

9.2.4.2.3 In High Vehicle Speed Region

When the vehicle speed is higher than V_H, as shown in Figures 9.18 and 9.19, the engine speed is controlled at its top $n_{e\text{-max}}$. In this case, the motor/generator works in the motoring mode, taking energy from the PPS and delivering it to the drive train. The motoring power is described by Equation 9.19. The torques of the engine and traction motor are controlled based on the commanded traction torque and energy level of the PPS.

When the commanded traction torque, $T_{t\text{-com}}$ (point G in Figure 9.19), is larger than the torque that the engine can produce with its optimal throttle at the speed of $n_{e\text{-max}}$, and the SOC of the PPS is lower than SOC_L, that is, the PPS cannot be discharged any more to support the motoring operation of the motor/generator and traction motor, the engine has to be forced to operate with a speed higher than the specified speed, $n_{e\text{-max}}$, to develop larger power. In this case, there are two options: one is to use the engine-alone mode with only torque coupling, which is the same as in the medium vehicle speed range; the other is to control the engine to operate with a speed somewhat higher than the speed that corresponds to the vehicle speed in the torque-coupling mode. That is,

$$n_e > \frac{30 i_{rw} V}{\pi k_{yr} r_w}. \tag{9.21}$$

The term on the right-hand side is the engine speed that corresponds to the vehicle speed V in the torque-coupling mode. In this way, the motor/generator can be operated in its generating mode as discussed above. The generating power from the motor/generator can feed the traction motor to generate additional traction torque. This operating mode is the EVT mode as discussed above.

If the SOC of the PPS is at its medium and high levels, that is, SOC > SOC_L, the engine is controlled at its specified speed, $n_{e\text{-max}}$, with the optimal

engine throttle (point H in Figure 9.19). The traction motor produces its torque, together with the engine torque, to meet the commanded traction torque.

In case the commanded traction torque is smaller than the engine torque with the optimal throttle as shown by point K in Figure 9.19, and the SOC of the PPS is below SOC_L, the engine is operated at point K and the traction motor works in its generating mode to charge the PPS. If the SOC is in the medium region ($SOC_L < SOC < SOC_H$), the traction motor may be de-energized and the engine alone propels the vehicle (point K). If the SOC of the PPS is at a high level ($SOC > SOC_H$), the engine may be shut down and the traction motor alone propels the vehicle.

9.2.4.3   Regenerative Braking Control

Similar to the parallel drive train control, when the commanded braking torque is larger than the maximum torque that the motor can produce in generating mode, both regenerative braking by the traction motor and mechanical braking are applied. Otherwise only regenerative braking is applied. For a detailed discussion, refer to Chapter 13.

It should be noted that the control strategies discussed above are only for guidance in a real control strategy design. More careful and insightful studies are necessary based on the special design constraints, design objectives, component characteristics, operation environments, and so on. More complicated and subtle approaches may be employed, such as fuzzy logic, dynamic programming, and so on. Further, computer simulations are very useful in designing a good control strategy.

9.3   Drive Train Parameters Design

The design principles of drive train parameters, such as engine power, motor power, and the power and energy capacity of the PPS, are very similar to those in series and parallel drive trains discussed in Chapters 7 and 8. Therefore, they are not discussed further in this chapter. However, the torque and power capacity design of the motor/generator may need further discussion.

From Equations 9.3 and 9.4 and Figure 9.5, it can be seen that the motor/regenerator torque is required to balance the engine torque at nearly full throttle, in the speed regions of lower than the minimum speed, $n_{e\text{-min}}$, and higher than the maximum speed, $n_{e\text{-max}}$. Thus, the torque capacity of the motor/generator is determined by the maximum engine torque in the low-speed and high-speed regions. However, for purposes of safety, the torque capacity of the motor/generator would be designed to be able to balance the maximum torque of the engine in its entire speed range. Figure 9.5

also indicates that this maximum motor torque should be available in its entire speed range, rather than a special point. Thus, the ideal torque–speed characteristic is a constant torque in its entire speed range, which can be expressed as

$$T_{\text{m/g-max}} = \frac{T_{\text{e-max}}}{k_{\text{ys}}}. \tag{9.22}$$

Here, $T_{\text{e-max}}$ is the maximum engine torque with fully open throttle.

From Equation 9.16, it is obvious that the generating power of the motor/generator is maximized at zero vehicle speed, that is, all the power produced by the engine goes to the motor/generator. Thus, the maximum generating power of the motor/generator can be determined by

$$P_{\text{m/g-max}} = \frac{2\pi}{60} T_{\text{e-max}} n_{\text{e-min}}. \tag{9.23}$$

Similarly, the maximum motoring power of the motor/generator occurs at the maximum vehicle speed, V_{max}, as indicated by Equation 9.19, which can be expressed as

$$P_{\text{m/g-ma}} = \frac{i_{\text{rw}}}{k_{\text{yr}} r_{\text{w}}} T_{\text{e-max}} V_{\text{max}} - \frac{2\pi}{60} T_{\text{e-max}} n_{\text{e-max}}. \tag{9.24}$$

9.4 Simulation of an Example Vehicle
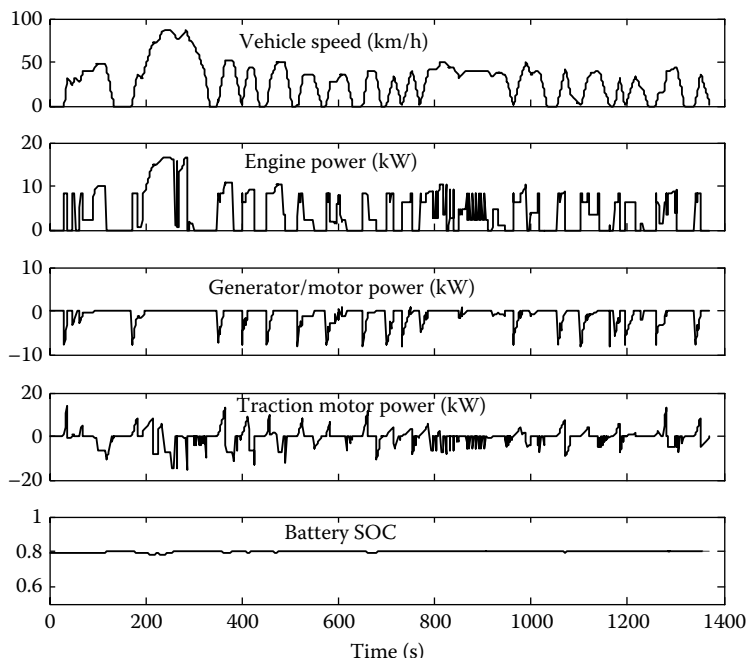
Based on the design and control principles discussed in previous sections, a 1500-kg passenger car has been simulated in FTP75 urban and highway driving cycles. The parameters of the vehicle simulated are listed in Table 9.1.

Figure 9.20 shows the simulation results of vehicle speed, engine power, motor/generator power, traction motor power, and SOC of the PPS in an FTP urban driving cycle. It can be seen that the motor/generator always

TABLE 9.1

Vehicle Parameters

Vehicle mass	1500 kg
Engine power	28 kW
Traction motor power	40 kW
Generator motor power	15 kW
Tire rolling resistance coefficient	0.01
Aerodynamic drag coefficient	0.3
Front area	2.2 m^2
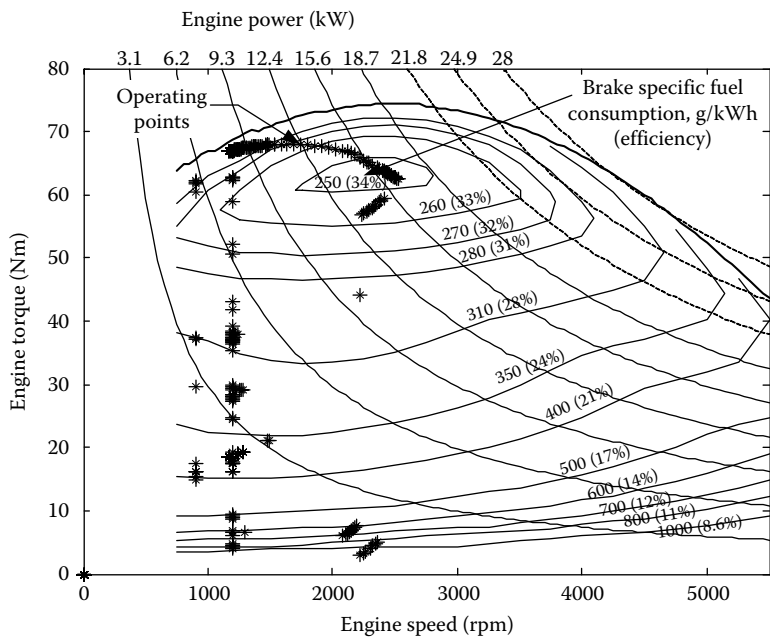
FIGURE 9.20 Vehicle speed, engine power, generator/motor power, traction motor power, and battery SOC in an FTP75 urban driving cycle.
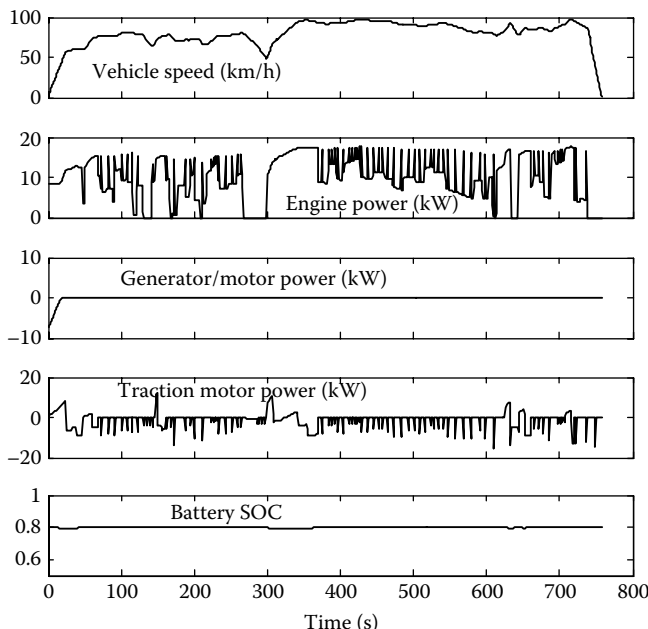
works in the generating mode (negative power) because of the low vehicle speeds. Through the regenerative braking and charging from the engine by the motor/generator, the PPS SOC can be easily maintained at a high level, which ensures that the PPS is always able to supply sufficient power to the drive train for acceleration.

Figure 9.21 shows the engine operating points on the engine fuel consumption map. This figure indicates that the engine, most of the time, operates in its high-efficiency area. Engine-alone traction with light load and high SOC of the PPS causes some engine operating points away from its high-efficiency area. The fuel consumption of the vehicle in an FTP urban driving cycle obtained from the simulation is 5.88 L per 100 km or 40.2 mpg.
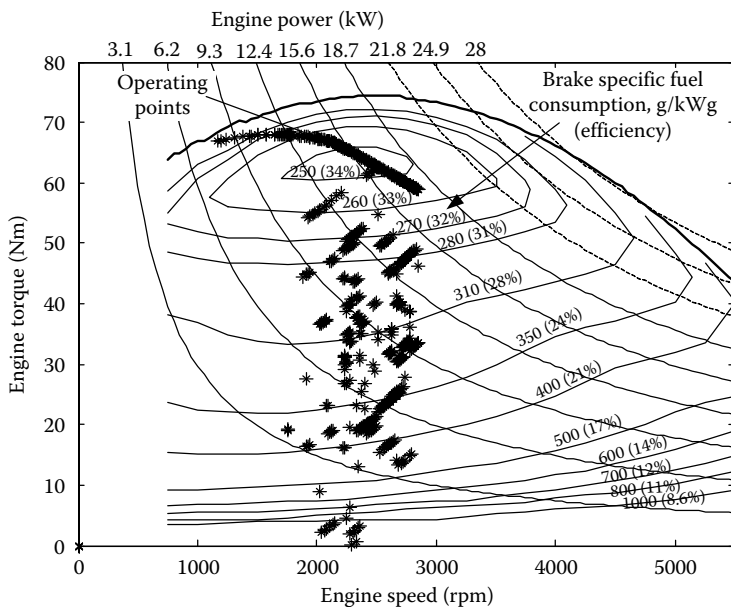
Figures 9.22 and 9.23 show the simulation results while driving in an FTP75 highway cycle. It can be seen that the generator/motor power is zero, except in a short time period of cycle start. This means that the drive train, most of the time, worked with a pure torque coupling (the sun gear and its motor/generator are locked to the vehicle frame). Simulation indicates that the fuel consumption of the vehicle in an FTP75 highway driving cycle is 4.96 L/100 km or 47.7 mpg.

FIGURE 9.21 Engine operating points on its fuel consumption map in an FTP75 urban driving cycle.

FIGURE 9.22 Vehicle speed, engine power generator/motor power, traction motor power, and battery SOC in an FTP75 highway driving cycle.

FIGURE 9.23 Engine operating points on its fuel consumption map in an FTP75 highway driving cycle.

References

1. Y. Gao and M. Ehsani, "A torque and speed coupling hybrid drive train—architecture, control, and simulation," *IEEE Transactions on Power Electronics*, 21 (3), 741–748, May 2006.
2. C. C. Chan and K. T. Chau, *Modern Electric Vehicle Technology*, Oxford University Press, New York, 2001.
3. I. Husani, *Electric and Hybrid Vehicles—Design and Fundamentals*, CRC Press LLC, New York, 2003.
4. M. Ehsani, Y. Gao, and K. Butler, "Application of electrically peaking hybrid (ELPH) propulsion system to a full size passenger car with simulated design verification," *IEEE Transaction On Vehicular Technology*, 48 (6), November 1999.
5. Nedunadi, M. Walls, and D. Dardalis, "A parallel hybrid drive train," *SAE*, SP-1466, Paper No. 1999-01-2928.
6. K. Yamaguchi, S. Moroto, K. Kobayashi, M. Kawamto, and Y, Miyaishi, "Development of a new hybrid system-duel system," *SAE*, SP-1156, Paper No. 960231, 1996.

10

Design and Control Principles of Plug-In Hybrid Electric Vehicles

As discussed in the previous chapters, in the PPS charge sustained hybrid drive train, the net energy consumption in PPS in a complete driving cycle is zero, that is, the energy level in the PPS at the beginning of the driving cycle is equal to the energy level at the end of the driving cycle. All the propulsion energy comes from the primary energy source: gasoline or diesel for IC engines; hydrogen or hydrogen-based fuel for fuel cells. During operation, the energy in the PPS fluctuates in a narrow window. The PPS size is determined by power rather than energy capacity. The energy-to-power ratio is in the range of 0.05–0.1 kWh/kW. That is to say, with a given power capacity, the energy storage in PPS is considered to be sufficient if it can sustain 0.05–0.1 h with the given power. Thus, the PPS is more an energy buffer than energy storage. This is also the origin of the name PPS (peaking power source). At present and in the immediate future, ultracapacitors and high-power batteries or their combination are the most promising candidates as the PPS of the PPS charge sustained HEVs (for details, refer to Chapter 12 of Peaking Power Source and Energy Storage).

With the development and maturing of advanced battery technologies, the energy storage capacity of batteries has significantly improved. Obviously, using high-energy batteries only as a PPS is a waste.

The plug-in hybrid electric drive train is designed to fully or partially use the energy of the energy storage to displace part of the primary energy source, such as gasoline, diesel, hydrogen, and so on.

All the configurations discussed in Chapter 5 can be employed in plug-in hybrid electric drive trains. Most of the differences from the PPS sustained hybrid drive train are in the drive train control strategy, energy storage design, and perhaps, slightly different electric motor power design. This chapter will concentrate on these three topics.
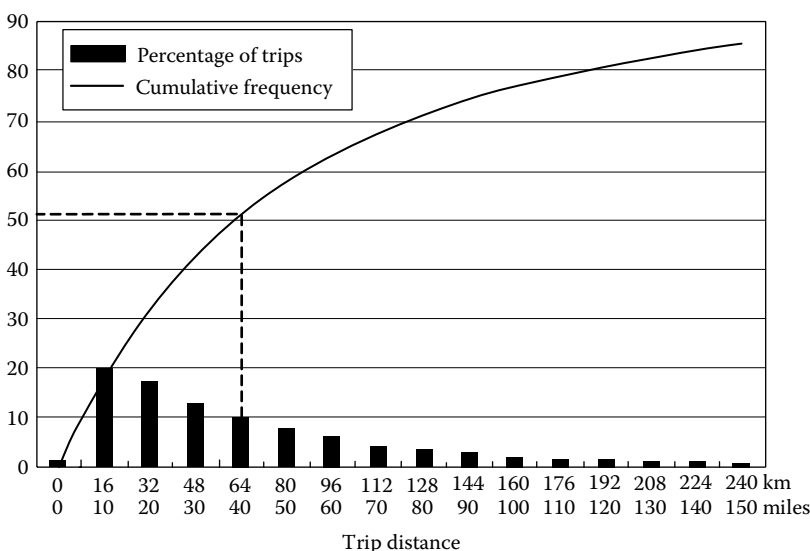
10.1 Statistics of Daily Driving Distance

Charging the energy in the energy storage device from the utility grid, to displace part of the petroleum fuel, is the major feature of the plug-in hybrid

electric vehicles (PHEVs). The amount of petroleum fuel displaced by the utility electricity depends mainly on the amount of electrical energy per recharge, that is, the energy capacity of the energy storage; total driving distance between recharges, that is, usual daily driving distance; and electrical power usage profiles, that is, the driving cycle features and control strategies. To achieve optimal design, especially for the energy storage system, understanding the daily driving distance in a typical environment is very helpful.

Figure 10.1 is a histogram showing the daily driving distance distribution and the cumulative frequency derived from the 1995 National Personal Transportation Survey data.[1,2] The cumulative frequency or utility factor in reference[1] represents the percentages of the total driving time (days) during which the daily driving distances are less than or equal to the said distance on the horizontal axis. Figure 10.1 reveals the fact that about half of the daily driving distance is less than 64 km (40 miles). If a vehicle is designed to have 64 km (40 miles) of pure EV range, that vehicle will have half of its total driving distance from the pure EV mode. Even if the daily traveling distance is beyond this 60 km (40 miles) pure EV range, a large amount of the petroleum fuel can be displaced by electricity, due to the pure EV mode taking a large portion of the daily travel. Research also shows that even if the pure EV range is less than 64 km (40 miles), such as 32 km (20 miles), there is still a large amount of petroleum that can be displaced in normal daily driving.[1]

FIGURE 10.1   Daily driving distance distribution and cumulative factor.

10.2 Energy Management Strategy

First, some definitions about PHEV are introduced:

- *Charge-Depleting (CD) Mode*: An operating mode in which the SOC of the energy storage may fluctuate, but on average decreases while driving.
- *Charge-Sustaining (CS) Mode*: An operating mode in which the SOC of the energy storage may fluctuate but on average is maintained at a certain level while driving.
- *All Electric Range (AER)*: After a full recharge, the total miles (kilometers) driven electrically (engine off) before the engine turns on for the first time.
- *Electric Vehicle Miles (EVM) or Kilometers (EVKM)*: After a full recharge, the cumulative miles or kilometers driven electrically (engine off) before the vehicle reaches CS mode.
- *Charge-Depleting Range (CDR)*: After a full recharge, the total miles or kilometers driven before the vehicle reaches CS mode. It should be noted that EVM or EVKM dictates pure electric driving. However, CDR may include engine propulsion, but the on-average SOC of the energy storage decreases till the sustaining level.
- *PHExx*: A PHEV with useable energy storage equivalent to *xx* miles of driving energy on a reference driving cycle, where *xx* stands for the mileage number. For example, PHEV20 can displace petroleum energy equivalent to 20 miles of driving on the reference driving cycle with off-board electricity. A similar definition can be made in kilometers. It should be noted that PHEV20, for example, does not imply that the vehicle will achieve 20 miles of AER, EVM, or CDR on the reference cycle, nor any other cycle. Operating characteristics also depend on the power ratings of components, the power train control strategy, and the nature of the driving cycle.[1]

10.2.1 AER-Focused Control Strategy

The idea of this control strategy is to use the energy of the energy storage intensively in the AER.[3,4] One possibility is to allow the driver to manually select between a CS mode and a full EV operating mode. This design could be useful for vehicles that may be used in the region where combustion engine use is restricted. This design provides flexibility for the driver to determine the times that the pure EV mode is used. For example, in a trip that includes places where pure EV operation is required, the driver can select the pure EV operating mode just prior to entering this area in order to have sufficient

range. In other places, the vehicle may be operated in pure EV mode or CS mode, depending on the energy status of the energy storage and the power demand. In normal conditions, where the trip does not include mandatory pure EV operation, the driver could select the pure EV mode at the start of the trip in order to fully use the energy of the energy storage to displace the petroleum fuel, until the energy of the energy storage reaches its specified level at which the CS mode will start automatically.

This energy management approach clearly divides the whole trip into pure EV and CS modes. Thus, the design and control techniques developed for EV and HEV in the previous chapters can be used. When series hybrid configuration is used, the power rating designs of the motor, engine, and energy storage are almost the same as in the CS hybrid. The motor power guarantees the acceleration and gradeability performance, the engine/generator power supports the vehicle driving at a constant speed on flat or mild grades, and the energy storage power is larger (or at least not smaller) than the motor power minus the engine/generator power. However, the energy storage has to be designed so that its useable energy can meet the requirement of the pure EV range. When parallel or series/parallel configuration is used, the motor power should be designed to meet the peaking power requirements of the reference driving cycles. Otherwise, the vehicle cannot follow the speed profile of the drive cycle, and will be somewhat sluggish, compared to the driver expectation.
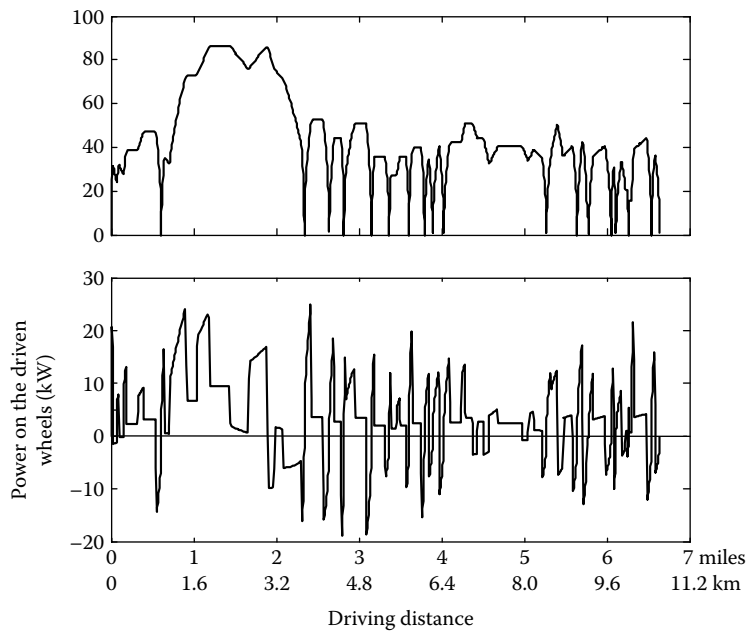
The traction power computations in typical driving cycles have been discussed in detail in previous chapters. However, for the reader's convenience, it is repeated below.

The traction power on the driven wheels includes the rolling resistance, aerodynamic drag, inertial force of acceleration, and grade resistance, which can be expressed as

$$P_t = \frac{V}{1000}\left(Mgf_r + \frac{1}{2}\rho_a C_D A_f V^2 + M\delta\frac{dV}{dt} + Mgi\right)(kW), \qquad (10.1)$$

where M is the vehicle mass in kg, V is the vehicle speed in m/s, g is the gravity acceleration, 9.81 m/s^2, ρ_a is the air mass density, 1.205 kg/m^3, C_D is the aerodynamic drag coefficient of the vehicle, A_f is the front area of the vehicle in m^2, δ is the rotational inertia factor, dV/dt is the acceleration in m/s^2, and i is the road grade. In standard driving cycles, flat roads are used.

Figure 10.2 is a diagram showing the vehicle speed and the traction power, on the driven wheels, versus the traveling distance in the FTP75 urban driving cycle. The vehicle parameters used in this computation are listed in Table 10.1. Figure 10.2 indicates that the peaking traction power on the driven wheels is about 25 kW. However, there are power losses in the path from the energy storage to the driven wheels. In order to meet the power requirement, the motor output power should be designed to account for the power losses from the motor shaft to the driven wheels. Suppose that the efficiency from the

FIGURE 10.2 Vehicle speed and traction power in an FTP75 urban driving cycle.

motor shaft to the driven wheels is 90%; then the motor shaft power rating is about 28 kW. It should be noted that this required motor power is also related to the vehicle speed at which this peak power occurs. For example, the peaking power in Figure 10.2 occurs at a vehicle speed of 50 km/h (31.25 mph). In the motor power design, we must be sure that the motor can produce this peak power at this vehicle speed. Similarly, the peaking power of the energy storage should include the losses in the electric motor, the power electronics, and the transmission. Suppose that the efficiencies of the motor and power electronics are 0.85 and 0.95, respectively; then the power capacity of the energy storage is about 34.7 kW in this example. Table 10.2 lists the motor power and the energy storage power in FTP75 urban, FTP75 highway, LA92, and US06 driving cycles.

TABLE 10.1

Vehicle Parameters Used in Power Computation

Vehicle mass (kg)	1700
Rolling resistance coefficient	0.01
Aerodynamic drag coefficient	0.3
Front area (m^2)	2.2
Rotational inertia factor	1.05

TABLE 10.2
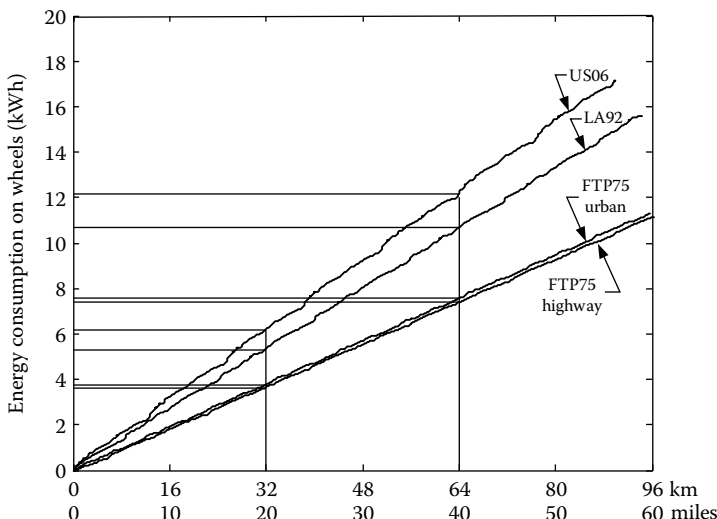
Powers of Motor and Energy Storage in Typical Driving Cycles

Cycles Power (kW) Item	FTP75 Urban	FTP75 Highway	LA92	US06
Motor at vehicle speed	28 at 50 km/h (31 mph)	32 at 72 km/h (57 mph)	55 at 57 km/h (36 mph)	98 at 117 km/h (73 mph)
Energy storage	35.7	39	68.5	121

Integrating Equation 10.1, over the driving time in a driving cycle, can give the energy consumption by the driven wheels as shown in Figure 10.3. Here, no regenerative braking is included. When including energy losses in the power electronics, the motor, and the transmission, the useable energy in the energy storage, for 32 km (20 miles) and 64 km (40 miles) of pure EV driving in typical driving cycles, is listed in Table 10.3.

In vehicle design, an appropriate reference driving cycle should be selected. An aggressive driving cycle, such as US06, will need a large motor drive and energy storage, but will also give good vehicle acceleration and gradeability performance. On the contrary, a mild driving cycle, such as FTP75, will lead to a small motor drive and energy storage, but also a sluggish vehicle performance.

The following figures show simulation results of the drive train in the reference driving cycle, FTP75 urban. The vehicle parameters listed in Table 10.1

FIGURE 10.3 Energy consumption by the driven wheels versus driving distance in typical driving cycles.

TABLE 10.3
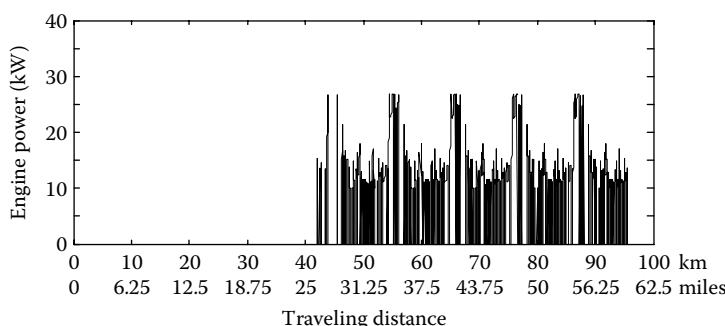
Energy Consumption in Typical Driving Cycles

Cycles Energy (kWh) Distance	FTP75 Urban	FTP75 Highway	LA92	US06
32 km (20 miles)	5.2	5.14	7.29	8.4
64 km (40 miles)	10.4	10.28	14.58	16.8
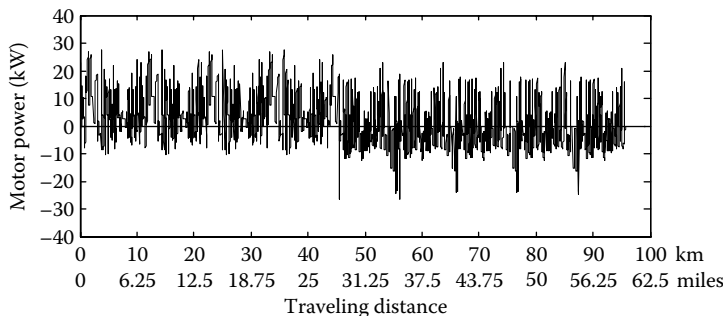
were used. The total energy in the energy storage, fully charged, is 10 kWh. The simulation ran nine sequential cycles and the pure EV mode was started at the beginning of the simulation, until the SOC reached about 30%, beyond which the CS mode was started. The control strategy in the CS mode employed the constrained engine on–off control strategy, discussed in Section 8.2.3. In the simulation, 400 W of constant auxiliary power was added at the terminal of the energy storage.

Figures 10.4 and 10.5 show the engine power and the motor power. Figure 10.6 shows the SOC of the energy storage, and the remaining energy in the energy storage, versus the traveling distance. The pure EV mode range is about 32 km (20 miles). Figure 10.7 shows the engine operating points overlapping its brake-specific fuel consumption map.
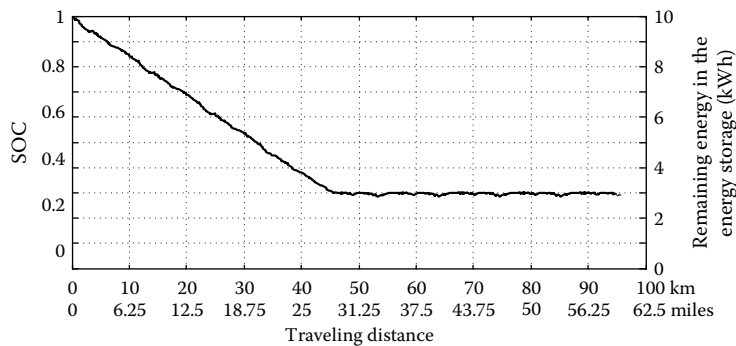
Figures 10.8 and 10.9 show the fuel and electric energy consumption scenarios, in metric and English units, respectively. It can be seen that when the traveling distance is less than four driving cycles (42.5 km or 26.6 miles), the vehicle can completely displace the petroleum fuel with electricity with pure EV mode. The total electric energy consumed is about 7.1 and 15.5 kWh per 100 km, or 4.05 miles/kWh (Figure 10.9). With the increasing total traveling distance, the percentage of the fuel displacement decreases, since the CS modes take larger percentages of the trip. For nine sequential driving cycles (96 km or 60 miles), the fuel and electrical energy consumptions are about 3.2 L/100 km (Figure 10.8) or 74 mpg (Figure 10.9), and 7.42 kWh/100 km (Figure 10.8) or 8.43 mile/kWh (Figure 10.9).
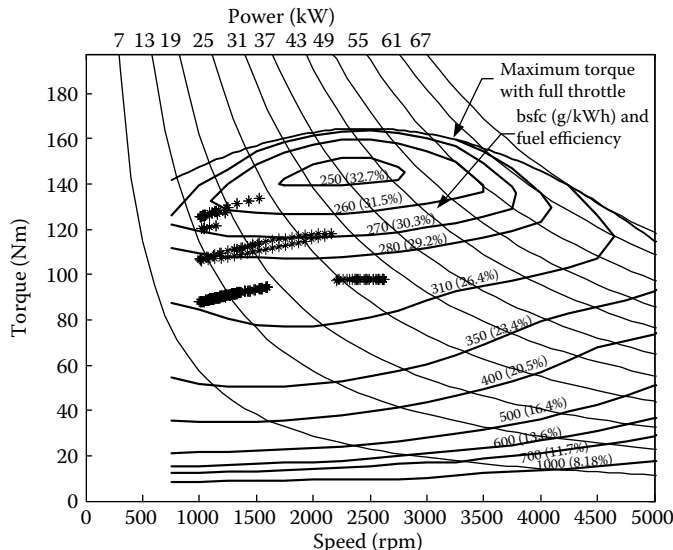
FIGURE 10.4 Engine power versus traveling distance in FTP75 urban driving cycle with AER mode.
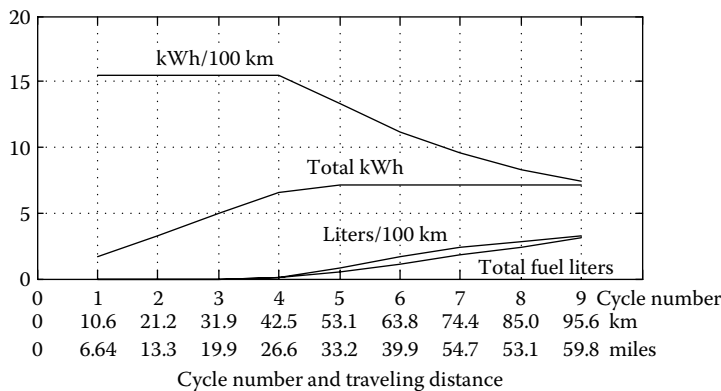
FIGURE 10.5   Motor power versus traveling distance in FTP75 urban driving cycle with AER mode.

FIGURE 10.6   SOC and the remaining energy in the energy storage versus traveling distance in FTP75 urban driving cycle with AER mode.

FIGURE 10.7   Engine operating points overlapping its fuel consumption map in FTP75 urban driving cycle with AER mode.
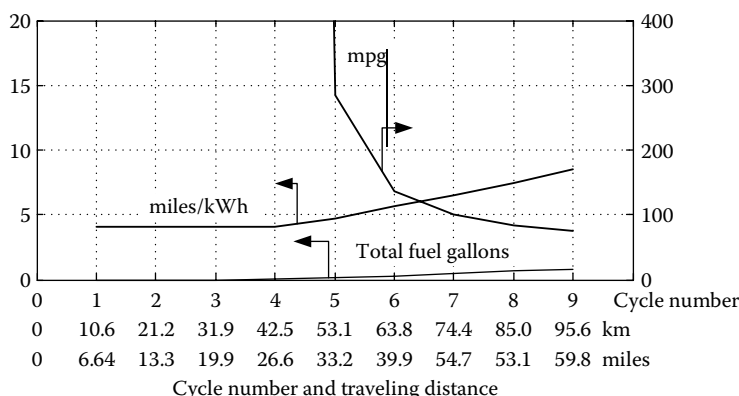
FIGURE 10.8 Fuel and electric energy consumption versus the number of FTP75 urban driving cycle and traveling distance with AER mode in metric unit.
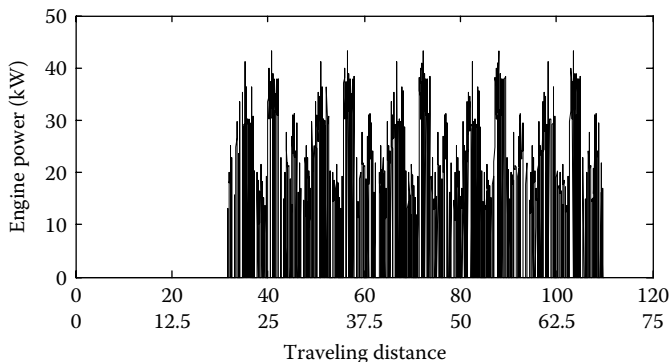
Simulation of the same design in the LA92 driving cycle has also been performed. The results are illustrated in the following figures (Figures 10.10 through 10.15). Comparing the two driving cycles, the LA92 driving cycle has higher vehicle speed and larger acceleration rate. The pure EV range is shorter, and the fuel and electric energy consumptions are higher than in FTP75 urban driving cycles.

10.2.2 Blended Control Strategy
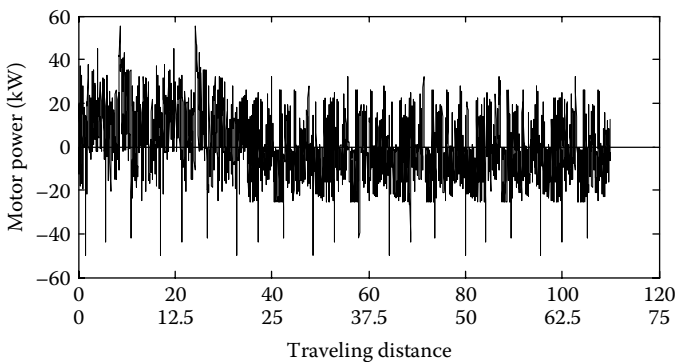
Unlike the AER-focused control strategy, in which a pure EV range is designed, the blended control strategy uses both the engine and the motor for traction, with CD mode, until the SOC of the energy storage reaches the specified low threshold, beyond which the vehicle will operate in the CS mode.
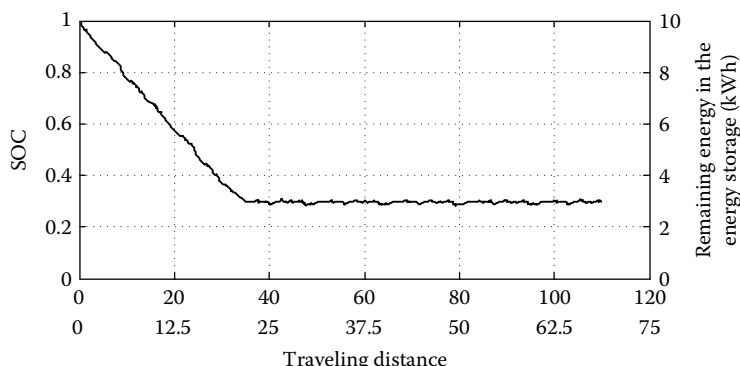
FIGURE 10.9 Fuel and electric energy consumption versus the number of FTP75 urban driving cycle and traveling distance with AER mode in English unit.
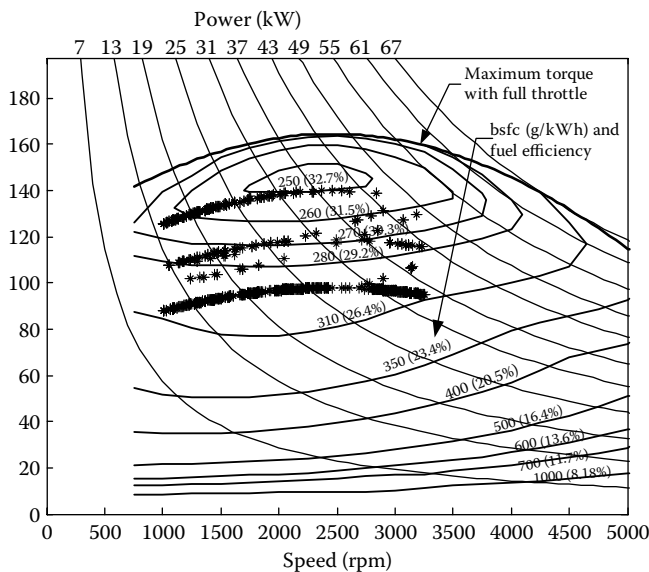
FIGURE 10.10   Engine power versus traveling distance in LA92 driving cycle with AER mode.

FIGURE 10.11   Motor power versus traveling distance in LA92 driving cycle with AER mode.
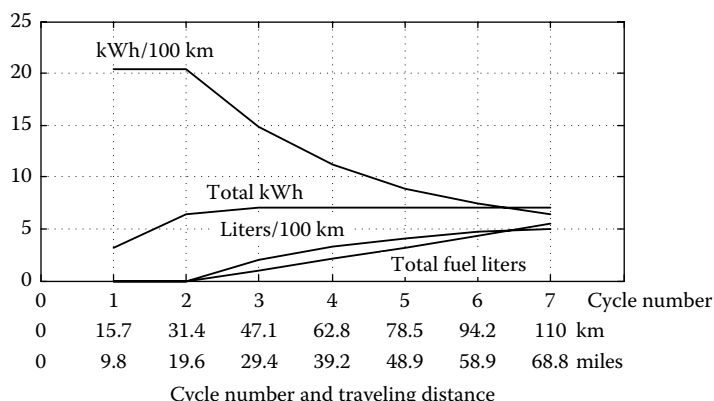
FIGURE 10.12   SOC and the remaining energy in the energy storage versus traveling distance in LA92 driving cycle with AER mode.
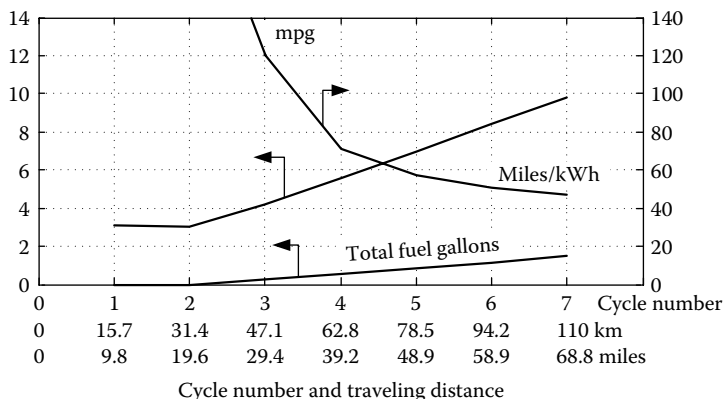
FIGURE 10.13   Engine operating points overlapping its fuel consumption map in LA92 driving cycle with AER mode.

In the CD mode, both the engine and the motor may operate at the same time. The range before entering the CS mode is longer than in the pure EV mode. Control strategies are needed to control the engine and the motor to meet the load demand. There are many possible control strategies. The following is the one in which the engine and the motor alternately propel the vehicle with no battery charging from the engine. The engine is constrained to operate in its optimal fuel economy region. The details are as follows.
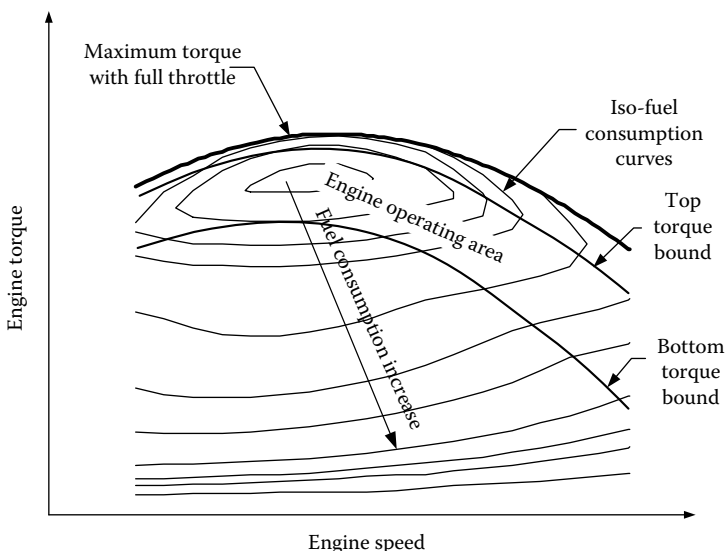
FIGURE 10.14   Fuel and electric energy consumption versus the number of LA92 driving cycle and traveling distance with AER mode in metric unit.
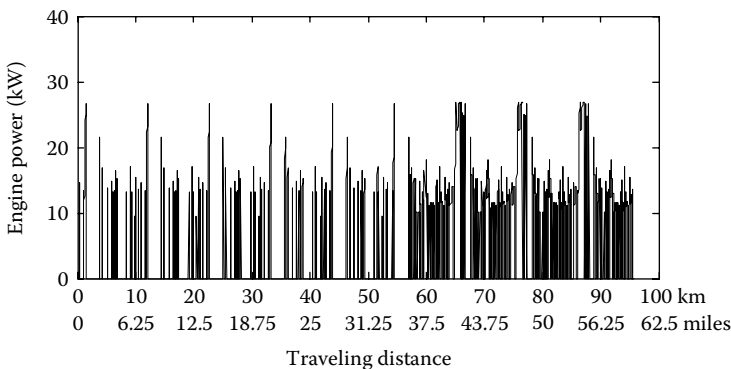
FIGURE 10.15   Fuel and electric energy consumption versus the number of LA92 driving cycle and traveling distance with AER mode in English unit.

Figure 10.16 schematically shows the engine operating area. When the requested engine torque is larger than the upper torque boundary, the engine is controlled to operate on this boundary and the remaining torque is supplied by the electric motor. When the requested engine torque falls below the upper boundary, the engine alone propels the vehicle. When the requested engine torque is below the lower torque boundary, the engine is shut down and the electric motor alone propels the vehicle. In this way, the engine operation is constrained within its optimal region. Due to the absence of battery charging

FIGURE 10.16   Operation area of the engine in the CD mode.
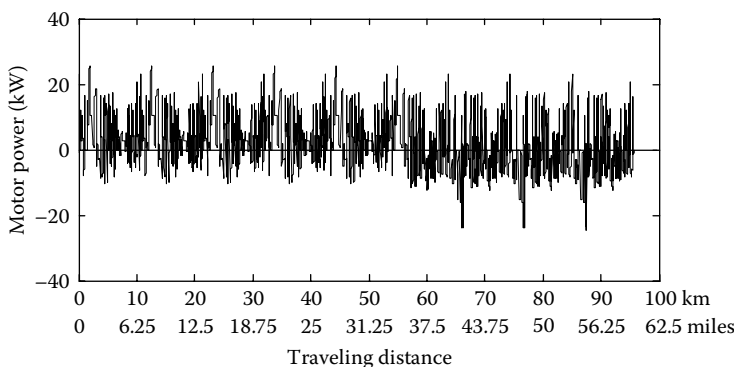
FIGURE 10.17 Engine power versus traveling distance in FTP75 urban driving cycle with CD mode.

from the engine, the battery energy level will continuously fall to its specified lower level. Then the drive train goes into CS mode.
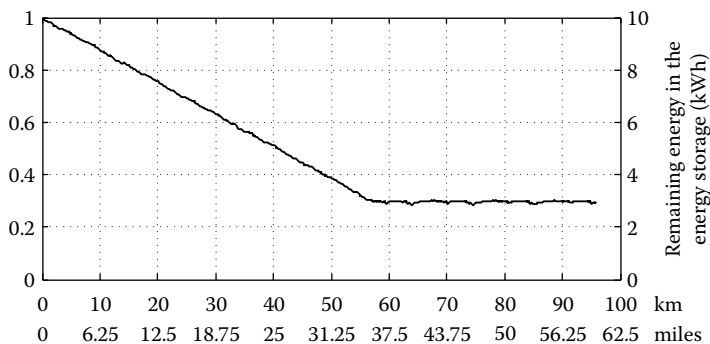
The example vehicle mentioned above has been simulated with the control strategy discussed above in nine sequences of the FTP75 urban driving cycle. The results are shown in Figures 10.17 through 10.22.

Similarly, simulation results in seven sequences of the LA92 driving cycles are shown in Figures 10.23 through 10.28.

It should be noted that the pure EV range is mostly determined by the capacity of the energy storage and its SOC level, at which the CS mode started. The range in the CD mode is also related to the drive train control strategy, especially the specified engine operating region as shown in Figure 10.16. When the engine lower torque boundary is moved downward, that is, the engine operating area is enlarged, the CD mode range is increased. However, the fuel displacement is reduced when the travel distance between chargings

FIGURE 10.18 Motor power versus traveling distance in FTP75 urban driving cycle with CD mode.
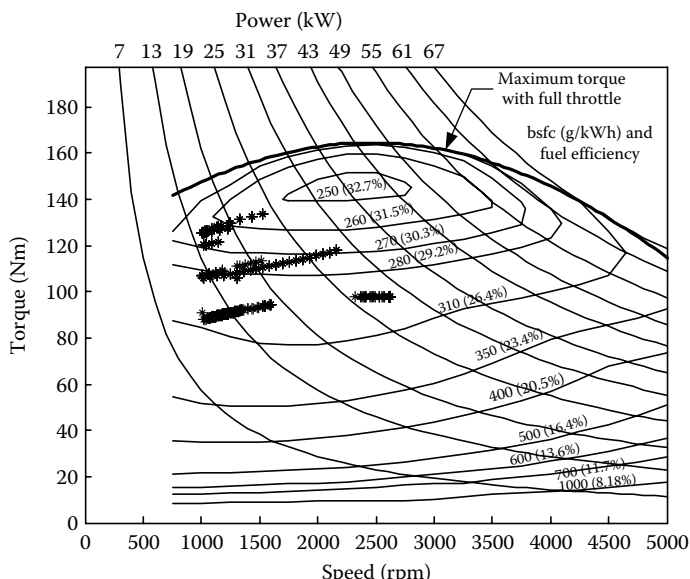
FIGURE 10.19 SOC and the remaining energy in the energy storage versus traveling distance in FTP75 urban driving cycle with CD mode.
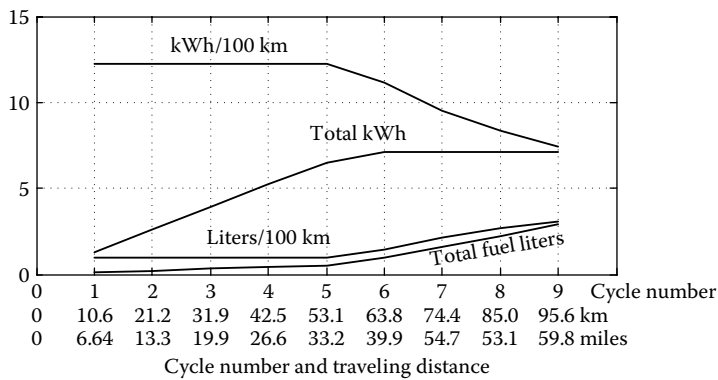
is shorter than the full CD mode range, and the SOC of the energy storage does not hit its lower limit, leaving useable energy in the energy storage.

10.3   Energy Storage Design
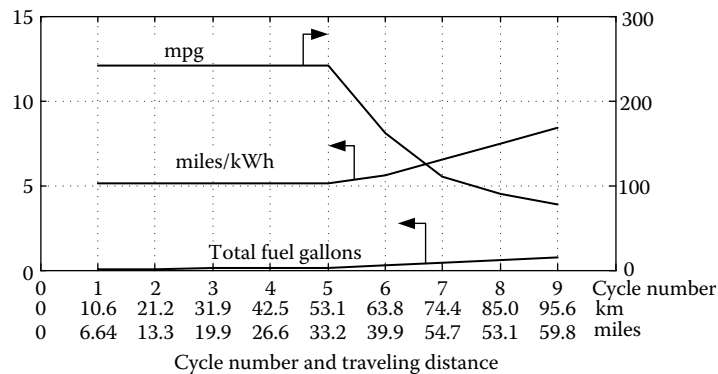
Energy storage is one of the most important components in the plug-in hybrid vehicle. It is closely related to vehicle performance, fuel consumption, fuel
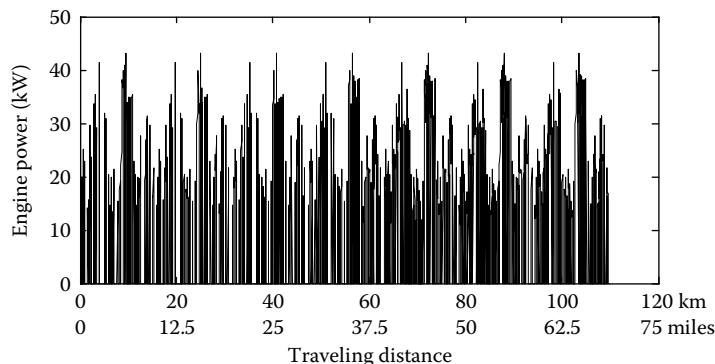
FIGURE 10.20   Engine operating points overlapping its fuel consumption map in FTP75 urban driving cycle with CD mode.
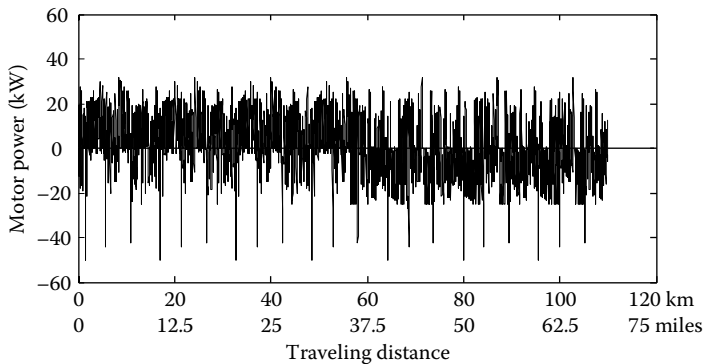
FIGURE 10.21 Fuel and electric energy consumption versus the number of FTP75 urban driving cycle and traveling distance with CD mode in metric unit.

FIGURE 10.22 Fuel and electric energy consumption versus the number of FTP75 urban driving cycle and traveling distance with CD mode in English unit.

FIGURE 10.23 Engine power versus traveling distance in LA92 driving cycle with CD mode.
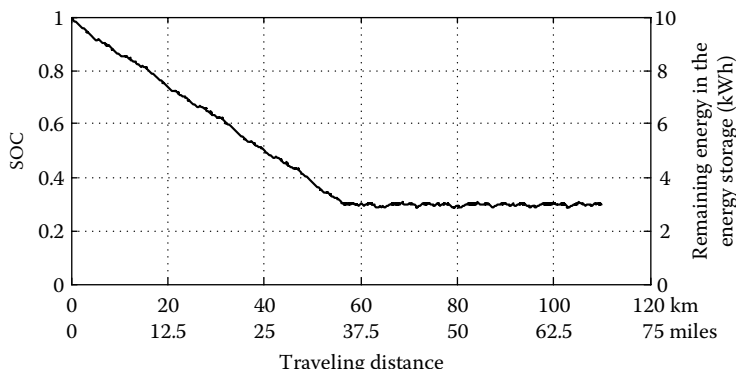
FIGURE 10.24 Motor power versus traveling distance in LA92 driving cycle with CD mode.
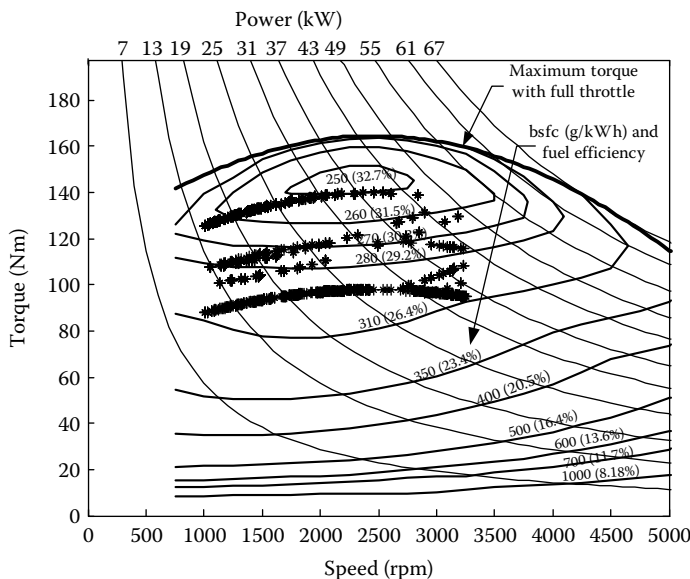
displacement, initial cost, and operation cost. The most important parameters in the energy storage design are the storage energy and power capacities. By simulation, similar to the above, the useable energy in the energy storage can be determined. The total energy capacity can be obtained by

$$E_c = \frac{E_{usable}}{SOC_{top} - SOC_{bottom}}, \tag{10.2}$$

where E_{usable} is the useable energy, in the energy storage, consumed in the pure EV or CD modes, SOC_{top} is the top SOC with fully charged energy storage (which is usually equal to 1), and SOC_{bottom} is the SOC of the energy storage at which the operation mode is switched from the pure EV or CD modes to the CS mode. In the above example, the useable energy is about 7 kWh (refer to Figures 10.6, 10.8, 10.12, 10.14, 10.19, 10.21, 10.25, and 10.27)
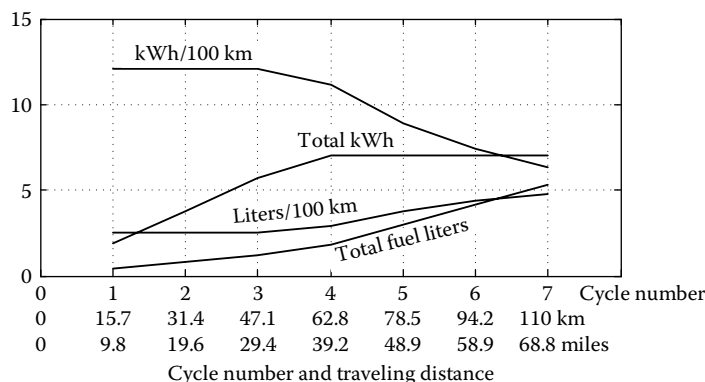
FIGURE 10.25 SOC and the remaining energy in the energy storage versus traveling distance in LA92 driving cycle with CD mode.
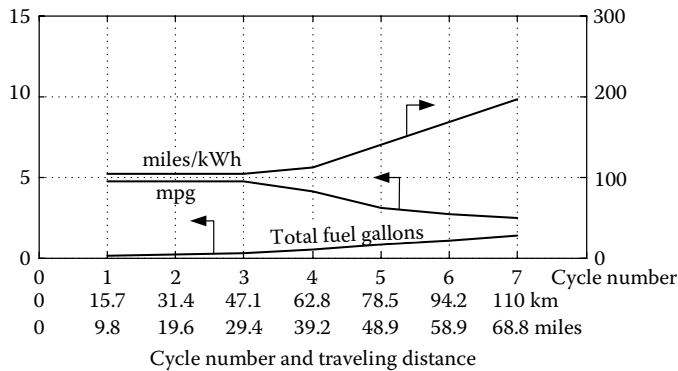
FIGURE 10.26 Engine operating points overlapping its fuel consumption map in LA92 driving cycle with CD mode.

and the SOC operating window is 0.7 (from 1 to 0.3). The total energy capacity of the energy storage is about 10 kWh.

It should be noted that the depth of discharge (DOD) of batteries is closely related to battery life. Figure 10.29 illustrates the battery cycle life with the DOD.[5,6] If one deep discharge per day is assumed, a total of 4000+ deep charges would be required for a 10–15-year lifetime. With the characteristics shown in Figure 10.29, a 70% DOD, for NiMH, and a 50% DOD, for Li-ion batteries, may be the proper designs.

FIGURE 10.27 Fuel and electric energy consumption versus the number of LA92 driving cycle and traveling distance with CD mode in metric unit.
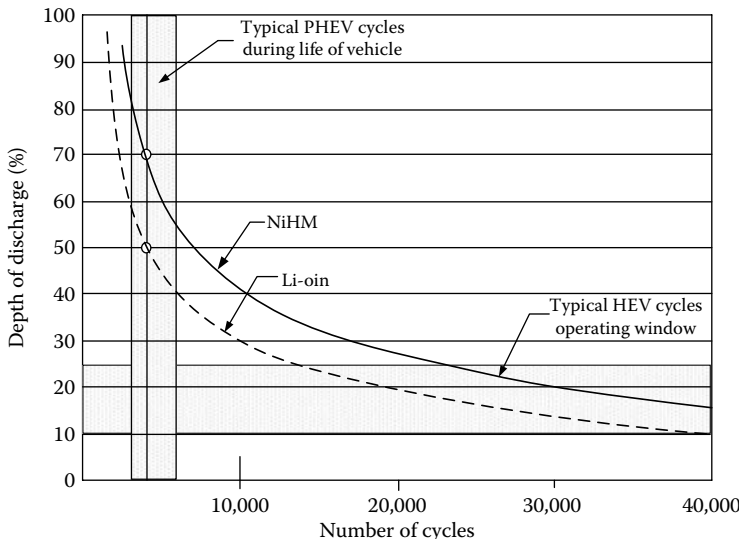
FIGURE 10.28 Fuel and electric energy consumption versus the number of LA92 driving cycle and traveling distance with CD mode in English unit.
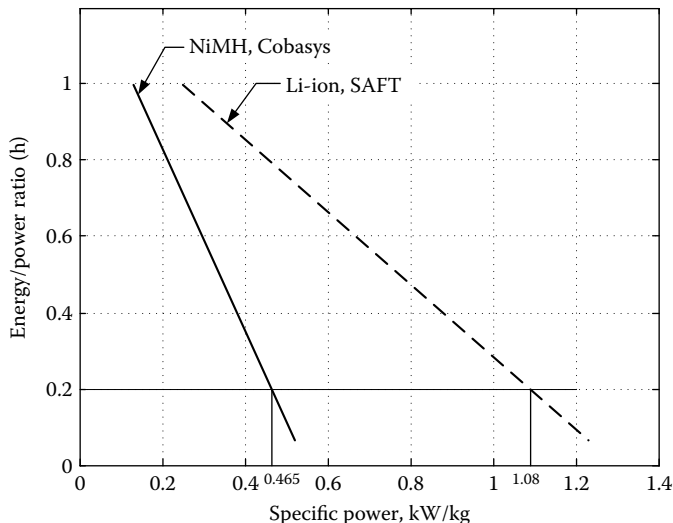
The power requirement of the energy storage is completely determined by the electric motor power rating, which can be expressed as

$$P_{es} \geq \frac{P_m}{\eta_m \eta_{pe}}, \tag{10.3}$$

where P_m is the motor power rating, measured on the motor shaft, and η_m and η_{pe} are the efficiencies of the motor and the power electronics between the energy storage and the motor. This power should be designed to work at

FIGURE 10.29 Cycle life characteristics of Varta energy storage technologies.[5]

FIGURE 10.30   Typical energy/power ratios versus specific power.

low SOC levels, such as 30%, since the energy storage always works at this low SOC level in the CS mode.

The energy/power ratio of an energy storage is a good measure of suitability. The size of the energy storage will be minimized when its energy/power ratio equals the required one. The energy/power ratio is defined as

$$R_{e/p} = \frac{\text{total energy}}{\text{power at operating SOC}}. \tag{10.4}$$

In the example vehicle simulated above, the total energy required is about 10 kWh and the power required is about 60 kW, which is defined at 30% of the battery SOC, yielding an $R_{e/p}$ of 0.167 h at 30% battery SOC. Figure 10.30 shows a typical energy/power ratio versus the specific power of energy storage technologies.[5] If 0.2 h of energy/power ratio is used in the design, Cobasys' NiMH battery will yield a total weight of 129 kg (60/0.465), which carries 12 kWh of total energy (0.2 × 60). However, when SAFT's Li-ion battery is used, the total weight will be about 56 kg (60/1.08), carrying the same amount of energy of 12 kWh.

References

1. T. Markel, "Plug-In HEV vehicle design options and expectations," *ZEV Technology Symposium*, California Air Resources Board, Sacramento, CA, September 27, 2006.

2. A. Simpson, "Cost–benefit analysis of plug-in hybrid electric vehicle technology," presented at the *22nd International Battery, Hybrid and Fuel Cell Electric Vehicle Symposium and Exhibition (EVS-22)*, Yokohama, Japan, October 23–28, 2006.
3. J. Gonder and T. Markel, "*Energy Management Strategies for Plug-In Hybrid Electric Vehicles*," SAE Paper no. 2007-01-0290, Society of Automotive Engineers, Warrendale, PA, 2007.
4. T. Markel and K. Wipke, "Modeling grid-connected hybrid electric vehicles using ADVISOR," *The 16th IEEE Annual Battery Conference on Application and Advances,* January 9, 2001, Long Beach, CA, 2001.
5. T. Markel and A. Simpson, "Energy storage systems considerations for grid-charged hybrid electric vehicles," *Vehicle Power and Propulsion, 2005 IEEE Conference*, September 7–9, 2005.
6. T. Markel and A. Simpson, "Plug-in hybrid electric vehicle energy storage system design," to be presented at *Advanced Automotive Battery Conference*, Baltimore, MD, May 17–19, 2006.

11

Mild Hybrid Electric Drive Train Design

Full HEVs with parallel, series, or series–parallel configurations can significantly reduce fuel consumption by operating the engine optimally and using effective regenerative braking.[1–3] However, a high electric power demand requires a bulky and heavy energy storage pack. This causes difficulties for packing the drive train under the hood and reduces the loading capacity, and also increases the energy losses in the rolling tires. Full hybrid drive trains have structures totally different from conventional drive trains. To turn totally from conventional drive trains to full hybrids, a huge investment of time and money is needed. A compromise is to develop an intermediate product that is easier to convert from the current products, and yet is more efficient than those products. One solution is to put a small electric motor behind the engine to constitute the so-called mild or soft hybrid electric drive train. This small electric motor can operate as an engine starter as well as an electrical generator. It can also add additional power to the drive train when high power is demanded and can convert part of the braking energy into electric energy. This small motor can potentially replace the clutch or the torque converter, which is inefficient when operating with a high slip ratio.
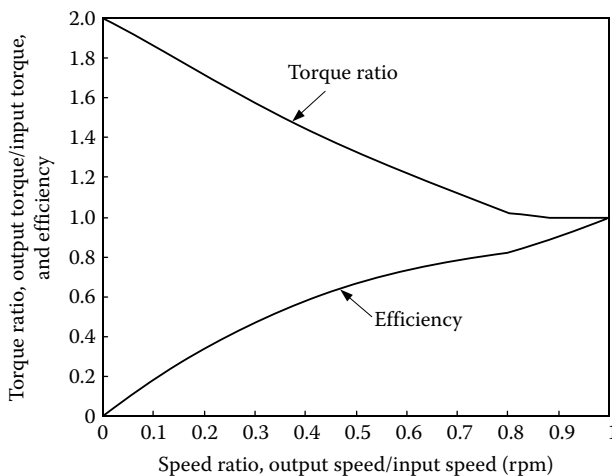
A mild hybrid electric drive train does not require high-power energy storage due to the small power rating of the electric motor. A 42-V electrical system may be able to meet the requirements. Other subsystems of the conventional vehicle, such as engine, transmission (gearbox), and brake, do not require many changes.

This chapter introduces two typical configurations of mild hybrid drive trains. Their control and parametric design are explained along with a design example.

11.1 Energy Consumed in Braking and Transmission
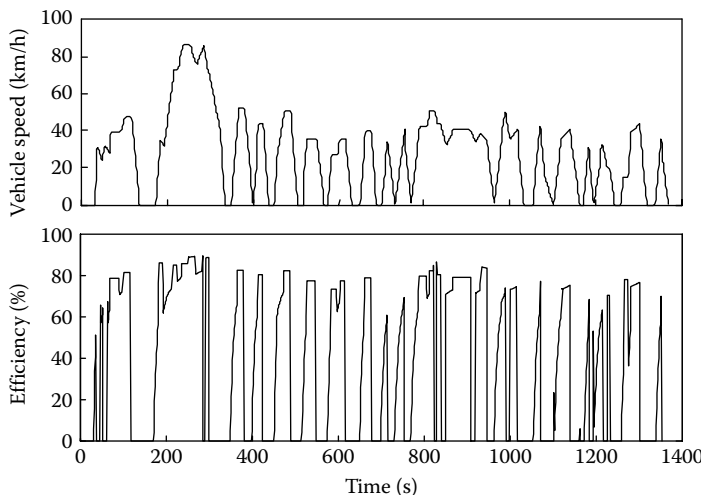
As indicated in Chapter 13, a significant amount of energy is consumed in braking, especially when driving in urban areas. Chapter 13 also indicates that the braking power in normal driving is not large (refer to Figure 13.6).[1,4] Thus, a small motor would be able to recover most of the braking energy.

FIGURE 11.1 Characteristics of a typical dynamic hydraulic torque converter.

Another source of energy loss in conventional vehicles is the transmission. Conventional vehicles are usually equipped with automatic transmissions, especially in North America. In the automatic transmission, the dynamic hydraulic torque converter is the basic element and has low efficiency when operating with a low-speed ratio (high-speed slip), as shown in Figure 11.1.

When the vehicle is operating with a stop-and-go driving pattern in urban areas, the frequent accelerating of the vehicle leads to a low-speed ratio in the torque converter, thus resulting in low operation efficiency. Figure 11.2 shows

FIGURE 11.2 Vehicle speed and operating efficiency of an automatic transmission while driving in an FTP75 urban drive cycle.

the operating efficiency of a typical automatic transmission in an FTP75 urban drive cycle. In this drive cycle, the average efficiency is about 0.5.[5,6]

In addition, when driving in urban areas, the engine idling time during standstill and braking is significant. In the FTP75 drive cycle the percentage of engine idling time reaches 44%, and in New York City it reaches about 57%. When the engine is idling, not only does the engine itself consume energy, but also the energy is needed to drive the transmission. For instance, about 1.7 kW of engine power is needed to drive the automatic transmission when the vehicle is at a standstill.

Using a small electric motor to replace the torque converter and then constitute a mild hybrid electric drive train is considered to be an effective approach to saving the energy losses in an automatic transmission, and in braking and engine idling operation.

11.2 Parallel Mild Hybrid Electric Drive Train

11.2.1 Configuration

A parallel connected mild hybrid electric drive train is shown in Figure 11.3. A small electric motor, which can function as engine starter, generator, and traction motor, is placed between the engine and the automatically shifted multigear transmission (gearbox). The clutch is used to disconnect the gearbox from the engine when required, such as during gear shifting and low vehicle speed. The power rating of the electric motor may be in the range of about 10% of the engine power rating. The electric motor can be smoothly controlled to operate at any speed and torque; thus, isolation between the electric motor and transmission is not necessary. The operation of the drive train and each individual component is controlled by the drive train controller and component controllers.
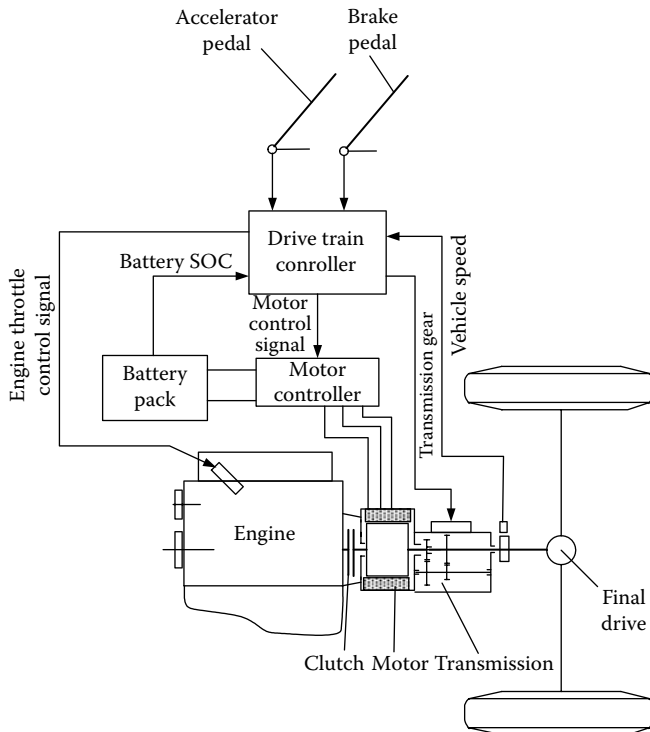
11.2.2 Operating Modes and Control Strategy

The drive train has several operating modes, depending on the operation of the engine and the electric motor.

Engine-alone traction mode—In this mode, the electric motor is de-energized, and the vehicle is propelled by the engine alone. This mode may be used when the SOC of the batteries is in the high region, and the engine alone can handle the power demand.

Motor-alone traction mode—In this mode, the engine is shut down and the clutch is disengaged (open). The vehicle is propelled by the electric motor alone. This operating mode may be used at low vehicle speed, less than 10 km/h, for example.

Battery charge mode—In this mode, the electric motor operates as a generator and is driven by the engine, to charge the batteries.

FIGURE 11.3 Configuration of the parallel connected mild hybrid electric drive train.

Regenerative braking mode—In this mode, the engine is shut down and the clutch is disengaged. The electric motor is operated to produce a braking torque to the drive train. Part of the kinetic energy of the vehicle mass is converted into electric energy and stored in the batteries.

Hybrid traction mode—In this mode, both the engine and the electric motor deliver traction power to the drive train.

Which of the above operating modes is used in real operation depends on the power demand, which is commanded by the driver through the accelerator or brake pedal, the SOC of the batteries, and vehicle speed.

The control strategy is the preset control logic in the drive train controller. The drive train controller receives the real-time signals from the driver and each individual component (refer to Figure 11.3) and then commands the operation of each component, according to the preset control logic. A proposed control logic is illustrated in Table 11.1 and Figure 11.4.[5]
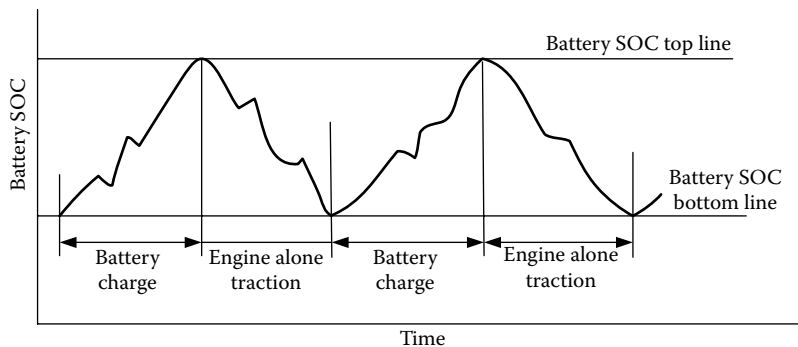
11.2.3   Drive Train Design

The design of the mild hybrid electric drive train is very similar to the design of the conventional drive train, because both are very close. The following is

TABLE 11.1

Illustration of the Control Logic

Driving Condition	Control Operation
Standstill	Both engine and motor are shut down
Low speed (<10 km/h)	Electric motor-alone traction
Braking	Regenerative braking
High-power demand (greater than the power that the engine can produce)	Hybrid traction
Middle and low power demand	Battery charge mode or engine-alone traction mode, depending on the battery SOC (see Figure 11.4)

FIGURE 11.4   Battery charge and engine-alone traction, depending on the battery SOC.
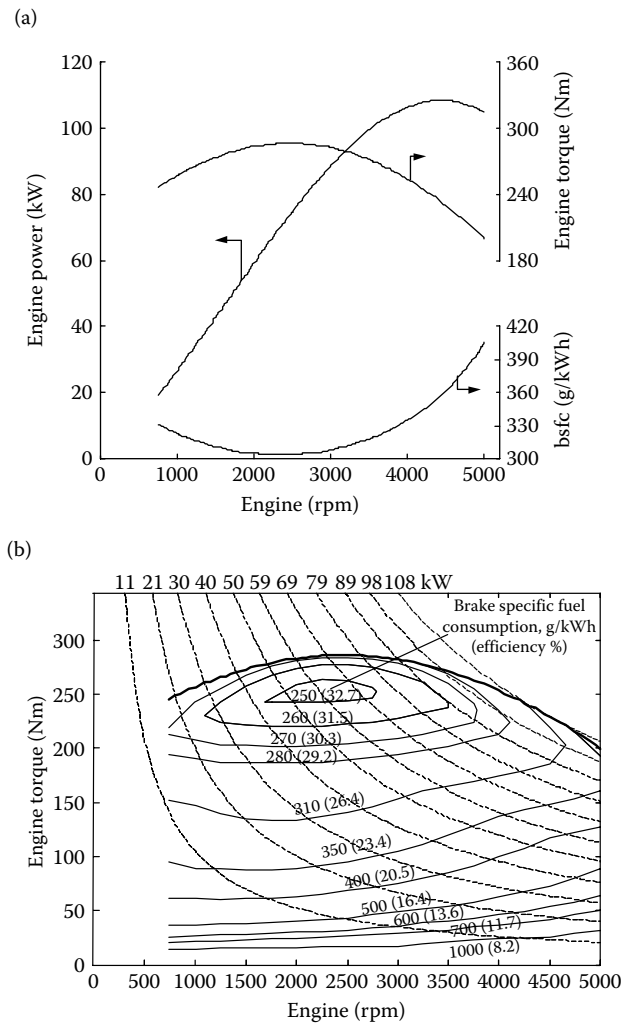
an example of the systematic design of a 1500-kg passenger car drive train. The major parameters of the vehicle are listed in Table 11.2.

Referring to the similar conventional drive train, the engine is designed to have a peak power of 108 kW. The engine characteristics of performance are shown in Figure 11.5.

TABLE 11.2

Major Parameters of the Mild Hybrid Electric Drive Train
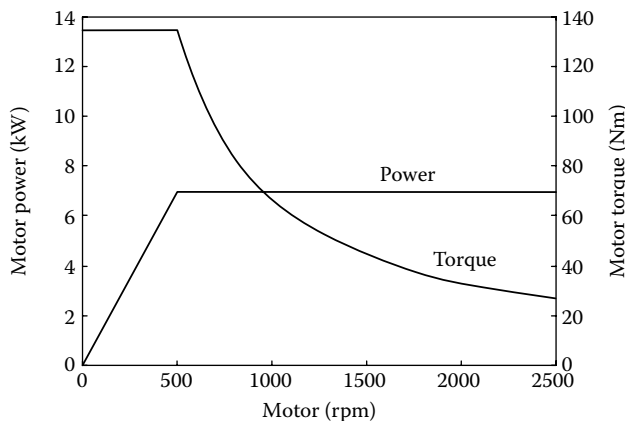
Vehicle Mass	1500 kg
Rolling resistance coefficient	0.01
Aerodynamic drag coefficient	0.28
Front area	2.25 m^2
Four-gear transmission	
Gear ratio:	
First gear	2.25
Second gear	1.40
Third gear	1.00
Fourth gear	0.82
Final gear ratio	3.50

(a)

(b)

FIGURE 11.5 Performance of the engine: (a) performance with full throttle and (b) fuel consumption map.

In this design, a small motor with 7-kW rating power is used, which can operate as an engine starter and alternator and assist regenerative braking. Figure 11.6 shows the torque and power characteristics versus speed of this motor.

The batteries in this design example are lead–acid batteries. Lead–acid batteries are popularly used in automobiles, due to their mature technology and low cost. They have relatively high power density, compared with other kinds of common batteries.[7] Thus they are considered to be the proper selection for mild HEVs, in which power density is more important than energy density.

FIGURE 11.6 Power and torque of the electric motor versus motor speed.
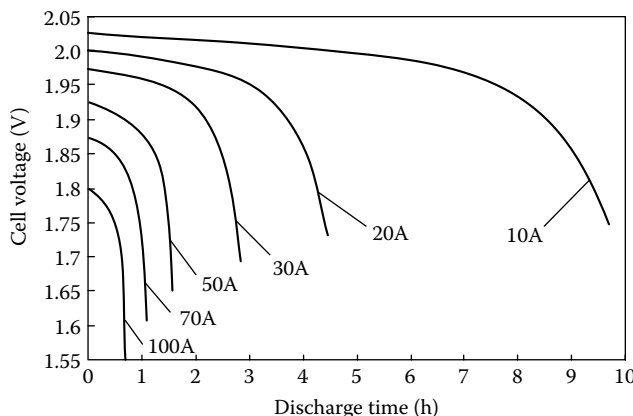
A cell of a lead-acid battery has the characteristics shown in Figure 11.7. The terminal voltage varies with discharging current and time, which in turn represent the SOC of the battery. These characteristics may be simply modeled as shown in Figure 11.8.

In the discharging process, the battery terminal voltage can be expressed as
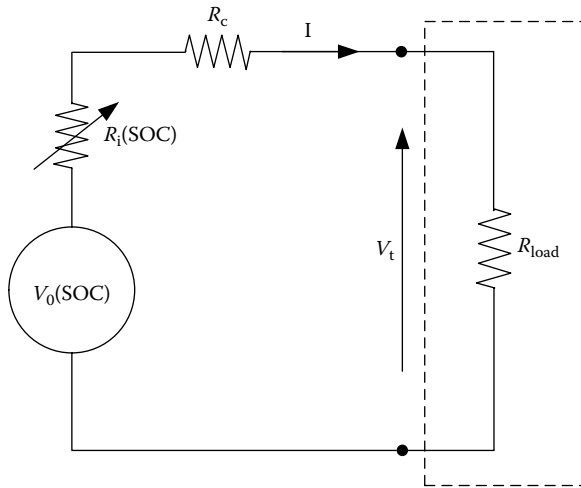
$$V_t = V_o(SOC) - [R_i(SOC) + R_c]I, \tag{11.1}$$

where $V_o(SOC)$ and $R_i(SOC)$ are the open circuit voltage and internal resistance of the battery, respectively, which are functions of battery SOC, and R_c is the conductor resistance. The discharging power at the terminals can be expressed as

$$P_t = I\,V_o(SOC) - [R_i(SOC) + R_c]I^2. \tag{11.2}$$

FIGURE 11.7 Discharge characteristics of the lead–acid battery.

FIGURE 11.8 Battery model.

The maximum power that the load can obtain at the terminals can be expressed as

$$P_{t\,max} = \frac{V_o^2(\text{SOC})}{4[R_i(\text{SOC}) + R_c]}. \tag{11.3}$$
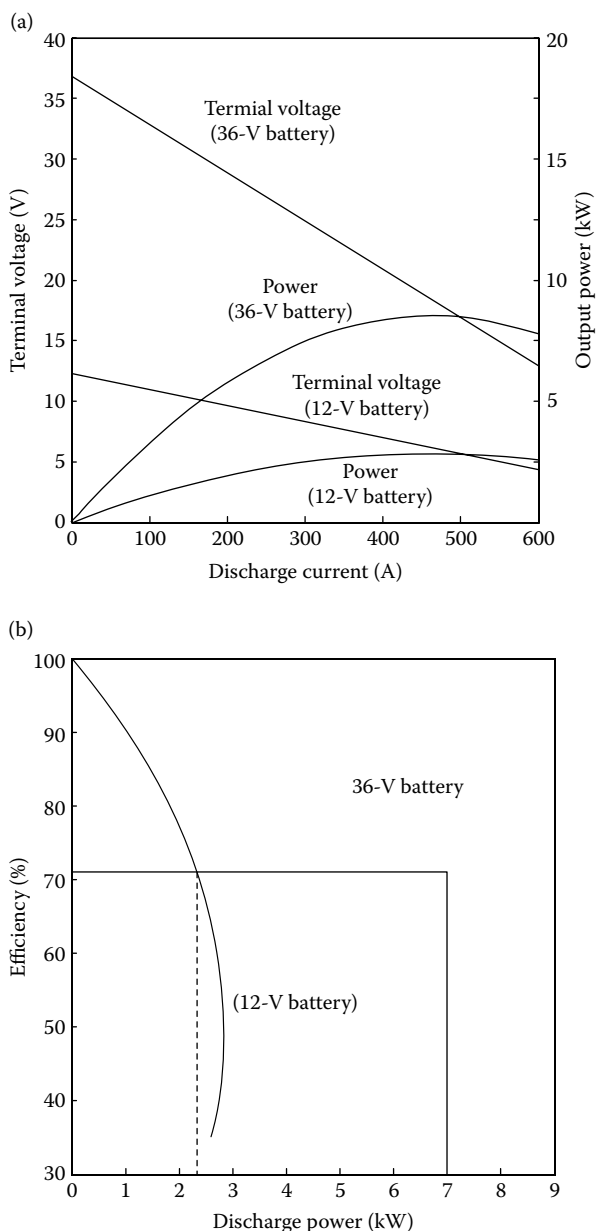
This maximum power is obtained when the discharging current is

$$I = \frac{V_o}{2\,[R_i(\text{SOC}) + R_c]}. \tag{11.4}$$
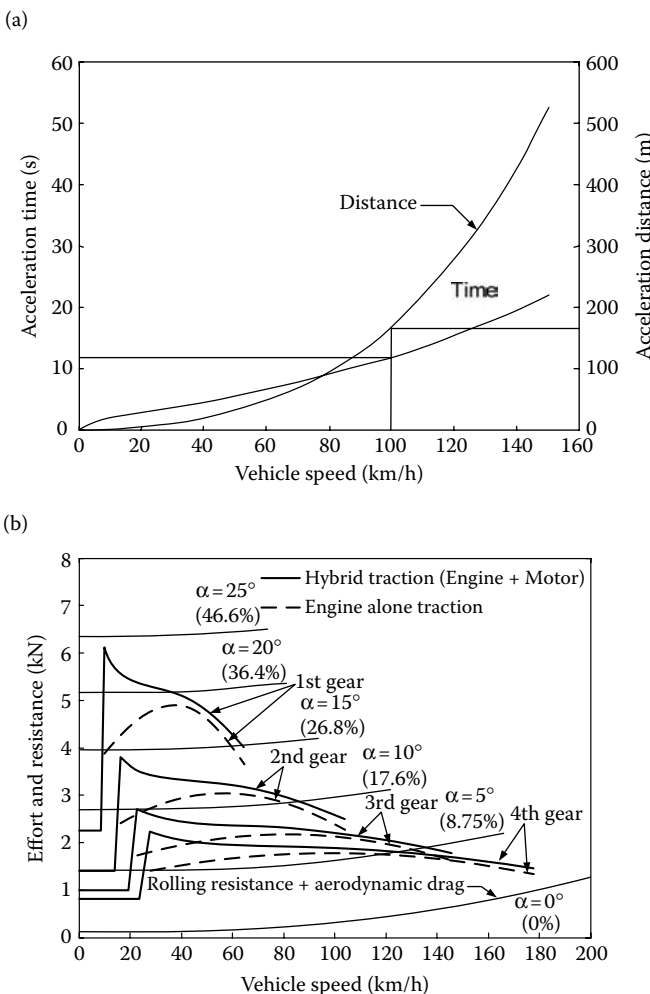
Figure 11.9a shows the terminal voltages and currents of 36 V and 12 V batteries with a current capacity of 100 Ah versus load power (discharge power). It indicates that for the 36-V battery, the maximum power that the battery can supply is about 8.5 kW. But for 12 V, it is less than 3 kW. Figure 11.9b shows that the 36-V battery has a discharge efficiency of over 70% at a power of less than 7 kW. For 12 V voltage, it is less than 2.5 kW. Thus, for the mild hybrid electric drive train proposed in this chapter, a 42-V electric system (36-V battery) can support the operation of the electric motor (rated power of 7 kW).

11.2.4 Performance

Because there are few differences from the conventional drive train (engine, transmission, etc.), the mild hybrid electric drive train is expected to have similar acceleration and gradeability performance. Figure 11.10 shows the performance of an example 1500-kg mild hybrid passenger car.
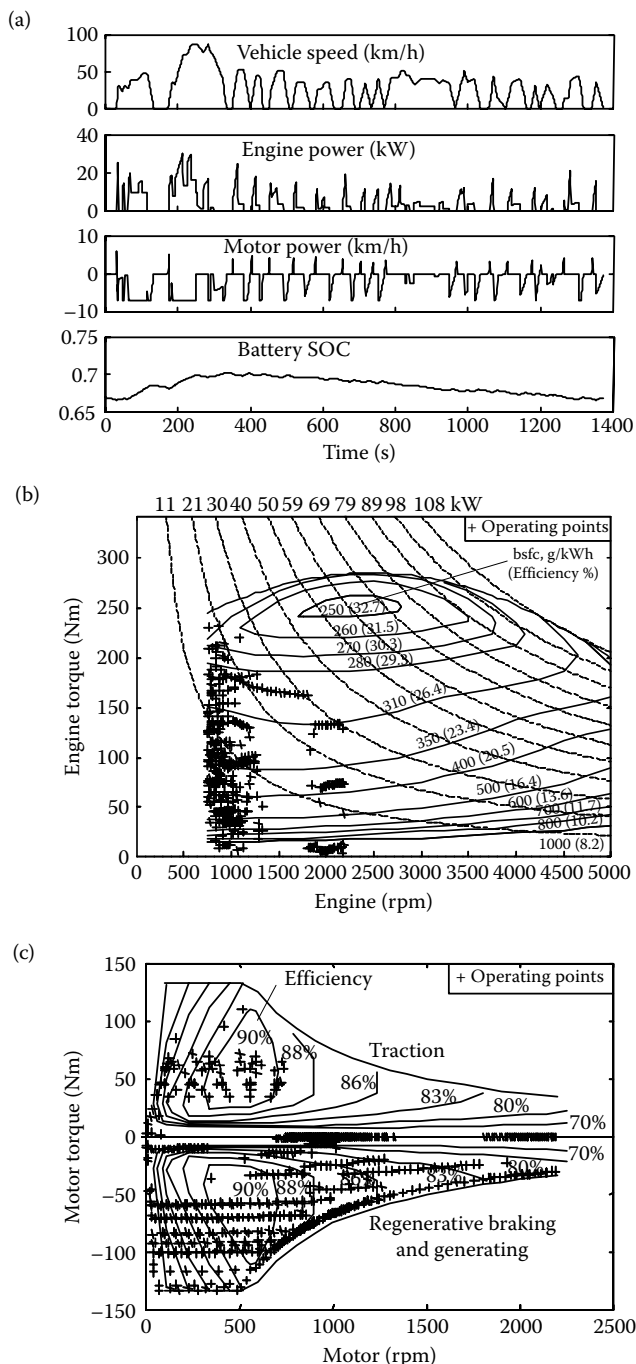
FIGURE 11.9 Battery performance with 36 and 12 V rated voltages: (a) battery power and terminal voltage versus discharge current and (b) battery discharge efficiency.

(a)

(b)
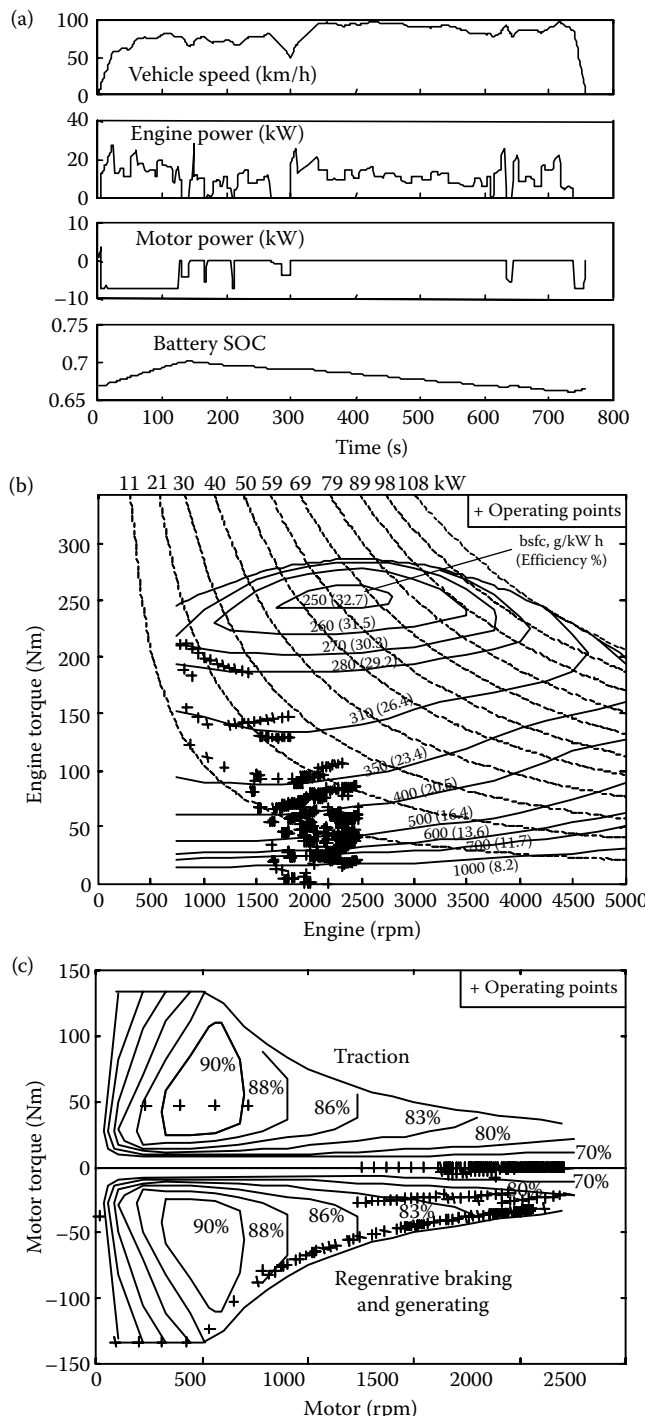
FIGURE 11.10   Performance of the hybrid electric drive train: (a) acceleration and (b) tractive effort versus vehicle speed.

Figure 11.11 shows the simulation results of a 1500-kg hybrid passenger car in an FTP75 urban cycle. Figure 11.11b indicates that a mild hybrid electric drive train with a small motor cannot significantly improve engine operating efficiency, because most of the time the engine still operates in a low load region. However, because of the elimination of engine idling and of the inefficient torque converter and utilization of regenerative braking, fuel economy in urban driving is significantly improved. The simulation shows that for the 1500-kg passenger car mentioned above, the fuel consumption is 7.01 L per 100 km (33.2 mpg). The simulated fuel consumption for a similar conventional vehicle is 10.7 L per 100 km (22 mpg), whereas the Toyota Camry (1445 kg curb

FIGURE 11.11 Simulation in an FTP75 urban drive cycle: (a) vehicle speed, engine power, motor power, and battery SOC, (b) engine fuel consumption map and operating points, and (c) motor efficiency map and operating points.

FIGURE 11.12 Simulation in an FTP75 highway drive cycle: (a) vehicle speed, engine power, motor power, and battery SOC, (b) engine fuel consumption map and operating points, and (c) motor efficiency map and operating points.
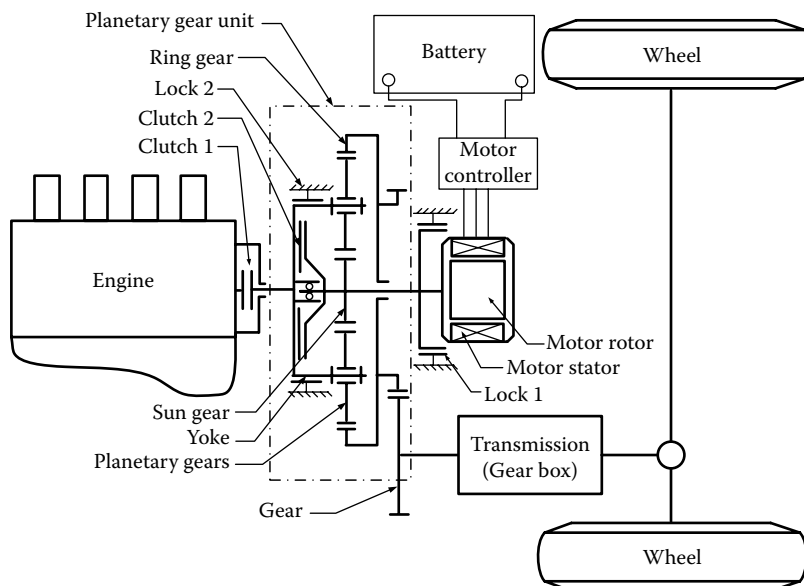
weight, four-cyclinder, 2.4 L, 157 hp, or 117 kW maximum engine power, automatic transmission) has a fuel economy of about 10.3 L/100 km (23 mpg).[8] With mild hybrid technology, fuel consumption can be reduced by more than 30%. Figure 11.11c shows the motor efficiency map and operating points. They indicate that the electric motor operates as a generator more than a traction motor, to support the electric load of auxiliaries and maintain the battery SOC balanced.

Figure 11.12 shows the simulation results of the same vehicle on an FTP75 highway drive cycle. Compared to urban driving, the speeds of both engine and motor are higher, due to higher vehicle speed. The fuel consumption is 7.63 L per 100 km (31 mpg) (Toyota Camry: 7.38 L/100 km or 32 mpg).[8] The fuel economy has not improved compared to conventional vehicles. The reason is that the highway vehicle has less energy losses in engine idling, braking, and transmission than during urban driving, and thus not much room exists for fuel economy improvement using mild hybrid technology.

11.3 Series–Parallel Mild Hybrid Electric Drive Train

11.3.1 Configuration of the Drive Train with a Planetary Gear Unit

Figure 11.13 shows the configuration of a series–parallel (speed coupling and torque coupling) mild hybrid electric drive train, which uses a planetary gear

FIGURE 11.13 Series–parallel mild hybrid electric drive train with a planetary gear unit.

unit to connect the engine, motor, and transmission (gearbox) together. This configuration is very similar to that shown in Figure 9.6 in Chapter 9, but by removing the traction motor and placing a multigear transmission. The engine is connected to the yoke of the planetary gear unit through clutch 1, which is used to couple or decouple the engine from the yoke. Lock 2 is used to lock the yoke of the planetary gear unit to the vehicle frame. The electric motor is connected to the sun gear. Clutch 2 is used to couple or decouple the sun gear (electric motor) to or from the yoke. Lock 1 is used to lock the sun gear and the rotor of the electric motor to the vehicle frame. The transmission (gearbox) is driven by the ring gear of the planetary gear unit through a gear.

The operating characteristics of the planetary gear unit have been discussed in detail in Chapter 9. They are repeated here for the reader's convenience.

The speeds, in rpm, of the sun gear, n_s, ring gear, n_r, and the yoke, n_y, have the relationship
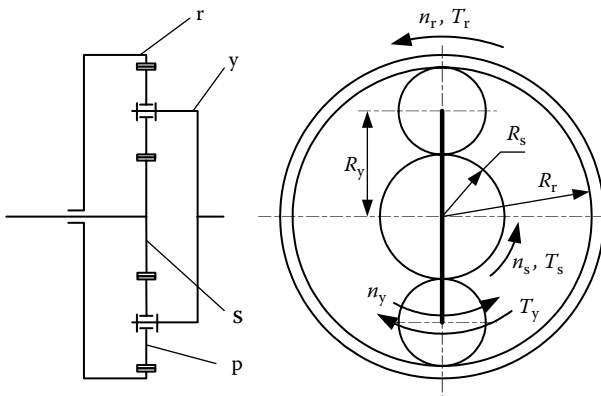
$$n_y = \frac{1}{1+i_g}n_s + \frac{i_g}{1+i_g}n_r, \tag{11.5}$$

where i_g is the gear ratio defined as R_r/R_s as shown in Figure 11.14. The speeds n_s, n_r, and n_y are defined as positive in the direction shown in Figure 11.14. Defining $k_{ys} = (1+i_g)$ and $k_{yr} = (1+i_g)/i_g$, Equation 11.5 can be further expressed as

$$n_y = \frac{1}{k_{ys}}n_s + \frac{1}{k_{yr}}n_r. \tag{11.6}$$

Ignoring the energy losses in the steady-state operation, the torques acting on the sun gear, ring gear, and yoke have the relationship

$$T_y = -k_{ys}T_s = -k_{yr}T_r. \tag{11.7}$$

FIGURE 11.14   Planetary gear unit used as a speed coupling.

Element fixed	Speed	Torque
Sun gear	$n_y = \dfrac{1}{k_{yr}} n_r$	$T_y = -k_{yr} T_r$
Ring gear	$n_y = \dfrac{1}{k_{ys}} n_s$	$T_y = -k_{ys} T_s$
Yoke	$n_s = -\dfrac{k_{ys}}{k_{ys}} n_r$	$T_s = \dfrac{k_{yr}}{k_{ys}} T_r$

FIGURE 11.15   Speed and torque relationships while one element is fixed.

Equation 11.7 indicates that the torques acting on the sun gear, T_s, and ring gear, T_r, always have the same sign. In other words, they have to always be in the same direction. However, the torque acting on the yoke, T_y, is always in the opposite direction of T_s and T_r. Equation 11.7 also indicates that with $i_g > 1$, which is the general case since $R_r > R_s$, T_s is the smallest, T_y is the largest, and T_r is in between. This means that the torque acting on the yoke is balanced by torques acting on the sun gear and ring gear.

When one element among the sun gear, ring gear, and yoke is locked to the vehicle stationary frame, that is, one degree of freedom of the unit is constrained, the unit becomes a single-gear transmission (one input and one output). The speed and torque relationships, with different elements fixed, are shown in Figure 11.15.

11.3.2   Operating Modes and Control

As suggested by the configurations of the drive trains, there are two distinct basic operating modes: speed coupling and torque coupling between the engine and gearbox, depending on the engagement or disengagement states of the clutches and the lock.

11.3.2.1   *Speed-Coupling Operating Mode*

When the vehicle is starting from zero speed, and because the engine cannot run at zero speed and transmission has only a finite gear ratio, slip must exist between the input shaft and output shaft of the transmission. The slip usually occurs in a clutch in manual transmissions or in a hydrodynamic torque converter in an automatic transmission. Thus, a certain amount of energy is lost in this slip. However, in the case of the drive train shown in Figure 11.13, this slip is performed between the engine and the electric motor (yoke and sun gear). In this case, clutch 1 connects the engine shaft to the yoke, clutch 2 releases the sun gear from the yoke, and locks 1 and 2 release the sun gear (motor) and yoke (engine) from the vehicle frame at a given

engine (yoke) speed and ring gear speed, which is proportional to the vehicle speed, according to Equation 11.6, the motor speed is

$$n_s = k_{ys}\left(n_y - \frac{n_r}{k_{yr}}\right). \tag{11.8}$$

When the first term on the right-hand side of Equation 11.8 is larger than the second term, that is, at low vehicle speed, the motor velocity is positive. However, from Equation 11.7, it is known that the motor torque must be negative, as expressed by

$$T_s = -\frac{T_y}{k_{ys}}. \tag{11.9}$$

Thus, the motor power is negative and it operates as a generator. The generating power can be expressed as

$$P_{m/g} = \frac{2\pi}{60}T_s n_s = \frac{2\pi}{60}(-n_y T_y + n_t T_r) = -P_e + P_t, \tag{11.10}$$

where $P_{m/g}$ is the generating power of the motor (negative), P_e is the engine power, and P_t is the power going to the transmission for propelling the vehicle.

The vehicle speed (proportional to n_r) at which the value that makes n_s equal to zero is defined as synchronous speed. With further increase of vehicle speed, n_s becomes negative and the electric motor goes into the motoring state.

In the speed-coupling operating mode, the engine speed is decoupled from the vehicle speed and can be controlled by the motor torque and engine throttle as discussed before.

11.3.2.2 Torque-Coupling Operating Mode

When clutch 1 is engaged, lock 2 releases the yoke and clutch 2 engages the sun gear (motor) and yoke (engine). The engine and motor speeds are forced to be the same. The ring gear speed and yoke (engine) speed have the relationship (from Equation 11.6)

$$n_r = k_{yr}\left(1 - \frac{1}{k_{ys}}\right)n_y. \tag{11.11}$$

From the definitions of k_{yr} and k_{ys} by Equations 11.4 and 11.5, Equation 11.11 can be rewritten as

$$n_r = n_y. \tag{11.12}$$

Equation 11.12 implies that the gear ratio from the engine and motor to the ring gear is 1.

The engine torque and motor torque are added together by the planetary gear unit and then delivered to the transmission from the ring gear, which can be expressed as

$$T_r = T_e + T_{m/g},\qquad(11.13)$$

where T_e and T_m are the engine torque and motor torque, respectively.

11.3.2.3 Engine-Alone Traction Mode

The engine-alone traction mode can be realized in two ways. One is with the same operation of clutch 1, clutch 2, and lock 2 as in the torque-coupling mode (the previous section). But here the motor is de-energized. In this case, the torque delivered to the transmission is expressed as

$$T_r = T_e.\qquad(11.14)$$

The other is to lock the sun gear (motor shaft) to the vehicle frame by lock 1 and both clutch 2 and lock 2 are released. From Equation 11.6, the ring gear speed and the yoke (engine) speed have the relationship

$$n_r = k_{yr}n_y.\qquad(11.15)$$

The torque delivered to the transmission can be expressed as

$$T_r = \frac{T_e}{k_{yr}}.\qquad(11.16)$$

It is seen from the above discussion that the planetary gear unit plays the role of a two-gear transmission. The lower gear ratio is $1/k_{yr} < 1$ and the higher gear ratio is 1.

11.3.2.4 Motor-Alone Traction Mode

In this mode, the engine is shut down and clutch 1 disengages the engine from the yoke. The motor alone is used to propel the vehicle. There are two ways of doing this. One method is by coupling the sun gear to the yoke by clutch 2. In this way, the motor delivers its speed and torque to the ring gear as

$$n_m = n_r\qquad(11.17)$$

and

$$T_m = T_r.\qquad(11.18)$$

The gear ratio from the motor to the ring gear is 1.

The other method is by releasing the sun gear from the yoke by clutch 2 and locking the yoke to the vehicle frame by lock 2. In this manner, the speed and torque of the motor are related to the speed and torque of the ring gear by

$$n_{m/g} = -\frac{k_{ys}}{k_{yr}} n_r \qquad (11.19)$$

and

$$T_{m/g} = \frac{k_{yr}}{k_{ys}} T_r. \qquad (11.20)$$

Equation 11.19 indicates that the motor turns in a direction opposite to that of the ring gear.

11.3.2.5 Regenerative Braking Mode

During braking, part of the braking energy can be recovered by the motor/generator. The operation of the drive train is the same as in electric traction mode, but the motor produces its torque in the direction opposite to that for traction.

11.3.2.6 Engine Starting
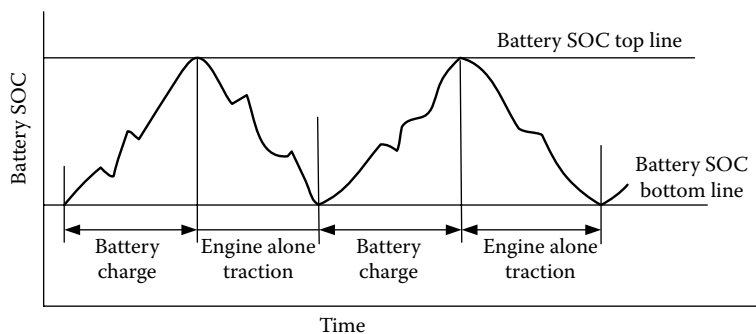
The engine can be started by the electric motor by engaging the sun gear to the yoke by clutch 2. The motor directly delivers its torque to the engine to start it.

11.3.3 Control Strategy

When the vehicle speed is lower than the synchronous speed, the speed-coupling operation mode is used. As explained in Section 11.3.2.1, the electric motor operates with a positive speed and negative power. One part of the engine power is used to charge the batteries and the other part is used to propel the vehicle.

When the vehicle speed is higher than the synchronous speed, the torque-coupling operation mode is used, and the drive train control strategy in this mode is as follows.

1. When the traction power demand is greater than the power that the engine can develop with full throttle, a hybrid traction mode is used. In this case, the engine is operated with full throttle and the electric motor supplies extra power to meet the traction power demand.

2. When the traction power demand is less than the power that the engine can develop with full throttle, the operations of the engine and electric motor are determined by the SOC of the batteries, as shown in
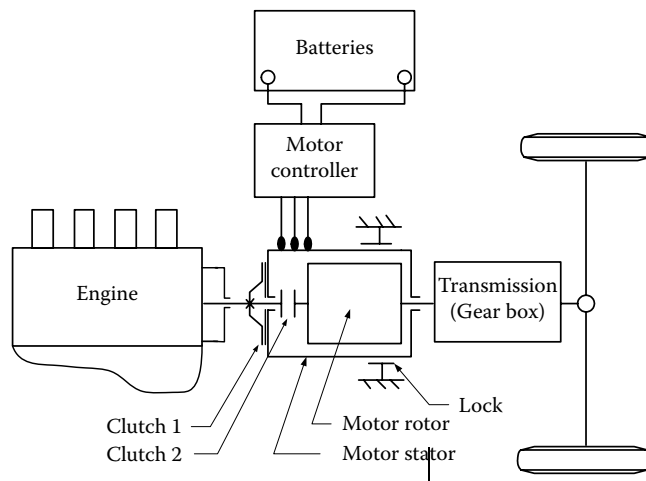
FIGURE 11.16 Battery charge and engine-alone traction, depending on battery SOC.

Figure 11.16. In the battery charging mode the battery charging power may be determined by the maximum power of the electric motor or by the maximum engine power and demanded traction power.
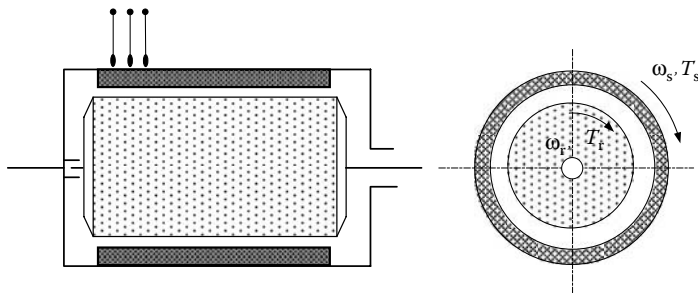
11.3.4 Drive Train with a Floating-Stator Motor

An alternative mild hybrid electric drive train, which has characteristics similar to the drive train discussed above, is shown in Figure 11.17.[6] This drive train uses an electric motor, which has a floating stator, to replace the planetary gear unit and the electric motor.

As mentioned in Chapter 5, the angular velocity of the rotor is the summation of the angular velocities of the stator and the relative angular velocity

FIGURE 11.17 Series–parallel mild hybrid electric drive train with a floating-stator motor.

FIGURE 11.18 An electric motor with a floating stator.

between the stator and rotor, that is,

$$\omega_r = \omega_s + \omega_{rr}. \tag{11.21}$$

Due to the action and reaction effect, the torque acting on the stator and rotor is always equal to the electromagnetic torque produced in the air gap (refer to Figure 11.18), which is, in a general sense, the electric motor torque. This relationship is described as

$$T_r = T_s = T_m, \tag{11.22}$$

where T_m is the electromagnetic torque in the air gap.

Comparing Equations 11.21 and 11.22 with Equations 11.6 and 11.7, it is known that both the planetary gear unit and the floating stator motor have the same operating characteristics. Therefore the mild hybrid electric drive trains as shown in Figures 11.13 and 11.17 have the same operating principles and use the same control strategy. However, the design of the drive train with a planetary gear unit is more flexible since the gear ratio, i_g, is selectable.

References

1. Y. Gao, L. Chen, and M. Ehsani, "Investigation of the effectiveness of regenerative braking for EV and HEV," *Society of Automotive Engineers (SAE) Journal*, SP-1466, Paper No. 1999-01-2901, 1999.
2. Y. Gao, K. M. Rahman, and M. Ehsani, "The energy flow management and battery energy capacity determination for the drive train of electrically peaking hybrid," *Society of Automotive Engineers (SAE) Journal*, SP-1284, Paper No. 972647, 1997.
3. Y. Gao, K. M. Rahman, and M. Ehsani, "Parametric design of the drive train of an electrically peaking hybrid (ELPH) vehicle," *Society of Automotive Engineers (SAE) Journal*, SP-1243, Paper No. 970294, 1997.

4. H. Gao, Y. Gao, and M. Ehsani "Design issues of the switched reluctance motor drive for propulsion and regenerative braking in EV and HEV," *Society of Automotive Engineers (SAE) Future Transportation Technology Conference*, Costa Mesa, CA, Paper No. 2001-01-2526, August 2001.
5. Y. Gao and M. Ehsani, "A mild hybrid drive train for 42 V automotive power system—design, control, and simulation," *Society of Automotive Engineers (SAE) World Congress*, Detroit, MI, Paper No. 2002-02-1082, 2002.
6. Y. Gao and M. Ehsani, "A mild hybrid vehicle drive train with a floating stator motor—configuration, control strategy, design, and simulation verification," *Society of Automotive Engineers (SAE) Future Car Congress*, Crystal City, VA, Paper No. 2002-01-1878, June 2002.
7. Y. Gao and M. Ehsani, "Investigation of battery technologies for the Army's hybrid vehicle application," *Proceedings of the IEEE 56th Vehicular Technology Conference,* Vancouver, British Columbia, Canada, September 2002.
8. Y. Gao and M. Ehsani, "Electronic braking system of EV and HEV—integration of regenerative braking, automatic braking force control and ABS," *Society of Automotive Engineers (SAE) Future Transportation Technology Conference,* Costa Mesa, CA, Paper No. 2001-01-2478, August 2001.

12

Peaking Power Sources and Energy Storages

"Energy storages" are defined in this book as devices that store energy, deliver energy outside (discharge), and accept energy from outside (charge). There are several types of energy storages that have been proposed for EV and HEV applications. These energy storages, so far, mainly include chemical batteries, ultracapacitors or supercapacitors, and ultra-high-speed flywheels. The fuel cell, which essentially is a type of energy converter, will be discussed in Chapter 14.
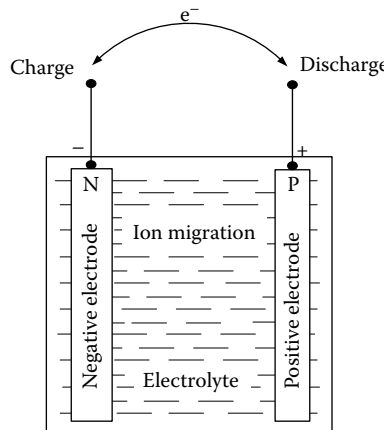
There are a number of requirements for energy storages applied in an automotive application, such as specific energy, specific power, efficiency, maintenance requirement, management, cost, environmental adaptation and friendliness, and safety. For application on an EV, specific energy is the first consideration since it limits the vehicle range. On the other hand, for HEV applications, specific energy becomes less important and specific power is the first consideration, because all the energy is from the energy source (engine or fuel cell) and sufficient power is needed to ensure vehicle performance, particularly during acceleration, hill climbing, and regenerative braking. Of course, other requirements should be fully considered in the vehicle drive train development.

12.1 Electrochemical Batteries

Electrochemical batteries, more commonly referred to as "batteries," are electrochemical devices that convert electrical energy into potential chemical energy during charging, and convert chemical energy into electric energy during discharging. A battery is composed of several cells stacked together. A cell is an independent and complete unit that possesses all the electrochemical properties. Basically, a battery cell consists of three primary elements: two electrodes (positive and negative), immersed into electrolyte as shown in Figure 12.1.
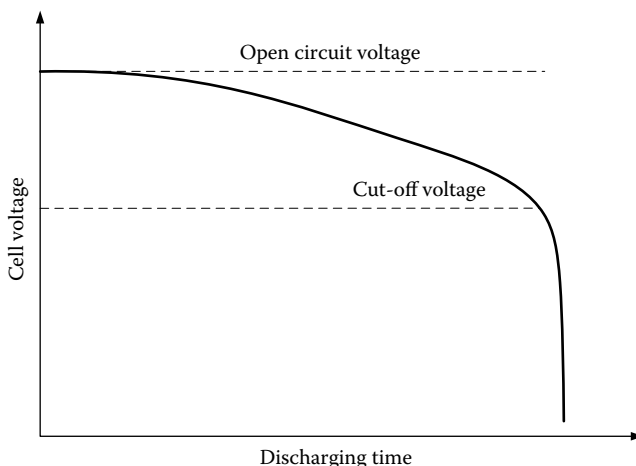
Battery manufacturers usually specify the battery with coulometric capacity (ampere-hours), which is defined as the number of ampere-hours gained when discharging the battery from a fully charged state until the terminal
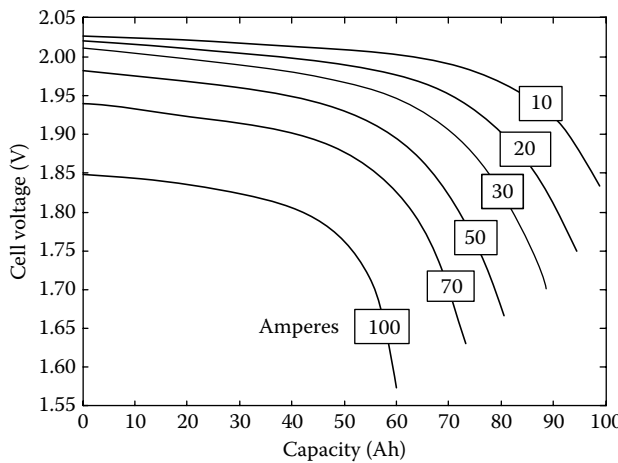
FIGURE 12.1 A typical electrochemical battery cell.

voltage drops to its cut-off voltage, as shown in Figure 12.2. It should be noted that the same battery usually has a different number of ampere-hours at different discharging current rates. Generally, the capacity will become smaller with a large discharge current rate, as shown in Figure 12.3. Battery manufacturers usually specify a battery with a number of ampere-hours along with a current rate. For example, a battery labeled as 100 Ah at C/5 rate has a 100 Ah capacity at a 5-h discharge rate (discharging current = 100/5 = 20 A).

Another important parameter of a battery is the SOC. SOC is defined as the ratio of remaining capacity to fully charged capacity. With this definition, a fully charged battery has an SOC of 100% and a fully discharged battery

FIGURE 12.2 Cut-off voltage of a typical battery.

FIGURE 12.3   Discharge characteristics of a lead–acid battery.

has an SOC of 0%. However, the term "fully discharged" sometimes causes confusion, because of the different capacities at different discharge rates, and different cut-off voltages (refer to Figure 12.3). The change in SOC in a time interval, dt, with discharging or charging current i may be expressed as

$$\Delta \text{SOC} = \frac{i \, \mathrm{d}t}{Q(i)}, \tag{12.1}$$

where $Q(i)$ is the ampere-hour capacity of the battery at current rate i. For discharging, i is positive, and for charging, i is negative. Thus, the SOC of the battery can be expressed as

$$\text{SOC} = \text{SOC}_0 - \int \frac{i \, \mathrm{d}t}{Q(i)}, \tag{12.2}$$

where SOC_0 is the initial value of the SOC.
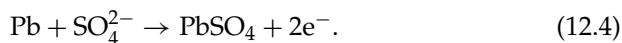
For EVs and HEVs, the energy capacity is considered to be more important than the coulometric capacity (ampere-hours), because it is directly associated with vehicle operation. The energy delivered from the battery can be expressed as

$$E_C = \int_0^t V(i, \text{SOC}) i(t) \mathrm{d}t, \tag{12.3}$$
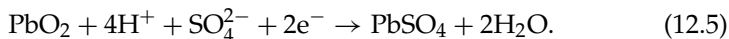
where $V(i, \text{SOC})$ is the voltage at the battery terminals, which is a function of battery current and SOC.

12.1.1 Electrochemical Reactions

For simplicity, and because it is the most widespread battery technology in today's automotive applications, the lead–acid battery case is used as an example to explain the operating principle theory of electrochemical batteries. A lead–acid battery uses an aqueous solution of sulfuric acid ($2H^+ + SO_4^{2-}$) as electrolyte. The electrodes are made of porous lead (Pb, anode, electrically negative) and porous lead oxide (PbO_2, cathode, electrically positive). The processes taking place during discharging are shown in Figure 12.4a, where the lead is consumed and lead sulfate is formed. The chemical reaction on the anode can be written as

$$Pb + SO_4^{2-} \rightarrow PbSO_4 + 2e^-. \tag{12.4}$$
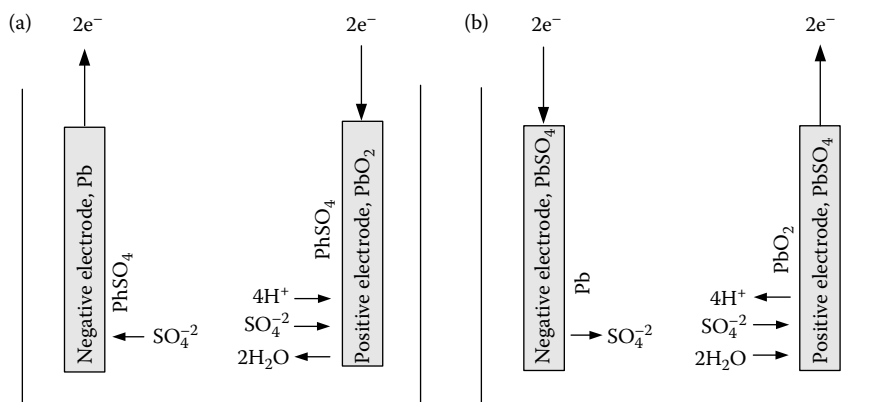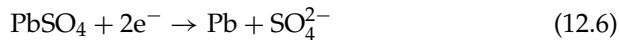
This reaction releases two electrons and, thereby, gives rise to an excess negative charge on the electrode that is relieved by a flow of electrons through the external circuit to the positive (cathode) electrode. At the positive electrode the PbO_2 is also converted to $PbSO_4$ and, at the same time, water is formed. The reaction can be expressed as

$$PbO_2 + 4H^+ + SO_4^{2-} + 2e^- \rightarrow PbSO_4 + 2H_2O. \tag{12.5}$$

During charging, the reactions on the anode and cathode are reversed as shown in Figure 12.4a and can be expressed as follows:
Anode:

$$PbSO_4 + 2e^- \rightarrow Pb + SO_4^{2-} \tag{12.6}$$
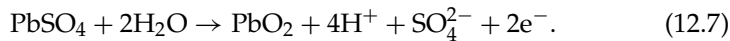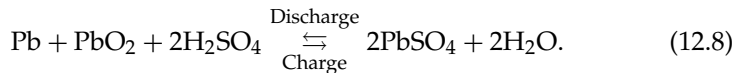
FIGURE 12.4 Electrochemical processes of a lead–acid battery cell: (a) discharging and (b) charging.

and

Cathode:

$$PbSO_4 + 2H_2O \rightarrow PbO_2 + 4H^+ + SO_4^{2-} + 2e^-. \tag{12.7}$$

The overall reaction in a lead–acid battery cell can be expressed as follows:

Overall:

$$Pb + PbO_2 + 2H_2SO_4 \underset{\text{Charge}}{\overset{\text{Discharge}}{\rightleftharpoons}} 2PbSO_4 + 2H_2O. \tag{12.8}$$

The lead–acid battery has a cell voltage of about 2.03 V at standard conditions, which is affected by the concentration of the electrolyte.

12.1.2 Thermodynamic Voltage

The thermodynamic voltage of a battery cell is closely associated with the energy released and the number of electrons transferred in the reaction. The energy released by a battery cell reaction is given by the change in Gibbs free energy, ΔG, usually expressed in per mole quantities. The change in Gibbs free energy in a chemical reaction can be expressed as

$$\Delta G = \sum_{\text{Products}} G_i - \sum_{\text{Reactants}} G_j, \tag{12.9}$$

where G_i and G_j are the free energy in species i of products and species j of reactants. In a reversible process, ΔG is completely converted into electric energy, that is,

$$\Delta G = -nFV_r, \tag{12.10}$$

where n is the number of electrons transferred in the reaction, $F = 96{,}495$ is the Faraday constant in coulombs per mole, and V_r is the reversible voltage of the cell. At standard conditions (25°C temperature and 1 atm pressure), the open circuit (reversible) voltage of a battery cell can be expressed as

$$V_r^0 = -\frac{\Delta G^0}{nF}, \tag{12.11}$$

where ΔG^0 is the change in Gibbs free energy at standard conditions.

The change of free energy, and thus the cell voltage, in a chemical reaction is a function of the activities of the solution species. From Equation 12.10 and the dependence of ΔG on reactant activities, the Nernst relationship is derived as

$$V_r = V_r^0 - \frac{RT}{nF} \ln \left[\frac{\prod (\text{activities of products})}{\prod (\text{activities of reactants})} \right], \tag{12.12}$$

where R is the universal gas constant, 8.31 J/mol K, and T is the absolute temperature in K.

12.1.3 Specific Energy

Specific energy is defined as the energy capacity per unit battery weight (Wh/kg). The theoretical specific energy is the maximum energy that can be generated per unit total mass of cell reactants. As discussed above, the energy in a battery cell can be expressed by the Gibbs free energy ΔG. With respect to the theoretical specific energy, only the effective weights (molecular weights of reactants and products) are involved; then

$$E_{spe,theo} = -\frac{\Delta G}{3.6 \sum M_i} = \frac{nFV_r}{3.6 \sum M_i} \text{ (Wh/kg)}, \qquad (12.13)$$

where $\sum M_i$ is the sum of the molecular weight of the individual species involved in the battery reaction. Taking the lead–acid battery as an example, $V_r = 2.03$ V, $n = 2$, and $\sum M_i = 642$ g, then $E_{spe,theo} = 170$ Wh/kg. From Equation 12.13, it is clear that the "ideal" couple would be derived from a highly electronegative element and a highly electropositive element, both of low atomic weight. Hydrogen, lithium, or sodium would be the best choice for the negative reactants, and the lighter halogens, oxygen, or sulfur would be the best choice for the positive reactants. To put such couples together in a battery requires electrode designs for effective utilization of the contained active materials, as well as electrolytes of high conductivity compatible with the materials in both electrodes. These constraints result in oxygen and sulfur being used in some systems as oxides and sulfides, rather than as the elements themselves. For operation at ambient temperature, aqueous electrolytes are advantageous because of their high conductivities. Here, alkali-group metals cannot be employed as electrodes since these elements react with water. It is necessary to choose other metals, which have a reasonable degree of electropositivity, such as zinc, iron, or aluminum. When considering electrode couples, it is preferable to exclude those elements that have a low abundance in the earth's crust, are expensive to produce, or are unacceptable from a health or environmental point of view.[1]

Examination of possible electrode couples has resulted in the study of more than 30 different battery systems with a view to developing a reliable, high-performance, inexpensive high-power energy source for electric traction. The theoretical specific energies of the systems championed for EVs and HEVs are presented in Table 12.1.[1] Practical specific energies, however, are well below the theoretical maxima. Apart from electrode kinetic and other restrictions that serve to reduce the cell voltage and prevent full utilization of the reactants, there is a need for construction materials, which add to the battery weight but are not involved in the energy producing reaction.

In order to appreciate the extent to which the practical value of the specific energy is likely to differ from the theoretical values, it is instructive to consider the situation of the well-established lead–acid battery. A breakdown of the various components of a lead–acid battery designed to give a practical specific energy of 45 Wh/kg is shown in Figure 12.5.[1] It shows that only about
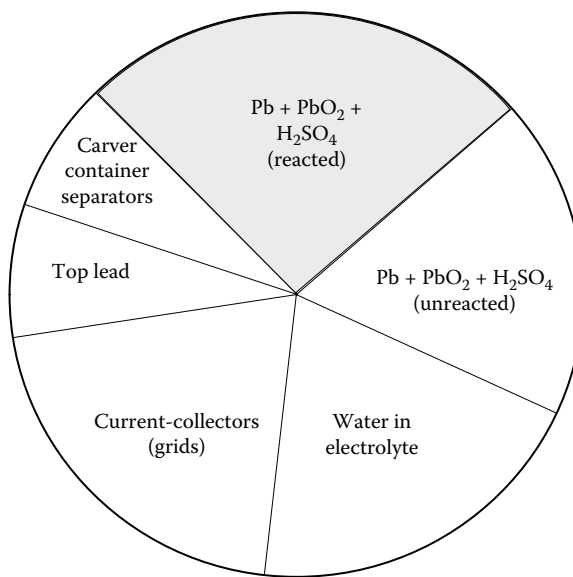
TABLE 12.1

Theoretical Specific Energies of Candidate Batteries for EVs and HEVs[1]

Battery		Cell Reaction		Specific Energy (Wh/kg)
(+)	(−)	Charge $\Leftarrow$	Discharge $\Rightarrow$	
Acidic Aqueous Solution				
PbO_2	Pb	$PbO_2 + 2H_2SO_4 + Pb$	$\Leftrightarrow 2PbSO_4 + 2H_2O$	170
Alkaline Aqueous Solution				
NiOOH	Cd	$2NiOOH + 2H_2O + Cd$	$\Leftrightarrow 2Ni(OH)_2 + Cd(OH)_2$	217
NiOOH	Fe	$2NiOOH + 2H_2O + Fe$	$\Leftrightarrow 2Ni(OH)_2 + Fe(OH)_2$	267
NiOOH	Zn	$2NiOOH + 2H_2O + Zn$	$\Leftrightarrow 2Ni(OH)_2 + Zn(OH)_2$	341
NiOOH	H_2	$2NiOOH + H_2$	$\Leftrightarrow 2Ni(OH)_2$	387
MnO_2	Zn	$2MnO_2 + H_2O + Zn$	$\Leftrightarrow 2MnOOH + ZnO$	317
O_2	Al	$4Al + 6H_2O + 3O_2$	$\Leftrightarrow 4Al(OH)_3$	2815
O_2	Fe	$2Fe + 2H_2O + O_2$	$\Leftrightarrow 2Fe(OH)_2$	764
O_2	Zn	$2Zn + 2H_2O + O_2$	$\Leftrightarrow 2Zn(OH)_2$	888
Flow				
Br_2	Zn	$Zn + Br_2$	$\Leftrightarrow ZnBr_2$	436
Cl_2	Zn	$Zn + Cl_2$	$\Leftrightarrow ZnCl_2$	833
$(VO_2)2SO_4$	VSO_4	$(VO_2)2SO_4 + 2HVSO_4 + 2H_2SO_4$	$2VOSO_4 + V_2(SO_4)_3 + 2H_2O$	114
Molten Salt				
S	Na	$2N3S \ a +$	$\Leftrightarrow Na_2S_3$	760
$NiCl_2$	Na	$2Na + NiCl_2$	$\Leftrightarrow 2NaCl$	790
FeS_2	LiAl	$4LiAl + FeS_2$	$\Leftrightarrow 2Li_2S + 4Al + Fe$	650
Organic Lithium				
$LiCoO_2$	Li − C	$Li(y+x)C6 + Li(1-(y-x))CoO_2$	$\Leftrightarrow LiyC6 + Li(1-y)CoO_2$	320[a]

[a] For maximum values of $x = 0.5$ and $y = 0$.

26% of the total weight of the battery is directly involved in producing electrical energy. The remainder is made up of (1) potential cell reactants that are not discharged at the rates required for EV operation, (2) water used as the solvent for the electrolyte (sulfuric acid alone is not suitable), (3) lead grids for current collection, (4) "top lead," that is, terminals, straps, and intercell connectors, and (5) cover, connector, and separators.

A similar ratio of practical-to-theoretical specific energy is expected for each of the candidate systems listed in Table 12.1. Present values realized by experimental cells and prototype batteries are listed in Table 12.2.[1] In recent years, some high-power batteries have been developed for application of HEVs.[2]

FIGURE 12.5   Weight distribution of the components of a lead–acid EV battery with a specific energy of 45 Wh/kg at the C5/5 rate.[1]

12.1.4   Specific Power

Specific power is defined as the maximum power of per unit battery weight that the battery can produce in a short period. Specific power is important in the reduction of battery weight, especially in high-power demand applications, such as HEVs. The specific power of a chemical battery depends mostly on the battery's internal resistance. With the battery model as shown in Figure 12.6, the maximum power that the battery can supply to the load is

$$P_{\text{peak}} = \frac{V_0^2}{4\left(R_c + R_{\text{int}}\right)}, \tag{12.14}$$

where R_c is the conductor resistance (ohmic resistance) and R_{int} is the internal resistance caused by chemical reaction.

Internal resistance, R_{int}, represents the voltage drop, ΔV, which is associated with battery current. The voltage drop ΔV, termed overpotential in battery terminology, includes two components: one caused by reaction activity ΔV_A and the other by electrolyte concentration ΔV_C. General expressions of ΔV_A and ΔV_C are[3]

$$\Delta V_A = a + b \log I \tag{12.15}$$
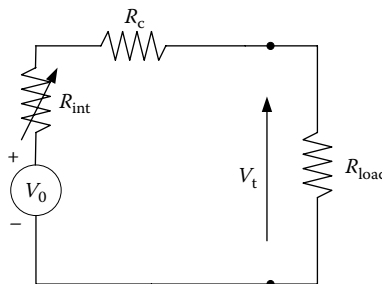
and

$$\Delta V_C = -\frac{RT}{nF} \ln\left(1 - \frac{I}{I_L}\right), \tag{12.16}$$

TABLE 12.2

Status of Battery System for Automotive Application

System	Specific Energy (Wh/kg)	Peak Power (V/kg)	Energy Efficiency (%)	Cycle Life	Self-Discharge (% per 48 h)	Cost (US$/kWh)
Acidic Aqueous Solution						
Lead/acid	35–50	150–400	>80	500–1000	0.6	120–150
Alkaline Aqueous Solution						
Nickel/cadmium	50–60	80–150	75	800	1	250–350
Nickel/iron	50–60	80–150	75	1500–2000	3	200–400
Nickel/zinc	55–75	170–260	65	300	1.6	100–300
Ni–MH	70–95	200–300	70	750–1200+	6	200–350
Aluminum/air	200–300	160	<50	?	?	?
Iron/air	80–120	90	60	500+	?	50
Zinc/air	100–220	30–80	60	600+	?	90–120
Flow						
Zinc/bromine	70–85	90–110	65–70	500–2000	?	200–250
Vanadium redox	20–30	110	75–85	–	–	400–450
Molten Salt						
Sodium/sulfur	150–240	230	80	800+	0[a]	250–450
Sodium/nickel chloride	90–120	130–160	80	1200+	0[a]	230–345
Lithium/iron sulfide (FeS)	100–130	150–250	80	1000+	?	110
Organic/Lithium						
Li–I	80–130	200–300	>95	1000+	0.7	200

[a] No self-discharge, but some energy loss by cooling.

FIGURE 12.6   Battery circuit model.

where a and b are constants, R is the gas constant, 8.314 J/K mol, T is the absolute temperature, n is the number of electrons transferred in the reaction, F is the Faraday constant, 96,495 ampere-seconds per mole, and I_L is the limit current. Accurate determination of battery resistance or voltage drop by analysis is difficult and is usually obtained by measurement.[1] The voltage drop increases with increase in discharging current, decreasing the stored energy in it (refer to Figure 12.3).

Table 12.2 also shows the status of battery systems potentially available for EV. It can be seen that although specific energies are high in advanced batteries, specific powers have to improve. About 300 W/kg might be the optimistic estimate. However, SAFT has reported their Li-ion high power for HEV application with a specific energy of 85 Wh/kg and a specific power of 1350 W/kg and their high-energy batteries for EV application with about 150 Wh/kg and 420 W/kg (at 80% state-of-discharge, 150 A current, and 30 s), respectively.[2]

12.1.5   Energy Efficiency

The energy or power losses during battery discharging and charging appear in the form of voltage loss. Thus the efficiency of the battery during discharging and charging can be defined at any operating point as the ratio of the cell operating voltage to the thermodynamic voltage, that is,

During discharging
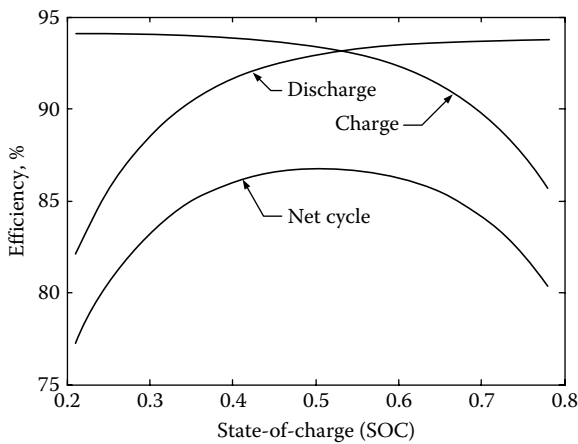
$$\eta = \frac{V}{V_0} \tag{12.17}$$

and

During charging

$$\eta = \frac{V_0}{V}. \tag{12.18}$$

The terminal voltage, as a function of battery current and energy stored in it or SOC, is lower in discharging and higher in charging than the electrical

FIGURE 12.7 Typical battery charge and discharge efficiency.

potential produced by chemical reaction. Figure 12.7 shows the efficiency of the lead–acid battery during discharging and charging. The battery has a high discharging efficiency with high SOC and a high charging efficiency with low SOC. The net cycle efficiency has a maximum in the middle range of the SOC. Therefore, the battery operation control unit of an HEV should control the battery SOC in its middle range so as to enhance the operating efficiency and depress the temperature rise caused by energy loss. High temperature would damage the battery.

12.1.6 Battery Technologies

The viable EV and HEV batteries consist of the lead–acid battery, nickel-based batteries, such as nickel/iron, nickel/cadmium, and nickel–metal hydride (Ni–MH) batteries, and lithium-based batteries such as lithium–polymer (Li–P) and lithium–ion (Li–I) batteries.[4] It seems that cadmium-based and lithium-based batteries would be the major candidates for EVs and HEVs.

12.1.6.1 Lead–Acid Battery

The lead–acid battery has been a successful commercial product for over a century and is still widely used as the electrical energy storage in the automotive field and other applications. Its advantages are its low cost, mature technology, and relatively high-power capability. These advantages are attractive for application in HEVs, where high power is the first consideration. The materials involved (lead, lead oxide, and sulfuric acid) are rather low cost when compared with their more advanced counterparts. Lead–acid batteries also have several disadvantages. The energy density is low, mostly because

of the high molecular weight of lead. The temperature characteristics are poor.[3] Below 10°C, specific power and specific energy are greatly reduced. This aspect severely limits the application of lead–acid batteries for the traction of vehicles operated in cold climates.

The presence of highly corrosive sulfuric acid is a potential safety hazard for vehicle occupants. The hydrogen released by the self-discharge reactions is another potential danger, since this gas is extremely flammable even in tiny concentrations. The hydrogen emission is also a problem for hermetically sealed batteries. Indeed, in order to provide a good level of protection against acid spills, it is necessary to seal the battery, thus trapping the parasitic gases in the casing. As a result, pressure may build up in the battery, causing swelling and mechanical constraints on the casing and sealing. The lead in the electrodes is an environmental problem because of its toxicity. The emission of lead consecutive to the use of lead–acid batteries may occur during the fabrication of the batteries, in the case of vehicle wreck (spill of electrolyte through cracks), or during their disposal at the end of battery life.

Different lead–acid batteries with improved performance are being developed for EVs and HEVs. Improvements of the sealed lead–acid batteries in specific energy over 40 Wh/kg, with the possibility of rapid charge, have been attained. One of these advanced sealed lead–acid batteries is the Electrasource's Horizon battery. It adopts the lead-wire-woven horizontal plate and hence offers competitive advantages of high specific energy (43 Wh/kg), high specific power (285 W/kg), long cycle life (over 600 cycles for on-road EV application), rapid recharge capability (50% capacity in 8 min and 100% in less than 30 min), low cost (US$2000–3000 per EV), mechanical ruggedness (robust structure of the horizontal plate), maintenance-free character (sealed battery technology), and environmental friendliness. Other advanced lead–acid battery technologies include bipolar designs and micro-tubular grid designs.

Advanced lead–acid batteries have been developed to remedy their disadvantages. The specific energy has been increased through the reduction of inactive materials such as the casing, current collector, separators, and so on. The lifetime has been increased by over 50%—at the expense of cost, however. The safety issue has been improved, with electrochemical processes designed to absorb the parasitic releases of hydrogen and oxygen.

12.1.6.2 Nickel-Based Batteries

Nickel is a lighter metal than lead and has very good electrochemical properties desirable for battery applications. There are four different nickel-based battery technologies: nickel–iron, nickel–zinc, nickel–cadmium, and Ni–MH.

12.1.6.2.1 Nickel/Iron Battery

The nickel/iron system was commercialized during the early years of the 20th century. Applications included fork-lift trucks, mine locomotives, shuttle

vehicles, railway locomotives, and motorized hand trucks.[1] The system comprises a nickel (III) hydroxy-oxide (NIOOH) positive electrode and a metallic iron negative electrode. The electrolyte is a concentrated solution of potassium hydroxide (typically 240 g/L) containing lithium hydroxide (50 g/L). The cell reaction is given in Table 12.1 and its nominal open-circuit voltage is 1.37 V.

Nickel/iron batteries suffer from gassing, corrosion, and self-discharge problems. These problems have been partially or totally solved in prototypes that have yet to reach the market. These batteries are complex due to the need to maintain the water level and the safe disposal of the hydrogen and oxygen released during the discharge process. Nickel–iron batteries also suffer from low temperatures, although less than lead–acid batteries. Finally, the cost of nickel is significantly higher than that of lead. Their greatest advantages are high power density compared with lead–acid batteries, capable of withstanding 2000 deep discharges.

12.1.6.2.2 Nickel/Cadmium Battery

The nickel/cadmium system uses the same positive electrodes and electrolyte as the nickel/iron system, in combination with metallic cadmium negative electrode. The cell reaction is given in Table 12.1 and its nominal open-circuit voltage is 1.3 V. Historically, the development of the battery has coincided with that of nickel/iron and they have similar performance.

Nickel/cadmium technology has gained enormous technical improvement because of the advantages of high specific power (over 220 W/kg), long cycle life (up to 2000 cycles), high tolerance of electric and mechanical abuse, a small voltage drop over a wide range of discharge currents, rapid charge capability (about 40–80% in 18 min), wide operating temperature (−40°C to −85°C), low self-discharge rate (<0.5% per day), excellent long-term storage due to negligible corrosion, and availability in a variety of size designs. However, the nickel/cadmium battery has some disadvantages, including high initial cost, relatively low cell voltage, and the carcinogenicity and environmental hazard of cadmium.
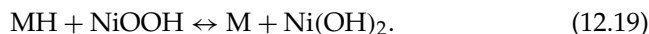
The nickel/cadmium battery can be generally divided into two major categories, namely the vented and sealed types. The vented type consists of many alternatives. The vented sintered plate is a more recent development, which has a high specific energy but is more expensive. It is characterized by its flat discharge voltage profile and superior high current rate and low-temperature performance. A sealed nickel/cadmium battery incorporates a specific cell design feature to prevent a build-up of pressure in the cell caused by gassing during overcharge. As a result, the battery requires no maintenance.

The major manufacturers of the nickel/cadmium battery for EV and HEV allocation are SAFT and VARTA. Recent EVs powered by the nickel/cadmium battery have included the Chrysler TE Van, Citroën AX, Mazda Roadster, Mitsubishi EV, Peugeot 106, and Renault Clio.[4,5]

12.1.6.2.3   *Ni–MH Battery*

The Ni–MH battery has been on the market since 1992. Its characteristics are similar to those of the nickel/cadmium battery. The principal difference between them is the use of hydrogen, absorbed in a metal hydride, for the active negative electrode material in place of cadmium. Because of superior specific energy to Ni–Cd and since it is free from toxicity or carcinogenicity, such as cadmium, the Ni–MH battery is superseding the Ni–Cd battery.

The overall reaction in an Ni–MH battery is

$$MH + NiOOH \leftrightarrow M + Ni(OH)_2. \tag{12.19}$$

When the battery is discharged, metal hydride in the negative electrode is oxidized to form metal alloy, and nickel oxyhydroxide in the positive electrode is reduced to nickel hydroxide. During charging, the reverse reaction occurs.

At present, Ni–MH battery technology has a nominal voltage of 1.2 V and attains a specific energy of 65 Wh/kg and a specific power of 200 W/kg. A key component of the Ni–MH battery is the hydrogen storage metal alloy, which should be formulated to obtain a material that is stable over a large number of cycles. There are two major types of metal alloys being used. These are the rare-earth alloys based on lanthanum nickel, known as AB_5, and alloys consisting of titanium and zirconium, known as AB_2. The AB_2 alloys have a higher capacity than the AB_5 alloys. However, the trend is to use AB_5 alloys because of better charge retention and stability characteristics.

Because the Ni–MH battery is still under continual development, its advantages based on present technology are summarized as follows: it has the highest specific energy (70–95 Wh/kg) and highest specific power (200–300 W/kg) of nickel-based batteries; environmental friendliness (cadmium free); a flat discharge profile (smaller voltage drop); and rapid recharge capability. However, this battery still suffers from its high initial cost. It may also have a memory effect and be exothermic during charging.

The Ni–MH battery has been considered as an important near-term choice for EV and HEV applications. A number of battery manufacturers, such as GM Ovonic, GP, GS, Panasonic, SAFT, VARTA, and YUASA, have actively engaged in the development of this battery technology, especially for powering EVs and HEVs. Since 1993, Ovonic has installed its Ni–MH battery in the Solectric GT Force EV for testing and demonstration. A 19-kWh battery has delivered over 65 Wh kg, 134 km/h, acceleration from zero to 80 km/h in 14 s, and a city driving range of 206 km. Toyota and Honda have used the Ni–MH battery in their HEVs—Prius and Insight, respectively.[4,5]

12.1.6.3   **Lithium-Based Batteries**

Lithium is the lightest of all metals and presents very interesting characteristics from an electrochemical point of view. Indeed, it allows a very high thermodynamic voltage, which results in a very high specific energy and

specific power. There are two major technologies of lithium-based batteries: Li–P and Li–I.

12.1.6.3.1 Li–P Battery

Li–P batteries use lithium metal and a transition metal intercalation oxide (M_yO_z) for the negative and positive electrodes, respectively. This M_yO_z possesses a layered structure into which lithium ions can be inserted, or from which they can be removed on discharge and charge, respectively. A thin solid polymer electrolyte (SPE) is used, which offers the merits of improved safety and flexibility in design. The general electrochemical reactions are

$$x\text{Li} + M_yO_z \leftrightarrow \text{Li}_xM_yO_z. \tag{12.20}$$

On discharge, lithium ions formed at the negative electrode migrate through the SPE and are inserted into the crystal structure at the positive electrode. On charge, the process is reversed. By using a lithium foil negative electrode and a vanadium oxide (V_6O_{13}) positive electrode, the $Li/SPE/V_6O_{13}$ cell is the most attractive one within the family of Li–Ps. It operates at a nominal voltage of 3 V and has a specific energy of 155 Wh/kg and a specific power of 315 W/kg. The corresponding advantages are a very low self-discharge rate (about 0.5% per month), capability of fabrication in a variety of shapes and sizes, and safe design (reduced activity of lithium with solid electrolyte). However, it has the drawback of relatively weak low-temperature performance due to its temperature dependence of ionic conductivity.[4]

12.1.6.3.2 Li–I Battery

Since the first announcement of the Li–I battery in 1991, the Li–I battery technology has seen an unprecedented rise to what is now considered to be the most promising rechargeable battery of the future. Although still in the stage of development, the Li–I battery has already gained acceptance for EV and HEV applications.

The Li–I battery uses a lithiated carbon intercalation material (Li_xC) for the negative electrode instead of metallic lithium, a lithiated transition metal intercalation oxide ($\text{Li}_{1-x}M_yO_z$) for the positive electrode, and a liquid organic solution or a solid polymer for the electrolyte. Lithium ions are swinging through the electrolyte between the positive and negative electrodes during discharge and charge. The general electrochemical reaction is described as

$$\text{Li}_xC + \text{Li}_{1-x}M_yO_z \leftrightarrow C + \text{LiM}_yO_z. \tag{12.21}$$

On discharge, lithium ions are released from the negative electrode, migrate via the electrolyte, and are taken up by the positive electrode. On charge the process is reversed. Possible positive electrode materials include $\text{Li}_{1-x}\text{CoO}_2$, $\text{Li}_{1-x}\text{NiO}_2$, and $\text{Li}_{1-x}\text{Mn}_2\text{O}_4$, which have the advantages of stability in air, high voltage, and reversibility for the lithium intercalation reaction.

The $Li_xC/Li_{1-x}NiO_2$ type, loosely written as $C/LiNiO_2$ or simply called the nickel-based Li–I battery, has a nominal voltage of 4 V, a specific energy of 120 Wh/kg, an energy density of 200 Wh/L, and a specific power of 260 W/kg. The cobalt-based type has higher specific energy and energy density, but with a higher cost and significant increase of the self-discharge rate. The manganese-based type has the lowest cost and its specific energy and energy density lie between those of the cobalt-based and nickel-based types. It is anticipated that the development of the Li–I battery will ultimately move to the manganese-based type because of the low cost, abundance, and environmental friendliness of the manganese-based materials.

Many battery manufacturers, such as SAFT, GS Hitachi, Panasonic, SONY, and VARTA, have actively engaged in the development of the Li–I battery. Starting in 1993, SAFT focused on the nickel-based Li–I battery. Recently, SAFT reported the development of Li–I high-power batteries for HEV applications with a specific energy of 85 Wh/kg and a specific power of 1350 W/kg. SAFT also announced high-energy batteries for EV applications with about 150 Wh/kg and 420 W/kg (at 80% SOC, 150 A current, and 30 s), respectively.[2]

12.2 Ultracapacitors

Because of the frequent stop-and-go operation of EVs and HEVs, the discharging and charging profile of the energy storage is highly varied. The average power required from the energy storage is much lower than the peak power for acceleration and hill climbing in a relatively short duration. The ratio of peak power to average power can reach over 10:1 (Chapter 2). In HEV design, the peak power capacity of the energy storage is more important than its energy capacity, and usually constrains its size reduction (refer to Chapters 8 and 9). Based on present battery technology, battery design has to carry out the trade-off among specific energy, specific power, and cycle life. The difficulty in simultaneously obtaining high values of specific energy, specific power, and cycle life has led to some suggestions that the energy storage system of EV and HEV should be a hybridization of an energy source and a power source. The energy source, mainly batteries and fuel cells, has high specific energy, whereas the power source has high specific power. Power sources can be recharged from the energy source during less demanding driving or regenerative braking. The power source that has received wide attention is the ultracapacitor.
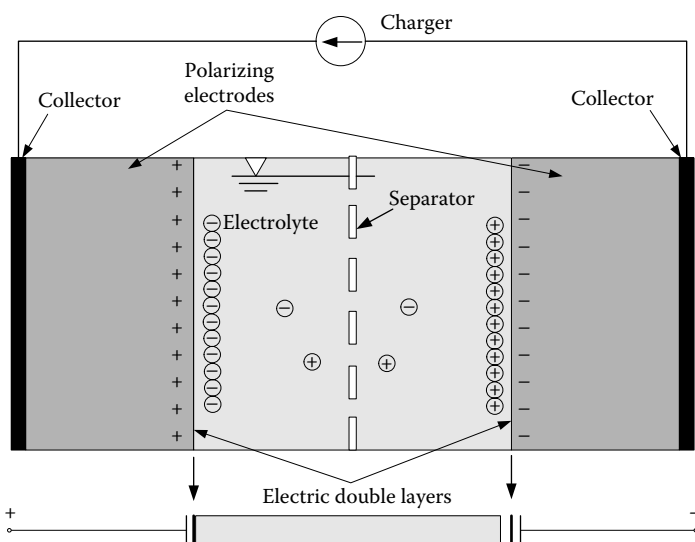
12.2.1 Features of Ultracapacitors

The ultracapacitor is characterized by a much higher specific power but a much lower specific energy compared to batteries. Its specific energy is in

the range of a few watt-hours per kilogram. However, its specific power can reach up to 3 kW/kg, much higher than any type of battery. Due to the low specific energy density and the dependence of terminal voltage on SOC, it is difficult to use ultracapacitors alone as an energy storage for EVs and HEVs. Nevertheless, there are a number of advantages that can result from using the ultracapacitor as an auxiliary power source. One promising application is the so-called battery and ultracapacitor hybrid energy storage system for EVs and HEVs.[4,6] Specific energy and specific power requirements can be decoupled, thus affording an opportunity to design a battery that is optimized for specific energy and cycle life with little attention being paid to specific power. Due to the load leveling effect of the ultracapacitor, the high current discharging from the battery and the high current charging to the battery by regenerative braking are minimized so that available energy, endurance, and life of the battery can be significantly increased.

12.2.2 Basic Principles of Ultracapacitors

Double-layer capacitor technology is the major approach to achieving the ultracapacitor concept. The basic principle of a double-layer capacitor is illustrated in Figure 12.8. When two carbon rods are immersed into a thin sulfuric acid solution, separated from each other and applied with increasing voltage from zero to 1.5 V, almost nothing happens up to 1 V; then at a little over 1.2 V, a small bubble appears on the surface of both electrodes. Bubbles at a voltage above 1 V indicate the electrical decomposition of water. Below the

FIGURE 12.8 Basic principles of a typical electric double-layer capacitor.

decomposition voltage, while the current does not flow, an "electric double layer" occurs at the boundary of electrode and electrolyte. The electrons are charged across the double layer and for a capacitor.

An electrical double layer works as an insulator only below the decomposing voltage. The stored energy, E_{cap}, is expressed as

$$E_{cap} = \frac{1}{2}CV^2, \tag{12.22}$$

where C is the capacitance in faraday and V is the usable voltage in volts. This equation indicates that the higher rated voltage V is desirable for larger energy density capacitors. Up to now, a capacitor's rated voltage with aqueous electrolyte has been about 0.9 V per cell, and with nonaqueous electrolyte it is 2.3–3.3 V for each cell.

There is great merit in using an electric double layer in place of plastic or aluminum oxide films in a capacitor, since the double layer is very thin—as thin as one molecule with no pin holes—and the capacity per area is quite large, at 2.5–5 $\mu F/cm^2$.

Even if a few $\mu F/cm^2$ are obtainable, the energy density of capacitors is not large when using aluminum foil. For increasing the capacitance, electrodes are made from specific materials that have a very large area, such as activated carbons, which are famous for their surface areas of 1000–3000 m^2/g. Ions are adsorbed on those surfaces, and result in 50 F/g ($1000\,m^2/g \times 5\,F/cm^2 \times 10,000\,cm^2/m^2 = 50\,F/g$). Assuming that the same weight of electrolyte is added, 25 F/g is quite a large capacity density. Nevertheless, the energy density of these capacitors is far smaller than that of batteries; the typical specific energy of ultracapacitors is at present about 2 Wh/kg, only 1/20 of 40 Wh/kg, which is the available value of typical lead–acid batteries.

12.2.3 Performance of Ultracapacitors
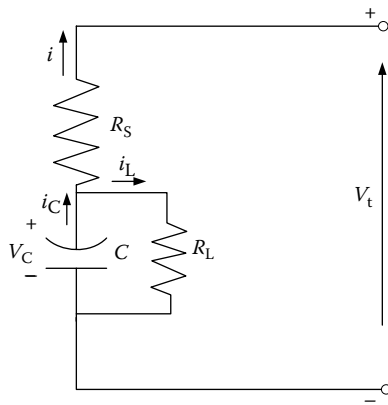
The performance of an ultracapacitor may be represented by terminal voltages during discharge and charge with different current rates. There are three parameters in a capacitor: the capacitance itself (its electric potential V_C), the series resistance R_S, and the dielectric leakage resistance, R_L, as shown in Figure 12.9. The terminal voltage of the ultracapacitor during discharge can be expressed as

$$V_t = V_C - iR_S. \tag{12.23}$$

The electric potential of the capacitor can be expressed as

$$\frac{dV_C}{dt} = -\left(\frac{i + i_L}{C}\right), \tag{12.24}$$

where C is the capacitance of the ultracapacitor.

FIGURE 12.9 Ultracapacitor equivalent circuit.

On the other hand, the leakage current i_L can be expressed as
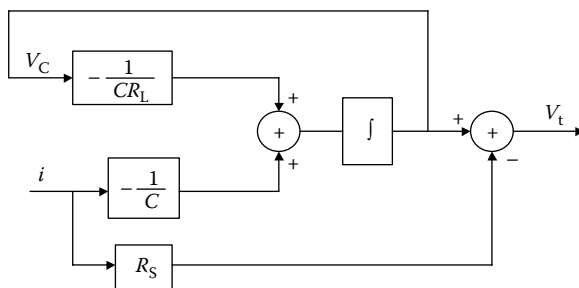
$$i_L = \frac{V_C}{R_L}. \tag{12.25}$$

Substituting Equation 12.25 into Equation 12.24, one can obtain
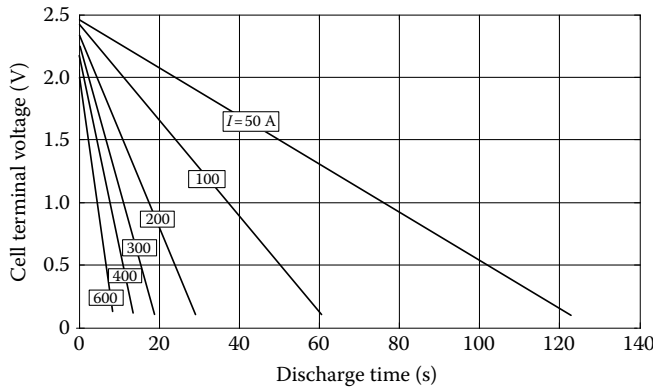
$$\frac{dV_C}{dt} = -\left(\frac{V_C}{CR_L} + \frac{i}{C}\right). \tag{12.26}$$

The terminal voltage of the ultracapacitor cell can be represented by the diagram shown in Figure 12.10. The analytical solution of Equation 12.26 is

$$V_C = \left[V_{C0} - \int_0^t \frac{i}{C} e^{t/CR_L} dt\right] e^{-(t/CR_L)}, \tag{12.27}$$

FIGURE 12.10 Block diagram of the ultracapacitor model.

FIGURE 12.11   Discharge characteristics of the 2600F Maxwell Technologies ultracapacitor.

where i is the discharge current and is a function of time in real operation. The discharge characteristics of a Maxwell 2600F ultracapacitor are shown in Figure 12.11. At different discharge current rates, the voltage linearly decreases with discharge time. At a large discharge current, the voltage decreases much faster than at a small current rate.

A similar model can be used to describe the charging characteristics of an ultracapacitor and readers who are interested may carry out their own analysis.

The operation efficiency in discharging and charging can be expressed as follows:

Discharging:

$$\eta_d = \frac{V_t I_t}{V_C I_C} = \frac{(V_C - I_t R_S)\, I_t}{V_C\, (I_t + I_L)} \tag{12.28}$$

and
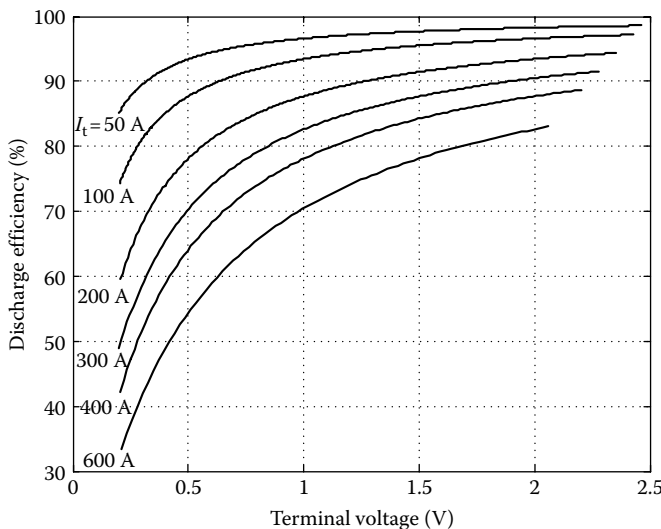
Charging:

$$\eta_c = \frac{V_C I_C}{V_t I_t} = \frac{V_C\, (I_t - I_L)}{(V_C + I_t R_S)\, I_t}, \tag{12.29}$$

where V_t is the terminal voltage and I_t is the current input to or output from the terminal. In actual operation, the leakage current I_L is usually very small (few mA) and can be ignored. Thus, Equations 12.28 and 12.29 can be rewritten as

Discharging:

$$\eta_d = \frac{V_C - R_S I_t}{V_c} = \frac{V_t}{V_c} \tag{12.30}$$

FIGURE 12.12 Discharge efficiency of the 2600F Maxwell Technologies ultracapacitor.

and
Charging:
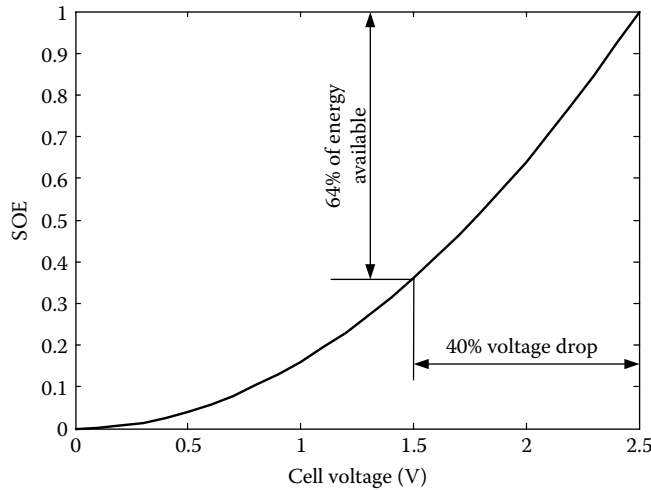
$$\eta_c = \frac{V_C}{V_C + R_S I_t} = \frac{V_C}{V_t}. \tag{12.31}$$

The above equations indicate that the energy loss in an ultracapacitor is caused by the presence of series resistance. The efficiency decreases at high current rate and low cell voltage, as shown in Figure 12.12. Thus, in actual operation, the ultracapacitor should be kept at its high-voltage region, for higher than 60% of its rated voltage.

The energy stored in an ultracapacitor can be obtained through the energy needed to charge it to a certain voltage level, that is,

$$E_C = \int_0^t V_C I_C dt = \int_0^V C V_C dV_C = \frac{1}{2} C V_C^2, \tag{12.32}$$

where V_C is the cell voltage in volts. At its rated voltage, the energy stored in the ultracapacitor reaches its maxima. Equation 12.32 indicates that increasing the rated voltage can significantly increase the stored energy since the energy increases with the voltage squared. In real operation, it is impossible to completely utilize the stored energy because of the low power in the low state-of-energy (SOE). Thus, an ultracapacitor is usually given a bottom voltage, V_{Cb}, below which the ultracapacitor will stop delivering energy. Consequently, the available or useful energy for use is less than its fully

FIGURE 12.13   SOE versus cell voltage.

charged energy, which can be expressed as

$$E_u = \frac{1}{2}C\left(V_{CR}^2 - V_{Cb}^2\right),$$ (12.33)

where V_{CR} is the rated voltage of the ultracapacitor.

   The usable energy in an ultracapacitor can also be expressed in SOE, which is defined as the ratio of the energy in the ultracapacitor at a voltage of V_C to the energy at full charged voltage, V_{CR}, as expressed by

$$SOE = \frac{0.5\,CV_C^2}{0.5\,CV_{CR}^2} = \left(\frac{V_C}{V_{CR}}\right)^2.$$ (12.34)

   For example, 60% of the rated voltage is the bottom voltage and 64% of the total energy is available for use, as shown in Figure 12.13.

12.2.4   Ultracapacitor Technologies

According to the goals set by the U.S. Department of Energy for the inclusion of ultracapacitors in EVs and HEVs, the near-term specific energy and specific power should be better than 5 Wh/kg and 500 W/kg, respectively, while the advanced performance values should be over 15 Wh/kg and 1600 W/kg. So far, none of the available ultracapacitors can fully satisfy these goals. Nevertheless, some companies are actively engaged in the research and development of ultracapacitors for EV and HEV applications. Maxwell Technologies has claimed that its power BOOSTCAP® ultracapacitor cells (2600 F at 2.5 V) and integrated modules (145 F at 42 V and 435 F at 14 V) are in production. The technical specifications are listed in Table 12.3.

TABLE 12.3

Technical Specifications of Maxwell Technologies Ultracapacitor Cell and Integrated Modules[7]

	BCA P0010 (Cell)	BMOD0115 (Module)	BMOD0117 (Module)
Capacitance (farads, −20%/+20%)	2600	145	435
Maximum series resistance ESR at 25°C (mΩ)	0.7	10	4
Voltage (V): continuous (peak)	2.5 (2.8)	42 (50)	14 (17)
Specific power at rated voltage (W/kg)	4300	2900	1900
Specific energy at rated voltage (Wh/kg)	4.3	2.22	1.82
Maximum current (A)	600	600	600
Dimensions (mm) (reference only)	60 × 172 (cylinder)	195 × 165 × 415 (box)	195 × 265 × 145 (box)
Weight (kg)	0.525	16	6.5
Volume (L)	0.42	22	7.5
Operating temperature[a] (°C)	−35 to +65	−35 to +65	−35 to +65
Storage temperature (°C)	−35 to +65	−35 to +65	−35 to +65
Leakage current (mA) 12 h, 25°C	5	10	10

[a] Steady-state case temperature.

12.3 Ultra-High-Speed Flywheels

The use of flywheels for storing energy in mechanical form is not a new concept. More than 25 years ago, the Oerlikon Engineering Company in Switzerland made the first passenger bus solely powered by a massive flywheel. This flywheel, weighing 1500 kg and operating at 3000 rpm, was recharged by electricity at each bus stop. The traditional flywheel is a massive steel rotor with hundreds of kilograms that spins on the order of ten hundreds of rpm. On the contrary, the advanced flywheel is a lightweight composite rotor with tens of kilograms and rotates on the order of ten thousands of rpm; it is the so-called ultra-high-speed flywheel.

The concept of ultra-high-speed flywheels appears to be a feasible means for fulfilling the stringent energy storage requirements for EV and HEV applications, namely high specific energy, high specific power, long cycle life, high energy efficiency, quick recharge, maintenance-free characteristics, cost effectiveness, and environmental friendliness.

12.3.1 Operation Principles of Flywheels
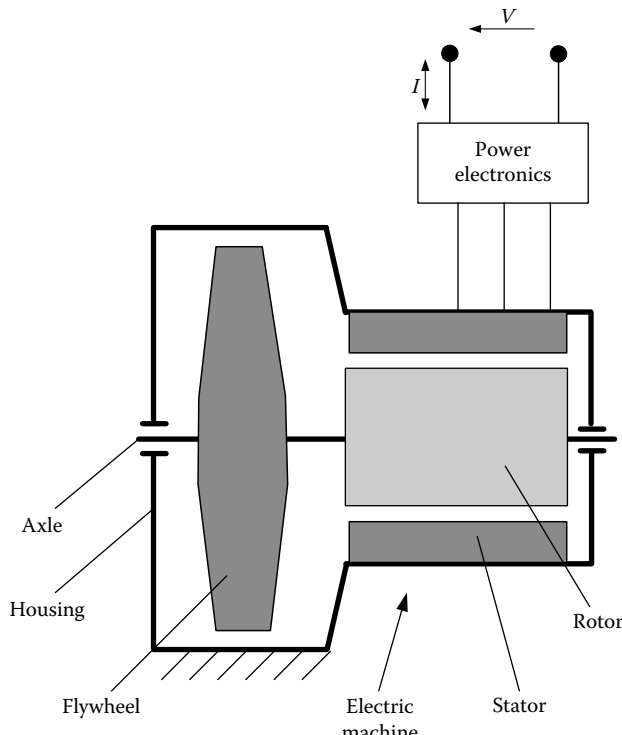
A rotating flywheel stores energy in the kinetic form as

$$E_f = \frac{1}{2} J_f \omega_f^2, \tag{12.35}$$
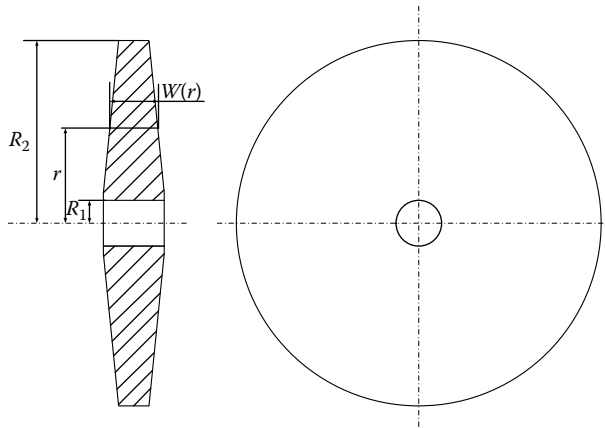
where J_f is the moment of inertia of the flywheel in $kg\,m^2/s$ and ω_f is the angular velocity of the flywheel in rad/s. Equation 12.35 indicates that enhancing the angular velocity of the flywheel is the key technique to increasing its energy capacity and reducing its weight and volume. At present, a speed of over 60,000 rpm has been achieved in some prototypes.

With current technology it is difficult to directly use the mechanical energy stored in a flywheel to propel a vehicle, due to the need for continuous variation transmission with a wide gear ratio variation range. The commonly used approach is to couple an electric machine to the flywheel directly or through a transmission to constitute a so-called mechanical battery. The electric machine, functioning as the energy input and output port, converts the mechanical energy into electric energy or vice versa, as shown in Figure 12.14.

Equation 12.35 indicates that the energy stored in a flywheel is proportional to the moment of inertia of the flywheel and flywheel rotating speed squared. A lightweight flywheel should be designed to achieve a large moment of inertia per unit mass and per unit volume by properly designing its

FIGURE 12.14   Basic structure of a typical flywheel system (mechanical battery).

FIGURE 12.15 Geometry of a typical flywheel.

geometric shape. The moment of inertia of a flywheel can be calculated by

$$J_f = 2\pi\rho \int_{R_1}^{R_2} W(r)r^3 \, dr, \tag{12.36}$$

where ρ is the material mass density and $W(r)$ is the width of the flywheel corresponding to radius r, as shown in Figure 12.15. The mass of the flywheel can be calculated by

$$M_f = 2\pi\rho \int_{R_1}^{R_2} W(r)r \, dr. \tag{12.37}$$

Thus, the specific moment of inertia of a flywheel, defined as the moment of inertia per unit mass, can be expressed as

$$J_{fs} = \frac{\int_{R_1}^{R_2} W(r)r^3 \, dr}{\int_{R_1}^{R_2} W(r)r \, dr}. \tag{12.38}$$

Equation 12.38 indicates that the specific moment of inertia of a flywheel is independent of its material mass density and dependent solely on its geometric shape $W(r)$.

For a flywheel with equal width, the moment of inertia is

$$J_f = 2\pi\rho(R_2^4 - R_1^4) = 2\pi\rho(R_2^2 + R_1^2)(R_2^2 - R_1^2). \tag{12.39}$$

The specific moment of inertia is

$$J_{fs} = R_2^2 + R_1^2. \tag{12.40}$$

The volume density of the moment of inertia, defined as the moment of inertia per unit volume, is, indeed, associated with the mass density of the material. The volume of the flywheel can be obtained by

$$V_f = 2\pi \int_{R_2}^{R_2} W(r)r \, dr. \tag{12.41}$$

The volume density of the moment of inertia can be expressed as

$$J_{fV} = \frac{\rho \int_{R_1}^{R_2} W(r)r^3 \, dr}{\int_{R_1}^{R_2} W(r)r \, dr}. \tag{12.42}$$

For a flywheel with equal width, the volume density of the moment of inertia is

$$J_{fV} = \rho \left(R_2^2 + R_1^2 \right). \tag{12.43}$$

Equations 12.42 and 12.43 indicate that heavy material can, indeed, reduce the volume of the flywheel with a given moment of inertia.

12.3.2   Power Capacity of Flywheel Systems
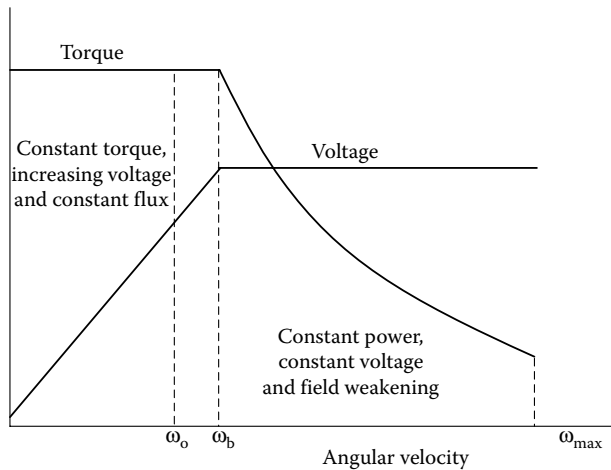
The power that a flywheel delivers or obtains can be obtained by differentiating Equation 12.35 with respect to time, that is,

$$P_f = \frac{dE_f}{dt} = J_f \omega_f \frac{d\omega_f}{dt} = \omega_f T_f, \tag{12.44}$$

where T_f is the torque acting on the flywheel by the electric machine. When the flywheel discharges its energy, the electric machine acts as a generator and converts the mechanical energy of the flywheel into electric energy. On the other hand, when the flywheel is charged, the electric machine acts as a motor and converts electric energy into mechanical energy stored in the flywheel. Equation 12.44 indicates that the power capacity of a flywheel system depends completely on the power capacity of the electric machine.

An electric machine usually has the characteristics shown in Figure 12.16, which has two distinct operating regions—constant-torque and constant-power regions. In the constant-torque region, the voltage of the electric machine is proportional to its angular velocity, and the magnetic flux in the air gap is constant. However, in the constant-power region, the voltage is constant and the magnetic field is weakened with the increase of machine angular velocity. During charging of the flywheel, that is, accelerating the flywheel from a low speed, ω_0, to a high speed, the maximum speed, ω_{max}, for example, the torque delivered from the electric machine is

$$T_m = J_f \frac{d\omega_f}{dt}, \tag{12.45}$$

FIGURE 12.16 Typical torque and voltage profile versus rotational speed.

where it is assumed that the electric machine is directly connected to the flywheel. The time, t, needed can be expressed as

$$t = \int_{\omega_0}^{\omega_{max}} \frac{J_f}{T_m} \, d\omega = \int_{\omega_0}^{\omega_b} \frac{J_f}{p_m/\omega_b} \, d\omega + \int_{\omega_b}^{\omega_{max}} \frac{J_f}{p_m/\omega} \, d\omega. \qquad (12.46)$$

With the given accelerating time, t, the maximum power of the electric machine can be obtained from Equation 12.46 as

$$P_m = \frac{J_f}{2t} \left(\omega_b^2 - 2\omega_0\omega_b + \omega_{max}^2 \right). \qquad (12.47)$$

Equation 12.47 indicates that the power of the electric machine can be minimized by designing its corner speed or base speed, ω_b, equal to the bottom speed of the flywheel, ω_0. This conclusion implies that the effective operating speed range of the flywheel should coincide with the constant-power region of the electric machine. The power of the electric machine can be minimized as

$$P_m = \frac{J_f}{2t} \left(\omega_{max}^2 - \omega_0^2 \right). \qquad (12.48)$$

Another advantage achieved by coinciding the operating speed range of the flywheel with the constant-power speed range is that the voltage of the electric machine is always constant (refer to Figure 12.16), therefore thus significantly simplifying the power management system, such as DC/DC converters and their controls.
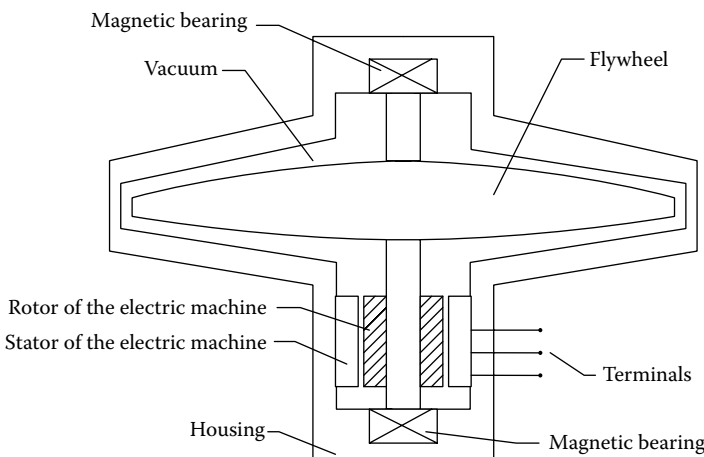
TABLE 12.4

Composite Materials for Ultra-High-Speed Flywheel[4]

	Tensile Strength σ (MPa)	Specific Energy ρ (kg/m^3)	Ratio σ/ρ (Wh/kg)
E-glass	1379	1900	202
Graphite epoxy	1586	1500	294
S-glass	2069	1900	303
Kevlar epoxy	1930	1400	383

12.3.3   Flywheel Technologies

Although higher rotational speed can significantly increase the stored energy (Equation 12.35), there is a limit beyond which the tensile strength σ of the material constituting the flywheel cannot withstand the stress resulting from the centrifugal force. The maximum stress acting on the flywheel depends on its geometry, specific density ρ, and rotational speed. Maximum benefit can be obtained by adopting flywheel materials that have the maximum ratio of σ/ρ. Note that if the speed of the flywheel is limited by material strength, the theoretical specific energy is proportional to the ratio of σ/ρ. Table 12.4 summarizes the characteristics of some composite materials for ultra-high-speed flywheels.

A constant-stress principle may be employed for the design of ultra-high-speed flywheels. To achieve maximum energy storage, every element in the rotor should be equally stressed to its maximum limit. This results in a shape of gradually decreasing thickness that theoretically approaches zero as the radius approaches infinity, as shown in Figure 12.17.[4]

FIGURE 12.17   Basic structure of a typical flywheel system.

Due to the extremely high rotating speed and in order to reduce the aerodynamic loss and frictional loss, the housing inside which the flywheel is spinning is always highly vacuumed, and noncontact, magnetic bearings are employed.

The electric machine is one of the most important components in the flywheel system, since it has a critical impact on the performance of the system. At present, PM brushless DC motors are usually accepted in the flywheel system. Apart from possessing high power density and high efficiency, the PM brushless DC motor has the unique advantage that no heat is generated inside the PM rotor, which is particularly essential for the rotor to work in a vacuum environment to minimize windage loss.

A switched reluctance machine (SRM) is also a very promising candidate for application in a flywheel system. SRM has a very simple structure and can operate efficiently at very high speed. In addition, SRM presents a large extended constant-power speed region, which allows more energy in the flywheel that can be delivered (refer to Section 12.3.2). In this extended speed region, only the machine excitation flux is varied, which is easily realized. On the contrary, the PM brushless motor shows some difficulty in weakening the field flux induced by the PM.

In contrast to applying the ultra-high-speed flywheel for energy storage in stationary plants, its application to EVs and HEVs suffers from two specific problems. First, gyroscopic forces occur whenever a vehicle departs from its straight-line course, such as in turning and in pitching upward or downward from road grades. These forces essentially reduce the maneuverability of the vehicle. Second, if the flywheel is damaged, its stored energy in mechanical form will be released in a very short period of time. The corresponding power released will be very high, which can cause severe damage to the vehicle. For example, if a 1-kWh flywheel breaks apart in 1–5 s, it will generate a huge power of 720–3600 kW. So containment in the case of failure is presently the most significant obstacle to implementing the ultra-high-speed flywheel in EVs and HEVs.

The simplest way of alleviating gyroscopic forces is to use multiple smaller flywheels. By operating them in pairs (one half spinning in one direction and another half in the opposite direction), the net gyroscopic effect becomes theoretically zero. Practically, it still has some problems related to the distribution and coordination of these flywheels. Also the overall specific energy and specific power of all flywheels may be smaller than a single one. Similarly, the simplest way of minimizing the damage due to breakage of the ultra-high-speed flywheel is to adopt multiple small modules, but this means vehicle performance suffers from the possible reduction of specific energy and specific power. Recently, a new failure containment has been proposed. Instead of diminishing the thickness of the rotor's rim to zero based on the maximum stress principle, the rim thickness is purposely enlarged. Hence, the neck area just before the rim (virtually a mechanical fuse) will break first at the instant the rotor suffers from a failure. Owing to the use of this mechanical

fuse, only the mechanical energy stored in the rim needs to be released or dissipated in the casing on failure.[4]

Many companies and research agencies (such as Lawrence Livermore National Laboratory (LLNL) in the United States, Ashman Technology, AVCON, Northrop Grumman, Power R&D, Rocketdyne/Rockwell Trinity Flywheel US Flywheel Systems, Power Center at UT Austin, and so on) have engaged in the development of ultra-high-speed flywheels as energy storages of EVs and HEVs. However, technologies of ultra-high-speed flywheels are still in their infancy. Typically, the whole ultra-high-speed flywheel system can achieve a specific energy of 10–150 Wh/kg and specific power of 2–10 kW/kg. LLNL has built a prototype (20 cm diameter and 30 cm height) that can achieve 60,000 rpm, 1 kWh, and 100 kW.
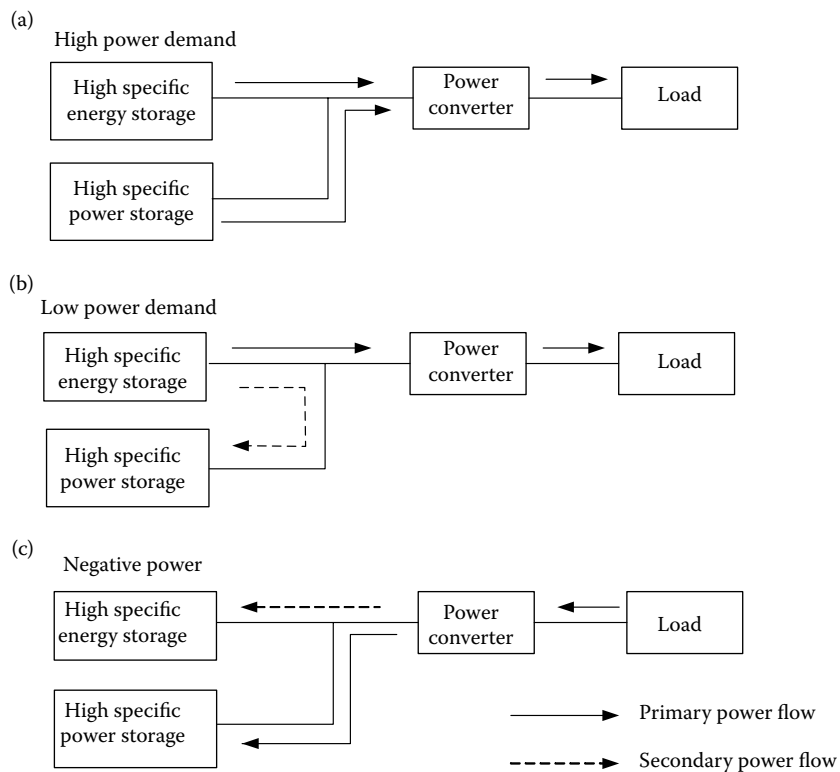
12.4   Hybridization of Energy Storages

12.4.1   Concept of Hybrid Energy Storage

The hybridization of energy storage involves to combining two or more energy storages together so that the advantages of each can be brought out and the disadvantages can be compensated by others. For instance, the hybridization of a chemical battery with an ultracapacitor can overcome problems such as the low specific power of chemical batteries and low specific energy of ultracapacitors, thus achieving high specific energy and high specific power. Basically, the hybridized energy storage consists of two basic energy storages, one with high specific energy and the other with high specific power. The basic operation of this system is illustrated in Figure 12.18. In high-power demand operation, such as acceleration and hill climbing, both basic energy storages deliver their power to the load as shown in Figure 12.18a. On the other hand, in low-power demand operation, such as constant-speed cruising operation, the high specific energy storage will deliver its power to the load and charge the high specific power storage to recover its charge lost during high-power demand operation, as shown in Figure 12.18b. In regenerative braking operation, the peak power will be absorbed by the high specific power storage, and only a limited part is absorbed by the high specific energy storage. In this way, the whole system would be much smaller in weight and size than if any one of them alone was the energy storage.

12.4.2   Passive and Active Hybrid Energy Storage with Battery and Ultracapacitor
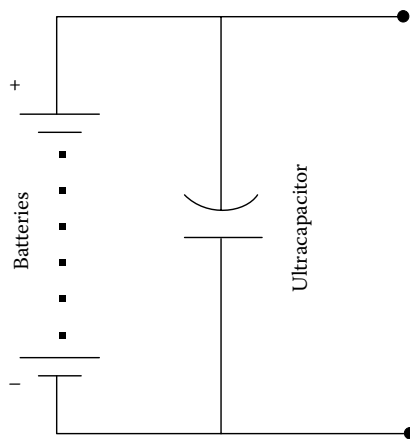
Based on the available technologies of various energy storages, there are several viable hybridization schemes for EVs and HEVs: typically, battery

FIGURE 12.18 Concept of a hybrid energy storage operation. (a) Hybrid powering, (b) power split, and (c) hybrid charging.

and battery hybrids, and battery and ultracapacitor hybrids. The latter is more natural because the ultracapacitor can offer a much higher power than batteries, and it collaborates with various batteries to form the battery and ultracapacitor hybrids. During the hybridization, the simplest way is to directly and parallelly connect the ultracapacitors to the batteries as shown in Figure 12.19. In this configuration, the ultracapacitors simply act as a current filter, which can significantly level the peak current of the batteries and reduce the battery voltage drop as shown in Figures 12.20 and 12.21. The major disadvantages of this configuration are that the power flow cannot be actively controlled and the ultracapacitor energy cannot be fully used.
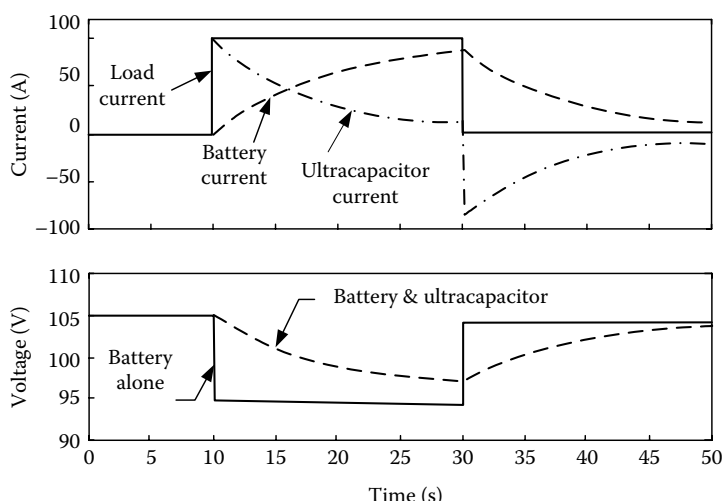
Figure 12.22 shows a configuration in which a two-quadrant DC/DC converter is placed between the batteries and ultracapacitors. This design allows the batteries and the ultracapacitors to have a different voltage; also the power flow between them can be actively controlled and the energy in the ultracapacitors can be fully used. In the long term, an ultra-high-speed flywheel will replace the batteries in hybrid energy storage to obtain a high efficiency, compact, and long-life storage system for EVs and HEVs.
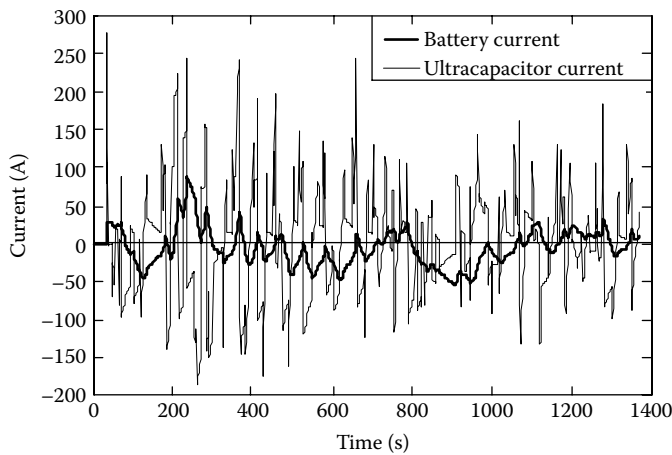
FIGURE 12.19   Direct and parallel connection of batteries and ultracapacitors.

12.4.3   Battery and Ultracapacitor Size Design

The best design of a hybrid energy storage with a battery and an ultracapacitor is that the overall energy and power capacities just meet the energy and power requirements of the vehicle without much margins.[8] The energy and power requirements of a vehicle to its energy storage can be represented by the

FIGURE 12.20   Variation of battery and ultracapacitor currents and voltages with a step current output change.
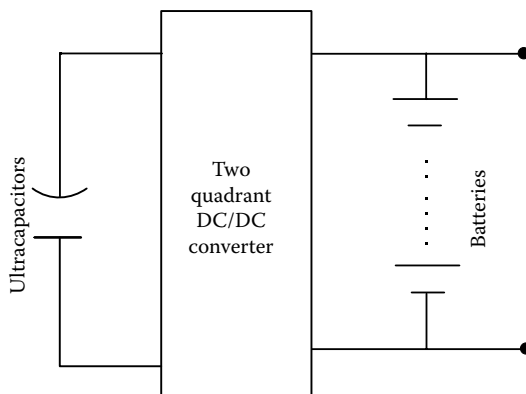
FIGURE 12.21 Battery and ultracapacitor currents during operation of HEV in an FTP75 urban drive cycle.

energy/power ratio, which is defined as

$$R_{e/p} = \frac{E_r}{P_r},$$ (12.49)

where E_r and P_r are the energy and power required by the vehicle, respectively.

The energy and power requirements mostly depend on the design of the vehicle drive train and control strategy as discussed in Chapters 7 through 9. When $R_{e/p}$ is known, the battery and ultracapacitor in the hybrid storage can be designed so that the energy/power ratio of the hybrid energy storage is

FIGURE 12.22 Actively controlled hybrid battery/ultracapacitor energy storage.

equal to $R_{e/p}$, which is expressed as[8]

$$\frac{W_b E_b + W_c E_c}{W_b P_b + W_c P_c} = R_{e/p}, \tag{12.50}$$

where W_b and W_c are the weights of the battery and ultracapacitor, respectively, E_b and E_c are the specific energies of the battery and ultracapacitor, respectively, and P_b and P_c are the specific powers of the battery and ultracapacitor, respectively.

Equation 12.50 can be further written as

$$W_c = kW_b, \tag{12.51}$$

where

$$k = \frac{E_b - R_{e/p}P_b}{R_{e/p}P_c - E_c}. \tag{12.52}$$

Thus, the specific energy of the hybrid energy storage is

$$E_{spe} = \frac{W_b E_b + W_c E_c}{W_b + W_c} = \frac{E_b + kE_c}{1 + k} \tag{12.53}$$

and the specific power of the hybrid energy storage is

$$P_{spe} = \frac{W_b P_b + W_c P_c}{W_b + W_c} = \frac{P_b + kP_c}{1 + k}. \tag{12.54}$$

An example is shown in the following.

Suppose that a vehicle needs a 50-kW energy storage; the desired energy/power ratio $R_{e/p} = 0.07$ h, that is, 3.5-kWh energy is required and the battery and ultracapacitor characteristics are shown in Tables 12.5 and 12.6. The weights needed for a single source and hybrid sources are listed in

TABLE 12.5

Major Parameters of CHPS Battery Alternative at Standard Testing[8]

CHPS Battery Alternative	Specific Energy (Wh/kg)	Specific Power (W/kg)	Energy/Power (h)
Lead–acid	28	75	0.373
NiCd	50	120	0.417
Ni–MH	64	140	0.457
Li–I (CHPS)[a]	100	1000[b]	0.1

[a] Combat Hybrid Power System sponsored by TACOM.
[b] Power capabilities depend on pulse length and temperature.

TABLE 12.6

Characteristic Data of a 42-V Ultracapacitor[7]

Rated capacitance (DCC[a], 25°C)	(F)	145
Capacitance tolerance	(%)	±20
Rated voltage	(V)	42
Surge voltage	(V)	50
Max. series resis., ESR (DCC, 25°C)	(mΩ)	10
Specific power density (42 V)	(W/kg)	2900
Max. current	(A)	600
Max. stored energy	(J)	128,000
Specific energy density (42 V)	(Wh/kg)	2.3
Max. leakage current (12 h, 25°C)	(mA)	30
Weight	(kg)	15
Volume	(l)	22
Operating temperature	(°C)	−35 to +65
Storage temperature	(°C)	−35 to +65
Lifetime (25°C)	(year)	10, C < 20% of initial value, ESR < 200% of initial value
Cyclability (25°C, $I = 20$ A)		500,000, C < 20% of initial value, ESR < 200% of initial value

^a a   DCC: discharging at constant current.

Tables 12.7 and 12.8. Comparing the total weights in Tables 12.7 and 12.8, it is obvious that the hybrid energy storage can save the weight significantly, especially with a battery that has low power density.

TABLE 12.7

Characteristic Data of a 42-V Ultracapacitor[7]

	Lead/Acid	**Ni/Cd**	**Ni/MH**	**Li–I**	**Ultracap**
Specific power (W/kg)	75	120	140	1000	2500
Specific energy (Wh/kg)	30	50	64	100	2
Total weight (kg)	667	417	357	50	1750

TABLE 12.8

Characteristic Data of a 42-V Ultracapacitor[7]

	Lead/Acid	**Ni/Cd**	**Ni/MH**	**Li–I**
Specific power (W/kg)	378.5	581.4	703	1222
Specific energy (Wh/kg)	26.5	40.7	49.2	85.5
Battery weight (kg)	116	69	54	35
Ultracap weight (kg)	16.5	16.7	16.9	6.05
Total weight (kg)	132	86	71	41

References

1. D. A. J. Rand, R. Woods, and R. M. Dell, *Batteries for Electric Vehicles*, Society of Automotive Engineers (SAE), Warrendale, PA, 1988.
2. Available at http://www.saftbatteries.com, SAFT, The Battery Company, 2007.
3. T. R. Crompton, *Battery Reference Book*, Society of Automotive Engineers (SAE), Warrendale, PA, 1996.
4. C. C. Chan and K. T. Chau, *Modern Electric Vehicle Technology*, Oxford University Press, Oxford, 2001.
5. Y. Gao and M. Ehsani, "Investigation of battery technologies for the army's hybrid vehicle application," *Proceedings of the IEEE 56th Vehicular Technology Conference*, pp. 1505–1509, Fall 2002.
6. Y. Gao, H. Moghbelli, M. Ehsani, G. Frazier, J. Kajs, and S. Bayne, "Investigation of high-energy and high-power hybrid energy storage systems for military vehicle application," *Society of Automotive Engineers (SAE) Journal*, Paper No. 2003-01-2287, Warrendale, PA, 2003.
7. Available at http://www.maxwell.com, Maxwell Technologies, 2007.
8. Y. Gao and M. Ehsnai, "Parametric design of the traction motor and energy storage for series hybrid off-road and military vehicles," *Power Electronics, IEEE Transactions*, 21 (3), 749–755, May 2006.

13

Fundamentals of Regenerative Breaking

One of the most important features of EVs, HEVs, and fuel cell vehicles (FCVs) is their ability to recover significant amounts of braking energy. The electric motors in EVs, HEVs, and FCVs can be controlled to operate as generators to convert the kinetic or potential energy of vehicle mass into electric energy that can be stored in the energy storage and then reused.

The braking performance of a vehicle is an important factor in vehicle safety. A successfully designed braking system for a vehicle must always meet the distinct demand of quickly reducing vehicle speed and maintaining vehicle direction controllable by the steering wheel. The former requires the braking system to be able to supply sufficient braking torque on all wheels. The latter requires proper braking force distribution on all wheels, as discussed in Chapter 2.
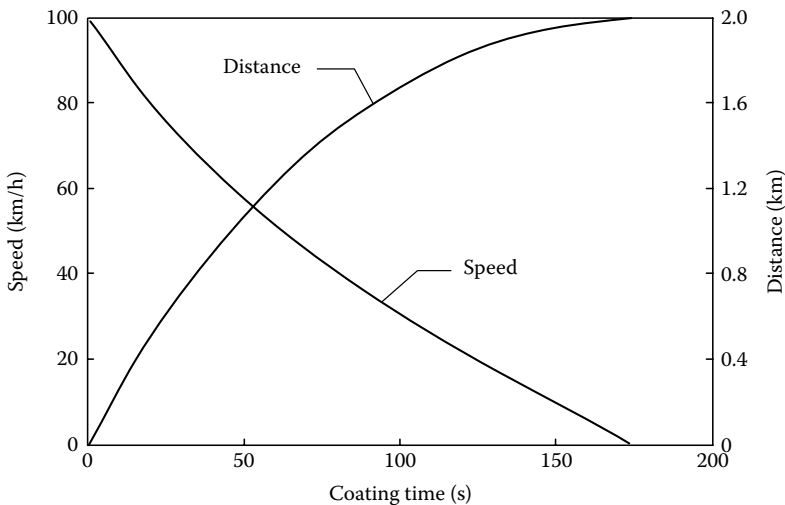
Generally, the braking torque required is much larger than the torque that an electric motor can produce, especially in heavy braking. In EVs, HEVs, and FCVs, mechanical friction braking systems have to coexist with electrical regenerative braking. Therefore, this is a hybrid braking system. As in the hybrid propulsion system, there are many configurations and control strategies. However, the final goal of the design and control of such systems is to ensure the vehicle's braking performance and its ability to recover as much braking energy as possible.

13.1 Braking Energy Consumed in Urban Driving

A significant amount of energy is dissipated by braking.[1–3] Braking a 1500-kg vehicle from 100 km/h to zero speed dissipates about 0.16 kWh of energy $[(1/2)MV^2]$ in a few tens of meters. If this amount of energy is dissipated by coasting and only by drag forces (rolling resistance and aerodynamic drag) without braking, the vehicle will travel about 2 km, as shown in Figure 13.1.

When a vehicle is driving in a stop-and-go pattern in urban areas, a significant amount of energy is dissipated by frequent braking. Successful design of the hybrid braking system for recovering as much of the braking energy as possible requires a full understanding of braking behavior and its

FIGURE 13.1 Coasting speed and distance.

characteristics with respect to vehicle speed, braking power, deceleration rate, and so on during typical urban driving cycles.[2,3,4] The typical urban driving cycles that are used in this chapter are EPA FTP75, LA92, US06, New York City, and ECE-15.
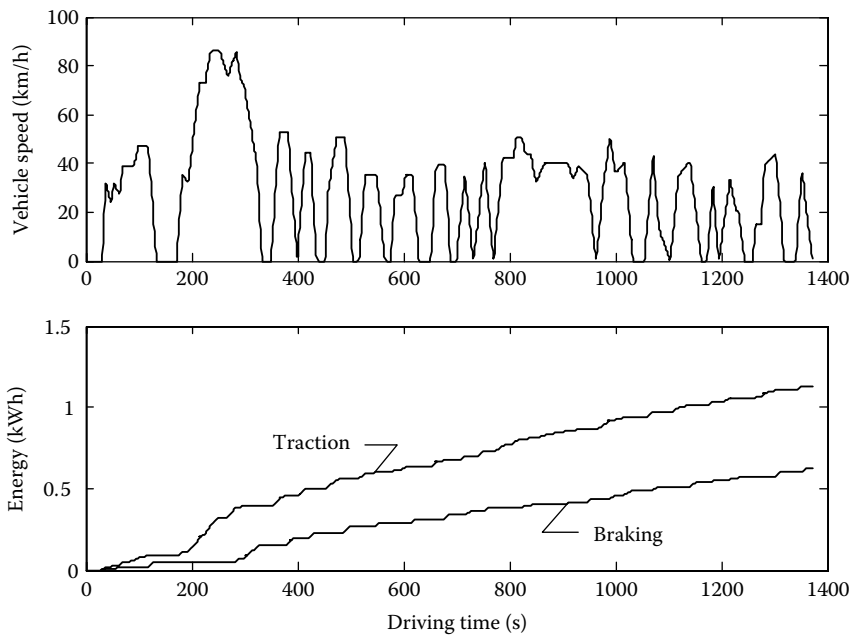
While driving on a flat road, the driving power on the vehicle wheels can be calculated by

$$P_d = \frac{V}{1000} \left(Mgf_r + \frac{1}{2}\rho_a C_D A V^2 + M\delta \frac{dV}{dt} \right) (\text{kW}), \qquad (13.1)$$

where M is the vehicle mass in kg, g is the gravitational acceleration, 9.81 m/s^2, f_r is the tire rolling resistance coefficient, ρ_a is the air mass density, 1.205 kg/m^3, C_D is the aerodynamic drag coefficient, A is the frontal area of the vehicle in m^2, V is the vehicle speed in m/s, δ is the rotational inertia factor, and dV/dt is the vehicle acceleration in m/s^2 (and is negative for deceleration). For $P_d > 0$, the traction wheels accept power from the power plants and push the vehicle forward. In this case, the braking power is zero. In contrast, $P_d < 0$ when braking and the kinetic energy of the vehicle mass is dissipated by the brake system. In this case, the driving power is zero.

Integrating Equation 13.1 over the driving time in a given driving cycle can give both the traction energy and braking energy, as shown in Figure 13.2, for a typical passenger car with the parameters listed in Table 13.1 in the FTP75 urban driving cycle. The vehicle parameters used in this chapter are shown in Figure 13.3 and Table 13.1.

Figure 13.2 and Table 13.2 indicate that the braking energy in typical urban areas may reach up to more than 34% of the total traction energy. In large cities, such as New York City, it may reach up to 80%.

FIGURE 13.2 Traction and braking energy dissipation in an FTP75 urban driving cycle.
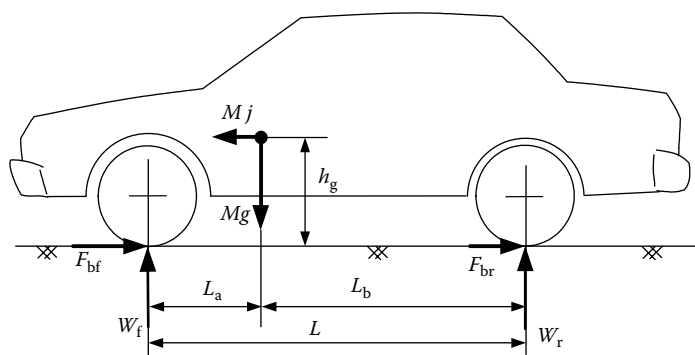
13.2 Braking Energy versus Vehicle Speed

Braking energy distribution over vehicle speed in typical urban driving cycles is useful information for the design and control of the regenerative brake system. In the speed range in which the braking energy is most dissipated, the operating efficiency of the electric motor, functioning as a generator, may be of most concern. In other speed ranges, regenerative braking may be abandoned

TABLE 13.1

Vehicle Parameters Used in this Paper

Item	Symbol	Unit	Value
Vehicle mass	M	kg	1500 (fully, loaded), 1250 (unloaded)
Rolling resist. coefficient	f_r		0.01
Aerodynamic drag coefficient	C_D		0.3
Front area	A	m^2	2.2
Wheel base	L	m	2.7
Distance from gravity center to front wheel center	L_a	m	1.134 (fully loaded), 0.95 (unloaded)
Gravity center height	h_g	m	0.6 (fully loaded), 0.5 (unloaded)

FIGURE 13.3   Forces acting on a vehicle in braking.
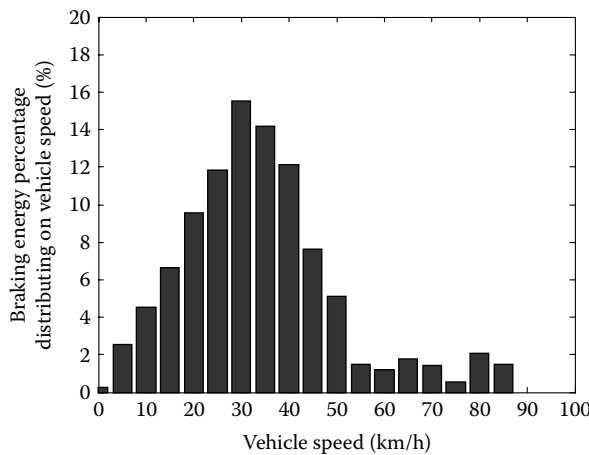
with no significant compromise on energy recovered. Figure 13.4 shows such a diagram of braking energy distribution over vehicle speed while driving in the FTP75 urban driving cycle for a vehicle whose parameters are listed in Table 13.1. Figure 13.5 further shows the braking energy dissipated in a speed range that is less than a given speed. These two figures indicate that only 10% of the total braking energy is dissipated in the speed range below 15 km/h. Table 13.3 shows the braking energy dissipated in the speed range below 15 km/h while driving in other typical urban driving cycles.

The braking energy dissipated in the low-speed range, such as below 15 km/h in all the typical driving cycles, is insignificant. This result indicates that we need not attempt to obtain high operating efficiency at low speeds in

TABLE 13.2

Maximum Speed, Average Speed, Total Traction Energy, and Energies Dissipated by the Drag and Braking per 100 km Traveling Distance in Different Drive Cycles
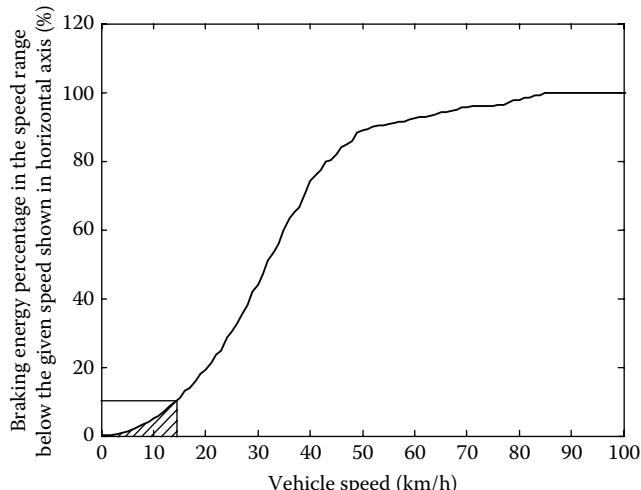
	FTP75 Urban	LA92	US06	New York	ECE15
Max. speed (km/h)	86.4	107.2	128.5	44.6	120
Ave. speed (km/h)	27.9	39.4	77.4	12.2	49.8
Traveling distance per cycle (km)	10.63	15.7	12.8	1.90	7.95
Traction energy (kWh)					
Per cycle	1.1288	2.3559	2.2655	0.2960	0.9691
Per km	1.1062	0.15	0.1769	0.1555	0.1219
Braking energy (kWh)					
Per cycle	0.6254	1.3666	0.9229	0.2425	0.3303
Per km	0.0589	0.0870	0.0721	0.1274	0.0416
Percentage of braking energy to traction energy	55.4	58.01	40.73	81.9	34.08

FIGURE 13.4 Braking energy distribution over vehicle speed in an FTP75 urban driving cycle.

the design and control of regenerative braking. In fact, it is difficult to regenerate at low speeds, because of the low motor electromotive force (voltage) generated at low motor rotational speeds.

It should be noted that the rotational speed of the vehicle driven wheels, which is proportional to motor angular speed, is decoupled from the translatory speed of the vehicle body when the vehicle wheels are close to being locked. Thus, the operation of the hybrid brake system must be at speeds

FIGURE 13.5 Braking energy dissipated over the speed range below the given speed.

TABLE 13.3

Braking Energy Dissipated in the Speed Range Below 15 km/h in Typical
Urban Driving Cycles

	FTP75 Urban	LA92	US06	New York	ECE-15
Braking energy $\mid_{V<15\,km/h}$ (%)	10.93	5.51	3.27	21.32	4.25

higher than a minimum threshold value. Electric regenerative braking should
be applied primarily to recapture as much braking energy as possible. At
speeds lower than this threshold, mechanical braking should be primarily
applied to ensure the vehicle's braking performance.

13.3   Braking Energy versus Braking Power

Another important factor is braking energy versus braking power. Under-
standing braking energy versus braking power in a typical driving cycle
is very helpful for power capacity design of the electric motor drive and
on-board energy storage, so that they are capable of recovering most of the
braking energy without oversize design.

Figure 13.6 shows the braking simulation results for the vehicle whose
parameters are listed in Table 13.1 while driving in an FTP75 urban driving
cycle. This figure indicates that around 15% of the total braking energy is dis-
sipated in the braking power range greater than 14.4 kW. This result implies
that a 15-kW electric motor can recover about 85% of the total braking energy
in this driving cycle. Table 13.4 shows the simulation results for other urban
driving cycles, which also indicates the braking power range in which 85% of
the total braking energy is dissipated. These data are good indicators of the
design of the power capacity of the electric motor and the on-board energy
storage from the braking point of view.
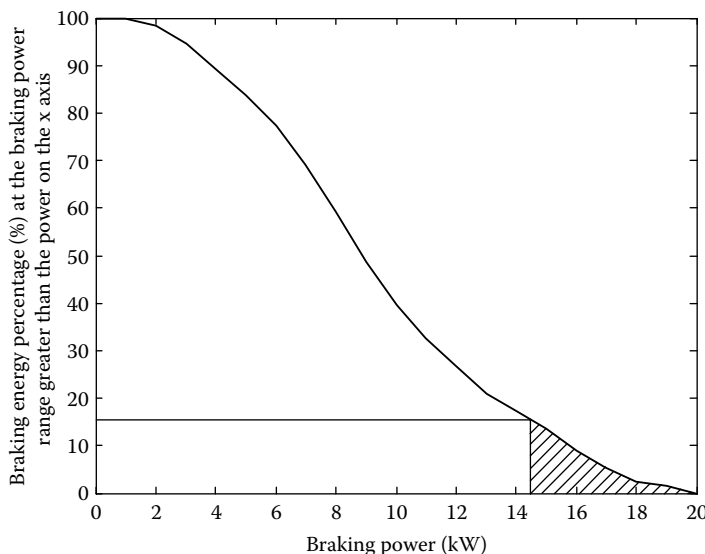
13.4   Braking Power versus Vehicle Speed

Another important consideration is the braking power characteristics ver-
sus vehicle speed in typical urban driving cycles. Understanding this is very

TABLE 13.4

The Braking Power Range in which 85% of Braking Energy is Dissipated
in Typical Urban Driving Cycles

	FTP75 Urban	LA92	US06	New York	ECE-15
Power range in which 85% of total energy is consumed	0–14.4	0–44.5	0–46.5	0–18.5	0–33.5
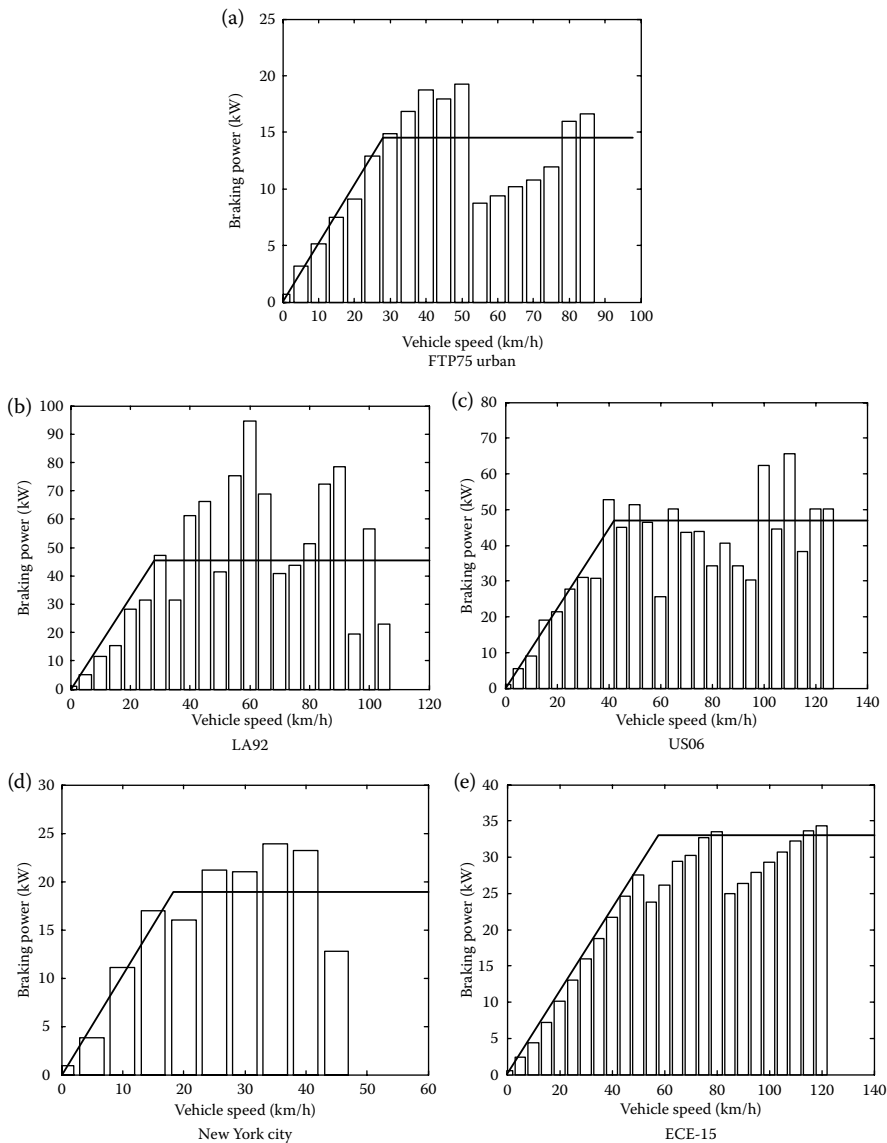
FIGURE 13.6 Braking energy percentage in the range that is greater than the power shown in the horizontal axis.

helpful for proper design and control of the speed–power profile of electric motors in order to optimally match the driving application. Figure 13.7 shows the simulation results for the vehicle mentioned above. The bars in Figure 13.7 represent the maximum braking power in particular driving cycles at specified vehicle speeds. The solid lines represent the supposed motor speed–power profiles that can recover at least 85% of the braking energy as indicated in Table 13.4.

It can be seen that the braking power versus vehicle speed profiles naturally match the power–speed characteristics of the motor, in that the power is proportional to the speed from zero speed to base speed (constant torque) and is constant beyond the base speed. Thus, electric motors do not need a special design and control for regenerative braking purposes.
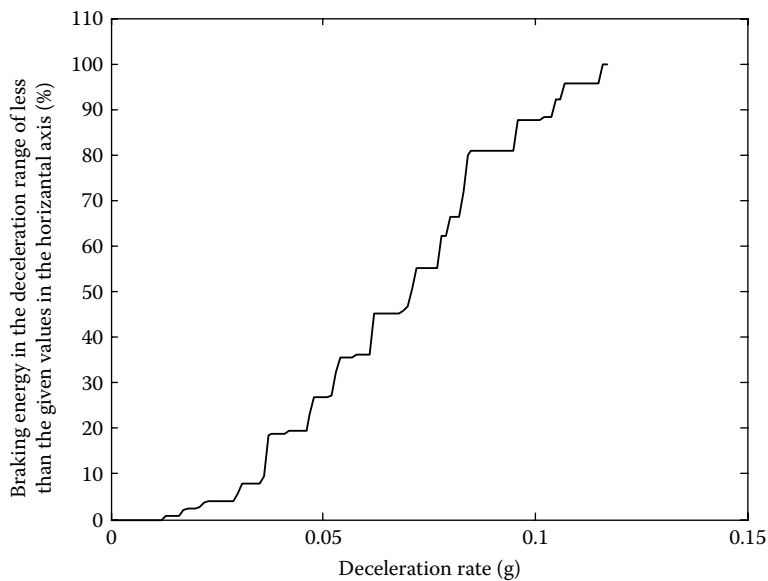
13.5 Braking Energy versus Vehicle Deceleration Rate

Another important consideration is the braking energy distribution over the vehicle deceleration rate, which reflects the required braking force. Understanding this feature will also help the design and control of the hybrid braking system of EVs, HEVs, and FCVs. Figure 13.8 shows the braking energy consumed in the vehicle deceleration range of less than a value shown in the horizontal axis for the vehicle mentioned above while driving

FIGURE 13.7   Braking power versus vehicle speed in typical urban driving cycles. (a) FTP75 urban, (b) LA92, (c) US06, (d) New York city, and (e) ECE-15.

in the FTP75 urban driving cycle. It can be seen in this figure that braking in this diving cycle is very gentle (the maximum deceleration rate is less than 0.15*g*). Table 13.5 shows the maximum deceleration rates and braking energy in a deceleration rate of less than 0.15*g* in other typical urban driving cycles.

FIGURE 13.8 Braking energy dissipated in various vehicle deceleration rates.

TABLE 13.5

Maximum Deceleration Rates and Braking Energy Dissipated
in the Deceleration Range of Less Than 0.15g

	FTP75 Urban	LA92	US06	New York	ECE-15
Maximum deceleration rate, g	0.12	0.40	0.31	0.27	0.14
% of braking energy consumed in the deceleration range of less than 0.15 g	100	56	59	69	100

13.6 Braking Energy on Front and Rear Axles

The braking performance for passenger cars requires the braking force distribution on the front and rear axles to be below the I curve, but above the braking regulation curve as shown in Figures 2.40 and 2.41 in Chapter 2. This requirement implies that most of the braking force is applied on the front axle. Consequently, regenerative braking on the front axle is better than that on the rear axle. However, for other kinds of vehicles, such as trucks, the rear axle may be better.

13.7   Brake System of EV, HEV, and FCV

Regenerative braking in EVs, HEVs, and FCVs introduces slight complexity to the braking system design. Two basic questions arise: how to distribute the total required braking forces among regenerative braking and frictional braking to recover as much braking energy as possible and how to distribute the total braking forces on the front and rear axles to achieve stable braking performance. Usually, regenerative braking is effective only for the driven axle (the front axle for passenger cars). The electric motor must be controlled to produce the proper amount of braking force for recovering braking energy as much as possible and, at the same time, the total braking force must be sufficient to meet vehicle deceleration commanded by the driver. This chapter introduces two configurations of hybrid braking systems and their corresponding design and control principles. One is the parallel hybrid brake system, which has a simple structure and control and retains all the major components of the conventional brakes. The other is a fully controllable hybrid brake system, which can fully control the braking force for each individual wheel, thus greatly enhancing the vehicle's braking performance on all types of roads.
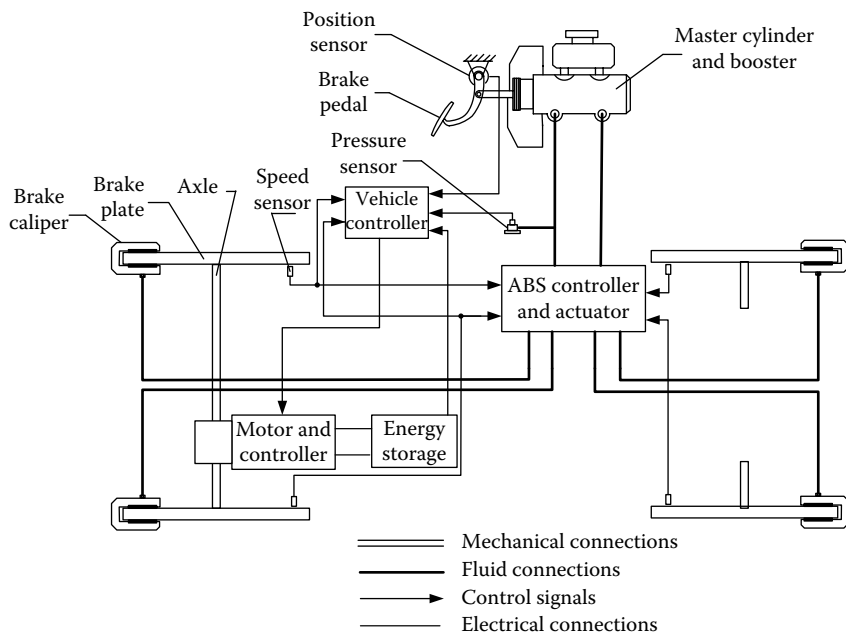
The analysis in the following sections is based on the braking performance described in Section 2.9 of Chapter 2.

13.7.1   Parallel Hybrid Braking System
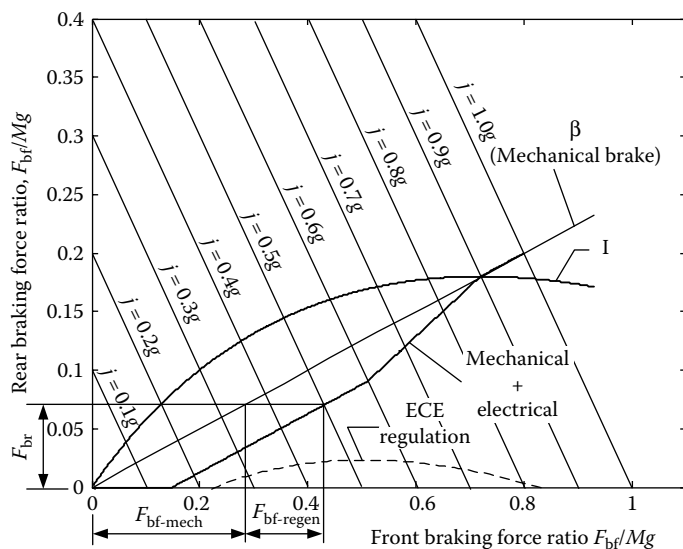
Perhaps the simplest and closest to conventional pure mechanical brakes (hydraulic or pneumatic) is the parallel hybrid brake system,[1,3] which retains all the major components of conventional mechanical brakes and adds electric braking directly on the front axle as shown in Figure 13.9. The mechanical brake system consists of a master cylinder and booster. It may or may not have an ABS controller and actuator, but will have a brake caliper and brake disks. The electric motor directly applies its braking torque to the front axle and is controlled by the vehicle controller, based on vehicle speed and brake pedal position signals, which represent the desired braking strength and braking control strategy embedded in the vehicle controller. The feature of the parallel hybrid braking system is that only the electric braking force (torque) is electronically controlled, and the mechanical braking force (torque) is controlled by the driver through the brake pedal before the ABS starts its function. However, the mechanical braking force is controlled by the ABS when the wheels are about to be locked, as in the conventional brake systems. The key problem in the design and control of such a system is to properly control the electric braking force for recovering as much braking energy as possible.

13.7.1.1   *Design and Control Principles with Fixed Ratios between Electric and Mechanical Braking Forces*

Figure 13.10 shows a braking force allocation strategy, in which the mechanical brake has a fixed ratio of braking force distribution on the front and

FIGURE 13.9 Schematic structure of the parallel hybrid brake system.

FIGURE 13.10 Braking forces varying with deceleration rate.

rear wheels represented by the β line. Curve I is the ideal braking force distribution of the vehicle. The ECE regulation, which stipulates the minimum rear braking force, is also plotted. The total braking force is the curve labeled mechanical + electrical. The braking force on the front wheels consists of mechanical braking, $F_{bf-mech}$, and electric braking, $F_{bf-regen}$, as shown in Figure 13.10. When the wheel speed is lower than a given threshold, 15 km/h for example, either very low vehicle speed or speed close to wheel lock-up, the electric regenerative braking will produce no braking force and the braking is completely done by the mechanical system.
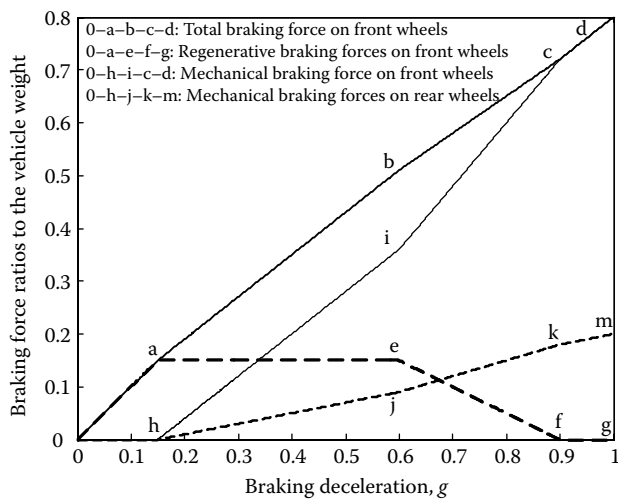
When the wheel speed is higher than the given threshold and the desired vehicle deceleration is less than a given value (0.15g in Figure 13.10), which is represented by the stroke of the brake pedal, all the braking force is produced by electric regenerative braking and no mechanical braking force is applied to the front and rear wheels. As described in Section 11.7, most of the braking energy is in this deceleration range. Zero mechanical force may be implemented by employing larger clearances between the brake pads and plates or by carrying out small modifications to the conventional master cylinders. When the desired deceleration is greater than the given value (0.15g in Figure 13.10), both mechanical and electric braking share the total front wheel braking force as shown in Figure 13.10. The design of the electric braking portion is associated with the power capacity of the electric motor and onboard energy storage. But the total braking force curve in Figure 13.10 must be above the ECE regulation curve. When the desired deceleration is higher than a given value (0.6g in Figure 13.10), the electric regenerative braking force is gradually reduced to zero with increase of the desired deceleration (0.9g in Figure 13.10). This design will ensure that the actual front and rear wheel braking forces are close to the ideal braking distribution curve, resulting in short braking distances, and strong mechanical braking that may be more relied upon for emergency cases. Figure 13.11 shows the total braking force, regenerative braking force, and mechanical braking forces on the front and rear wheels, respectively, along with vehicle deceleration rate.

With the design principle described above and the electric regenerative braking control rule with respect to wheel speed, the braking energy available for recovering can be computed in various typical driving cycles by using a computer model. The simulation results are listed in Table 13.6. The data indicate that in normal urban driving, most of the braking energy can be recovered.

It should be noted that the maximum braking torque required of the electric motor is that which can produce 0.15g of deceleration. Thus, a large-sized electric motor would not be needed.

13.7.1.2   Design and Control Principles for Maximum Regenerative Braking

This design and control principle will follow the rule that allocates the total braking force to the front wheels as much as possible, under the condition of

FIGURE 13.11 Braking force ratios relative to the vehicle weight varying with deceleration rate.
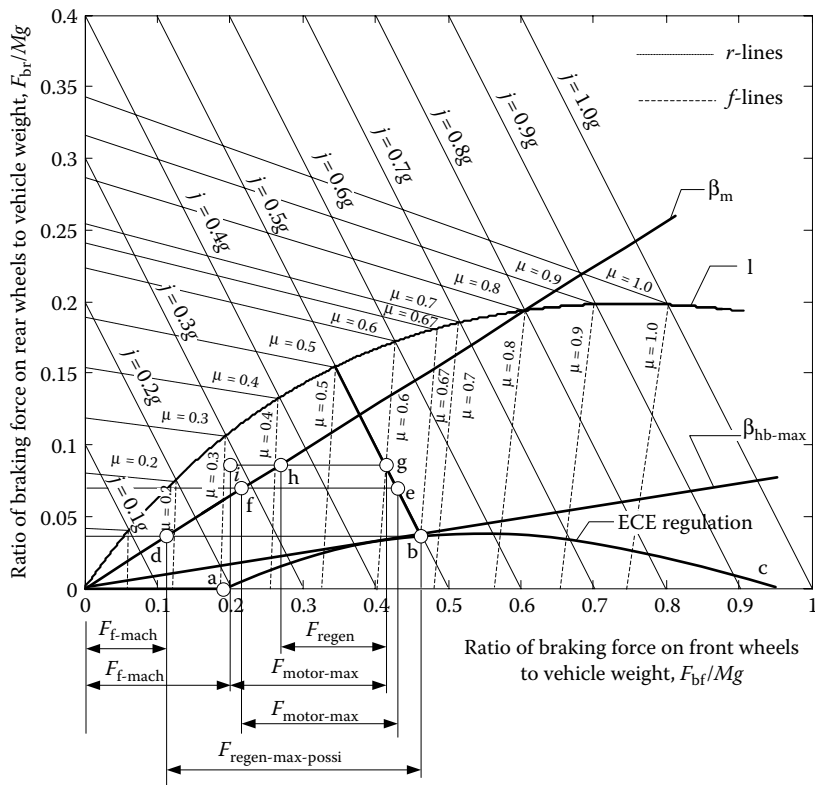
meeting the braking regulations (the ECE regulation used here), that is, the total braking force distribution will follow the maximum front braking force curve (minimum rear braking force) stipulated by the ECE regulation, which is represented by curve 0–a–b–c as shown in Figure 13.12. More details are described below.

When the braking strength is less than 0.2g, all the braking force is allocated to the front wheels for regenerative braking and no mechanical braking force is applied to the front or rear wheels. Motor torque may be controlled through sensing the braking pedal position. In this case, the master cylinder will not establish hydraulic pressure. When the braking strength is greater than 0.2g, the mechanical system starts creating pressure and the mechanical braking forces on the front and rear wheels start increasing, following the β_m line. At the same time, the electric motor adds its electric braking torque on the front wheels to make the total braking force follow the ECE regulation line. For example, when the braking strength required is 0.5g, the total braking force is at point b and the mechanical braking force on the front and rear wheels is at point d. The maximum possible braking force for regenerative braking is the segment of d–b, labeled $F_{regen\text{-}max\text{-}possi.}$. However, for fully recovering all

TABLE 13.6

Percentage of Total Braking Energy Available for Recovering

FTP75 Urban	LA92	US06	New York	ECE-15
89.69	82.92	86.55	76.16	95.75

FIGURE 13.12 Schematic illustration of braking force distribution on the front wheels (electrical + mechanical) and the rear wheels.

this maximum possible braking power, two conditions have to be satisfied. One condition is that the electric motor should be capable of producing this braking force. Assuming that the maximum electric motor braking force is limited to that shown in Figure 13.12 by segment f–e, with a braking strength of $0.5g$, the operating point of the total braking force should be at point e and the mechanical braking force at point f. Assuming that the electric motor is powerful enough, another condition will have to be met to recover the maximum possible braking power limited by the ECE regulation. This condition is that the road adhesive coefficients must be larger than 0.67. Otherwise, the front wheels will be locked. Figure 13.12 shows a case of braking strength $j = 0.5\,g$ and $\mu = 0.6$ and an operating point of total braking force at point g. In this case, the operation will be different for brake systems with and without a mechanical ABS. For the system without ABS, to meet the braking force requirement on the rear wheels, the mechanical brake has to operate at point h. Thus the regenerative braking force takes the segment h–g, which is smaller than the maximum braking force that the electric motor can produce.

However, for the brake system with a mechanical ABS, when the front wheels are close to being locked, the ABS will start its function and the mechanical braking force on the front wheels will be decoupled from the β line, instead following the f line of μ = 0.6; this limits further increase in the mechanical braking force on the front wheels. In this case, the electric motor can still produce its maximum braking force for maximum braking energy recovery as shown in Figure 13.12 by the segment i–g and the operating point of the mechanical braking is at point i.

The above design and control principle for maximum regenerative braking is based on the idea that the maximum possible braking force on the front wheels is limited by the ECE regulation. However, it can be seen from Figure 13.12 that the ECE regulation produces a nonlinear braking force distribution curve. This nonlinearity may lead to a complex design and control. A simple straight line can be used to replace the ECE regulation in the design and control of the hybrid brake system as shown in Figure 13.12 by the line $\beta_{hb\text{-}max}$. The line $\beta_{hb\text{-}max}$ is generated as follows.

The minimum braking force on the rear wheels (maximum braking force on the front wheels) when the front wheels are locked, stipulated by the ECE regulation, is expressed as

$$\frac{F_{bf}}{W_f} \leq \frac{q + 0.07}{0.85}, \tag{13.2}$$

where F_{bf} is the total braking force on the front wheels, W_f is the vertical loading on the front wheels, and q is the braking strength, $q = j/g$ (refer to Figure 13.3). As in the definition of the β line in Section 2.9, the front wheel braking force can be expressed as

$$F_{bf} = \beta_{hb} F_b, \tag{13.3}$$

where F_b is the total braking force of the vehicle, which is related to the braking strength, q, as

$$F_b = Mj = Mgq. \tag{13.4}$$

The braking strength, q, and the vertical loading on the front wheels, W_f, have the relationship

$$W_f = \frac{Mg}{L}\left(L_b + qh_g\right), \tag{13.5}$$

where M is the mass of the vehicle, L is the wheel base, and L_b is the length from the vehicle center of gravity to the rear axle as shown in Figure 13.3.

Combining Equations 13.3 through 13.5, we obtain

$$\frac{F_{bf}}{W_f} = \frac{\beta_{bh}qL}{L_b + qh_g}. \tag{13.6}$$

From Equations 13.2 and 13.6, we obtain

$$\beta_{bh} \leq \frac{(q + 0.07)(L_b + qh_g)}{0.85qL}. \tag{13.7}$$

It can be seen from Equation 13.7 that the upper limit of β_{hb} to meet the ECE regulation is a function of braking strength q. The q, at which the maximum β_{hb} is achieved, can be obtained by

$$\frac{d\beta_{bh}}{dq}\bigg|_{q=q^0} = 0 \tag{13.8}$$

with $q^0 = \sqrt{0.07L_b/h_g}$; then we obtain
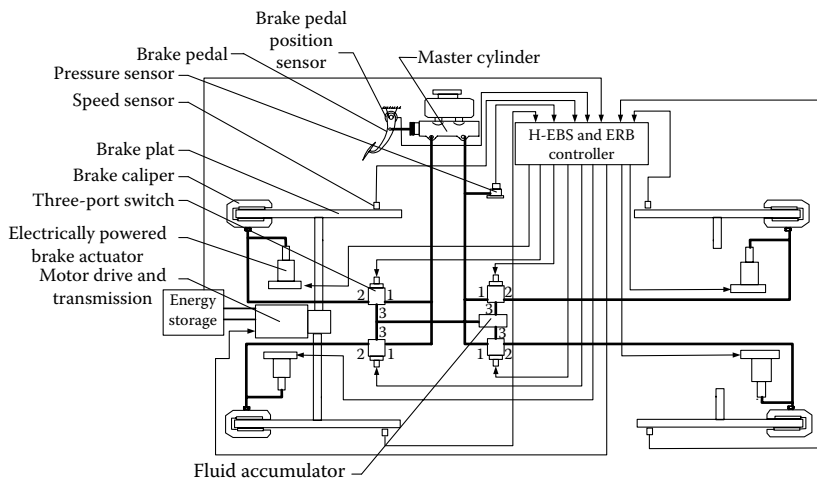
$$\beta_{bh\text{-}max} = \frac{2\sqrt{0.07L_bh_g} + L_b + 0.07h_g}{0.85L}. \tag{13.9}$$

Equation 13.9 indicates that this braking force distribution ratio is only determined by the vehicle parameters. With $\beta_{bh\text{-}max}$, the braking force distribution on the front and rear wheels can be plotted as shown in Figure 13.12. This line can be used to replace the ECE regulation curve and the design and control of the braking system may be simplified. The analysis for the braking process is similar to the above and is left to the reader.

13.7.2   Fully Controllable Hybrid Brake System

In recent years, more advanced braking systems are emerging that allow controlling the braking force on each wheel independently.[1,2,5] Hydraulic electric brake systems (H-EBSs) and mechanical electric brake systems are two typical examples. Figure 13.13 schematically shows a fully controllable hybrid brake system, which consists of a hydraulic electric brake and an electric regenerative brake.

   The mechanical brake system consists mainly of a brake pedal and its position sensor, a master cylinder, an electrically operated and controlled brake actuator, electrically controlled three-port switches, a fluid accumulator, and a pressure sensor. In normal operation, ports 1 and 3 of the three-port switches are open and port 2 is closed. The mechanical braking torque applied on each wheel is independently produced by the corresponding brake actuator, which is commanded by the H-EBS controller. The torque command to each wheel is generated in the H-EBSs, based on the pressure signal from the pressure sensor, the brake pedal stroke signal from the brake pedal position sensor, wheel speed signal from the wheel speed sensor, and the embedded control rule in the H-EBS controller. The brake fluid from the master cylinder flows into the fluid accumulator through the three-port switches to establish pressure and

FIGURE 13.13 Fully controllable hybrid brake system with H-EBS and electric regenerative braking.

emulate the braking feeling of a conventional brake system. In the case of failure in any brake actuator, the corresponding three-port switch will switch to the mode of ports 1 and 2 open and port 3 closed for the brake fluid from the master cylinder to directly go to the brake caliper cylinder and therefore to maintain the braking torque.
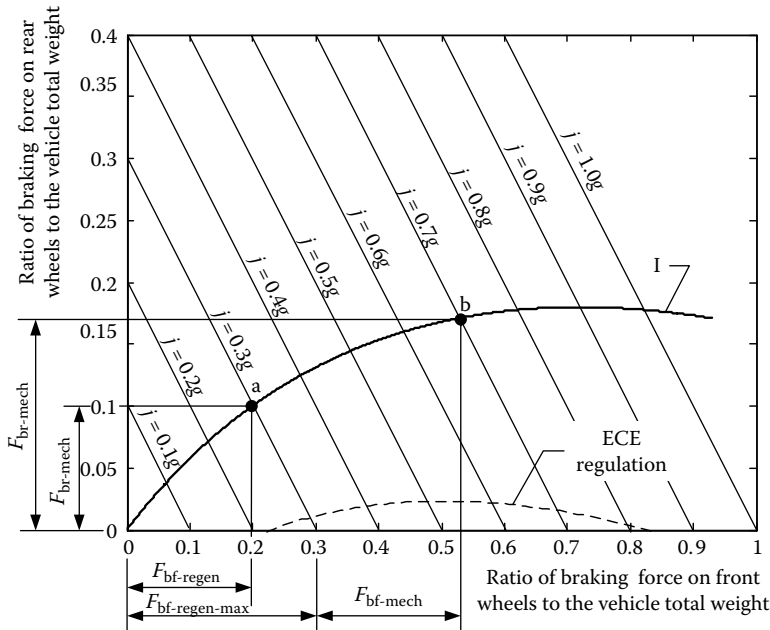
The electric regenerative brake mainly includes an electric motor and its controller (drive) and an on-board energy storage. An ERB controller is used to control electric braking, based on wheel speed, brake pedal stroke, charge condition in the energy storage, and control rules embedded in the controller.

One of the key problems in this system is how to control the mechanical and electric braking torques to obtain acceptable braking performance and to recover, as much as possible, the available regenerative braking energy. In this chapter, two typical control strategies are introduced; one emphasizes the braking performance and the other the maximum regenerative braking energy recovery.

13.7.2.1 Control Strategy for Optimal Braking Performance

Due to the independent control of braking force on each wheel, the fully controllable hybrid brake system can be controlled to apply braking forces on the front and rear wheels in the way of following the ideal braking force distribution curve. This control strategy can yield optimal brake performance.

Figure 13.14 illustrates the principle of this control strategy for a vehicle, on which electric regenerative braking is available only on the front wheels. When the required total braking force on the front wheels is smaller than that produced by the electric motor, the electric motor produces the total braking

FIGURE 13.14   Control strategy for the best braking performance.

force and no mechanical braking force is applied. However, the mechanical braking produces the total braking force for the rear wheels to follow the I curve, as shown by point a in Figure 13.14. When the required total braking force on the front wheels is greater than that produced by the electric motor, both electric braking and mechanical braking have to be applied. For more braking energy recapture, the electric motor should be controlled to produce its maximum braking force that is limited by the electric motor or energy storage. The remaining is applied by the mechanical brake as shown by point b in Figure 13.14.

It should be noted that at low front wheel speeds caused by actual low vehicle speed or close to locked wheels, it is hard to produce braking torque by the electric motor due to its low electromotive force (voltage) generated in the stator windings of the electric motor. Therefore, in this case, the mechanical brake has to produce the total braking force as required.

As seen in Figure 13.14, a significant amount of braking energy is dissipated by the rear brakes, especially in weak braking (small deceleration). For example, at $j = 0.3\,g$, around 33% of the total braking energy is dissipated in the rear brakes. At $j = 0.1\,g$, this percentage reaches 37.8%. Unfortunately, this is just the case for most of the urban driving cycles. Considering no regenerative braking at low wheel speeds ($<15\,km/h$), the braking energy available for recovery on the front wheels is considerably reduced. The simulation results, shown in Table 13.7, prove this conclusion.

TABLE 13.7

Scenarios of Braking Energy in Typical Urban Driving Cycles
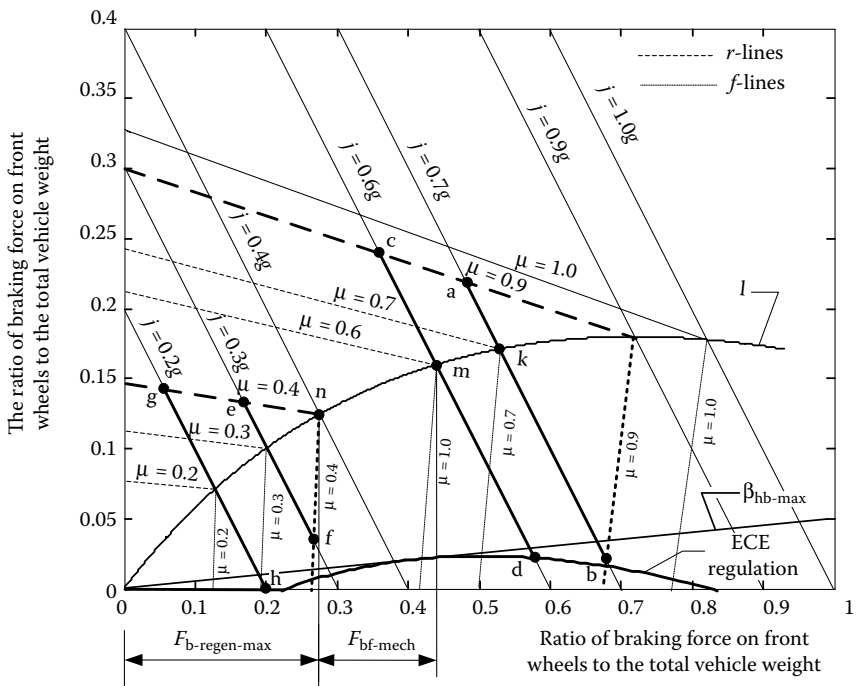
	FTP75 Urban	LA92	US06	New York	ECE-15
Percentage of braking energy on front wheels to total braking energy	61.52	63.16	62.98	62.57	61.92
Percentage of braking energy on rear wheels to total braking energy	38.48	36.84	37.02	37.43	38.08
Percentage of available regenerative braking energy on front wheels to total braking energy	55.16	59.85	60.89	50.26	59.27

13.7.2.2 Control Strategy for Optimal Energy Recovery

The principle of this control strategy aims to allocate more braking force to the front wheels under the condition of the front wheels never locking earlier than the rear wheels on a road with any adhesive coefficient. Thus, more braking energy will be available for regenerative braking.

The details of this control strategy are explained below with the help of Figure 13.15.

When the vehicle brakes with an acceleration rate j on a road with an adhesive coefficient μ, and $j/g < \mu$, the braking forces on the front and rear wheels can be arbitrarily applied as long as the total braking force meets the requirements, that is, $F_{bf} + F_{br} = Mj$. However, braking performance requires that no wheel be locked and that the braking force on the rear wheels be above the ECE regulation curve as shown in Figure 13.15. Thus, the braking forces on the front and rear wheels are variable in a certain range, which is dependent on vehicle deceleration rate and road adhesive coefficient. Figure 13.15 shows the braking force ranges of a–b and c–d for the deceleration rates of $j/g = 0.7$ and $j/g = 0.6$ (strong braking), respectively, on a road with adhesive coefficient $\mu = 0.9$ (concrete road). Obviously, for $j/g = 0.7$, the maximum braking force on the front wheels is determined by point b, which is dictated by the f line (front wheel locked) of $\mu = 0.9$. However, for $j/g = 0.6$, the maximum braking force on the front wheels is determined by point d, which is dictated by the ECE regulation. Actually, on this high adhesive road, when $j/g < 0.7$, the braking force on the rear wheels can be very small and almost all the braking force can be applied to the front wheels. However, when the road adhesive coefficient is smaller (slippery road), the braking force variable range is much smaller. Figure 13.15 shows a case with $\mu = 0.4$ (wet mud road), and $j/g = 0.3$ and $j/g = 0.2$. Obviously point f determines the maximum braking force on the front wheels for $j/g = 0.3$ and point h for $j/g = 0.2$.

FIGURE 13.15   Depicted control strategy for optimal energy recovery.

The above analysis provides only a control principle for the hybrid brake system to obtain maximum braking energy on the front wheels to make more braking energy recoverable. However, the power capacities of the electric motor and energy storage are usually not big enough to handle the huge braking power when the braking is very strong. In this case, it is supposed that the electric motor provides its maximum braking torque and the mechanical brake provides the remaining. Figure 13.15 shows an electric motor that produces its maximum braking force on the front wheels to brake the vehicle at point n ($j/g = 0.4$). It is obvious that when the vehicle deceleration is less, $j/g = 0.4$, the electric motor itself can handle it and no mechanical braking is needed. However, when the braking deceleration is bigger, $j/g = 0.6$ for example, the required braking force for the front wheels is bigger than the electric motor can handle. In this case, the mechanical brake has to apply additional braking force to make the operation at any point in the range m–d. It is obvious that the best operation point is m.

With a simplified straight line $\beta_{hb\text{-}max}$ replacing the ECE regulation, very similar analysis can be done for this control strategy. This work is left to the reader.

References

1. S. R. Cikanek and K. E. Bailey, *Energy Recovery Comparison Between Series and Parallel Braking System for Electric Vehicles Using Various Drive Cycles*, Advanced Automotive Technologies, American Society of Mechanical Engineers (ASME), New York, DSC vol. 56/DE Vol. 86, pp. 17–31, 1995.
2. Y. Gao, L. Chu, and M. Ehsani, "Design and control principle of hybrid braking system for EV, HEV and FCV," *2007 IEEE VPPC*.
3. Y. Gao, L. Chen, and M. Ehsani, "Investigation of the effectiveness of regenerative braking for EV and HEV," *Society of Automotive Engineers (SAE) Journal*, SP-1466, Paper No. 1999-01-2901, 1999.
4. H. Gao, Y. Gao, and M. Ehsani, "Design issues of the switched reluctance motor drive for propulsion and regenerative braking in EV and HEV," in *Proceedings of the SAE 2001 Future Transportation Technology Conference*, Costa Mesa, CA, Paper No. 2001-01-2526, August 2001.
5. Y. Gao and M. Ehsani, "Electronic braking system of EV and HEV—integration of regenerative braking, automatic braking force control and ABS," in *Proceedings of the SAE 2001 Future Transportation Technology Conference*, Costa Mesa, CA, Paper No. 2001-01-2478, August 2001.

14

Fuel Cells

In recent decades, the application of fuel cells in vehicles has been the focus of increased attention. In contrast to a chemical battery, the fuel cell generates electric energy rather than storing it and continues to do so as long as a fuel supply is maintained. Compared with the battery-powered EVs, the fuel-cell-powered vehicle has the advantages of a longer driving range without a long battery charging time. Compared with the ICE vehicles, it has the advantages of high energy efficiency and much lower emissions due to the direct conversion of free energy in the fuel into electric energy, without undergoing combustion.
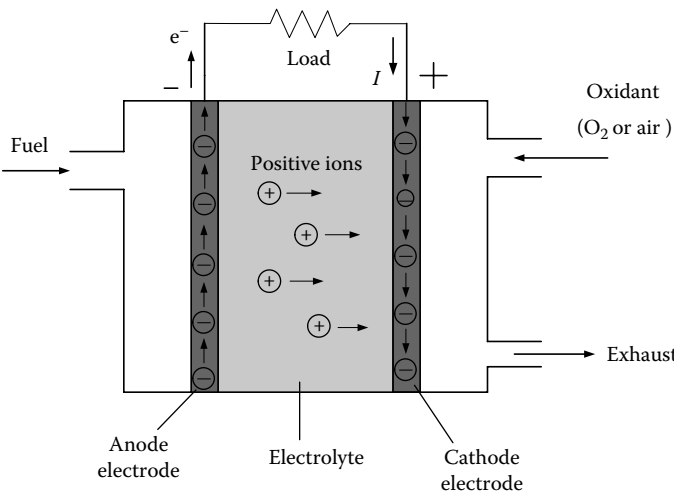
14.1 Operating Principles of Fuel Cells

A fuel cell is a galvanic cell in which the chemical energy of a fuel is converted directly into electrical energy by means of electrochemical processes. The fuel and oxidizing agent are continuously and separately supplied to the two electrodes of the cell, where they undergo a reaction. Electrolyte is necessary to conduct the ions from one electrode to the other as shown in Figure 14.1. Fuel is supplied to the anode or positive electrode, where electrons are released from the fuel under catalyst. The electrons, under the potential difference between these two electrodes, flow through the external circuit to the cathode electrode or negative electrode, where combining positive ions and oxygen, reaction products, or exhaust are produced.

The chemical reaction in a fuel cell is similar to that in a chemical battery. The thermodynamic voltage of a fuel cell is closely associated with the energy released and the number of electrons transferred in the reaction.[1,2] The energy released by the cell reaction is given by the change in Gibbs free energy, ΔG, usually expressed in per mole quantities. The change in Gibbs free energy in a chemical reaction can be expressed as

$$\Delta G = \sum_{\text{Products}} G_i - \sum_{\text{Reactants}} G_j, \qquad (14.1)$$

FIGURE 14.1   Basic operation of a fuel cell.

where G_i and G_j are the free energies in species i of products and species j of reactants. In a reversible process, ΔG is completely converted into electric energy, that is,

$$\Delta G = -nFV_r, \tag{14.2}$$

where n is the number of electrons transferred in the reaction, $F = 96,495$ is the Faraday constant in coulombs per mole, and V_r is the reversible voltage of the cell. At standard conditions (25°C temperature and 1 atm pressure), the open-circuit (reversible) voltage of a cell can be expressed as

$$V_r^0 = -\frac{\Delta G^0}{nF}, \tag{14.3}$$

where ΔG^0 is the change in Gibbs free energy at standard conditions. ΔG is expressed as

$$\Delta G = \Delta H - T\,\Delta S, \tag{14.4}$$

where ΔH and ΔS are the enthalpy and entropy changes, respectively, in the reaction at absolute temperature T. Table 14.1 shows the values of standard enthalpy, entropy, and Gibbs free energy of some typical substances.[3] Table 14.2 shows the thermodynamic data for some reactions in a fuel cell at 25° and 1 atm pressure.[3]

The "ideal" efficiency of a reversible galvanic cell is related to the enthalpy for the cell reaction by

$$\eta_{id} = \frac{\Delta G}{\Delta H} = 1 - \frac{\Delta S}{\Delta H}T. \tag{14.5}$$

TABLE 14.1

Standard Enthalpy of Formation and Gibbs Free Energy for Typical Fuels

Substance	Formula	ΔH^0_{298} (kJ/mol)	ΔS^0_{298} (kJ/mol K)	ΔG^0_{298} (kJ/mol)
Oxygen	O (g)	0	0	0
Hydrogen	H (g)	0	0	0
Carbon	C (s)	0	0	0
Water	H_2O (l)	−286.2	−0.1641	−237.3
Water	H_2O (g)	−242	−0.045	−228.7
Methane	CH_4 (g)	−74.9	−0.081	−50.8
Methanol	CH_3OH (l)	−238.7	−0.243	−166.3
Ethanol	C_2H_5OH (l)	−277.7	−0.345	−174.8
Carbon monoxide	CO (g)	−111.6	0.087	−137.4
Carbon dioxide	CO_2	−393.8	0.003	−394.6
Ammonia	NH_3 (g)	−46.05	−0.099	−16.7

η_{id} will be 100% if the electrochemical reaction involves no change in the number of gas moles, that is, when ΔS is zero. This is the case for reactions $C + O_2 = CO_2$. However, if the entropy change, ΔS, of a reaction is positive, then the cell—in which this reaction proceeds isothermally and reversibly—has at its disposal not only the chemical energy, ΔH, but also (in analogy to a heat pump) a quantity of heat, $T\Delta S$, absorbed from the surroundings for conversion into electrical energy (see Table 14.2) (Figure 14.2).

The change of free energy, and thus cell voltage, in a chemical reaction is a function of the activities of the solution species. The dependence of cell voltage on the reactant activities is expressed as
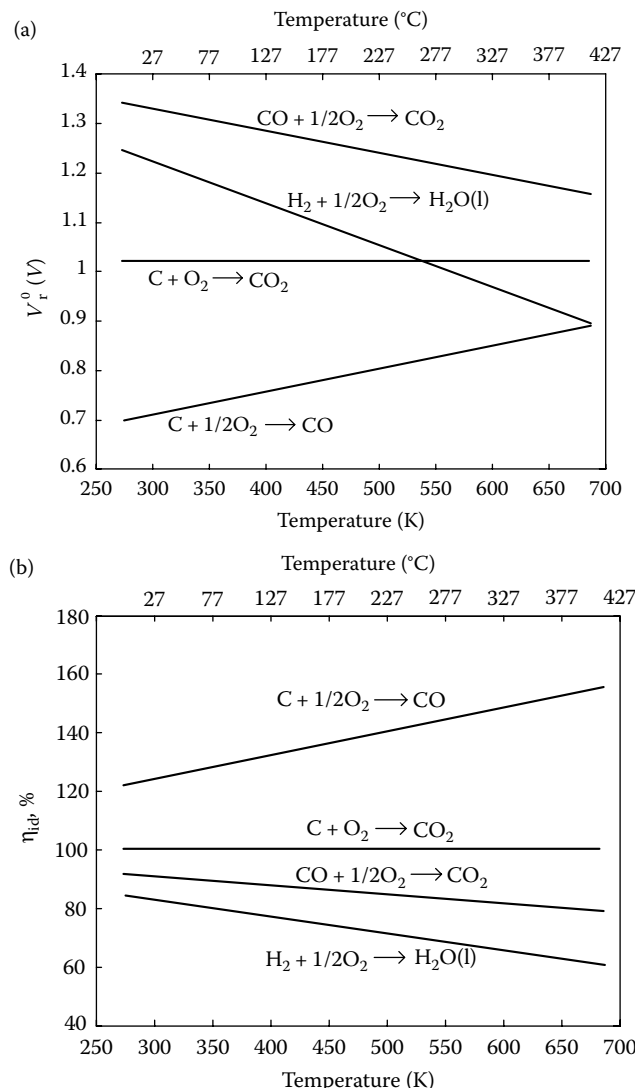
$$V_r = V_r^0 - \frac{RT}{nF} \ln \left[\frac{\prod(\text{activities of products})}{\prod(\text{activities of reactants})} \right], \quad (14.6)$$

where R is the universal gas constant, 8.31 J/mol K, and T is the absolute temperature in K. For gaseous reactants and products, Equation 14.6 can be

TABLE 14.2

Thermodynamic Data for Different Reactions at 25°C and 1°atm Pressure

	ΔH^0_{298} (kJ/mol)	ΔS^0_{298} (kJ/mol K)	ΔG^0_{298} (kJ/mol)	n	E (V)	η_{id} (%)
$H_2 + \frac{1}{2}O_2 \rightarrow H_2O$ (l)	−286.2	−0.1641	−237.3	2	1.23	83
$H_2 + \frac{1}{2}O_2 \rightarrow H_2O$ (g)	−242	−0.045	−228.7	2	1.19	94
$C + \frac{1}{2}O_2 \rightarrow CO$ (g)	−116.6	0.087	−137.4	2	0.71	124
$C + O_2 \rightarrow CO_2$ (g)	−393.8	0.003	−394.6	4	1.02	100
$CO + \frac{1}{2}O_2 \rightarrow CO_2$ (g)	−279.2	−0.087	−253.3	2	1.33	91

FIGURE 14.2 Temperature dependence of cell voltage (a) and reversible efficiency (b).

expressed as

$$V_r = V_r^0 - \frac{RT}{nF} \sum_i v_i \ln\left(\frac{p_i}{p_i^0}\right),$$ (14.7)

where V_r is the voltage of the cell in which the reaction proceeds with gaseous participants at nonstandard pressure p_i, V_r^0 is the corresponding cell voltage

with all gases at the standard pressure p_i^0 (normally 1 atm), and v_i is the number of moles of species i accounted as positive for products and negative for reactants.

14.2   Electrode Potential and Current–Voltage Curve

Experiments have shown that the rest voltage, V, is usually lower than the reversible voltage, V_r^0, calculated from the ΔG value. The voltage drop is called the rest voltage drop, ΔV_0. The reason may be the existence of a significant kinetic hindrance to the electrode process, or because the process does not take place in the manner assumed in the thermodynamic calculation of V_r^0. This rest voltage drop depends, in general, on the electrode materials and the kind of electrolyte.

When current is drawn from a cell, voltage drop is caused by the existence of ohmic resistance in the electrode and electrolyte, which increases in direct proportion to the current density, that is,

$$\Delta V_\Omega = R_e i, \tag{14.8}$$

where R_e is the equivalent ohmic resistance per area and i is the current density.

In a fuel cell, part of the generated energy is lost in pushing the species to react, because extra energy is required to overcome the activation barriers. These losses are called activation losses and are represented by an activation voltage drop, ΔV_a. This voltage drop is closely related to the materials of electrodes and the catalysts. The Tafel equation is most commonly used to describe this behavior, by which the voltage drop is expressed as[3]

$$\Delta V_a = \frac{RT}{\beta nF} \ln\left(\frac{i}{i_0}\right). \tag{14.9}$$

Or more conveniently, it is written as

$$\Delta V_a = a + b \ln(i), \tag{14.10}$$

where $a = -(RT/\beta nF)\ln(i_0)$ and $b = RT/\beta nF$; i_0 is the exchange current at equilibrium state and b is constant depending on the process. For a more detailed theoretical description, refer to pp. 230–236 of Messerle.[3]

When current flows, ions are discharged near the negative electrode, and as a result the concentration of ions in this region tends to decrease. If the current is to be maintained, ions must be transported to the electrode. This takes place naturally by diffusion of ions from the bulk electrolyte and by direct transport due to fields caused by concentration gradients. Bulk

movement of the electrolyte by convection or stirring also helps to bring the ions up.

The voltage drop caused by the lack of ions is called concentration voltage drop, since it is associated with a decrease in the concentration of the electrolyte in the immediate vicinity of the electrode. For small current densities, the concentration voltage drop is generally small. However, as the current density increases, it reaches a limit, when the maximum possible rate of transport of ions to the electrode is approached as the concentration at the electrode surface falls to zero.

The voltage drop caused by the concentration at the electrode where ions are removed (cathode electrode in fuel cell) can be expressed as[3]

$$\Delta V_{c1} = \frac{RT}{nF} \ln\left(\frac{i_L}{i_L - i}\right) \tag{14.11}$$

and at the electrode where ions are formed (anode electrode in fuel cell) as

$$\Delta V_{c2} = \frac{RT}{nF} \ln\left(\frac{i_L + i}{i_L}\right), \tag{14.12}$$

where i_L is the limiting current density.

The voltage drop caused by concentration is not only restricted to the electrolyte. When either the reactant or the product is gaseous, a change in partial pressure in the reacting zones also represents a change in concentration. For example, in a hydrogen–oxygen fuel cell, oxygen may be introduced into air. When the reaction takes place, oxygen is removed near the electrode surface in the pores of the electrode and the partial pressure of oxygen drops there when compared with that in bulk air. The change in partial pressure causes a voltage drop, which is determined by
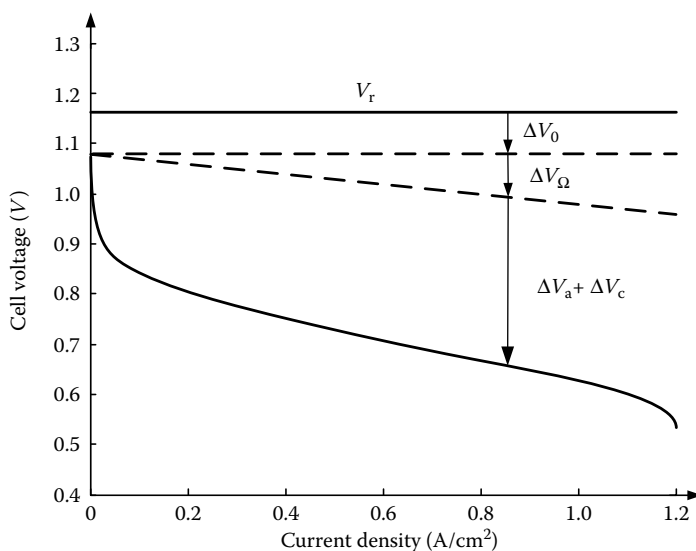
$$\Delta V_{cg} = \frac{RT}{nF} \ln\left(\frac{p_s}{p_0}\right), \tag{14.13}$$

where p_s is the partial pressure at the surface and p_0 is the partial pressure in the bulk feed. For more details, see pp. 236–238 of Messerle.[3]

Figure 14.3 shows the voltage–current curves of a hydrogen–oxygen fuel cell with a temperature of 80°C. It can be seen that the drop caused by the chemical reaction, including activation and concentration, is the source of the voltage drop. This figure also indicates that improving the electrode materials and manufacturing using advanced technology, such as nanotechnology, and advanced catalysts will significantly reduce the voltage drop and will consequently improve the efficiency of the fuel cell.
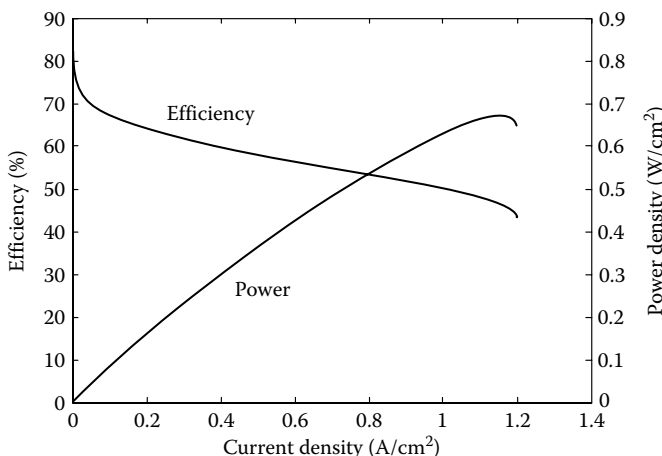
The energy loss in a fuel cell is represented by the voltage drop. Thus the efficiency of the fuel cell can be written as

$$\eta_{fc} = \frac{V}{V_r^0}, \tag{14.14}$$

FIGURE 14.3 Current–voltage curves for a hydrogen–oxygen fuel cell at $T = 80°C$.

where V_r^0 is the cell reversible voltage at standard conditions ($T = 298$ K and $p = 1$ atm). The efficiency curve is strictly homothetic to the voltage curve. An efficiency–current curve for a hydrogen–oxygen fuel cell (refer to Figure 14.3) is shown in Figure 14.4. Figure 14.4 indicates that the efficiency decreases, and power increases, with the increase of current. Therefore, operating a fuel cell at its low current, and then at low power, results in high operating efficiency. However, taking account of the energy consumed by its auxiliaries, such as

FIGURE 14.4 Operating efficiency and power density along with the current density in a hydrogen–oxygen fuel cell.

the air circulating pump, the cooling water circulating pump, and so on, very low power ($<10\%$ of its maximum power) results in low operating efficiency, due to the larger percentage of power consumption in the auxiliary. This will be discussed in more detail later.

14.3   Fuel and Oxidant Consumption

The fuel and oxidant consumptions in a fuel cell are proportional to the current drawn from the fuel cell. The chemical reaction in a fuel cell can be generally described by Equation 14.15, where A is the fuel, B is the oxidant, C and D are the products:

$$A + x_B B \rightarrow x_C C + x_D D. \tag{14.15}$$

The mass flow of the fuel, associated with the current drawn from the fuel cell, can be expressed as

$$\dot{m}_A = \frac{W_A I}{1000\, nF} \ \text{(kg/s)}, \tag{14.16}$$

where W_A is the molecular weight of fuel A, I is the fuel cell current, n is the electrons transferred in the reaction of Equation 14.15, and $F = 96,495\,\text{C/mol}$ is the Faraday constant. The stoichiometric ratio of oxidant mass flow to fuel mass flow can be expressed as

$$\frac{\dot{m}_B}{\dot{m}_A} = \frac{x_B W_B}{W_A}, \tag{14.17}$$

where W_B is the molecular weight of oxidant B.

For a hydrogen–oxygen fuel cell (see Table 14.2 for the reaction), the stoichiometric ratio of hydrogen to oxygen is

$$\left(\frac{\dot{m}_H}{\dot{m}_O}\right)_{\text{stoi}} = \frac{0.5\, W_O}{W_H} = \frac{0.5 \times 32}{2.016} = 7.937. \tag{14.18}$$

The equivalent ratio of oxidant to fuel is defined as the ratio of the actual oxidant/fuel ratio to the stoichiometric ratio, that is,

$$\lambda = \frac{(\dot{m}_B/\dot{m}_A)_{\text{actual}}}{(\dot{m}_B/\dot{m}_A)_{\text{stoi}}}. \tag{14.19}$$

When $\lambda < 1$, the reaction is fuel rich; when $\lambda = 1$, the reaction is stoichiometric; and when $\lambda > 1$, the reaction is fuel lean. In practice, fuel cells are always operated with $\lambda > 1$, that is, excessive air over the stoichiometric value is

supplied in order to reduce the voltage drop caused by concentration. For fuel cells using O_2 as oxidant, air is usually used rather than pure oxygen. In this case, the stoichiometric ratio of fuel to air can be expressed as
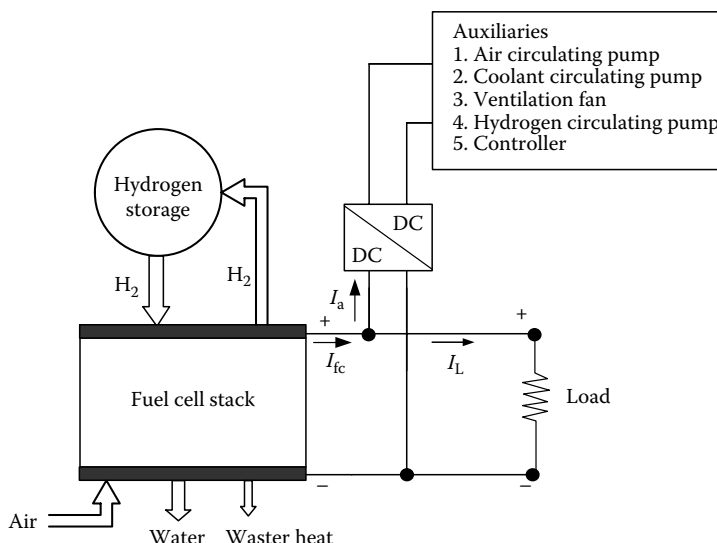
$$\frac{\dot{m}_{air}}{\dot{m}_A} = \frac{(x_O W_O)/0.232}{W_A},$$ (14.20)

where it is assumed that oxygen mass takes 23.2% of the air mass. For hydrogen–air fuel cells, Equation 14.19 becomes

$$\left(\frac{\dot{m}_{air}}{\dot{m}_H}\right)_{stoi} = \frac{(0.5 W_O)/0.232}{W_H} = \frac{(0.5 \times 32)/0.232}{2.016} = 34.21.$$ (14.21)

14.4 Fuel Cell System Characteristics

In practice, fuel cells need auxiliaries to support their operation. The auxiliaries mainly include an air circulating pump, a coolant circulating pump, a ventilation fan, a fuel supply pump, and electrical control devices as shown in Figure 14.5. Among the auxiliaries, the air circulating pump is the largest energy consumer. The power consumed by the air circulating pump (including its drive motor) may take about 10% of the total power output of the fuel cell stack. The other auxiliaries consumed much less energy compared with the air circulating pump.

FIGURE 14.5 A hydrogen–air fuel cell system.

In a fuel cell, the air pressure on the electrode surface, p, is usually higher than the atmospheric pressure, p_0, in order to reduce the voltage drop (see Equation 14.13). According to thermodynamics, the power needed to compress air from low-pressure p_0 to high-pressure p with a mass flow $\dot{m}_{air}$ can be calculated by[1,2]
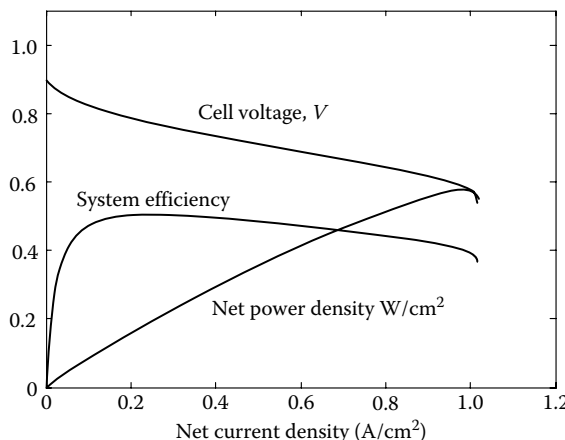
$$P_{air-comp} = \frac{\gamma}{\gamma - 1} \dot{m}_{air} RT \left[\left(\frac{p}{p_0} \right)^{\gamma - 1/\gamma} - 1 \right] (W), \qquad (14.22)$$

where γ is the ratio of specific heats of air ($\gamma = 1.4$), R is the gas constant of air ($R = 287.1\,J/kg\,K$), and T is the temperature at the inlet of the compressor in K. When calculating the power consumed by the air circulating pump, the energy losses in the air pump and motor drive must be taken into account. Thus, the total power consumed is

$$P_{air-cir} = \frac{P_{air-comp}}{\eta_{ap}}, \qquad (14.23)$$

where η_{ap} is the efficiency of the air pump plus motor drive.

Figure 14.6 shows an example of the operation characteristics of the hydrogen–air fuel cell system, where $\lambda = 2$, $p/p_0 = 3$, and $\eta_{ap} = 0.8$, and the net current and net power are the current and power that flow to the load (see Figure 14.5). This figure indicates that the optimal operation region of the fuel cell system is in the middle region of the current range, say, 7–50% of the maximum current. A large current leads to low efficiency due to the large voltage drop in the fuel cell stack and, on the other hand, a very small current leads to low efficiency due to the increase in the percentage of the auxiliaries' energy consumption.

FIGURE 14.6 Cell voltage, system efficiency, and net power density varying with net current density of a hydrogen–air fuel cell.

14.5 Fuel Cell Technologies

It is possible to distinguish six major types of fuel cells, depending on the type of their electrolyte.[4,5] They are proton exchange membrane (PEM) or polymer exchange membrane fuel cells (PEMFCs), alkaline fuel cells (AFCs), phosphoric acid fuel cells (PAFCs), molten carbonate fuel cells (MCFCs), solid oxide fuel cells (SOFCs), and direct methanol fuel cells (DMFCs). Table 14.3 lists their normal operation temperature and the state of electrolyte.

14.5.1 Proton Exchange Membrane Fuel Cells

PEMFCs use solid polymer membranes as the electrolyte. The polymer membrane is perfluorosulfonic acid, which is also referred to as Nafion (Dupont®). This polymer membrane is acidic; therefore the ions transported are hydrogen ions (H^+) or protons. The PEMFC is fueled with pure hydrogen and oxygen or air as oxidant.

The polymer electrolyte membrane is coated with a carbon-supported catalyst. The catalyst is directly in contact with both the diffusion layer and the electrolyte for a maximized interface. The catalyst constitutes the electrode. Directly on the catalyst layer is the diffusion layer. The assembly of the electrolyte, catalyst layers, and gas diffusion layers is referred to as the membrane–electrode assembly.

The catalyst is a critical issue in PEMFCs. In early realizations, very high loadings of platinum were required for the fuel cell to operate properly. Tremendous improvements in catalyst technology have made it possible to reduce the loading from 28 mg to $0.2\,mg/cm^2$. Because of the low operating temperature of the fuel cell and the acidic nature of the electrolyte, noble metals are required for the catalyst layer. The cathode is the most critical electrode because the catalytic reduction of oxygen is more difficult than the catalytic oxidation of hydrogen.

TABLE 14.3

Operating Data of Various Fuel Cell Systems[4,5]

Cell System	Operating Temperature (°C)	Electrolyte
PEMFCs	60–100	Solid
AFCs	100	Liquid
PAFCs	60–200	Liquid
MCFCs	500–800	Liquid
SOFCs	1000–1200	Solid
DMFCs	100	Solid

Another critical issue in PEMFCs is water management. In order to operate properly, the polymer membrane needs to be kept humid. Indeed, the conduction of ions in polymer membranes requires humidity. If the membrane is too dry, there will not be enough acid ions to carry the protons. If it is too wet (flooded), the pores of the diffusion layer will be blocked and reactant gases will not be able to reach the catalyst.

In PEMFCs, water is formed on the cathode. It can be removed by keeping the fuel cell at a certain temperature and flowing enough to evaporate the water and carry it out of the fuel cell as a vapor. However, this approach is difficult because the margin of error is narrow. Some fuel cell stacks run on a large excess of air that would normally dry the fuel cell, and use an external humidifier to supply water by the anode.
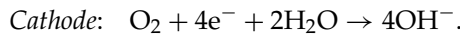
The last major critical issue in PEMFCs is poisoning. The platinum catalyst is extremely active and thus provides great performance. The trade-off of this great activity is a greater affinity for carbon monoxide (CO) and sulfur products than oxygen. The poisons bind strongly to the catalyst and prevent hydrogen or oxygen from reaching it. The electrode reactions cannot take place on the poisoned sites and the fuel cell performance is diminished. If hydrogen is fed from a reformer, the stream will contain some carbon monoxide. The carbon monoxide may also enter the fuel cell in the air stream if the air is pumped from the atmosphere of a polluted city. The poisoning by carbon monoxide is reversible, but comes at a cost and requires the individual treatment of each cell.

The first PEMFCs were developed in the 1960s for the needs of the U.S.-manned space program. It is nowadays the most investigated fuel cell technology for automotive applications by manufacturers such as Ballard. It is operated at 60–100°C and can offer a power density of 0.35–0.6 W/cm^2. The PEMFC has some definite advantages in its favor for EV and HEV applications.[6] First, its low-temperature operation and hence its fast start-up are desirable for an EV and HEV. Second, the power density is the highest among all the available types of fuel cells. The higher the power density, the smaller the size of the fuel cell that needs to be installed for the desired power demand. Third, its solid electrolyte does not change, move, or vaporize from the cell. Finally, since the only liquid in the cell is water, the possibility of any corrosion is essentially delimited. However, it also has some disadvantages, such as the expensive noble metal needed, expensive membrane, and easily poisoned catalyst and membrane.[7]

14.5.2 Alkaline Fuel Cells

AFCs use an aqueous solution of potassium hydroxide (KOH) as the electrolyte to conduct ions between electrodes. Potassium hydroxide is alkaline. Because the electrolyte is alkaline, the ion conduction mechanism is different from PEMFCs. The ion carried by the alkaline electrolyte is a hydroxide ion

(OH^-). This affects several other aspects of the fuel cell. The half reactions are as follows

$$Anode: \quad 2H_2 + 4OH^- \rightarrow 4H_2O + 4e^-.$$

$$Cathode: \quad O_2 + 4e^- + 2H_2O \rightarrow 4OH^-.$$

Unlike in acidic fuel cells, water is formed on the hydrogen electrode. In addition, water is needed at the cathode by oxygen reduction. Water management becomes an issue that is sometimes resolved by making the electrodes waterproof and keeping the water in the electrolyte. The cathode reaction consumes water from the electrolyte where as the anode reaction rejects its product water. The excess water ($2°$mol per reaction) is evaporated outside the stack.
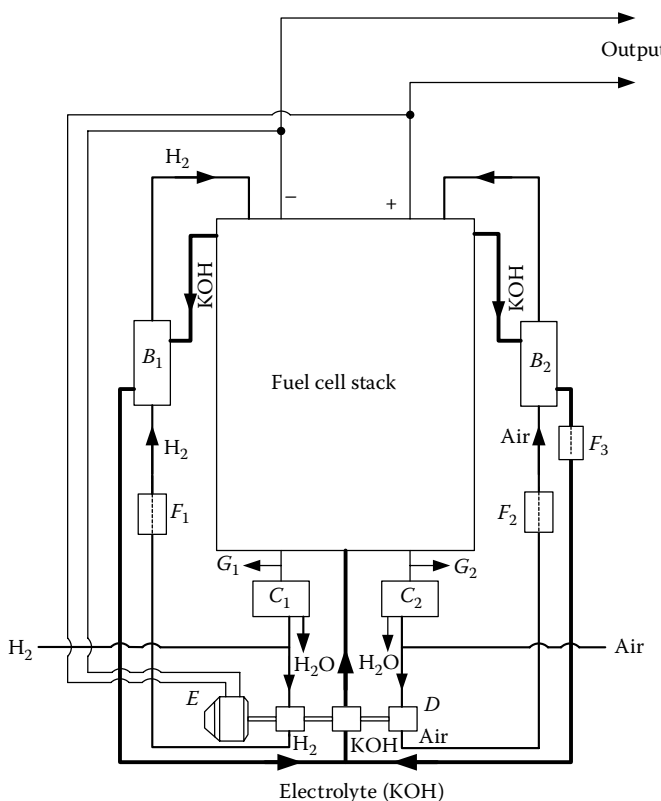
AFCs are capable of operating over a wide range of temperatures (from $80°C$ to $230°C$) pressures[3] (from 2.2 to 45 atm). High-temperature AFCs also make use of a highly concentrated electrolyte, so highly concentrated that the ion transport mechanism changes from aqueous solution to molten salt.

AFCs are capable of achieving very high efficiencies because of the fast kinetics allowed by the hydroxide electrolyte. The oxygen reaction ($O_2 \rightarrow OH^-$) in particular is easier than the oxygen reduction in acidic fuel cells. As a result, the activation losses are very low. The fast kinetics in AFCs allows using silver or nickel as catalysts instead of platinum. The cost of the fuel cell stack is thus greatly reduced.

AFC kinetics is further improved by the eventual circulation of the electrolyte. When the electrolyte is circulated, the fuel cell is said to be a "mobile electrolyte fuel cell." The advantages of such an architecture are as follows: a easy thermal management because the electrolyte is used as coolant; more homogeneous electrolyte concentration, which solves problems of concentration around the cathode; the possibility of using the electrolyte for water management; the possibility of replacing the electrolyte if it has been too polluted by carbon dioxide; and, finally, the possibility of removing the electrolyte from the fuel cell when it is turned off, which has the potential to greatly lengthen the lifetime of the stack.

The use of a circulated electrolyte, however, poses some problems. The greatest problem is the increased risk of leakage: potassium hydroxide is highly corrosive and has a natural tendency to leak even through the tightest seals. The construction of the circulation pump and heat exchanger and eventual evaporator is further complicated. Another problem is the risk of internal electrolytic short-circuit between two cells if the electrolyte is circulated too violently or if the cells are not isolated enough. A circulating electrolyte AFC is pictured in Figure 14.7.[8]

The greatest problem with AFCs is the poisoning by carbon dioxide. The alkaline electrolyte has great affinity for carbon dioxide and together they form carbonate ions (CO_3^{2-}). These ions do not participate in the fuel cell reaction and diminish its performance. There is also a risk that the carbonate

FIGURE 14.7   Circulating electrolyte and supplies of hydrogen and air in an AFC; B_1, B_2, heater exchangers; C_1, C_2, condensers; D, pampers; E, motor; F_1, F_2, F_3, controls; and G_1, G_2, outlets.[8]

will precipitate and obstruct the electrodes. This last issue may be taken care of by circulating the electrolyte. The solution, which adds to the cost and complexity, is to use a carbon dioxide scrubber that will remove the gas from the air stream.

The advantages of AFCs are that they require cheap catalyst, cheap electrolyte, and high-efficiency and low-temperature operation. However, they also have some disadvantages such as impaired durability due to corrosive electrolyte, water produced on the fuel electrode, and poisoning by carbon dioxide.

14.5.3   Phosphoric Acid Fuel Cells[8]

PAFCs rely on an acidic electrolyte, like PEMFCs, to conduct hydrogen ions. The anode and cathode reactions are the same as the PEMFC reactions. Phosphoric acid (H_3PO_4) is a viscous liquid that is contained by capillarity in the fuel cell in a porous silicon carbide matrix.

PAFC was the first fuel cell technology to be marketed. Many hospitals, hotels, and military bases make use of a PAFC to cover part or the totality of their electricity and heat requirements. Very little work has been done to apply this technology to vehicles, probably because of temperature problems.
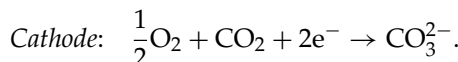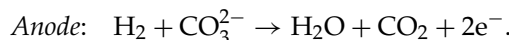
The phosphoric acid electrolyte temperature must be kept above 42°C, which is its freezing point. Freezing and rethawing the acid unacceptably stresses the stack. Keeping the stack above this temperature requires extra hardware, which adds to the cost, complexity, weight, and volume. Most of these issues are minor in the case of a stationary application, but are incompatible with a vehicular application. Another problem arising from the high operating temperature (above 150°C) is the energy consumption associated with warming up the stack. Every time the fuel cell is started, some energy (i.e., fuel) must be spent to heat it up to operating temperature, and every time the fuel cell is turned off, the heat (i.e., energy) is wasted. The loss is significant for short travel times, which usually occurs during city driving. However, this issue seems to be minor in the case of mass transportation such as buses.

The advantages of PAFCs are that they require a cheap electrolyte, a low operating temperature, and a reasonable start-up time. The disadvantages are the expensive catalyst (platinum), corrosion by acidic electrolyte, CO poisoning, and low efficiency.

14.5.4 Molten Carbonate Fuel Cells

MCFCs are high-temperature fuel cells (500–800°C). They rely on a molten carbonate salt to conduct ions, usually lithium–potassium carbonate or lithium–sodium carbonate. The ions conducted are carbonate ions (CO_3^{2-}). The ion conduction mechanism is that of a molten salt like in PAFCs or highly concentrated AFCs.

The electrode reactions are different from other fuel cells:

$$\textit{Anode}: \quad H_2 + CO_3^{2-} \rightarrow H_2O + CO_2 + 2e^-.$$

$$\textit{Cathode}: \quad \frac{1}{2}O_2 + CO_2 + 2e^- \rightarrow CO_3^{2-}.$$
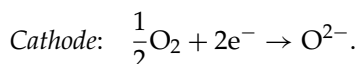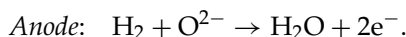
The major difference from other fuel cells is the necessity of providing carbon dioxide at the cathode. It is not necessary to have an external source since it can be recycled from the anode. MCFCs are never used with pure hydrogen but rather with hydrocarbons. Indeed, the major advantage of high-temperature fuel cells is their capability to, almost, directly process hydrocarbon fuels because the high temperature allows their decomposition to hydrogen on the electrodes. This would be a tremendous advantage for automotive applications because of the present availability of hydrocarbon fuels. In addition, the high temperatures enhance the kinetics to the point that cheap catalysts may be used.

MCFCs, however, pose many problems because of the nature of the electrolyte and the operating temperature required. The carbonate is an alkali and is extremely corrosive, especially at high temperature. Not only is this unsafe, but there is also the problem of corrosion on the electrodes. It is unsafe to have a large device at 500–800°C under the hood of a vehicle. While it is true that temperatures in internal combustion engines do reach above 1000°C, these temperatures are restricted to the gases themselves and most parts of the engine are kept cool (around 100°C) by the cooling system. The fuel consumption associated with heating up the fuel cell is also a problem, worsened by the very high operating temperature and the latent heat necessary to melt the electrolyte. These problems are likely to confine MCFCs to stationary or steady power applications such as ships.
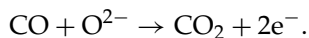
The major advantages of MCFCs are that they are fueled with hydrocarbon fuels, require a low-cost catalyst, have improved efficiency due to fast kinetics, and have a lower sensitivity to poisoning. The major disadvantages are slow start-up and reduced material choice due to high temperature, a complex fuel cell system due to CO_2 cycling, corrosive electrolyte, and slow power response.

14.5.5 Solid Oxide Fuel Cells
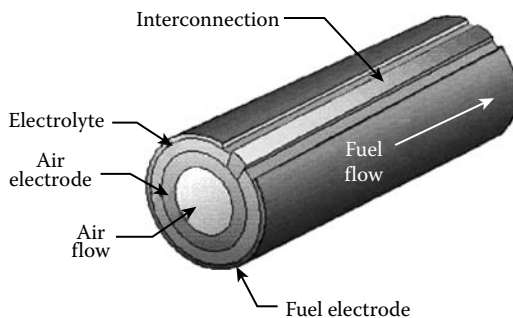
SOFCs conduct ions in a ceramic membrane at high temperature (1000–1200°C). Usually, the ceramic is a yttrium-stabilized zirconia (YSZ) that will conduct oxygen ions (O^{2-}), but other ceramics conduct hydrogen ions. The conduction mechanism is similar to that observed in semiconductors, often called solid-state devices. The name of the fuel cell is derived from this similarity. The half reactions are as follows:

$$\text{\textit{Anode}:}\quad H_2 + O^{2-} \rightarrow H_2O + 2e^-.$$

$$\text{\textit{Cathode}:}\quad \frac{1}{2}O_2 + 2e^- \rightarrow O^{2-}.$$

Water is produced at the fuel electrode. The greatest advantage of SOFCs is this static electrolyte. There is no moving part, except perhaps in the ancillaries. The very high operating temperature allows the use of hydrocarbon fuels as in MCFCs. It should also be noted that SOFCs are not poisoned by carbon monoxide and that they process it about as efficiently as hydrogen. The anode reaction is then

$$CO + O^{2-} \rightarrow CO_2 + 2e^-.$$

SOFCs also benefit from reduced activation losses due to their high operating temperature. The losses are dominated by the ohmic component. SOFCs may be of two kinds: planar and tubular. The planar type is a bipolar

FIGURE 14.8 Tubular SOFC.
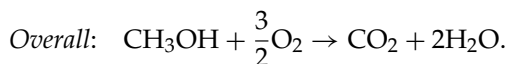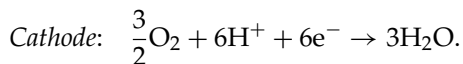
stack similar to other fuel cell technologies. A tubular SOFC is described in Figure 14.8. The major advantages of tubular technologies include easier sealing and reduced constraints on the ceramics. Disadvantages include lower efficiency and power density.

Like MCFCs, the disadvantages of SOFCs are mostly associated with their high operating temperature (safety and fuel economy). Supplementary problems arise because the ceramic electrolyte and electrodes are extremely brittle. This is a major disadvantage for vehicular applications where vibrations are a common occurrence. Thermal cycling further stresses the ceramics and is a major concern for planar fuel cells.

14.5.6 Direct Methanol Fuel Cells

Instead of using hydrogen, methanol can be directly used as the fuel for a fuel cell; this is the so-called DMFC. There are some definite motivations for applying DMFCs to vehicles. First, methanol is a liquid fuel that can be easily stored, distributed, and marketed for vehicle application; hence the current infrastructure of fuel supply can be used without much further investment. Second, methanol is the simplest organic fuel that can be most economically and efficiently produced on a large scale from relatively abundant fossil fuel, namely coal and natural gas. Furthermore, methanol can be produced from agriculture products, such as sugar cane.[9]

In the DMFCs, both the anode and cathode adopt platinum or platinum alloys as electro catalyst. The electrolyte can be trifluoromethane sulfonic acid or PEM. The chemical reaction in a DMFC is given below:

$$\textit{Anode}: \quad CH_3OH + H_2O \rightarrow CO_2 + 6H^+ + 6e^-.$$

$$\textit{Cathode}: \quad \frac{3}{2}O_2 + 6H^+ + 6e^- \rightarrow 3H_2O.$$

$$\textit{Overall}: \quad CH_3OH + \frac{3}{2}O_2 \rightarrow CO_2 + 2H_2O.$$

The DMFC is relatively immature among the aforementioned fuel cells. At the present status of DMFC technology, it generally operates at 50–100°C. Compared with direct hydrogen fuel cells, DMFCs have low power density, slow power response, and low efficiency.[9–11]

14.6 Fuel Supply

Fuel supply to the on-board fuel cells is the major challenge for fuel cell vehicle applications. As mentioned before, hydrogen is the ideal fuel for fuel-cell-powered vehicles.[4,5] Hence, hydrogen production and storage on-board are the major concern. Generally, there are two ways of supplying hydrogen to fuel cells. One is to produce hydrogen in ground stations and store pure hydrogen on-board. The other is to produce hydrogen on-board from an easy-carrying hydrogen carrier and directly feed the fuel cells.

14.6.1 Hydrogen Storage

So far, there are three methods for storage of hydrogen on-board: compressed hydrogen in a container at ambient temperature, cryogenic liquid hydrogen at low temperature, and the metal hydride method. All these methods have their advantages and disadvantages.

14.6.1.1 *Compressed Hydrogen*
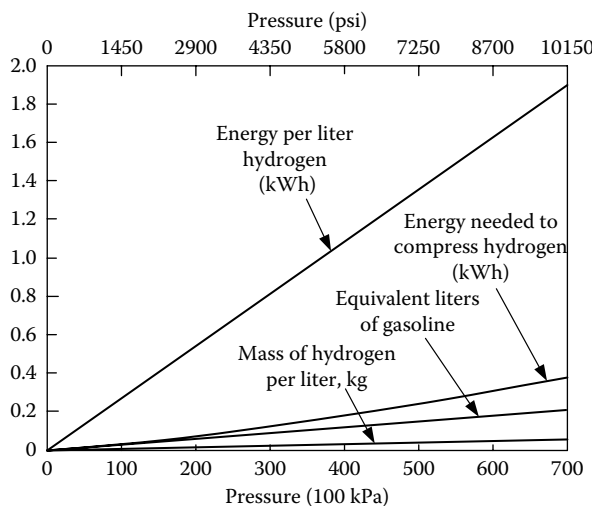
Pure hydrogen may be stored on-board the vehicle under pressure in a tank. The ideal gas equation can be used to calculate the mass of hydrogen stored in a container with volume V and pressure p, that is,

$$m_H = \frac{pV}{RT} W_H,$$ (14.24)

where p and V are the pressure and volume of the container, R is the gas constant (8.31 J/mol K), T is the absolute temperature, and W_H is the molecular weight of hydrogen (2.016 g/mol). The energy stored in hydrogen can be calculated as

$$E_H = m_H \, HV,$$ (14.25)

where HV is the heating value of hydrogen. The heating value is either the high heating value ($HHV_H = 144 \, mJ/kg$) or the low heating value ($LHV_H = 120 \, mJ/kg$), depending on the condensation energy of produced water. For a convenient comparison with internal combustion engines, LHV_H is most often used.

FIGURE 14.9 Energy per liter of hydrogen and equivalent liters of gasoline versus pressure.

Figure 14.9 shows the mass and energy in 1 L of hydrogen and the equivalent liters of gasoline under different pressure and at room temperature (25°C). The equivalent liters of gasoline are defined as the number of liters of gasoline in which the same amount of energy is contained as that in 1 L of hydrogen. Figure 14.9 also indicates that at a pressure of 350 bar, the energy per liter of hydrogen is less than 1 kWh and is equivalent to about 0.1 L of gasoline. Even if the pressure is increased to 700 bar, which is believed to be the maximum pressure that can be reached, the energy per liter of hydrogen is still less than 2.0 kWh and is equivalent to about 0.2 L of gasoline.

In addition, a certain amount of energy is needed to compress hydrogen from low pressure to high pressure. The process in hydrogen compression may be assumed to be an adiabatic process, that is, no heat exchange occurs during the process. The energy consumed can be expressed as

$$E_{comp} = \frac{\gamma}{\gamma - 1} \frac{m}{W_H} RT \left[\left(\frac{p}{p_0} \right)^{\gamma - 1/\gamma} - 1 \right], \tag{14.26}$$

where m is the mass of hydrogen, W_H is the molecular weight of hydrogen, γ is the ratio of the specific heat ($\gamma = 1.4$), p is the pressure of hydrogen, and p_0 is atmospheric pressure. This energy consumption is also drawn in Figure 14.9. It shows that about 20% of hydrogen energy must be consumed to compress it to high pressure. Taking into account the inefficiency of the compressor and the electric motor, it is estimated that about 25% of hydrogen energy is consumed.

To contain a gas at several hundred atmospheres requires a very strong tank. In order to keep the weight as low as possible and the volume reasonable,

today's hydrogen tanks for automotive applications use composite materials such as carbon fiber. The cost of a compressed hydrogen tank is thus likely to be high.

The hazards of compressed hydrogen on-board a vehicle must be taken into account. Besides the risk of leakages through cracks in the tank walls, seals, and so on, there is the problem of permeation of hydrogen through the material of the wall. The hydrogen molecule is so small that it can diffuse through some materials.

In addition, a compressed gas tank is a potential bomb in case of a crash. The dangers are even greater in the case of hydrogen, which has a very wide explosive range in air from 4% to 77%[12] and is capable of mixing very quickly with air. This is to be compared with gasoline, which has an explosive range from only 1% to 6% and is a liquid. It should be noted that hydrogen has a high autoignition temperature of 571°C, whereas gasoline autoignites at around 220°C but must be vaporized first.

So far, the technology of compressed hydrogen storage on-board is still a huge challenge for vehicle application.

14.6.1.2 *Cryogenic Liquid Hydrogen*

Another alternative solution to storing hydrogen on-board a vehicle is to liquefy the gas at cryogenic temperatures ($-259.2°C$). The thus stored hydrogen is commonly referred to as "LH_2." LH_2 storage is affected by the same density problems that affect compressed hydrogen. Indeed, the density of liquid hydrogen is very low and 1 L of liquid hydrogen only weighs 71×10^{-3} kg. This low density results in an energy content of about 8.52 mJ/L of liquid hydrogen.

Containing a liquid at such a low temperature as $-259.2°C$ is technically challenging. It requires a heavily insulated tank to minimize the heat transfer from the ambient air to the cryogenic liquid and thus prevent it from boiling. The approach usually taken is to build a significantly insulated tank and to make it strong enough to withstand some of the pressure resulting from the boil-off. The excess pressure is then released to the atmosphere by means of a safety valve. The tank insulation, strength, and safety devices also add significantly to the weight and cost of LH_2 storage.

The boil-off is a problematic phenomenon: if the vehicle is parked in a closed area (garage, underground parking) there is the risk that hydrogen will build up in the confined atmosphere and that the explosive mixture thus formed will explode at the first spark (light switch, lighter, etc.). The refueling of a tank with liquid hydrogen requires specific precautions: air must be kept out of the circuit. The commonly used method is to fill the tank with nitrogen prior to fueling in order to evacuate the residual gas in the tank. It is also necessary to use specialized equipment, designed to handle the explosion hazard and the cryogenic hazards. Indeed, a cryogenic liquid is a dangerous compound for living beings, as it burn-freezes the skin and organs. It may well be, however,
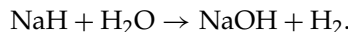
that the ambient temperature would evaporate the cryogenic hydrogen fast enough to limit or eliminate this risk.

14.6.1.3 Metal Hydrides

Some metals are capable of combining with hydrogen to form stable compounds that can later be decomposed under certain pressure and temperature conditions. These metals may be iron, titanium, manganese, nickel, lithium, and some alloys of these metals. Metal hydrides are stable under normal temperature and pressure conditions and are capable of releasing hydrogen only when required.

The hydrogen storage metals and metal alloys are Mg, Mg_2Ni, FeTi, and $LaNi_5$. These metals and metal alloys absorb hydrogen to form $Mg–H_2$, $Mg_2Ni–H_4$, $FeTi–H_2$, and $LaNi_5–H_6$. Theoretically, metal and metal alloys store hydrogen at a higher density than pure hydrogen, as shown in Table 14.4. In practice, the hydrogen storage capacity depends heavily on the surface area of the material, on which the hydrogen molecules are absorbed. A large surface area per unit weight of material can be obtained by fine porous modules made of finely ground powder of the metals or metal alloys. Figure 14.10 shows the practical mass and volume needed to store 6 kg of hydrogen (22 L of gasoline equivalent). This figure indicates that $Mg–H_2$ is the promising technology.

Alkaline metal hydrides are possible alternatives to metal hydride absorption. These hydrides react violently with water to release hydrogen and a hydroxide. The example of sodium hydride is shown below:

$$NaH + H_2O \rightarrow NaOH + H_2.$$
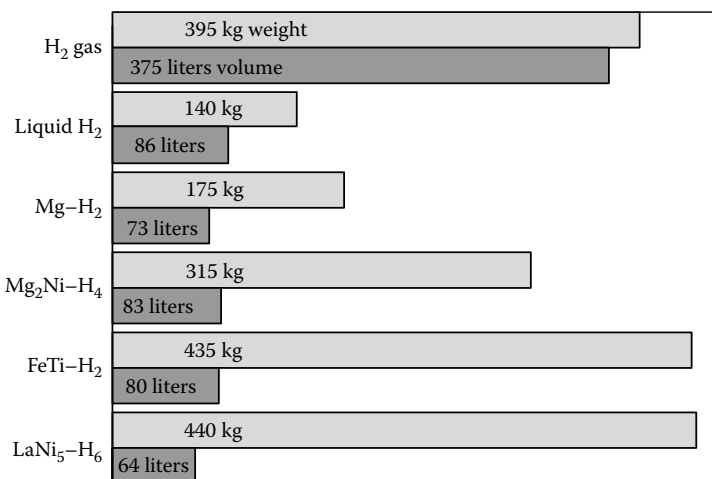
The major disadvantage is the necessity of carrying a highly reactive hydride and a corrosive solution of hydroxide in the same vehicle. The storage density is good enough in comparison to many other hydrogen storage techniques,

TABLE 14.4

Theoretical Hydrogen Storage Densities in Compressed, Liquid, and Metal Hydride Approaches[12]

Material	H-Atoms per cm^3 ($\times 10^{22}$)	% of Weight that is Hydrogen
H_2 gas, 200 bar (2900 psi)	0.99	100
H_2 liquid, 20°K (−253°C)	4.2	100
H_2 liquid, 4.2°K (−269°C)	5.3	100
$Mg–H_2$	6.5	7.6
$Mg_2Ni–H_2$	5.9	3.6
$FeTi–H_2$	6.0	1.89
$LaNi–H_6$	5.5	1.37

FIGURE 14.10 Current mass and volume needed to store 6 kg of hydrogen (22 L of gasoline equivalent) in various hydrogen storage devices.[14]

but falls short in comparison to gasoline. The manufacture of these hydrides and their recycling are also challenging.

Carbon nanotubes, discovered in 1991, would be a prospective method for hydrogen storage systems, because of their potential high hydrogen absorbing capability and light weight. However, carbon nanotube technology is still in its infancy and has a long way to go before its practical utility can be assessed.

14.6.2   Hydrogen Production
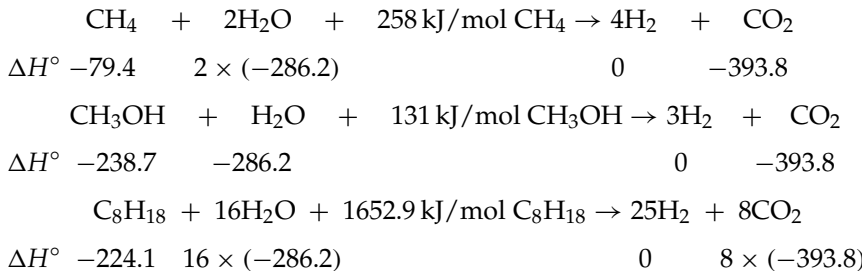
At present, hydrogen is mostly produced from hydrocarbon fuels through reforming. Reforming is a chemical reaction that extracts hydrogen from hydrocarbons. During this reaction, the energy content of the fuel is transferred from the carbon–hydrogen bonds to the hydrogen gas. Hydrocarbons such as gasoline, methane, or methanol are the most likely candidates because of their ease of reforming.

There are three major methods of reforming: steam reforming (SR), autothermal reforming (ATR), and partial oxidation (POX) reforming. SR may be used with methanol, methane, or gasoline, whereas ATR and POX reforming are the most commonly used for processing gasoline.
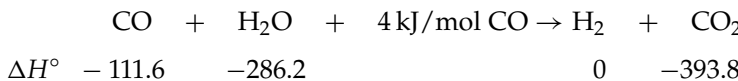
14.6.2.1   Steam Reforming

SR is a chemical process in which hydrogen is produced through the chemical reaction between hydrocarbon fuels and water steam at high temperature.

The following chemical equations describe the reforming, using methane (CH_4), methanol (CH_3OH), and gasoline (iso-octane C_8H_{18}) as the fuels:

$$CH_4 \; + \; 2H_2O \; + \; 258\,kJ/mol\,CH_4 \rightarrow 4H_2 \; + \; CO_2$$

$\Delta H°$ -79.4 $2 \times (-286.2)$ 0 -393.8

$$CH_3OH \; + \; H_2O \; + \; 131\,kJ/mol\,CH_3OH \rightarrow 3H_2 \; + \; CO_2$$

$\Delta H°$ -238.7 -286.2 0 -393.8

$$C_8H_{18} \; + \; 16H_2O \; + \; 1652.9\,kJ/mol\,C_8H_{18} \rightarrow 25H_2 \; + \; 8CO_2$$

$\Delta H°$ -224.1 $16 \times (-286.2)$ 0 $8 \times (-393.8)$
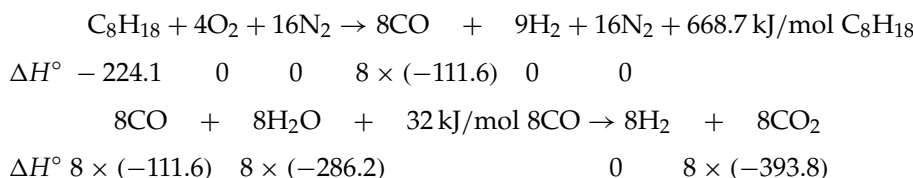
The above reactions are highly endothermic and need to be powered by some burning of fuels. Also, these reactions yield some carbon monoxide (CO) in the products, which is a poison to some electrolytes such as PEMFCs, AFCs, and PAFCs. The carbon monoxide can be further converted into hydrogen and carbon dioxide by means of a water–gas shift reaction:

$$CO \; + \; H_2O \; + \; 4\,kJ/mol\,CO \rightarrow H_2 \; + \; CO_2$$

$\Delta H°$ -111.6 -286.2 0 -393.8
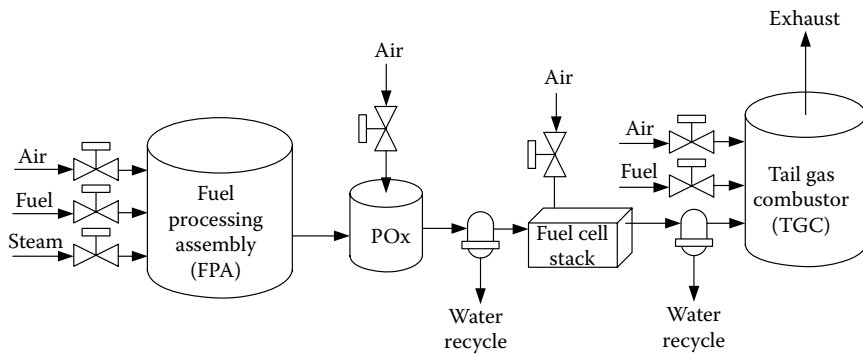
In SR, it is particularly preferred to use methanol as the fuel, since there is no theoretical need for a water–gas shift reaction and since the processing temperature is low (250°C). The hydrogen yield is also particularly high. Among its disadvantages, the most significant are the poisoning of the reformer catalysts by impurities in methanol and the need for external heat input to the endothermic reaction. The heat requirements slow the reaction down and impose a slow start-up time between 30 and 45 min.[13] The methanol steam reformer also has slow output dynamics. Although feasible, the SR of gasoline is not commonly used.

14.6.2.2 POX Reforming

POX reforming combines fuel with oxygen to produce hydrogen and carbon monoxide. This approach generally uses air as the oxidant, and results in a reformate that is diluted with nitrogen. Then the carbon monoxide further reacts with water steam to yield hydrogen and carbon dioxide (CO_2), as mentioned above. POX reforming usually uses gasoline (iso-octane) as its fuel. The reaction is expressed as

$$C_8H_{18} + 4O_2 + 16N_2 \rightarrow 8CO \; + \; 9H_2 + 16N_2 + 668.7\,kJ/mol\,C_8H_{18}$$

$\Delta H°$ -224.1 0 0 $8 \times (-111.6)$ 0 0

$$8CO \; + \; 8H_2O \; + \; 32\,kJ/mol\,8CO \rightarrow 8H_2 \; + \; 8CO_2$$

$\Delta H°$ $8 \times (-111.6)$ $8 \times (-286.2)$ 0 $8 \times (-393.8)$
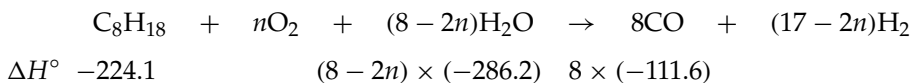
FIGURE 14.11   Fuel processing diagram.[13]

POX reforming is highly exothermic, which thus has the advantages of very fast response to transients and being capable of very fast start-ups. POX reformers are also fuel flexible, and are capable of treating a wide variety of fuels. The disadvantages include a high operating temperature (800–1000°C) and a difficult construction due to heat-integration problems between the different steps of the reaction.[13] In addition, it can be seen from the above chemical equation that the heat produced from the first reaction is much more than that absorbed in the second reaction, and hence POX reforming is somewhat less efficient than the SR of methanol.

Figure 14.11 shows a fuel processing system developed by Epyx Co-operation.[13]

14.6.2.3   Autothermal Reforming

ATR combines fuel with both water and steam so that the exothermic heat from the POX reaction is balanced by the endothermic heat of the SR reaction. The chemical equation in this reaction is

$$C_8H_{18} \quad + \quad nO_2 \quad + \quad (8-2n)H_2O \quad \rightarrow \quad 8CO \quad + \quad (17-2n)H_2$$
$$\Delta H° \quad -224.1 \qquad\qquad (8-2n) \times (-286.2) \quad 8 \times (-111.6)$$
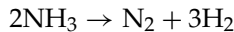
Zero heat produced in the above equation yields $n = 2.83$. The CO produced in the above reaction can further react with water steam to produce hydrogen by the water-shift reaction mentioned above.

ATR yields a more concentrated hydrogen stream than POX reforming, but less than SR. The heat integration is easier than for POX reforming but a catalyst is required. ATR is potentially more efficient than POX reforming.

14.6.3 Ammonia as Hydrogen Carrier

Ammonia is a non-carbon-based chemical that presents interesting characteristics as a hydrogen source. The extraction of hydrogen from ammonia, called "cracking," is shown below:

$$2NH_3 \rightarrow N_2 + 3H_2$$

The above reaction is easily achieved by heating ammonia, either alone or over a catalyst bed, which has the advantage of lowering the reaction temperature. The energy requirement for this reaction is minimal because it is reversible. Ammonia presents great advantages in terms of storage as it is easily liquefied at low pressure (about 10 atm) or at mildly low temperatures ($-33°C$). Other advantages include a very high autoignition temperature ($651°C$) and a limited explosive range in air (15–28%).

Despite its many advantages, ammonia has a major disadvantage: it is toxic. Ammonia is an alkali that has an extreme affinity for water; hence it strongly attacks the eyes and lungs and causes severe burns. This causticity makes it challenging to conceive of ammonia as a fuel-for fuel cell-powered automobiles.

14.7 Non-Hydrogen Fuel Cells

Some fuel cell technologies can directly process fuels other than hydrogen.[4,5] Some likely couples are listed below:

- Direct methanol PEMFCs
- Ammonia AFCs
- Direct hydrocarbon MCFCs or SOFCs

Like their hydrogen counterparts, direct methanol PEMFCs are actively studied and present many advantages such as the absence of a reformer, the handling of a liquid fuel, and the absence of high temperatures in the system. The major disadvantages are the necessity of diluting the methanol in liquid water to feed the fuel electrode and a strong crossover of methanol—due to its absorption in the polymer membrane, but due mostly to its slow kinetics.

Ammonia AFCs[14] are possible alternatives to the thermal cracking of ammonia. Ammonia gas is directly fed to the fuel cell and is catalytically cracked on the anode. The ammonia fuel cell reaction yields a slightly lower thermodynamic voltage and higher activation losses than hydrogen AFCs. The activation losses may be reduced by improving the catalyst layer. Interestingly, it would be possible to use ammonia directly with other fuel cell

technologies if it were not for the fact that the acidic nature of their electrolyte would be destroyed by the alkaline ammonia.

MCFCs and SOFCs have the capability of directly cracking hydrocarbons because of their high operating temperature. Therefore, they are not directly consuming the hydrocarbons, but are internally extracting the hydrogen from them. This option obviously has all the disadvantages of high-temperature fuel cells as discussed in the section on fuel cell technologies.

References

1. J. Bevan Ott and J. Boerio-Goates, *Chemical Thermodynamics—Advanced Applications*, Academic Press, New York, ISBN 0-12-530985-6, 2000.
2. S. I. Sandler, *Chemical and Engineering Thermodynamics*, Third Edition, John Wiley & Sons, New York, ISBN 0-471-18210-9, 1999.
3. H. K. Messerle, *Energy Conversion Statics*, Academic Press, New York, 1969.
4. P. J. Berlowitz and C. P. Darnell, "Fuel choices for fuel cell powered vehicles," *Society of Automotive Engineers (SAE) Journal*, Paper No. 2000-01-0003, Warrendale, PA, 2002.
5. P. J. Berlowitz and C. P. Darnell "Fuel choices for fuel cell powered vehicles," *Society of Automotive Engineers (SAE) Journal*, Paper No. 2001-01-0003, Warrendale, PA, 2002.
6. F. Michalak, J. Beretta, and J.-P. Lisse, "Second generation proton exchange membrane fuel cell working with hydrogen stored at high pressure for fuel cell electric vehicle," *Society of Automotive Engineers (SAE) Journal*, Paper No. 2002-01-0408, Warrendale, PA, 2002.
7. J. Larminie and A. Dicks, *Fuel Cell Systems Explained*, John Wiley & Sons, New York, 2000.
8. W. Vielstich, *Fuel Cells—Modern Processes for Electrochemical Production of Energy*, John Wiley & Sons, New York, ISBN 0-471-90695-6, 1970.
9. R. M. Moore, "Direct methanol fuel cells for automotive power system," in *Fuel Cell Technology for Vehicles*, R. Stobart (ed.), Society of Automotive Engineers (SAE), ISBN: 0-7680-0784-4, Warrendale, PA, 2001.
10. N. Q. Minh and T. Takahashi, *Science and Technology of Ceramic Fuel Cells*, Elsevier, Amsterdam, 1995.
11. M. Baldauf and W. Preidel, "Status of the development of a direct methanol fuel cell," in *Fuel Cell Technology for Vehicles*, R. Stobart (ed.), Society of Automotive Engineers (SAE), ISBN: 0-7680-0784-4, Warrendale, PA, 2001.
12. S. E. Gay, J. Y. Routex, M. Ehsani, and M. Holtzapple, "Investigation of hydrogen carriers for fuel cell based transportation," *Society of Automotive Engineers (SAE) Journal*, Paper No. 2002-01-0097, Warrendale, PA, 2002.
13. "Hydrogen at GKSS: Storage Alternative," available at http://www.gkss.de/, last visited in May 2003.
14. C. E. Thomas, B. D. James, F. D. Lomax Jr, and I. F. Kuhn Jr, "Societal impacts of fuel options for fuel cell vehicles," *Society of Automotive Engineers (SAE) Journal*, Paper No. 982496, Warrendale, PA, 2002.

15

Fuel Cell Hybrid Electric Drive Train Design
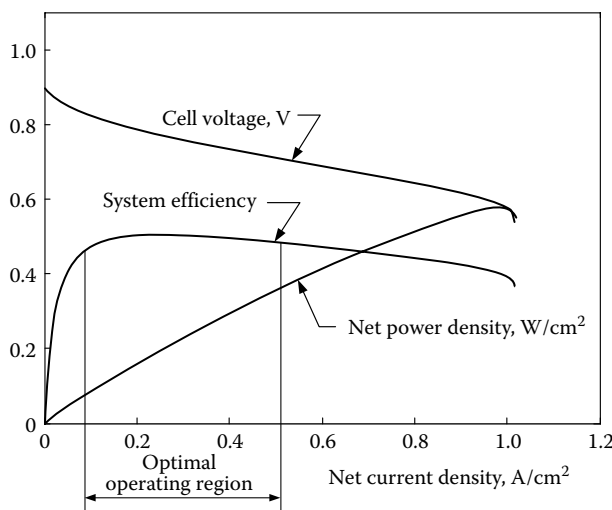
Fuel cells, as discussed in Chapter 14, are considered to be one of the advanced power sources for applications in transportation. Compared with the IC engines, fuel cells have the advantages of high energy efficiency and much lower emissions. This is because they directly convert the free energy in fuel into electrical energy, without undergoing combustion. However, vehicles powered solely by fuel cells have some disadvantages, such as a heavy and bulky power unit caused by the low power density of the fuel cell system, long start-up time, and slow power response. Furthermore, in propulsion applications, the extremely large power output at sharp acceleration and the extremely low power output at low-speed driving lead to low efficiency, as shown in Figure 15.1.

Hybridization of the fuel cell system with a peaking power source is an effective technology to overcome the disadvantages of the fuel-cell-alone-powered vehicles. The fuel cell HEV is totally different from the conventional IC engine-powered vehicles and IC engine-based hybrid drive trains. Therefore, a totally new design methodology is necessary.[1] In this chapter, a general systematic design methodology and a control strategy for the fuel cell hybrid electric drive trains are discussed. Along with the discussion, a design example for a passenger car drive train is introduced.
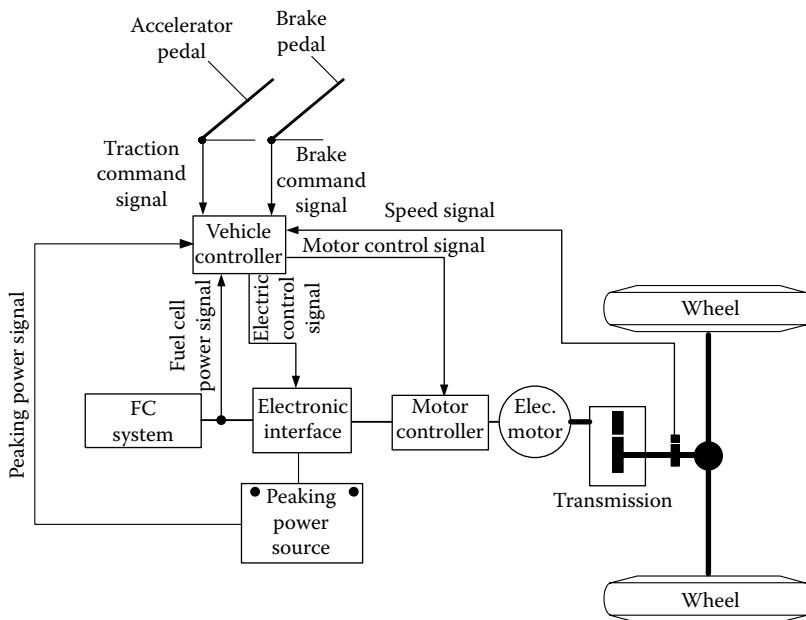
15.1 Configuration

The fuel-cell-powered hybrid drive train has the construction as shown in Figure 15.2.[1,2] It mainly consists of a fuel cell system as the primary power source, a PPS, an electric motor drive (motor and its controller), a vehicle controller, and an electronic interface between the fuel cell system and the PPS.[1] According to the power or torque command received from the accelerator or the brake pedal and other operating signals, the vehicle controller controls the motor power (torque) output and the energy flows between the fuel cell system, the PPS, and the drive train. For peak power demand, for instance,

FIGURE 15.1   Typical operating characteristics of a fuel cell system.

in sharp acceleration, both the fuel cell system and the PPS supply propulsion power to the electric motor drive. In braking, the electric motor, working as a generator, converts part of the braking energy into electric energy and stores it in the PPS. The PPS can also restore the energy coming from the fuel cell system when the load power is less than the rated power of the fuel cell

FIGURE 15.2   Configuration of a typical fuel cell hybrid drive train.

system. Thus, with proper design and control strategy, the PPS will never need to be charged from outside of the vehicle.

15.2 Control Strategy

The control strategy that is preset in the vehicle controller is to control the power flow between the fuel cell system, the PPS, and the drive train. The control strategy should ensure the following:

1. The power output of the electric motor always meets the power demand.
2. The energy level in the PPS is always maintained within its optimal region.
3. The fuel cell system operates within its optimal operating region.

The driver gives a traction command or brake command through the accelerator pedal or brake pedal (refer to Figure 15.3), which is represented

P_{comm}	--Commanded power
$P_{fc-rated}$	--Rated power of the fuel cell system
P_{fc}	--Power of the fuel cell system
P_{fc-min}	--Minimum power of the fuel cell system
$P_{pps-traction}$	--Traction power drawn from the PPS
$P_{pps-charging}$	--Charging power in to the PPS
E	--Energy level of the PPS
E_{min}	--Bottom line of the energy storage in the PPS
E_{max}	--Top line of the energy storage in the PPS
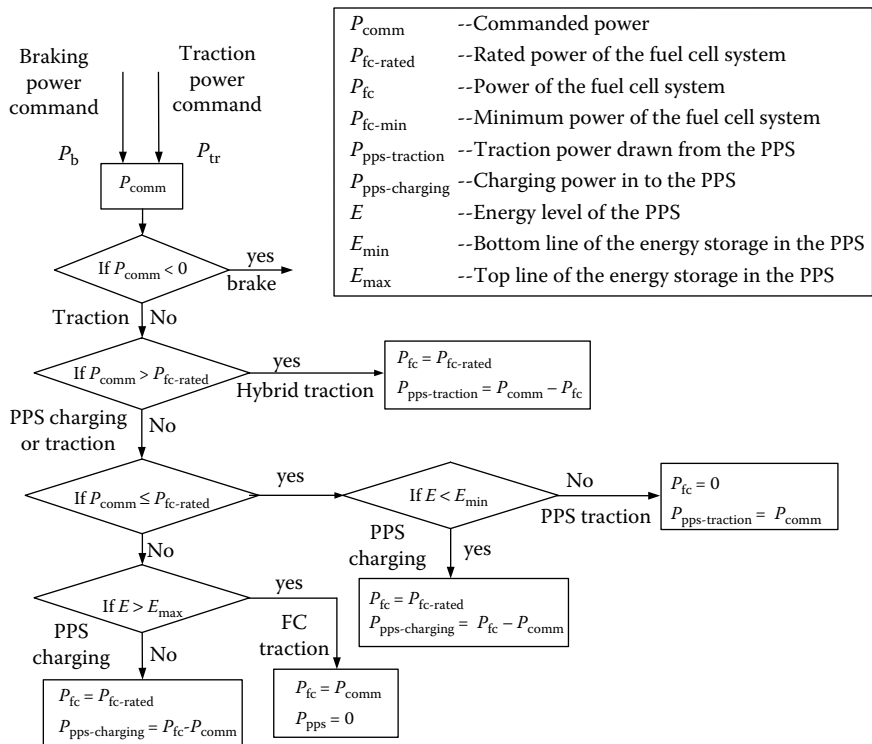
FIGURE 15.3 Flowchart of the control strategy.

by a power command, P_{comm}, that the motor is expected to produce. Thus, in traction mode, the electric power input to the motor drive can be expressed as

$$P_{m\text{-}in} = \frac{P_{comm}}{\eta_m},\tag{15.1}$$

where η_m is the efficiency of the motor drive. However, in braking, the motor drive functions as a generator, and the electric power output from the motor is expressed as

$$P_{m\text{-}out} = P_{mb\text{-}comm}\eta_m,\tag{15.2}$$

where $P_{mb\text{-}comm}$ is the braking power command to the motor, which may be different from the power command, P_{comm}, coming from the brake pedal, since not all the braking power, P_{comm}, may be supplied by the regenerative braking, as discussed in Chapter 13.

According to the motor power command and other vehicle information, such as energy level in the PPS and minimum operating power of the fuel cell system—below which the efficiency of the fuel cell will decrease significantly (see Figure 15.1)—the fuel cell system and the PPS are controlled to produce the corresponding power. Various operating modes of the drive train and the corresponding power control strategy are described in detail below.

Standstill mode: Neither the fuel cell system nor the PPS supplies power to the drive train. The fuel cell system may operate at idle.

Braking mode: The fuel cell system operates at idle, and the PPS absorbs the regenerative braking energy, according to the brake system operating characteristics.

Traction mode:

1. If the commanded motor input power is greater than the rated power of the fuel cell system, the hybrid traction mode is used, in which the fuel cell system operates with its rated power, and the remaining power demanded is supplied by the PPS. The rated power of the fuel cell system may be set as the top line of the optimal operating region of the fuel cell.

2. If the commanded motor input power is smaller than the preset minimum power of the fuel cell system, and the PPS needs charging (the energy level is less than the minimum value), the fuel cell system operates with its rated power—part of which goes to the drive train, while the other part goes to the PPS. Otherwise, if the PPS does not need charging (the energy level is near its maximum value), the fuel cell system operates at idle and the PPS alone drives the vehicle. In the latter case, the peak power that the PPS can produce is greater than the commanded motor input power.

3. If the load power is greater than the preset minimum power and less than the rated power of the fuel cell, and the PPS does not need charging, the fuel cell system alone drives the vehicle. Otherwise, if the PPS does need charging, the fuel cell system operates with its rated power—part of which goes to the drive train to drive the vehicle, while the other part is used to charge the PPS.

Figure 15.3 illustrates the flowchart diagram of this control strategy.

15.3 Parametric Design

Similar to the design of the engine-based hybrid drive train, the parametric design of the fuel-cell-powered hybrid drive train includes the design of the traction motor power, the fuel cell system power, and the PPS power and energy capacity.

15.3.1 Motor Power Design

The motor power is required to meet the acceleration performance of the vehicle as discussed in previous chapters. Figure 15.4 shows the motor power for a 1500-kg passenger car, with respect to the acceleration time from zero to 100 km/h and a constant speed on a flat road and a 5% grade road. The parameters used in this example are vehicle mass 1500 kg, rolling resistance
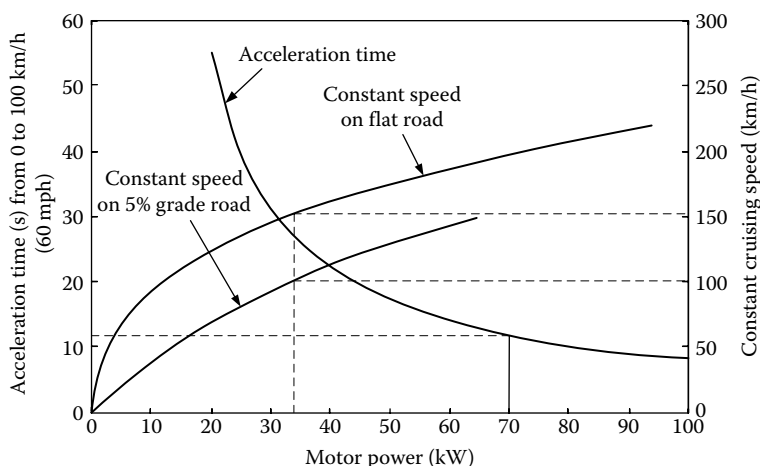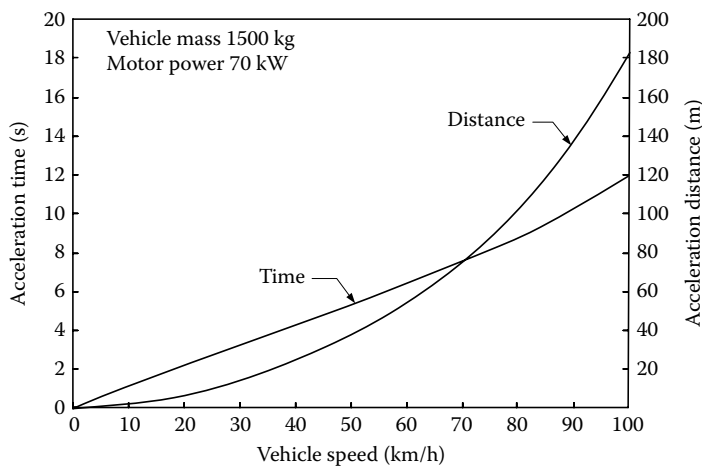
FIGURE 15.4 Motor power versus acceleration time and vehicle cruising speed.

FIGURE 15.5 Acceleration time and distance versus vehicle speed of the passenger car example.

coefficient 0.01, aerodynamic drag coefficient 0.3, and front area $2\,m^2$. It can be seen that accelerating the vehicle from zero speed to 100 km/h in 12 s needs about 70 kW of motor power. Figure 15.4 also shows the required power while driving at a constant speed on a flat road and a 5% grade road. It can be seen that 33 kW of motor power can support the vehicle driving at about 150 and 100 km/h on a flat road and a 5% grade road, respectively. In other words, the motor power required for acceleration performance is much greater than that required for constant speed driving. Thus, a 70-kW traction motor is considered to be the proper design for this vehicle example. Figure 15.5 shows the acceleration time and distance covered by the vehicle during acceleration driving.

15.3.2   Power Design of the Fuel Cell System

The PPS, as discussed in previous chapters, is only used to supply peak power in short time periods and has a limited amount of energy in it. Thus, the fuel cell system must be able to supply sufficient power to support the vehicle while it drives at high constant speeds on a long trip (e.g., highway driving between cities), and to support the vehicle to overcome a mild grade at a specified speed without the help of the PPS.

For the 1500-kg example passenger car, as indicated in Figure 15.4, 33 kW of motor power is sufficient to meet the power demand with about 150 km/h of constant speed on a flat road and 100 km/h on a 5% grade road. Considering the inefficiency of the motor drive, a fuel cell system of about 40 kW power will be needed to support long trip driving (in the fuel cell system design, the maximum power may be designed slightly larger than that dictated by the constant speed driving).[1]

15.3.3   Design of the Power and Energy Capacity of the PPS

15.3.3.1   *Power Capacity of the PPS*

Based on the maximum power of the motor determined by the specified acceleration performance, and the rated power of the fuel cell system determined by the constant speed driving, the rated power of the peaking power source can be determined by

$$P_{pps} = \frac{P_{motor}}{\eta_{motor}} - P_{fc}, \tag{15.3}$$
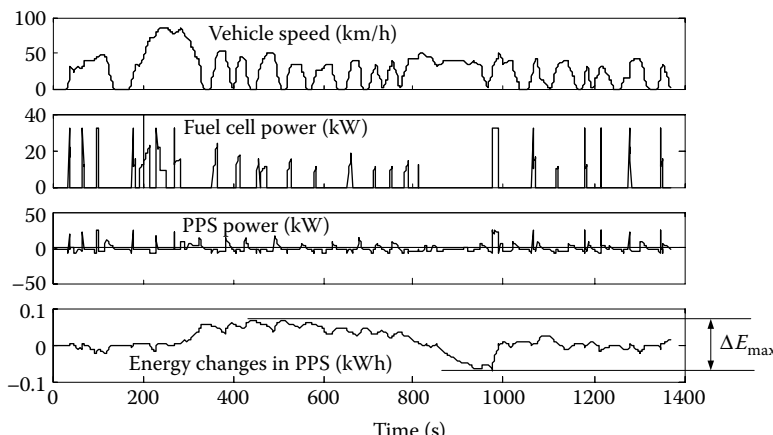
where P_{pps} is the rated power of the peaking power source, P_{motor} is the maximum motor power, η_{motor} is the efficiency of the motor drive, and P_{fc} is the rated power of the fuel cell system. The rated power of the PPS in the example passenger car is about 43 kW.

15.3.3.2   *Energy Capacity of the PPS*
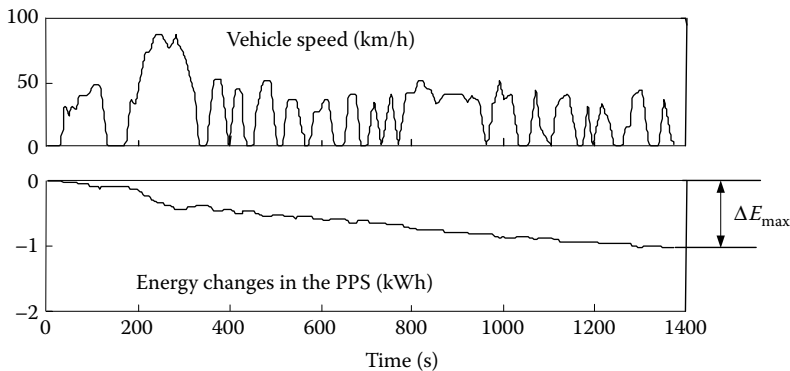
The PPS supplies its energy to the drive train when peaking power is needed, and restores its energy storage from regenerative braking or from the fuel cell system. The energy changes in the PPS in a driving cycle can be expressed as

$$E = \int_t (P_{pps\text{-}charge} - P_{pps\text{-}discharge}) \, dt \tag{15.4}$$

where $P_{pps\text{-}charge}$ and $P_{pps\text{-}discharge}$ are the charge and discharge power of the PPS, respectively. The energy changes, E, in the PPS depend on the size of the fuel cell system, the vehicle control strategy, and the load power profile along with time. Figure 15.6 shows the time profiles of the vehicle speed, the power of the fuel cell system, the PPS power, and the energy change in the PPS for

FIGURE 15.6   Vehicle speed, fuel cell power, power of the PPS, and energy changes in the PPS.

FIGURE 15.7 Energy changes in the PPS while powered by PPS alone in an FTP75 urban drive cycle.

a 1500-kg passenger car with a 40-kW rated power fuel cell system, driving in an FTP75 urban driving cycle and using the control strategy mentioned above. Figure 15.6 indicates that the maximum energy change, ΔE_{max}, in the PPS is quite small (about 0.1 kWh). This result implies that the PPS does not need much stored energy to support the vehicle driving in this driving cycle.

It should be noted that the power producing capability of the fuel cell system is limited before the fuel cell system is warmed up, and the propulsion of the vehicle relies on the PPS. In this case, the energy in the PPS will be delivered quickly. Figure 15.7 shows the energy changes in the PPS in an FTP75 urban driving cycle for a 1500-kg passenger car, while PPS alone propels the vehicle. It indicates that about 1 kWh of energy in the PPS is needed to complete the driving cycle [approximately 10.62 km (6.64 miles) in 23 min], and about 43.5 Wh of energy from the PPS will be discharged each minute. Assuming that 10 min are needed to warm up the fuel cell system,[3] about 435 Wh of energy in the PPS will be discharged.

Based on the maximum discharged energy in the PPS discussed above, the energy capacity of the PPS can be determined by

$$C_E = \frac{\Delta E_{max}}{C_p},$$ (15.5)
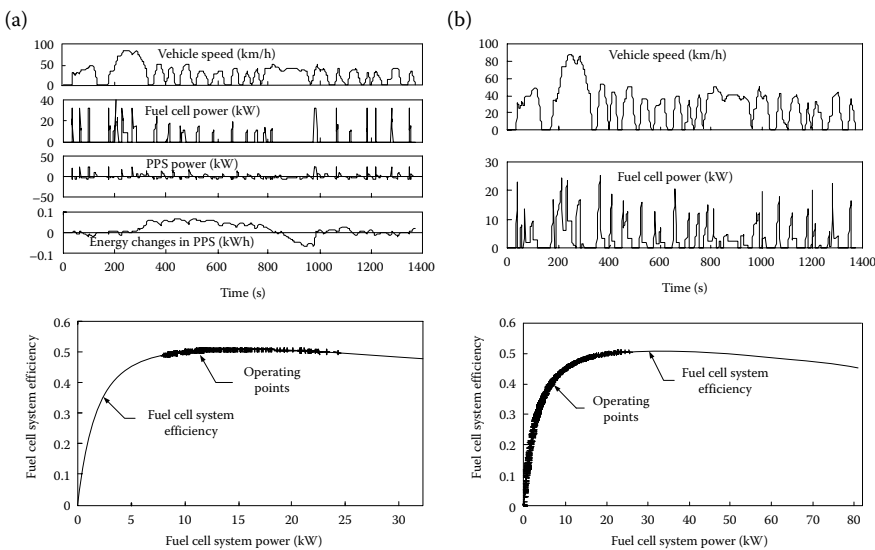
where C_E is the total energy capacity of the PPS and C_p is the percentage of the total energy capacity that is allowed to be used, according to the characteristics of the PPS.

15.4 Design Example
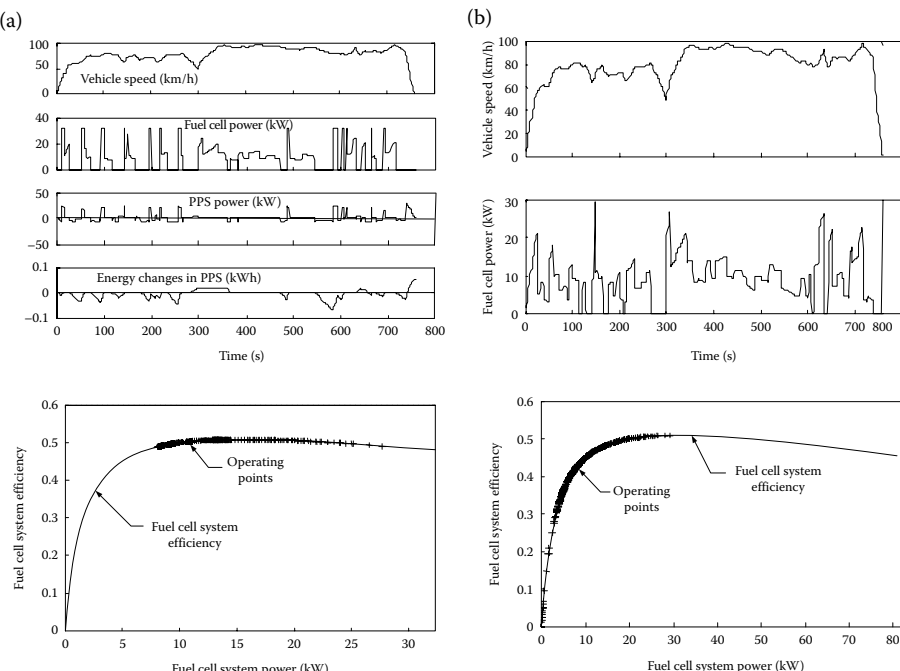
Using the design methodology developed in previous sections, a fuel-cell-powered hybrid drive train for a passenger car has been designed.[1] For

TABLE 15.1

Simulation Results for the 1500-kg Hybrid and Fuel-Cell-Alone-Powered Passenger Cars

	Hybrid	Fuel Cell
Vehicle mass (kg)	1500	1500
Rated motor power (kW)	70	70
Rated power of fuel cell system (kW)	40	83
Maximum power of PPS (kW)	43	—
Maximum energy storage in PPS (kWh)	1.5	—
Acceleration time (0–100 km/h or 60 mph) (s)	12	12
Gradeability (at 100 km/h or 60 mph) (%)	5	5
Fuel economy		
Constant speed, at 100 km/h or 60 mph	1.81 L/100 km or 130 mpg (gas. equi.) 0.475 kg H_2/100 km or 131 mile/kg H_2	1.91 L/100 km or 123 mpg (gas. equi.) 0.512 kg H_2/100 km or 124 mile/kg H_2
FTP75 urban driving cycle	2.93 L/100 km or 80 mpg (gas. equi.) 0.769 kg H_2/100 km or 80.4 mile/kg H_2	4.4 L/100 km or 53.4 mpg (gas. equi.) 1.155 kg H_2/100 km or 53.7 mile/kg H_2
FTP75 highway driving cycle	2.65 L/100 km or 88.7 mpg (gas. equi.) 0.695 kg H_2/100 km or 89.1 mile/kg H_2	2/9 L/100 km or 81 mpg (gas. equi.) 0.762 kgH_2/100 km or 81.4 mile/kg H_2

FIGURE 15.8 Operating simulation of the fuel cell hybrid and fuel-cell-alone-powered passenger car in an FTP75 urban drive cycle: (a) hybrid drive train and (b) fuel-cell-alone-powered drive train.

FIGURE 15.9 Operating simulation of the fuel cell hybrid and fuel-cell-alone-powered passenger car in an FTP75 highway drive cycle: (a) hybrid drive train and (b) fuel-cell-alone-powered drive train.

comparison, a fuel-cell-system-alone-powered passenger car with the same size has also been simulated. The simulation results are shown in Table 15.1 and Figures 15.8 and 15.9. The design and simulation results indicate that the hybrid vehicle has much higher fuel efficiency and the same performance, when compared with the fuel-cell-system-alone-powered vehicle.

References

1. Y. Gao and M. Ehsani, "Systematic design of FC powered hybrid vehicle drive trains," *Society of Automotive Engineers (SAE) Journal*, Paper No. 2001-01-2532, Warrendale, PA, 2001.
2. D. Tran, M. Cummins, E. Stamos, J. Buelow, and C. Mohrdieck, "Development of the Jeep Commander 2 FC hybrid electric vehicle," *Society of Automotive Engineers (SAE) Journal*, Paper No. 2001-01-2508, Warrendale, PA, 2001.
3. T. Simmons, P. Erickson, M. Heckwolf, and V. Roan, "The effects of start-up and shutdown of a FC transit bus on the drive cycle," *Society of Automotive Engineers (SAE) Journal*, Paper No. 2002-01-0101, Warrendale, PA, 2002.

16

Design of Series Hybrid Drive Train for Off-Road Vehicles

Off-road vehicles (military, agricultural, and construction) usually operate on unprepared ground and need to overcome very complex and difficult ground obstacles, such as steep grade and very soft ground. Depending on the functional requirements, different criteria are used to evaluate the performance of various types of off-road vehicles. For tractors, their main function is to provide adequate draft to pull various types of implement and machinery: drawbar performance is of primary interest. This may be characterized by the ratio of drawbar pull to vehicle weight, drawbar power, and drawbar efficiency. For off-road transport vehicles, the transport productivity and efficiency are often used as basic criteria for evaluating their performance. For military vehicles, the maximum feasible operating speed at two specific points in a given area may be employed as a criterion for evaluation of their agility.[1]

Although different criteria are used to evaluate the performance of different types of off-road vehicles, there is a common requirement for all: mobility over unprepared terrain. Mobility, in the broad sense, is concerned with performance of the vehicle in relation to soft terrain, obstacle negotiation and avoidance, ride quality over rough terrain, water crossing, and so on.

This chapter discusses the design principle of an off-road hybrid electric tracked vehicle, focusing on power ratings of the traction motor, engine/generator, and energy storage for satisfying specified vehicle performance indices, such as gradeability, acceleration, and steering on various types of ground. For drive train control, refer to Chapter 7.

16.1 Motion Resistance

In addition to aerodynamic drag, rolling distance caused by tire deformation, and track friction as discussed in Chapter 2, the motion resistance of an off-road vehicle mostly stems from significant deformation of the ground while a vehicle is moving on it. In off-road operations, various types of terrain with different characteristics, ranging from desert sand through deep mud

to snow, may be encountered. The mechanical properties of the terrain quite
often impose severe limitations on the mobility and performance of off-road
vehicles. The study of the relationship between the performance of an off-
road vehicle and its physical environment (terrain) has now become known
as "Terranmechanics."[1]

Although a study of "Terranmechanics" is beyond the scope of this book,
for proper design of a vehicle power train it is necessary to briefly introduce
some terranmechanics concepts, especially the motion resistance and thrust
that a terrain can support for off-road vehicle normal operation.

This section will briefly explain the calculation method of the tracked vehi-
cle motion resistance and thrust, accompanied by an example tracked vehicle.
For more details on wheeled vehicles, see Wong[1] and Bekker.[2–4]
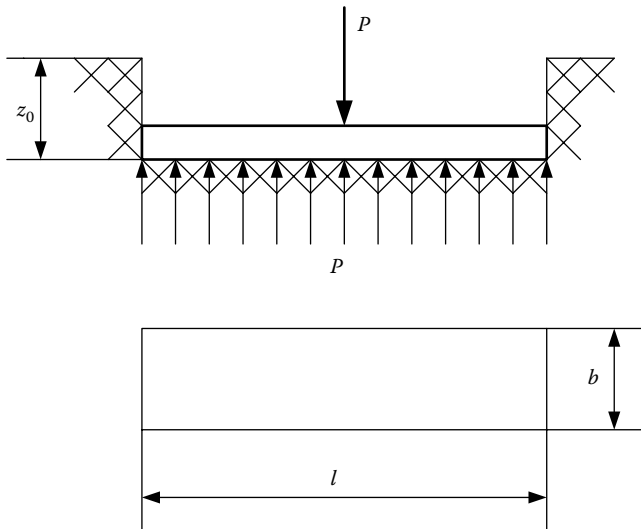
16.1.1   Motion Resistance Caused by Terrain Compaction

The motion resistance, supported by consuming vehicle energy, to compact
terrain is studied by using penetration tests as shown in Figure 16.1. A plate
is used to simulate the contact area of a track. A vertical load, P, is placed on
the plate, resulting in sinkage, z, and terrain reaction pressure, p.

The work done by the load P can be expressed as

$$W = bl \int_0^{z_0} p \, dz, \qquad (16.1)$$

where b and l are the plate dimensions of the short and long sides as shown
in Figure.16.1. The relationship between pressure, p, and sinkage, z, depends

FIGURE 16.1   Terrain penetration test.

on the terrain characteristic, which is determined by experiment and has the expression[1]

$$z = \left(\frac{p}{k_c/b + k_\phi} \right)^{1/n},$$ (16.2)

where k_c, $k_{\phi,g}$ and n are terrain parameters and b is the dimension of the shorter side of the plate. Parameter k_c reflects the cohesion characteristic and k_ϕ the internal friction characteristic of the terrain. Parameter n reflects the "hardness" of the terrain. The terrain has a linear characteristic when $n = 1$, a hard characteristic when $n < 1$, and a soft characteristic when $n > 1$. Typical terrain parameters are listed in Table 16.1.

Substituting for p from Equation 16.2 into Equation 16.1 yields

$$W_c = bl \left(\frac{k_c}{b} + k_\phi \right) \left(\frac{z_0^{n+1}}{n+1} \right).$$ (16.3)

The interaction between the track of a tracked vehicle and the terrain is similar to that between a plate and the terrain as shown in Figure 16.1. Using Equation 16.3, the vehicle motor resistance caused by terrain compaction can be expressed as

$$R_c = \frac{W_c}{l} = b \left(\frac{k_c}{b} + k_\phi \right) \left(\frac{z_0^{n+1}}{n+1} \right).$$ (16.4)

Example: A tracked vehicle with 196 kN gross weight and track dimensions of $l = 3.6$ m and $b = 1.0$ m is operating on the terrain with parameters $n = 1.6$, $k_c = 4.37$ kN/m$^{2.6}$, and $k_\phi = 196.73$ kN/m$^{3.6}$. The vehicle resistance caused by terrain compaction can be calculated as follows:

Pressure:

$$p = \frac{P}{bl} = \frac{196/2}{3.6 \times 1.0} = 27.2 \, \text{kN/m}^2.$$

Sinkage:

$$z_0 = \left(\frac{p}{k_c/b + k_\phi} \right)^{1/n} = \left(\frac{27.2}{4.37/1.0 + 196.73} \right)^{1/1.6} = 0.2864 \, \text{m}.$$

Motion resistance:

$$R_c = \frac{W_c}{l} = 2b \left(\frac{k_c}{b} + k_\phi \right) \left(\frac{z_0^{n+1}}{n+1} \right)$$

$$= 2 \times 1.0 \left(\frac{4.37}{1.0} + 196.73 \right) \left(\frac{0.2864^{2.6}}{2.6} \right) = 5.99 \, \text{kN}.$$

TABLE 16.1
Terrain Values

Terrain	Moisture Content (%)	n	k_c		k_p		c		ϕ (deg)
			lb/in.$^{n+1}$	kN/m$^{(n+1)}$	lb/in.$^{(n+2)}$	kN/m$^{(n+2)}$	lb/in.^{2}	kPa	
Dry sand [Land Locomotion Lab. (LLL)]	0	1.1	0.1	0.95	3.9	1528.43	0.15	1.04	28
Sand loam (LLL)	15	0.7	2.3	5.27	16.8	1515.04	0.25	1.72	29
	22	0.2	7	2.56	3	43.12	0.2	1.38	38
Sand loam Michigan (strong Buchele)	11	0.9	11	52.53	6	1127.97	0.7	4.83	20
Sandy loam (Hanamoto)	23	0.1	15	11.42	27	808.96	1.4	9.65	35
	26	0.3	5.3	2.79	6.8	141.11	2.0	13.79	22
	32	0.5	0.7	0.77	1.2	51.91	0.75	5.17	11
Clayey soil (Thailand)	38	0.5	12	13.91	16	692.15	0.6	4.14	13
	55	0.7	7	16.03	14	1262.53	0.3	2.07	10
Heavy clay [Waterways Experiment Station (WES)]	25	0.13	45	12.70	140	1555.95	10	68.95	31
Lean clay (WES)	10	0.11	7	1.81	10	103.27	3	20.69	6
	22	0.2	45	16.43	120	1724.69	10	68.95	20
	32	0.15	5	1.52	10	119.61	2	13.79	11
Snow (Harrison)		1.6	0.07	4.37	0.08	196.72	0.15	1.03	19.7
		1.6	0.04	2.49	0.10	245.90	0.09	0.62	23.2

16.1.2 Motion Resistance Caused by Terrain Bulldozing

Another motion resistance may exist, caused by bulldozing the soil in front of the vehicle track. This motion resistance is called bulldozing resistance. In this section, only the equations and diagrams are introduced for the purpose of calculating the bulldozing resistance.[1]

In predicting the bulldozing resistance, Bekker[2,3] suggested equations by assuming that it is equivalent to the horizontal force acting on a vertical blade:

$$R_b = b\left(cz_0 K_{pc} + 0.5z_0^2 \gamma_s K_{p\gamma}\right), \tag{16.5}$$

where b is the width of the track, c is the cohesion of the terrain (refer to Table 16.1), γ_s is the specific weight of the terrain, z_0 is sinkage, and

$$K_{pc} = (N_c - \tan\phi)\cos^2\phi$$

and

$$K_{p\gamma} = \left(\frac{2N_\gamma}{\tan\phi} + 1\right)\cos^2\phi.$$
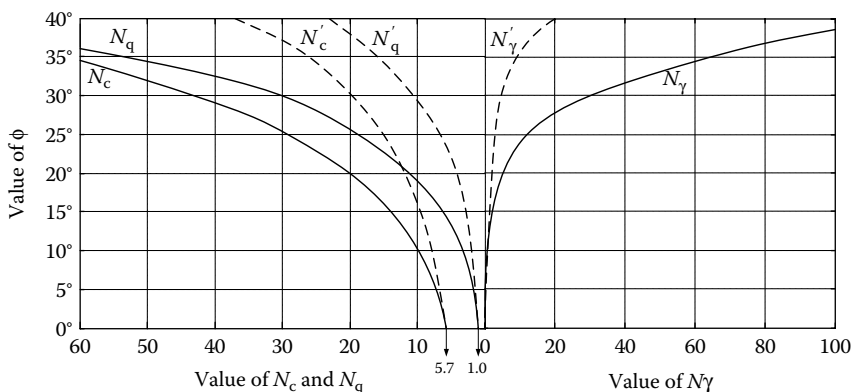
where, N_c and N_γ are the terrain's bearing capacity factors as shown in Figure 16.2, and ϕ is the angle of internal shearing resistance of the terrain. In soft terrain or loose soils, local failure in front of the wheel or track may be assumed, and the bulldozing resistance may be estimated using the following equation[1]:

$$R_b = b\left(0.67cz_0 K'_{pc} + 0.5z_0^2 \gamma_s K'_{p\gamma}\right), \tag{16.6}$$

where

$$K'_{pc} = \left(N'_c - \tan\phi'\right)\cos^2\phi'$$

FIGURE 16.2 Variation of terrain bearing capacity factors with angle of internal shearing resistance.[1]

and

$$K'_{p\gamma} = \left(\frac{2N'_\gamma}{\tan \phi'} + 1 \right) \cos^2 \phi'.$$

N'_c and N'_γ are bearing capacity factors for local shear failure shown in Figure 16.2, and $\tan \phi' = \frac{2}{3} \tan \phi$.

Example: The same vehicle as above is operating on the same terrain as shown in the example in Section 16.1.1, with $c = 1.0\,\text{kPa}$, internal shear angle $\phi = 19.7$, and $\gamma_s = 2646\,\text{N/m}^3$.

From Figure 16.2, for $\phi = 19.7$, $N'_c = 11.37$, and $N'_\gamma = 1.98$, then $K'_{pc} = 10.53$ and $K'_{p\gamma} = 16.64$. By Equation 16.6, $R_b = 7.79\,\text{kN}$ is obtained.

The total motion resistance, compacting and bulldozing terrain, is $R_{terr} = 5.99 + 7.79 = 13.78\,\text{kN}$. The resistance coefficient defined as the motion resistance per unit vehicle weight is $f_{terr} = 13.78/196 = 0.07$.

16.1.3 Internal Resistance of the Running Gear

For wheeled vehicles, the internal resistance of the running gear is mainly caused by the hysteresis of tire materials as discussed in Chapter 2. For tracked vehicles, the internal resistance of the track and the associated suspension system may be substantial. Frictional losses in track pins, driving sprockets and sprocket hubs, and road wheel bearing constitute the major portion of the internal resistance of the track and associated suspension system.[1]

Because of the complex nature of the internal resistance in the track and suspension system, it is difficult to establish an analytical procedure to predict the internal resistance with sufficient accuracy. As a first approximation, the following formula, proposed by Bekker, may be used for calculating the average value of the internal resistance, R_{in}, of a conventional tracked vehicle[1,4]:

$$R_{in} = W(222 + 3V), \tag{16.7}$$
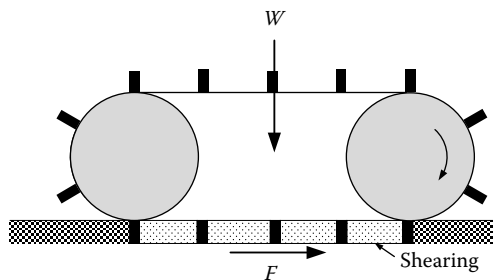
where R_{in} is in newtons, W is the vehicle weight in tons, and V is the vehicle speed in km/h.

For modern lightweight tracked vehicles, the internal resistance may be less and the empirical formula is[1,4]

$$R_{in} = W(133 + 2.5\,V). \tag{16.8}$$

16.1.4 Tractive Effort of a Terrain

The tractive effort of a track is produced by the shearing of the terrain as in Figure 16.3. The maximum tractive effort, $F_{t,max}$, that can be developed

FIGURE 16.3 Shearing action of a track.

by a track is determined by the shear strength of the terrain, which can be expressed by[1]

$$F_{t,max} = Ac + W \tan \phi, \tag{16.9}$$

where W and A are the vertical load and contact area of the track to the ground, respectively, and c and ϕ are the apparent cohesion and angle of internal shearing resistance of the terrain, respectively. Their typical values are shown in Table 16.1.

When the vehicle motion resistance is greater than the maximum tractive effort that the terrain can develop, complete skidding will occur if the torque developed by the mover is large enough, and the vehicle cannot move.

For the example vehicle in Sections 16.1.2 and 16.1.3, the terrain parameters are $c = 1.0 \, \text{kPa}$, internal shear angle $\phi = 19.7$, $W = 196 \, \text{kN}$, and $A = 2 \times l \times B = 7.2 \, \text{m}^2$. The maximum tractive effort is

$$F_{t,max} = Ac + W \tan \phi = 7.2 + 196 \times \tan 19.7° = 77.4 \, \text{kN}.$$

16.1.5 Drawbar Pull

For off-road vehicles designed for traction (i.e., tractors), drawbar performance is of prime importance, as it stands for the ability of the vehicle to pull or push various types of working machinery, including implements and construction and earthmoving equipment. Drawbar pull, F_d, is the force available at the drawbar and is equal to the difference between the tractive effort and the total resistance $\sum R$. That is,

$$F_d = F_t - \sum R. \tag{16.10}$$
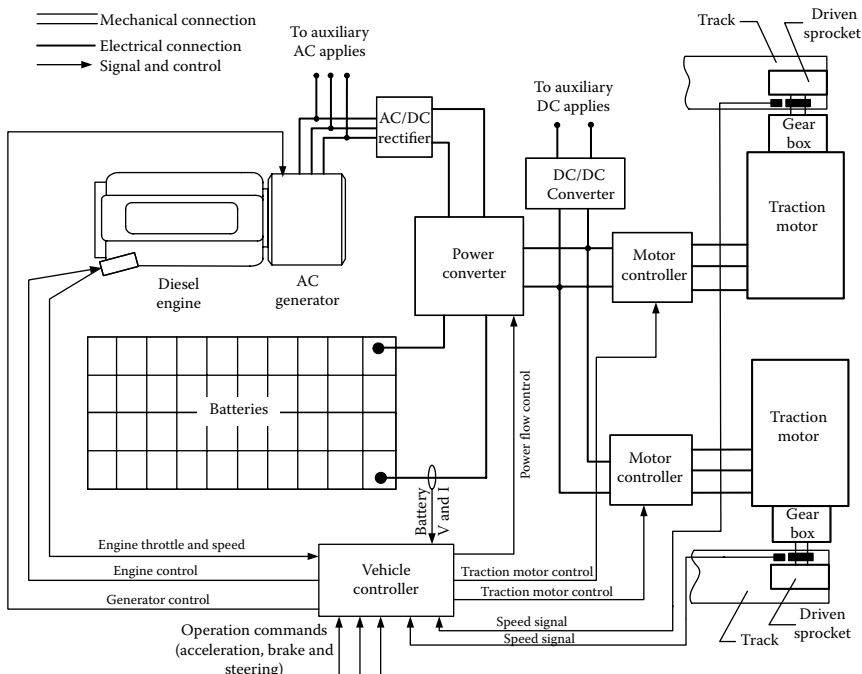
The tractive effort, F_t, may be determined by the power plant and transmission of the vehicle on a strong terrain, for example, a paved road, or by the maximum thrust that the terrain can support on a soft terrain as discussed in Section 16.1.4. Because this book focuses on transportation vehicles, drawbar performance will not be discussed further. However, the principles

developed in this book can be directly applied to the analysis of vehicle drawbar performance.

16.2 Tracked Series Hybrid Vehicle Drive Train Architecture

A tracked series hybrid off-road vehicle drive train mainly contains subsystems of a primary power source, a secondary power source, traction motors and their controllers, a power converter, and a vehicle controller, as shown in Figure 16.4.

Primary power source: The primary power source, generally a diesel engine and a generator, is used to provide power to meet the average power demand of the load. The diesel engine drives the generator to generate electricity to charge the secondary power source and the batteries/ultracapacitors. Or, it directly provides power to the electric motor drives. The generator generates AC power. The nontraction AC power devices may be directly connected to the output of the generator through transformers if the voltages of the AC devices are different from the output voltage of the generator. An AC/DC converter (rectifier) is used to convert the AC power into DC power.

FIGURE 16.4   Tracked series hybrid off-road vehicle architecture.

Secondary power source: The secondary power source, generally a battery/ultracapacitor, is used to supply peaking power to the traction motor drives to meet the peak power demand of the load. The secondary power source can be charged from the primary power source and/or the regenerative braking in which the motor functions as a generator to convert all or part of the braking power of the vehicle into electrical power to charge the secondary power source. In normal operation, the total output energy from the secondary power source should be equal to the total charging energy over the mission period. Furthermore, the charging rate should be controlled to be in an acceptable range.

Traction motors and controllers: The traction motors deliver their torque to the sprockets through transmissions to propel the vehicle. The motor drives are powered by the primary and/or secondary power sources and controlled by their controllers to provide correct torques and speeds that meet the maneuver requirements, according to the commands of the driver. These maneuvers include acceleration, deceleration, forward and reverse moving, and steering.

Power converter: The power converter is an assembly of controllable power electronics. It is used to control the power flow between the primary power source, the secondary power source, and the motor drives. All of the operation modes of the drive train are implemented by controlling the power converter. The operation modes of the drive train mainly include engine/generator-alone powered operation, batteries/ultracapacitors-alone powered operation, both engine/generator and batteries/ultracapacitors powered operation (hybrid traction), regenerative braking operation, and batteries/ultracapacitors charging operation. The various architectures of the power converter have been discussed in Chapter 7.

Vehicle controller: The vehicle controller is the highest-level, microprocessor-based system controller. The vehicle controller receives operation commands from the driver (acceleration, deceleration, forward or reverse moving, steering, etc.) and drive train real-time operating information, such as vehicle speed, and component real-time operating information, such as the voltages and currents of batteries/ultracapacitors, engine throttle position, speed, etc. Based on all the information received and the control strategy (software code stored in the vehicle controller), the vehicle controller will generate the necessary control signals and send them to the components (engine/generator, power converter, motor drives, etc.). The components follow the control commands of the vehicle controller.

16.3 Parametric Design of the Drive Train

The parametric design of the drive train mainly includes traction motor power design, engine/generator power design, and energy storage (battery/ultracapacitor) power and energy design.

16.3.1   Traction Motor Power Design
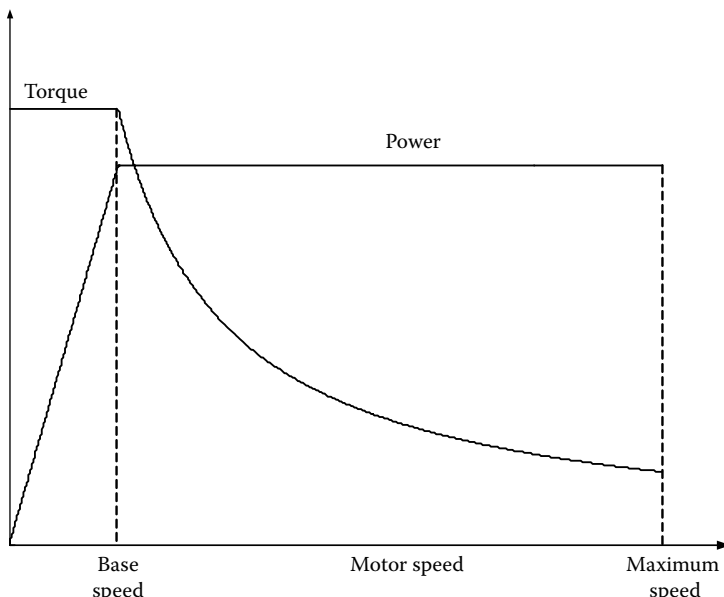
In motor power design, the acceleration performance, maximum gradeability, and steering are the highest considerations.

16.3.1.1   *Vehicle Thrust versus Speed*
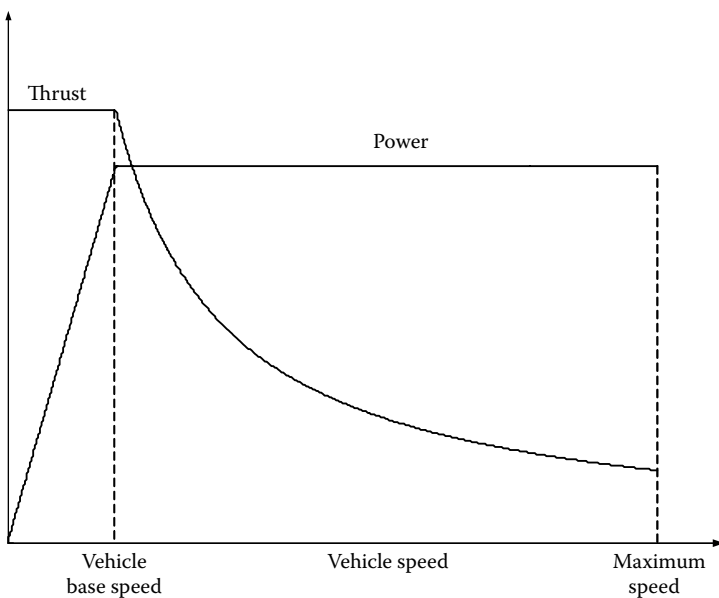
A well-controlled traction motor usually has the torque and power characteristics of constant torque in the low-speed range and constant power in the high-speed range, as shown in Figure 16.5. The corner speed is referred to as the base speed. In traction motor design, two important parameters, maximum power and extended speed ratio x, which is defined as the ratio of its maximum speed to its base speed, must be determined first. For a given power rating, that is, power in the constant power range, motor torque is expressed as

$$T_{\mathrm{m}} = \frac{30P_{\mathrm{m}}}{\pi n_{\mathrm{mb}}}, \quad n_{\mathrm{m}} \leq n_{\mathrm{mb}}$$

$$= \frac{30P_{\mathrm{m}}}{\pi n_{\mathrm{m}}}, \quad n_{\mathrm{m}} > n_{\mathrm{mb}}, \quad\quad\quad (16.11)$$

where P_{m} is the motor power rating defined above, n_{mb} is the motor base speed (rpm) as shown in Figure 16.5, and n_{m} is the motor speed (rpm) varying from zero to its maximum.

FIGURE 16.5   Typical torque and power profiles of traction motor versus motor speed.

FIGURE 16.6 Typical thrust and power profiles versus vehicle speed with an electric motor as its mover.

The motor torque and power profiles can be translated into the thrust of the vehicle versus vehicle speed by

$$F_t = \frac{T_m \eta_t i_g}{r} \tag{16.12}$$

and

$$V = \frac{\pi n_m r}{30 i_g}, \tag{16.13}$$

where η_t and i_g are the transmission efficiency and gear ratio from the traction motor to the driving sprockets, and r is the radius of driving sprockets. The transmission may be single gear or multigear (for more details, see Chapter 4). The typical thrust and power profiles are illustrated in Figure 16.6. The motor power design given below is based on these profiles.

16.3.1.2 Motor Power and Acceleration Performance

The motor power required by the acceleration performance includes the power for overcoming various mechanical resistances (losses in the locomotive mechanism as described by Equations 16.7 and 16.8, losses caused by road deformation as discussed in Section 16.1, and aerodynamic drag) and

TABLE 16.2

Vehicle Parameter Values

M	20,000 kg
t_a	8 s
V_f	48 km/h (30 mph)
C	0.0138[a]
D	0.000918[a]
C_D	1.17
A_f	6.91 m^2

[a] c and d correspond to the constants of 133 and 2.5 with vehicle weight in newtons and V in m/s.

the power for accelerating vehicle mass (inertial resistance). On a hard surface road, the loss due to road deformation is negligible, and the motor power for acceleration can be expressed as

$$P_{acc} = \frac{M}{2t_a}\left(V_b^2 + V_f^2\right) + MV_f\left(\frac{2}{3}c + \frac{1}{2}dV_f\right) + \frac{1}{5}\rho_aC_DA_fV_f^3 (\text{W}), \qquad (16.14)$$

where M is the vehicle mass in kg, t_a is the time in seconds for accelerating the vehicle from zero speed to a specified final speed, V_f, V_b is the base speed in m/s, as shown in Figure 16.6, ρ_a is the air mass density in kg/m^3, C_D is the coefficient of aerodynamic drag, A_f is the front area of the vehicle in m^2, and c and d are constants, representing the constant term and the term proportional to the vehicle speed of the resistance of the locomotive mechanism as described in Equation 16.8. The resistance coefficient is expressed as $f_r = c + dV$. The vehicle parameters used in the motor power design are shown in Table 16.2.
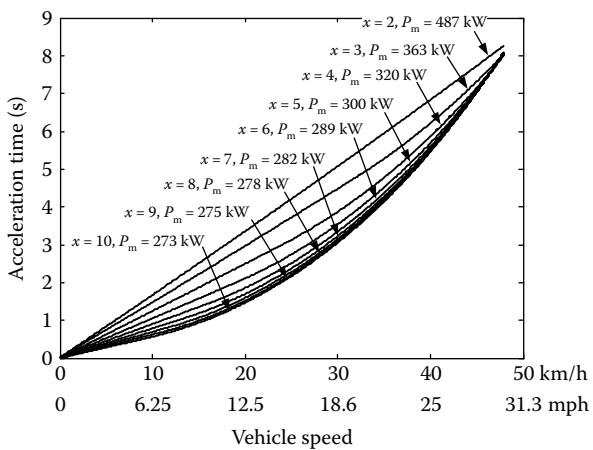
The motor powers required for acceleration performance (8 s from 0 to 48 km/h [30 mph]) with different extended speed ratios, x, of the thrust are shown in Figure 16.7. It can be seen that the motor power decreases with increasing extended speed ratio, x. However, when $x \geq 6$, further decrease in the motor power is not significant with further increase in the extended speed ratio, x.

16.3.1.3 Motor Power and Gradeability

The motor power requirement in an uphill operation can be expressed as

$$P_{grade} = \left(Mgf_r + \frac{1}{2}\rho_aC_DA_fV^2 + Mg\sin\alpha\right)V (\text{W}), \qquad (16.15)$$

where α is the slope angle of the road and V is the vehicle speed specified by the gradeability. When the vehicle is climbing its maximum slope (60%) in
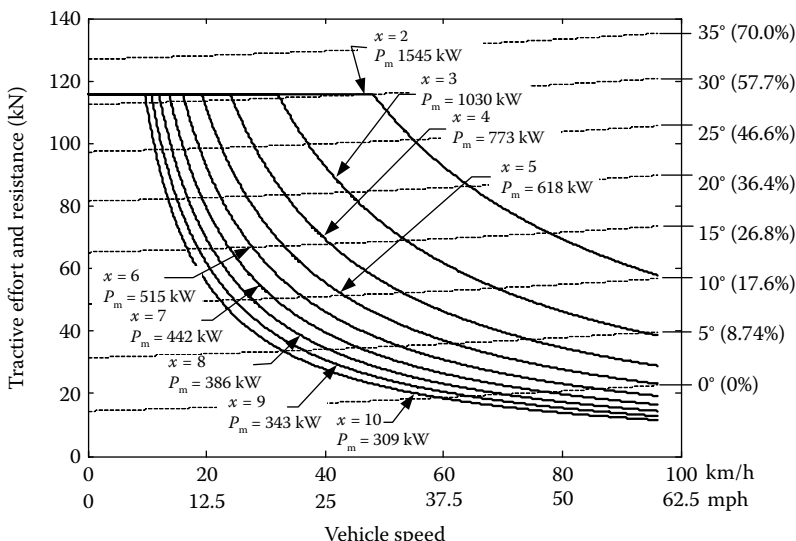
FIGURE 16.7 Motor power required by acceleration performance with different extended speed ratios, x.

real operation, the ground surface is usually unprepared and thus resistance is much larger than on prepared roads. Therefore, in the calculation of motor power required by gradeability, additional resistance should be included to reflect this situation. The resistance due to terrain deformation can be obtained as discussed in Section 16.1. In the following sections, 0.06 of additional resistance coefficient is introduced (snow or sandy loam with about 21% moisture content).[5,6]

Based on the specified gradeability, for example 60%, the tractive effort profiles versus vehicle speed with different extended speed ratios and motor powers are shown in Figure 16.8. It can be seen that with the same gradeability, a larger extended speed ratio, x, will result in smaller motor power demand.
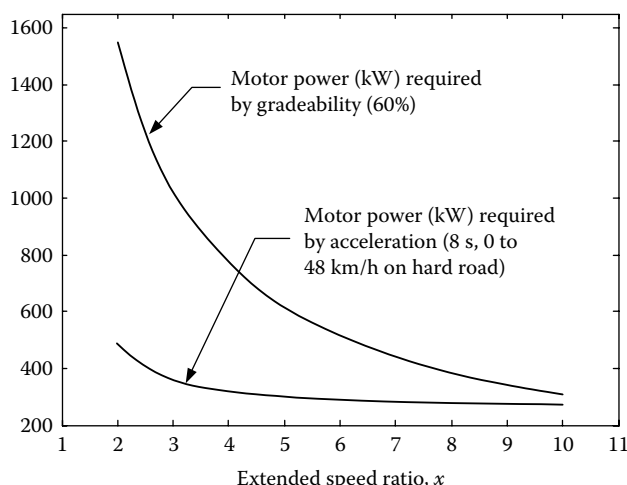
Figure 16.9 summarizes the motor power demand by acceleration and gradeability performances along with the extended speed ratio, x, of the motor drive. It can be clearly seen that the motor power required by gradeability is larger than the motor power required by acceleration, especially with a small x.

The above analysis indicates that one of the effective approaches for reducing the motor power rating is to increase the extended speed ratio. However, the extended speed ratio of the motor drive is closely and naturally related to motor type. PM motor drives have very small x, usually less than 2, due to their rather limited field weakening capability.[7] To keep the power of the motor drive in a reasonable range and meet the gradeability requirement, they will need a multigear transmission with three or four gears. A common induction motor with speed adjustment control usually has an extended speed ratio of 2. Nevertheless, a properly designed induction motor, for example a spindle motor, with field orientation control can achieve field weakening in the range

FIGURE 16.8   Tractive effort versus vehicle speed with different x and motor power.

of about 3–5 times its base speed.[8–11] Even with this special design, a double-gear transmission is still needed. An SRM drive can inherently operate with extremely long constant power range. Both 6–4 and 8–6 SRMs can reach 6–8[12]; thus a single-gear transmission would serve this requirement.

FIGURE 16.9   Motor power required by acceleration and gradeability along with extended speed ratios, x.

16.3.1.4 Steering Maneuver of a Tracked Vehicle
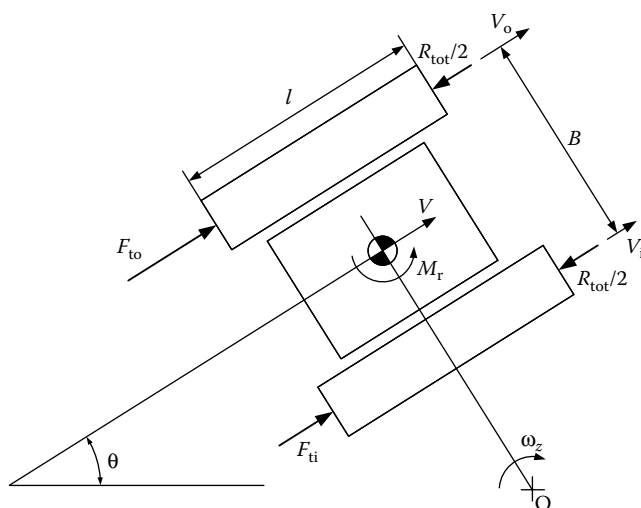
Steering maneuver of a tracked vehicle is quite different from that of wheeled vehicles. There are a number of possible methods that can accomplish the steering of a tracked vehicle. These include skid-steering, steering by articulation in multibody vehicles, and curved track steering. For single-body vehicles, skid-steering is the common method. In this book, only skid-steering is discussed, which is closely related to the thrusts on both side tracks. For other steering methods, readers are refered to Wong.[1]

In skid-steering, the thrust of one track is increased and that of the other is reduced, so as to create a turning moment to overcome the moment of resistance due to the skidding of the track on the ground and the rotational inertia of the vehicle. Since the moment of the turning resistance is usually considerable, significantly more power may be required during a turn than in straight line motion.[1]

The turning behavior of a tracked vehicle using skid-steering depends on the thrusts of the outside and inside tracks, F_{to} and F_{ti}, the resultant resisting force, R_{tot}, the moment of turning resistance, M_r, exerted on the track by the ground, and vehicle parameters as shown in Figure 16.10. At low speeds on level ground, the centrifugal force may be neglected, and the behavior of the vehicle can be described by the following motion equations:

$$M\frac{dV}{dt} = F_{to} + F_{ti} - R_{tot}, \tag{16.16}$$

$$I_z\frac{d\omega_z}{dt} = \frac{B}{2}(F_{to} - F_{ti}) - M_r, \tag{16.17}$$

FIGURE 16.10 Skid steering behavior.

where I_z is the moment of inertia of the vehicle about the vertical axis passing through its center of gravity and ω_z is the turning angle velocity of the vehicle.

At low speeds and under steady-state conditions with zero linear and angular acceleration, that is, $dV/dt = 0$ and $d\omega_z/dt = 0$, the thrusts of the outside and inside tracks can be expressed as

$$F_{to} = \frac{R_{tot}}{2} + \frac{M_r}{B} = \frac{Mgf_r}{2} + \frac{M_r}{B}, \tag{16.18}$$
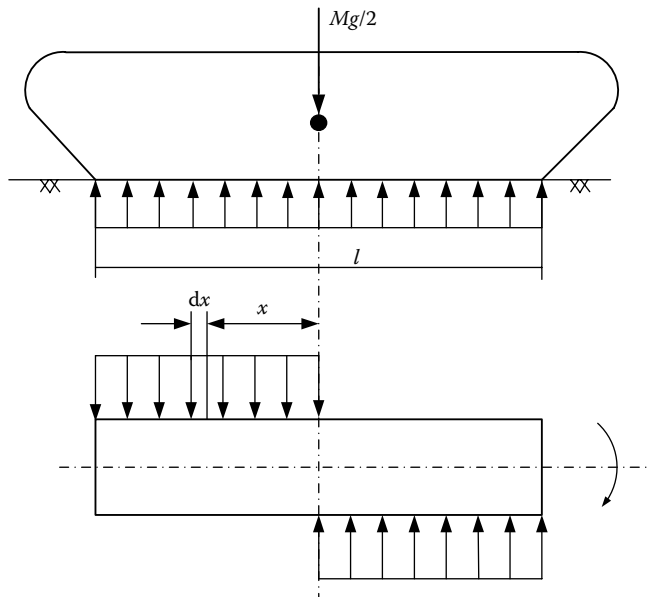
$$F_{ti} = \frac{R_{tot}}{2} - \frac{M_r}{B} = \frac{Mgf_r}{2} - \frac{M_r}{B}, \tag{16.19}$$

where M and g are the vehicle mass and the acceleration of gravity, respectively, and f_r is the resistance coefficient due to ground deformation.

The moment of turning resistance, M_r, can be determined experimentally or analytically. If the normal pressure is assumed to be uniformly distributed along the track, the lateral resistance per unit length of the track, R_l, can be expressed by

$$R_l = \frac{\mu_t Mg}{2l}, \tag{16.20}$$

where μ_t is the coefficient of lateral resistance and l is the contact length of the track as shown in Figure 16.11. The value of μ_t depends not only on the terrain, but also on the design of the track. Over soft terrain, the vehicle sinks

FIGURE 16.11 Moment of turning resistance of a track.

TABLE 16.3

Values of Lateral Resistance of Tracks Over Various Surfaces

Track Materials	Coefficient of Lateral Resistance, μ_t		
	Concrete	Hard Ground (not Paved)	Grass
Steel	0.50–0.51	0.55–0.85	0.87–1.11
Rubber	0.09–0.91	0.65–0.66	0.67–1.14

Source: J. W. Wong, *Theory of Ground Vehicle,* John Wiley & Sons, New York, 1978.

into the ground and the tracks together with the grousers will be sliding on the surface as well as displacing the soil laterally during steering. The lateral force acting on the track and grousers due to displacing the soil laterally forms part of the lateral resistance. Table 16.3 shows the values of μ_t for steel and rubber tracks over various types of ground.[1]

By referring to Figure 16.11, the resultant moment of the lateral resistance about the center of the two tracks (i.e., moment of turning resistance) can be determined by

$$M_r = 4 \int_0^{l/2} R_l x \, dx = 4 \frac{Mg\mu_t}{2l} \int_0^{l/2} x \, dx = \frac{Mgl\mu_t}{4}. \tag{16.21}$$

Accordingly, Equations 16.18 and 16.19 can be rewritten as

$$F_{to} = \frac{Mg}{2} \left(f_r + \frac{l\mu_t}{2B} \right), \tag{16.22}$$

$$F_{ti} = \frac{Mg}{2} \left(f_r - \frac{l\mu_t}{2B} \right). \tag{16.23}$$

From Equation 16.23, it can be seen that if $l\mu_t/2B > f_r$, the thrust of the inside track, F_{ti}, will be negative. This implies that to achieve a steady state, a conventional vehicle with a diesel engine as its mover must apply a braking force on the inside track. In a series hybrid drive train, as shown in Figure 16.3, the inside track motor can apply a negative torque (regenerative braking) to this track.
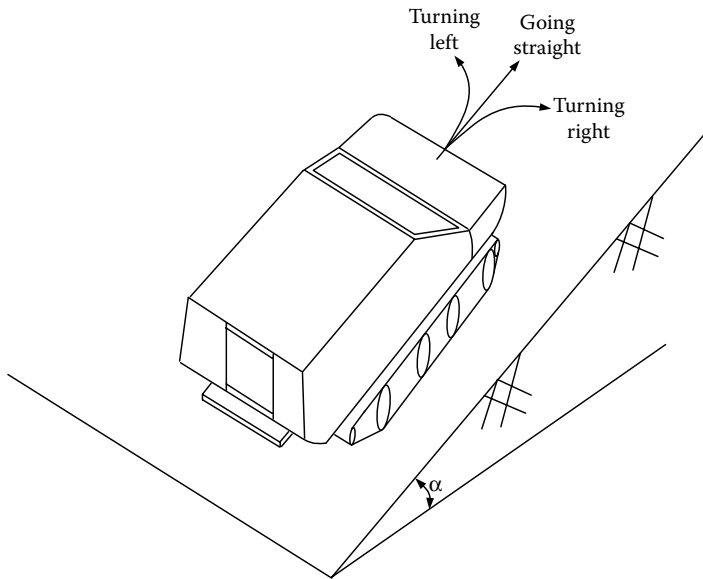
Referring to the maximum terrain tractive effort and for normal operation and steerability, the thrust of the outside track should be smaller than the maximum terrain tractive effort, that is,

$$F_{to} \leq cbl + \frac{Mg \tan \phi}{2}, \tag{16.24}$$

$$\frac{l}{B} \leq \frac{1}{\mu_r} \left(\frac{4cA}{Mg} + 2 \tan \phi - 2f_r \right), \tag{16.25}$$

or

$$\frac{l}{B} \leq \frac{2}{\mu_r} \left(\frac{c}{p} + \tan \phi - f_r \right), \tag{16.26}$$

FIGURE 16.12   A vehicle going straight and steering on a slope ground.
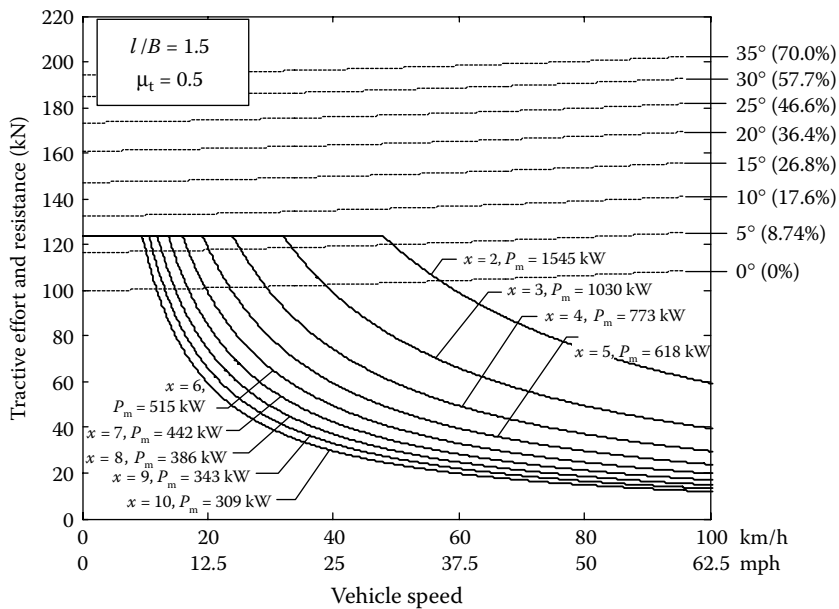
where A is the contact area of the track ($A = b \times l$) and p is the normal pressure, which is equal to $Mg/2A$.

From Equation 16.22, it can be seen that, in addition to overcoming motion resistance, the motor drive of the outside track has to produce additional thrust to overcome the turning resistance. The most difficult situation is steering on a slope as shown in Figure 16.12. In this case, the traction motor of the outside track has to produce a large traction torque to overcome terrain resistance, grade resistance, and steering resistance. The total resistance of the vehicle, in this case, can be expressed by

$$R_o = Mg \left(f_r + \frac{l\mu_t}{2B} \right) + \frac{1}{2}\rho_a C_D A_f V^2 + Mg \sin a, \qquad (16.27)$$

where f_r is the resistance coefficient that includes the internal resistance of the track and resistance caused by terrain deformation.

Figure 16.13 shows vehicle resistance that includes motion resistance, aerodynamic drag, grade resistance, and steering resistance as expressed in Equation 16.27. The thrusts produced by the electric motors have the same powers as shown in Figure 16.8 (e.g., straight line on 60% slope ground) and different extended speed ratios, x. Since significant steering resistance is involved, the ground grade, on which the vehicle can operate, is greatly reduced. In motor and transmission design, this situation should be taken into consideration.
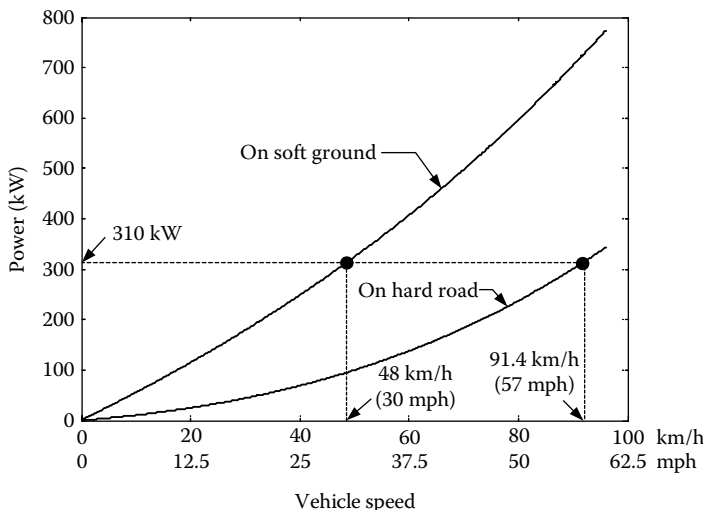
FIGURE 16.13 Vehicle gradeability with steering versus vehicle speed with respect to various x and motor powers.

16.4 Engine/Generator Power Design

The engine/generator power should be designed to meet the requirements of constant speed operation at high speed (near its maximum speed) on hard surface roads, and medium speed on soft surface roads for long distance trips, and also be larger than the average power at variable speed (driving cycle) in order to prevent the energy storage from being fully discharged during the mission. The engine/generator unit also needs to produce additional power to support the nontraction, continuous power, such as communication, lights, hotel loads, reconnaissance, and the auxiliaries (coolant circulation, cooling fans, etc.). The peaking powers required by acceleration, hill climbing, steering, and high-magnitude pulsed power needed by nontraction devices are provided by the PPS: batteries or a combination of batteries and ultracapacitors.

Due to the absence of sufficient information about variable speed operation (driving cycle) for off-road vehicles, the engine/generator power design will be based on the constant speed operation on hard roads and soft grounds and can be expressed by

$$P_{\mathrm{m/g}} = \eta_{\mathrm{t}}\eta_{\mathrm{m}}\left(Mgf_{\mathrm{r}} + \frac{1}{2}\rho_{\mathrm{a}}C_{\mathrm{D}}A_{\mathrm{f}}V^2\right)V, \tag{16.28}$$

FIGURE 16.14   Traction power on hard road and soft ground at constant speeds.

where η_t and η_m are transmission efficiency and motor drive efficiency, respectively. On hard roads, the resistance coefficient, f_r, includes only the internal resistance of run gear, which is described by $c + dV$ as shown in Table 16.2, and no road deformation loss. However, on soft roads, an additional resistance coefficient of 0.06 caused by ground deformation is added. Using the parameters shown in Table 16.2 and assuming the total efficiency of converters and electric motor drives as 0.85, the traction powers of the engine/generator versus vehicle speeds on soft and hard surfaces are shown in Figure 16.14.

The engine/generator unit needs to produce additional power to support nontraction continuous loads, such as communications, lights, hotel loads, reconnaissance, and the auxiliaries (coolant circulation, cooling fans, etc.). Due to the lack of accurate data from the nontraction loads for off-road vehicles, we take civilian vehicles as reference. The nontraction continuous power may be estimated as 40–50 kW. Thus, the total engine/generator power is designed around 350 kW.

It should be noted that the power of the engine/generator, designed above, is the maximum power. In real-time operation, this power may be smaller, depending on the real operation conditions and the overall drive train control strategy.

16.5   Power and Energy Design of Energy Storage

Batteries or a combination of batteries and ultracapacitors are commonly employed as the energy storage for providing peaking power to the drive

train. Peaking power can be divided into traction power and nontraction power. Traction power for peaking operation mainly includes the power in acceleration, hill climbing, and steering, and nontraction power mainly includes the power needed, for example, by high-power detection devices and electric weapon systems in military vehicles.[5,6]

16.5.1 Peaking Power for Traction

In high-power traction, the drive train is powered by both the engine/generator and batteries/ultracapacitors, and the maximum power is constrained by the designed maximum power of the traction motors as previously specified. Thus, the traction peaking power for batteries/ultracapacitors is

$$P_b = \frac{P_{m,max}}{\eta_m} - P_{e/g}, \tag{16.29}$$
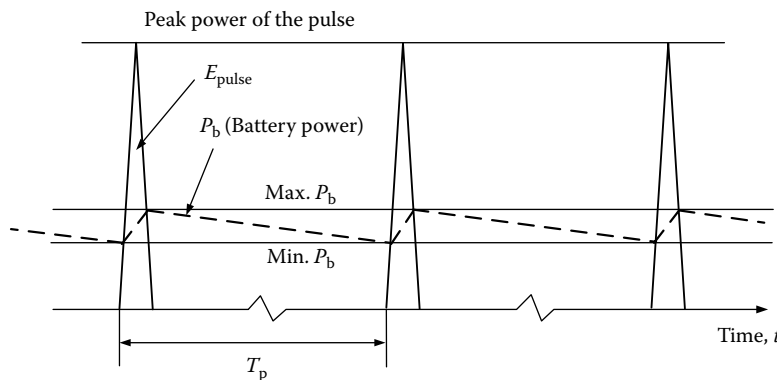
where $P_{m,maxr}$ and η_m are the maximum output power and efficiency of the motor drives, respectively, and $P_{e/g}$ is the engine/generator output power. It should be noted that in acceleration and hill climbing operations, the engine is not called upon to always operate at its maximum power, due to efficiency concerns. Suppose, in the example vehicle above, the traction motor drives have an efficiency of 0.85; the batteries/ultracapacitors power for traction is then around 375 kW (515/0.85–230), where the engine/generator is delivering 230 kW of power to the traction motor (75% of maximum traction power of the engine/generator [310 kW]).

16.5.2 Peaking Power for Nontraction

It is hard to accurately estimate the magnitude of the nontraction peaking power. In military vehicles, the most significant nontraction pulsed loads may be presented by "electric weapon" systems, for example, lasers, electrothermal chemical guns, electromagnetic armor, high-power microwaves, and so on. The magnitude of the required pulsed power may reach 1 GW (10^9 W) for a very short time period (10^{-3} s). It is clear that the on-board batteries/ultracapacitors cannot supply this huge pulsed power, due to their internal impedances. Thus, a pulse forming system that mainly consists of capacitors, inductors, and resistors is needed. This system can be charged from the main DC bus and can then discharge its energy to the pulsed load with a huge power for a short time. Figure 16.15 conceptually illustrates the time profiles of the pulsed power and the battery/ultracapacitor power, which may be expressed as

$$\frac{1}{2\varepsilon} t_p (P_{b,max} + P_{b,min}) = E_{pulse}. \tag{16.30}$$
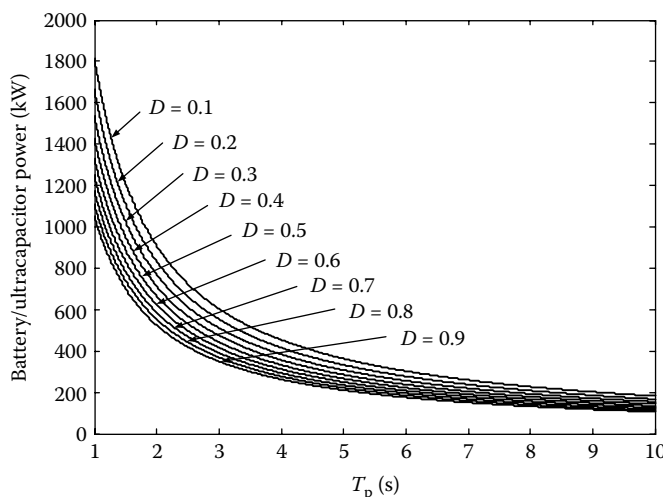
FIGURE 16.15   Conceptual illustration of the time profiles of pulsed power and battery power.

Thus,
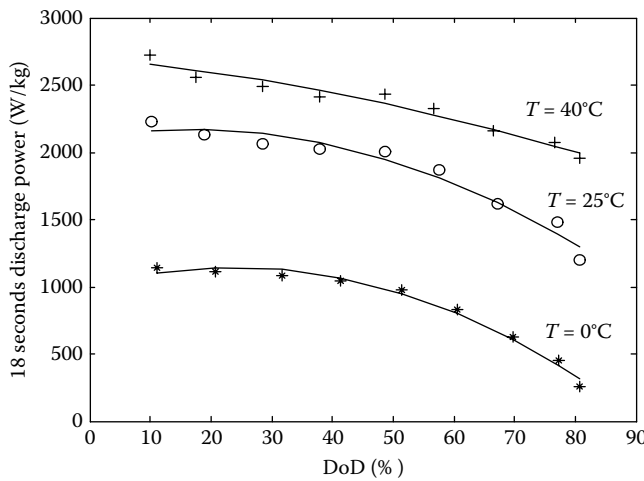
$$P_{b,max} = \frac{2E_{pulse}}{t_p(1+D)},\qquad(16.31)$$

where $D = P_{b,max}/P_{b,min}$ is the charging power ratio and T_p is the period of the pulsed power load.

Figure 16.16 illustrates the battery/ultracapacitor power for the pulsed power load, varying with the charging power ratio D, and the period of the pulsed power load, T_p. In this design, $T_p = 4\,s$ and $D = 0.6$ would be a good estimate. Thus the maximum battery/ultracapacitor power will be around

FIGURE 16.16   Peaking power of the batteries for pulsed power load varying with D and T_p.

FIGURE 16.17 Eight-second discharge power of the SAFT Li-ion batteries at different operation temperatures and DoD.

300 kW. Adding this to the traction power, the total power requirement is estimated around 675 kW.

It should be noted that the battery/ultracapacitor power capacity must be maintained above the designed value for a certain period of time to support the peaking power operation. For traction power demand, this time period is required by acceleration, hill climbing, obstacle negotiation, and steering and may be over 20–30 s. For nontraction peaking power demand, it is dependent on the mission requirements.

Figure 16.17 shows the discharging power characteristics, in 18 s, of the Li-ion batteries provided by SAFT America and tested by CHPS (Combat Hybrid Power System sponsored by TACOM). It indicates that the battery power is very dependent on temperature and DoD. Table 16.4 gives the

TABLE 16.4

Major Parameters of CHPS Battery Alternatives at Standard Testing

CHPS Battery Alternative	Specific Energy (Wh/kg)	Specific Power (Wh/kg)	Energy Density (Wh/L)
Lead acid	28	75	73
Ni–Cd	50	120	80
Ni–MH	64	140	135
Li-ion (high energy)	144	700	308
Li-ion (CHPS)	100	1000[a]	214
Li-ion (high power)	80	1400[a]	150

[a] Power capabilities depends on pulse length and temperature.

specific power, specific energy, and energy density of the CHPS battery alternatives at standard testing. In this design, 1000 W/kg of specific power and 100 Wh/kg of specific energy would be a good estimate.

16.5.3 Energy Design of Batteries/Ultracapacitors

The energy requirements for batteries/ultracapacitors depend on the specific mission requirements, for example the required time for stealth operation, silent watch, "electric weapon" operation, and so on. However, when the power capacity is determined, the energy capacity of the batteries can be obtained from the energy/power ratio of the selected batteries.

As mentioned above, the battery power demand is around 675 kW and the energy/power ratio of Li-ion battery is 0.1 h (specific energy/specific power). Thus, 67.5 kWh of energy capacity is obtained. The battery weight is around 675 kg.

16.5.4 Combination of Batteries and Ultracapacitors

In addition to batteries, ultracapacitors are another possible PPS. Compared with batteries, ultracapacitors have some advantages, such as 2–3 times the specific power density of Li-ion batteries (see Tables 16.4 and 16.5), wide temperature adaptability, high efficiency (low resistance), and fast response to charging and discharging. Hence, it may be a good selection as a pulsed power source. However, the ultracapacitor has the major disadvantage of a low specific energy density of less than 5°W/kg. It cannot sustain its power for more than a couple of minutes. Thus, it is difficult for ultracapacitors alone to supply the peaking power for a vehicle.

TABLE 16.5

Technical Specifications of Maxwell MBOD 0115 Ultracapacitor Module

Capacitance		145 Faradays ($-20\%/+20\%$)
Max. series resistance ESR	25 C	10 mohm
Specific power density	42 V	2900 W/kg
Voltage	Continuous	42 V
	Peak	50 V
Max. current		600 A
Dimensions	(Reference only)	$195 \times 265 \times 415$ mm
Weight		16 kg
Volume		22 L
Temperature[a]	Operating	$-35°C$ to $65°C$
	Storage	$-35°C$ to $65°C$
Leakage current	12 h, 25°C	10 mA

Source: Available at http://www.maxwell.com, Maxwell Technologies.
[a] Steady-state temperature.

A good design for the PPS of a hybrid vehicle may be to combine Li-ion batteries and ultracapacitors to constitute a hybrid energy storage, in which the batteries supply the energy and the ultracapacitors supply the power.[6] The combination of batteries and ultracapacitors meets the power and energy requirements, that is,

$$P_{tot} = W_b P_b + W_c P_c, \tag{16.32}$$
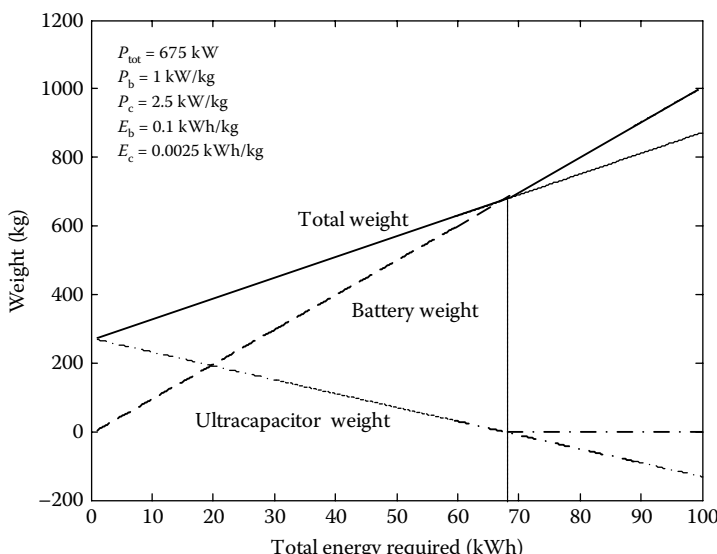
$$E_{tot} = W_b E_b + W_c E_c, \tag{16.33}$$

where P_{tot} and E_{tot} are the total power and energy required, W_b and W_c are the weights of the battery and the ultracapacitor, P_b and P_c are the specific powers of the battery and the ultracapacitor, and E_b and E_c are the specific energies of the battery and the ultracapacitor. For a given P_{tot}, E_{tot}, P_b, P_c, E_b, and E_c, the battery and ultracapacitor weights can be obtained as
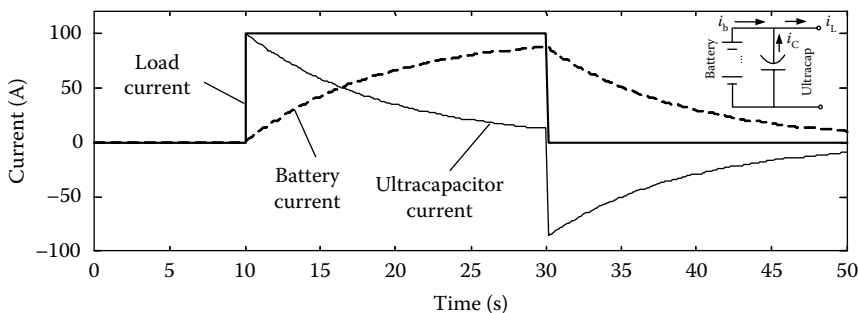
$$W_b = \frac{P_c E_{tot} - P_{tot} E_c}{P_c E_b - P_b E_c}, \tag{16.34}$$

$$W_c = \frac{P_{tot} E_b - P_b E_{tot}}{P_c E_b - P_b E_c}. \tag{16.35}$$

Figure 16.18 shows the weights of batteries, ultracapacitors, and the hybrid energy storage that is capable of supplying 675 kW of total power. It can be

FIGURE 16.18 Battery weight, ultracapacitor weight, and total weight of the hybrid energy storage versus total energy.

FIGURE 16.19   Current profiles of the battery/ultracapacitor energy storage.

seen that when the total energy requirement is less than 67.5 kWh, the hybrid energy storage has less weight than the battery-alone energy storage. When the total energy requirement is greater than 67.5 kWh, battery alone should be used.

Other advantages of hybrid energy storage include leveling of the battery peak current, as shown in Figure 16.19. This will simplify thermal management of the batteries, extend the battery life cycle, and offer fast power response due to the very low resistance in the ultracapacitors. Other advanced configurations of hybrid energy storage may be used for better performance (refer to Chapter 12 for more details).

References

1. J. W. Wong, *Theory of Ground Vehicle*, John Wiley & Sons, New York, 1978.
2. M. G. Bekker, *Theory of Land Locomotion*, University of Michigan Press, Ann Arbor, 1956.
3. M. G. Bekker, *Off-the-Road Locomotion*, University of Michigan Press, Ann Arbor, 1960.
4. M. G Bekker, *Introduction of Terrain-Vehicle Systems*, University of Michigan Press, Ann Arbor, 1969.
5. Y. Gao and M. Ehsani, "Parametric design of the traction motor and energy storage for series hybrid off-road and military vehicles," *IEEE Transactions on Power Electronics*, 21 (3), 749–755, May 2006.
6. Y. Gao and M. Ehsani, "Investigation of battery technologies for the army's hybrid vehicle application," *Vehicular Technology Conference, 2002. Proceedings, VTC 2002-Fall, 2002 IEEE 56th*, Vol. 3, pp. 1505–1509, September 24–28, 2002.
7. M. Ehsani, K. Rahman, and A. Toliyat, "Propulsion system design of electric and hybrid vehicles," *IEEE Transactions on Industrial Electronics*, 44 (1), 19–27, February 1997.
8. A. Boglietti, P. Ferraris, and M. Lazzari, "A new design criteria for spindle induction motors controlled by field orientated technique," *Electric Machine and Power Systems*, 21, 171–182, 1993.

9. T. Kume, T. Iwakane, T. Yoshida, and I. Nagai, "A wide constant power range vector-controlled AC motor drive using winding changeover technique," *IEEE Transactions on Industry Applications*, 27 (5), 934–939, September/October 1991.

10. M. Osama and T. A. Lipo, "A new inverter control scheme for induction motor drives requiring speed range," *Proceedings of the IEEE-IAS Annual Meeting*, Orland, FL, pp. 350–355, 1995.

11. R. J. Kerkman, T. M. Rowan, and D. Leggate, "Indirect field-oriented control of an induction motor in the field weakened region," *IEEE Transactions on Industry Applications*, 28 (4), 850–857, 1992.

12. K. Rahman, B. Fahimi, G. Suresh, A. Rajarathnam, and M. Ehsani, "Advanced of switched reluctance motor applications to EV and HEV: Design and control issues," *IEEE Transactions on Industry Applications*, 36 (1), 11, January/February 2000.

13. Available at http://www.maxwell.com, Maxwell Technologies.

Appendix

Technical Overview of Toyota Prius

More and more hybrid vehicle products are being introduced to the market. Among them, Toyota Prius was the pioneer and has the largest number of units on the road. To give the reader a case study of a commercially successful hybrid vehicle, the Toyota Prius technology is described in this Appendix. This appendix will review the important technical features of this product, including the architecture, control, and component characteristics. The main resource for this material is autoshop101.com (http://www.autoshop101.com/forms/Hybrid01.pdf). However, the diagrams have been redrawn. We gratefully acknowledge the use of material available in autoshop101.com.

A.1   Vehicle Performance

Prius is a Latin word meaning "to go before." When the Prius was first released, it was selected as the world's best-engineered passenger car for 2002. The car was chosen because it is the first hybrid vehicle that seats four to five people plus their luggage, and is one of the most economical and environmentally friendly vehicles available. Then in 2004, the second-generation Prius won the prestigious Motor Trend Car of the Year award and Best-Engineered Vehicle of 2004.

Both the Toyota Hybrid System (THS) power train in the original Prius and the Toyota Hybrid System II (THSII) power train in the second-generation Prius provide impressive electric power steering (EPS) fuel economy numbers and extremely clean emissions as shown in Table A.1.

A.2   Overview of Prius Hybrid Power Train and Control Systems

The hybrid power train of Toyota Prius uses the series–parallel architecture as discussed in Chapters 5 and 9. Figure A.1 shows an overview of the hybrid

TABLE A.1

EPA Fuel Economy and Emissions

THS (2002–2003 Prius)		THS-II (2004 and Later)	
City	52 mpg	City	60 mpg
Highway	45 mpg	Highway	51 mpg
SULEV		AT-PZEV	
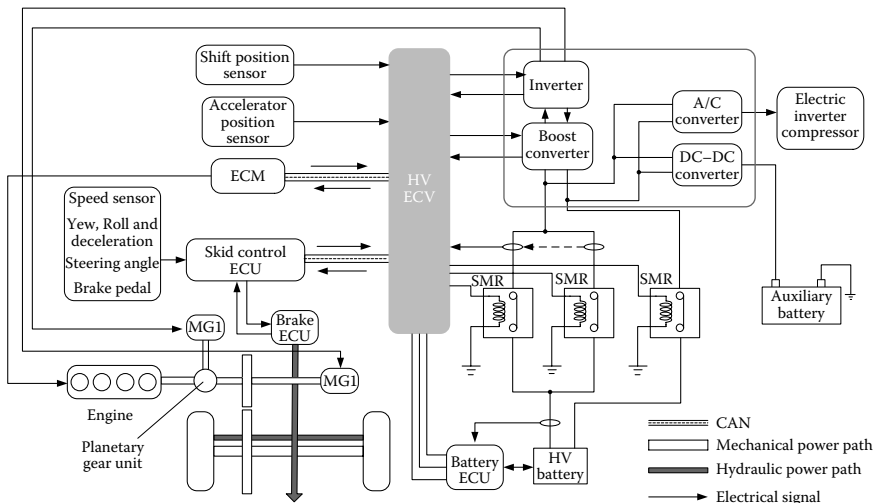
Notes: SULEV standards are about 75% more stringent than ULEV and nearly 90% than LEV for smog forming exhaust gases.

SULEV vehicles will emit less than a single pound of HCs during 100,000 miles of driving (about the same as spilling a half quarter of gasoline).

AT-PZEV vehicles use advanced technology capable of producing zero emission during at least part of the vehicle's driving cycle.

power train and control systems. The hybrid system components include the following:

- Hybrid transaxle, consisting of motor/generator 1 (MG1), motor/generator 2 (MG2), and a planetary gear unit (refer to Figure A.3 for more details)
- 1NZ-FXE engine
- Inverter assembly containing an inverter, a booster converter, a DC–DC converter, and an AC inverter
- Hybrid vehicle electronic control unit (HV ECU), which gathers information from the sensors and sends calculated results to the engine

FIGURE A.1 Overview of Prius power train and control systems.

control module (ECM), inverter assembly, battery ECU, and skid control ECU to control the hybrid system

- Shift position sensor
- Accelerator pedal position sensor, which converts accelerator angle into an electrical signal
- Skid control ECU that controls regenerative braking
- ECM
- High-voltage (HV) battery
- Battery ECU, which monitors the charging condition of the HV battery and controls cooling fan operation
- Service plug, which shuts off the system
- The system main relay (SMR) that connects and disconnects the HV power circuit
- Auxiliary battery, which stores 12 V DC for the vehicle's control systems

A.3 Major Components

A.3.1 Engine

The 1NZ-FXE engine is a 1.5-L inline four-cylinder gasoline engine with variable valve timing intelligence (VVTi) and Electric Throttle Control System with Intelligence (ETCS-i). In the 2004 and later models, there is a special coolant heat storage system that recovers hot coolant from the engine and stores it in an insulated tank where it stays hot for up to three days. Later, an electric pump precirculates the hot coolant through the engine to reduce HC emission normally associated with a cold start.

Table A.2 shows the specifications of the 1NZ-FEX engine.

A.3.2 Hybrid Transaxle

Referring to Figure A.2, the hybrid transaxle contains

- MG1 that generate electric power
- MG2 that drives the vehicle
- A planetary gear unit that provides continuously variable gear ratios and serves as a power splitting device
- A reduction unit consisting of a silent chain, counter gears, and final gears
- A standard two-pinion differential

TABLE A.2

Specifications of 1NZ-FEX Engine

Model	2004 Prius	2003 Prius
Engine type	1NZ-FXE	←
No. of cycles and arrangement	Four-cylinder, in-line	←
Value mechanism	Sixteen-value DOHC, chain drive (with VVTi)	←
Combustion chamber	Pentroof type	←
Manifolds	Cross-flow	←
Fuel system	SFI	←
Displacement (cm^3) (cu. in.)	1497 (91.3)	←
Bore × Stroke (mm) (in.)	75 × 84.7 (2.95 × 3.33)	←
Compression ratio	13.0:1	←
Max. output (SAE-Net)	57 kW at 5000 rpm (76 hp at 5000 rpm)	52 kW at 4500 rpm (70 hp at 4500 rpm)
Max. torque (SAE-Net)	111 Nm at 4200 rpm (82 ft.lbf at 4200 rpm)	←
Value timing		
Intake		
Open	18° to −15° BTDC	18° to −25° BTDC
Close	72° to −105° ABDC	18° to −15° ABDC
Exhaust		
Open	34° BBDC	←
Close	34° ATDC	←
Firing order	1-3-4-2	←
Research octane number	91 or higher	←
Octane rating	87 or higher	←
Engine service mass[a] (kg) (lb)	86.1 (198.8)	86.6 (190.9)
(References)		
Oil grade	API SJ, SL, EC or ILSAC	API SH, SJ, EC or ILSAC
Tail emission regulation	SULEV	←
Evaporative emission regulation	AT-PZEV, ORVR	LEV-II, ORVR
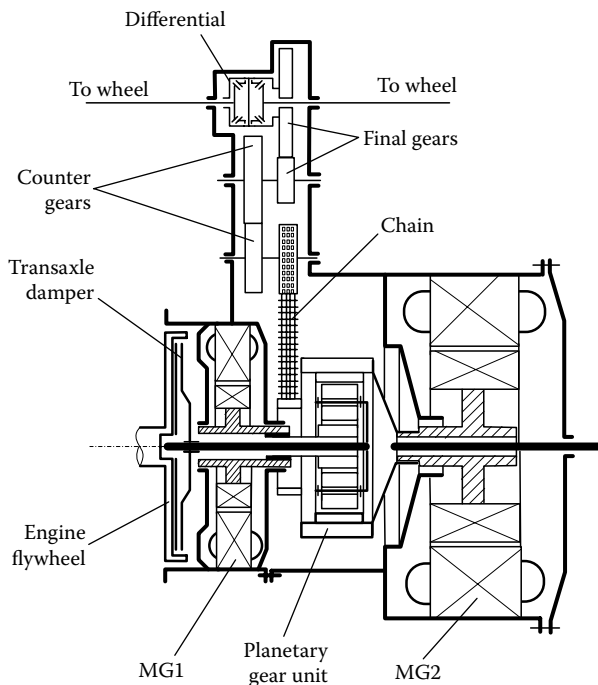
[a]   Weight shows the figure with the oil and the engine coolant fully filled.

Table A.3 shows the main parameters of the hybrid transaxle. Table A.4 shows the specifications of MG1 and MG2.

A.3.3   HV Battery

The HV batteries are Ni–MH. Six 1.2 V cells connected together in series constitute a battery module that has a voltage of 7.2 V.

In the 2001–2003 Prius, 38 battery modules are divided into two holders and connected in series and have a rated voltage of 273.6 V.

FIGURE A.2 Schematic illustration of the hybrid transaxle.

In the 2004 and later models, 28 battery modules are connected for a rated voltage of 201.6 V. The cells are connected in two places to reduce the internal resistance of the battery.

Table A.5 shows the HV battery information.

The battery ECU provides the following functions:

- It estimates the charging/discharging amperage and the outputs charge and discharge requests to the HV ECU so that the SOC can be constantly maintained at a middle level.
- It estimates the amount of heat generated during charging and discharging, and adjusts the cooling fan to maintain HV battery temperature.
- It monitors the temperature and voltage of the battery, and if a malfunction is detected can restrict or stop charging and discharging to protect the HV battery.

The SOC of the battery is controlled by the HV battery ECU. The target SOC is 60%. When the SOC drops below the target range, the battery ECU informs the HV ECU and then signals the engine ECM to increase its power

TABLE A.3

Main Parameters of the Transaxle

	2004 Model	2003 Model
Transaxle type	P112	P111
Planetary gear		
Number of ring gear teeth	78	←
Number of pinion gear teeth	23	←
Number of sun gear teeth	30	←
Differential gear ratio		
Chain		
Number of links	72	74
Drive sprocket	36	39
Drive sprocket	35	36
Counter gear		
Drive gear	30	←
Driven gear	35	←
Final gear		
Drive gear	26	←
Driven gear	75	←
Fluid capacity		
Liters (US qts, lmp qts)	3.8 (4.0, 3.3)	4.6 (4.9, 4.0)
Fluid type	ATF WS or equivalent	ATF type T-IV or equivalent

TABLE A.4

Specification of the MG1 and MG2

MG1 Specification	2004 Model	2003 Model
Item		
Type	Permanent magnet motor	
Function	Generate engine starter	
Maximum voltage (V)	AC 500	AC 273.6
Cooling system	Water-cooled	
MG2 specification	2004 model	2003 model
Item		
Type	Permanent magnet motor	
Function	Generate engine starter	
Maximum voltage(V)	AC 500	AC 273.6
Maximum output kW(PS)/rpm	50 (68)/1200–1540	33 (45)/1040–5600
Maximum torque Nm (kgf.m)/rpm	400 (40.8)/0–1200	350 (35.7)/0–400
Cooling system	Water cooled	

TABLE A.5

HV Battery Information

HV Battery Pack	2004 and Later	2001–2003
Battery pack voltage	206.6 V	273.6 V
Number of Ni–MH battery modules in the pack	28	38
Number of cells	168	228
Ni–MH battery modules voltage	7.2	←

to charge the HV battery. The normal low to high SOC deviation is 20% as shown in Figure A.3.
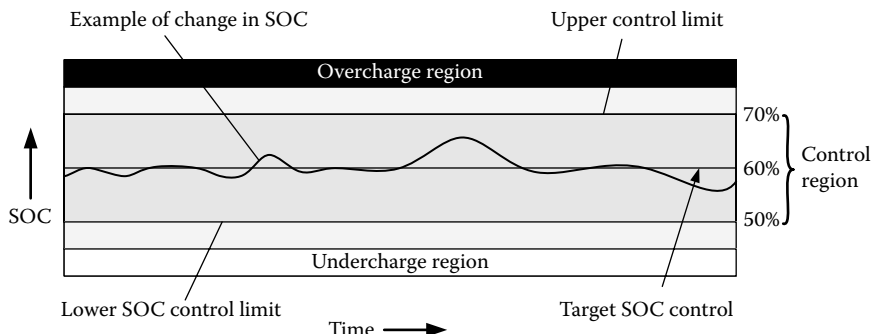
The HV battery is air cooled. The battery ECU detects battery temperature via three temperature sensors in the HV battery and one intake air temperature sensor. Based on their readings, the battery ECU adjusts the duty cycle of the cooling fan to maintain the temperature of the HV battery within the specified range.
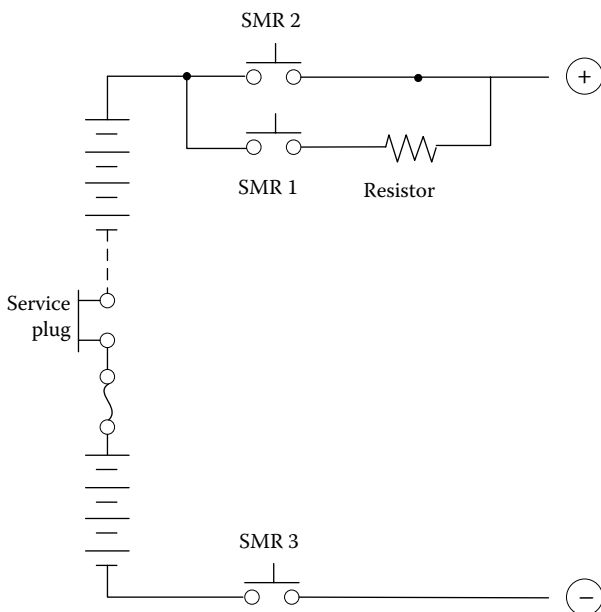
Three SRMs are used to connect or disconnect power to the HV circuit based on commands from the HV ECU. Two SRMs are placed on the positive side and one is placed on the negative side, as shown in Figure A.4.

When the circuit is energized, SMR1 and SMR3 are turned on. The resistor in line with SRM1 protects the circuit from excessive initial current (called inrush current). Next, SRM2 is turned on and SRM1 is turned off.

When de-energized, SMR2 and SMR3 are turned off in that order and the HV ECU verifies that the respective relays have been properly turned off.

A service plug is placed between the two battery holders. When the service plug is removed, the HV circuit is shut off. The service plug assembly also contains a safety interlock reed switch. Lifting the clip on the service plug opens the reed switch, shutting off the SMR. There is also a main fuse for the HV circuit within the service plug assembly.

FIGURE A.3 Battery SOC control region.

FIGURE A.4   SMRs and service plug.

Toyota Prius uses an absorbed glass mat 12-V maintenance-free auxiliary battery. This 12-V battery powers the vehicle's electrical system similar to a conventional vehicle.

A.3.4   Inverter Assembly

The inverter assembly includes an inverter, a booster converter, a DC–DC converter, and an AC converter as shown in Figures A.1 and A.5.
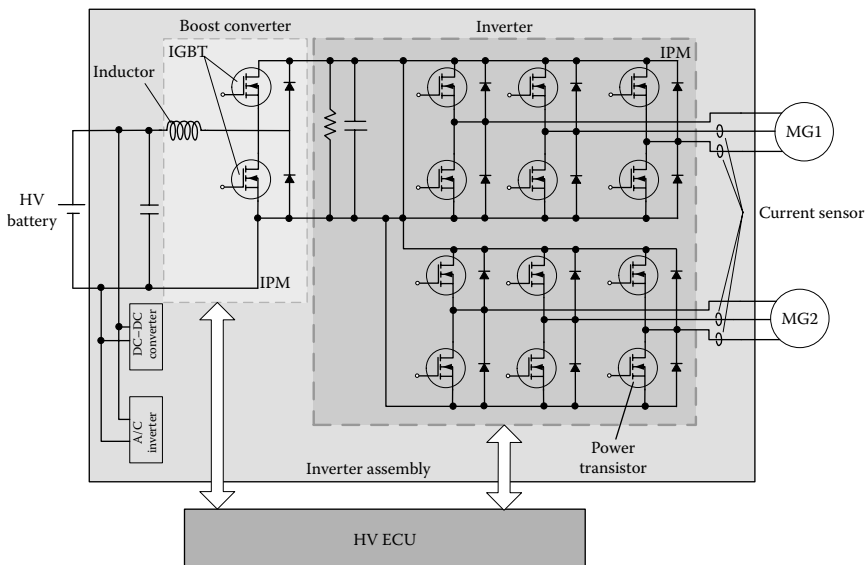
A.3.4.1   Booster Converter (2004 and Later)

The booster converter boosts the nominal voltages of 206.1 V DC that is output by the HV battery to the maximum voltage of 500 V DC. To boost the voltage, the converter uses a boost integrated power module with a built-in insulated-gate bipolar transistor (IGBT) for switching control and a reactor to store the energy, as shown in Figure A.5.

When MG1 or MG2 acts as a generator, the inverter AC, generated by either motor, is converted to DC. Then the booster converter drops the voltage to 201.6 V DC to charge the HV battery.

A.3.4.2   Inverter

The inverter changes the HV DC from the HV battery into three-phase AC for MG1 and MG2 as shown in Figure A.5. The HV ECU controls the activation

FIGURE A.5   Inverter assembly.

of the power transistors. In addition, the inverter transmits information that is needed to control the current, such as the output amperage or voltage, to the HV ECU.

The inverter, MG1, and MG2 are cooled by a dedicated radiator and coolant system that is separated from the engine coolant system. The HV ECU controls the electric water pump for this system.

A.3.4.3   DC–DC Converter
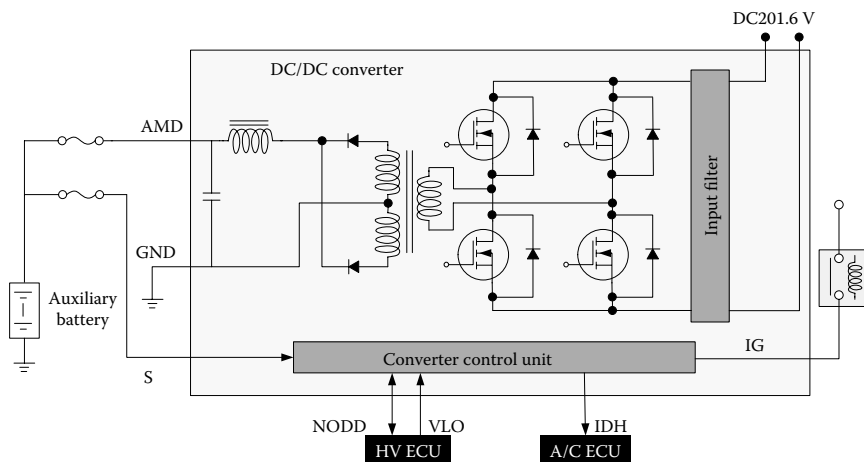
A DC–DC converter is used to transform the HV into 12 V to recharge the 12-V auxiliary battery. The structure of the DC–DC converter is shown in Figure A.6. In the 2001–2003 models, it transforms 273.6 V DC to 12 V DC. In the 2004 and later models, it transforms 201.6 V DC to 12 V DC.

A.3.4.4   AC Inverter

The inverter assembly in the 2004 and later models includes a separate inverter for the air conditioner system that changes the HV battery's nominal voltage of 201.6 V DC into 206.6 V AC to power the air conditioner system's electric motor as shown in Figure A.7.
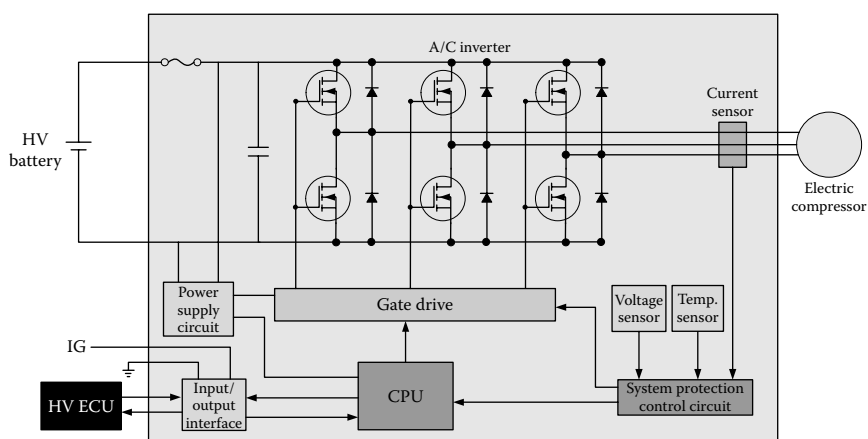
A.3.5   Brake System

The hybrid vehicle brake system includes both standard hydraulic brakes and a regenerative braking system that uses the vehicle's kinetic energy to
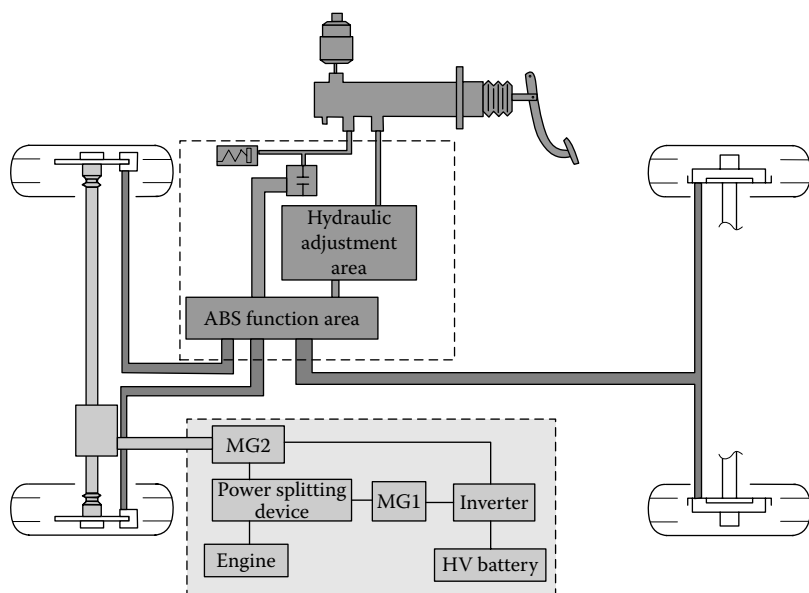
FIGURE A.6   DC–DC converter.

recharge the battery. As soon as the accelerator pedal is released, the HV ECU initiates the regenerative braking. MG2 is turned by the wheels and used as a generator to recharge the battery. During this phase of braking, the hydraulic brakes are not used. When more rapid deceleration is required, the hydraulic brakes are activated to provide additional stopping power. To increase energy efficiency, the system uses the regenerative brakes whenever possible. Selecting "B" on the shift lever will maximize regenerative efficiency and is useful for controlling downhill speeds. The overall structure of the hybrid brake system is shown in Figure A.8.

FIGURE A.7   AC inverter.

FIGURE A.8 The hybrid brake system.
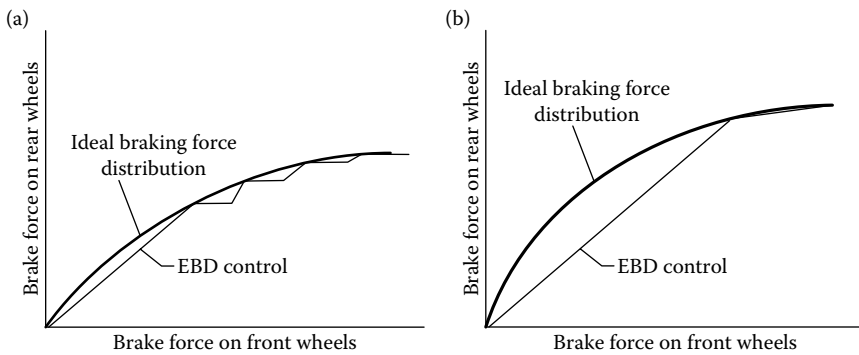
A.3.5.1 Regenerative Brake Cooperative Control

Regenerative brake cooperative control balances the brake force of the regenerative and the hydraulic brakes to minimize the amount of kinetic energy lost to heat and friction. It recovers the energy by converting it into electrical energy.

A.3.5.2 Electronic Brake Distribution Control (2004 and Later Models)

In the 2004 and later models, brake force distribution is performed under electrical control of the skid control ECU. The skid control ECU precisely controls the braking force in accordance with the vehicle's driving conditions.

1. Braking force distribution, front and rear (2004 and later models) Generally, when the brakes are applied the vehicle's weight shifts forward, reducing the load on the rear wheels. When the skid control ECU senses this condition (based on the speed sensor output), it signals the brake actuator to regulate rear braking force so that the vehicle will remain under control during the stop. The amount of brake force applied to the rear wheels varies based on the amount of deceleration. The amount of brake force that is applied to the real wheels also varies based on road conditions. Figure A.9a and b show the braking force on the front and rear wheels without and with load on the rear wheels.

FIGURE A.9 Braking force on the front and rear wheels: (a) without load on the rear wheels and (b) with load in the rear wheels.

2. Brake force distribution, left and right (2004 and later models) When the brakes are applied while the vehicle is cornering, the load applied to the inner wheels decreases whereas the load applied to the outer wheels increases. When the skid control ECU senses this situation (based on speed sensor output), it signals the brake actuator to regulate the brake force between the left and right wheels to prevent a skid.

A.3.5.3 Brake Assist System (2004 and Later Models)
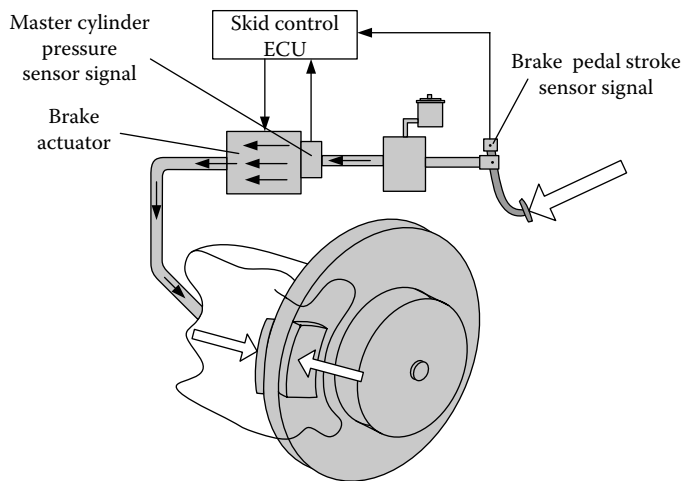
In emergencies, drivers often panic and do not apply sufficiently fast pressure to the brake pedal. So in the 2004 and later models, a brake assist system (as shown in Figure A.10) is used to interpret a quick push of the brake pedal as emergency braking and supplements braking power accordingly.

To determine the need for an emergency stop, the skid control ECU looks at the speed and the amount of brake pedal application based on signals from the master cylinder pressure sensors and the brake pedal stroke sensor. If the skid control ECU determines that the driver is attempting an emergency stop, it signals the brake actuator to increase the hydraulic pressure.

A key feature of the brake assist system is that the timing and the degree of braking assistance are designed to ensure that the driver does not discern anything unusual about the braking operation. As soon as the driver eases up on the brake pedal, the system reduces the amount of assistance it provides.

A.3.6 Electric Power Steering
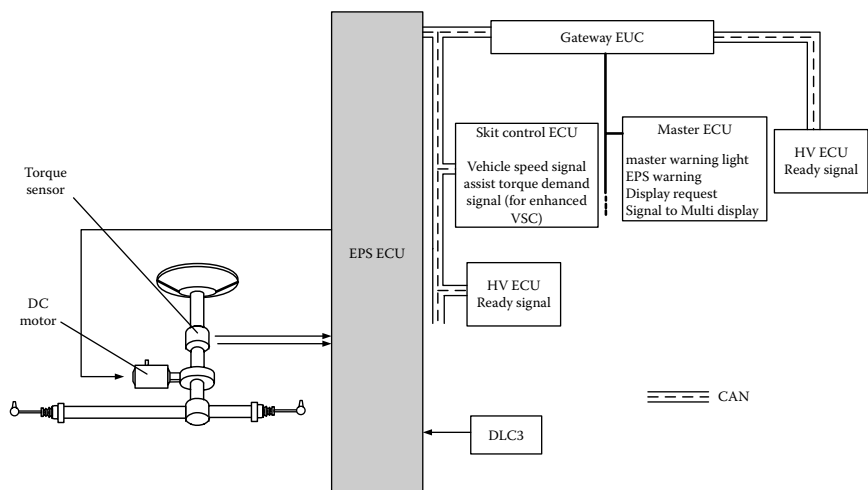
A 12-V motor powers the EPS system so that steering feel is not affected when the engine shuts off. The EPS ECU uses torque sensor output along with information from skid control ECU about vehicle speed and torque assist demand to determine the direction and force of the power assist. It then

FIGURE A.10   Brake assist.

actuates the DC motor accordingly. The structure of the EPS system is shown in Figure A.11.

The EPS ECU uses signals from the torque sensor to interpret the driver's steering intention. It combines this information with data from other sensors regarding the current vehicle condition to determine the amount of steering assist that will be required. It can then control the current to the DC motor that provides steering assist.

FIGURE A.11   The EPS system.

When the steering wheel is turned, torque is transmitted to the pinion causing the input shaft to rotate. The torsion bar that links the input shaft and the pinion twists until the torque and reaction force equalize. The torque sensor detects the twist of the torsion bar and generates an electrical signal that is proportional to the amount of torque applied to the torsion bar. The EPS ECU uses that signal to calculate the amount of power assist that the DC motor should provide.

A.3.7   Enhanced Vehicle Stability Control (VSC) System (2004 and Later Prius)

The enhanced vehicle stability control (VSC) system in the 2004 and later models helps maintain stability when the vehicle's tires exceed their lateral grip. The system helps control the vehicle by adjusting the motive force and the brakes at each wheel when

- the front wheels lose traction but the rear wheels do not (front wheel skid tendency known as "understeer,"
- the rear wheels lose traction but the front wheels do not (rear wheel skid tendency, or "oversteer").

When the skid control ECU determines that the vehicle is in understeer or oversteer condition, it decreases engine output and applies the brakes to the appropriate wheels individually to control the vehicle.

- When the skid control ECU senses understeer, it brakes the front and rear inside wheel. This slows the vehicle, shifts the load to the outside front wheel, and limits the front wheel skid.
- When the skid control ECU senses oversteer condition, it brakes the front and rear outside wheel. This restrains the skid and moves the vehicle back toward its intended path.
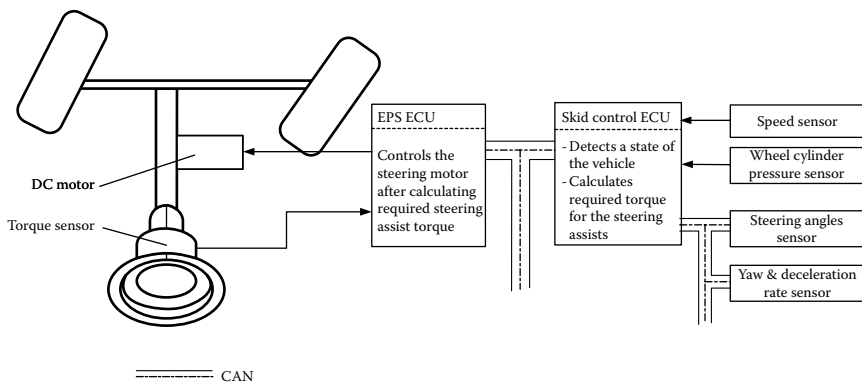
Enhanced VSC also provides the appropriate amount of steering assist based on driving conditions by coordinating EPC and VSC control as shown in Figure A.12.

A.4   Hybrid System Control Modes

Toyota Prius hybrid system uses series–parallel hybrid configuration that has many operation modes, as was discussed in previous chapters. Prius uses the following control strategies:

1. When starting off and traveling at low speed, MG2 provides the primary motive force. The engine may start immediately if the HV battery

FIGURE A.12   Cooperative control with EPS.

SOC is low. As the speed increases above 24 km/h to 32 km/h (15–20 mph), the engine will start.
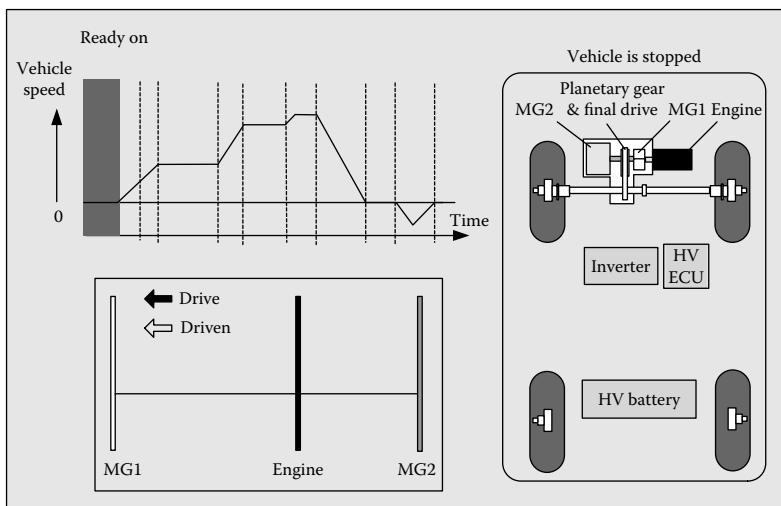
2. When driving under normal conditions, the engine's power is divided into two paths: a portion drives the wheels and a portion drives MG1 to produce electricity. The HV ECU controls the energy distribution ratio for maximum efficiency.

3. During full acceleration, the power generated by the engine and MG1 is supplemented by power from the HV battery. Engine torque combined with MG2 torque delivers the power required to accelerate the vehicle.

4. During deceleration or braking, the wheels drive MG2. MG2 acts as a generator for regenerative energy recovery. The recovered energy from braking is stored in the HV battery pack.

The operation modes of the engine, MG1, and MG2 are depicted in response to different driving conditions as follows.

Stopped: If HV battery is fully charged and the vehicle is not moving, the engine may stop. The engine will start up automatically if the HV battery needs charging. Also, if MAX AC is selected in the 2001–2003 models, the engine will run continuously due to the engine-driven compressor. The 2004 and later models use an electrically driven compressor. Figure A.13 shows the depicted operation modes of the engine, MG1, and MG2.
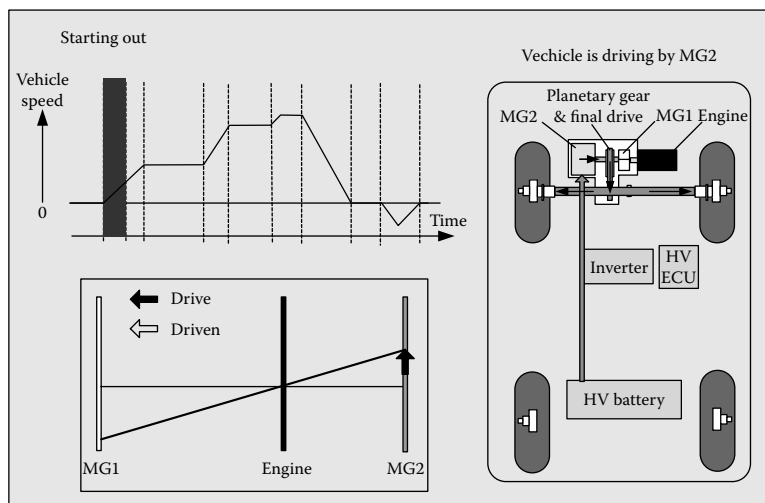
Starting out: When starting out under light load and light throttle, only MG2 turns to provide power. The engine does not run and the vehicle runs on electric power only. MG1 rotates backwards and just idles. It does not generate electricity, as illustrated in Figure A.14.

Engine starting: As the speed increases above 24 km/h to 32 km/h (15–20 mph), the engine starts. The engine is started by MG1. The operations of the engine, MG1, and MG2 are shown in Figure A.15.
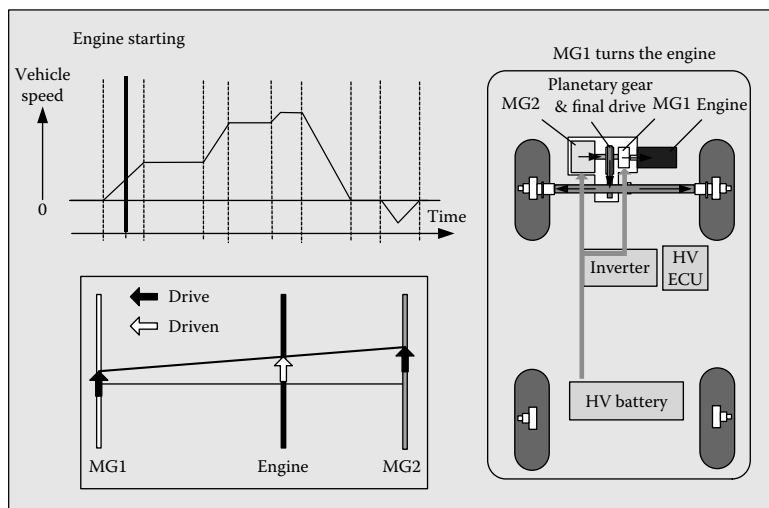
FIGURE A.13 Operation with stopped vehicle.

Light acceleration with engine: In this mode, the engine delivers its power to the driven wheels and MG1, which is generating. MG2 may assist the engine for propulsion if required, depending on the engine power and the requested driving power. In this mode, the energy generated by MG1 may be equal to the energy delivered to MG2. The drive train operates as an EVT. The operations of the engine, MG1, and MG2 are shown in Figure A.16.
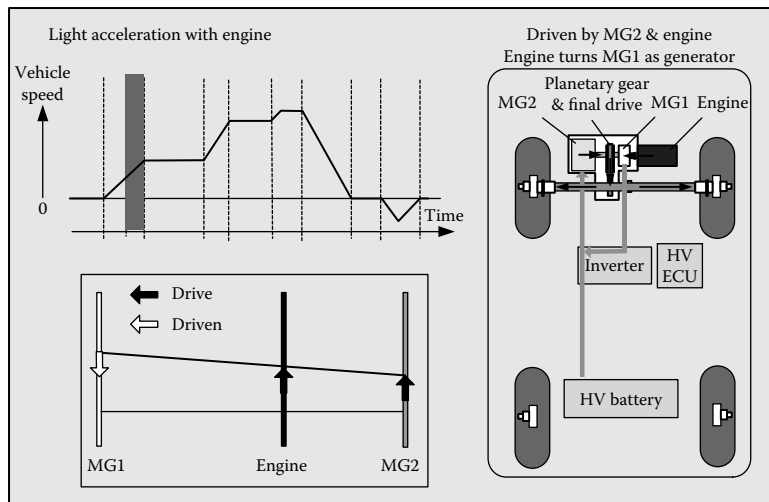
FIGURE A.14 Operation mode of starting out.
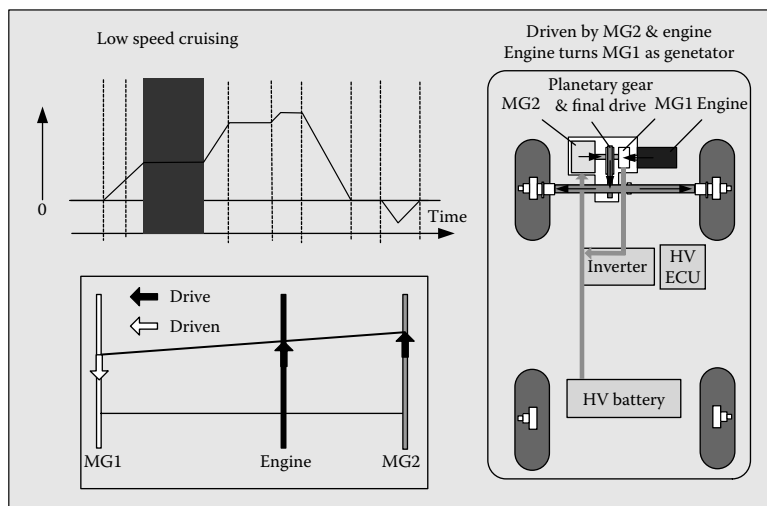
FIGURE A.15 Operation mode of engine starting.

Low-speed cruising: This mode is similar to the mode of light acceleration with the engine as shown in Figure A.17.

Full acceleration: In this mode, the engine delivers its power to the wheels and to MG1, which is in the generating mode. MG2 adds its power to the engine power and is delivered to the wheels as shown in Figure A.18. The power drawn by MG2 from HV battery power is greater than the power

FIGURE A.16 Operation mode of light acceleration with engine.
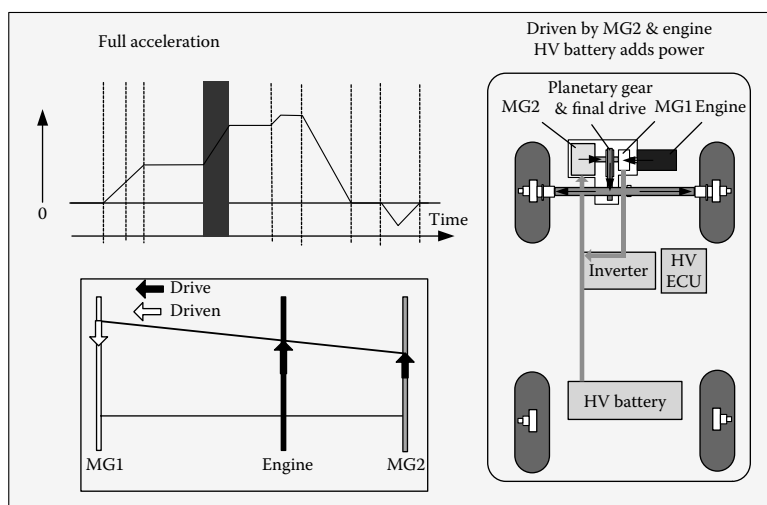
FIGURE A.17   Operation mode of low-speed cruising.
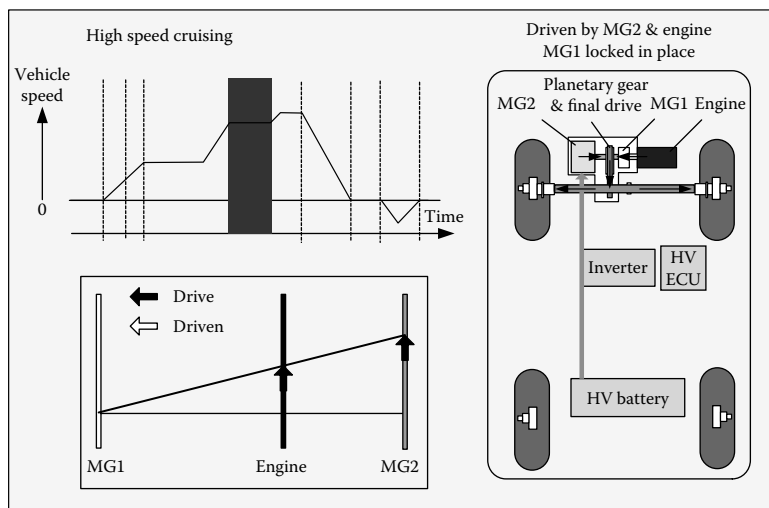
generated by MG1. Thus, the HV battery pack contributes energy to the drive train and its SOC drops.

High-speed cruising: In this mode, the shaft of MG1 is fixed to the vehicle stationary frame and the drive train is operated in pure torque-coupling mode. Both the engine and MG2 propel the vehicle as shown in Figure A.19.

Driving with maximum speed: In this mode, both MG1 and MG2 receive power from the HV battery pack and deliver their mechanical power to the
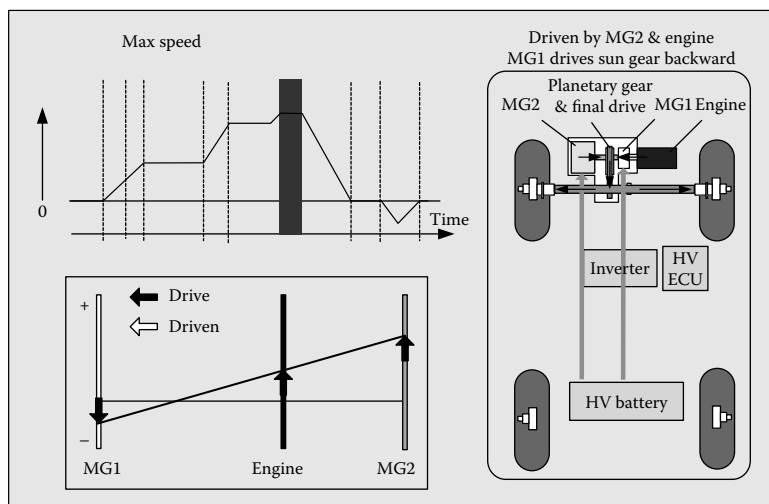
FIGURE A.18   Operation mode in full acceleration.
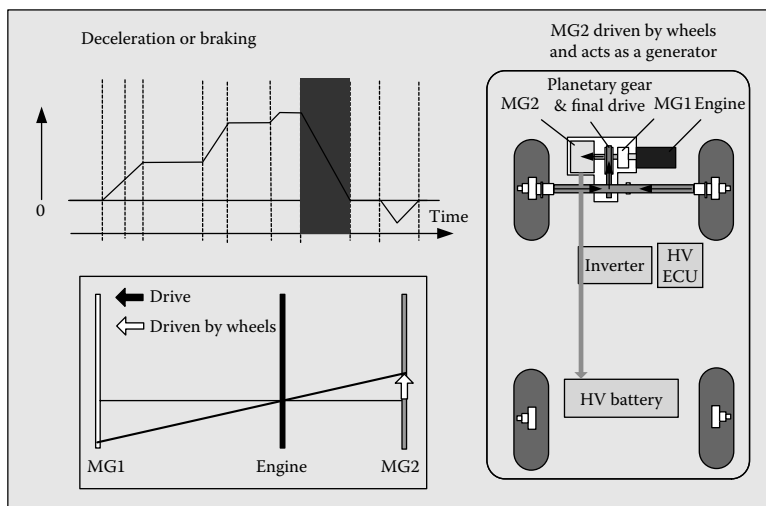
FIGURE A.19 Operation mode at high-speed cruising.

drive train. In this case, MG1 turns in the opposite direction as shown in Figure A.20.

Deceleration or braking: When the vehicle is decelerating or braking, the engine is shut down. MG2 becomes a generator and is turned by the drive wheels and generates electricity to recharge the HV battery pack. The operation is shown in Figure A.21.
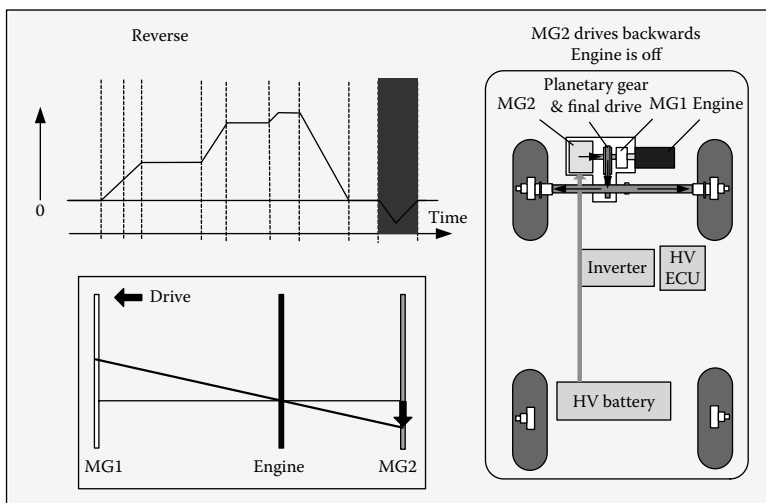
FIGURE A.20 Operation mode in driving with maximum speed.

FIGURE A.21   Operation mode in deceleration or braking.

Reverse: When the vehicle moves in reverse direction, MG2 turns in the reverse direction as an electric motor. The engine is shut down. MG1 turns in the forward direction and just idles as shown in Figure A.22.

FIGURE A.22   Reverse operation.

Index

Modern Electric, Hybrid Electric, and Fuel Cell Vehicles
Fundamentals, Theory, and Design
SECOND EDITION

Air pollution, global warming, and the steady decrease in petroleum resources continue to stimulate interest in the development of safe, clean, and highly efficient transportation. Building on the foundation of the bestselling first edition, **Modern Electric, Hybrid Electric, and Fuel Cell Vehicles: Fundamentals, Theory, and Design, Second Edition** updates and expands its detailed coverage of the vehicle technologies that offer the most promising solutions to these issues affecting the automotive industry.

Proven as a useful in-depth resource and comprehensive reference for modern automotive systems engineers, students, and researchers, this book speaks from the perspective of the overall drive train system and not just its individual components.

New to the second edition

- A case study appendix that breaks down the Toyota Prius hybrid system
- Corrections and updates of the material in the first edition
- Three new chapters on drive train design methodology and control principles
- A completely rewritten chapter on *Fundamentals of Regenerative Braking*

The first edition of this book gave practicing engineers and students a systematic reference to fully understand the essentials of this new technology. This edition introduces newer topics and offers deeper treatments than those included in the first. Revised many times over many years, it will greatly aid engineers, students, researchers, and other professionals who are working in automotive-related industries, as well as those in government and academia.